SPOTLIGHT ON CHINA - MATERIALS SCIENCE

EDITED BY: Limin Wang, Xiaotian Wang, Yunchao Tang, Weiliang Wang, Yongtao Sun, Dake Xu, Wenbo Wang, Dongxiang Li, Xufeng Dong, Qihui Wu and Lin Xu

PUBLISHED IN: Frontiers in Materials

frontiers Research Topics

ISSN 1664-8714
ISBN 978-2-83250-576-2
DOI 10.3389/978-2-83250-576-2

About Frontiers

Frontiers is more than just an open-access publisher of scholarly articles: it is a pioneering approach to the world of academia, radically improving the way scholarly research is managed. The grand vision of Frontiers is a world where all people have an equal opportunity to seek, share and generate knowledge. Frontiers provides immediate and permanent online open access to all its publications, but this alone is not enough to realize our grand goals.

Frontiers Journal Series

The Frontiers Journal Series is a multi-tier and interdisciplinary set of open-access, online journals, promising a paradigm shift from the current review, selection and dissemination processes in academic publishing. All Frontiers journals are driven by researchers for researchers; therefore, they constitute a service to the scholarly community. At the same time, the Frontiers Journal Series operates on a revolutionary invention, the tiered publishing system, initially addressing specific communities of scholars, and gradually climbing up to broader public understanding, thus serving the interests of the lay society, too.

Dedication to Quality

Each Frontiers article is a landmark of the highest quality, thanks to genuinely collaborative interactions between authors and review editors, who include some of the world's best academicians. Research must be certified by peers before entering a stream of knowledge that may eventually reach the public - and shape society; therefore, Frontiers only applies the most rigorous and unbiased reviews.
Frontiers revolutionizes research publishing by freely delivering the most outstanding research, evaluated with no bias from both the academic and social point of view. By applying the most advanced information technologies, Frontiers is catapulting scholarly publishing into a new generation.

What are Frontiers Research Topics?

Frontiers Research Topics are very popular trademarks of the Frontiers Journals Series: they are collections of at least ten articles, all centered on a particular subject. With their unique mix of varied contributions from Original Research to Review Articles, Frontiers Research Topics unify the most influential researchers, the latest key findings and historical advances in a hot research area! Find out more on how to host your own Frontiers Research Topic or contribute to one as an author by contacting the Frontiers Editorial Office: frontiersin.org/about/contact

SPOTLIGHT ON CHINA - MATERIALS SCIENCE

Topic Editors:
Limin Wang, Yanshan University, China
Xiaotian Wang, Southwest University, China
Yunchao Tang, Zhongkai University of Agriculture and Engineering, China
Weiliang Wang, Sun Yat-sen University, China
Yongtao Sun, Tianjin University, China
Dake Xu, Northeastern University, China
Wenbo Wang, Inner Mongolia University, China
Dongxiang Li, Qingdao University of Science and Technology, China
Xufeng Dong, Dalian University of Technology, China
Qihui Wu, Jimei University, China
Lin Xu, Jilin University, China

Citation: Wang, L., Wang, X., Tang, Y., Wang, W., Sun, Y., Xu, D., Wang, W., Li, D., Dong, X., Wu, Q., Xu, L., eds. (2022). Spotlight on China - Materials Science. Lausanne: Frontiers Media SA. doi: 10.3389/978-2-83250-576-2

Table of Contents

frontiers in Materials

ORIGINAL RESEARCH
published: 10 June 2021
doi: 10.3389/fmats.2021.705453

Rainfall Erosion Damage of Residual Soil Slope in Intermittently Frozen Area Based on Discrete Element Method

Yunbin Ke[1], *Yanyu Chen*[2], *Zhenliang Jiang*[2,3]* *and Yonghui Qiu*[4]

[1]School of Civil Engineering and Architecture, Taizhou University, Taizhou, China, [2]Department of Civil and Environmental Engineering, The Hong Kong University of Science and Technology, Hong Kong, China, [3]College of Civil Engineering, Fuzhou University, Fuzhou, China, [4]Zijin Mining Group Co., Ltd., Longyan, China

This study developed a discrete element simulation model based on the 2D particle flow code (PFC^{2D}), of which the mesoscopic parameters were calibrated by the indoor experiments, to investigate the rainfall erosion damage of residual soil slope in the intermittently frozen area. It is to be noted that the runoff scouring action was simulated according to the equivalent rainfall method, the soil particles on the slope were given initial velocity, and the water absorption was considered by increasing the unit weight. The results indicated that the scouring action only caused superficial erosion with the main damage region at the foot, regardless of the FT effect. A splitting phenomenon was observed in the lower part of the steeper slope under the FT effect. Moreover, regardless of the FT effect, the gentler slope tended to incur spalling rather than a splitting phenomenon, where the soil particles slid along the structural plane with strong anti-scouring ability. Besides, the gentler slope maintained higher stability and shorter scouring time. Finally, the scouring velocity increased the erosion damage to a large extent.

Keywords: residual soil slope, erosion, rainfall scouring, PFC 2D, freeze–thaw, intermittently frozen

OPEN ACCESS

Edited by:
Yunchao Tang,
Zhongkai University of Agriculture and Engineering, China

Reviewed by:
Yun Que,
Fuzhou University, China
Peiyuan Lin,
Sun Yat-Sen University, China

***Correspondence:**
Zhenliang Jiang
zhenliang.jiang@ryerson.ca

Specialty section:
This article was submitted to Mechanics of Materials, a section of the journal Frontiers in Materials

Received: *05 May 2021*
Accepted: *17 May 2021*
Published: *10 June 2021*

Citation:
Ke Y, Chen Y, Jiang Z and Qiu Y (2021) Rainfall Erosion Damage of Residual Soil Slope in Intermittently Frozen Area Based on Discrete Element Method. Front. Mater. 8:705453. doi: 10.3389/fmats.2021.705453

INTRODUCTION

The intermittently frozen area was defined as an area where the near-surface soil is frozen annually from one to fifteen days per year (Willmott and Matsuura, 2001; Zhang et al., 2003; Chen, et al., 2020). Intermittently frozen areas are widely distributed in the world, accounting for 6.6% of the exposed lands in the coldest month of the year in the Northern Hemisphere (Baranov, 1964; Zhang et al., 2003; Lu et al., 2017). Taking China, for example, it is mostly distributed in the south of the Yangtze River and the north of the Pearl River Basin, covering an area of about 1.9 million square kilometers and accounting for about 20% of the total national area (Que et al., 2017; Que et al., 2021).

Compared with the permafrost and seasonal frozen soils, the intermittently frozen soil experiences high-frequency freeze–thaw cycles, resulting from the frequently fluctuated ambient temperature around the freezing point (Woo and Winter, 1993; Chen and Li, 2008; Thomas et al., 2009). It should be noted that Que et al. (2017) observed 16 freeze–thaw times a day in December 2013 to mid-February 2014 in Wuyi Mountain, Fujian Province, China. Usually, it will experience superficial spalling occurring on the soil slope, especially under the influence of continuous rainfall or rainstorm. That might develop the instability of soil further, causing potential safety problems and economic loss to the vehicles and pedestrians along with the projects (Que et al., 2017; Li, 2013). Therefore, there is a great need to study further the strength reduction of soil slopes under the short-term freeze–thaw cycle and the mechanism of superficial spalling induced by rainfall erosion.

Recently, the discrete element technique, like particle flow code (PFC) (Zhang et al., 2013; Liang et al., 2017; Wang et al., 2020; Wang et al., 2021), has been found to be suitable for not only dealing with large deformation discontinuity problems but also illustrating the force and motion pattern from the mesoscopic scale (Li et al., 2013; Saman et al., 2014; Shi and Xu, 2015; Xu, 2017; Zhang, 2017; Wang et al., 2021). Hence, it has been currently used in geotechnical engineering, including the superficial freeze–thaw spalling of slope (Evans et al., 2009; Park and Song, 2009; Zhu et al., 2021).

Several studies have been carried out on the erosion of the slope surface caused by rainfall through PFC. Tsuji et al. (1993) introduced computational fluid dynamics to the discrete element method and verified the reliability of the fluid–solid coupling analysis method in simulating two-phase flows using discrete elements. Zeghal and Shamy (2005) implemented the fluid–solid coupling analysis method to analyze saturated sand, which simplified the N-S equation and by which the seepage problem of the soil slope was investigated. Based on this, Bai et al. (2012) determined the permeability coefficient for the PFC method. Xiong et al. (2013) performed a three-dimensional simulation of the rainfall slope collapse by fluid–solid coupling analysis, where the rainfall was simulated by applying pressure on the boundary. The results manifested that it was feasible to study the collapse formation mechanism *via* PFC using the fluid–solid coupling methods. Song (2013) and Wu et al. (2014) analyzed the evolution process of slope erosion and the distribution of slope erodibility by using the aforementioned method. Hu (2014) performed the rainfall equivalent *via* increasing the gravity and reducing shear strength, but the strength-reduced parameters were not calibrated. Ma (2012) and Wu et al. (2013) carried out an erosion failure simulation of steep slopes *via* a two-dimensional PFC (PFC^{2D}) model, where the effect of runoff scouring was simulated by the particles' movement on the slope surface.

Overall, it can be found that rainfall erosion can be simulated through the fluid–solid coupling analysis method *via* PFC. However, most studies were limited to the saturated soil. There is no research related to the rainfall equivalent method. Besides, the parameter effects are still unclear either, such as slope gradient, freeze–thaw, and scouring velocity.

To fulfill this gap, this paper carries out an in-depth study about the effects of rainfall erosion damage of residual soil slope in the intermittently frozen area. Specifically, this paper addresses three questions: How to build a slope scouring model? What are the basic effects of scouring on the slope? How the slope gradient, freeze–thaw action, and scouring velocity affect the erosion damage? The objective of the present study is threefold: 1) to build a PFC^{2D} scouring model, where the mesoscopic parameters are calibrated by indoor experiments, 2) to investigate the basic characteristics of slope under the runoff erosion, and 3) to perform parameter effects on the rainfall erosion, including slope gradient, freeze–thaw action, and scouring velocity.

METHODOLOGY

Experimental Design

As shown in **Figure 1**, in order to investigate the effects of freeze–thaw on erosion damage of the residual soil slope induced by rainfall, the indoor test and PFC^{2D} simulation are performed in depth. First, the freeze–thaw experiments are conducted to verify the feasibility of the PFC simulating models by comparing the stress–strain curves. At the same time, the details of the two aforementioned experiments will be fully presented, especially the numeric scouring model. Then, based on the PFC^{2D} models of which the mesoscopic parameters were calibrated, both the basic behaviors and the parameter effects of scouring action on the slope are going to be thoroughly analyzed, including the slope morphology, contact, and denudation amount. Finally, a discussion will be made on the mechanism of freeze–thaw on erosion damage of the residual soil slope induced by rainfall.

Indoor Experiments

Soil Sample

The soil samples were taken from the site where the spalling disease occurred. The basic physical properties of the soil samples are natural moisture content (w), density (ρ), dry density (ρ_d), specific gravity (G_s), void ratio (e), porosity (n), liquid limit (w_L), plastic limit (w_p), liquidity index (I_L), and plasticity index (I_p), whose values are 19.6%, 1.78 g/cm^3, 1.49 g/cm^3, 2.655, 0.76, 43.22%, 33.4%, 19.6%, 0.01, and 13.79, respectively. The mass percentage of each soil grain size (gradation) >5 mm, 2–5 mm, 1–2 mm, 0.5–1 mm, 0.25–0.5 mm, 0.075–0.25 mm, 0.03–0.075 mm, 0.01–0.03 mm, and <0.01 mm is 3.94, 7.98, 3.92, 12.71, 11.14, 13.35, 20.51, 19.42, and 7.03, respectively.

Experimental Scheme

The water content of samples is set at 21.5%, and the dry density is 1.49 g/cm^3. The testing temperature range is −7–15°C. The FT cycles were set under 0, 2, 4, 6, and 8 times. The water supplement was conducted at the sealed condition. It is to be noted that the triaxial shear test was performed under the consolidated drainage condition. The temperature range was determined according to the field detection and the historical record.

Specimen Preparation and Freeze–Thaw Triaxial Shear Test

Specimen Preparation

The specimens were prepared according to JTG E40-2007 (Research Institute of Highway Science, 2010). It is noted that the soil was screened by a 2 mm sieve in order to maintain the homogeneity and the similarity of the initial soil structure. The mass percentage of each soil grain size (gradation) 1–2 mm, 0.5–1 mm, 0.25–0.5 mm, 0.075–0.25 mm, 0.03–0.075 mm, 0.075–0.03 mm, and <0.075 mm is 4.45, 14.43, 12.66, 15.17, and 53.29, respectively.

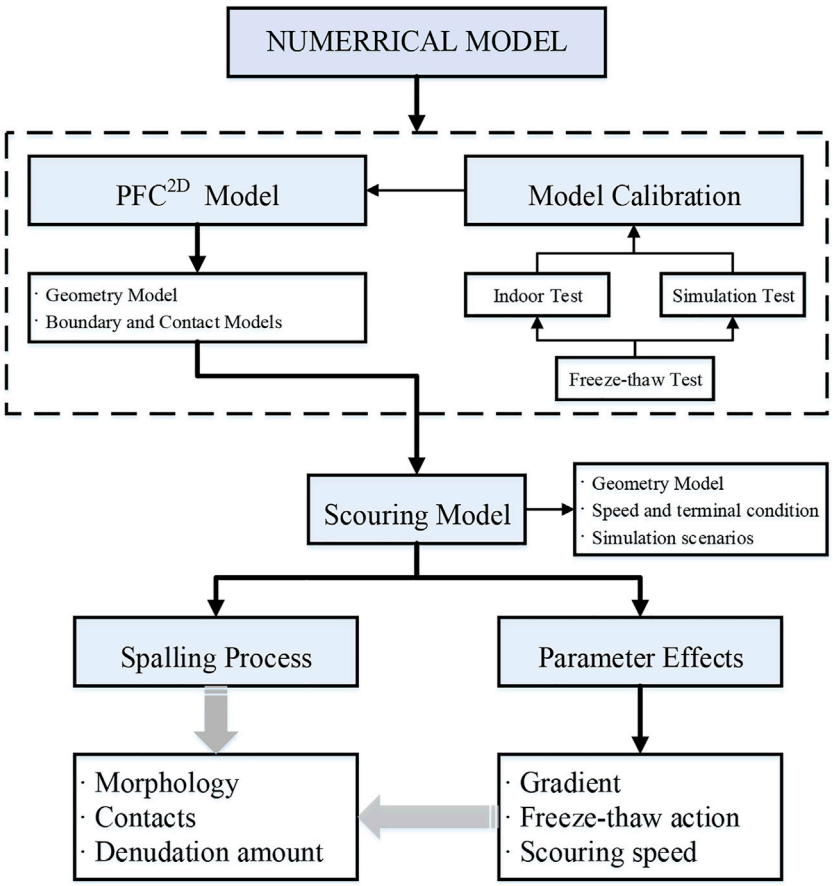

FIGURE 1 | Experimental design.

Freeze–Thaw Triaxial Shear Test

The equipment utilized in this research is TCK-1, which was produced by Nanjing Soil Instrument Co., Ltd. To avoid misoperation, five specimens were prepared for each group. Three of them were used for shear tests under different confining pressures (100, 150, 200 kPa), and the other two were set as a standby.

Mesoscopic Parameter Calibration

Model Generation and Initial Setting of Calibration Modes

Porosity Conversion

In PFC^{2D} simulation, the porosity can be converted from the practical soil model by an empirical equation (He et al., 2014). Wang believed that the parabolic modes seemed to be more appropriate after performing the comparison between several methods (Wang et al., 2014). By using the same approach in this research, shown in the following equation, the converted porosity is 18.65%:

$$p2D = 0.42 \times p3D^2 + 0.25 \times p3D, \quad (1)$$

where p2D and p3D are the porosity in 2D and 3D, respectively.

Geometry

The dimension of the specimen is 32 mm × 15.64 mm, the soil particle radius is set between 0.65 and 1.3 mm, and the density is 2,655 kg/m^3. The model consists of two pairs of rigid walls: the vertical panel that is applying the load in the vertical direction and the servo panel that is controlling pressure on the lateral side of the specimen.

Contact Models and Boundary Conditions

Contact models. Two models were utilized to consider the bonding and debonding conditions of the contacts between particles. For contacts that have not yet broken, it is widely accepted that the contact model is much more appropriate in simulating the clay material in this case. However, the opinions about which model is more appropriate are diverse, although the accuracy of the stress and strain curves from the default model is extensively acknowledged in the debonding case.

In most studies, the linear contact model is selected as the default model. However, it was found that increasing the inter-particle friction cannot change the peak strength of the specimen, which was similar to that in the studies performed by Skinner (1969) and Oda et al. (1982). However, Suiker and Fleck (2004)

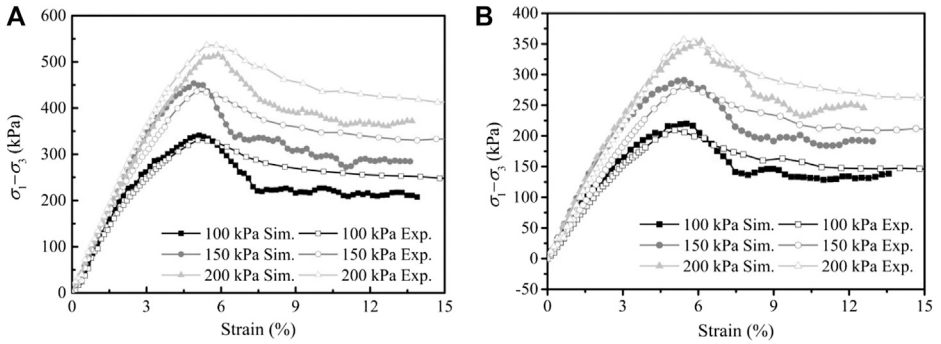

FIGURE 2 | Stress–strain curves of the simulated and experimental results. **(A)** Before FT. **(B)** After FT. Note: "After FT" means the soil experienced eight times of freeze–thaw action, of which the damage was the most serious (Fu, 2017).

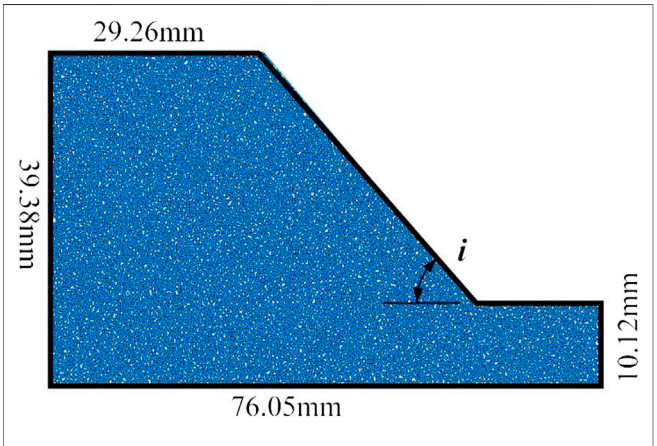

FIGURE 3 | Slope model (i = 45°).

and Thornton (2000) believed that it could be explained by particle rolling, which is also supported in this paper. It has been acknowledged that the rotational velocity will be enormous while the material reaches its yield point. This shows a rolling effect on the surface, which undoubtedly reduces the friction coefficient. Thus, the established rotation resistance linear model (rrlinear) was selected as the default model (Iwashita and Oda, 1998; Iwashita and Oda, 2000; Jiang et al., 2005; Jiang et al., 2009; Liu et al., 2013).

Boundary. The flexible boundary condition was achieved by setting the lateral wall stiffness 1/10 of the particle stiffness, while the vertical wall stiffness was the same as that of the particles.

Calibration of the Stress and Strain Curves

The stress–strain curves of the simulated and experimental results are shown in **Figures 2A,B**. It can be found that the correlation between these two curves is very high before the peak shear strength. Although both curves tend to decrease first and then remain unchanged after the peak value, the simulated curves seem to decrease rapidly at the initial stage after the peak strength (generally around 4% axial strain). And then, they remain basically unchanged, and the final residual strength is also lower than that in the testing curves. This is mainly due to the complicated nature of the size, shape, distribution, and stress characteristics of the practical soil particles, and the residual strength is provided by friction and structural occlusion force. Additionally, the particles are two-dimensional discs in the 2D simulation, where the point-type inter-particle contacts tended to slip under high force, which resulted in the attenuation of the residual strength.

Numerical Model

Sample Generation

As shown in **Figure 3**, two slope models with a gradient of 45° and 60° were established. According to the study performed by Ni et al. (2000), changing the particle size appropriately has little effect on the simulation results. Besides, by integrating the operation ability of the computer and the running timing of the model, the radius of the soil particles was determined in a range from 0.1625 to 0.325 mm. Finally, 9,124 and 8,057 particle elements were generated in the 60° and 45° slopes, respectively.

Scouring Simulation

Generally, the simulation of equivalent rainfall is realized by changing the macroscopic and mesoscopic parameters of soil. For example, Hu et al. increased gravity and reduced the shear strength of soil to consider the effect of rainfall. Wu et al. carried out simulations by altering the mesoscopic soil parameters to simulate the moisture content change during the process of rainfall. Moreover, Ma et al. performed the slope erosion failure induced by rainfall by giving velocity to the particles on the slope surface *via* PFC^{2D}.

Therefore, in order to simulate the equivalent rainfall scouring process more precisely, this study improves the method proposed by Ma (2012) in two aspects. On the one hand, the soil particles on the slope are given an initial velocity; on the other hand, the water absorption was considered by increasing the unit weight of soil particles. Specifically, the scouring process can be generally divided into the following four steps. Firstly, the generation and gravity balance of the soil particles are performed. Then, the allocation of the contact models is carried out based on the freeze–thaw zoning. Here, it was assumed that the width of the freeze–thaw zone (Zone B) accounts for 1/10 of the total width of the top of the slope. After that, the identification of the surface

TABLE 1 | Simulation scheme and main parameters.

Scenarios	Slope (°)	Scouring velocity(m/s)	Zone A		Zone B	
			Tensile strength (Pa)	Shear strength (Pa)	Tensile strength (Pa)	Shear strength (Pa)
Before FT	45	0.1	2.8e5	1.4e5	2.8e5	1.4e5
	60					
After FT	45	0.1	2.8e5	1.4e5	1.4e5	0.7e5
	60	0.1, 0.15, 0.2				

Note: Zones A and B mean the slope region without and with the action of freeze–thaw, respectively.

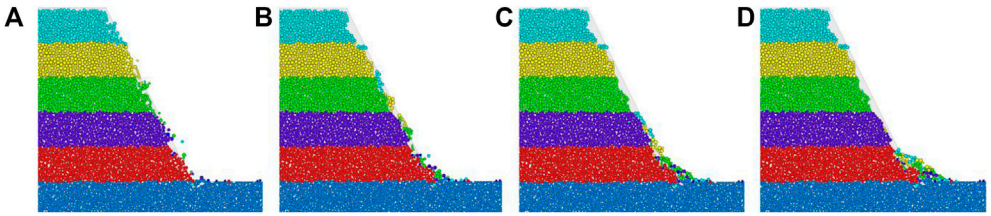

FIGURE 4 | Superficial erosion process of the 60° slope (before FT). **(A)** 0.1, **(B)** 0.8, **(C)** 1.5, and **(D)** 2.5 (×million steps).

particles is made by the programmed codes. Finally, the walls are going to be removed, and the velocity and the extra gravity will be imposed on the surface particles.

Scouring Velocity and Terminal Condition

Scouring velocity. When setting the scouring velocity, the particles will impact each other and bump away from the slope under high velocity; on the contrary, it does not work due to the cohesion between the particles. After repeated trials, a scouring velocity of 0.1 m/s was determined. In this study, the velocity is also variable to discuss the influence of flow velocity on the slope stability. Due to the change in direction of particle motion after collision, it is impossible to apply a constant flow velocity to the slope particles at present. Hence, only the influence of single scouring action on the slope stability will be discussed here.

Terminal condition. The original balance of superficial soil particles is broken under scouring, and the particles begin to move down the slope with water flow until a new balance is reached, where the movement of the particle is nearly stationary. After several trials, it is found that when the operation reaches 2.5 million cycles, the particles are stationary, and the maximum velocity is less than 1e-3 m/s. Therefore, the terminal condition was set when the total cycles reached 2.5 million times.

Simulation Scenarios and Parameters

The simulation scheme and main parameters are set, as shown in **Table 1**.

RESULTS AND DISCUSSION

Basic Behaviors of Scouring Action

Morphology

As shown in **Figure 4**, in order to distinguish easily, the slope is evenly divided into six layers by colors from top to bottom according to height. It can be found that only the shallow layer of the slope was destroyed after being scoured, while the other parts of the slope were not deformed. It is to be noted that the gray background represents the initial slope area, which does not participate in the calculation.

From **Figures 4A–D**, it can be found that the runoff only caused damage to the slope surface, leaving a little slide of soil particles, candle holes, and cavity prototypes at the top and foot of the slope. Besides, the particles at the slope foot are first washed and denuded and then accumulated on the slope feet, thereby making the soil in the upper layer in an unbalanced state to move downward. And then, under the continuous action of runoff shearing force, the shallow soil particles on the upper slope are gradually eroded, resulting in the particles in the deeper layer being disturbed and slid down along the structural surface with higher erosion resistance and accumulation at the foot of the slope, which finally can be called the spalling phenomenon.

Contacts

The contacts between particles can be illustrated in **Figures 5A–D**. As noted, the contacts in blue and red represent the initial and the default anti-rotation contact model, respectively. It can be found that most of the particles slide and pile up at the foot of the slope, which is in good agreement with the aforementioned slope morphology. Besides, the rotation resistance model is the major contact model of spalling fragments, which indicates that the spalling objects are non-sticky and loose soil granules. This is in line with the practical field investigation. However, part of them still obey the contact-bonding model, which is mainly due to the scouring effect that destroyed the soil structure at the weakest point of anti-scouring ability, avoiding the contact model there, which can be classified as fragmentary spalling.

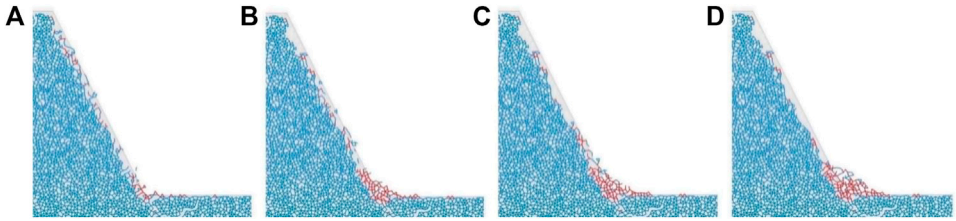

FIGURE 5 | Contact distribution of soil particles under scouring. **(A)** 0.1, **(B)** 0.8, **(C)** 1.5, and **(D)** 2.5 (×million steps).

TABLE 2 | Denudation amount.

Slope		First layer	Second layer	Third layer	Fourth layer	Fifth layer	Total	Scenarios
60°	Before FT	25	15	19	21	29	109	Basic
	After FT	17	23	41	28	47	156	Contrastive
45°	Before FT	4	12	11	18	35	80	Contrastive
	After FT	22	31	20	31	43	147	Contrastive

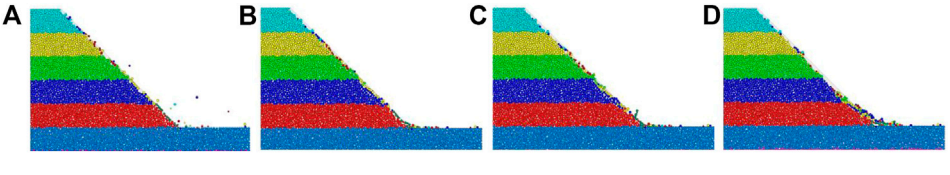

FIGURE 6 | Surperfical erosion process of the 45° slope (before FT). **(A)** 0.1, **(B)** 0.8, **(C)** 1.5, and **(D)** 2.5 (×million steps).

Denudation Amount

The rotation angle of the particles is near zero when the soil structure is stable, while it increases when being spalled. Here, it is assumed that the contacts of soil particles have been denuded when the finial absolute rotation angle is greater than 0.5°. Therefore, by monitoring the particle rotation angle, the damage degree of the superficial slope can be quantified. It can be seen from **Table 2** that, under runoff scouring, the amount of each layer is sorted as the foot (fifth layer) > top layer (first layer) > fourth layer > third layer > second layer, indicating that the most of the spalling occurred at the lower part of the slope.

Parameter Effects

Slope Gradient

Morphology

The erosion failure process of the 45° slope before the FT effect is shown in **Figures 6A–D**. As noted, the scouring time of the 45° slope is shorter than that of the steeper one (60° slope). For example, the shape of the 45° slope changes slightly after 0.8 M steps, while the shape change of the 60° slope can still be observed at 2.5 M steps. This is mainly because the scouring force was counteracted by adhesion and friction between the particles, leaving the particles of the 45° slope to maintain a stable state more easily. This indicates that the slope gradient has a significant influence on stability under the action of runoff scouring, and the smaller slope has a stronger anti-scouring ability.

Denudation Amount

The denudation amount of 45° and 60° slopes is shown in **Table 2**. As noted, it is evident that the amount of spalling particles was decreased significantly under the lower gradient slope, while the amount of each layer was the same as that of the steeper slope.

Freeze–Thaw Action

Morphology

The erosion failure process of 45° and 60° slopes after the FT effect is shown in **Figures 7A–H** from a to d and e to h, respectively. Compared with **Figures 4**, **6**, it can be found that, at the initial stage of erosion (within 0.8 M steps), the runoff only caused damage to the slope surface both with and without the FT effect. Moreover, in the middle and late stages (after 0.80 M steps), considering the FT effects, the particles cut into the lower layer of soil rather than rolling down under scouring action, resulting in a splitting effect on the shallow particles in the lower slope. The split blocks are dispersed into smaller blocks and particles under

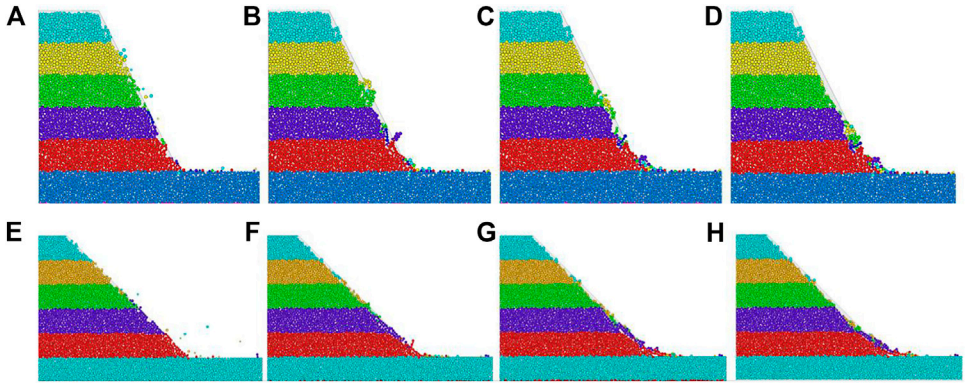

FIGURE 7 | Spalling process of slopes (after FT). **(A–D)** are for 60° slope and **(E–H)** are 45° slope. **(A–D)** and **(E–H)** refer to numerical steps under 0.1, 0.8, 1.5, and 2.5, respectively (× million).

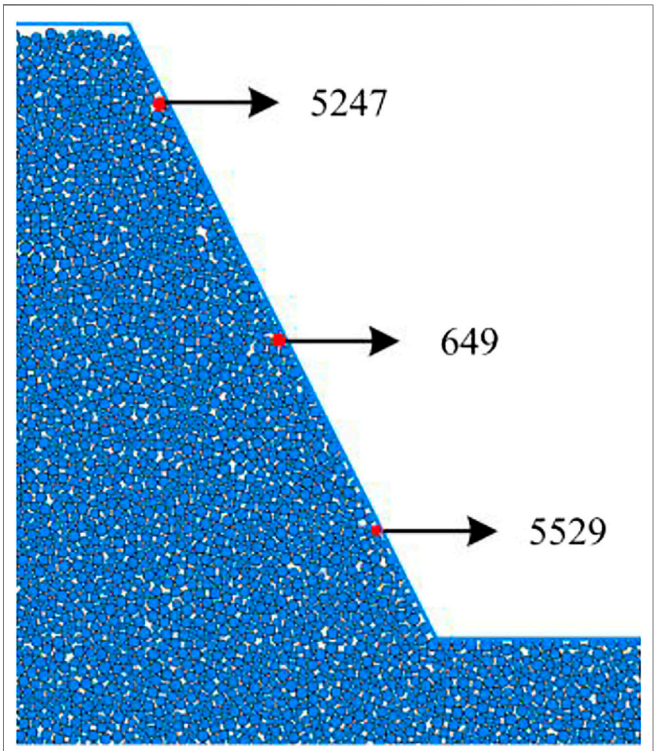

FIGURE 8 | Monitoring spheres on the slope surface.

the scouring effect and then piling up at the foot of the slope. The underlying reason for splitting was the poor cohesion among soil particles in the freeze–thaw zone. When the runoff was wrapping up the soil particles and moving downward, the soil in that zone was likely to be punched, and the phenomenon tended to occur.

Besides, in the final stage (above 2.5 M steps), the slope foot was damaged more significantly with the action of FT, which can be ascribed to the stress concentration at the foot of the slope. So, the particles deformed more largely under frequent FT disturbances. Finally, compared to the 60° slope, the impacts of runoff scouring on the 45° slope are quite limited on the top, regardless of the FT effect. During this process, the splitting from the upper layer soil to the lower does not occur.

Denudation Amount

The denudation of 45° and 60° slopes is shown in **Table 2**. As noted, it is evident that the number of spalling particles was increased significantly after considering the FT effect, which can be seen from the increased total number of 45° and 60° slopes by 147 and 156, rising 83.75 and 43.1%, respectively. Besides, the FT effect has a larger impact on the lower parts of the slope. For example, the denudation amount in the fourth and fifth layers of the slope considering the FT effect is much larger than that without.

Particle Movement

In order to detect the FT effect on the particle movement at different locations during the scouring process, three measurement spheres were selected on the 60° slope to record the position changes under different conditions, as shown in **Figure 8**, and the corresponding trajectories are presented in **Figures 9A–C**. It can be found that the soil particles on the lower layer of the slope surface reach the steady state first than those on the upper layer. This is mainly due to the shorter movement distance of the former particles, resulting in smaller potential energy, which is faster dissipated by the bonding and friction between the particles. Besides, when considering the FT effect, the spheres (5,247 and 649) located on the upper and middle layers reach a steady state faster than those without. The reason is that the adhesion between the particles of the shallow soil after the FT effect is reduced, leaving less kinetic energy needed to be consumed to destroy the contacts between the particles. Finally, the time of the sphere (5,529) located on a lower layer to reach the steady state is the same in both scenarios. However, when considering the FT effect, the particles move first downward and then upward, which indicates particles at the foot move more actively.

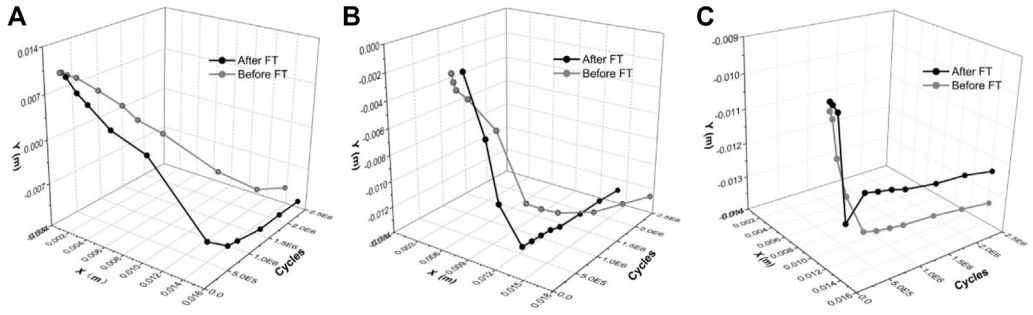

FIGURE 9 | Trajectories of different monitoring points. **(A)**, **(B)**, and **(C)** are for 5,247, 649, and 5,529 measuring spheres, respectively.

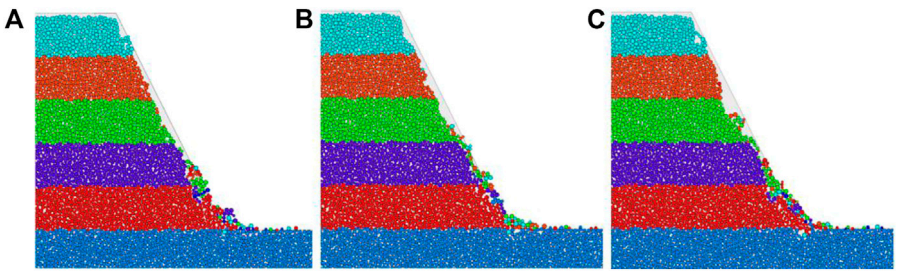

FIGURE 10 | Morphology under different scouring velocities of the 60° slope. **(A)** 0.1, **(B)** 0.15, and **(C)** 0.2 m/s.

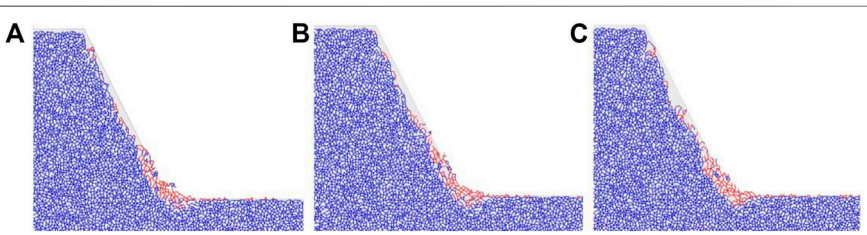

FIGURE 11 | Contact distribution under different scouring velocities of the 60° slope. **(A)** 0.1, **(B)** 0.15, and **(C)** 0.2 m/s.

TABLE 3 | Denudation amount of the 60° slope under the FT effect.

Scouring velocity (m/s)	First layer	Second layer	Third layer	Fourth layer	Fifth layer	Growth*
0.1	25	15	19	21	29	-
0.15	28	28	45	29	46	59%
0.2	25	27	53	33	54	86%

**means that growth is calcualted based on the amount under 0.1 m/s.*

Scouring Velocity

Morphology and Contacts

The effects, including morphology and contact distribution, under different scouring velocities (0.1, 0.15, and 0.2 m/s) on a 60° slope, are shown in **Figures 10A–C**, **11A–C**. As noted, the contact model distribution is clearer in demonstrating the spalling process of the slope. It can be found that although the velocity does not affect the type of slope failure, it impacts diversely on the foot of the slope, showing an increasing pit size at the foot under greater velocity.

Denudation Amount

The denudation amount of each layer under the FT effect is shown in **Table 3**. It can be found that the denudation amount

increases significantly as the velocity is increased. With the increase in velocity, the denudation amount of particles in the top layer (the first layer) of the slope is unchanged, while that in the lower layer increases gradually. The reason for that is the flow was only loaded once rather than continuously, leaving short disturbance time to the top layers and producing shallow superficial spalling in the lower layer. Increasing the velocity resulted in a larger erosion load on the lower surface. So, the erosion amount increases gradually.

CONCLUSIONS

A PFC^{2D} scouring model, of which the mesoscopic parameters were calibrated by the indoor experiments, was developed to investigate the rainfall erosion damage of residual soil slope in the intermittently frozen area. The main conclusions are addressed in the following three aspects:

- At the beginning of erosion, only the slope surface was damaged under both with and without the FT effect. And then, the splitting phenomenon was observed rather than rolling down in the middle and late stages. The most damaged part was at the foot, as was more evident under the action of FT in the final stage. Moreover, the FT effect caused less damage to the gentler slope.
- The denudation amount of spalling particles was increased significantly after considering the FT effect. Finally, regardless of the FT effect, the particles in the lower layer reached the stable state first, and the time was the same under these two conditions.
- The pit size at the foot and the denudation amount were both increased under higher scouring velocity.

The future study will focus on the development of more realistic contact models and computing effective methods, which facilitate revealing the freeze–thaw effect on the slope surface. Besides, the coupling effects of water flow and soil particle movement on slope stability will also be explored.

DATA AVAILABILITY STATEMENT

The original contributions presented in the study are included in the article/Supplementary Material, and further inquiries can be directed to the corresponding author.

AUTHOR CONTRIBUTIONS

ZJ and YK conceptualized the idea. YK performed the methodology. ZJ and YC ran the software. YK, YC, ZJ, and YQ wrote the original draft.

REFERENCES

Bai, R. X., Chen, X. S., and Zheng, G. (2012). Study on Microcosmic Parameters of Soil Permeability Coefficient Particle Flow. *Low Temp Archit Technol.* 34 (1), 64–67. doi:10.3969/j.issn.1001-6864.2012.01.028

Baranov, I. Y. (1964). *Geographical Distribution of Seasonally Frozen Ground and Permafrost*. National research council of Canada. Division of Building Research. doi:10.4224/20359041

Chen, B., and Li, J. P. (2008). Characteristics of Spatial and Temporal Variation of Seasonal and Short- Term Frozen Soil in China in Recent 50 Years. *Chin. J. Atmos. Sci.* 32 (3), 432–443. doi:10.3724/SP.J.1148.2008.00288

Chen, J., Wu, Y., O'Connor, M., Cardenas, M. B., Schaefer, K., Michaelides, R., et al. (2020). Active Layer Freeze-Thaw and Water Storage Dynamics in Permafrost Environments Inferred from InSAR. *Remote Sensing Environ.* 248, 112007. doi:10.1016/j.rse.2020.112007

Evans, M. T., Chall, S. L., Zhao, X. L., and Rhyne, T. M. (2009). Visualization and Analysis of Microstructure in Three-Dimensional Discrete Numerical Models. *J. Comput. Civil Eng.* 23 (4), 277–287. doi:10.1061/(ASCE)0887-380110.1061/(asce)0887-3801(2009)23:5(277)

Fu, Y. S. (2017). *Study on the Mechanism of Shallow Surface Spalling of Residual Soil Slope in Short Time Frozen Area*. Fuzhou University.

He, Y. R., Zhu, S., and Wu, L. Q. (2014). Research on the Corresponding Relationship between Two-Dimensional Porosity and Three-Dimensional Porosity of Coarse Materials. *Water Power* 40 (5), 27–29. doi:10.3969/j.issn.0559-9342.2014.05.008

Hu, Z. R. (2014). *The Granular Flow Analysis for Volume Change Characteristics of Gravel Soil Slope the under Equivalent Rainfall Infiltration*. Xiangtan: Xiangtan University.

Iwashita, K., and Oda, M. (2000). Micro-deformation Mechanism of Shear Banding Process Based on Modified Distinct Element Method. *Powder Tech.* 109 (1-3), 192–205. doi:10.1016/S0032-5910(99)00236-3

Iwashita, K., and Oda, M. (1998). Rolling Resistance at Contacts in Simulation of Shear Band Development by DEM. *J. Eng. Mech.* 124 (3), 285–292. doi:10.1061/(ASCE)0733-939910.1061/(asce)0733-9399(1998)124:3(285)

Jiang, M. J., Li, X. M., Sun, Y. G., and Hu, H. J. (2009). Discrete Element Simulation of Biaxial Compression Test Considering Rolling Resistance. *Rock Soil Mech.* 30 (z2), 514–517. doi:10.16285/j.rsm.2009.s2.108

Jiang, M. J., Yu, H.-S., and Harris, D. (2005). A Novel Discrete Model for Granular Material Incorporating Rolling Resistance. *Comput. Geotechnics* 32 (5), 340–357. doi:10.1016/j.compgeo.2005.05.001

Li, S. B., Wang, C. M., Wang, N. Q., Wang, G. C., and Yao, K. (2013). Numerical Simulation of Loess Triaxial Shear Test by PFC^{3D}. *China J. Highw. Transport* 26 (06), 22–29. doi:10.19721/j.cnki.1001-7372.2013.06.004

Li, Z. Y. (2013). *Instable Mechanism of Granite Residual Soil Slope in Intermittently Frozen Soil Area*. Fuzhou: Fuzhou University.

Liang, J. X., Hu, X. W., and Xu, X. J. (2017). Particle Flow Simulation of Earthquake Induced Deformation Failure of Soil Slopes with Different Geological Factors under Earthquake. *J. Eng. Geology.* 25 (06), 1537–1546. doi:10.13544/j.cnki.jeg.2017.06.017

Liu, Y. M., Yang, C. H., Huo, Y. S., Li, L., Xu, Y. L., and Du, C. (2013). Discrete Element Modeling of Behaviors of Coarse Grained Soils Considering Rolling Resistance. *Rock Soil Mech.* 34 (S1), 486–493. doi:10.16285/j.rsm.2013.s1.023

Lu, Q., Zhao, D., and Wu, S. (2017). Simulated Responses of Permafrost Distribution to Climate Change on the Qinghai-Tibet Plateau. *J. Scientific Rep.* 7 (1), 3845. doi:10.1038/s41598-017-04140-7

Ma, D. H. (2012). *A Study of Water-Soil Mechanics Coupling Mechanism and Model for Loess Slope Surface Erosion on Highway*. Jilin: Jilin University.

Ni, Q., Powrie, W., Zhang, X., and Harkness, R. (2000). Effect of Particle Properties on Soil Behavior: 3-D Numerical Modeling of Shearbox Tests. *Numer. Methods Geotechnical Eng. GSP* 96. doi:10.1061/40502(284)5

Oda, M., Nemat-Nasser, S., and Mehrabadi, M. M. (1982). A Statistical Study of Fabric in a Random Assembly of Spherical Granules. *Int. J. Numer. Anal. Methods Geomech.* 6 (1), 77–94. doi:10.1002/nag.1610060106

Park, J.-W., and Song, J.-J. (2009). Numerical Simulation of a Direct Shear Test on a Rock Joint Using a Bonded-Particle Model. *Int. J. Rock Mech. Mining Sci.* 46 (8), 1315–1328. doi:10.1016/j.ijrmms.2009.03.007

Que, Y., Deng, X. Y., and Chen, J. (2017). Mechanism Analysis of Non-equilibrium Seepage and Stability Mechanism of Residual Soil Slopes by Ice and Snow

Ablation in Intermittently Frozen Area. *Eng. Sci. Tech.* 49 (6), 73–83. doi:10.15961/j.jsuese.201600767

Que, Y., Chen, X., Chen, Y., Jiang, Z., Qiu, Y., and Easa, S. M. (2021). Stability Analysis of Double V-Shaped Gully Embankment: A Dimension-Reduced Calculation Method. *Can. J. Civ. Eng.*. In press. doi:10.1139/cjce-2019-0783

Research Institute of Highway Science, Ministry of Communications (2010). *Highway Geotechnical Test Code, JTG E40-2007*. Beijing: China communication press.

Saman, A., Zhao, C. G., and Kang, K. (2014). Study on Sample Size and Grain Size Influence on Shear Strength of Coarse-Grained Soil in Triaxial Test. *J. Beijing Jiaotong Univ.* 38 (4), 133–136. doi:10.11860/j.issn.1673-0291-2014.04.023

Shi, C., and Xu, Y. W. (2015). *Numerical Simulation Technique and Practice of Granular Flow*. China Architecture Building Press. doi:10.2991/asei-15.2015.314

Skinner, A. E. (1969). A Note on the Influence of Interparticle Friction on the Shearing Strength of a Random Assembly of Spherical Particles. *Géotechnique* 19 (19), 150–157. doi:10.1680/geot.1969.19.1.150

Song, P. R. (2013). *The Erosion Damage Characteristics and Numerical Simulation of Loess Slope*. Jilin: Jilin University.

Suiker, A. S. J., and Fleck, N. A. (2004). Frictional Collapse of Granular Assemblies. *J. Appl. Mech.* 71 (3), 350–358. doi:10.1115/1.1753266

Thomas, H. R., Cleall, P., Li, Y.-C., Harris, C., and Kern-Luetschg, M. (2009). Modelling of Cryogenic Processes in Permafrost and Seasonally Frozen Soils. *Géotechnique* 59 (3), 173–184. doi:10.1680/geot.2009.59.3.173

Thornton, C. (2000). Numerical Simulations of Deviatoric Shear Deformation of Granular media. *Géotechnique* 50 (1), 43–53. doi:10.1680/geot.2000.50.1.43

Tsuji, Y., Kawaguchi, T., and Tanaka, T. (1993). Discrete Particle Simulation of Two-Dimensional Fluidized Bed. *Powder Tech.* 77 (1), 79–87. doi:10.1016/0032-5910(93)85010-7

Wang, X., Nie, Z., Gong, J., and Liang, Z. (2021). Random Generation of Convex Aggregates for DEM Study of Particle Shape Effect. *Construction Building Mater.* 268, 121468. doi:10.1016/j.conbuildmat.2020.121468

Wang, X., Yin, Z. Y., Wu, X. X., Su, D., and Zhao, J. D. (2021). A Novel Approach of Random Packing Generation of Complex-Shaped 3D Particles with Controllable Sizes and Shapes. *Acta Geotechnica*. doi:10.1007/s11440-021-01155-3

Wang, Z., Ruiken, A., Jacobs, F., and Ziegler, M. (2014). A New Suggestion for Determining 2D Porosities in DEM Studies. *Geomech. Eng.* 7 (6), 665–678. doi:10.12989/gae.2014.7.6.665

Willmott, C. J., and Matsuura, K. (2001). Terrestrial Air Temperature and Precipitation: Monthly and Annual Time Series (1950 - 1999). Available at: http: //climate.geog.udel.edu/ ~climate/html_pages (Accessed May 04, 2021). doi:10.1029/2017eo074939

Woo, M., and Winter, T. C. (1993). The Role of Permafrost and Seasonal Frost in the Hydrology of Northern. *J. Hydrol.* 141 (1-4), 5–31. doi:10.1016/0022-1694(93)90043-9

Wu, Q., Wang, C. M., Ma, D. H., and Song, P. R. (2013). Mechanism of Steep Loess Slop Rainfall Erosion in Western Liaoning. *J. Jilin Univ.* 43 (5), 1563–1571. doi:10.13278/j.cnki.jjuese.2013.05.026

Wu, Q., Wang, C. M., Song, P. R., Zhu, H. B., and Ma, D. H. (2014). Rainfall Erosion experiment for Steep Loess Slope and Fluid-Soil Coupling Simulation with PFC^{3D}. *Rock Soil Mech.* 2014 (4), 977–985. doi:10.16285/j.rsm.2014.04.031

Xiong, C. X., Wang, T., and Lu, X. B. (2013). Meso-mechanical Simulation of Slope Disintegration Erosion under Rainfall. *J. Mountain Sci.* 31 (6), 710–715. doi:10.16089/j.cnki.1008-2786.2013.06.015

Xu, Z. L. (2017). *Numerical Analysis of Unsaturated Soil Strength with PFC3D*. Beijing Jiaotong University.

Zeghal, M., and Shamy, U. E. (2005). Coupled Continuum-Discrete Model for Saturated Granular Soils. *J. Eng. Mech.*, 2005, 131(4): 413–426. doi:10.1061/(ASCE)0733-9399

Zhang, D., Huang, X., and Zhao, Y. (2013). Algorithms for Generating Three-Dimensional Aggregates and Asphalt Mixture Samples by the Discrete-Element Method. *J. Comput. Civ. Eng.* 27 (2), 111–117. doi:10.1061/(asce)cp.1943-5487.0000210

Zhang, T., Barry, R. G., Knowles, K., Ling, F., and Armstrong, R. L. (2003). "Distribution of Seasonally and Perennially Frozen Ground in the Northern Hemisphere," in Proceedings of the 8th International Conference on Permafrost, Zürich, Switzerland. Editors M. Phillips, S. M. Springman, and L. U. Arenson (AA Balkema Publishers) 2, 1289–1294.

Zhang, Y. (2017). *Microscopic Numerical Simulation of Deformation and Failure Process of Rock under True Triaxial Stress*. China University of Mining and Technology.

Zhu, T., Chen, J., Huang, D., Luo, Y., Li, Y., and Xu, L. (2021). A DEM-Based Approach for Modeling the Damage of Rock under Freeze-Thaw Cycles. *Rock Mech. Rock Eng.*, 1–16. doi:10.1007/s00603-021-02465-4

Conflict of Interest: The author YQ was employed by Zijin Mining Group Co., Ltd.

The remaining authors declare that the research was conducted in the absence of any commercial or financial relationships that could be construed as a potential conflict of interest.

frontiers in Materials

ORIGINAL RESEARCH
published: 30 July 2021
doi: 10.3389/fmats.2021.736180

A Complete Two-Dimensional Avalanche Photodiode Based on $MoTe_2$–WS_2–$MoTe_2$ Heterojunctions With Ultralow Dark Current

Tenghui Ouyang, Ximiao Wang, Shaojing Liu, Huanjun Chen and Shaozhi Deng*

State Key Laboratory of Optoelectronic Materials and Technologies, Guangdong Province Key Laboratory of Display Material and Technology, School of Electronics and Information Technology, Sun Yat-sen University, Guangzhou, China

Two-dimensional (2D)-material-based photodetectors have recently received great attention due to their potentials in developing ultrathin and highly compact devices. Avalanche photodiodes (APDs) are widely used in a variety of fields such as optical communications and bioimaging due to their fast responses and high sensitivities. However, conventional APDs based on bulk materials are limited by their relatively high dark current. One solution to tackle this issue is by employing nanomaterials and nanostructures as the active layers for APDs. In this study, we proposed and fabricated an atomically-thick APD based on heterojunctions formed by 2D transition metal dichalcogenides (TMDs). A typical device structure was formed by stacking a semiconducting monolayer WS_2 onto two metallic few-layer $MoTe_2$ flakes. Due to the Schottky barrier formed between the TMD layers and their atomic thicknesses, the dark current of the APD is greatly reduced down to 93 pA. In addition, the APD can operate through a broad spectral range from visible to near-infrared region, with a responsivity of 6.02 A/W, an external quantum efficiency of 1,406%, and an avalanche gain of 587. We believe that the 2D APD demonstrated here provides a feasible approach for developing all-2D optoelectronic devices with simultaneous high-sensitivity and low noise.

Keywords: MoTe2, WS2, avalanche photodiodes, transition metal dichalcogenides, heterojunctions

OPEN ACCESS

Edited by:
Dongxiang Li,
Qingdao University of Science and Technology, China

Reviewed by:
Lei Shao,
Beijing Computational Science Research Center (CSRC), China
Zhang Zhang,
South China Normal University, China

****Correspondence:***
Huanjun Chen
chenhj8@mail.sysu.edu.cn

Specialty section:
This article was submitted to Semiconducting Materials and Devices, a section of the journal Frontiers in Materials

Received: *06 July 2021*
Accepted: *20 July 2021*
Published: *30 July 2021*

Citation:
Ouyang T, Wang X, Liu S, Chen H and Deng S (2021) A Complete Two-Dimensional Avalanche Photodiode Based on $MoTe_2$–WS_2–$MoTe_2$ Heterojunctions With Ultralow Dark Current. Front. Mater. 8:736180. doi: 10.3389/fmats.2021.736180

2D atomic crystals have attracted extensive interests during the past decade due to their excellent electrical, optical, and optoelectronic properties. Echo with their ultrathin structure, a broad range of potential applications can be envisioned, including high-performance 2D transistors (Yoon et al., 2013; Liu et al., 2015; Choi et al., 2016; Chuang et al., 2016; Liu et al., 2019; Zheng et al., 2020), photodetectors (Mittendorff et al., 2013; Cheng et al., 2014; Mudd et al., 2015; Tao et al., 2015; Wang et al., 2015; Shim et al., 2016; Vu et al., 2017; Yu et al., 2017; Zeng et al., 2019; Wang et al., 2020), ultra-compact and flexible light-emitting diodes (Withers et al., 2015; Wang et al., 2017; Shang et al., 2018), sensors (Burman et al., 2016; Shokri and Salami, 2016; Guo et al., 2017), to name but a few. In particular, 2D transition metal dichalcogneides (TMDs) are usually semiconductors with exotic characteristics which can open up new avenues for both of fundamental research and practical applications. For example, monolayer WS_2 is shown to be a direct bandgap semiconductor with strong room-temperature exciton binding energy. It has been widely employed as quantum emitters for studying of strong light–matter interactions in different types of micro- and nanocavities (Wen et al., 2017). In addition, monolayer WS_2 exhibits strong absorption across the visible spectral range, as well as excellent chemical stability (Bernardi et al., 2013; Zhang et al., 2013). These allow it to act as

TABLE 1 | Comparison of device performances.

Device structure	R (A/W)	RT (ms)	λ (nm)	I_{dark} (A)	EQE	NPDR (W^{-1})	AG	References
Gr–WS_2–Gr	0.1	---	633	10^{-7}	0.3	1×10^{6}	---	Britnell et al. (2013)
Gr–InSe–Gr	60	0.12	400–1,000	5×10^{-10}	148.5	1.2×10^{11}	---	Luo et al. (2015)
Gr–$MoTe_2$–Gr	5	0.03	600–1,350	---	0.4	---	---	Wu et al. (2020)
Gr–WSe_2–Gr	0.04	5.5×10^{-6}	---	---	0.07	---	---	Massicotte et al. (2016)
Gr–WS_2–Gr	3.5	>2000	532	10^{-8}	9.3	3.5×10^{8}	---	Tan et al. (2016)
Gr–WSe_2/GeSe–Gr	6.2	0.03	520	---	14.9	---	---	Wei et al. (2017)
Gr–WS_2/MoS_2–Gr	2,340	>10,000	---	10^{-6}	---	2.34×10^{9}	---	Tan et al. (2017)
Gr–$MoTe_2$–Gr	0.11	0.024	1,064	5×10^{-7}	0.13	2.2×10^{5}	---	Zhang et al. (2017)
Gr–$MoTe_2$–Gr	0.03	6.15×10^{-3}	550	6×10^{-8}	---	4.6×10^{5}	---	Wei et al. (2019)
MoS_2 APD	2.2	---	633	2×10^{-7}	---	1.1×10^{7}	903	Lopez-sanchez et al. (2014)
InSe APD	---	0.06	400–800	1.3×10^{-9}	3.4	---	152	Lei et al. (2015a)
BP APD	---	---	532	1.05×10^{-5}	2.7	---	272	Atalla and Koester (2017)
BP APD	130	---	500–1,100	2×10^{-6}	310	6.5×10^{7}	7	Jia et al. (2019)
InSe APD	11,000	1	405–785	5×10^{-9}	---	2.5×10^{12}	500	Yang et al. (2019)
APD120A	25	---	400–1,000	---	---	---	50	Com
LSSAPD9-230	0.57	3×10^{-5}	400–1,000	10^{-9}	---	---	60	Com
AD100-8 TO	50	1.8×10^{-5}	400–1,100	10^{-10}	---	---	100	Com
MTAPD-06-001	50	3×10^{-5}	400–1,100	4×10^{-10}	---	---	100	Com
$MoTe_2$–WS_2–$MoTe_2$	6.02	475	400–700	9.3×10^{-11}	14.1	6.47×10^{10}	587	This work

Com. stands for commercial.

active layers for photodetectors. The few-layer $MoTe_2$ is reported to be a type-II Weyl semimetal, which can be employed as electrodes in the 2D devices for its high carrier mobility and good electric conduvtivity (Zhang et al., 2014; Beams et al., 2016; Chen et al., 2016). Furthermore, one can also explore new physical phenomena associated with the semimetal phase in the few-layer $MoTe_2$ (Keum et al., 2015).

Avalanche photodiodes (APDs), which consist of p–n junctions or Schottky junctions, are able to convert the incoming photons into charge carriers undergoing cascade amplifications upon reverse bias (Johnson, 1965; Anderson and McMurtry, 1966; Aull et al., 2002). When operating in the avalanche regime, APDs can exhibit high internal gain for photodetection of ultrahigh sensitivity, making them widely used in optical communications (Liu et al., 1992; Ferraro et al., 2015), single-photon detection (Huntington et al., 2007; Faramarzpour et al., 2008; Ren et al., 2011), and bioimaging (Vo-Dinh et al., 2010; Wohnhaas et al., 2013). However, conventional APDs based on bulk materials are usually limited by their relatively high dark current. This issue can be alleviated by reducing the volume of the devices, which is typically accompanied by sacrifice of device responsivity and quantum efficiency. During the past decade, due to their atomic thicknesses, strong optical absorption, and high photocurrent conversion efficiencies, 2D crystals have been demonstrated to provide a new avenue for developing high-performance photodetectors with low dark current and high responsivity (**Table 1**).

Generally, in 2D photodetectors bulk metals such as titanium and gold are utilized as electrodes. A limitation of these electrodes is that acquiring defect-free interface between metal and 2D crystals without Fermi level pinning or carrier scattering is still a challenge, because defects and dangling bonds in these metal electrodes will introduce plentiful interfacial states (Gong et al., 2014; Kim et al., 2017). In contrast, the passivated and dangling-bond-free surfaces of 2D crystals can make them integrate layer-by-layer to form heterojunctions bonded through van der Waals (vdW) force. Accordingly, devices free of interface defects can be formed through stacking different types of 2D crystals. Specifically, all-2D photodetectors have been developed by respectively adopting the 2D crystals as electrodes and active layers (Britnell et al., 2013; Luo et al., 2015; Massicotte et al., 2016; Tan et al., 2016; Padilha et al., 2017; Tan et al., 2017; Wei et al., 2017; Zhang et al., 2017; Yao and Yang, 2018; Wei et al., 2019; Yang et al., 2019; Wu et al., 2020). Although these all-2D devices exhibit excellent photodetection performances, their room-temperature dark currents are still relatively high (in the range of ~0.1 nA–1 μA, **Table 1**). Such high dark currents will deteriorate the signal-to-noise (S/N) ratio of the photodetectors and consequently limit the device applications in sensing of low photon flows.

In this study, we present an all-2D APD composed of a monolayer WS_2 and two few-layer $MoTe_2$ flakes ($MoTe_2$–WS_2–$MoTe_2$ heterostructure). The metallic $MoTe_2$ flakes act as electrodes. A Schottky barrier can thereafter be formed at the interface between the semiconducting WS_2 and metallic $MoTe_2$. Upon reverse bias, the APD is demonstrated with a responsivity (R) of 6.02 A/W, an external quantum efficiency (EQE) of 1,406%, and an avalanche gain (AG) of 587. In particular, due to the Schottky barrier, a dark current as low as 93 pA can be obtained. The *R* and EQE is at the forefront of the all-2D photodetectors, while the dark current is even better than many state-of-the-art commercial APDs. In addition, wavelength scanned measurements further indicated that the APD operated in a broad spectral range from 400 to 700 nm. Our results therefore demonstrate a facile approach for design and fabrication of room-temperature all-2D photodetectors with simultaneous high-sensitivity and low noise.

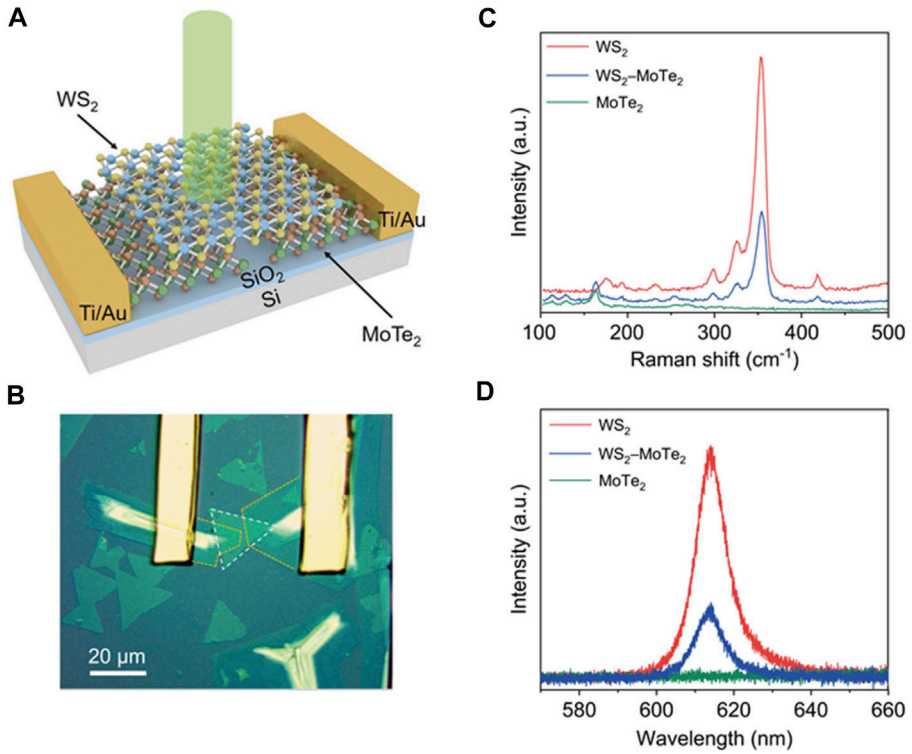

FIGURE 1 | Material characterizations of the $MoTe_2$–WS_2–$MoTe_2$ heterojunction device. **(A)** Schematic showing the APD composed of a monolayer WS_2 flake overlaid onto two few-layer $MoTe_2$ flakes. The green cylinder delegates the incidence light. **(B)** Optical microscope image of the fabricated $MoTe_2$–WS_2–$MoTe_2$ heterostructure. The WS_2 region is marked with white dashed lines. The $MoTe_2$ regions are marked with yellow dashed lines. **(C, D)** Raman **(C)** and PL **(D)** spectra of the $MoTe_2$–WS_2–$MoTe_2$ heterostructure. The spectra are collected from the monolayer WS_2 (red), few-layer $MoTe_2$ (green), and WS_2–$MoTe_2$ heterojunction (blue) regions. The excitation laser is of 532-nm wavelength.

EXPERIMENTAL

Materials

Monolayer WS_2 was purchased from 6Carbon Technology company in China. Few-layer $MoTe_2$ was grown on the silicon substrate covered with 300-nm-thick SiO_2 layer according to the process reported previously (Chen et al., 2017).

Device Fabrications

The $MoTe_2$–WS_2–$MoTe_2$ heterostructure was fabricated using a wet-transfer method (Wen et al., 2017). Specifically, Polystyrene (PS) was first coated on the surface of the substrate covered with monolayer WS_2 flakes. Then, the substrate covered with PS film was put into water so that the PS film pasted with WS_2 was stripped off from the substrate. Subsequently, the WS_2 adhered onto the PS film was transferred onto two few-layer $MoTe_2$ flakes separated with a micrometer-scale gap. After incubation at 110°C for 60 s, the sample was immersed into toluene solution for 2 hours to dissolve the PS film, whereby heterojunctions were formed between the WS_2 and two $MoTe_2$ flakes.

To fabricate the $MoTe_2$–WS_2–$MoTe_2$ heterojunction device structure, maskless lithography (uPG501, Wavetest) was employed to pattern the two electrodes. Afterwards, titanium (Ti, 10-nm thick) and gold (Au, 100-nm thick) were deposited using an electron-beam evaporation system (DE400, Wavetest). The heterojunction device structure was obtained after the lift-off process.

Characterizations

Raman and photoluminescence (PL) spectra were measured using a micro-Raman spectrometer (inVia Reflex, Renishaw). The excitation laser with a wavelength of 532 nm was focused onto the samples through a ×50 objective (numerical aperture 0.80). The diameter of the focusing spot is ~1 μm. The thicknesses of the WS_2 and $MoTe_2$ flakes were measured using an atomic force microscope (AFM, NTEGRA Spectra, NT-MDT). The photocurrents were measured by a sourcemeter (Keithley 2636B, Tektronix), with incidence wavelengths of 405, 532, 633, 785, and 1,064 nm. In addition, a supercontinuum laser source with an output wavelength range of 400–2400 nm (Fianium, SC400-4-PP) was employed to measure the photocurrent spectrum. The noise power spectra of the device under different bias voltages were collected using a semiconductor characterization system (FS-Pro™, Hongkong Base For Information Technology).

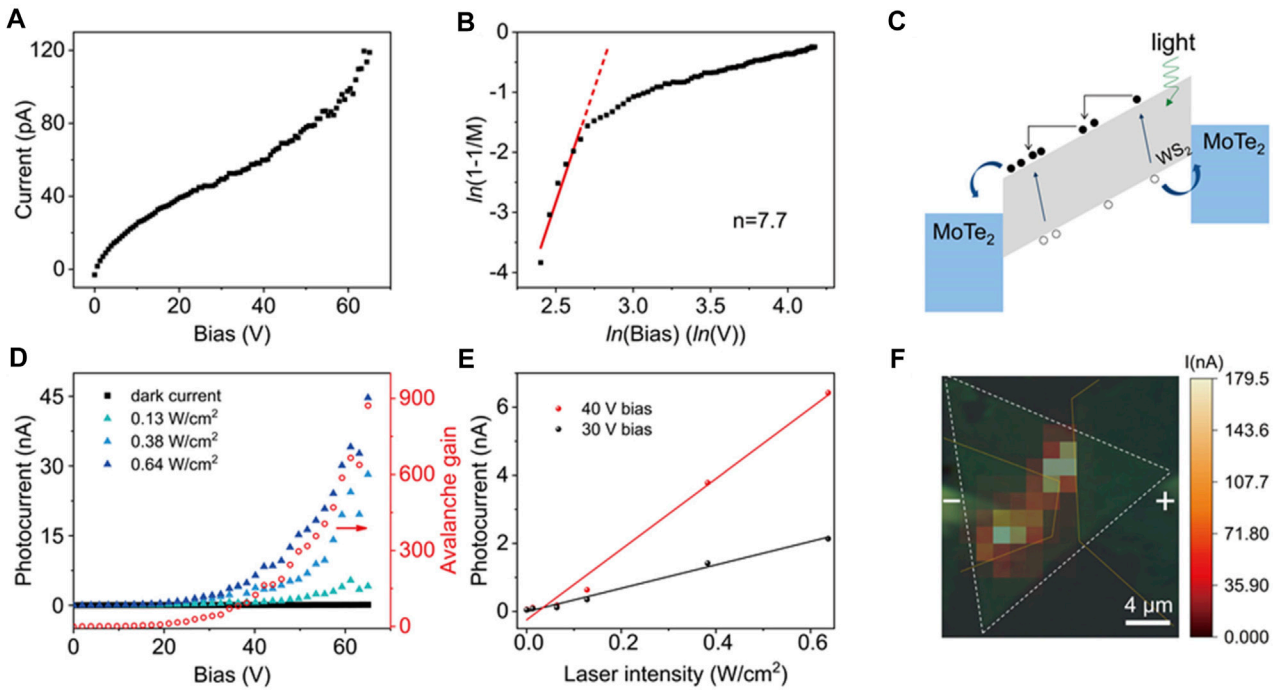

FIGURE 2 | Electrical and photocurrent characterizations of the $MoTe_2$–WS_2–$MoTe_2$ heterojunction device. **(A)** Dependence of dark current on bias voltage of the heterojunction device. **(B)** Relationship between ln(1−1/*M*) and ln(*V*). *M* is the multiplication factor. V is the bias voltage. Red dashed line is the linear fit. **(C)** Schematic showing the operation principle of the heterojunction device. **(D)** Photocurrent response of the $MoTe_2$–WS_2–$MoTe_2$ heterojunction device under different light illumination intensities. Red opened circles show the corresponding AGs upon an excitation intensity of 0.64 W/cm^2. The illumination wavelength is 532 nm. **(E)** Intensity-dependent photocurrent of the $MoTe_2$–WS_2–$MoTe_2$ heterojunction device. The applied bias voltages are 30 V (black) and 40 V (red). **(F)** Photocurrent mapping of $MoTe_2$–WS_2–$MoTe_2$ heterojunction device. White dashed lines mark out the WS_2 region. Yellow solid lines mark out the $MoTe_2$ region. Symbols "+" and "−" indicate the direction of the bias voltage.

RESULTS AND DISCUSSION

The configuration of the all-2D APD device is schematically shown in **Figure 1A**, which consists of a monolayer WS_2 overlaid onto two few-layer $MoTe_2$ flakes. The metallic $MoTe_2$ flakes act as electrodes in the APD. In this way two heterojunctions were formed at the overlapped regions between the WS_2 and $MoTe_2$. Afterwards, titanium and gold layers were consecutively deposited on the $MoTe_2$ flakes as electrodes for electrical readout. Optical microscope image of the APD is displayed in **Figure 1B**. The channel length (i.e., separation between the two $MoTe_2$ flakes) of the device is measured as 2 μm. The thickness of the WS_2 flake is 1.0 nm, and those of the two $MoTe_2$ flakes are 4.3 and 4.5 nm, respectively (**Supplementary Figure S1**, Supporting Information). The monolayer nature of the WS_2 can be further confirmed by Raman spectroscopy characterizations (**Figure 1C**). Two strong peaks are observed at 352 cm^{-1} and 418 cm^{-1}, corresponding to the 2LA(M) and $A_{1g}(\Gamma)$ modes of WS_2, respectively. The peak intensity ratio of 2LA(M)/$A_{1g}(\Gamma)$ can be determined as 6.6, which is a typical feature of monolayer WS_2 (Cong et al., 2014; Xu et al., 2015). For Raman spectrum collected from the $MoTe_2$ region, a small peak at 188.91 cm^{-1} can be observed, which is the B_g mode of $MoTe_2$ in 1T′ phase (Kan et al., 2015; Naylor et al., 2016; Chen et al., 2017). 1T′-$MoTe_2$ is a semimetal and a good candidate of 2D electrode material because of its low resistance and high carrier mobility (Zhang et al., 2014; Beams et al., 2016; Chen et al., 2016). Due to its strong exciton transition at room temperature, the pristine monolayer WS_2 exhibits a strong PL peak at 614 nm (**Figure 1D**). In contrast, because of its semimetal nature, negligible PL signal can be observed in the 1T′-$MoTe_2$ region. It is noted that in the heterostructure regions both the Raman and PL signals from WS_2 are reduced (**Figures 1C,D**). Such a phenomenon suggests intimate contact between the monolayer WS_2 and few-layer $MoTe_2$. Once the intimate contact is formed, the WS_2 excitons or lattice vibrations will transfer their energies to the $MoTe_2$ underneath through electromagnetic coupling. Subsequently, the lattice vibration energy or exciton energy will be dissipated by the impurities, defects, and free electrons in the semimetal layer. As a result, the Raman and PL signals of the WS_2 will be quenched.

Schottky junctions can be formed at the two heterojunctions between the semiconducting WS_2 and semimetal $MoTe_2$ layer. **Figure 2A** shows the dependence of current on bias voltage in a representative device. Specifically, the current increases along with the increase of bias voltage and saturates at 10.4 V. Afterwards, the current increases notably when the bias is further increased. Such bias voltage dependence is typical of Schottky diodes. Due to the Schottky barrier, the device exhibits a dark current as low as 93 pA under a bias voltage of 59 V. Such a dark current is much lower than many

photodetectors based on 2D materials and even lower than typical commercial APDs (**Table 1**). The Schottky barriers at the heterojunctions can trigger electron avalanche effect upon applying a large electrical field across the device. The current at 10.4 V (26 pA) is defined as the saturation current I_{sat}[59]. Bias voltages above 10.4 V will accelerate the charge carriers passing through the heterojunction, giving rise to ionization collisions of the lattice and generation of additional charge carriers, i.e., occurrence of electron avalanche effect. To further demonstrate the avalanche effect, a charge carrier multiplication factor, M, is defined as $M = I/I_{sat}$, with I the current above 10.4 V. When the avalanche effect occurs, parameter M will follow the behavior (Miller, 1957),

$$M = \frac{1}{1 - \left(\frac{V}{V_b}\right)^n} \tag{1}$$

where n represents ionization rate, V_b is a fitting parameter. **Equation (1)** can be rewritten as,

$$\ln\left(1 - \frac{1}{M}\right) = n\left[\ln(V) - \ln(V_b)\right] \tag{2}$$

suggesting a linear dependence of $\ln\left(1 - \frac{1}{M}\right)$ on $\ln(V)$. As shown in **Figure 2B**, for bias voltage above 10.4 V, $\ln\left(1 - \frac{1}{M}\right)$ varies linearly against $\ln(V)$, which is a direct indicator of avalanche carrier multiplication. By fitting the experimental data using **Eq. (2)**, the n and V_b are determined as 7.7 and 17.6 V. It is noted that the n in our $MoTe_2$–WS_2–$MoTe_2$ is about 6 times that of a previous report (Lei et al., 2015a), where Schottky junction was formed between a layered InSe and metal electrode ($n = 1.3$). The larger n and smaller V_b means that the avalanche effect is easier to be initiated in the $MoTe_2$–WS_2–$MoTe_2$ heterostructure. Moreover, once the avalanche effect is triggered, more electrons will be generated due to the larger M under a certain bias voltage. We ascribe these merits to the atomic thickness of our device, where a much larger electric field can be induced across the Schottky junction under a moderate bias.

The avalanche effect and small dark currents of the $MoTe_2$–WS_2–$MoTe_2$ heterostructure can greatly benefit photodetection. **Figure 2C** illustrates the operation principle of the heterostructure APD. Electron–hole pairs will be generated in both of the 2D layers and Schottky junctions upon light illumination. When a bias voltage is applied to initiate the avalanche effect, carrier multiplications will occur, giving rise to a rapid increase of the photocurrent with the applied bias. Additionally, a larger S/N ratio will be obtained as well. **Figure 2D** shows the current responses of the device measured in the dark and under 532-nm laser excitations of different intensities (green: 0.13 W/cm^2; cyan: 0.38 W/cm^2; blue: 0.64 W/cm^2). The dark current remains below 100 pA even when the bias voltage is above 60 V. In contrast, the photocurrent increases slowly with applied bias smaller than 10.4 V, then dramatically grows when the bias voltage become larger due to the avalanche effect. Moreover, the photocurrent increases against illumination intensity. By plotting the photocurrent as a function of the laser intensity, linear dependences can be observed at two typical bias voltages (30 and 40 V, **Figure 2E**) for laser intensity upto 0.64/cm^2.

R, EQE, and AG are three important parameters evaluating the performance of an APD. Specifically, R, EQE, and AG can be calculated according to the following formulae (Yu et al., 2013; Long et al., 2019),

$$\begin{cases} R = \dfrac{I_{ph}}{P_{in}} \\ EQE = \dfrac{I_{ph}hc}{P_{in}e\lambda} \\ AG = \dfrac{I_{ph} - I_{dark}}{I_{ph0} - I_{dark0}} \end{cases} \tag{3}$$

where I_{ph}, I_{dark}, and P_{in} represent photocurrent, dark current, and incidence light intensity, respectively. Parameter h is the Planck constant ($h = 6.62607015 \times 10^{-34}$ J s), c is the speed of light ($c = 2.99792458 \times 108$ m/s), e is quantity of a unit electric charge ($e = 1.602176634 \times 10^{-19}$ C), λ is wavelength of incidence light. Parameters I_{ph0} and I_{dark0} are the photocurrent and dark current before the occurrence of avalanche effect, respectively. In our analyses, I_{ph0} and I_{dark0} were taken at the bias of 10.4 V.

We evaluate the R, EQE, and AG of the heterojunction device with an illumination intensity of 0.64 W/cm^2. As shown in **Figure 2D**, the AG increases distinctly as a function of the bias voltage. At a bias of 59 V, the R and EQE are calculated to be 6.02 A/W and 1,406%, respectively, corresponding to an AG of 587. **Table 1** summarizes the performances of various 2D photodetectors, including APD and non-APD types, as well as typical APDs that are commercially available. It is seen that although the R of the $MoTe_2$–WS_2–$MoTe_2$ heterojunction device is moderate, its EQE and AG are among the best ones. In particular, the AG of the heterojunction device is much better than the listed commercial APDs can exhibit. Moreover, the dark current of our device is merely 93 pA at a bias of 59 V, which is at the lowest level among both of the 2D and commercial photodetectors. The normalized photocurrent-to-dark current ratio (NPDR) can be further calculated as NPDR = $R/I_{dark} = 6.47 \times 10^{10}$ W^{-1}, which is better than most of the 2D photodetectors can provide (**Table 1**). These results suggest that our 2D APD can provide an excellent S/N ratio and favor the detection of low-level signals.

Figure 2F shows a typical 2D photocurrent map of the $MoTe_2$–WS_2–$MoTe_2$ heterojunction APD. To avoid electrical breakdown of the device, a relatively small voltage of 25 V is applied to reversely bias the left Schottky junction. According to **Figure 2A**, such a bias can already trigger the avalanche effect. In addition, to induce strong enough photocurrent for the 2D mapping, a relatively large incidence intensity of 305.73 W/cm^2 was used. As shown in **Figure 2F**, photocurrent was visible near the left Schottky junction (reversely bias) and the channel region. However, negligible photocurrent can be found at the right Schottky junction which is forward biased. These observations can be understood by considering that in the avalanche regime, the photocurrent is proportional the magnitude of collision ionization. The photo-generated

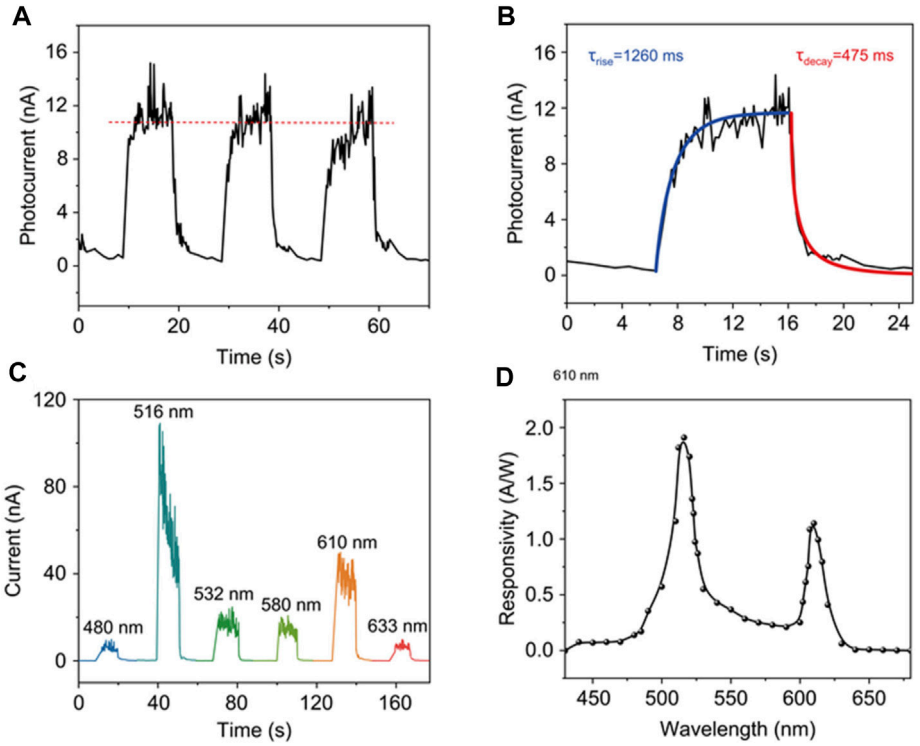

FIGURE 3 | Time- and spectrum-resolved photoresponses of the $MoTe_2$–WS_2–$MoTe_2$ heterojunction device. **(A)** Photocurrents of the device in response to three ON/OFF illumination cycles. The red dashed line suggests that the photocurrent maxima of the three cycles are the same. **(B)** Photocurrent of the device during one typical ON/OFF illumination cycle. Blue and red curves are fitting results by assuming that the rise and decay processes of the photocurrent are exponential dependences. **(C)** Representative switching behaviors of the heterojunction device under illuminations at 480, 516, 532, 580, 610, and 633 nm. **(D)** Photocurrent spectrum of the heterojunction device.

electrons in the reversely-biased Schottky junction and regions nearby will experience a longer acceleration path, which will therefore undergo more collision events. These additional collisions will generate more electrons, giving rise to stronger photocurrents.

Figure 3A illustrates the switching characteristic of the broadband photoresponse of $MoTe_2$–WS_2–$MoTe_2$ heterojunction APD under a bias voltage of 50 V at 532-nm excitation. The three ON/OFF cycles are similar with each other, suggesting that photodetection performance of our APD is repeatable. Response time (RT), which is another important parameter characterizing a photodetector, can be deduced from one typical cycle. As shown in **Figure 3B**, the RTs are revealed as 1,260 and 475 ms for the laser-on and–off processes, respectively. As an APD, the RTs of our heterojunction photodetector is ordinary among the 2D photodetectors (**Table 1**). The origin of such long RTs can be possibly due to introduction of carrier trapping centers during the device manufacturing processes. It is known that impurities and defects will be generated at the interface of the heterojunction by stacking different 2D materials *via* wet-transfer method (Rooney et al., 2017). These impurities and defects will act as trapping states for electrons and holes, which will increase the photocurrent gain but largely compromise the RT of the photodetectors (Hu et al., 2012; Lopez-Sanchez et al., 2013; Lei et al., 2015a; Lei et al., 2015b). To fasten the device responses, improvement of the device manufacturing processes is required.

We further study the broadband photocurrent performance of the $MoTe_2$–WS_2–$MoTe_2$ APD by illuminating the device at different wavelengths. To that end, the bias voltage was fixed at 30 V, the laser spot was focused onto the center of the left Schottky junction shown in **Figure 2F**. The incidence wavelength was selected by placing a specific narrowband optical filter in front of the exit of the supercontinuum laser. Representative switching behaviors of the APD illuminated at 480, 516, 532, 580, 610, and 633 nm are shown in **Figure 3C**. The device exhibits similar ON/OFF behaviors and same dark currents at different excitation wavelengths. Moreover, two clear photocurrent maxima were observed at 516 and 610 nm, respectively. This can be seen more clearly by plotting the R against illumination wavelength, i.e., the photocurrent spectrum (**Figure 3D**). The peak at 610 nm should correspond to the exciton-A transition in the monolayer WS_2, as corroborated with the PL spectrum shown in **Figure 1D**. The peak at 516 nm with a larger R can be ascribed to exciton-B in monolayer WS_2. The separation between the two photocurrent maxima is 0.37 eV, which is consistent with the splitting energy of the valence band minimum in WS_2 arising from the spin-orbit coupling at K (K′) valley (Zeng et al., 2013; Zhao et al., 2013; Zhu et al., 2015). Previous studies have demonstrated that the recombination rate of exciton-B is

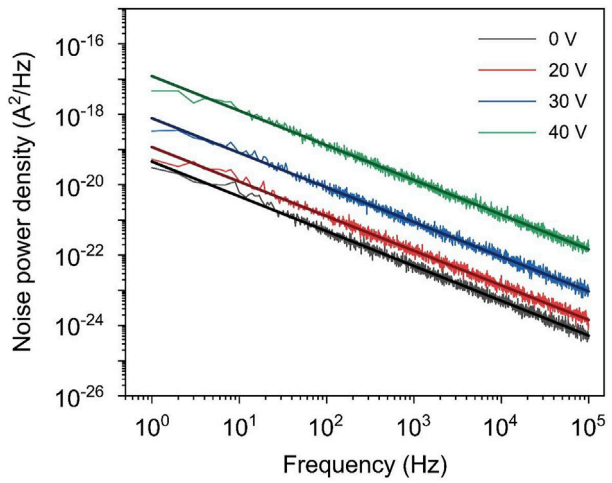

FIGURE 4 | Noise power spectra of the $MoTe_2$–WS_2–$MoTe_2$ heterojunction APD under different applied bias voltages. The black straight lines are linear fittings of the noise power spectra under different bias voltages.

much smaller than that of exciton-A, giving rise to a much lower PL quantum yield of exciton-B (Zeng et al., 2013; Zhao et al., 2013; Zhu et al., 2015). Accordingly, more photo-generated carriers will undergo avalanche multiplications under optical excitation associated with exciton-B, leading to a stronger photocurrent response. Another important observation is that the photocurrent response can extend to wavelengths larger than 614 nm, i.e., the exciton transition energy of WS_2. Such an effect can be ascribed to photo-generated electron transmitting over the Schottky barrier from the Fermi energy of the metallic $MoTe_2$[59]. On the basis of the photocurrent spectrum shown in **Figure 3D**, the Schottky barrier height can be extracted as 1.93 eV (**Supplementary Figure S2**, Supporting Information), corresponding to a wavelength of 642 nm. This low Schottky barrier height guarantees photocurrent response of the APD under optical excitation with energy smaller than the exciton transition energy of the monolayer WS_2.

With the knowledge of dark current, AG, RT, and M, the S/N ratio can be readily calculated according to (Lei et al., 2015a),

$$\begin{cases} \frac{S}{N} = \frac{I_{ph}^2}{\sigma^2} \\ \sigma^2 = 2e \times I_{dark} \times BW \times M^2 \end{cases} \quad (4)$$

where BW is the bandwidth. In a specific calculation, BW is set as inverse of the RT (Lei et al., 2015a). Under an illumination intensity of 0.64 W/cm^2 and a bias voltage of 59 V, the S/N ratio is calculated as 71 dB, which is 10 times larger than that of a 2D APD (60 dB) consisted of layered InSe and bulk metal electrode (Lei et al., 2015a). The enhanced S/N ratio in our device is attributed to its ultralow dark current even in the avalanche regime.

Finally, we characterized the current noise density of the $MoTe_2$–WS_2–$MoTe_2$ APD, whereby the noise equivalent power (NEP) and normalized detectivity (D*) can be calculated. **Figure 4** shows the low-frequency noise power spectra of the device under different applied bias voltages. The noise increases against the bias voltage. In addition, all of the four noise power spectra can be well fitted using the equation $S_n(f) = K\left(\frac{I_{dark}^{\beta}}{f^{\alpha}}\right)$ (Chang et al., 2011), where $S_n(f)$ is the spectral density of the noise power, K is a constant, and α and β are two fitting parameters. The fitting results suggest that the 1/*f* noise prevails at low frequencies (1–100 Hz) for our APD. The 1/*f* noise usually exists in 2D photodetectors (Balandin, 2013; Na et al., 2014), which is induced by the disorder or defects (Clément et al., 2010). By optimizing the fabrication processes, especially the stacking of the 2D crystals, it is expected that the 1/*f* noise can be further reduced.

By integrating $S_n(f)$ within a given bandwidth B (usually B is set as 1 Hz), the total noise current power can be expressed as (Chang et al., 2011),

$$\langle in^2 \rangle = \int_0^B S_n(f) df \quad (5)$$

The NEP and D* can thereafter be obtained as (Chang et al., 2011),

$$\begin{cases} NEP = \frac{\sqrt{\langle in^2 \rangle}}{R} \\ D* = \frac{\sqrt{A}\sqrt{B}}{NEP} \end{cases} \quad (6)$$

where A is the effective APD area used to normalized the noise, which is 294 μm^2 according to the triangular WS_2 region shown in **Figure 1B**. Parameter B is the test bandwidth which is set as 100 kHz. Therefore, for a bias voltage of 40 V, the corresponding NEP and D* are calculated as 7.49×10^{-11} W/Hz$^{0.5}$ and 7.24×10^9 Jones, respectively.

CONCLUSION

In summary, we successfully demonstrate an all-2D APD structure with ultralow dark current. By stacking a monolayer semiconducting WS_2 onto two few-layer semimetal $MoTe_2$ flakes, two back-to-back Schottky barriers were formed at the two heterojunctions between the WS_2 and $MoTe_2$. Due to the double Schottky barriers and good crystallinity of the 2D crystals, the fabricated device structure can exhibit excellent electrical avalanche effect. When operating in the avalanche regime, the heterojunction structure can act as an APD with improved photodetection performances and a remarkably low dark current. The EQE of our APD is 1,406%, with an AG of 587 and dark current as low as 93 pA. Moreover, due to the small Schottky barrier height, the 2D APD can operate in a broadband spectrum range from 400 to 700 nm. Further optimization of the APD performances is possible. For example, by selecting 2D crystals with favorable energy band structures and alignments, it is possible to establish proper Schottky barriers to further minimize the dark currents and expand the operation wavelength ranges. Additionally, by improving the processing

techniques of the 2D stacked heterostructures, one can reduce the *RT* and current noise. We therefore believe that the results obtain in the current study can pave the way for design and fabrication of miniaturized all-2D optoelectronic devices with supreme performances.

DATA AVAILABILITY STATEMENT

The original contributions presented in the study are included in the article/**Supplementary Material**, further inquiries can be directed to the corresponding author.

AUTHOR CONTRIBUTIONS

HC and SD conceived the study and supervised the project. TO fabricated the all-2D APD device and characterized the device performances. XW and SL helped prepare the samples and characterizations. TO, XW, SL, HC, and SD analyzed the data and discussed the results. The manuscript was written through contributions of all authors. All authors have given approval to the final version of the manuscript.

FUNDING

We acknowledge support from the National Key Basic Research Program of China (grant no. 2019YFA0210203), the National Natural Science Foundation of China (grant nos. 91963205 and 11904420), Guangdong Basic and Applied Basic Research Foundation (grant no. 2020A1515011329). HC acknowledges the support from Changjiang Young Scholar Program.

SUPPLEMENTARY MATERIAL

The Supplementary Material for this article can be found online at: https://www.frontiersin.org/articles/10.3389/fmats.2021.736180/full#supplementary-material

REFERENCES

Anderson, L. K., and McMurtry, B. J. (1966). High-Speed Photodetectors. *Proc. IEEE* 54 (10), 1335–1349. doi:10.1109/proc.1966.5121

Atalla, M. R. M., and Koester, S. J. (2017). "Black Phosphorus Avalanche Photodetector," in 75th Annual Device Research Conference (DRC), South Bend, IN, June 25–28, 2017.

Aull, B. F., Loomis, A. H., Young, D. J., Heinrichs, R. M., Felton, B. J., Daniels, P. J., et al. (2002). Geiger-Mode Avalanche Photodiodes for Three- Dimensional Imaging. *Lincoln Lab. J.* 13 (2), 335–350.

Balandin, A. A. (2013). Low-Frequency 1/f Noise in Graphene Devices. *Nat. Nanotech* 8 (8), 549–555. doi:10.1038/nnano.2013.144

Beams, R., Cançado, L. G., Krylyuk, S., Kalish, I., Kalanyan, B., Singh, A. K., et al. (2016). Characterization of Few-Layer 1T′ MoTe2 by Polarization-Resolved Second Harmonic Generation and Raman Scattering. *ACS Nano* 10 (10), 9626–9636. doi:10.1021/acsnano.6b05127

Bernardi, M., Palummo, M., and Grossman, J. C. (2013). Extraordinary Sunlight Absorption and One Nanometer Thick Photovoltaics Using Two-Dimensional Monolayer Materials. *Nano Lett.* 13 (8), 3664–3670. doi:10.1021/nl401544y

Britnell, L., Ribeiro, R. M., Eckmann, A., Jalil, R., Belle, B. D., Mishchenko, A., et al. (2013). Strong Light-Matter Interactions in Heterostructures of Atomically Thin Films. *Science* 340 (6138), 1311–1314. doi:10.1126/science.1235547

Burman, D., Ghosh, R., Santra, S., and Guha, P. K. (2016). Highly Proton Conducting MoS2/graphene Oxide Nanocomposite Based Chemoresistive Humidity Sensor. *RSC Adv.* 6 (62), 57424–57433. doi:10.1039/c6ra11961a

Chang, S.-P., Lu, C.-Y., Chang, S.-J., Chiou, Y.-Z., Hsueh, T.-J., and Hsu, C.-L. (2011). Electrical and Optical Characteristics of UV Photodetector with Interlaced ZnO Nanowires. *IEEE J. Select. Top. Quan. Electron.* 17 (4), 990–995. doi:10.1109/jstqe.2010.2046884

Chen, K., Chen, Z., Wan, X., Zheng, Z., Xie, F., Chen, W., et al. (2017). A Simple Method for Synthesis of High-Quality Millimeter-Scale 1T′ Transition-Metal Telluride and Near-Field Nanooptical Properties. *Adv. Mater.* 29 (38), 1–9. doi:10.1002/adma.201700704

Chen, S.-Y., Goldstein, T., Venkataraman, D., Ramasubramaniam, A., and Yan, J. (2016). Activation of New Raman Modes by Inversion Symmetry Breaking in Type II Weyl Semimetal Candidate T′-MoTe2. *Nano Lett.* 16 (9), 5852–5860. doi:10.1021/acs.nanolett.6b02666

Cheng, R., Li, D., Zhou, H., Wang, C., Yin, A., Jiang, S., et al. (2014). Electroluminescence and Photocurrent Generation from Atomically Sharp WSe2/MoS2 Heterojunction P-N Diodes. *Nano Lett.* 14 (10), 5590–5597. doi:10.1021/nl502075n

Choi, K., Lee, Y. T., Kim, J. S., Min, S.-W., Cho, Y., Pezeshki, A., et al. (2016). Non-Lithographic Fabrication of All-2D α-MoTe2Dual Gate Transistors. *Adv. Funct. Mater.* 26 (18), 3146–3153. doi:10.1002/adfm.201505346

Chuang, H.-J., Chamlagain, B., Koehler, M., Perera, M. M., Yan, J., Mandrus, D., et al. (2016). Low-Resistance 2D/2D Ohmic Contacts: A Universal Approach to High-Performance WSe2, MoS2, and MoSe2 Transistors. *Nano Lett.* 16 (3), 1896–1902. doi:10.1021/acs.nanolett.5b05066

Clément, N., Nishiguchi, K., Fujiwara, A., and Vuillaume, D. (2010). One-by-One Trap Activation in Silicon Nanowire Transistors. *Nat. Commun.* 1 (1), 92. doi:10.1038/ncomms1092

Cong, C., Shang, J., Wu, X., Cao, B., Peimyoo, N., Qiu, C., et al. (2014). Synthesis and Optical Properties of Large-Area Single-Crystalline 2D Semiconductor WS2Monolayer from Chemical Vapor Deposition. *Adv. Opt. Mater.* 2 (2), 131–136. doi:10.1002/adom.201300428

Faramarzpour, N., Deen, M. J., Shirani, S., and Fang, Q. (2008). Fully Integrated Single Photon Avalanche Diode Detector in Standard CMOS 0.18- μm Technology. *IEEE Trans. Electron. Devices* 55 (3), 760–767. doi:10.1109/ted.2007.914839

Ferraro, M. S., Clark, W. R., Rabinovich, W. S., Mahon, R., Murphy, J. L., Goetz, P. G., et al. (2015). InAlAs/InGaAs Avalanche Photodiode Arrays for Free Space Optical Communication. *Appl. Opt.* 54 (31), F182–F188. doi:10.1364/ao.54.00f182

Gong, C., Colombo, L., Wallace, R. M., and Cho, K. (2014). The Unusual Mechanism of Partial Fermi Level Pinning at Metal-MoS2 Interfaces. *Nano Lett.* 14 (4), 1714–1720. doi:10.1021/nl403465v

Guo, H., Lan, C., Zhou, Z., Sun, P., Wei, D., and Li, C. (2017). Transparent, Flexible, and Stretchable WS2 Based Humidity Sensors for Electronic Skin. *Nanoscale* 9 (19), 6246–6253. doi:10.1039/c7nr01016h

Hu, P., Wen, Z., Wang, L., Tan, P., and Xiao, K. (2012). Synthesis of Few-Layer GaSe Nanosheets for High Performance Photodetectors. *ACS Nano* 6 (7), 5988–5994. doi:10.1021/nn300889c

Huntington, A. S., Compton, M. A., and Williams, G. M. (2007). "Linear-Mode Single-Photon APD Detectors," in Proceeding of SPIE, South Bend, IN, June 25–28, 2017, 6771.

Jia, J., Jeon, J., Park, J. H., Lee, B. H., Hwang, E., and Lee, S. (2019). Avalanche Carrier Multiplication in Multilayer Black Phosphorus and Avalanche Photodetector. *Small* 15 (38), 1805352. doi:10.1002/smll.201805352

Johnson, K. M. (1965). High-Speed Photodiode Signal Enhancement at Avalanche Breakdown Voltage. *IEEE Trans. Electron. Devices* 12 (2), 55–63. doi:10.1109/t-ed.1965.15453

Kan, M., Nam, H. G., Lee, Y. H., and Sun, Q. (2015). Phase Stability and Raman Vibration of the Molybdenum Ditelluride (MoTe2) Monolayer. *Phys. Chem. Chem. Phys.* 17 (22), 14866–14871. doi:10.1039/c5cp01649e

Keum, D. H., Cho, S., Kim, J. H., Choe, D.-H., Sung, H.-J., Kan, M., et al. (2015). Bandgap Opening in Few-Layered Monoclinic MoTe2. *Nat. Phys* 11 (6), 482–486. doi:10.1038/nphys3314

Kim, C., Moon, I., Lee, D., Choi, M. S., Ahmed, F., Nam, S., et al. (2017). Fermi Level Pinning at Electrical Metal Contacts of Monolayer Molybdenum Dichalcogenides. *ACS Nano* 11 (2), 1588–1596. doi:10.1021/acsnano.6b07159

Lei, S., Wen, F., Ge, L., Najmaei, S., George, A., Gong, Y., et al. (2015). An Atomically Layered InSe Avalanche Photodetector. *Nano Lett.* 15 (5), 3048–3055. doi:10.1021/acs.nanolett.5b00016

Lei, S., Wen, F., Li, B., Wang, Q., Huang, Y., Gong, Y., et al. (2015). Optoelectronic Memory Using Two-Dimensional Materials. *Nano Lett.* 15 (1), 259–265. doi:10.1021/nl503505f

Liu, L., Xu, N., Zhang, Y., Zhao, P., Chen, H., and Deng, S. (2019). Van der Waals Bipolar Junction Transistor Using Vertically Stacked Two-Dimensional Atomic Crystals. *Adv. Funct. Mater.* 29 (17), 1807893. doi:10.1002/adfm.201807893

Liu, Y., Forrest, S. R., Hladky, J., Lange, M. J., Olsen, G. H., and Ackley, D. E. (1992). A Planar InP/InGaAs Avalanche Photodiode with Floating Guard Ring and Double Diffused Junction. *J. Lightwave Technol.* 10 (2), 182–193. doi:10.1109/50.120573

Liu, Y., Wu, H., Cheng, H.-C., Yang, S., Zhu, E., He, Q., et al. (2015). Toward Barrier Free Contact to Molybdenum Disulfide Using Graphene Electrodes. *Nano Lett.* 15 (5), 3030–3034. doi:10.1021/nl504957p

Long, M., Wang, P., Fang, H., and Hu, W. (2019). Progress, Challenges, and Opportunities for 2D Material Based Photodetectors. *Adv. Funct. Mater.* 29 (19), 1803807. doi:10.1002/adfm.201803807

Lopez-sanchez, O., Dumcenco, D., Charbon, E., and Kis, A. (2014). *Avalanche Photodiodes Based on MoS_2/Si Heterojunctions*. Lausanne, Switzerland: arXiv. arXiv:1411.3232.

Lopez-Sanchez, O., Lembke, D., Kayci, M., Radenovic, A., and Kis, A. (2013). Ultrasensitive Photodetectors Based on Monolayer MoS2. *Nat. Nanotech.* 8 (7), 497–501. doi:10.1038/nnano.2013.100

Luo, W., Cao, Y., Hu, P., Cai, K., Feng, Q., Yan, F., et al. (2015). Gate Tuning of High-Performance InSe-Based Photodetectors Using Graphene Electrodes. *Adv. Opt. Mater.* 3 (10), 1418–1423. doi:10.1002/adom.201500190

Massicotte, M., Schmidt, P., Vialla, F., Schädler, K. G., Reserbat-Plantey, A., Watanabe, K., et al. (2016). Picosecond Photoresponse in Van Der Waals Heterostructures. *Nat. Nanotech.* 11 (1), 42–46. doi:10.1038/nnano.2015.227

Miller, S. L. (1957). Ionization Rates for Holes and Electrons in Silicon. *Phys. Rev.* 105 (4), 1246–1249. doi:10.1103/physrev.105.1246

Mittendorff, M., Winnerl, S., Kamann, J., Eroms, J., Weiss, D., Schneider, H., et al. (2013). Ultrafast Graphene-Based Broadband THz Detector. *Appl. Phys. Lett.* 103 (2), 021113. doi:10.1063/1.4813621

Mudd, G. W., Svatek, S. A., Hague, L., Makarovsky, O., Kudrynskyi, Z. R., Mellor, C. J., et al. (2015). High Broad-Band Photoresponsivity of Mechanically Formed InSe-Graphene Van Der Waals Heterostructures. *Adv. Mater.* 27 (25), 3760–3766. doi:10.1002/adma.201500889

Na, J., Lee, Y. T., Lim, J. A., Hwang, D. K., Kim, G.-T., Choi, W. K., et al. (2014). Few-Layer Black Phosphorus Field-Effect Transistors with Reduced Current Fluctuation. *ACS Nano* 8 (11), 11753–11762. doi:10.1021/nn5052376

Naylor, C. H., Parkin, W. M., Ping, J., Gao, Z., Zhou, Y. R., Kim, Y., et al. (2016). Monolayer Single-Crystal 1T′-MoTe2 Grown by Chemical Vapor Deposition Exhibits Weak Antilocalization Effect. *Nano Lett.* 16 (7), 4297–4304. doi:10.1021/acs.nanolett.6b01342

Padilha, J. E., Miwa, R. H., Da Silva, A. J. R., and Fazzio, A. (2017). Two-Dimensional Van Der Waals P-N Junction of InSe/Phosphorene. *Phys. Rev. B* 95 (19), 2–7. doi:10.1103/physrevb.95.195143

Ren, M., Gu, X., Liang, Y., Kong, W., Wu, E., Wu, G., et al. (2011). Laser Ranging at 1550 Nm with 1-GHz Sine-Wave Gated InGaAs/InP APD Single-Photon Detector. *Opt. Express* 19 (14), 13497–13502. doi:10.1364/oe.19.013497

Rooney, A. P., Kozikov, A., Rudenko, A. N., Prestat, E., Hamer, M. J., Withers, F., et al. (2017). Observing Imperfection in Atomic Interfaces for Van Der Waals Heterostructures. *Nano Lett.* 17 (9), 5222–5228. doi:10.1021/acs.nanolett.7b01248

Shang, Y., Li, G., Liu, W., and Ning, Z. (2018). Quasi-2D Inorganic CsPbBr3Perovskite for Efficient and Stable Light-Emitting Diodes. *Adv. Funct. Mater.* 28 (22), 1801193. doi:10.1002/adfm.201801193

Shim, J., Oh, A., Kang, D.-H., Oh, S., Jang, S. K., Jeon, J., et al. (2016). High-Performance 2D Rhenium Disulfide (ReS2) Transistors and Photodetectors by Oxygen Plasma Treatment. *Adv. Mater.* 28 (32), 6985–6992. doi:10.1002/adma.201601002

Shokri, A., and Salami, N. (2016). Gas Sensor Based on MoS2 Monolayer. *Sensors Actuators B. Chem.* 236, 378–385. doi:10.1016/j.snb.2016.06.033

Tan, H., Fan, Y., Zhou, Y., Chen, Q., Xu, W., and Warner, J. H. (2016). Ultrathin 2D Photodetectors Utilizing Chemical Vapor Deposition Grown WS2 with Graphene Electrodes. *ACS Nano* 10 (8), 7866–7873. doi:10.1021/acsnano.6b03722

Tan, H., Xu, W., Sheng, Y., Lau, C. S., Fan, Y., Chen, Q., et al. (2017). Lateral Graphene-Contacted Vertically Stacked WS_2/MoS_2 Hybrid Photodetectors with Large Gain. *Adv. Mater.* 29 (46), 1–8. doi:10.1002/adma.201702917

Tao, Y., Wu, X., Wang, W., and Wang, J. (2015). Flexible Photodetector from Ultraviolet to Near Infrared Based on a SnS2 Nanosheet Microsphere Film. *J. Mater. Chem. C* 3 (6), 1347–1353. doi:10.1039/c4tc02325k

Vo-Dinh, T., Wang, H. N., and Scaffidi, J. (2010). Plasmonic Nanoprobes for SERS Biosensing and Bioimaging. *J. Biophoton.* 3 (1-2), 89–102. doi:10.1002/jbio.200910015

Vu, Q. A., Lee, J. H., Nguyen, V. L., Shin, Y. S., Lim, S. C., Lee, K., et al. (2017). Tuning Carrier Tunneling in Van Der Waals Heterostructures for Ultrahigh Detectivity. *Nano Lett.* 17 (1), 453–459. doi:10.1021/acs.nanolett.6b04449

Wang, L., Jie, J., Shao, Z., Zhang, Q., Zhang, X., Wang, Y., et al. (2015). MoS2/Si Heterojunction with Vertically Standing Layered Structure for Ultrafast, High-Detectivity, Self-Driven Visible-Near Infrared Photodetectors. *Adv. Funct. Mater.* 25 (19), 2910–2919. doi:10.1002/adfm.201500216

Wang, Q., Zhou, C., and Chai, Y. (2020). Breaking Symmetry in Device Design for Self-Driven 2D Material Based Photodetectors. *Nanoscale* 12 (15), 8109–8118. doi:10.1039/d0nr01326a

Wang, S., Wang, J., Zhao, W., Giustiniano, F., Chu, L., Verzhbitskiy, I., et al. (2017). Efficient Carrier-to-Exciton Conversion in Field Emission Tunnel Diodes Based on MIS-Type Van Der Waals Heterostack. *Nano Lett.* 17 (8), 5156–5162. doi:10.1021/acs.nanolett.7b02617

Wei, X., Yan, F., Lv, Q., Shen, C., and Wang, K. (2017). Fast Gate-tunable Photodetection in the Graphene Sandwiched WSe2/GaSe Heterojunctions. *Nanoscale* 9 (24), 8388–8392. doi:10.1039/c7nr03124f

Wei, X., Yan, F., Lv, Q., Zhu, W., Hu, C., Patanè, A., et al. (2019). Enhanced Photoresponse in $MoTe_2$ Photodetectors with Asymmetric Graphene Contacts. *Adv. Opt. Mater.* 7 (12), 1–8. doi:10.1002/adom.201900190

Wen, J., Wang, H., Wang, W., Deng, Z., Zhuang, C., Zhang, Y., et al. (2017). Room-Temperature Strong Light-Matter Interaction with Active Control in Single Plasmonic Nanorod Coupled with Two-Dimensional Atomic Crystals. *Nano Lett.* 17 (8), 4689–4697. doi:10.1021/acs.nanolett.7b01344

Withers, F., Del Pozo-Zamudio, O., Mishchenko, A., Rooney, A. P., Gholinia, A., Watanabe, K., et al. (2015). Light-Emitting Diodes by Band-Structure Engineering in Van Der Waals Heterostructures. *Nat. Mater* 14 (3), 301–306. doi:10.1038/nmat4205

Wohnhaas, C., Mailänder, V., Dröge, M., Filatov, M. A., Busko, D., Avlasevich, Y., et al. (2013). Triplet-Triplet Annihilation Upconversion Based Nanocapsules for Bioimaging Under Excitation by Red and Deep-Red Light. *Macromol. Biosci.* 13 (10), 1422–1430. doi:10.1002/mabi.201300149

Wu, G., Wang, X., Chen, Y., Wu, S., Wu, B., Jiang, Y., et al. (2020). $MoTe_2$ P–N Homojunctions Defined by Ferroelectric Polarization. *Adv. Mater.* 32 (16), 1–8. doi:10.1002/adma.201907937

Xu, Z.-Q., Zhang, Y., Lin, S., Zheng, C., Zhong, Y. L., Xia, X., et al. (2015). Synthesis and Transfer of Large-Area Monolayer WS2 Crystals: Moving Toward the Recyclable Use of Sapphire Substrates. *ACS Nano* 9 (6), 6178–6187. doi:10.1021/acsnano.5b01480

Yang, Y., Jeon, J., Park, J.-H., Jeong, M. S., Lee, B. H., Hwang, E., et al. (2019). Plasmonic Transition Metal Carbide Electrodes for High-Performance InSe Photodetectors. *ACS Nano* 13 (8), 8804–8810. doi:10.1021/acsnano.9b01941

Yao, J., and Yang, G. (2018). Flexible and High-Performance All-2D Photodetector for Wearable Devices. *Small* 14 (21), 2–9. doi:10.1002/smll.201704524

Yoon, J., Park, W., Bae, G. Y., Kim, Y., Jang, H. S., Hyun, Y., et al. (2013). Highly Flexible and Transparent Multilayer MoS_2 Transistors with Graphene Electrodes. *Small* 9 (19), 3295–3300. doi:10.1002/smll.201370112

Yu, J., Shan, C. X., Huang, X. M., Zhang, X. W., Wang, S. P., and Shen, D. Z. (2013). ZnO-Based Ultraviolet Avalanche Photodetectors. *J. Phys. D. Appl. Phys.* 46 (30), 305105. doi:10.1088/0022-3727/46/30/305105

Yu, W., Li, S., Zhang, Y., Ma, W., Sun, T., Yuan, J., et al. (2017). Near-Infrared Photodetectors Based on $MoTe_2$/Graphene Heterostructure with High Responsivity and Flexibility. *Small* 13 (24), 1–8. doi:10.1002/smll.201700268

Zeng, H., Liu, G.-B., Dai, J., Yan, Y., Zhu, B., He, R., et al. (2013). Optical Signature of Symmetry Variations and Spin-Valley Coupling in Atomically Thin Tungsten Dichalcogenides. *Sci. Rep.* 3 (1), 1608. doi:10.1038/srep01608

Zeng, L. H., Wu, D., Lin, S. H., Xie, C., Yuan, H. Y., Lu, W., et al. (2019). Controlled Synthesis of 2D Palladium Diselenide for Sensitive Photodetector Applications. *Adv. Funct. Mater.* 29 (1), 1–9. doi:10.1002/adfm.201970005

Zhang, K., Fang, X., Wang, Y., Wan, Y., Song, Q., Zhai, W., et al. (2017). Ultrasensitive Near-Infrared Photodetectors Based on a Graphene-MoTe2-Graphene Vertical van der Waals Heterostructure. *ACS Appl. Mater. Inter.* 9 (6), 5392–5398. doi:10.1021/acsami.6b14483

Zhang, W., Huang, Z., Zhang, W., and Li, Y. (2014). Two-Dimensional Semiconductors with Possible High Room Temperature Mobility. *Nano Res.* 7 (12), 1731–1737. doi:10.1007/s12274-014-0532-x

Zhang, Y., Zhang, Y., Ji, Q., Ju, J., Yuan, H., Shi, J., et al. (2013). Controlled Growth of High-Quality Monolayer WS2 Layers on Sapphire and Imaging its Grain Boundary. *ACS Nano* 7 (10), 8963–8971. doi:10.1021/nn403454e

Zhao, W., Ghorannevis, Z., Chu, L., Toh, M., Kloc, C., Tan, P.-H., et al. (2013). Evolution of Electronic Structure in Atomically Thin Sheets of WS2 and WSe2. *ACS Nano* 7 (1), 791–797. doi:10.1021/nn305275h

Zheng, Z., Sun, F., Huang, W., Jiang, J., Zhan, R., Ke, Y., et al. (2020). Phonon Polaritons in Twisted Double-Layers of Hyperbolic Van Der Waals Crystals. *Nano Lett.* 20 (7), 5301–5308. doi:10.1021/acs.nanolett.0c01627

Zhu, B., Chen, X., and Cui, X. (2015). Exciton Binding Energy of Monolayer WS_2. *Sci. Rep.* 5 (1), 9218. doi:10.1038/srep09218

Conflict of Interest: The authors declare that the research was conducted in the absence of any commercial or financial relationships that could be construed as a potential conflict of interest.

The reviewer LS declared a past co-authorship with one of the authors HC to the handling Editor.

Publisher's Note: All claims expressed in this article are solely those of the authors and do not necessarily represent those of their affiliated organizations, or those of the publisher, the editors and the reviewers. Any product that may be evaluated in this article, or claim that may be made by its manufacturer, is not guaranteed or endorsed by the publisher.

frontiers in Materials

ORIGINAL RESEARCH
published: 09 August 2021
doi: 10.3389/fmats.2021.731627

Nonlinear Buckling of Fixed Functionally Graded Material Arches Under a Locally Uniformly Distributed Radial Load

Hanwen Lu[1], *Jinman Zhou*[1], *Zhicheng Yang*[2]*, *Airong Liu*[3]* and *Jian Zhu*[1]

[1]School of Transportation, Civil Engineering and Architecture, Foshan University, Foshan, China, [2]College of Urban and Rural Construction, Zhongkai University of Agriculture and Engineering, Guangzhou, China, [3]Guangzhou University-Tamkang University Joint Research Centre for Engineering Structure Disaster Prevention and Control, Guangzhou University, Guangzhou, China

Functionally graded material (FGM) arches may be subjected to a locally radial load and have different material distributions leading to different nonlinear in-plane buckling behavior. Little studies is presented about effects of the type of material distributions on the nonlinear in-plane buckling of FGM arches under a locally radial load in the literature insofar. This paper focuses on investigating the nonlinear in-plane buckling behavior of fixed FGM arches under a locally uniformly distributed radial load and incorporating effects of the type of material distributions. New theoretical solutions for the limit point buckling load and bifurcation buckling loads and nonlinear equilibrium path of the fixed FGM arches under a locally uniformly distributed radial load that are subjected to three different types of material distributions are derived. The comparisons between theoretical and ANSYS results indicate that the theoretical solutions are accurate. In addition, the critical modified geometric slendernesses of FGM arches related to the switches of buckling modes are also derived. It is found that the type of material distributions of the fixed FGM arches affects the limit point buckling loads and bifurcation buckling loads as well as the nonlinear equilibrium path significantly. It is also found that the limit point buckling load and bifurcation buckling load increase with an increase of the modified geometric slenderness, the localized parameter and the proportional coefficient of homogeneous ceramic layer as well as a decrease of the power-law index p of material distributions of the FGM arches.

Keywords: functionally graded material, fixed arch, limit point buckling, bifurcation buckling, critical modified geometric slenderness

OPEN ACCESS

Edited by:
Lin Xu,
Jilin University, China

Reviewed by:
Man-Tai Chen,
Shanghai Jiao Tong University, China
Qiang Feng,
Shandong University of Science and Technology, China

***Correspondence:**
Zhicheng Yang
zhicheng.yang@zhku.edu.cn
Airong Liu
liuar@gzhu.edu.cn

Specialty section:
This article was submitted to Mechanics of Materials, a section of the journal Frontiers in Materials

Received: *28 June 2021*
Accepted: *27 July 2021*
Published: *09 August 2021*

Citation:
Lu H, Zhou J, Yang Z, Liu A and Zhu J (2021) Nonlinear Buckling of Fixed Functionally Graded Material Arches Under a Locally Uniformly Distributed Radial Load. Front. Mater. 8:731627. doi: 10.3389/fmats.2021.731627

INTRODUCTION

Arch structure has been widely used in the practice, because of the unique characteristics about aesthetics and safety. Arch structure is often subjected to different forms of load and different boundary constraints in practical engineering, which may lead to structural damage of arches. (Timoshenko et al., 1962), (Schreyer, 1972) and (Plaut and Raymond, 1990) started the research of arches early. Then, (Bradford et al., 2002) researched the in-plane buckling behavior of symmetrical cross-section arches under a central point load. (Pi et al., 2002) used an energy method to build the nonlinear equilibrium equation and the buckling equilibrium equation of arches, and the analytical

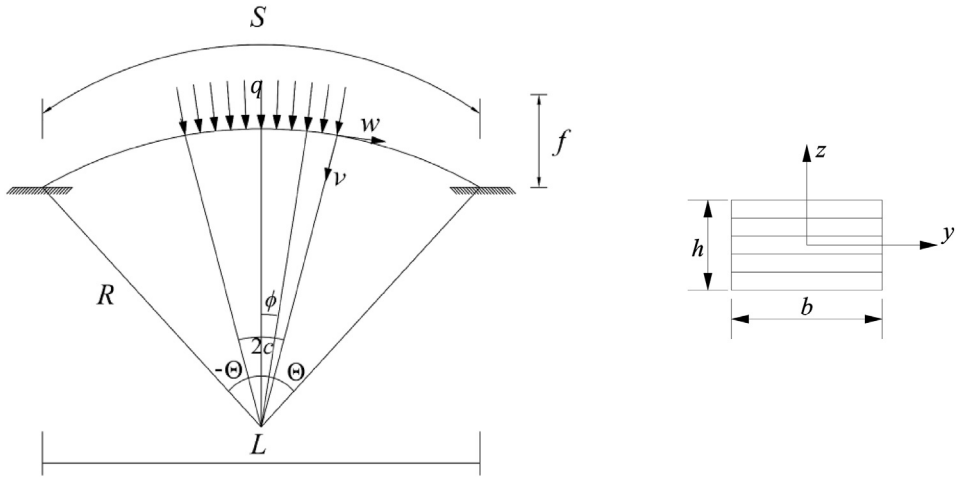

FIGURE 1 | FGM arch under a locally uniformly distributed radial load.

result of nonlinear buckling was obtained. (Pi et al., 2008) also presented a theoretical research on the nonlinear in-plane buckling of pin-ended circular arches subjected to a central point load with rotational restraints elastic end. (Pi and Bradford, 2009) developed the virtual work approach was used to establish post-buckling equilibrium differential equation and the nonlinear buckling, and the exact solution of the nonlinear bifurcations. (Cai and Feng, 2010) carried out the in-plane buckling of parabolic arches whose rotational stiffness of supports increases according to loaded. (Cai et al., 2012) carried out the buckling equations and nonlinear equilibrium by virtual work principal method. (Cai et al., 2013) also analyzed the buckling equilibrium path according to the bistable strut by using fixed arches subjected to a central point load. According to the principle of virtual work, (Han et al., 2016) studied the in-plane nonlinear buckling behavior of circular arches with elastic horizontal supports under a uniform radial load. (Yan et al., 2017) made an analytical study about the non-uniform shallow arch subjected to a central point load. (Pi et al., 2017) revealed in-plane buckling of fixed shallow circular arches with the arbitrary radial point load. (Lu et al., 2018) explored the nonlinear in-plane buckling and post-buckling behavior of the fixed arches subjected to a localized uniform radial load. (Lu et al., 2020) also explored effects of movement and rotation of supports on nonlinear instability of fixed shallow arches under a localized uniform radial load. (Hu et al., 2021) presented an analytical investigates for nonlinear buckling of pin-ended arch-beam structures. In addition to the optimization of the cross section can make the stability of the structure better (Chen and Young, 2021; Chen et al., 2021), the improvement of material engineering technology also can make the stability of the structure better.

Most of the arches studied in the above literatures are homogeneous solid materials, however, functionally graded material (FGM) has been widely used because their mechanical properties are better than those of homogeneous materials in recent years. FGM arches are usually composed of two or more materials, which can contribute to the superior performance of each material, but the stress and buckling of FGM arches become complicated. (Bateni and Eslami, 2015) conducted nonlinear buckling behavior of FG circular arches under the uniformly radial load using an analytical method. (Simsek, 2016) assumed the material properties of the beam vary as the power-law form in both axial and thickness directions. (Al-shujairi and Mollamahmutoğlu, 2018) concerned with the sandwich FG micro-beams is made of the ceramic-metal FG skin and homogenous ceramic core, based on the classical rule and the Mori-Tanaka homogenization scheme of composite material properties of the part of the FG sandwich size according to beam changes continuously by the thickness of the beam. For different boundary condition analysis, (Bateni and Eslami, 2014) explored the nonlinear in-plane buckling behavior of FGMs arches. Simply supported–simply supported and clamped–clamped boundary conditions are considered as two types of well-known symmetric boundary conditions for this analysis. (Simsek, 2016) investigated first two-dimensional FGM to research the buckling of beams with different boundary conditions, using adding auxiliary functions the boundary conditions are met. For different load form analysis, (Rastgo et al., 2005) explored the spatial buckling of pinned FGM arches being subjected to a thermal loading for using the Galerkin method. (Song and Li, 2008) using Kirchhoff" s assumption conducted nonlinear governing equations of FG arches under thermal and mechanical loads. (Asgari et al., 2014) focused the nonlinear thermo-elastic behavior of pin-ended FGM arches. The stability equation of the nonlinear primary equilibrium path was developed using adjacent equilibrium criterion. (Moita et al., 2018) studied the discrete model of the structural by the theory of high order shear deformation, and the finite element formulation is carried out to meet general FGM plate-shell type structures. (Yang et al., 2020a; Yang et al., 2020b; Yang et al., 2020c; Yang et al., 2021a; Yang et al., 2021b) have published a series of papers on in-plane buckling and free vibrations of functionally graded composite arches with

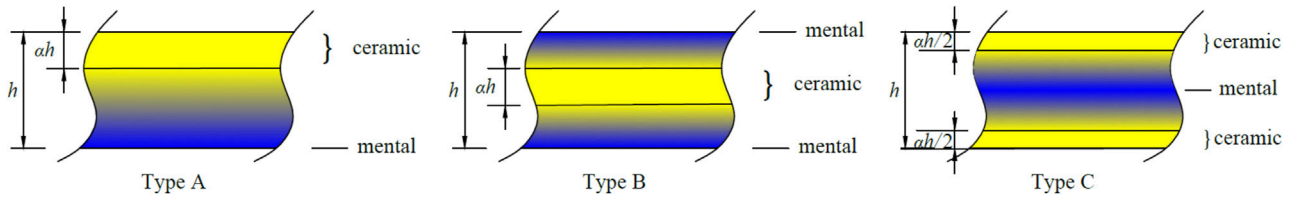

FIGURE 2 | Type A, Type B and Type C of material distributions of FGM arch.

graphene reinforcements. However, FGM arches may be subjected to a locally radial load and have different material distributions leading to different nonlinear in-plane buckling behavior. Little studies is presented about effects of the type of material distributions on the nonlinear in-plane buckling of FGM arches under a locally radial load in the literature.

This paper, therefore, aims at studying the in-plane buckling of a fixed functionally graded material arch under a locally uniformly distributed radial load incorporating effects of the type of material distributions. To illustrate the nonlinear in-plane buckling behavior of FGM arches, three types of material distributions containing functionally graded material layer and homogeneous material layer are considered. Theoretical solutions for the limit point buckling load and bifurcation buckling loads and nonlinear equilibrium path of the fixed FGM arches under a locally uniformly distributed radial load that are subjected to three different types of material distributions are derived. Comparisons with the ANSYS results present the theoretical solutions are enough accurate. The critical modified geometric slendernesses of FGM arches that are switches of buckling modes are also derived. In addition, the effects of the proportional coefficient of homogeneous ceramic layer, the type and power-law index p of material distributions on the buckling load and critical modified geometric slendernesses are discussed and examined.

MATERIAL DISTRIBUTION OF FUNCTIONALLY GRADED MATERIAL ARCHES

The FGM shallow arches under a locally uniformly distributed radial load q with a central angle 2Θ, and radius R and length S are made from ceramic Al_2O_3 and metal Al, as shown in **Figure 1**. In addition, $2c$ represents the subtended angle of the arch segment where the locally uniformly distributed radial load acts, also as shown in **Figure 1**. The total cross-sectional thickness and width are h and b, respectively.

In this research, the metal-ceramic material Al-Al_2O_3 is adopted. According to power-law function, the FGM arch through the thickness are graded continuously as

$$\Xi = \Xi_m V_m + \Xi_c V_c, \tag{1}$$

where Ξ_c and Ξ_m are the properties of ceramic and metal, respectively. V_c and V_m is the volume fraction of ceramic and metal, and they meet the following conditions as

$$V_m + V_c = 1. \tag{2}$$

In order to illustrate the nonlinear in-plane buckling behavior of FGM arches, three types of material distributions containing functionally graded material layer and homogeneous material layer are considered, including Type A, Type B, and Type C as shown in **Figure 2**. The cross-section of Type A represents that the top layer is the metal layer with the thickness αh and the material distributions of bottom layer is that the weight fraction of metal increase from the top surface to the bottom and the weight fraction of ceramic decrease from the top surface to the bottom surface. The cross-section of Type B have three layers, the middle layer of Type B is the metal layer with the thickness αh, the top and bottom layers of Type B is symmetric about the midline of the cross-section, and the material distributions of bottom layer of Type B is same to the bottom layer of Type A. The cross-section of Type C have four layers, the top and the bottom layers of Type C is the metal layer with the thickness $\alpha h/2$, the second and third layers of Type B is symmetric about the midline of the cross-section, and the material distributions of the second layer of Type C is same to the bottom layer of Type A.

The volume fractions V_c for three distribution modes that are shown in **Figure 2** are expressed as

$$\text{Type A}: V_c = \begin{cases} \left[\dfrac{z+0.5h}{(1-\alpha)h}\right]^p & -0.5h \le z \le (0.5-\alpha)h \\ 1 & (0.5-\alpha)h \le z \le 0.5h \end{cases}, \tag{3}$$

$$\text{Type B}: V_c = \begin{cases} \left[\dfrac{z+0.5h}{0.5(1-\alpha)h}\right]^p & -0.5h \le z \le -0.5\alpha h \\ 1 & -0.5\alpha h \le z \le 0.5\alpha h \\ \left[\dfrac{-z+0.5h}{0.5(1-\alpha)h}\right]^p & 0.5\alpha h \le z \le 0.5h \end{cases}, \tag{4}$$

and

$$\text{Type C}: V_c = \begin{cases} 1 & -0.5h \le z \le -0.5(1-\alpha)h \\ \left[-\dfrac{z}{0.5(1-\alpha)h}\right]^p & -0.5(1-\alpha)h \le z \le 0 \\ \left[\dfrac{z}{0.5(1-\alpha)h}\right]^p & 0 \le z \le 0.5(1-\alpha)h \\ 1 & 0.5(1-\alpha)h \le z \le 0.5h \end{cases}, \tag{5}$$

where p is the power-law index of material distributions and α is the proportional coefficient of homogeneous ceramic layer. According to **Eq. 1**, the elastic modulus of FGM arch can be expressed as (Bateni and Eslami, 2015).

$$E(z) = E_m(1 - V_c) + E_c V_c \tag{6}$$

where E_c and E_m are the elastic modulus of ceramic and metal, respectively.

NONLINEAR EQUILIBRIUM

The nonlinear in-plane buckling behavior of a fixed FGM arch subjected to a locally uniformly distributed radial load is investigated, which is shown in **Figure 1**. The potential energy Π of the FGM arch can then be given by

$$\Pi = \frac{1}{2}\int_{-\Phi}^{\Phi} Rb \int_{-h/2}^{h/2} E(z)\varepsilon^2 dz d\phi - R^2 \int_{-\Phi}^{\Phi} q\widetilde{v} H_1(\phi, c) d\phi \tag{7}$$

with the function $H_1(\phi, c)$ being given by

$$H_1(\phi, c) = \text{Heaviside}(\phi + c) - \text{Heaviside}(\phi - c), \tag{8}$$

where Heaviside() represents Heaviside function. The longitudinal strain of an arbitrary point at the cross-section can be expressed as

$$\varepsilon = \varepsilon_m + \varepsilon_b \tag{9}$$

where ε_m and ε_b are the membrane and bending strains of the FGM arch, respectively, which are given by

$$\varepsilon_m = -\widetilde{v} + \frac{1}{2}\widetilde{v}'^2 + \widetilde{w}', \tag{10}$$

$$\varepsilon_b = -\frac{z\widetilde{v}''}{R} \tag{11}$$

with $\widetilde{w} = w/R$ and $\widetilde{v} = v/R$, where $(\,)' \equiv d(\,)/d\phi$, z is the coordinate of the point P_0 at the cross-sectional axis oz, w and v are the axial and radial displacements respectively.

For nonlinear equilibrium of FGM arch using the principle of minimum total potential energy, the variation of the total potential energy obtained from **Eq. 7** should vanish as

$$\delta\Pi = \int_{-\Theta}^{\Theta} Rb \int_{-h/2}^{h/2} E(z)\varepsilon\delta\varepsilon dz d\phi - R^2 \int_{-\Theta}^{\Theta} q\delta\widetilde{v} H_1(\phi, c) d\phi = 0 \tag{12}$$

By substituting **Eqs 10**, **11** into **Eq. 12**, the **Eq. 12** can then be rewritten as

$$\begin{aligned}\delta\Pi = &\int_{-\Theta}^{\Theta} \left[-NR\left(\delta\widetilde{w}' - \delta\widetilde{v} + \widetilde{v}'\delta\widetilde{v}'\right) - M\delta\widetilde{v}'' \right] d\phi \\ &- R^2 \int_{-\Theta}^{\Theta} q\delta\widetilde{v} H_1(\phi, c) d\phi = 0\end{aligned} \tag{13}$$

where N and M are the axial and bending actions of the FGM arch, respectively, which can be given by

$$N = -A_k\left(\widetilde{w}' - \widetilde{v} + \frac{\widetilde{v}'^2}{2}\right) + \frac{B_k}{R}\widetilde{v}'' \tag{14}$$

$$M = B_k\left(\widetilde{w}' - \widetilde{v} + \frac{\widetilde{v}'^2}{2}\right) - \frac{D_k}{R}\widetilde{v}'' \tag{15}$$

with A_k, B_k, and D_k being the stiffness components of the FGM arch, respectively, which are defined as

$$\{A_k B_k D_k\} = b\int_{-0.5h}^{0.5h} E(z)\{1 z z^2\} \mathrm{d}z. \tag{16}$$

When material distributions of the FGM arch is subjected to Type A, the stiffness components of the FGM arch A_k, B_k, and D_k can be given by

$$A_k = \frac{bh\{[(E_c - E_m)\alpha + E_m]p + E_c\}}{p + 1} \tag{17}$$

$$B_k = \frac{bh^2 p(1 - \alpha)(E_c - E_m)(\alpha p + \alpha + 1)}{2p^2 + 6p + 4} \tag{18}$$

$$\begin{aligned}D_k = &\frac{bh^3 p^2\{(E_c - E_m)[(4\alpha^3 - 6\alpha^2 + 3\alpha - 1)p + 12\alpha^3 - 12\alpha^2 + 3\alpha - 3] + E_c(6 + p)\}}{12(p^3 + 6p^2 + 11p + 6)} \\ &+ \frac{bh^3\{[(8\alpha^3 - 6\alpha^2 + 6\alpha - 8)(E_c - E_m) + 11E_c]p + 6E_c\}}{12(p^3 + 6p^2 + 11p + 6)}\end{aligned} \tag{19}$$

When material distributions of the FGM arch is subjected to Type B, the stiffness components of the FGM arch A_k, B_k, and D_k can be given by

$$A_k = \frac{bh\{[(E_c - E_m)\alpha + E_m]p + E_c\}}{p + 1} \tag{20}$$

$$B_k = 0 \tag{21}$$

$$\begin{aligned}D_k = &\frac{bh^3 p^2\{(E_c - E_m)[p(\alpha^3 - 1) + 3\alpha^3 + 3\alpha^2 - 6] + E_c(6 + p)\}}{12(p^3 + 6p^2 + 11p + 6)} \\ &+ \frac{bh^3[(2\alpha^3 + 3\alpha^2 + 6\alpha - 11)(E_c - E_m)p + E_c(11p + 6)]}{12(p^3 + 6p^2 + 11p + 6)}\end{aligned} \tag{22}$$

When material distributions of the FGM arch is subjected to Type C, the stiffness components of the FGM arch A_k, B_k, and D_k can be given by

$$A_k = \frac{bh\{[(E_c - E_m)\alpha + E_m]p + E_c\}}{p + 1} \tag{23}$$

$$B_k = 0 \tag{24}$$

$$D_k = \frac{bh^3[(E_c - E_m)(\alpha^3 - 3\alpha^2 + 3\alpha)p + E_m p + 3E_c]}{12p + 36} \tag{25}$$

Integrating **Eq. 13** by parts, the differential equilibrium equations of a FGM arch under a locally uniformly distributed radial load can be derived as

$$(NR)' = 0 \tag{26}$$

$$NR + \left(NR\widetilde{v}'\right)' - M'' - qR^2 \mathrm{H}_1(\phi, c) = 0 \tag{27}$$

By Substituting **Eq. 14** into **Eq. 15**, the bending action of the FGM arch can be given by

$$M = -\left(D_k - \frac{B_k^2}{A_k}\right)\frac{\widetilde{v}''}{R} - \frac{B_k}{A_k}N \tag{28}$$

By Substituting **Eqs. 26**, **28** into **Eq. 27**, **Eq. 27** can then be rewritten as

$$\frac{\widetilde{v}^{iv}}{\varpi^2} + \widetilde{v}'' = \frac{qR\mathrm{H}_1(\phi, c)}{N} - 1 \tag{29}$$

where ϖ is non-dimensional axial force parameter, which is given by

$$\varpi^2 = \frac{NR^2}{\kappa} \tag{30}$$

with κ being the equivalent stiffness of the FGM arch, which is defined as

$$\kappa = D_k - \frac{B_k^2}{A_k} \tag{31}$$

Meanwhile, the essential boundary conditions at the both ends of FGM arch

$$\widetilde{v} = 0,\ \widetilde{w} = 0,\ \text{and}\ \widetilde{v}' = 0\ \text{at}\ \phi = \pm\Theta \tag{32}$$

also need to be satisfied. The non-dimensional radial displacement $\widetilde{v}$ of a FGM arch can be determined by solving **Eq. 29** under the boundary conditions obtained from **Eq. 32**.

$$\begin{aligned}\widetilde{v} = {} & \frac{P[\cos(\varpi\phi)(\beta_2 - \cos\beta_1 \sin\beta_2) - \beta_2(\beta_1 \sin\beta_1 + \cos\beta_1) + \sin\beta_2]}{\varpi^2 \sin\beta_1} + \frac{\beta_1^2 - \mu^2\phi^2}{2\varpi^2} \\ & + \frac{\beta_1[\cos\beta_1 - \cos(\varpi\phi)]}{\varpi^2 \sin\beta_1} + \frac{P\mathrm{H}_1(\phi, c)\left[2\cos\beta_2 \cos(\varpi\phi) + \beta_2^2 + (\varpi\phi)^2 - 2\right]}{2\varpi^2} \\ & - \frac{P\mathrm{H}_2(\phi, c)[\sin(\varpi\phi)\sin\beta_2 - \varpi\phi\beta_2]}{\varpi^2}\end{aligned} \tag{33}$$

where $\beta_1 = \mu\Theta$ and $\beta_2 = \mu c = \eta\beta_1$ with $\eta = c/\Theta$, the non-dimensional locally uniformly distributed radial load P is expressed as

$$P = \frac{Q}{2cN} \text{ with } Q = 2cqR, \tag{34}$$

and the $\mathrm{H}_2(\phi, c)$ is expressed as

$$\mathrm{H}_2(\phi, c) = -1 + Heaviside(-c + \phi) + Heaviside(-c + \phi). \tag{35}$$

Equation 33 indicates that the non-dimensional radial displacement $\widetilde{v}$ is dependent on P and ϖ, and so it is necessary to calculate the relationship of the axial force with the locally uniformly distributed radial load.

Therefore, substituting **Eq. 33** into **Eq. 14**, and integrating it along the arch length results in

$$\begin{aligned}2\Phi N &= \int_{-\Theta}^{\Theta}\left[-A_k\left(\widetilde{w}' - \widetilde{v} + \frac{\widetilde{v}'^2}{2}\right) + \frac{B_k}{R}\widetilde{v}''\right]d\phi \\ &= \int_{-\Theta}^{\Theta} -A_k\left(-\widetilde{v} + \frac{\widetilde{v}'^2}{2}\right)d\phi - \int_{-\Theta}^{\Theta} A_k\left(\widetilde{w}'\right)d\phi + \int_{-\Theta}^{\Theta}\frac{B_k}{R}\widetilde{v}''d\phi, \\ &= \int_{-\Theta}^{\Theta} -A_k\left(-\widetilde{v} + \frac{\widetilde{v}'^2}{2}\right)d\phi - \widetilde{w}|_{-\Theta}^{\Theta} + \left(\frac{B_k}{R}\widetilde{v}\right)\Big|_{-\Theta}^{\Theta}\end{aligned} \tag{36}$$

Considering the essential boundary conditions obtained from **Eq. 32**, the **Eq. 36** can be rewritten as

$$2\Phi N = \int_{-\Theta}^{\Theta} -A_k\left(-\widetilde{v} + \frac{\widetilde{v}'^2}{2}\right)d\phi \Rightarrow \int_{-\Theta}^{\Theta}\left(\widetilde{v} - \frac{\widetilde{v}'^2}{2}\right)d\phi + \frac{2\Phi N}{A_k} = 0, \tag{37}$$

Subsequently, Calculating **Eq. 37** leads to a quadratic equilibrium equation, as

$$A_1P^2 + B_1P + C_1 = 0, \tag{38}$$

where the coefficients A_1, B_1 and C_1 are expressed as

$$\begin{aligned}A_1 = {} & \frac{\left[3\beta_2^2 + 5\sin^2\beta_2 - \beta_2 \sin(2\beta_2)\right]\cos\beta_1 + 2\beta_2(\beta_2 \cos\beta_2 - 4\sin\beta_2)}{4\beta_1^3 \sin\beta_1} - \frac{5\sin(2\beta_2)}{8\beta_1^3} \\ & + \frac{\beta_2^2(2\sin^2\beta_1 + 1) + \sin^2\beta_2 - 2\beta_2 \sin\beta_2 \cos\beta_1}{4\beta_1^2\sin^2\beta_1} + \frac{6\cos^2\beta_2 + 9 - 4\beta_1^2}{12\beta_1^3},\end{aligned} \tag{39}$$

$$B_1 = \frac{2\sin\beta_2 - \beta_2(\cos\beta_1 + \cos\beta_2)}{2\beta_1^2 \sin\beta_1} + \frac{\sin\beta_2 \cos\beta_1 - \beta_2}{2\beta_1\sin^2\beta_1}, \tag{40}$$

$$C_1 = \frac{2\cos^2\beta_1 + 1}{12\sin^2\beta_1} - \frac{\cos\beta_1}{4\beta_1 \sin\beta_1} + \frac{\kappa\beta_1^2}{A_k(\lambda_s h)^2} \tag{41}$$

with λ_s being the modified geometric slenderness of the FGM arch, respectively, which can be express as

$$\lambda_s = \frac{S\Theta}{2h} \tag{42}$$

By solving **Eq. 38**, the relationship of the axial force with the locally uniformly distributed radial load can be obtained. Then, by substituting those relationship into **Eq. 33**, the non-dimensional radial displacement $\widetilde{v}$ can be obtained. Finally, the relationship of the locally uniformly distributed radial load with the non-dimensional radial displacement can be established, and the nonlinear instability behavior of FGM arches can be analyzed.

BUCKLING ANALYSIS

Limit Point Buckling and Bifurcation Buckling

The FGM arches under the locally uniformly distributed radial load may buckle in a limit point mode. According to the theory of (Lu et al., 2018) for an arches under the locally uniformly distributed radial load, the upper and lower limit point buckling loads can be derived using routine calculus, and the equation of equilibrium between β_1 and P at the upper and lower limit points can be expressed as

$$A_2P^2 + B_2P + B_2 = 0 \tag{43}$$

where

$$A_2 = \frac{\beta_1\partial A_1}{\partial\beta_1} - 4A_1,\ B_2 = \frac{\beta_1\partial B_1}{\partial\beta_1} - 2B_1,\ C_2 = \frac{\beta_1\partial C_1}{\partial\beta_1} \tag{44}$$

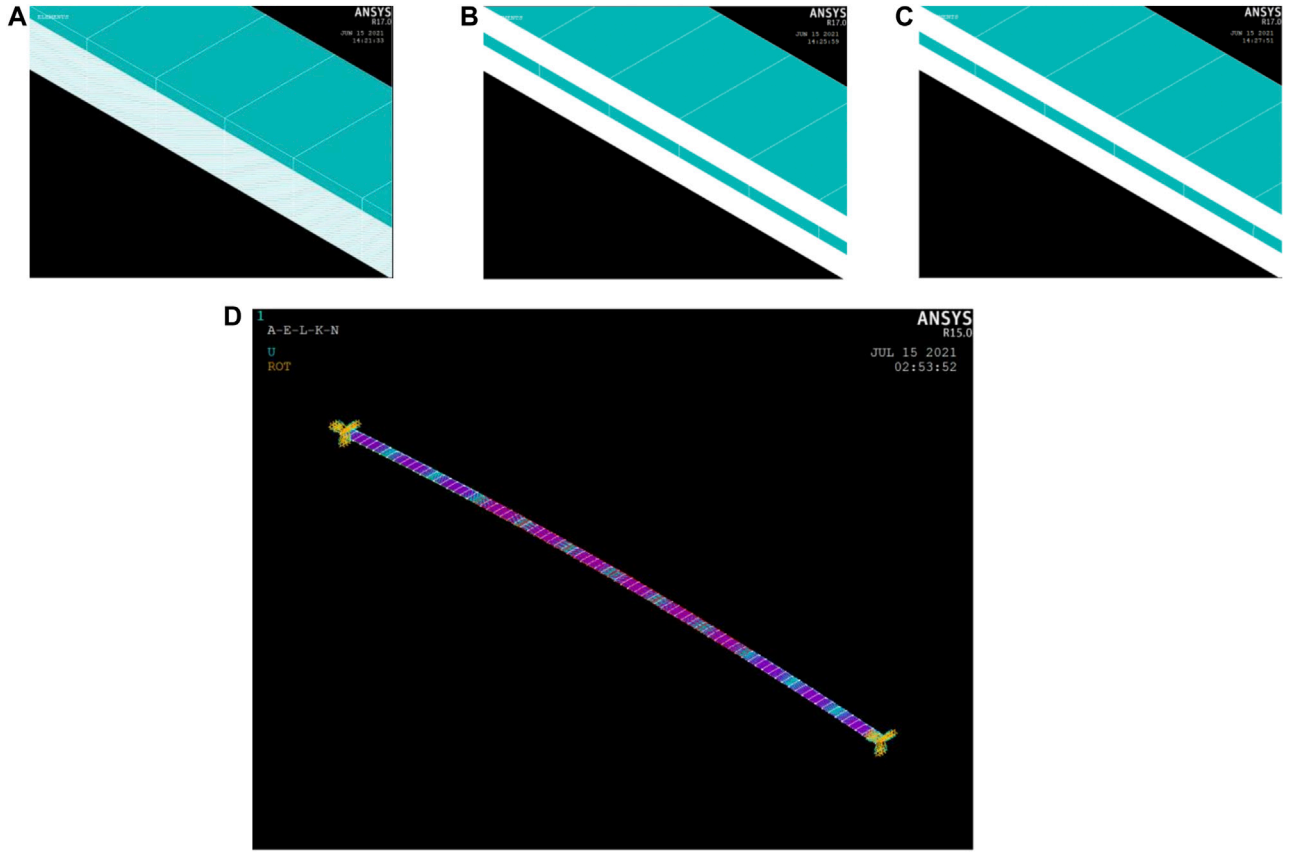

FIGURE 3 | ANSYS model of material distributions of FGM arch **(A)** Type A **(B)** Type B **(C)** Type C **(D)** ANSYS model with boundary conditions.

Therefore, the upper and lower limit point buckling loads can be obtained by solving **Eqs 38**, **43** simultaneously.

It can be found that the **Eq. 43** for equilibrium of limit point buckling mode of the FGM arches are the same as those for the homogeneous arches (Lu et al., 2018). Similarly, refer to limit point buckling theory of the homogeneous arches under the locally uniformly distributed radial load, the axial force parameter β_{b1} and the axial force N in the FGM arch during lowest possible limit point buckling are respectively given by

$$\beta_{b1} = \pi \text{ and } N = \frac{\pi^2 \kappa}{(S/2)^2} = N_{E1} \tag{45}$$

In addition, also refer to the above theory of homogeneous arch, the central displacement $\tilde{v}_{sc}$ corresponding to the lowest buckling load of the FGM arch as

$$\tilde{v}_{sc} = \frac{\Theta^2}{2} - \frac{2\Theta^2}{2\pi^2(\beta_2 + \sin\beta_2)}\left[\beta_2(\pi^2 - 2) + \pi(1 - \cos\beta_2) - 2\sin\beta_2 - \frac{\beta_2^2\pi}{2}\right] \pm 2\Theta^2\sqrt{\frac{1}{\pi^2}\left(\frac{B}{\pi^2} + \frac{5}{3}\right) - \frac{4\kappa}{A_k(\lambda_s h)^2}} \tag{46}$$

with

$$B = \frac{(5\pi - 6\beta_2)\cos\beta_2 - 6\beta_2}{\beta_2 + \sin\beta_2} + \beta_2^2 + 9 + 2(\pi - \beta_2)^2\left(\frac{1}{\beta_2 + \sin\beta_2} - 1\right) + \frac{\beta_2(\cos\beta_2 + 1)(2\beta_2 - 5\pi) - \beta_2^2(9\pi^2 - 10\pi\beta_2 + 3\beta_2^2)}{(\beta_2 + \sin\beta_2)^2} \tag{47}$$

The **Eq. 46** has a real solution only when

$$\frac{1}{\pi^2}\left(\frac{B}{\pi^2} + \frac{5}{3}\right) - \frac{4\kappa}{A_k(\lambda_s h)^2} \geq 0 \tag{48}$$

from which the modified geometric slenderness λ_s of the lowest buckling load of the FGM arch can be obtained once the type of the cross section and the locally uniformly distributed radial load are given.

The FGM arches under the locally uniformly distributed radial load may buckle in a bifurcation mode. The equation of equilibrium of the FGM arch in the primary equilibrium path is obtained from **Eq. 29**. Similarly, the differential equation of equilibrium of the FGM arch in the case of infinitely close to the bifurcation equilibrium path can be given by

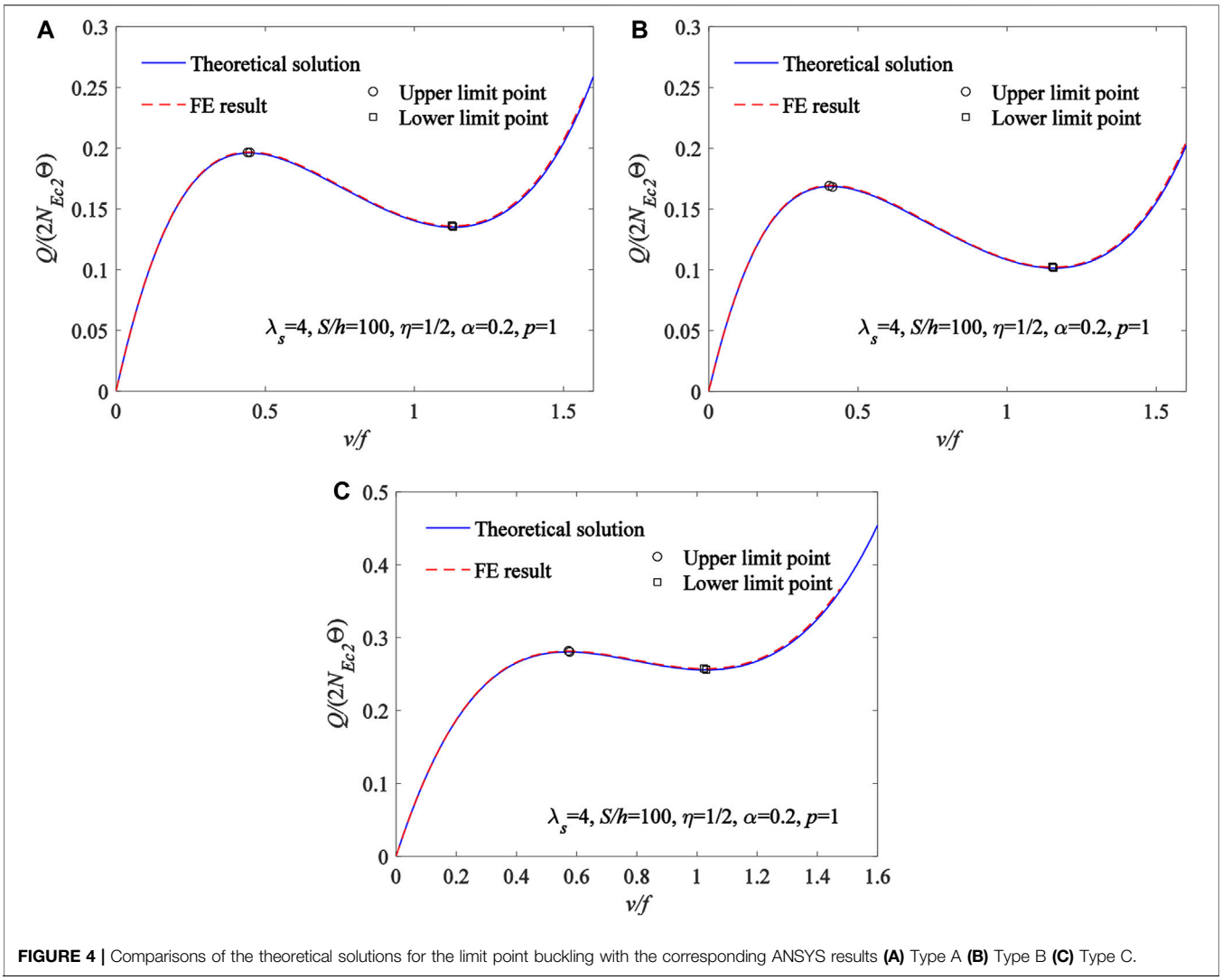

FIGURE 4 | Comparisons of the theoretical solutions for the limit point buckling with the corresponding ANSYS results **(A)** Type A **(B)** Type B **(C)** Type C.

$$\frac{\tilde{v}^{iv} + \tilde{v}_b^{iv}}{\bar{\omega}^2} + \tilde{v}'' + \tilde{v}''_b = P\mathrm{H}_1(\phi, c) - 1 \tag{49}$$

Therefore, the equation for equilibrium of bifurcation mode of the FGM arches can be built by substituting **Eq. 29** into **Eq. 49** as

$$\frac{\tilde{v}_b^{iv}}{\bar{\omega}^2} + \tilde{v}''_b = 0 \tag{50}$$

It's can be found that the equation for equilibrium of bifurcation mode of the FGM arches are the same as those for the homogeneous arches (Lu et al., 2018). Similarly, refer to bifurcation buckling theory of the homogeneous arches, the axial force parameter β_{b1} and the axial force N in the arch during bifurcation are respectively given by

$$\beta_{b1} = 1.4303\pi \text{ and } N = \frac{(1.4303\pi)^2\kappa}{(S/2)^2} = N_{E2} \tag{51}$$

In addition, the parameter β_{b2} for bifurcation mode can then be expressed as

$$\beta_{b2} = 1.4303\pi\frac{c}{\Theta} \tag{52}$$

By substituting **Eqs 51**, **52** into **Eq. 39**, the equation of equilibrium between β_{b1} and P at the upper and lower bifurcation points can be expressed as

$$A_3P^2 + B_3P + C_3 = 0 \tag{53}$$

where

$$A_3 = \frac{5\sin^2\beta_{b2} - \beta_{b2}\sin(2\beta_{b2})}{4\beta_{b1}^4} + \frac{4\beta_{b2}\cos^2\beta_{b2} - 5\sin(2\beta_{b2})}{8\beta_{b1}^3} + \frac{3\eta(\eta+1)}{4\beta_{b1}^2} + \frac{\eta^2(3-2\eta)}{6} + \frac{\eta(\beta_{b2}\cos\beta_{b2} - 5\sin\beta_{b2})}{2\beta_{b1}^2\sin\beta_{b1}} + \frac{\beta_{b2}^2 + \sin^2\beta_{b2}}{4\beta_{b1}^2\sin^2\beta_{b1}} \tag{54}$$

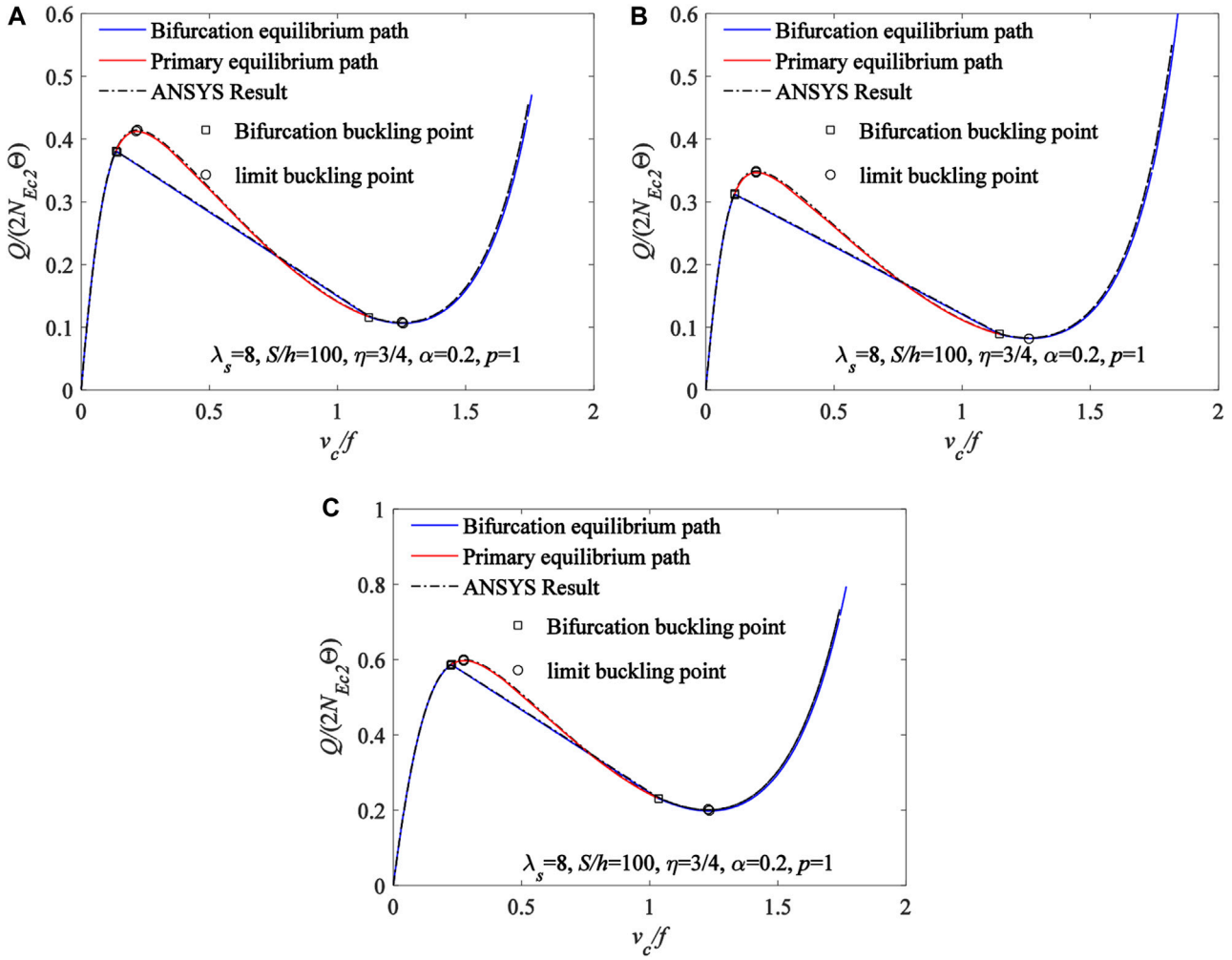

FIGURE 5 | Comparisons of the theoretical solutions for the bifurcation buckling with the corresponding ANSYS results **(A)** Type A **(B)** Type B **(C)** Type C.

$$B_3 = \frac{3\sin\beta_{b2} - \beta_{b2}\cos\beta_{b2}}{2\beta_{b1}^2\sin\beta_{b1}} - \frac{\eta}{\beta_{b1}}\left(\frac{1}{2} - \frac{1}{\beta_{b1}}\right) \tag{55}$$

$$C_3 = \frac{1}{12\sin^2\beta_1} - \frac{1}{12\beta_1^2} + \frac{\kappa\beta_{b1}^2}{A_k(\lambda_s h)^2} \tag{56}$$

with

$$\eta = \frac{c}{\Theta} \tag{57}$$

The bifurcation buckling load of a FGM arch under a locally uniformly distributed radial load can be obtained once the localized parameter η is given.

Comparisons of Theoretical Solutions with ANSYS Results

According to Donnell's shallow shell theory, in the ANSYS models of FGM arch, the geometry of the rectangular section was, the width b = 0.14 m, the total thickness h = 0.07 m, the power-law index p = 1 and the proportional coefficient of homogeneous ceramic layer α= 0.2. In addition, the geometric slenderness of the FGM arch S/h = 100. The Young's modulus of the metal-ceramic material Al-Al_2O_3 are 70GPa and 380GPa, respectively.

When a multilayer for metal-ceramic material Al-Al_2O_3 is used to simulate a continuous gradient properties, the accuracy of the FGM arch model increases with an increase of the number of layers of metal-ceramic material Al-Al_2O_3. As demonstrated in **Figure 3**, when material distributions of the FGM arch is subjected to Type A (**Figure 3A**), the cross-section of the FGM arch have 101 layers, the first layer is a homogeneous ceramic layer, and the second to the 101st layers are gradient layers from ceramic to metal. When material distributions of the FGM arch is subjected to Type B (**Figure 3B**), the cross-section of the FGM arch have 201 layers, the first to the 100st layers are gradient layers from

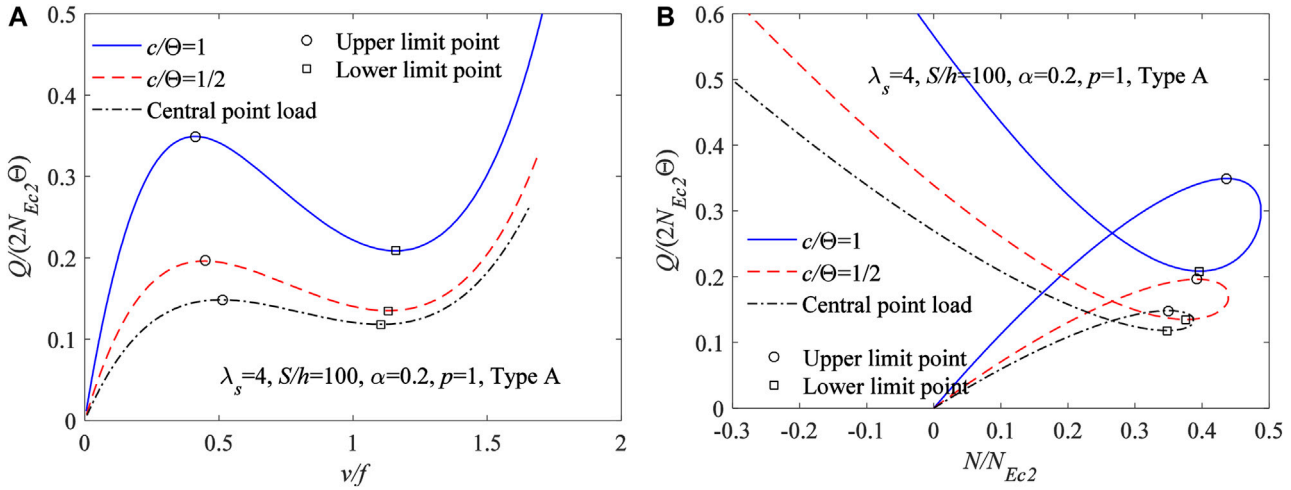

FIGURE 6 | Limit point buckling equilibrium path for FGM arches having different localized parameter **(A)** v_c/f *vs* $Q/(2N_{Ec2}\Theta)$ **(B)** N/N_{Ec2} *vs* $Q/(2N_{Ec2}\Theta)$.

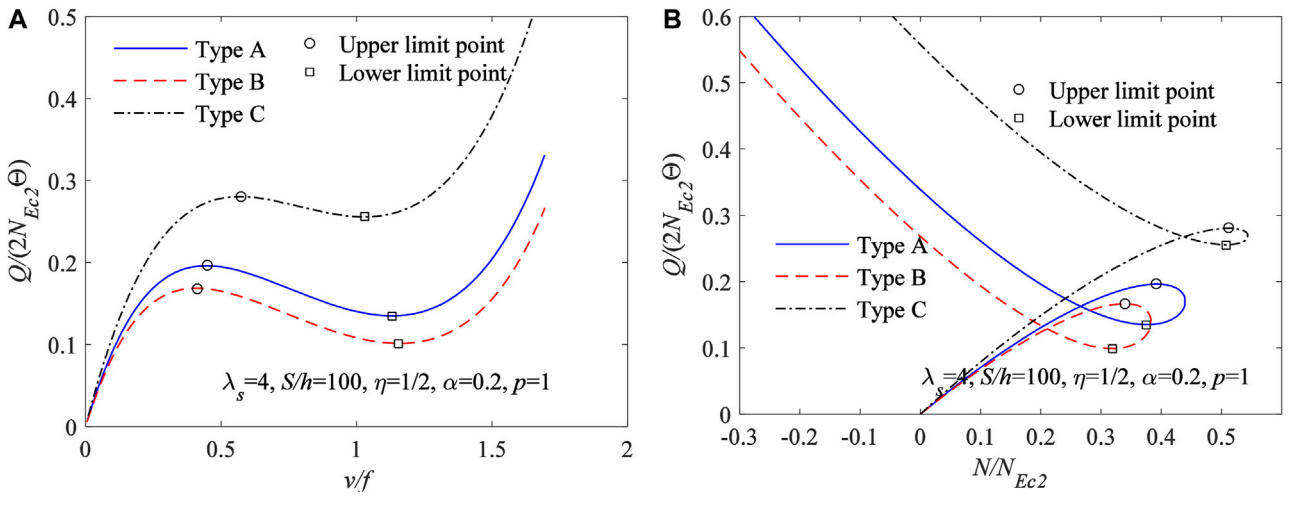

FIGURE 7 | Limit point buckling equilibrium path for FGM arches having different type of material distributions **(A)** v_c/f *vs* $Q/(2N_{Ec2}\Theta)$ **(B)** N/N_{Ec2} *vs* $Q/(2N_{Ec2}\Theta)$.

metal to ceramic, the 101st is a homogeneous ceramic layer, and the 102st to the 201st layers are gradient layers from ceramic to metal. When material distributions of the FGM arch is subjected to Type C (**Figure 3C**), the cross-section of the FGM arch have 202 layers, the first layer is a homogeneous ceramic layer, the second to the 101st layers are gradient layers from ceramic to metal, the 102st to the 201st layers are gradient layers from metal to ceramic, the 101st is a homogeneous ceramic layer, and the last layer is a homogeneous ceramic layer.

In addition, the proposed theoretical solution of the buckling equilibrium path, the limit point and bifurcation buckling load for the FGM arches under the locally uniformly distributed radial load are validated by ANSYS finite element results. Convergence researches for using the shell element shell181 of ANSYS show that 80 elements can produce convergent results. Therefore, 80 shell181 elements are chosen to simulate the FGM arches (**Figure 3D**).

Comparisons of the theoretical solutions of **Eqs. 33**, **38** for the limit point buckling equilibrium path and the limit point buckling load of the FGM arches with the corresponding ANSYS results are plotted in **Figure 4**. The variation curves of the dimensionless locally uniformly distributed radial load $Q/(2N_{Ec2}\Theta)$ with the dimensionless central displacement v_c/f are plotted in **Figure 4A** for material distributions of the FGM arch being subjected to Type A, in **Figure 4B** for material distributions of the FGM arch being subjected to Type B, and in **Figure 4C** for material distributions of the FGM arch being subjected to Type C, where the locally uniformly distributed radial load with $\eta = 0.5$, the modified geometric slenderness $\lambda_s = 4$ and $N_{Ec2} = (1.4303\pi)^2 E_c b h^3/[12(S/2)^2]$. It can be seen from **Figures 4A–C** that the theoretical solutions for the limit point buckling

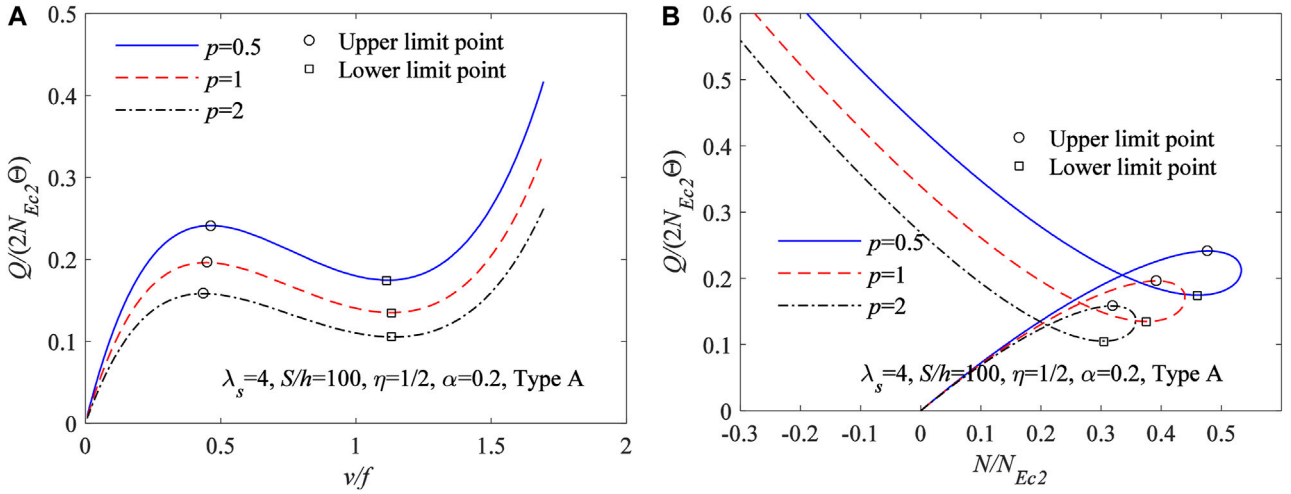

FIGURE 8 | Limit point buckling equilibrium path for FGM arches having different power-law index of material distributions **(A)** v_c/f *vs* $Q/(2N_{Ec2}\Theta)$ **(B)** N/N_{Ec2} *vs* $Q/(2N_{Ec2}\Theta)$.

equilibrium path and the limit point buckling load of the FGM arches are highly consistent with the corresponding ANSYS results.

Comparisons of the theoretical solutions of **Eqs 33**, **53** for bifurcation buckling equilibrium path and the bifurcation buckling load of the FGM arches with the corresponding ANSYS results are plotted in **Figure 5**. The variation curves of the dimensionless locally uniformly distributed radial load $Q/(2N_{Ec2}\Theta)$ with the dimensionless central displacement v_c/f are plotted in **Figure 5A** for material distributions of the FGM arch being subjected to Type A, in **Figure 5B** for material distributions of the FGM arch being subjected to Type B, and in **Figure 5C** for material distributions of the FGM arch being subjected to Type C, where the locally uniformly distributed radial load with $\eta = 0.75$, the modified geometric slenderness $\lambda_s = 8$. It can be seen from **Figures 5A–C** that the theoretical solutions for bifurcation buckling equilibrium path and the bifurcation buckling load of the FGM arches are highly consistent with the corresponding ANSYS results.

Hence, the theoretical solutions of **Eqs 33**, **38**, **53** can be used to predict the buckling equilibrium path, the limit point and bifurcation buckling load for the FGM arches under the locally uniformly distributed radial load.

Limit Point Buckling Analysis

This section investigates the effects of the localized parameter η of locally uniformly distributed radial load, the type and the power-law index p of material distributions of the FGM arch on the limit point buckling equilibrium path and the limit point buckling load for FGM arches under a locally uniformly distributed radial load.

Under the locally uniformly distributed radial load, the limit point buckling equilibrium path obtained from **Eqs 33**, **38** for FGM arches having different localized parameter η are plotted in **Figure 6A** with the variation curves of v_c/f *vs* $Q/(2N_{Ec2}\Theta)$, and in **Figure 6B** with the variation curves of N/N_{Ec2} *vs* $Q/(2N_{Ec2}\Theta)$, where the modified geometric slenderness $\lambda_s = 4$, the power-law index $p = 1$, the proportional coefficient of homogeneous ceramic layer $\alpha = 0.2$, the geometric slenderness $S/h = 100$ and the material distributions of FGM arches are subjected to Type A. Also plotted in **Figure 6** are the limit points given by **Eqs 38**, **43**. In **Figure 6**, when the upper limit point is reached, the load system and limit point buckling equilibrium path of FGM arches snaps through to the remote equilibrium branch, and the displacement become very large. Therefore, the upper limit point is the limit point buckling load. It can also be seen from **Figure 6** that the localized parameter η has a significant effect on the limit point buckling equilibrium path and the limit point buckling load, the limit point buckling load increases with an increase of localized parameter η, which indicates that FGM arches having a larger length of the locally uniformly distributed radial loading segment are more prone to limit point buckling.

In addition, the limit point buckling equilibrium path obtained from **Eqs 33**, **38** for FGM arches having different type of material distributions are plotted in **Figure 7A** with the variation curves of v_c/f *vs* $Q/(2N_{Ec2}\Theta)$, and in **Figure 7B** with the variation curves of N/N_{Ec2} *vs* $Q/(2N_{Ec2}\Theta)$, where $\lambda_s = 4$, $\eta = 0.5$, $\alpha = 0.2$, $S/h = 100$, $p = 1$. It can be seen from **Figure 7** that the type of material distributions has a significant effect on the limit point buckling equilibrium path and the limit point buckling load, Type C has a largest limit point buckling load among Type A, Type B and Type C, which indicates that under the same proportion of metal and ceramic materials, the distribution of ceramics on the upper and lower surfaces of the cross-section can greatly improve the stability of the FGM arch.

Similarly, **Figure 8A** plots the variation curves of v_c/f *vs* $Q/(2N_{Ec2}\Theta)$ and **Figure 8B** plots the variation curves of N/N_{Ec2} *vs* $Q/(2N_{Ec2}\Theta)$ for FGM arches having different power-law index p, where $\lambda_s = 4$, $\eta = 0.5$, $\alpha = 0.2$, $S/h = 100$ and the material distributions of FGM arches are subjected to Type A. It can

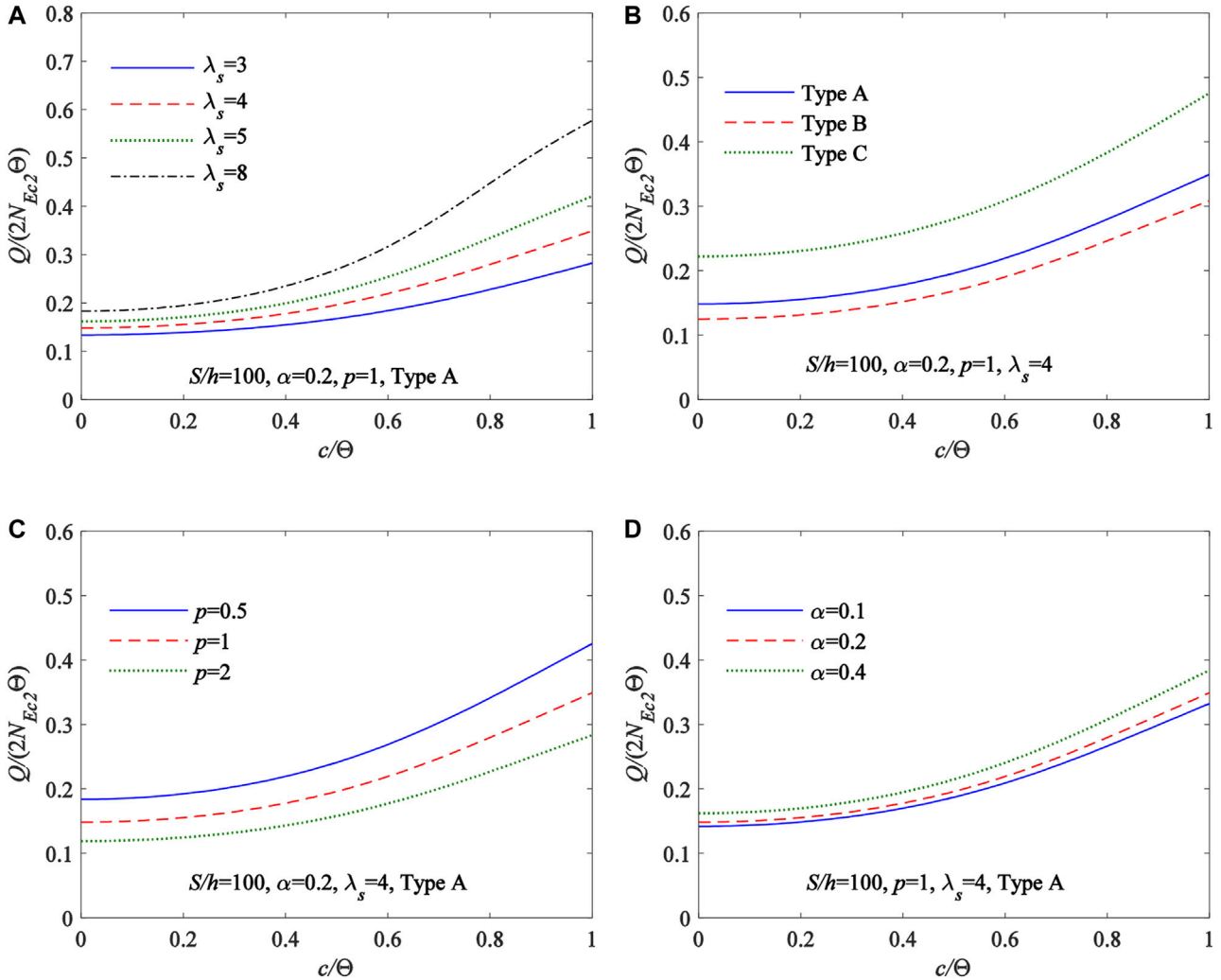

FIGURE 9 | η *vs* $Q/(2N_{Ec2}\Theta)$ **(A)** different modified geometric slenderness **(B)** different type of material distributions **(C)** different power-law index p of material distributions **(D)** different proportional coefficient of homogeneous ceramic layer.

also be seen from **Figure 8** that the power-law index p has a significant effect on the limit point buckling equilibrium path and the limit point buckling load, the limit point buckling load increases with a decrease of the power-law index p, which indicates that FGM arches having a smaller power-law index p of material distributions are more prone to limit point buckling.

Furthermore, the influences of the modified geometric slenderness λ_s, the type and the power-law index p of material distributions of the FGM arch, the proportional coefficient of homogeneous ceramic layer α and the localized parameter η of the locally uniformly distributed radial load on the limit point buckling load of the FGM arch are studied in detail as well. The variation curves of η *vs* $Q/(2N_{Ec2}\Theta)$ are plotted in **Figure 9A** for a FGM arch having different modified geometric slenderness λ_s, in **Figure 9B** for a FGM arch having different type of material distributions, in **Figure 9C** for a FGM arch having different power-law index p of material distributions and in **Figure 9D** for a FGM arch having different proportional coefficient of homogeneous ceramic layer α. It can be seen again from **Figure 9** that the limit point buckling load increases with an increase of localized parameter η. It can be seen from **Figure 9A** that the limit point buckling load increases with an increase of modified geometric slenderness λ_s. It can be seen again from **Figure 9B** that Type C has a largest limit point buckling load among Type A, Type B and Type C. In addition, because the composition proportion of ceramics increases with an increase of the proportional coefficient of homogeneous ceramic layer α and a decrease of the power-law index p of material distributions of the FGM arch. Therefore, **Figures 9C,D** show the limit point buckling load increases with an increase of the proportional coefficient of homogeneous ceramic layer α and a decrease of the power-law index p of material distributions of the FGM arch, and the power-law index p has a more obvious effect on the limit point buckling load.

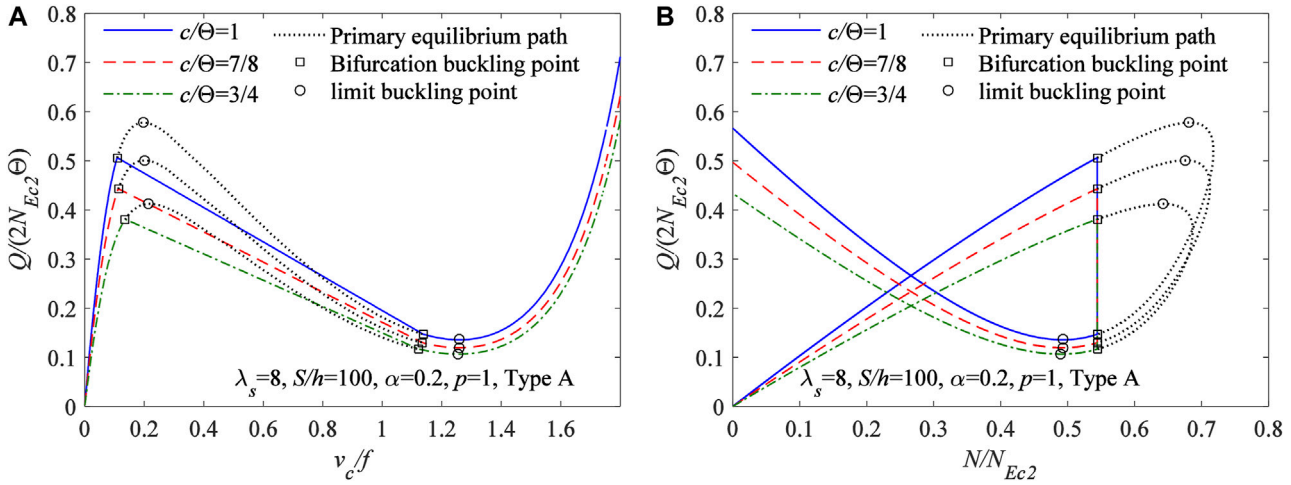

FIGURE 10 | Bifurcation equilibrium path for FGM arches having different localized parameter **(A)** v_c/f *vs* $Q/(2N_{Ec2}\Theta)$ **(B)** N/N_{Ec2} *vs* $Q/(2N_{Ec2}\Theta)$.

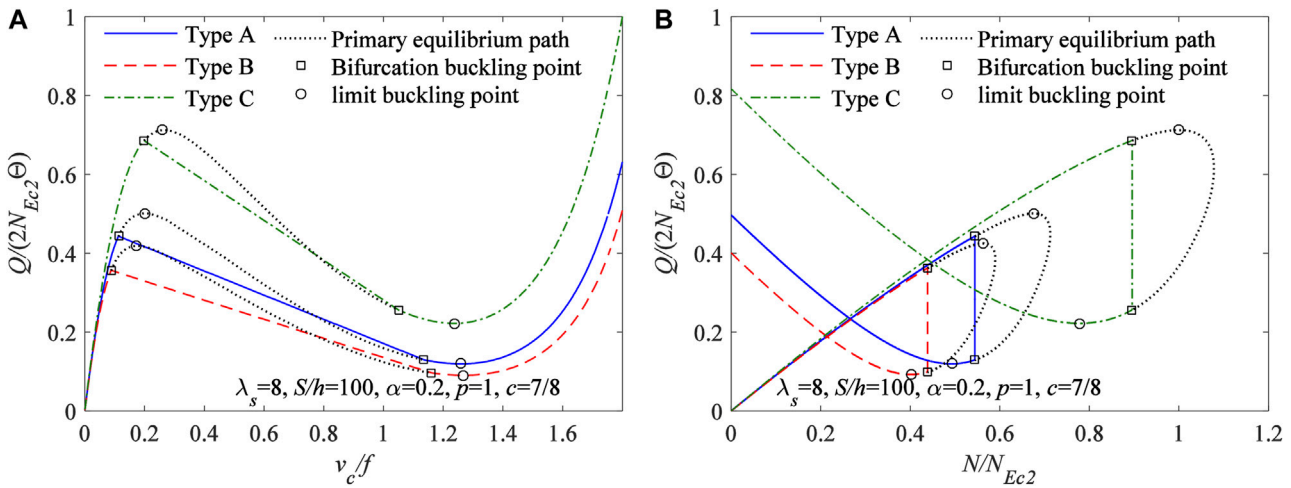

FIGURE 11 | Bifurcation equilibrium path for FGM arches having different type of material distributions **(A)** v_c/f *vs* $Q/(2N_{Ec2}\Theta)$ **(B)** N/N_{Ec2} *vs* $Q/(2N_{Ec2}\Theta)$.

Bifurcation Buckling Analysis

This section investigates the effects of the localized parameter η of locally uniformly distributed radial load, the type of material distributions of the FGM arch on the bifurcation buckling equilibrium path and the bifurcation buckling load for FGM arches under a locally uniformly distributed radial load.

Under the locally uniformly distributed radial load, the bifurcation buckling equilibrium path obtained from **Eqs 33**, **53** for FGM arches having different localized parameter η are plotted in **Figure 10A** with the variation curves of v_c/f *vs* $Q/(2N_{Ec2}\Theta)$, and in **Figure 6B** with the variation curves of N/N_{Ec2} *vs* $Q/(2N_{Ec2}\Theta)$, where the modified geometric slenderness $\lambda_s = 8$, the power-law index $p = 1$, the proportional coefficient of homogeneous ceramic layer $\alpha = 0.2$, the geometric slenderness $S/h = 100$ and the material distributions of FGM arches are subjected to Type A. Also plotted in **Figure 10** are the bifurcation buckling points given by **Eq. 53**. In **Figure 10**, the upper bifurcation buckling point is on the primary equilibrium path and bifurcation buckling equilibrium path, when this point is reached, the load decreases with an increase of the central displacement, and the dimensionless axial force parameter axial force N/N_{Ec2} still unchanged during this moment. When lower bifurcation buckling point is reached, the equilibrium path of the FGM arch returns from the bifurcation buckling equilibrium path back to the primary equilibrium path.

It can also be seen from **Figure 10** that the localized parameter η has a significant effect on the bifurcation buckling equilibrium path and the bifurcation buckling load, the bifurcation buckling load increases with an increase of localized parameter η, which indicates that FGM arches having a larger length of the locally uniformly

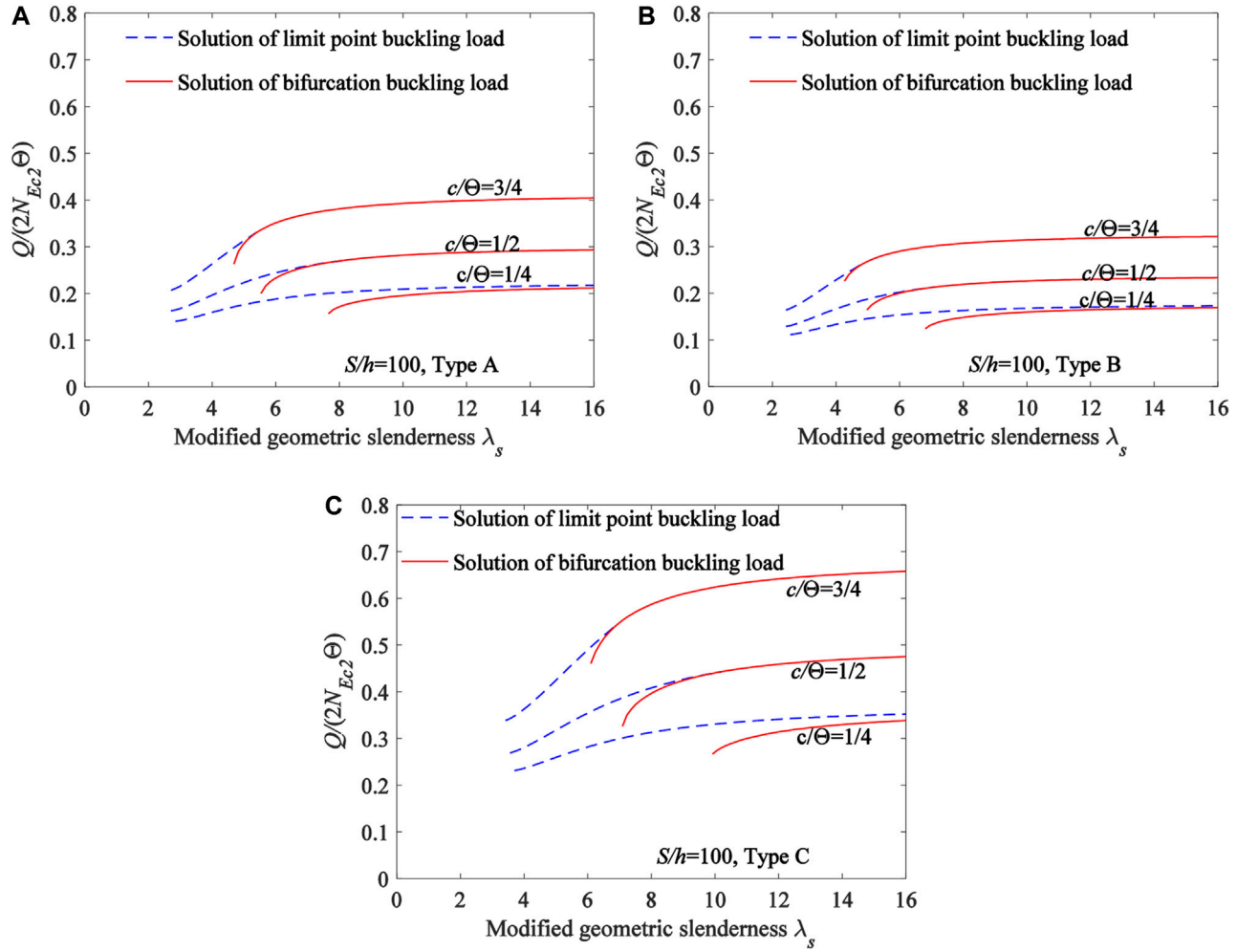

FIGURE 12 | Limit point buckling load and bifurcation buckling load of the FGM arch **(A)** Type A **(B)** Type B **(C)** Type C.

distributed radial loading segment are more prone to bifurcation buckling.

In addition, the bifurcation buckling equilibrium path obtained from **Eqs 33**, **53** for FGM arches having different type of material distributions are plotted in **Figure 11A** with the variation curves of v_c/f *vs* $Q/(2N_{Ec2}\Theta)$, and in **Figure 11B** with the variation curves of N/N_{Ec2} *vs* $Q/(2N_{Ec2}\Theta)$, where $\lambda_s = 8$, $\eta = 0.5$, $\alpha = 0.2$, $S/h = 100$, $p = 1$. It can be seen from **Figure 11** that the type of material distributions has a significant effect on the bifurcation buckling equilibrium path and the limit point buckling load, Type C has a largest bifurcation buckling load among Type A, Type B and Type C, which indicates again that under the same proportion of metal and ceramic materials, the distribution of ceramics on the upper and lower surfaces of the cross-section can greatly improve the stability of the FGM arch.

Furthermore, the influences of the localized parameter η of locally uniformly distributed radial load, the type of material distributions and the modified geometric slenderness λ_s of the FGM arch on the limit point buckling load and bifurcation buckling load of the FGM arch are studied in detail as well. The variation curves of λ_s *vs* $Q/(2N_{Ec2}\Phi)$ are plotted in **Figure 12A** for a Type A FGM arch having different localized parameter η, in **Figure 12B** for a Type B FGM arch having different localized parameter η and in **Figure 12C** for a Type C FGM arch having different localized parameter η. It can be seen from **Figure 12** that the limit point buckling load and bifurcation buckling load increase with an increase of the modified geometric slenderness λ_s and the localized parameter η. It can also be seen from **Figure 12** that Type C has a largest limit point buckling load and bifurcation buckling load among Type A, Type B and Type C. In addition, **Figure 12** shows that the limit point buckling loads are initially larger than the bifurcation buckling loads, and then smaller than the bifurcation buckling loads while the modified geometric slenderness λ_s reaches a certain value. However, when $\eta = 0.25$, the limit point buckling loads are larger than the bifurcation buckling loads with any modified geometric slenderness λ_s. Therefore, the modified geometric slenderness λ_s that is a switches of bifurcation buckling domination and limit point buckling domination may not exist within a certain range of the localized parameter η.

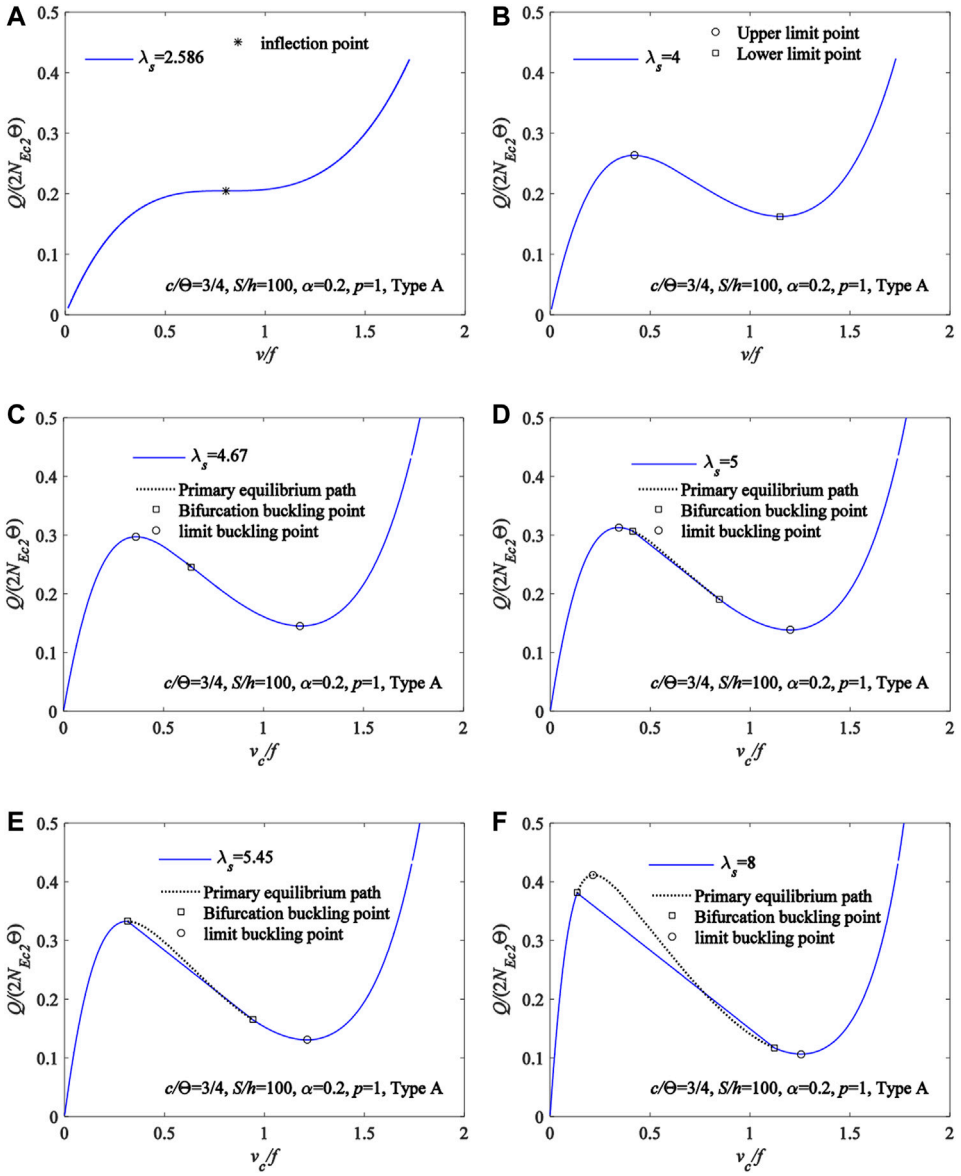

FIGURE 13 | Buckling equilibrium path for FGM arches having different modified geometric slenderness **(A)** λ_s = 2.586 **(B)** λ_s = 4 **(C)** λ_s = 4.67 **(D)** λ_s = 5 **(E)** λ_s = 5.45 **(F)** λ_s = 8.

CRITERIA FOR SWITCHES OF BUCKLING MODE OF FUNCTIONALLY GRADED MATERIAL ARCH

It can be seen from the above research that fixed FGM arches under a locally uniformly distributed radial load may buckle in a limit point buckling mode or in a bifurcation buckling mode. The buckling equilibrium path for FGM arches having different modified geometric slenderness are plotted in **Figure 13** with the variation curves of v_c/f *vs* $Q/(2N_{\mathrm{Ec2}}\Theta)$, where η = 0.75, α= 0.2, S/h = 100, p = 1 and the material distributions of FGM arches are subjected to Type A. **Figure 13A** shows that when λ_s = 2.586, the buckling equilibrium path is in the lowest limit point buckling mode, which only has a inflection point, this mode is a switches of limit point buckling and no limit point buckling. **Figure 13B** shows when λ_s = 4, the buckling equilibrium path is in the limit point buckling mode, which has two limit point. **Figure 13C** shows when λ_s = 4.67, the buckling equilibrium path is in the lowest bifurcation buckling mode, which only has a bifurcation buckling point, this mode is a switches of bifurcation buckling and limit point buckling. **Figure 13D** shows when λ_s = 5, the buckling equilibrium path is in the bifurcation

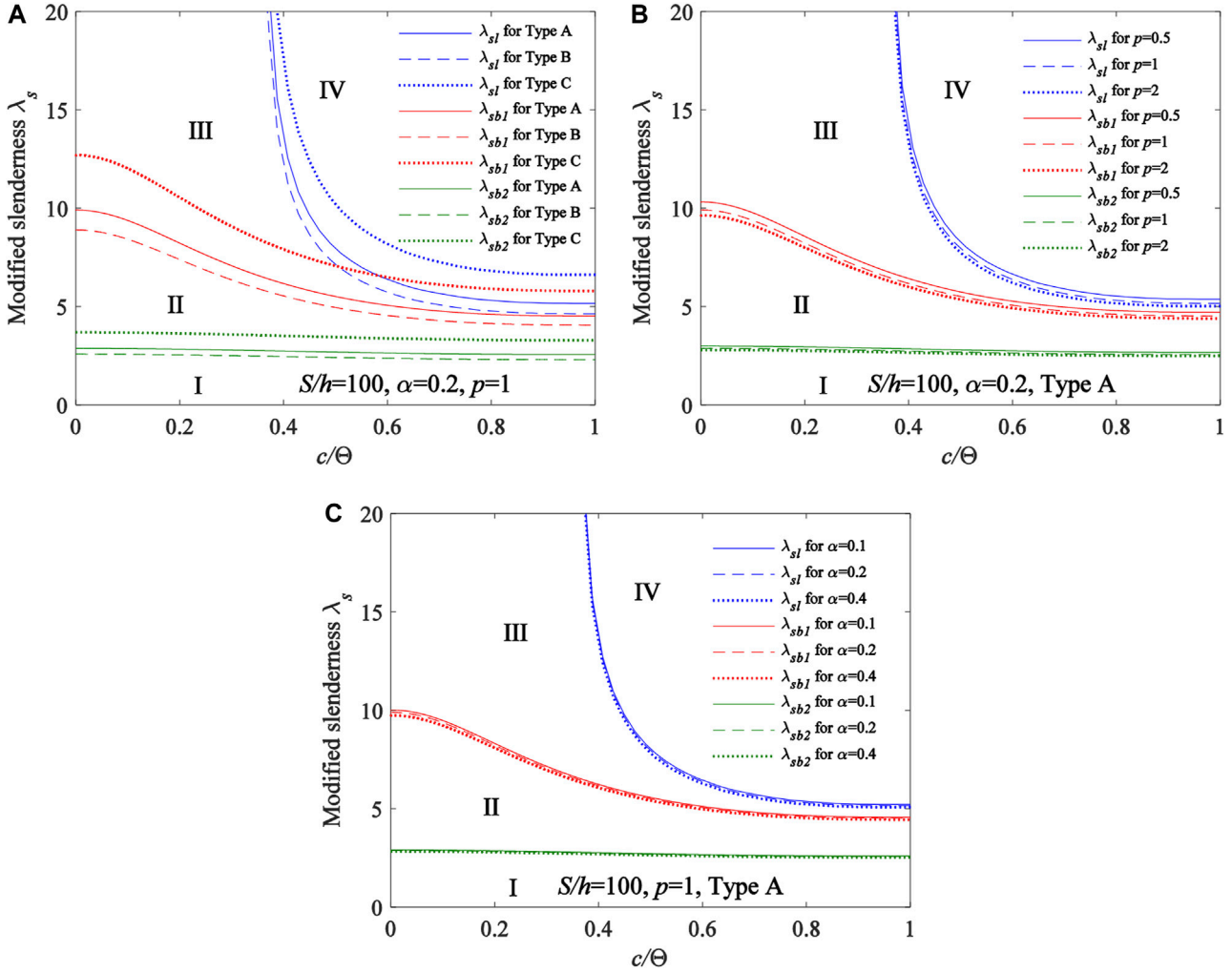

FIGURE 14 | Localized parameter η *vs* Modified geometric slenderness λ_{sl}, λ_{sb1}, and λ_{sb2} **(A)** different type of material distributions **(B)** different power-law index p of material distributions **(C)** different proportional coefficient of homogeneous ceramic layer.

buckling mode, which has two bifurcation buckling point. **Figure 13E** shows when λ_s = 5.45, the buckling equilibrium path is in the lowest bifurcation buckling dominant mode, which has the same upper limit point and upper bifurcation buckling point, this mode is a switches of bifurcation buckling domination and limit point buckling domination. **Figure 13F** shows when λ_s = 8, the buckling equilibrium path is in the bifurcation buckling dominant mode. Therefore, the modified geometric slenderness λ_s of a fixed FGM arch play an important role in determining its buckling mode.

The modified geometric slenderness λ_s obtained from **Eq. 48** can make fixed FGM arches lose its stability in the lowest limit buckling mode. This modified geometric slenderness λ_{sl} can be expressed as

$$\lambda_s \geq \lambda_{sl} = \frac{2\pi}{h}\sqrt{\frac{\kappa\pi}{A_k\left(\frac{B}{\pi^2}+\frac{5}{3}\right)}} \tag{58}$$

The modified geometric slenderness λ_s obtained from **Eq. 53** can make fixed FGM arches lose its stability in the lowest bifurcation buckling mode. This modified geometric slenderness λ_{sb1} can be expressed as

$$\lambda_s \geq \lambda_{sb1} = \frac{1}{h}\sqrt{\frac{\kappa\beta_{b1}^2}{A_k\left(\frac{B_3^2}{4A_3}-\frac{1}{12\sin^2\beta_{b1}}+\frac{1}{12\beta_{b1}^2}\right)}}, \tag{59}$$

When the fixed FGM arches lose its stability in the lowest bifurcation buckling dominant mode, the modified geometric slenderness λ_{sb2} corresponding to this mode can be obtained by equaling the upper bifurcation instability load to the upper limit point buckling load.

Typical variation curves of the localized parameter η *vs* the modified geometric slenderness λ_s are shown in **Figure 14A** for FGM arches having different type of material distributions, in **Figure 14B** for FGM arches having different power-law index p of

material distributions and in **Figure 14C** for FGM arches having different proportional coefficient of homogeneous ceramic layer α, where S/h = 100. It can be seen from **Figure 14** that the localized parameter η has a significant effect on the modified geometric slenderness λ_{sb1}, λ_{sb2}, and a slightly effect on the modified geometric slenderness λ_{sl}, the modified geometric slenderness λ_{sl}, λ_{sb1}, and λ_{sb2} increase with a decrease of the localized parameter η of the locally uniformly distributed radial load. **Figure 14** defines four regions, region I corresponding to FGM arches with $\lambda_s < \lambda_{sl}$ is subjected to the no buckling mode, region II corresponding to FGM arches with $\lambda_{sl} < \lambda_s < \lambda_{sb1}$ is subjected to the limit point buckling mode, region III corresponding to FGM arches with $\lambda_{sb1} < \lambda_s < \lambda_{sb2}$ is subjected to the bifurcation buckling mode, region IV corresponding to FGM arches with $\lambda_s > \lambda_{sb2}$ is subjected to the bifurcation buckling dominant mode. In addition, it can be seen from **Figure 14A** that the type of material distributions has a significant effect on the modified geometric slenderness λ_{sl}, λ_{sb1} and λ_{sb2}, Type C has largest modified geometric slenderness λ_{sl}, λ_{sb1} and λ_{sb2} among Type A, Type B and Type C, **Figures 14B,C** shows the modified geometric slenderness λ_{sl}, λ_{sb1} and λ_{sb2} increase with an decrease of the power-law index p of material distributions and the proportional coefficient of homogeneous ceramic layer α.

CONCLUSION

Theoretical studies of the nonlinear in-plane buckling of a fixed circular functionally graded material (FGM) arches under a locally uniformly distributed radial load have been explored in this paper. It was found that fixed FGM arches under a locally uniformly distributed radial load may buckle in a limit point buckling mode or in a bifurcation buckling mode. Theoretical solutions for the limit point buckling load and bifurcation buckling loads and nonlinear equilibrium path of the fixed FGM arches that are subjected to three different types of material distributions were obtained. It was found that the type of material distributions of the fixed FGM arches slight the limit point buckling loads and bifurcation buckling loads as well as the nonlinear equilibrium path significantly. Type C had a largest limit point buckling load and a largest bifurcation buckling load among Type A, Type B and Type C, it indicated that under the same proportion of metal and ceramic materials, the distribution of ceramics on the upper and lower surfaces of the cross-section can greatly improve the stability of the FGM arch. In addition, the limit point buckling load and bifurcation buckling load also increase with an increase of the modified geometric slenderness λ_s and the localized parameter η and the proportional coefficient of homogeneous ceramic layer α as well as a decrease of the power-law index p of material distributions of the FGM arch.

The critical modified geometric slendernesses λ_{sl}, λ_{sb1}, and λ_{sb2} that are switches of buckling modes were also derived. The localized parameter η has a significant effect on the modified geometric slenderness λ_{sb1}, λ_{sb2}, and limited effect on the modified geometric slenderness λ_{sl}, the modified geometric slenderness λ_{sl}, λ_{sb1}, and λ_{sb2} increase with a decrease of the localized parameter η of the locally uniformly distributed radial load. It was found that Region I corresponding to FGM arches with $\lambda_s < \lambda_{sl}$ is subjected to the no buckling mode, region II corresponding to FGM arches with $\lambda_{sl} < \lambda_s < \lambda_{sb1}$ is subjected to the limit point buckling mode, region III corresponding to FGM arches with $\lambda_{sb1} < \lambda_s < \lambda_{sb2}$ is subjected to the bifurcation buckling mode, region IV corresponding to FGM arches with $\lambda_s > \lambda_{sb2}$ is subjected to the bifurcation buckling dominant mode. In addition, it was also found that the type of material distributions has a significant effect on the modified geometric slenderness λ_{sl}, λ_{sb1} and λ_{sb2}, Type C has the largest modified geometric slenderness λ_{sl}, λ_{sb1} and λ_{sb2} among Type A, Type B and Type C, and the modified geometric slenderness λ_{sl}, λ_{sb1} and λ_{sb2} increase with an decrease of the power-law index p of material distributions and the proportional coefficient of homogeneous ceramic layer α. Theoretical solutions for FGM arches under a locally uniformly distributed radial load derived in this paper would be useful as a reference for the design of buckling of the FGM arches in the future.

DATA AVAILABILITY STATEMENT

The original contributions presented in the study are included in the article/supplementary material, further inquiries can be directed to the corresponding authors.

AUTHOR CONTRIBUTIONS

HL: Data curation, Formal analysis, Investigation, Methodology, Software, Visualization, Writing-review and editing. JZ: Formal analysis, Validation, Writing-review and editing. ZY: Formal analysis, Investigation, Methodology, Writing-original draft. AL: Data curation, funding acquisition. JZ: Project administration.

FUNDING

This work was funded by (Characteristic innovation projects of colleges and universities in Guangdong Province) with grant number (2019KTSCX190) and (National Natural Science Foundation of China) with grant number (51908146).

REFERENCES

Al-shujairi, M., and Mollamahmutoğlu, C. (2018). Buckling and Free Vibration Analysis of Functionally Graded sandwich Microbeams Resting on Elastic Foundation by Using Non Local Strain Gradient Theory in Conjunction with Higher Order Shear Theories under thermal Effect. *Compos. Part. B* 154, 292–312. doi:10.1016/j.compositesb.2018.08.103

Asgari, H., Bateni, M., Kiani, Y., and Eslami, M. R. (2014). Non-linear Thermo-Elastic and Buckling Analysis of FGM Shallow Arches. *Compos. Struct.* 109, 75–85. doi:10.1016/j.compstruct.2013.10.045

Bateni, M., and Eslami, M. R. (2015). Non-linear In-Plane Stability Analysis of FG Circular Shallow Arches under Uniform Radial Pressure. *Thin-Walled Structures* 94, 302–313. doi:10.1016/j.tws.2015.04.019

Bateni, M., and Eslami, M. R. (2014). Non-linear In-Plane Stability Analysis of FGM Circular Shallow Arches under central Concentrated Force. *Int. J. Non-Linear Mech.* 60, 58–69. doi:10.1016/j.ijnonlinmec.2014.01.001

Bradford, M. A., Uy, B., and Pi, Y.-L. (2002). In-plane Elastic Stability of Arches under a central Concentrated Load. *J. Eng. Mech.* 128, 710–719. doi:10.1061/(asce)0733-9399(2002)128:7(710)

Cai, J., and Feng, J. (2010). Buckling of Parabolic Shallow Arches when Support Stiffens under Compression. *Mech. Res. Commun.* 37, 467–471. doi:10.1016/j.mechrescom.2010.05.004

Cai, J., Xu, Y., Feng, J., and Zhang, J. (2012). In-plane Elastic Buckling of Shallow Parabolic Arches under an External Load and Temperature Changes. *J. Struct. Eng.* 138, 1300–1309. doi:10.1061/(asce)st.1943-541x.0000570

Cai, J., Zhou, Y., and Feng, J. (2013). Post-buckling Behavior of a Fixed Arch for Variable Geometry Structures. *Mech. Res. Commun.* 52, 74–80. doi:10.1016/j.mechrescom.2013.07.002

Chen, M.-T., and Young, B. (2021). Beam-column Design of Cold-Formed Steel Semi-oval Hollow Non-slender Sections. *Thin-walled Structures* 162, 107376. doi:10.1016/j.tws.2020.107376

Chen, M.-T., Young, B., Martins, A. D., Camotim, D., and Dinis, P. B. (2021). Experimental Investigation on Cold-Formed Steel Lipped Channel Beams Affected by Local-Distortional Interaction under Non-uniform Bending. *Thin-walled Structures* 161, 107494. doi:10.1016/j.tws.2021.107494

Han, Q., Cheng, Y., Lu, Y., Li, T., and Lu, P. (2016). Nonlinear Buckling Analysis of Shallow Arches with Elastic Horizontal Supports. *Thin-Walled Structures* 109, 88–102. doi:10.1016/j.tws.2016.09.016

Hu, C.-F., Li, Z., and Hu, Q.-S. (2021). On Non-linear Behavior and Buckling of Arch-Beam Structures. *Eng. Structures* 239 (2), 112214. doi:10.1016/j.engstruct.2021.112214

Lu, H., Liu, A., Pi, Y.-L., Bradford, M. A., Fu, J., and Huang, Y. (2018). Localized Loading and Nonlinear Instability and post-instability of Fixed Arches. *Thin-Walled Structures* 131, 165–178. doi:10.1016/j.tws.2018.06.019

Lu, H. W., Liu, L. L., Liu, A. R., Pi, Y.-L., Bradford, M. A., and Huang, Y. H. (2020). Effects of Movement and Rotation of Supports on Nonlinear Instability of Fixed Shallow Arches. *Thin-Walled Structures* 122, 2020. doi:10.1016/j.tws.2020.106909

Moita, J. S., Araújo, A. L., Correia, V. F., Mota Soares, C. M., and Herskovits, J. (2018). Material Distribution and Sizing Optimization of Functionally Graded Plate-Shell Structures. *Composites B: Eng.* 142, 263–272. doi:10.1016/j.compositesb.2018.01.023

Pi, Y.-L., Bradford, M. A., and Liu, A. (2017). Nonlinear Equilibrium and Buckling of Fixed Shallow Arches Subjected to an Arbitrary Radial Concentrated Load. *Int. J. Str. Stab. Dyn.* 17 (8), 1750082. doi:10.1142/s0219455417500821

Pi, Y.-L., and Bradford, M. A. (2009). Non-linear In-Plane Postbuckling of Arches with Rotational End Restraints under Uniform Radial Loading. *Int. J. Non-Linear Mech.* 44 (9), 975–989. doi:10.1016/j.ijnonlinmec.2009.07.003

Pi, Y.-L., Bradford, M. A., and Tin-Loi, F. (2008). Non-linear In-Plane Buckling of Rotationally Restrained Shallow Arches under a central Concentrated Load. *Int. J. Non-Linear Mech.* 43 (1), 1–17. doi:10.1016/j.ijnonlinmec.2007.03.013

Pi, Y.-L., Bradford, M. A., and Uy, B. (2002). In-plane Stability of Arches. *Int. J. Sol. Structures* 39 (1), 105–125. doi:10.1016/s0020-7683(01)00209-8

Plaut, R. H., and Raymond, H. (1990). Buckling of Shallow Arches with Supports that Stiffen when Compressed. *J. Eng. Mech.* 116 (4), 973–976. doi:10.1061/(asce)0733-9399(1990)116:4(973)

Rastgo, A., Shafie, H., and Allahverdizadeh, A. (2005). Instability of Curved Beams Made of Functionally Graded Material under Thermal Loading. *Int. J. Mech. Mater. Des.* 2, 117–128. doi:10.1007/s10999-005-4446-3

Schreyer, H. L. (1972). The Effect of Initial Imperfections on the Buckling Load of Shallow Circular Arches. *J. Appl. Mech.* 39 (2), 445–450. doi:10.1115/1.3422698

Simsek, M. (2016). Buckling of Timoshenko Beams Composed of Two-Dimensional Functionally Graded Material (2D-FGM) Having Different Boundary Conditions. *Compos. Struct.* 49, 304–314. doi:10.1016/j.compstruct.2016.04.034

Song, X., and Li, S. R. (2008). Nonlinear Stability of Fixed-Fixed Fgm Arches Subjected to Mechanical and thermal Loads. *Amr* 33-37, 699–706. doi:10.4028/www.scientific.net/amr.33-37.699

Timoshenko, S. P., Gere, J. M., Prager, W., Gere, J. M., and Prager, W. (1962). Theory of Elastic Stability, Second Edition. *J. Appl. Mech.* 29 (1), 220–221. doi:10.1115/1.3636481

Yan, S.-t., Shen, X., Chen, Z., and Jin, Z. (2017). On Buckling of Non-uniform Shallow Arch under a central Concentrated Load. *Int. J. Mech. Sci.* 133, 330–343. doi:10.1016/j.ijmecsci.2017.08.046

Yang, Z., Feng, C., Yang, J., Wang, Y., Lv, J., Liu, A., et al. (2020a). Geometrically Nonlinear Buckling of Graphene Platelets Reinforced Dielectric Composite (GPLRDC) Arches with Rotational End Restraints. *Aerospace Sci. Tech.* 107, 106326. doi:10.1016/j.ast.2020.106326

Yang, Z., Zhao, S., Yang, J., Lv, J., Liu, A., and Fu, J. (2020b). In-plane and Out-Of-Plane Free Vibrations of Functionally Graded Composite Arches with Graphene Reinforcements. *Mech. Adv. Mater. Structures*, 1–11. doi:10.1080/15376494.2020.1716420

Yang, Z., Tam, M., Zhang, Y., Kitipornchai, S., Lv, J., and Yang, J. (2020c). Nonlinear Dynamic Response of FG Graphene Platelets Reinforced Composite Beam with Edge Cracks in thermal Environment. *Int. J. Str. Stab. Dyn.* 20, 2043005. doi:10.1142/s0219455420430051

Yang, Z., Liu, A., Yang, J., Lai, S.-K., Lv, J., and Fu, J. (2021a). Analytical Prediction for Nonlinear Buckling of Elastically Supported FG-GPLRC Arches under a central point Load. *Materials* 14 (8), 2026. doi:10.3390/ma14082026

Yang, Z., Wu, D., Yang, J., Lai, S.-K., Lv, J., Liu, A., et al. (2021b). Dynamic Buckling of Rotationally Restrained FG Porous Arches Reinforced with Graphene Nanoplatelets under a Uniform Step Load. *Thin-Walled Structures* 166, 108103. doi:10.1016/j.tws.2021.108103

Conflict of Interest: The authors declare that the research was conducted in the absence of any commercial or financial relationships that could be construed as a potential conflict of interest.

Publisher's Note: All claims expressed in this article are solely those of the authors and do not necessarily represent those of their affiliated organizations, or those of the publisher, the editors and the reviewers. Any product that may be evaluated in this article, or claim that may be made by its manufacturer, is not guaranteed or endorsed by the publisher.

frontiers in Materials

ORIGINAL RESEARCH
published: 12 August 2021
doi: 10.3389/fmats.2021.719536

Biomechanical Properties of 3D-Printed Cervical Interbody Fusion Cage With Novel SF/nHAp Composites

*Shuang Chen[1†], Yi Meng[1†], Guozhi Wu[1†], Zhize Liu[1], Xiaodong Lian[1], Jianyu Hu[1], Dongfang Yang[1], Guiqi Zhang[1], Kun Li[2] and Hao Zhang[1]**

[1]Department of Orthopedics, Affiliated Dalian Municipal Central Hospital, Dalian Medical University, Dalian, China, [2]Department of Orthopedics, The Peoples Hospital of Langfang City, Langfang, China

Anterior cervical discectomy and fusion (ACDF) is a commonly used surgical method for the treatment of cervical spondylosis. As ACDF surgery is widely used in clinics, identifying suitable materials to design and prepare cervical interbody fusion cages is a hot research topic. Here, we describe a new three-dimensional (3D) printing approach to create stretchable and tough silk fibroin/nano-hydroxyapatite (SF/nHAp) composites with tunable mechanical properties. The compressive strength of the novel composites with biomimetic structure could reach more than 128 MPa. More importantly, the composites were prepared using 30% silk fibroin and 70% hydroxyapatite, a composition similar to the human bone tissue. Finite element analysis results indicate that the stress distribution of SF/nHAp composite cervical interbody fusion cages *in vivo* is more uniform than that of commercial Ti alloy cages. This study evaluates the effectiveness of SF/nHAp composites for application in cervical interbody fusion cages and in the field of bone tissue engineering.

Keywords: 3D printing, cervical interbody fusion cages, biomechanical properties, silk fibroin, nano-hydroxyapatite, composites

OPEN ACCESS

Edited by:
Xufeng Dong,
Dalian University of Technology, China

Reviewed by:
Ying Hu,
Hefei University of Technology, China
Qingyu Peng,
Harbin Institute of Technology, China

****Correspondence:***
Hao Zhang
691248842@qq.com

[†]These authors have contributed equally to this work

Specialty section:
This article was submitted to Polymeric and Composite Materials, a section of the journal Frontiers in Materials

Received: *02 June 2021*
Accepted: *29 June 2021*
Published: *12 August 2021*

Citation:
Chen S, Meng Y, Wu G, Liu Z, Lian X, Hu J, Yang D, Zhang G, Li K and Zhang H (2021) Biomechanical Properties of 3D-Printed Cervical Interbody Fusion Cage With Novel SF/nHAp Composites. Front. Mater. 8:719536. doi: 10.3389/fmats.2021.719536

INTRODUCTION

In cervical fusion surgery, it is always difficult to choose the appropriate bone implant (Park and Roh, 2013; Ming et al., 2015; Mazas et al., 2019). A bone tissue engineering scaffold not only plays the role of structural support in a human body but is also beneficial for cell adhesion, growth, and reproduction, providing a place for tissue regeneration and plasticity (Dias et al., 2021; Su et al., 2021). Therefore, bone tissue engineering scaffold materials should have good biocompatibility, degradability, osteoinduction, certain compressive strength, and toughness to meet the requirements of cell proliferation and differentiation on the surface of materials (Ming et al., 2015; Wei et al., 2019).

Currently, inorganic composite materials occupy a very important place in the research of bone tissue engineering scaffold materials. Among these inorganic materials, hydroxyapatite, the main component of human bones and teeth, has good biocompatibility and is a commonly used hard tissue material that can perfectly combine with human bones and induce the formation of new bones (Cho et al., 2017; Pitjamit et al., 2020; Thunsiri et al., 2020). However, a single hydroxyapatite particle has inherent defects such as high brittleness and low bending strength, which limit its further application in bone tissue engineering. Currently, the most commonly used method to improve the comprehensive properties of hydroxyapatite is by compounding it with metals and ceramics (Jin et al., 2014; Farokhi et al., 2018). However, hydroxyapatite/metal composites have some problems, such as metal corrosion, dense fibrous tissue, and stress shielding at the bone–graft interface (Larobina et al., 2012; Ming et al., 2015; Campo et al., 2017; Deng et al., 2017). However, hydroxyapatite/polymer composites have gradually become a

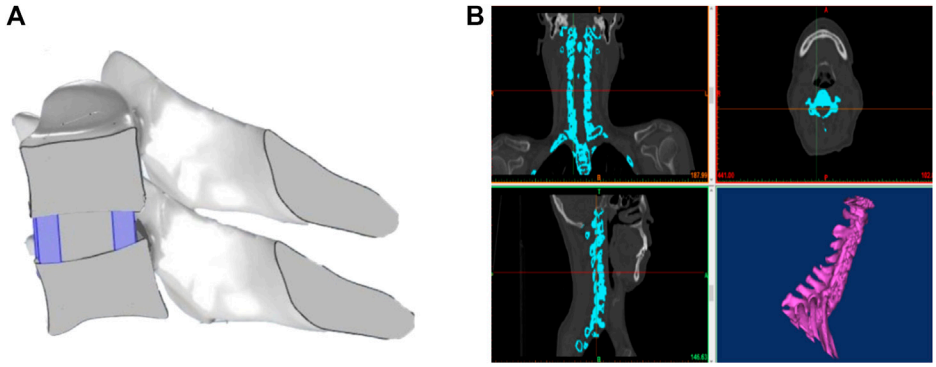

FIGURE 1 | (A) 3D model of the cervical interbody fusion cage obtained by Mimics. **(B)** Original 3D CT image of the cervical spine scanned from a healthy woman.

research hotspot because of their advantages of no tissue reaction, no inhibition of bone growth, and no need of secondary surgery (Jin et al., 2014; Cho et al., 2017; Farokhi et al., 2018).

With the rapid development of nanotechnology, the application of nano-hydroxyapatite is becoming more extensive. The nanostructure of nano-hydroxyapatite can provide an amazing interface effect, significantly improving its biomechanical strength and increasing its surface bioactivity (Ruan et al., 2018). In addition, some polymers, including synthetic and natural polymers, with good flexibility and degradability have gradually gained attention as promising candidate materials for compounding with hydroxyapatite (Hassanajili et al., 2019; Pei et al., 2019; Cakmak et al., 2020). Compared with synthetic polymers, natural polymers have attracted more attention in bone tissue engineering due to their unique biocompatibility and biodegradability. Chen et al. made a kind of bone implant material with nano-hydroxyapatite/collagen composite material which has high biocompatibility and strong biomechanical properties, and is an ideal bone tissue engineering scaffold choice (Chen et al., 2016). However, collagen materials are mainly extracted from animals or synthesized artificially, which makes it difficult to be widely used in experimental research and clinical practice (Sun et al., 2016; Kambe et al., 2017). Among natural polymers, silk fibroin derived from silk is a natural high-purity protein composed of a variety of amino acids and has a clear sequence of amino acids, and this natural polymer has high safety, which can eliminate the potential immune sensitization (Jin et al., 2014; Gholipourmalekabadi et al., 2015). The most striking feature is that silk fibroin also has excellent biological activity, which can support the adsorption, adhesion, diffusion, and differentiation of various cells on its surface (Ruan et al., 2018). In addition, silk fibroin has excellent vascular induction ability, which further promotes the repair of surrounding tissues. These excellent properties make silk fibroin an ideal choice to replace collagen (Kambe et al., 2017).

In this work, we constructed a composite material for bone tissue engineering by combining silk fibroin (SF) with nano-hydroxyapatite (nHAp) and prepared a cervical interbody fusion cage by 3D printing. The mechanical properties of the SF/nHAp composite cage were tested, and finite element analysis was conducted to compare the biomechanical properties of the SF/nHAp cage and commercial Ti alloy cages.

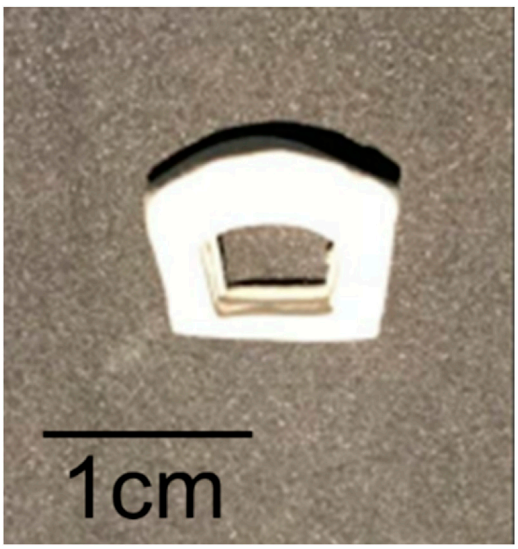

FIGURE 2 | Photos of the 3D-printed cervical interbody fusion cage.

MATERIALS AND METHODS

Materials

Silk fibroin was purchased from the Institute of Chemistry, Chinese Academy of Sciences; nano-hydroxyapatite was obtained from Beijing Deco Island Gold Technology Co., Ltd. Sodium carbonate, calcium chloride, ethanol, deionized water, diammonium hydrogen phosphate, and ammonia water were all purchased from Sinopharm Chemical Reagent Co., Ltd. (China) and used as received without further purification.

Fabrication of Silk Fibroin

First, 0.5% sodium carbonate solution in a beaker was heated to a slight boiling point, 15 g silk was added and the mixture stirred

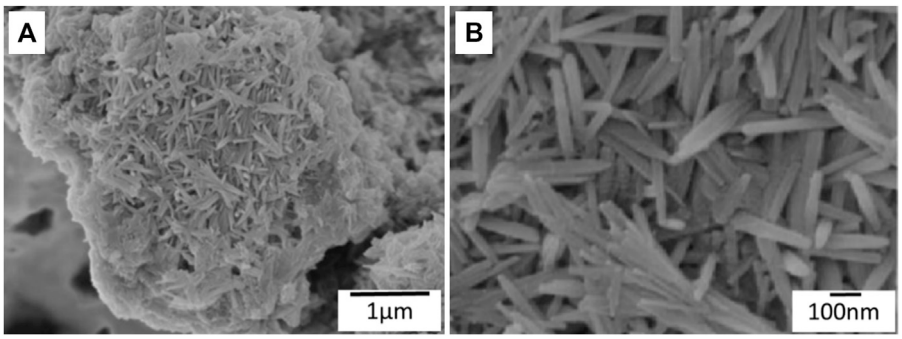

FIGURE 3 | (A) SEM images showing nano-hydroxyapatite needles formed on the silk fibroin substrate. **(B)** High magnification of SEM images of nano-hydroxyapatite needles.

for 0.5 h, the mixture was rinsed with deionized water, the above process was repeated for secondary degumming, and then the mixture was allowed to dry naturally. The degummed silk fibroin was weighed. Then, 13.8 g degummed silk fibroin was added into a ternary system of calcium chloride, ethanol, and water at a molar ratio of 1:2:8 and dissolved at 60°C for 2 h. After dissolution, 1.5 times deionized water (heated to 60°C in advance) was added, the mixture cooled to room temperature, filtered with a filter membrane, and transferred into a dialysis bag for dialysis for 3–5 days to obtain silk fibroin (SF) material (Huang et al., 2019).

Preparation of SF/nHAp Composites

15 g silk was soaked in 0.5% sodium carbonate solution (90°C) for 0.5 h, and then the aforementioned process was repeated for secondary degumming. Then, the mixture was air-dried naturally to obtain degummed silk fibroin. 3.25 g of degummed silk fibroin was dissolved in 36.5 ml of calcium chloride, ethanol, and water at a molar ratio of 1:2:8 at 60°C; temperature was adjusted to 75°C; and diammonium hydrogen phosphate solution was added dropwise. After 24 h, the product was washed with deionized water and freeze-dried to obtain SF/nHAp composites.

Cervical Interbody Fusion Cage Fabricated With 3D Printing Technique

A 3D bioprinter (EFD company, 2400) was used to prepare the 3D printing cage. The 3D model (**Figure 1A**) of the cage that was supposed to be implanted between C5 and C6 was obtained by Mimics. The original 3D CT image of the cervical spine (**Figure 1B**) was scanned from a healthy woman, who is 55 years old, 165 cm tall, and 70 kg in weight.

The prepared SF/nHAp composites were loaded into a syringe and centrifuged to exhaust air. Under the condition of pressure of 15Psi and linearity of 8 mm/s, 3D direct writing printing and layer-by-layer printing were carried out to make the cervical interbody fusion cage. The 3D printing cervical interbody fusion cage was soaked in 5% calcium chloride–water–ethanol solution for one night and dried naturally to obtain the cervical interbody fusion cage, as shown in **Figure 2**.

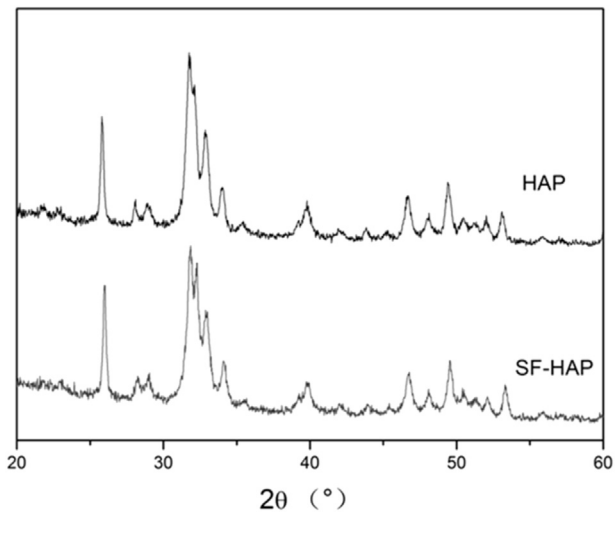

FIGURE 4 | XRD patterns of the pure HAp and SF/nHAp composites.

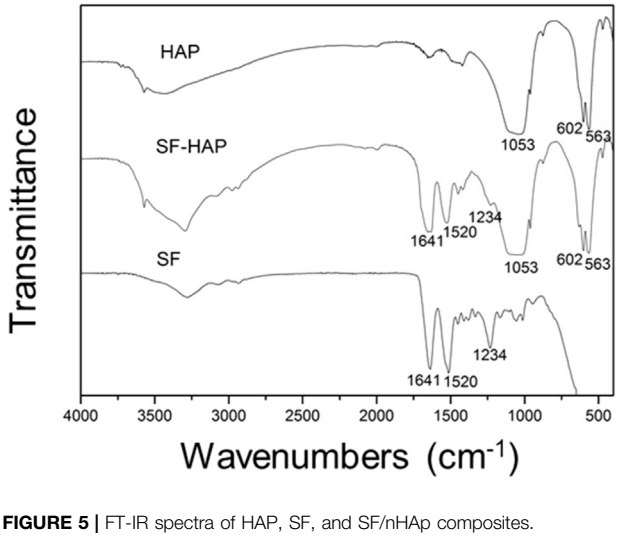

FIGURE 5 | FT-IR spectra of HAP, SF, and SF/nHAp composites.

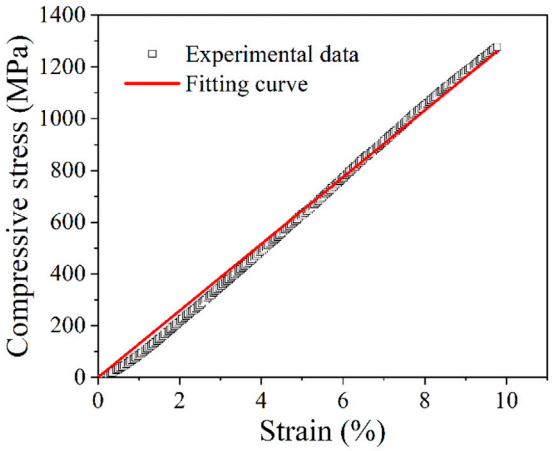

FIGURE 6 | Compression curve of SF/nHAp composites.

TABLE 1 | Mechanical properties of model components.

Model components	Young's modulus (GPa)	Poisson's ratio
Cortical bone	12	0.29
Cancellous bone	0.1	0.29
SF/nHAp composite cage	12.9	0.29
Titanium alloy cage	110	0.29

Characterization of SF/nHAp Composites

The crystalline structures and chemical compositions of the SF/nHAp composites were examined by X-ray diffraction (XRD; Empyrean, Panaco) and Fourier transform infrared spectroscopy (FTIR; iS10, Thermo Fisher Scientific). The morphologies of the SF/nHAp composites were determined by scanning electron microscopy (SEM; JSM7500F, JEOL).

Mechanical Property Testing of SF/nHAp Composites

An electronic universal material testing machine (Instron 3365, Instron) was used to test the compressive properties of the SF/nHAp composites. The unconstrained sample, with size 12.7 × 12.7 × 25.4 mm, was compressed between flat steel plates at a constant strain rate of 1 mm/min.

RESULTS AND DISCUSSION

The SEM images (**Figure 3** show the formation of nano-hydroxyapatite needles on the silk fibroin substrate. The length and width of the nano-hydroxyapatite needles are ~400 and ~24 nm, respectively.

Figure 4 presents the XRD patterns of the pure HAp and SF/nHAp composites. The XRD pattern shows that the peak position of SF/nHAp is the same as that of pure HAP, and there is no other phosphate diffraction peak, indicating that hydroxyapatite crystals are formed. It could be proved that although the silk fibroin material is present in the SF/nHAp composite material, it does not affect the formation of hydroxyapatite crystals in the composite material. In addition, the bottom of the SF/nHAp diffraction peak is broad and not sharp.

The FT-IR results show that SF/nHAp composites are formed, as shown in **Figure 5**. Among them, 1,053, 602,, and 563 cm^{-1} correspond to the characteristic peak of phosphate, indicating that the compositional and structural properties of hydroxyapatite are present in the composites, and 1,641, 1,520, and 1,234 cm^{-1} correspond to the characteristic peaks of amide I, II, and III, respectively, in the silk fibroin structure. Based on the above analysis, it can be seen that the structure and properties of SF/nHAp composites are clear.

With the development of nanotechnology, nano-hydroxyapatite with ultra-fine and nanostructures is being widely studied. Nano-hydroxyapatite materials can reduce the sintering temperature, improve the surface and interface effects of the nanomaterials, and degrade and absorb in the biological environment in the human body. Because of the excellent properties of silk fibroin and nano-hydroxyapatite materials, more and more research studies have used silk fibroin as a scaffold material combined with hydroxyapatite to make spinal intervertebral fusion cages. In this study, we successfully prepared SF/nHAp composites containing 30% silk

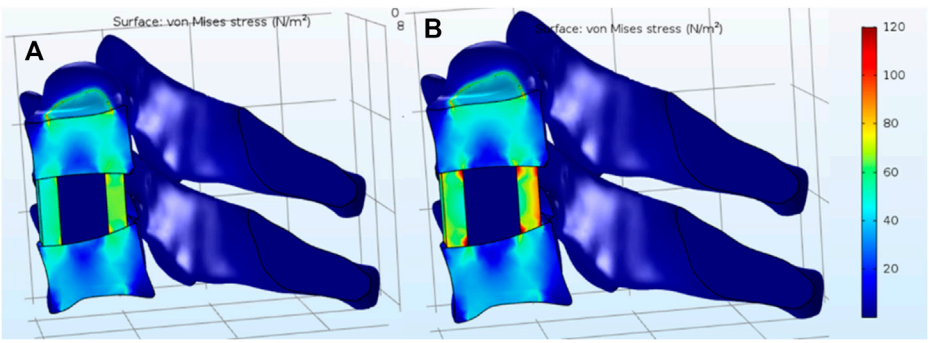

FIGURE 7 | Stress distribution under standing condition. **(A)** SF/nHAp composite cage. **(B)** Ti alloy cage.

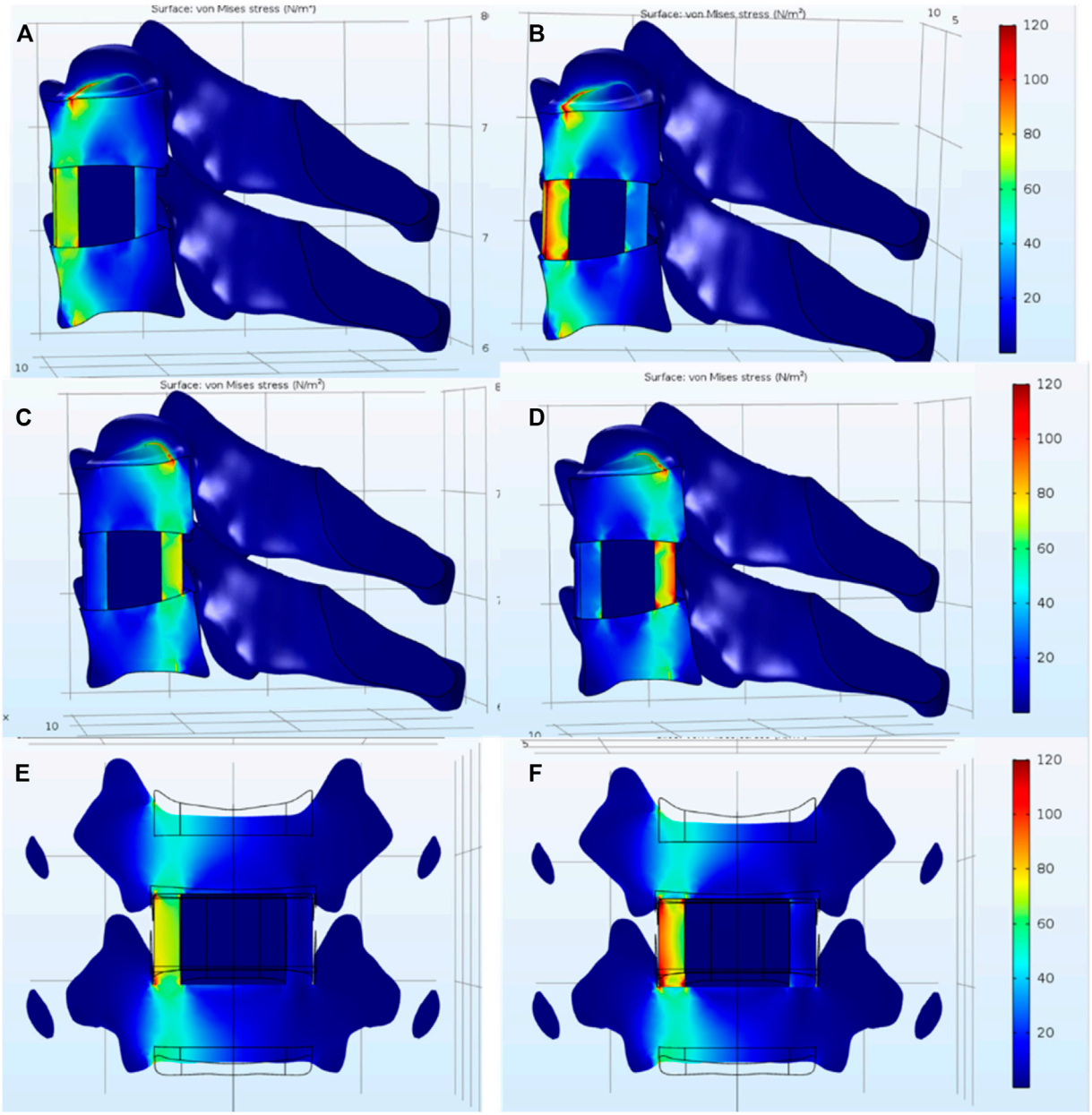

FIGURE 8 | Stress distribution under **(A)** anteflexion, **(C)** retro-extension, and **(E)** side bend with a SF/nHAp composite cage. Stress distribution under **(B)** anteflexion, **(D)** retro-extension, and **(F)** side bend with a Ti alloy cage.

fibroin and 70% hydroxyapatite. The composition (Ca/P ratio 1.67) is similar to that in the human bone tissue (Ca/P ratio 1.67).

The compression curve of the SF/nHAp composites is shown in **Figure 6**. The compressive stress linearly increases with increasing strain. The compressive stress at 9.77% strain is 1.28 GPa. The composite did not yield at ~10%, which indicates that its compressive strength is higher than 1.28 GPa. The stress vs. strain curve is fitted by a linear equation. Young's modulus of the composites is 12.9 GPa, which can be obtained as the slope of the fitting curve.

FINITE ELEMENT ANALYSIS

To compare the mechanical behavior of the SF/nHAp composite cage and commercial titanium alloy cages, a finite element model was established by using COMSOL Multiphysics. The mechanical properties of the model components are listed in **Table 1**.

Generally, the mass of a human head is 7% of the person's total body mass. Therefore, the weight of a woman's head is ~52N. It can be deduced that the moment applied on the C5 cervical vertebra is 1.8N•m. The stress distribution after implanting the cage is analyzed under various conditions, including standing,

anteflexion, retro-extension, and side bend. As shown in **Figure 7**, under standing condition, the stress distributes uniformly in the SF/nHAp composite cage, while the stress concentration can be observed on the edge of the end plate when the Ti alloy cage is implanted.

Figure 8 shows the stress distribution under anteflexion, retro-extension, and side bend. By comparison, the stress concentration in the SF/nHAp composite cage is less significant than that in the Ti alloy cage. The results indicate that by using SF/nHAp composites with similar mechanical properties as the natural bone, stress concentration could be reduced compared to that using traditional Ti alloys.

CONCLUSION

In this study, a novel 3D-printed SF/nHAp composite scaffold was fabricated by using the direct writing–based 3D printing technology. This scaffold with biomimetic structure and appropriate mechanical properties showed good biocompatibility and provided suitable templates for cervical interbody fusion cages. Importantly, composites containing 30% silk fibroin and 70% hydroxyapatite were prepared by a safe and effective mineral co-deposition method. This biomimetic preparation method could be used to successfully prepare a composition and structure similar to the human bone tissue, so it is expected that this new composite material could become the ideal object of bone implant materials that are suitable for spinal bone graft fusion in follow-up research studies. This will provide access to functional multi-materials that have applications in cervical interbody fusion cages.

DATA AVAILABILITY STATEMENT

The raw data supporting the conclusion of this article will be made available by the authors, without undue reservation.

ETHICS STATEMENT

Written informed consent was obtained from the individual(s) for the publication of any potentially identifiable images or data included in this article.

AUTHOR CONTRIBUTIONS

Conceptualization: SC and HZ; methodology: YM and GW; validation: ZL and XL; formal analysis: JH; investigation: SC; resources: DY; data curation: GZ and KL; writing—original draft preparation: SC and YM; writing—review and editing: GW and HZ; supervision: HZ; project administration: HZ; funding acquisition: HZ. All authors have read and agreed to the published version of the manuscript.

FUNDING

This research was funded by Dalian Medical Science Research Project (grant number 2011001).

REFERENCES

Cakmak, A. M., Unal, S., Sahin, A., Oktar, F. N., Sengor, M., Ekren, N., et al. (2020). 3D Printed Polycaprolactone/gelatin/bacterial Cellulose/hydroxyapatite Composite Scaffold for Bone Tissue Engineering. *Polymers* 12, 1962. doi:10.3390/polym12091962

Campo, R. D., Savoini, B., Muñoz, A., Monge, M. A., and Pareja, R. (2017). Processing and Mechanical Characteristics of Magnesium-Hydroxyapatite Metal Matrix Biocomposites. *J. Mech. Behav. Biomed. Mater.* 69, 135–143. doi:10.1016/j.jmbbm.2016.12.023

Chen, Y., Lü, G., Wang, B., Li, L., and Kuang, L. (2016). A Comparison of Anterior Cervical Discectomy and Fusion (ACDF) Using Self-Locking Stand-Alone Polyetheretherketone (PEEK) Cage with ACDF Using Cage and Plate in the Treatment of Three-Level Cervical Degenerative Spondylopathy: A Retrospective Study with 2-year Follow-Up. *Eur. Spine J.* 25, 2255–2262. doi:10.1007/s00586-016-4391-x

Cho, Y. S., Hong, M. W., Jeong, H.-J., Lee, S.-J., Kim, Y. Y., and Cho, Y.-S. (2017). The Fabrication of Well-Interconnected Polycaprolactone/hydroxyapatite Composite Scaffolds, Enhancing the Exposure of Hydroxyapatite Using the Wire-Network Molding Technique. *J. Biomed. Mater. Res.* 105, 2315–2325. doi:10.1002/jbm.b.33769

Deng, Y., Zhang, M., Chen, X., Pu, X., Liao, X., Huang, Z., et al. (2017). A Novel Akermanite/poly (Lactic-Co-Glycolic Acid) Porous Composite Scaffold Fabricated via a Solvent Casting-Particulate Leaching Method Improved by Solvent Self-Proliferating Process. *Regenerative Biomater.* 4, 233–242. doi:10.1093/rb/rbx014

Dias, D., Vale, A. C., Cunha, E. P. F., Paiva, M., Reis, R. L., Vaquette, C., et al. (2021). 3D -printed Cryomilled Poly(ε-caprolactone)/graphene Composite Scaffolds for Bone Tissue Regeneration. *J. Biomed. Mater. Res.* 109, 961–972. doi:10.1002/jbm.b.34761

Farokhi, M., Mottaghitalab, F., Samani, S., Shokrgozar, M. A., Kundu, S. C., Reis, R. L., et al. (2018). Silk Fibroin/hydroxyapatite Composites for Bone Tissue Engineering. *Biotechnol. Adv.* 36, 68–91. doi:10.1016/j.biotechadv.2017.10.001

Gholipourmalekabadi, M., Mozafari, M., Gholipourmalekabadi, M., Nazm Bojnordi, M., Hashemi-soteh, M. B., Salimi, M., et al. (2015). In Vitroandin Vivoevaluations of Three-Dimensional Hydroxyapatite/silk Fibroin Nanocomposite Scaffolds. *Biotechnol. Appl. Biochem.* 62, 441–450. doi:10.1002/bab.1285

Hassanajili, S., Karami-Pour, A., Oryan, A., and Talaei-Khozani, T. (2019). Preparation and Characterization of PLA/PCL/HA Composite Scaffolds Using Indirect 3D Printing for Bone Tissue Engineering. *Mater. Sci. Eng. C* 104, 109960. doi:10.1016/j.msec.2019.109960

Huang, T., Fan, C., Zhu, M., Zhu, Y., Zhang, W., and Li, L. (2019). 3D-printed scaffolds of biomineralized hydroxyapatite nanocomposite on silk fibroin for improving bone regeneration, *Applied Surface Science* 467-468, 345-353. doi:10.1016/j.apsusc.2018.10.166

Jin, J., Wang, J., Huang, J., Huang, F., Fu, J., Yang, X., et al. (2014). Transplantation of Human Placenta-Derived Mesenchymal Stem Cells in a Silk Fibroin/hydroxyapatite Scaffold Improves Bone Repair in Rabbits. *J. Biosci. Bioeng.* 118, 593–598. doi:10.1016/j.jbiosc.2014.05.001

Kambe, Y., Murakoshi, A., Urakawa, H., Kimura, Y., and Yamaoka, T. (2017). Vascular Induction and Cell Infiltration into Peptide-Modified Bioactive Silk Fibroin Hydrogels. *J. Mater. Chem. B* 5, 7557–7571. doi:10.1039/c7tb02109g

Larobina, D., Guarino, V., and Ambrosio, L. (2012). Modeling of Phase Separation Mechanism in Polycaprolactone/dioxane Binary Systems. *J. Appl. Biomater. Funct. Mater.* 10, 237–242. doi:10.5301/JABFM.2012.10363

Mazas, S., Benzakour, A., Castelain, J.-E., Damade, C., Ghailane, S., and Gille, O. (2019). Cervical Disc Herniation: Which Surgery?. *Int. Orthopaedics (Sicot)* 43, 761–766. doi:10.1007/s00264-018-4221-3

Ming, J., Jiang, Z., Wang, P., Bie, S., and Zuo, B. (2015). Silk Fibroin/sodium Alginate Fibrous Hydrogels Regulated Hydroxyapatite crystal Growth. *Mater. Sci. Eng. C* 51, 287–293. doi:10.1016/j.msec.2015.03.014

Park, J. H., and Roh, S. W. (2013). Anterior Cervical Interbody Fusion Using Polyetheretherketone Cage Filled with Autologous and Synthetic Bone Graft Substrates for Cervical Spondylosis: Comparative Analysis between PolyBone and Iliac Bone. *Neurol. Med. Chir.(Tokyo)* 53, 85–90. doi:10.2176/nmc.53.85

Pei, B., Wang, Z., Nie, J., and Hu, Q. (2019). Highly Mineralized Chitosan-Based Material with Large Size, Gradient mineral Distribution and Hierarchical Structure. *Carbohydr. Polym.* 208, 336–344. doi:10.1016/j.carbpol.2018.12.087

Pitjamit, S., Thunsiri, K., Nakkiew, W., Wongwichai, T., Pothacharoen, P., and Wattanutchariya, W. (2020). The Possibility of Interlocking Nail Fabrication from FFF 3D Printing PLA/PCL/HA Composites Coated by Local Silk Fibroin for Canine Bone Fracture Treatment. *Materials* 13, 1564. doi:10.3390/ma13071564

Ruan, S.-Q., Deng, J., Yan, L., and Huang, W.-l. (2018). Composite Scaffolds Loaded with Bone Mesenchymal Stem Cells Promote the Repair of Radial Bone Defects in Rabbit Model. *Biomed. Pharmacother.* 97, 600–606. doi:10.1016/j.biopha.2017.10.110

Su, X., Wang, T., and Guo, S. (2021). Applications of 3D Printed Bone Tissue Engineering Scaffolds in the Stem Cell Field. *Regenerative Ther.* 16, 63–72. doi:10.1016/j.reth.2021.01.007

Sun, K., Li, R., Jiang, W., Sun, Y., and Li, H. (2016). Comparison of Three-Dimensional Printing and Vacuum Freeze-Dried Techniques for Fabricating Composite Scaffolds. *Biochem. Biophysical Res. Commun.* 477, 1085–1091. doi:10.1016/j.bbrc.2016.07.050

Thunsiri, K., Pitjamit, S., Pothacharoen, P., Pruksakorn, D., Nakkiew, W., and Wattanutchariya, W. (2020). The 3D-Printed Bilayer's Bioactive-Biomaterials Scaffold for Full-Thickness Articular Cartilage Defects Treatment. *Materials* 13, 3417. doi:10.3390/ma13153417

Wei, L., Wu, S., Kuss, M., Jiang, X., Sun, R., Reid, P., et al. (2019). 3D Printing of Silk Fibroin-Based Hybrid Scaffold Treated with Platelet Rich Plasma for Bone Tissue Engineering. *Bioactive Mater.* 4, 256–260. doi:10.1016/j.bioactmat.2019.09.001

Conflict of Interest: The authors declare that the research was conducted in the absence of any commercial or financial relationships that could be construed as a potential conflict of interest.

Publisher's Note: All claims expressed in this article are solely those of the authors and do not necessarily represent those of their affiliated organizations, or those of the publisher, the editors and the reviewers. Any product that may be evaluated in this article, or claim that may be made by its manufacturer, is not guaranteed or endorsed by the publisher.

frontiers in Materials

ORIGINAL RESEARCH
published: 12 August 2021
doi: 10.3389/fmats.2021.712500

Strain Rate Effect on Mechanical Properties of the 3D-Printed Metamaterial Foams With Tunable Negative Poisson's Ratio

Di Gao[1,2], Bin Wang[3], Haoqiang Gao[2], Fuguang Ren[4]*, Chunxia Guo[5], Shuai Ma[6], Tiewa Cao[2], Yu Xia[2] and Yansen Wu[2]*

[1]Department of Orthopedics, The Sixth People's Hospital of Anyang, Anyang, China, [2]Tianjin Key Laboratory of Nonlinear Dynamics and Control, Tianjin University, Tianjin, China, [3]Key Laboratory of Soft Soils and Engineering Environment of Tianjin Province, Tianjin Chengjian University, Tianjin, China, [4]School of Mechanical Engineering, Hebei University of Technology, Tianjin, China, [5]Department of Mechanics, School of Science, Xi'an University of Architecture and Technology, Xi'an, China, [6]School of Mathematics and Physics, Qingdao University of Science and Technology, Qingdao, China

As a kind of metamaterial, the negative Poisson's ratio foams, which expand (shrink) in the transverse direction when stretched (compressed) in the longitudinal direction, have many potential applications in fields such as aerospace and mechanical and biomedical engineering. In this paper, the out-of-plane crushing behaviors of four types of the orthogonal isotropic NPR convex-concave foams (CCF) were extensively studied using an electronic universal testing machine and Instron machine at different strain rates where each test was conducted at a constant compressive velocity under uniaxial compression. Strain rate effect on mechanical properties of these foams is experimentally studied. When the strain rate increases, the compressive force enhancement of the foams is obvious and varies with different specimens. The difference in energy absorption and deformation patterns for these foams between quasi-static and dynamic loading conditions is also analyzed. We find that the deformation patterns for the specimens are not only related to the compressive velocities but also the topologies of the specimens. The research in this paper is expected to be meaningful for the optimization design of the foam structures/materials widely used in the fields of aerospace and mechanical and biomedical engineering.

Keywords: convex-concave foams, mechanical properties, strain rate effect, negative Poisson's ratio, optimization design

OPEN ACCESS

Edited by:
Limin Wang,
Yanshan University, China

Reviewed by:
Kai Zhang,
Northwestern Polytechnical University, China
Jiaxi Zhou,
Hunan University, China

****Correspondence:***
Haoqiang Gao
hqgao@tju.edu.cn
Fuguang Ren
renfuguang99@163.com

Specialty section:
This article was submitted to Mechanics of Materials, a section of the journal Frontiers in Materials

Received: *20 May 2021*
Accepted: *21 June 2021*
Published: *12 August 2021*

Citation:
Gao D, Wang B, Gao H, Ren F, Guo C, Ma S, Cao T, Xia Y and Wu Y (2021) Strain Rate Effect on Mechanical Properties of the 3D-Printed Metamaterial Foams With Tunable Negative Poisson's Ratio. Front. Mater. 8:712500. doi: 10.3389/fmats.2021.712500

INTRODUCTION

Negative Poisson's ratio (NPR) foams, which expand (shrink) in the transverse direction when stretched (compressed) in the longitudinal direction, are a typical kind of mechanical metamaterial (Yang et al., 2004). Compared with the conventional foams with positive Poisson's ratio, NPR foams have some enhanced mechanical properties, such as a higher fracture toughness, increased indentation resistance, superior damping and acoustic properties and enhanced sound absorption, and superior tensile fatigue performance (Lakes and Elms, 1993; Chen and Lakes, 1996; Choi and Lakes, 1996; Scarpa et al., 2003; Bezazi and Scarpa, 2007; Zhang et al., 2020b; Zhang et al., 2020c; Zhao et al., 2021).

Mechanical properties play a very important role in engineering applications of the NPR foams. To explore the mechanical properties of the NPR foams and thus promote their practical applications in the fields of vehicle, aerospace, and mechanical engineering, many kinds of NPR foams have been proposed by researchers in recent years. Lakes (1987) first developed novel re-entrant foams with negative Poisson's ratio. Theocaris et al. (1997) used the numerical homogenization theory for the investigation of composite structures with star-shaped inclusions, which are able to exhibit a negative Poisson's ratio. Evans et al. (1994) proposed a re-entrant three-dimensional, open-celled NPR foam. Based on the commercial soft polyurethane foam material as matrix and shape memory epoxy resin as functional phase, Yao et al. (2018) proposed such NPR foams with different re-entrant structures. Adopting an assembly method, Wang et al. (2018b) fabricated 3D double-arrow-head NPR foam structure and studied their mechanical properties. By using an initiator-integrated 3D printing technology, Zhang et al. (2018) introduced metal/polymer re-entrant foams with tunable NPR. Based on a classical re-entrant structure, Chen et al. (2018) proposed three kinds of novel lattice foams with NPR, which showed enhanced energy absorption capacity, stiffness, and strength. Fan et al. (2018) proposed a novel method based on steam penetration and condensation (SPC) process and fabricated foams with negative Poisson's ratio. Using an interlocking assembly method, Wang et al. (2018a) fabricated the three-dimensional re-entrant auxetic foams made from carbon fiber reinforced polymer. Through pressure infiltration technology, Xue et al. (2019) fabricated the Al-based auxetic foams with polymer fillers and investigated their compressive mechanical properties with experimental and finite element analyses methods, which showed higher elastic modulus, compressive strength, and better energy absorption capacity. Through the experimental and finite element methods, Cui et al. (2018) have systematically studied effects of geometrical morphology on elastic moduli, energy absorption, and damage properties of the convex-concave foams (NPR). The CCF are constructed by replacing cell edges of the conventional open cell foams (COF), whose straight cell edges of square cross sections are arranged in planes at forty-five degrees relative to each other (Dolla, 2014), with sin-shaped cell edges of equal mass but different cross sections.

In the practical engineering applications, strain rate effect plays also a vital role in the reliable design of the NPR foams. With respect to strain rate effect of the structural materials, much research work has been done by the researchers all over the world. Baker et al. (1998) investigated the strain rate effect on energy absorption capacity of metal honeycombs through static and dynamic tests. The group of Tao Yong studied the strain rate effect on mechanical behaviour of metallic honeycombs under out-of-plane dynamic compression through theoretical and experimental analyses (Tao et al., 2015a), numerical simulation, and theoretical analysis (Tao et al., 2015b), respectively. Through an experimental analysis, Nia and Sadeghi (2013) investigated the effects of strain rate on the mechanical behaviour of bare and foam-filled honeycomb structures under compression. Adopting a modified Johnson rate dependent model, Tabiei and Wu (2000) investigated the strain rate effect on the dynamic response of wood material. Vural and Ravichandran (2003) studied the influence of strain rate on dynamic and energy dissipation properties of balsa wood through experimental and theoretical analysis. Widehammar (2004) systematically investigated the mechanical properties of spruce wood under different strain rates, moisture content, and loading direction; the strain rate effect on their stress-strain relationships was obtained. Comley and Fleck (2009) conducted experiments on adipose tissue under shear and compression, the strain rate effect on the mechanical properties of porcine adipose tissue was investigated. Guo et al. (2015) proposed a three-dimensional constitutive model to investigate the influence of strain rate on the mechanical properties of the shape memory polymer (epoxy). By conducting experiments on the luffa sponge material under different strain rates, Shen et al. (2013) studied the influence of strain rate on the mechanical properties of luffa sponge. Using an Instron machine and a split Hopkinson pressure bar apparatus, Miao et al. (2016) investigated nanosilica filled epoxies under different strain rates and the effects of strain rate on the mechanical properties of nanosilica/epoxy was analyzed. Pastorino et al. (2007) studied the NPR open cell foams, which showed that the strain rate has a great influence on the stress-strain curves and magnitudes of the Poisson's ratio. Through finite element analysis, Yang et al. (2015) designed a metal foam model and investigated the strain rate effect on the foam structures. Dou et al. (2016) investigated the influence of strain rate on the aluminum foam sandwich panels based on the finite element models.

Taking into account their special properties originating from the effect of NPR, a variety of NPR foams have also been proposed for applications in the medical fields. By using custom-made digital micro-mirror device stereolithography technology, Soman et al. (2012) proposed and fabricated a multi-layer scaffold which exhibited simultaneous negative and positive Poisson's ratio behavior. Choi et al. (2016) fabricated the organic/inorganic composite scaffolds by mixing hydroxyapatite (HA) to poly (lactide-coglycolide) (PLGA) which possess negative Poisson's ratio (NPR) and investigated the mechanical properties and cyto-compatibility of the composite scaffold. Kim et al. (2017) investigated the influence of dynamic compressive stimulation on MG-63 cell proliferation on an auxetic PLGA scaffold which exhibits negative Poisson's ratio. Using the organic-inorganic photopolymer SZ 2080, Flamourakis et al. (2020) fabricated a re-entrant hexagonal geometry scaffold which possess a negative Poisson's ratio with the multiphoton lithography technique. Zhang et al. (2020) designed the unit cells of titanium alloy to mimic trabecular structure and investigated the difference between the design and fabrication of the trabecular structures, as well as mechanical properties and the progressive collapse behavior and failure mechanism of the scaffold. Park et al. (2005) fabricated the polyurethane foam with a negative Poisson's ratio for the insoles of the shoes of diabetic patients. Park et al. (Park and Kim, 2013) designed a structural polyurethane scaffold which exhibits negative Poisson's ratio for cartilage regeneration and the chondrocyte proliferation effectiveness

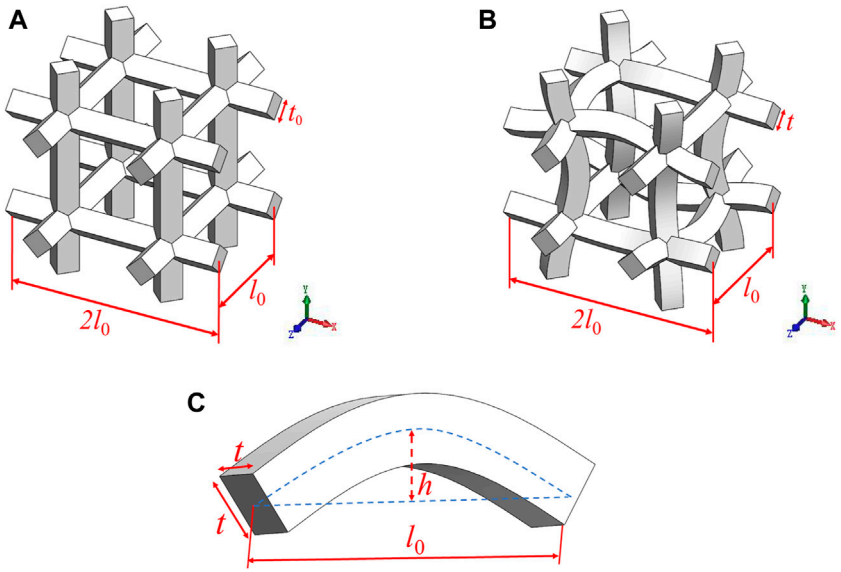

FIGURE 1 | (A) Cubic unit cell model of the conventional open-cell foams, in which the edge thickness is t_0 and the edge length is l_0; **(B)** Cubic unit cell model of the negative Poisson's ratio convex-concave foams; **(C)** Schematic diagram of the sine-shaped cell edges of the convex-concave foams (CCF) with chord span l_0, chord height h, and thickness t.

within the auxetic scaffold under mechanical (compression) stimulation was studied.

Dedicated to promoting their applications in the fields of vehicle, mechanical, aerospace, and medical engineering, in this paper, strain rate effects on mechanical behaviors of the NPR CCF are further systematically studied. In the open literature, mechanical behaviors of the NPR CCF under different compressive loading strain rates are still not clear. In fact, systematic and deep understanding of mechanical behaviors of the NPR CCF under different compressive loading speeds or strain rates is critical for their practical engineering applications. Choosing one conventional foam (COF) and three NPR convex-concave foams (CCF) of equal mass as examples for illustration, strain rate effects on force-displacement curves and energy absorption, the damage patterns of the NPR CCF, and the influence of geometrical morphology on the mechanical properties of NPR foams are experimentally investigated. The study of this paper plays a vital role in the optimization design of the foam structures/materials and facilitates their practical application in engineering fields.

SAMPLES AND EXPERIMENTS

3D-Print of the Negative Poisson's Ratio Convex-Concave Foams

In this paper, one kind of conventional foam and three kinds of NPR convex-concave foams (Cui et al., 2018) are investigated. Cubic unit cell models of the COF and CCF are shown in **Figures 1A,B**, respectively. t_0 and l_0 are the edge thickness and length of the COF, the CCF are constructed by replacing cell edges of the open-cell foam, whose square cross section cell walls are connected in the 45° diagonal direction, and the CCF have sin-shaped cell edges with chord span l_0, chord height h, and side thickness t. By using 3D-printed technology, one type of COF and three kinds of CCF structures with equal quality are printed. As depicted in **Figure 2A**, the four kinds of samples are named COF0, CCF1, CCF2, and CCF3, respectively. They are constructed by 5 × 5 × 7 arrays (**Figure 2B**) of their cubic unit cell (**Figures 1A,B**). The materials of these samples are a type of nylon material (PA2200), whose young's modulus and density (sintered) are 1500 MPa and 930 kg/m^3.

The curve of the sine-shaped cell edges (**Figure 1C**) of the CCF samples can be mathematically described as $y = h\sin(\pi x/l_o)(x \in [0,\ l_0\ ])$. To avoid the intersection of the sine-shaped cell edges, here $h/l_0 < 0.5$is assumed. Define the curve length of the sine-shaped cell edges as s, then s is expressed as:

$$s = \int_0^{l_0} \sqrt{1 + (y')^2}\,dx = \int_0^{l_0} \sqrt{1 + h^2\pi^2/l_0^2\cos^2(\pi x/l_0)}\,dx \qquad (1)$$

According to the equal-mass principle, we have $t^2 s = t_0^2 l_0$, which gives the side thickness t of the sine-shaped cell edges of the CCF samples

$$t = t_0\sqrt{l_0}/\sqrt{\int_0^{l_0} \sqrt{1 + h^2\pi^2/l_0^2\cos^2(\pi x/l_0)}\,dx} \qquad (2)$$

Here, the edge length and edge thickness of the COF0 are t_0 = 1 mm and l_0 = 5 mm. The chord height h of CCF1, CCF2, and CCF3 are 0.5, 1, and 1.5 mm, respectively. Apparently, when h = 0, the CCF becomes the COF. The chord height to span ratio of the COF0, CCF1, CCF2, and CCF3 are 0, 0.1, 0.2, and 0.3, respectively.

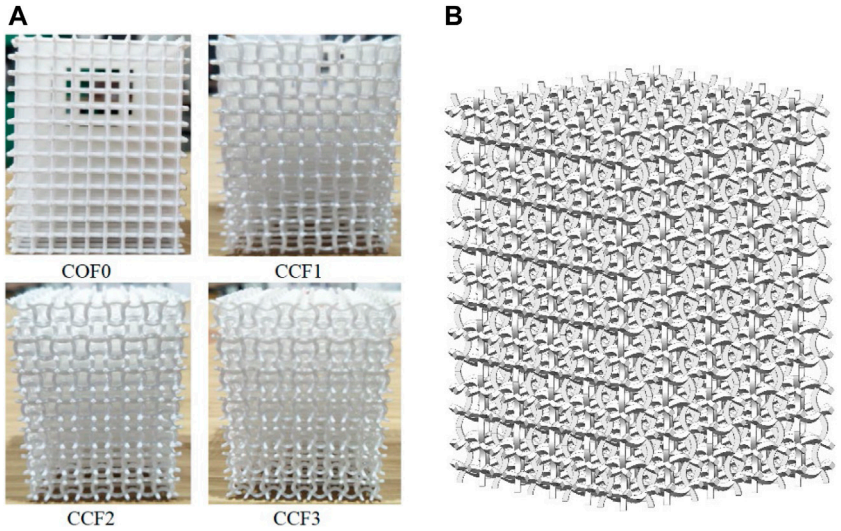

FIGURE 2 | (A) Front views of the COF sample and the corresponding three kinds of CCF samples of equal mass: COF0 (t_0 = 1 mm, l_0 = 5 mm); CCF1 (h = 0.5 mm); CCF2 (h = 1 mm); CCF3 (h = 1.5 mm); **(B)** Schematic diagram of the CCF samples constructed by 5 × 5 × 7 arrays of the cubic unit cell shown in **Panel 1B**.

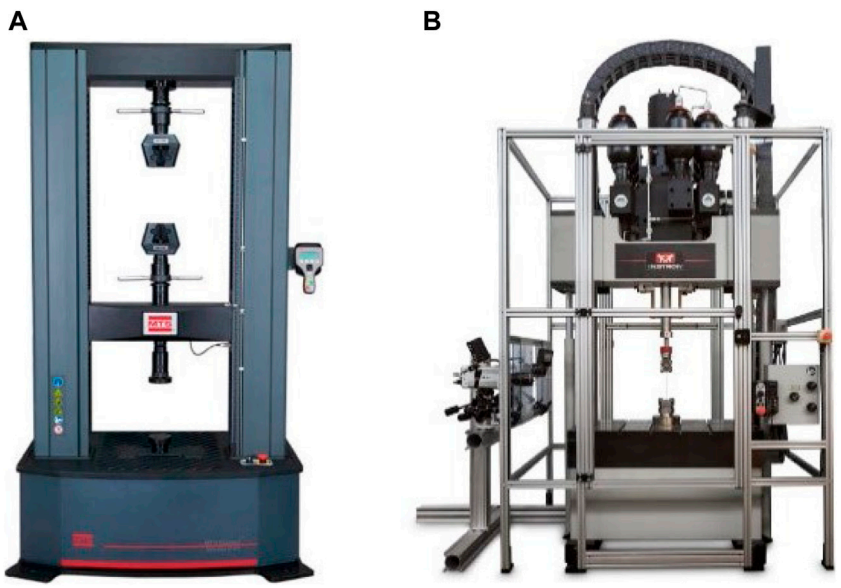

FIGURE 3 | Compressive testing machines for the experiments: **(A)** Universal testing machine for quasi-static tests, **(B)** Instron high rate testing system for dynamic tests.

Quasi-Static Experiments

The quasi-static compression tests were performed in an electronic universal testing machine which has a load capacity of 50 kN, as shown in **Figure 3A**. An iron cylinder with polished upper surface was put on the lower platen and then the foam specimen was placed on the polished surface in order to minimize friction. During the experiment, the lower surface of these specimens was enforced and given normal displacement to move upward to compress the specimen at a constant loading speed of 2 mm/min (3.33×10^{-5} m/s). In the experiment, a computer and digital camera were used to record the displacement and load signals from the testing machine during the entire loading process.

Dynamic Compression Experiments

The dynamic tests were performed using an Instron VHS High Rate Testing System, as shown in **Figure 3B**. The system is equipped with VHS software, which helps to maintain a constant velocity during the compression of the specimens. The Instron machine can achieve a maximum velocity of 20 m/s in

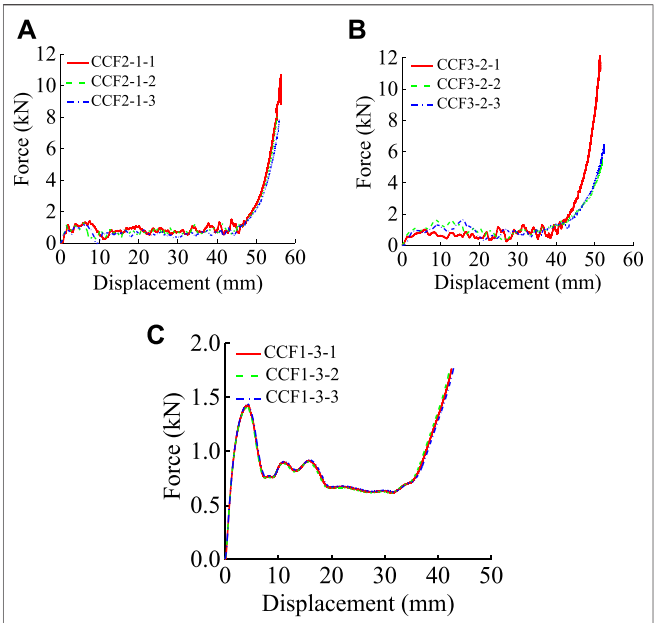

FIGURE 4 | Results of repeated experiments on NPR foams: **(A)** CCF2 ($\dot{\varepsilon}$ =71.4s^{-1}), **(B)** CCF3 ($\dot{\varepsilon}$ =2.14 × 10^{2} s^{-1}) and **(C)** CCF1 ($\dot{\varepsilon}$ =4.76 × 10^{-4} s^{-1}).

compression and has a load capacity of 100 kN. The specimens were placed on the bottom compression platen which was positioned at a considerably long distance from the top platen at the beginning of each test. During the compression, the upper platen moved downwards to impact with the lower fixed platen. Very thin and weak glue was used to stick the specimen to the lower platen in order to avoid any possible slippage of the specimens during the compression. The Instron machine was used on tests under 5 and 15 m/s, for which the corresponding nominal strain rates are 71.4 and 2.14×10^{2} s^{-1}, respectively, for specimens 70 mm high.

In this paper, each experiment was repeated three times at the same condition under quasi-static and dynamic loading for all specimens. **Figure 4** shows the force-displacement curves of three types of NPR foams for three repeated tests under strain rates 71.4, 2.14 × 10^{2} and 4.76 × 10^{-4} s^{-1}. Although the data of compressive force has a slight gap, the overall trend is basically the same and there is good repeatability.

RESULTS AND DISCUSSION

Force-Displacement Curves

In the experiments, four groups of foam specimens, namely COF0, CCF1, CCF2, CCF3, with different h/l_0 ratios were tested at 5 m/s, 15 m/s, and 2 mm/min, for which the corresponding strain rates are 71.4, 2.14 × 10^{2}, and 4.76 × 10^{-2}s^{-1}. Three experiments were conducted for each type of the specimen. **Table 1** gives the characteristics of different foam specimens with different h/l_0 ratios tested. The force-displacement curves for these foams are shown in **Figure 5**. Similar to some metal foams, the force-displacement curves can be divided into three stages, namely,

TABLE 1 | Summary of the tests on the foams and the results.

Test no	Mass	h/l_0	Velocity (m/s)	Strain rate (s^{-1})	Initial peak force (kN)
COF0-1-1	m	0	5	71.4	3.490
COF0-1-2	m	0	5	71.4	3.837
COF0-1-3	m	0	5	71.4	4.054
COF0-2-1	m	0	15	2.14 × 10^{2}	6.504
COF0-2-2	m	0	15	2.14 × 10^{2}	5.083
COF0-2-3	m	0	15	2.14 × 10^{2}	5.942
COF0-3-1	m	0	3 × 10^{-5}	4.76 × 10^{-4}	1.614
COF0-3-2	m	0	3 × 10^{-5}	4.76 × 10^{-4}	1.756
COF0-3-3	m	0	3 × 10^{-5}	4.76 × 10^{-4}	1.601
CCF1-1-1	m	0.1	5	71.4	3.024
CCF1-1-2	m	0.1	5	71.4	3.307
CCF1-1-3	m	0.1	5	71.4	2.883
CCF1-2-1	m	0.1	15	2.14×10^{2}	3.913
CCF1-2-2	m	0.1	15	2.14 × 10^{2}	4.014
CCF1-2-3	m	0.1	15	2.14 × 10^{2}	3.547
CCF1-3-1	m	0.1	3 × 10^{-5}	4.76 × 10^{-4}	1.425
CCF1-3-2	m	0.1	3 × 10^{-5}	4.76 × 10^{-4}	1.572
CCF1-3-3	m	0.1	3 × 10^{-5}	4.76 × 10^{-4}	1.453
CCF2-1-1	m	0.2	5	71.4	1.377
CCF2-1-2	m	0.2	5	71.4	1.401
CCF2-1-3	m	0.2	5	71.4	1.268
CCF2-2-1	m	0.2	15	2.14×10^{2}	1.724
CCF2-2-2	m	0.2	15	2.14 × 10^{2}	1.875
CCF2-2-3	m	0.2	15	2.14 × 10^{2}	1.691
CCF2-3-1	m	0.2	3 × 10^{-5}	4.76 × 10^{-4}	0.806
CCF2-3-2	m	0.2	3 × 10^{-5}	4.76 × 10^{-4}	0.74
CCF2-3-3	m	0.2	3 × 10^{-5}	4.76 × 10^{-4}	0.794
CCF3-1-1	m	0.3	5	71.4	1.200
CCF3-1-2	m	0.3	5	71.4	1.07
CCF3-1-3	m	0.3	5	71.4	1.214
CCF3-2-1	m	0.3	15	2.14×10^{2}	1.311
CCF3-2-2	m	0.3	15	2.14 × 10^{2}	1.637
CCF3-2-3	m	0.3	15	2.14 × 10^{2}	1.219
CCF3-3-1	m	0.3	3 × 10^{-5}	4.76 × 10^{-4}	0.724
CCF3-3-2	m	0.3	3 × 10^{-5}	4.76 × 10^{-4}	0.751
CCF3-3-3	m	0.3	3 × 10^{-5}	4.76 × 10^{-4}	0.736

the initial elastic, plastic collapse region, and densification regime. The force of these curves linearly increases with strain up to the elastic limit, then the curve reaches a peak point and becomes non-linear after the elastic limit, after which the force fluctuates during the plastic collapse plateau regime. In these curves, strong fluctuations can be seen in all the dynamic loading tests, but the fluctuation degree of these different specimens is different from each other at the same strain rate. The specimen, COF0, has the most volatile curve and it fluctuates around the *X*-axis. For the other three groups of specimens, CCF1, CCF2, CCF3, their curves are almost all over the *X*-axis and with the increase of the h/l_0 ratio, the degree of the fluctuation in the plateau region decreases. The specimens do not have an evident plateau region compared with metal foams and they have a wavy plateau stress which fluctuates significantly. For the specimen COF0 and CCF1 under dynamic loading, there is a negative value of the force in the curves after the initial peak, which indicates that, after the crushing of the first row of the specimen, there is a spring-back effect of the impactor mass; the reason for this phenomenon may be because of the property of the nylon or the failure modes of these specimens.

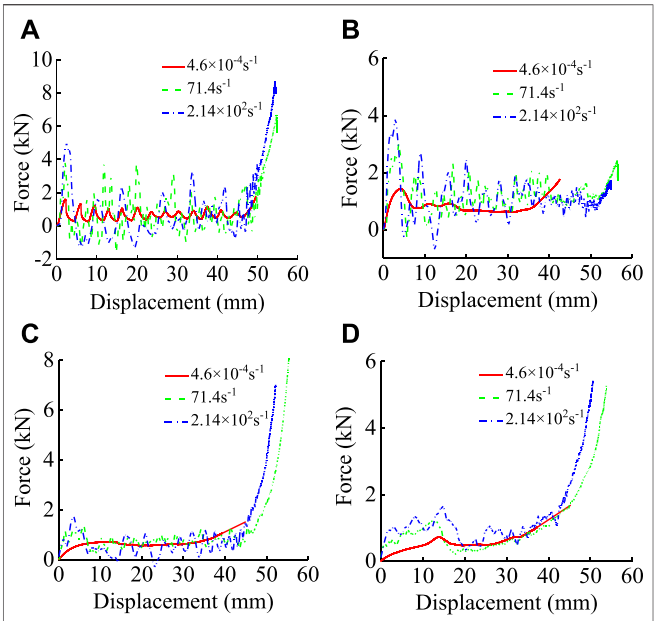

FIGURE 5 | Force-displacement curves for foam specimens under different strain rates: **(A)** COF0, **(B)** CCF1, **(C)** CCF2, **(D)** CCF3.

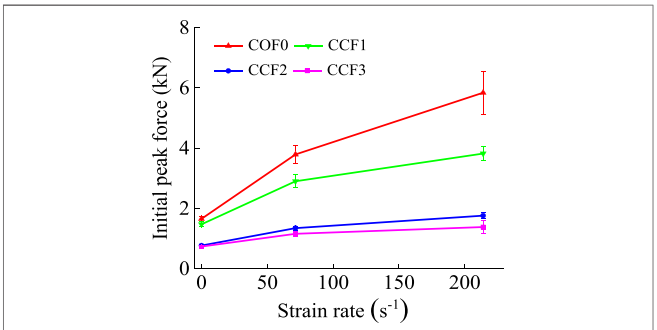

FIGURE 6 | The initial peak force-strain rate curve for the four types of foams: COF0,CCF1, CCF2, and CCF3.

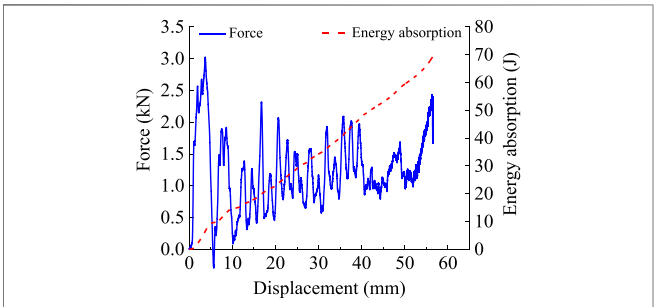

FIGURE 7 | Force and energy absorption-displacement curves for specimen CCF1 at 71.4 s^{-1}.

We can see from the force-displacement curves, compared with the quasi-static compression tests, the increase of the initial peak force under dynamic impact is obvious. The specimen COF0

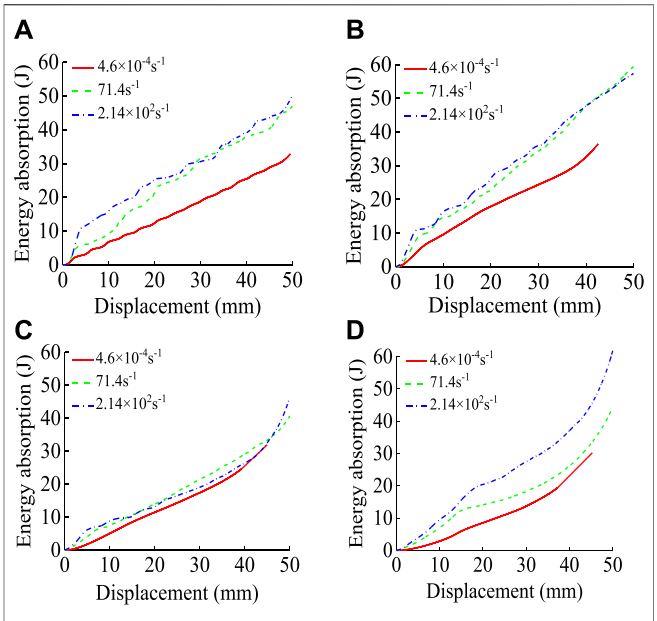

FIGURE 8 | Energy absorption-displacement curves for specimens; **(A)** COF0, **(B)** CCF1, **(C)** CCF2, **(D)** CCF3 under different strain rate.

TABLE 2 | The results of total energy absorption under different strain rates for specimens COF0, CCF1, CCF2, CCF3.

	4.6×10^{-4} s^{-1} (J)	71.4 s^{-1} (J)	2.14×10^{2} s^{-1} (J)
COF0	26.35	36.64	39.08
CCF1	34.08	48.61	46.98
CCF2	25.47	27.82	26.90
CCF3	22.86	28.50	34.95

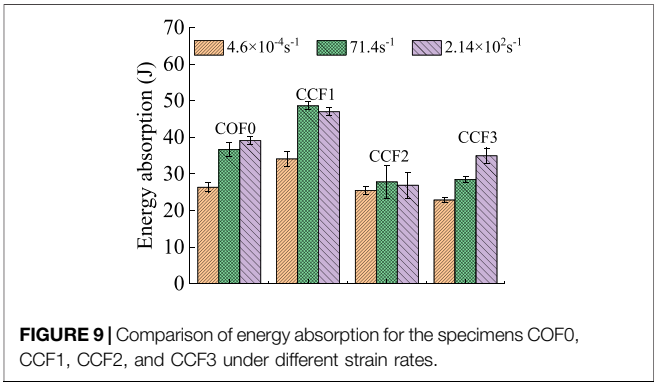

FIGURE 9 | Comparison of energy absorption for the specimens COF0, CCF1, CCF2, and CCF3 under different strain rates.

has the biggest peak force and the plateau region of its force-displacement curve exhibits a marked serration in the plateau region compared with the other three types of specimens, the other three foams have a relatively flat platform stage in their force-displacement curves.

Figure 6 depicts the experimental results of the initial peak force of these foams. We find that the strain rate has a great

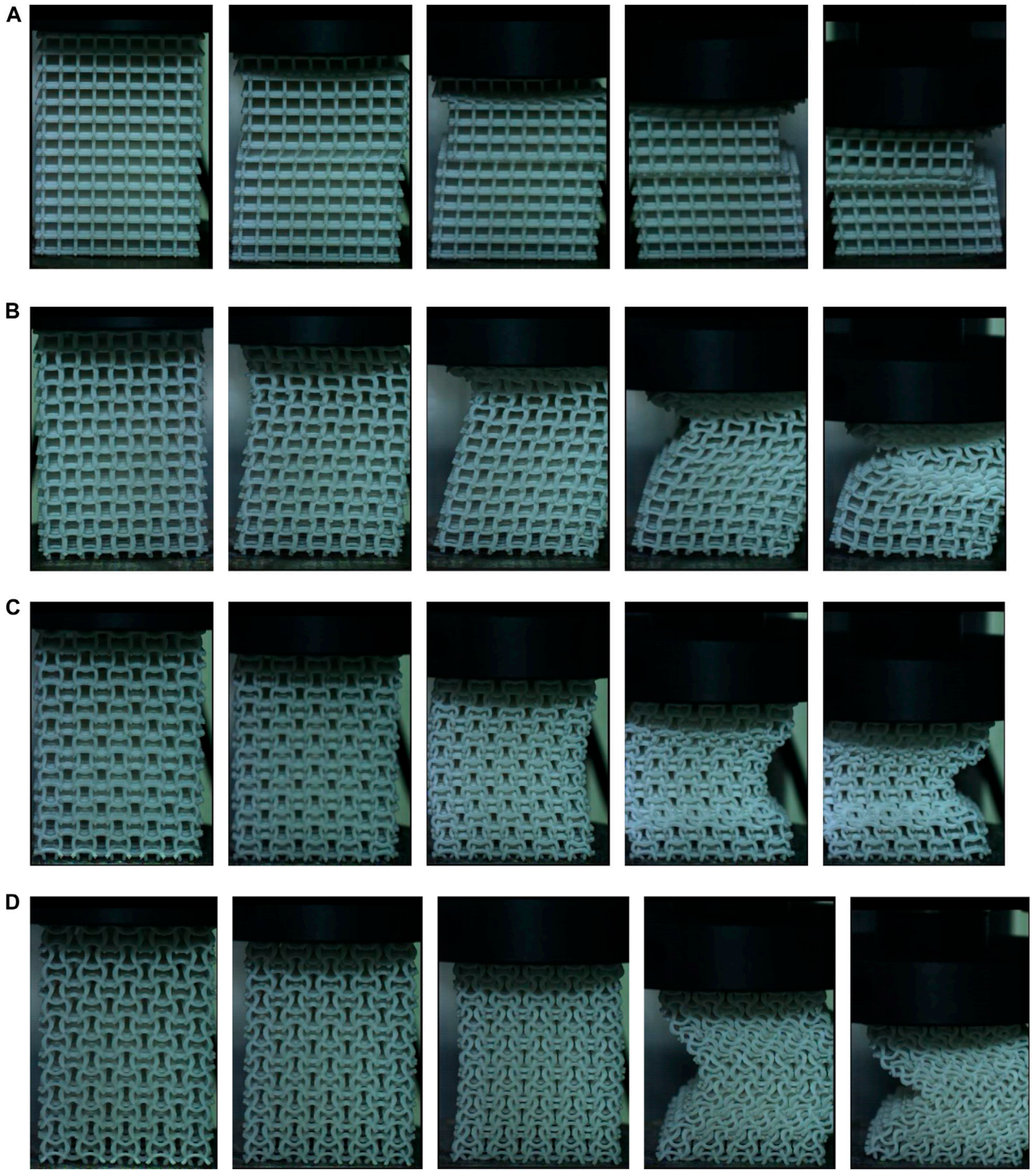

FIGURE 10 | The deformation patterns for the four types of specimens under quasi-static: **(A)** COF0, **(B)** CCF1, **(C)** CCF2, **(D)** CCF3.

influence on the force and such enhancement during the experiments is different between the four types of specimens. It is obvious that the initial peak force of the specimen COF0 under whether quasi-static or dynamic compression is bigger than the ones of these NPR foams. With the strain rate increasing, the peak stress will increase significantly. The peak force enhancement ratio under strain rate 2.14×10^{2} and $71.4^{\circ}s^{-1}$ is 248.8, 157.9, 128.6, 88.0, and 128.9, 107.8, 74.8, 58.4% for the specimen COF0, CCF1, CCF2 and CCF3 compared with the quasi-static compression under strain rate $4.76 \times 10^{-4}\,s^{-1}$,

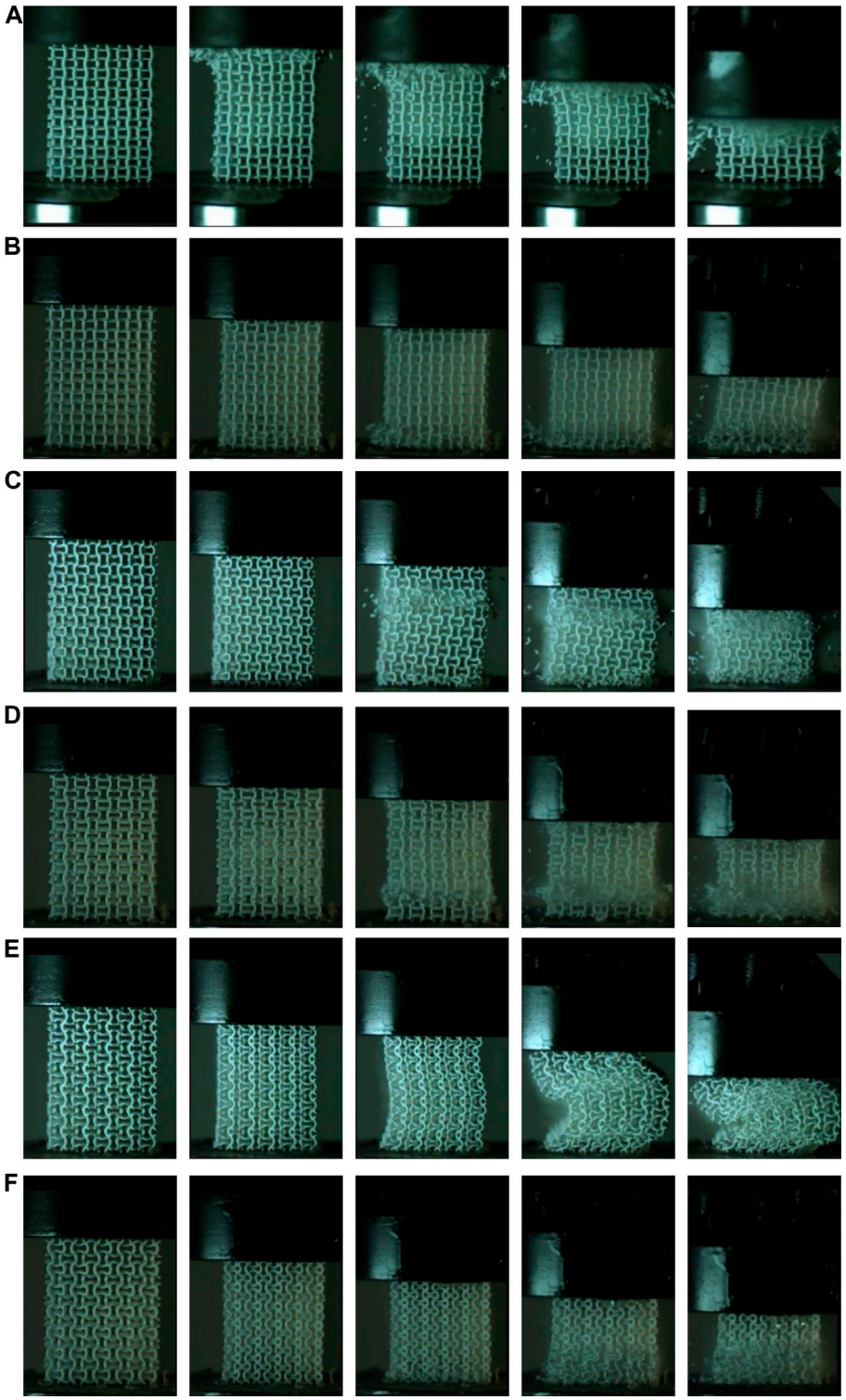

FIGURE 11 | The typical damage patterns for the NPR foams: specimen CCF1 **(A)** $\dot{\varepsilon}$ =71.4 s^{-1} and **(B)** $\dot{\varepsilon}$ =2.14 × 10^2 s^{-1}; specimen CCF2 **(C)** $\dot{\varepsilon}$ = 71.4 s^{-1} and **(D)** $\dot{\varepsilon}$ = 2.14 × 10^2 s^{-1}; specimen CCF3 **(E)** $\dot{\varepsilon}$ = 71.4 s^{-1} and **(F)** $\dot{\varepsilon}$ =2.14 × 10^2 s^{-1}.

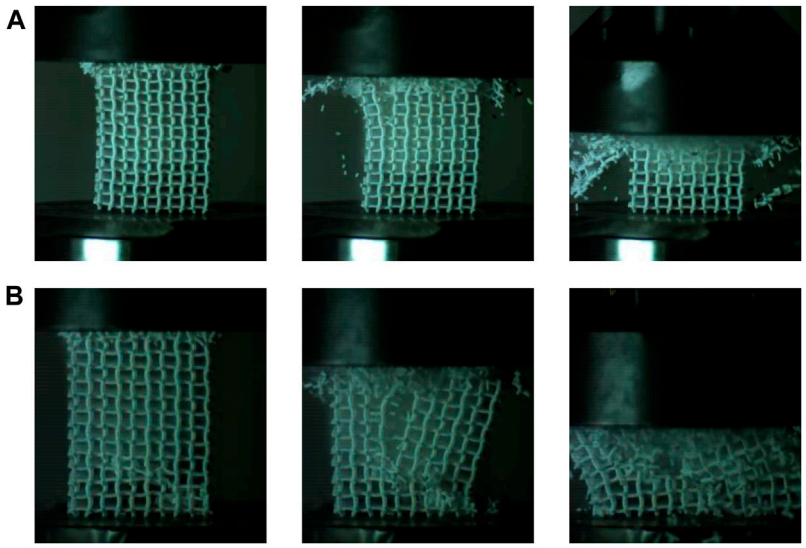

FIGURE 12 | Typical damage pattern for the specimen: **(A)** CCF1-1-1, $\dot{\varepsilon}$ = 71.4 s^{-1} **(B)** CCF1-2-1, $\dot{\varepsilon}$ = 2.14 × 10^2 s^{-1}.

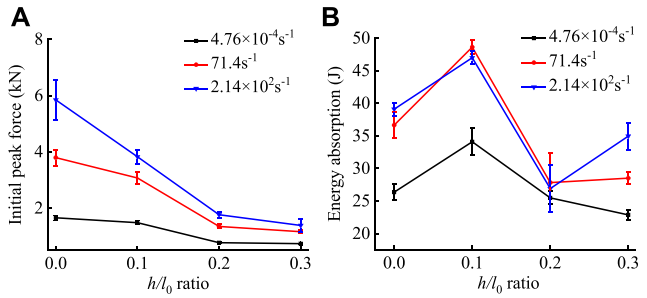

FIGURE 13 | The effects of the topology on the mechanical properties of these foams. **(A)** The quasi-static force-displacement curves for the four types of foams. **(B)** The peak force-h/l_0 ratio curves under different strain rates.

respectively. The force enhancement ratio at strain rate 2.14×10^2 s^{-1} is 54.0, 24.5, 30.8 and 18.7% for the specimen COF0, CCF1, CCF2, and CCF3 compared with the dynamic crushing at strain rate 71.4 s^{-1}, respectively. The conventional specimen COF0 has the largest increase in the force enhancement, which indicates that the conventional foam has a better enhancement capacity compared with the NPR foams. For the three types of NPR foams, the specimen CCF1 has the biggest dynamic enhancement and the specimen CCF3 has the least enhancement ratio compared with quasi-static compression.

Effect of Strain Rate on the Energy Absorption Properties of NPR CCF

Energy absorption (EA) is usually used as an indicator to evaluate the crashworthiness of a structure. By integrating the force-displacement curves of the specimens, the energy absorption is expressed as **Eq. 3**

$$EA = \int_0^d F(x)\,dx \tag{3}$$

where d is the effect total crushing length and F(x) is the crushing force in the force-displacement curves.

Choosing the specimen CCF1 as an example, the plot of compressive force and energy absorption is defined, as shown in **Figure 7**. By calculating the energy absorption of the four types of foams, the energy absorption-displacement curves for specimen COF0, CCF1, CCF2, and CCF3 under different strain rates are plotted in **Figure 8**. Analyzing the plots, the curves under dynamic loading condition for these specimens are above ones in static, which shows a good energy absorption enhancement, it is obvious that the strain rate has a great influence on the capacity of energy absorption of the NPR CCF.

For the specimen COF0, CCF1, and CCF2, the energy absorption curves under 71.4 and 2.14 × 10^2 s^{-1} are very close in the dynamic impact process. For specimen CCF3, when the strain rate increases from 71.4 to 2.14 × 10^2 s^{-1}, the energy absorption enhancement is obvious, which shows that CCF3 has a significant negative Poisson's ratio effect and it is more sensitive to strain rate than the other specimens.

In order to investigate the effect of strain rate on the total energy absorption of these specimens, we defined d = 40 mm as the effective total crushing length and obtained the average total energy absorption values of every specimen which is listed in **Table 2**. As shown in **Figure 9**, the values of energy absorption of these foams under dynamic loading (71.4 and 2.14 × 10^2 s^{-1}) are obviously bigger than the ones under the quasi-static condition (4.6 × 10^{-4} s^{-1}). For the specimen COF0 and CCF1, there is a big enhancement of the energy absorption when strain rate increases from 4.6 × 10^{-4} to 71.4 s^{-1}: 39.05% for COF0 and 42.63% for CCF1. The increase of energy absorption for the CCF2 and CCF3 is 9.23 and 24.67%, which is lower than the specimen COF0 and CCF1. When the strain rate increases from 71.4 to 2.14 × 10^2 s^{-1}, only the

specimen CCF3 has an obvious increase in energy absorption, the values of the specimen COF0 and CCF1 do not change much; the main reason for this could be the specimen CCF3 is relatively sensitive to the strain rate compared to other foams in the experiment.

Damage Patterns Under Quasi-Static and Dynamic Loadings

In the experiments, a high-speed camera was used to record the failure modes of the four types of foams in quasi-static and dynamic loading tests. Damage patterns have a direct relation to the material properties and the geometry topology of the structures. We will display diverse damage patterns under different strain rates later.

For the quasi-static compression, the damage pattern of the specimen COF0 was different from the other three kinds of NPR CCF. During the compression, they first began to buckle from the layer close to the interface near the upper platen and then the middle region of the specimen formed a fold, finally the specimen collapsed layer by layer and its deformation pattern is shown in **Figure 10A**. For the specimens NPR CCF, their deformation patterns were roughly the same. When the experiments began, the specimens CCF1, CCF2, and CCF3 first shrunk continuously and then buckled at the region near the upper platen, finally they displayed global bending. Little rebound was observed in the specimens after unloading and their deformation patterns are shown in **Figures 10B–D**.

For dynamic compression, we found that the damage pattern of the specimen COF0 was similar to one in the quasi-static. When the experiment began, a random layer was destroyed and then collapsed layer by layer until it compacted. For the three types of NPR foams, that may be because of the property of negative Poisson's ratio material, the specimens have a long elastic stage compared with the conventional specimen COF0. When the compression initial peak force is achieved, the specimens are destroyed and their deformation patterns are different from the ones of the specimen COF0. We list the damage patterns of the specimen CCF1, CCF2, and CCF3 under different strain rates respectively, as shown in **Figure 11**.

For the specimen CCF1, when the experiment began, they were first damaged at the layer near the upper or lower platen and then collapsed gradually, as shown in **Figures 11A,B**. Different from the specimen CCF1, the specimen CCF2 was first damaged at a layer near the interfaces between the specimen and platens, then they were crushed layer by layer. The typical deformation patterns of these specimens are shown in **Figures 11C,D**. For the specimen CCF3, they have a bigger h/l_0 ratio than the specimen CCF1 and CCF2; when they were compressed, they first produced a large deformation in the longitudinal direction and became thinner and thinner and then collapsed near the lower platen with the plastic buckling, as shown in **Figure 11F**. There is an interesting phenomenon that the deformation behavior of the specimen CCF3 under strain rate $71.4\ s^{-1}$ as shown in **Figure 11E** is similar to the one in the quasi-static compression as shown in **Figure 10D**.

One interesting deformation pattern should be mentioned, for the specimen CCF1-2-1 and CCF1-1-1, when the experiment began, they first shrunk continuously and then started to break at the layer near the platen and then there was a destruction in the longitudinal direction, finally they collapsed gradually, as shown in **Figure 12**.

Effect of Geometrical Morphology on the Mechanical Properties of the NPR CCF

In this part, the effects of the geometrical parameters on the mechanical properties (the initial peak force and energy absorption) of NPR CCF are studied. As shown in **Figure 13A**, with the fixed strain rates, initial peak force decreases with the h/l_0 increasing from 0 to 0.2. When the strain rate is 4.76×10^{-4} and $71.4\ s^{-1}$, the initial peak force almost keeps a constant value when h/l_0 increases from 0.2 to 0.3. **Figure 13B** depicts the change trend of energy absorption with h/l_0, for fixed strain rates, the energy absorption increases when h/l_0 increases from 0 to 0.1. Under strain rate $4.76 \times 10^{-4}\ s^{-1}$, when the h/l_0 increases from 0.1 to 0.3, the energy absorption decreases. However, for the strain rates 71.4 and $2.14 \times 10^{2}\ s^{-1}$, the energy absorption first decreases with h/l_0 increasing from 0.1 to 0.2 and then increases when h/l_0 increases from 0.2 to 0.3. We can find that CCF1($h/l_0 = 0.1$) has a better capacity of energy absorption compared to other NPR CCF.

CONCLUSION

In this paper, the mechanical properties of the four types of foams have been extensively investigated under different strain rates, namely, 4.76×10^{-4}, 71.4, and $2.14 \times 10^{2}\ s^{-1}$. All tests were conducted at constant compressive velocities and all the specimens are of equal quality and have the same dimension. By analyzing the force-displacement curves, there is an enhancement of initial peak force when the strain rate increases. The influence of strain rate on the energy absorption is also studied. Under quasi-static compression, the conventional foam buckles from the layer close to the upper interface or lower interface and then collapses layer by layer and the other three types of foams first have a lateral contraction and then bend at the section near the middle region. The effect of topologies on the initial peak force and energy absorption is also investigated. The study of this paper provides the theoretical foundations for optimization design of mechanical properties of the NPR CCF and thus could promote their practical applications in the engineering fields.

DATA AVAILABILITY STATEMENT

The original contributions presented in the study are included in the article/supplementary material, further inquiries can be directed to the corresponding authors.

AUTHOR CONTRIBUTIONS

DG, FR, and HG contributed to conception and design of the study. DG, HG, and BW performed the experiment. CG, SM, and TC performed the statistical analysis. DG wrote the first draft of the manuscript. HG, FR, YX, and YW wrote sections of the manuscript.

HG made major contributions to the manuscript revision, proofreading and communication process. All authors contributed to manuscript revision, read, and approved the submitted version.

FUNDING

The research of this paper is supported by Shaanxi Provincial Education Department (Grant No.18JK0437).

REFERENCES

Baker, W. E., Togami, T. C., and Weydert, J. C. (1998). Static and Dynamic Properties of High-Density Metal Honeycombs. *Int. J. Impact Eng.* 21 (3), 149–163. doi:10.1016/S0734-743X(97)00040-7

Bezazi, A., and Scarpa, F. (2007). Mechanical Behaviour of Conventional and Negative Poisson's Ratio Thermoplastic Polyurethane Foams under Compressive Cyclic Loading. *Int. J. Fatigue* 29 (5), 922–930. doi:10.1016/j.ijfatigue.2006.07.015

Chen, C. P., and Lakes, R. S. (1996). Micromechanical Analysis of Dynamic Behavior of Conventional and Negative Poisson's Ratio Foams. *J. Eng. Mater. Technol.* 118 (3), 285–288. doi:10.1115/1.2806807

Chen, Z., Wang, Z., Zhou, S., Shao, J., and Wu, X. (2018). Novel Negative Poisson's Ratio Lattice Structures with Enhanced Stiffness and Energy Absorption Capacity. *Materials* 11 (7), 1095. doi:10.3390/ma11071095

Choi, H. J., Lee, J. J., Lee, J. B., Sung, H.-J., Shin, J.-W., Shin, J. W., et al. (2016). MG-63 Cells Proliferation Following Various Types of Mechanical Stimulation on Cells by Auxetic Hybrid Scaffolds. *Biomater. Res.* 20 (1), 1–8. doi:10.1186/s40824-016-0079-x

Choi, J. B., and Lakes, R. S. (1996). Fracture Toughness of Re-entrant Foam Materials with a Negative Poisson's Ratio: experiment and Analysis. *Int. J. Fract.* 80 (1), 73–83. doi:10.1007/BF00036481

Comley, K., and Fleck, N. (2009). The Mechanical Response of Porcine Adipose Tissue. *ASME J. Biomech. Eng.* 1-30. Available at: http://www-mech.eng.cam.ac.uk/profiles/fleck/papers/259.pdf.

Cui, S., Gong, B., Ding, Q., Sun, Y., Ren, F., Liu, X., et al. (2018). Mechanical Metamaterials Foams with Tunable Negative Poisson's Ratio for Enhanced Energy Absorption and Damage Resistance. *Materials* 11 (10), 1869. doi:10.3390/ma11101869

Dolla, W. (2014). *Rotational Expansion Auxetic Structures*. Kansas: U.S. Patent Application Us3841508, doi:10.1017/cbo9781139946223

Dou, R., Qiu, S., Ju, Y., and Hu, Y. (2016). Simulation of Compression Behavior and Strain-Rate Effect for Aluminum Foam sandwich Panels. *Comput. Mater. Sci.* 112, 205–209. doi:10.1016/j.commatsci.2015.10.032

Evans, K. E., Nkansah, M. A., and Hutchinson, I. J. (1994). Auxetic Foams: Modelling Negative Poisson's Ratios. *Acta Metallurgica et Materialia* 42 (4), 1289–1294. doi:10.1016/0956-7151(94)90145-7

Fan, D., Li, M., Qiu, J., Xing, H., Jiang, Z., and Tang, T. (2018). Novel Method for Preparing Auxetic Foam from Closed-Cell Polymer Foam Based on the Steam Penetration and Condensation Process. *ACS Appl. Mater. Inter.* 10 (26), 22669–22677. doi:10.1021/acsami.8b02332

Flamourakis, G., Spanos, I., Vangelatos, Z., Manganas, P., Papadimitriou, L., Grigoropoulos, C., et al. (2020). Laser-made 3D Auxetic Metamaterial Scaffolds for Tissue Engineering Applications. *Macromol. Mater. Eng.* 305 (7), 2000238. doi:10.1002/mame.202000238

Guo, X., Liu, L., Zhou, B., Liu, Y., and Leng, J. (2015). Influence of Strain Rates on the Mechanical Behaviors of Shape Memory Polymer. *Smart Mater. Struct.* 24 (9), 095009, doi:10.1088/0964-1726/24/9/095009

Kim, M. J., Choi, H. J., Cho, J., Lee, J. B., Sung, H.-J., and Kim, J. K. (2017). MG-63 Cell Proliferation with Static or Dynamic Compressive Stimulation on an Auxetic PLGA Scaffold. *Int. J. Polym. Sci.* 2017, 1–6. doi:10.1155/2017/1286109

Lakes, R. (1987). Foam Structures with a Negative Poisson's Ratio. *Science* 235 (4792), 1038–1040. doi:10.1126/science.235.4792.1038

Lakes, R. S., and Elms, K. (1993). Indentability of Conventional and Negative Poisson's Ratio Foams. *J. Compos. Mater.* 27 (12), 1193–1202. doi:10.1177/002199839302701203

Miao, Y.-G., Liu, H.-Y., Suo, T., Mai, Y.-W., Xie, F.-Q., and Li, Y.-L. (2016). Effects of Strain Rate on Mechanical Properties of Nanosilica/epoxy. *Composites B: Eng.* 96, 119–124. doi:10.1016/j.compositesb.2016.04.008

Nia, A. A., and Sadeghi, M. (2013). An Experimental Investigation on the Effect of Strain Rate on the Behaviour of Bare and Foam-Filled Aluminium Honeycombs. *Mater. Des.* 52, 748–756. doi:10.1016/j.matdes.2013.06.006

Park, K. O., Park, J. C., Choi, J. B., Lee, S. J., Choi, H. H., and Kim, J. K. (2005). Polyurethane Foam with a Negative Poisson's Ratio for Diabetic Shoes. *Kem* 288-289, 677–670. doi:10.4028/www.scientific.net/KEM.288-289.677

Park, Y. J., and Kim, J. K. (2013). The Effect of Negative Poisson's Ratio Polyurethane Scaffolds for Articular Cartilage Tissue Engineering Applications. *Adv. Mater. Sci. Eng.* 2013, 1–5. doi:10.1155/2013/853289

Pastorino, P., Scarpa, F., Patsias, S., Yates, J. R., Haake, S. J., and Ruzzene, M. (2007). Strain Rate Dependence of Stiffness and Poisson's Ratio of Auxetic Open Cell PU Foams. *Phys. Stat. Sol. (B)* 244 (3), 955–965. doi:10.1002/pssb.200572714

Scarpa, F., Ciffo, L. G., and Yates, J. R. (2003). Dynamic Properties of High Structural Integrity Auxetic Open Cell Foam. *Smart Mater. Struct.* 13 (1), 49–56. doi:10.1088/0964-1726/13/1/006

Shen, J., Xie, Y. M., Huang, X., Zhou, S., and Ruan, D. (2013). Behaviour of luffa Sponge Material under Dynamic Loading. *Int. J. Impact Eng.* 57, 17–26. doi:10.1016/j.ijimpeng.2013.01.004

Soman, P., Lee, J. W., Phadke, A., Varghese, S., and Chen, S. (2012). Spatial Tuning of Negative and Positive Poisson's Ratio in a Multi-Layer Scaffold. *Acta Biomater.* 8 (7), 2587–2594. doi:10.1016/j.actbio.2012.03.035

Tabiei, A., and Wu, J. (2000). Three-dimensional Nonlinear Orthotropic Finite Element Material Model for wood. *Compos. Structures* 50 (2), 143–149. doi:10.1016/S0263-8223(00)00089-1

Tao, Y., Chen, M., Chen, H., Pei, Y., and Fang, D. (2015a). Strain Rate Effect on the Out-Of-Plane Dynamic Compressive Behavior of Metallic Honeycombs: Experiment and Theory. *Compos. Structures* 132, 644–651. doi:10.1016/j.compstruct.2015.06.015

Tao, Y., Chen, M., Pei, Y., and Fang, D. (2015b). Strain Rate Effect on Mechanical Behavior of Metallic Honeycombs under Out-Of-Plane Dynamic Compression. *J. Appl. Mech.* 82 (2). doi:10.1115/1.4029471

Theocaris, P. S., Stavroulakis, G. E., and Panagiotopoulos, P. D. (1997). Negative Poisson's Ratios in Composites with star-shaped Inclusions: a Numerical Homogenization Approach. *Archive Appl. Mech. (Ingenieur Archiv)* 67 (4), 274–286. doi:10.1007/s004190050117

Vural, M., and Ravichandran, G. (2003). Dynamic Response and Energy Dissipation Characteristics of Balsa wood: experiment and Analysis. *Int. J. Sol. Structures* 40 (9), 2147–2170. doi:10.1016/S0020-7683(03)00057-X

Wang, X.-T., Chen, Y.-L., and Ma, L. (2018a). The Manufacture and Characterization of Composite Three-Dimensional Re-entrant Auxetic Cellular Structures Made from Carbon Fiber Reinforced Polymer. *J. Compos. Mater.* 52 (23), 3265–3273. doi:10.1177/0021998318764021

Wang, X.-T., Wang, B., Wen, Z.-H., and Ma, L. (2018b). Fabrication and Mechanical Properties of CFRP Composite Three-Dimensional Double-Arrow-Head Auxetic Structures. *Composites Sci. Technology* 164, 92–102. doi:10.1016/j.compscitech.2018.05.014

Widehammar, S. (2004). Stress-strain Relationships for spruce wood: Influence of Strain Rate, Moisture Content and Loading Direction. *Exp. Mech.* 44 (1), 44–48. doi:10.1007/BF02427975

Xue, Y., Wang, W., and Han, F. (2019). Enhanced Compressive Mechanical Properties of Aluminum Based Auxetic Lattice Structures Filled with Polymers. *Composites Part B: Eng.* 171, 183–191. doi:10.1016/j.compositesb.2019.05.002

Yang, B., Liu, Z. J., Tang, L. Q., Jiang, Z. Y., and Liu, Y. P. (2015). Mechanism of the Strain Rate Effect of Metal Foams with Numerical Simulations of 3D Voronoi Foams during the Split Hopkinson Pressure Bar Tests. *Int. J. Comput. Methods* 12 (04), 1540010. doi:10.1142/S0219876215400101

Yang, W., Li, Z.-M., Shi, W., Xie, B.-H., and Yang, M.-B. (2004). Review on Auxetic Materials. *J. Mater. Sci.* 39 (10), 3269–3279. doi:10.1023/b:jmsc.0000026928.93231.e0

Yao, Y., Luo, Y., Xu, Y., Wang, B., Li, J., Deng, H., et al. (2018). Fabrication and Characterization of Auxetic Shape Memory Composite Foams. *Composites Part B: Eng.* 152, 1–7. doi:10.1016/j.compositesb.2018.06.027

Zhang, C., Zhang, L., Liu, L., Lv, L., Gao, L., Liu, N., et al. (2020). Mechanical Behavior of a Titanium alloy Scaffold Mimicking Trabecular Structure. *J. Orthop. Surg. Res.* 15 (1), 1–11. doi:10.1186/s13018-019-1489-y

Zhang, D., Xiao, J., Yu, W., Guo, Q., and Yang, J. (2018). Hierarchical Metal/polymer Metamaterials of Tunable Negative Poisson's Ratio Fabricated by Initiator-Integrated 3D Printing (i3DP). *Nanotechnology* 29 (50), 505704. doi:10.1088/1361-6528/aae283

Zhang, K., Zhao, C., Zhao, P., Luo, J., and Deng, Z. (2020b). Wave Propagation Properties of Rotationally Symmetric Lattices with Curved Beams. *The J. Acoust. Soc. America* 148 (3), 1567–1584. doi:10.1121/10.0001918

Zhang, K., Zhao, P., Zhao, C., Hong, F., and Deng, Z. (2020c). Study on the Mechanism of Band gap and Directional Wave Propagation of the Auxetic Chiral Lattices. *Compos. Structures* 238, 111952. doi:10.1016/j.compstruct.2020.111952

Zhao, P., Zhang, K., Zhao, C., and Deng, Z. (2021). On the Wave Propagation Properties and Poisson's Ratio of the Star-3/6 Structures. *Compos. Structures* 270, 114089. doi:10.1016/j.compstruct.2021.114089

Conflict of Interest: The authors declare that the research was conducted in the absence of any commercial or financial relationships that could be construed as a potential conflict of interest.

frontiers in Materials

ORIGINAL RESEARCH
published: 16 August 2021
doi: 10.3389/fmats.2021.718516

Deformation of Steel Slag Asphalt Mixtures Under Normal Temperature Water Immersion

Chao Wang[1,2] *and Caili Zhang*[2]*

[1]Jiangsu JITRI Road Engineering Technology and Equipment Research Institute Co., Ltd., XuZhou, China, [2]School of Civil Engineering and Transportation, Hebei University of Technology, Tianjin, China

To study the deformation resistance of steel slag asphalt mixtures (SSAMs) under rainy conditions, limestone–asphalt mixtures (LAMs) and SSAM were soaked in water at room temperature for 120 days and rutting tests and triaxial compression tests were carried out. The results show that the deformation resistance of SSAM was improved after 120 days of immersion, the cohesion did not decrease significantly, and the internal friction angle increased by 25.1%; the deformation resistance of LAM decreased significantly, the cohesion decreased by 27.1%, and the internal friction angle decreased by 21.1%. To better understand the reason for the increased anti-deformation ability, adhesion tests of asphalt and microscopic studies of the steel slag surface were performed. The experimental results showed that the cohesion of steel slag did not decrease significantly after immersion because of the excellent adhesion between steel slag and asphalt. The increased internal friction angle was caused by calcium hydroxide and other crystals formed on the surface of the steel slag mixture after immersion, which increased the surface roughness of the steel slag aggregates and the internal friction angle of the SSAM. The mechanical properties of semirigid asphalt pavement were analyzed by ANSYS. It was determined that the shear stress of this type of pavement is large, and it can easily produce permanent deformations. Under the influence of moisture, the anti-deformation ability of SSAMs can grow, which promotes the high-temperature deformation resistance of asphalt pavement. Based on a test road used for 2 years, the SSAM pavement exhibited no pavement problems, such as cracking, loosening, or rutting, which indicates good practical road performance.

Keywords: steel slag asphalt mixture, deformation resistance, cohesion, internal friction angle, crystalline matters

OPEN ACCESS

Edited by:
Yunchao Tang,
Guangxi University, China

Reviewed by:
Zhenliang Jiang,
Ryerson University, Canada
Shengjie Jiao,
Chang'an University, China
Wanhui Feng,
Zhongkai University of Agriculture and Engineering, China

***Correspondence:**
Caili Zhang
17695799230@163.com

Specialty section:
This article was submitted to Environmental Degradation of Materials, a section of the journal Frontiers in Materials

Received: *01 June 2021*
Accepted: *05 July 2021*
Published: *16 August 2021*

Citation:
Wang C and Zhang C (2021) Deformation of Steel Slag Asphalt Mixtures Under Normal Temperature Water Immersion. Front. Mater. 8:718516. doi: 10.3389/fmats.2021.718516

INTRODUCTION

China is the largest steel-producing country, accounting for about 50% of global steel production. By the end of 2020, China's steel production reached 1.05 billion tons, with an annual growth of 5.4%. Steel slag is the waste generated during steel making in the steel refining process, which corresponds to approximately 10–15% of crude steel output.

Steel slag is a reusable resource in many fields, and it can be employed as a soil conditioner or a steel slag cement compound (Lian et al., 2021). However, in order to be used in such applications, steel slag must go through a complex processing treatment. This process requires significant manpower and material resources and has a low utilization rate. Therefore, to date, the comprehensive utilization rate of steel slag in China is only about 38.7%.

Considering conventional methods of industrial and construction waste utilization, most solid waste is used as concrete aggregate (Tang et al., 2020; Tang et al., 2021a; Tang et al., 2021b). If a significant amount of steel slag can be applied in road-engineering projects, this would not only solve the urgent challenges regarding material shortages but would also help to reduce steel slag pollution on land. Therefore, numerous researchers around the world have evaluated whether steel slag can be used in asphalt mixtures.

The chemical composition of steel slag has an important influence on its applicability. The iron content in steel slag impacts its heating efficiency, such that a high iron content corresponds to a high heating efficiency (Wan et al., 2018). Additionally, as the steel slag content in asphalt mixtures increases, the thermal conductivity of the asphalt mixture first increases and then decreases (Barišić et al., 2017). Alkaline substances in steel slag can increase the concentration of asphalt components on the aggregate surface and enhance the adhesion between asphalt and steel slag (Jiao et al., 2020). Some heavy metals may also exist in steel slag. Reports have shown that the application of steel slag in highways does not lead to environmental pollution (Liu et al., 2020).

Steel slag asphalt mixtures (SSAMs) have many unique characteristics. If the free calcium oxide content in steel slag is too high, expansion cracking may occur during use, which could lead to performance degradation of the mixture. However, the influence of steel slag expansion on asphalt pavement can be reduced by properly designing the surface water isolation structure (Ma et al., 2020). If steel slag aggregates are used in an asphalt mixture, its permanent deformation resistance will be improved (Ameri et al., 2013). This means that replacing the skeleton of coarse aggregates with steel slag aggregates could improve the rutting resistance of the mixture (Ameli et al., 2020). Furthermore, it has been demonstrated that it is technically feasible to use steel slag as the coarse aggregate (Chen and Wei, 2016).

In addition to enhancing the deformation resistance of SSAM, steel slag aggregates can improve the anti-fatigue cracking performance of asphalt mixtures (Qazizadeh et al., 2018; Ziaee and Behnia, 2020), as well as their low-temperature performance (Chai et al., 2020). The improvement mechanism is governed by the alkalinity and a large specific surface area of steel slag (Zhu et al., 2020) and benefits from the physical anchoring and chemical adhesion effects between steel slag and asphalt (Pathak et al., 2020).

In an open-graded friction course, replacing part of the coarse aggregate with steel slag can improve the water damage resistance of the material. Incorporating 75% steel slag aggregate into OGFC promoted good road performance (Pattanaik et al., 2021). It was also demonstrated that using steel slag as coarse aggregate improved the friction resistance of OGFC; specifically, it was suggested that in hilly and rainy areas, 50% steel slag should be used instead of coarse aggregate in OGFC mixtures to improve the water damage resistance of roads (Preti et al., 2019).

In snow melting pavement, steel slag can improve the microwave heating efficiency to enhance snow melting on the road. Asphalt concrete mixed with 60% steel slag can effectively improve the snow melting efficiency of thermally conductive asphalt concrete and pavement temperature distribution (Lyu et al., 2021). When steel slag is used as the microwave deicing aggregate in an asphalt mixture, the steel slag serves as a microwave absorption reinforcement material to improve the heating efficiency of the asphalt mixture (Gao et al., 2017). Previously, a co-precipitation method was used to modify the steel slag particles, which increased the Fe_3O_4 content on the surface to completely replace the fine aggregate; after microwave heating, the internal temperature of the modified SSAM was 74.4% higher than that of the basalt asphalt mixture (Gulisano et al., 2020). Overall, adding steel slag and using microwave heating can clearly improve the performance of emulsified asphalt repair materials (Liu et al., 2017).

The application of steel slag in the gravel seal can recover industrial waste, reduce the consumption of natural resources, and promote the development of economic pavement maintenance technology by reducing CO_2 emissions (Bonoli et al., 2020). In a warm mixture, adding steel slag can improve the water damage resistance of the asphalt mixture (Wei et al., 2020).

Objective

Although research regarding steel slag in general has been fruitful, the enhancement of SSAM's anti-deformation ability is still not entirely understood. Steel slag is a material that is easily affected by water. Therefore, in the rainy season, changes in the anti-deformation performance of SSAMs must be considered to evaluate the potential applicability of steel slag aggregates in road engineering.

The main purpose of the present work was to study the causes and magnitudes of the changes to SSAMs' anti-deformation performance under normal temperature immersion. The water stability, low-temperature deformation performance, and fatigue performance of SSAMs were also studied following normal temperature immersion.

Research Approach

In this study, SSAM was used as the research object, and a limestone–asphalt mixture was used as a reference. Rutting tests, triaxial compression tests, adhesion tests, and atomic force scanning tests were conducted to study the macroscopic and microscopic changes in the anti-deformation properties of asphalt mixtures immersed in water at 30°C for 120 days during the summer. A water stability test, a low-temperature bending test, and a fatigue test were also employed to detect the changes in the performance of SSAMs after immersion.

MATERIALS AND METHODS

Raw Materials and Specimens

For the asphalt base of penetration (70 ± 0.01 mm), steel slag aggregates and limestone aggregates from Tangshan, Hebei, were selected as the raw materials. After testing, the raw materials met the relevant requirements of Chinese standard JTG F40-2004. The parameters of these aggregate-related materials are shown in **Table 1**.

TABLE 1 | Measured parameters of steel slag and limestone aggregates.

Aggregate type	Particle size specification (mm)	Apparent density ($g \cdot cm^{-3}$)	Water absorption (%)	Crushing value (%)	Los Angeles abrasion value (%)
Steel slag	10–15	3.416	2.3	9.0	11.0
	5–10	3.455	2.7	—	—
	0–5	3.495	3.0	—	—
Limestone	10–15	2.725	0.4	13.8	24.5
	5–10	2.736	0.5	—	—
	0–5	2.748	0.6	—	—

TABLE 2 | Marshall indices of asphalt mixtures.

Type of mixture	Oil stone ratio (%)	Void fraction (%)	Stability (kN)	Flow value (0.1 mm)	Bulk specific gravity ($g \cdot cm^{-3}$)
SSAM	5.1	4.0	11.3	28	2.753
LAM	4.7	4.3	10.0	33	2.498

TABLE 3 | Preliminary gradation quality.

Mesh size (mm)	16	13.2	9.5	4.75	2.36	1.18	0.6	0.3	0.15	0.075
Passing mass (%)	100.0	95.0	68.9	46.2	30.0	20.3	14.2	9.9	7.0	5.0

Steel slag was used for the coarse aggregate and fine aggregate of the AC-13 SSAM, and limestone powder was used as a filler. Limestone was used for the coarse aggregate, fine aggregate, and mineral powder of the AC-13 limestone–asphalt mixture (LAM). The relevant Marshall volume parameters are shown in **Table 2**, and the unified mixture gradation is presented in **Table 3**.

According to the Marshall test's results, and to ensure consistent height and uniformity of the test specimens, a press machine and rut-forming machine were used to separately generate specimens' triaxial compression and rutting tests. The size of the static pressure specimen was 250 mm in diameter and 160 mm in height, and these specimens were further processed into samples 150 mm in diameter and 150 mm in height; the size of each rutting specimen was 300 mm × 300 mm × 50 mm.

The micro test samples required special treatments because atomic force microscopy (AFM) generally adopts a tapping mode. The sample size is typically less than 1 cm^2, the height should be controlled below 0.5 cm, and the surface fluctuation of the sample should not exceed 15 μm, otherwise the needle tip may be damaged. It was, therefore, necessary to cut the Marshall specimen into 3–5 mm slices, dissolve them in trichloroethylene, select the slices that met the test requirements, and wrap them with a layer of asphalt film.

The prepared triaxial compression specimens, rutting specimens, Marshall specimens, trabecular specimens, and microscopic specimens were immersed in normal temperature water in the summer for 120 days.

TABLE 4 | Fatigue test parameters.

Test parameters	Value
Prestress (*N*)	50
Loading frequency (Hz)	10
Loading waveform	Sine wave
Test temperature (°C)	15
Stress ratio	0.5

The stress ratio is the ratio of the test pressure to the maximum pressure that the specimen could bear.

Testing Methods

Water Stability Test Method

Water resistance tests, rutting tests, and low-temperature bending tests were conducted on the asphalt mixtures in strict accordance with the technical requirements of Chinese standard JTG E20-2011.

Fatigue Tests

The fatigue testing machine used in this study was a universal testing machine (UTM), a multifunctional testing machine. The equipment was mainly composed of a refrigeration system, a hydraulic system, a temperature system, a pressure system, splitting accessories, a transverse displacement sensor, and a spindle displacement sensor. The instrument continuously applied pressure to the splitting accessories through the spindle, and the splitting accessories applied force to the Marshall specimen. The transverse displacement sensor was used to measure the transverse deformation of each Marshall specimen under pressure.

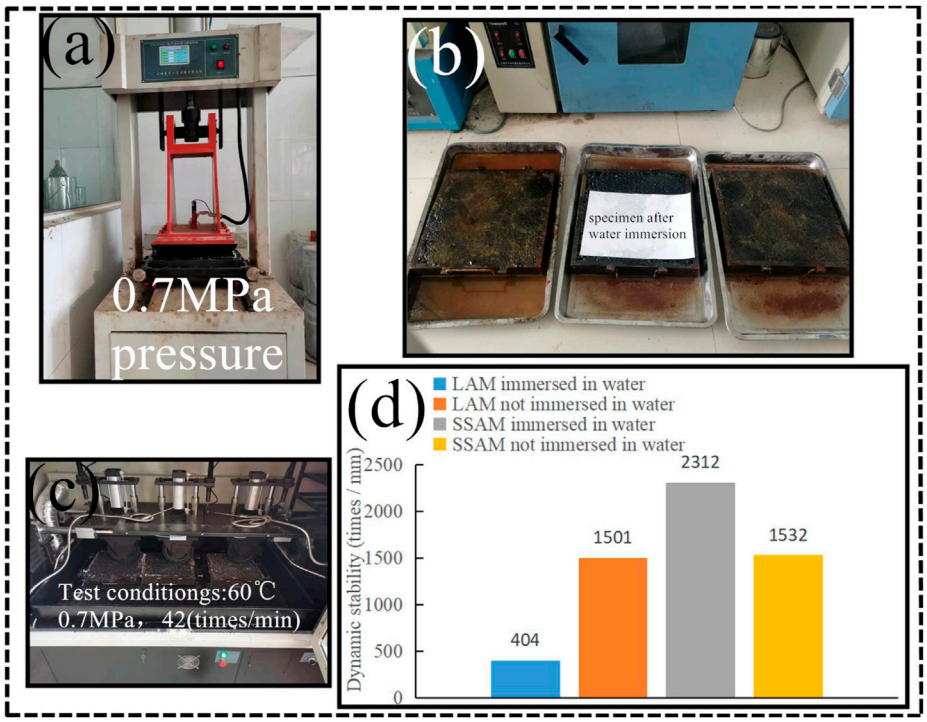

FIGURE 1 | Rutting performance of asphalt mixtures: **(A)** test piece formation; **(B)** test piece soaking; **(C)** rutting test; and **(D)** results.

During these tests, the displacement sensor accessories were first installed on the Marshall specimen. Then the specimens were maintained at 15°C for at least 6 h. At that time, the test was begun immediately, according to the parameters compiled in **Table 4**.

Triaxial Tests

The equipment used for the triaxial tests was a UTM-30 multifunctional testing machine, and the test temperature was 60°C. The instrument was mainly composed of a pressure chamber, an axial pressure system, a confining pressure application system, data acquisition system, and a control system.

The standard size of each specimen for the triaxial test was 100 mm in diameter and 150 mm in height. During the test, the control and acquisition systems of the triaxial apparatus were turned on, the designated confining pressure was applied, and the axial load was applied according to the constant loading rate. For specimens with a height of 150 mm, the constant loading rate was 7.5 mm/min, which corresponds to an axial strain rate of about 0.05 mm/(mmmin). When the peak value of axial pressure was reached, the test was stopped. If there was no peak value, the test was stopped when the strain reached 20%. After each test, the computer automatically calculated the cohesion and internal friction angle.

RESULTS AND DISCUSSION

Analysis of Rutting Test Results

Numerous studies have demonstrated that the deformation of asphalt pavement under a certain load undergoes the following three stages: 1) a further compaction stage, wherein the asphalt mixture is further compacted before about 1,000 load cycles; 2) the creep stability stage, wherein the asphalt mixture has been fully compacted (this deformation stage mainly involves slow creep under the load cycle); and 3) spalling in the accelerated deformation stage, wherein part of the asphalt spalling generates strain, and the strain rate of the asphalt mixture increases rapidly with time because of the influence of moisture. Therefore, moisture must be considered when evaluating the asphalt mixtures' permanent deformation resistance to understand its performance during the rainy season.

In China, the evaluation index of the rutting test is dynamic stability, which refers to the walking times of a standard axle load borne by the asphalt mixture when a deformation of 1 mm occurs at 60°C; the larger the value, the better the anti-rutting performance of the asphalt mixture. The process of forming the test pieces is shown in **Figure 1A**, the soaking of the specimen is shown in **Figure 1B**, the rutting test is shown in **Figure 1C**, and the test results are shown in **Figure 1**D.

As shown in the figure, the dynamic stability of LAM after immersion decreased by 73% relative to the sample that was not immersed. In contrast, the dynamic stability of SSAM after immersion increased by 50% relative to that without immersion. These results indicated that the deformation resistance of LAM decreased after immersion, whereas SSAM endured some changes that increased the deformation resistance of SSAM upon immersion in water. The changes in deformation resistance are closely related to the cohesion and internal friction of the asphalt mixtures. Therefore, to further explore

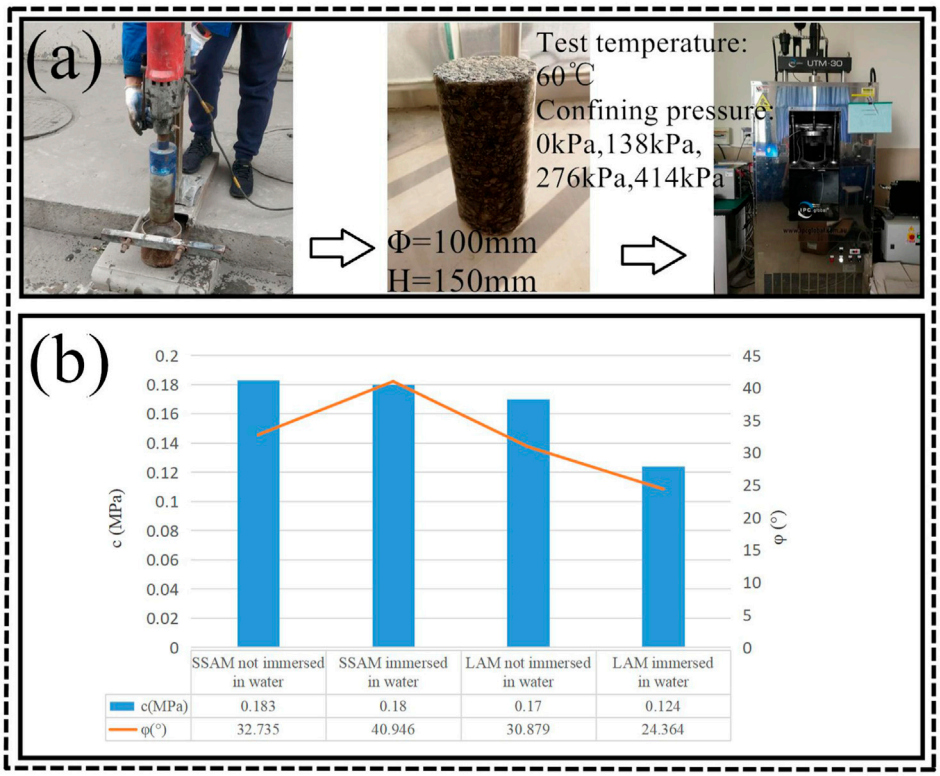

FIGURE 2 | Triaxial tests: **(A)** testing process and **(B)** results.

the origin of this phenomenon, triaxial compression tests were performed.

Triaxial Compression Tests

Asphalt mixtures are viscoelastic materials, meaning that under the action of shear stress, viscoelastic deformation of asphalt mixture occurs. The main properties that contribute to the shear capacity of an asphalt mixture are cohesion (c) and the internal friction angle (φ). To study the cohesion and internal friction angles of LAM and SSAM before and after immersion, triaxial compression tests were performed. The test procedures are shown in **Figure 2A**, and the test results are shown in **Figure 2B**.

The results of the triaxial compression tests indicate that the cohesion of SSAM does not decrease significantly, but that of LAM decreases by 27.1%; the internal friction angle of SSAM increases by 25.1% and that of LAM decreases by 21.1%. The reduction in LAM cohesion and the internal friction angle are the main reasons for this material's decreased deformation resistance after immersion, while the increase in the SSAM internal friction angle and the stability of its cohesion are the main reasons for the improvement of deformation resistance in the case of SSAM. To further explore the reasons why the cohesion of the SSAM remained unchanged and the internal friction increased after immersion, it was necessary to carry out asphalt adhesion and micro tests.

Asphalt Adhesion Tests

The adhesion test of asphalt is typically used to evaluate the adhesion between the aggregate surface and the asphalt to understand the anti-stripping ability of the asphalt film on the aggregate surface. According to the anti-stripping ability, the adhesion can be divided into five grades, where grade 5 is the best and grade 1 is the worst. The sample should be boiled for 3 min in a conventional laboratory, but to further study the aggregate adhesion, the boiling time in this study was extended to 6 min; the test results are shown in **Figure 3C**.

As the boiling time increased, the adhesion grade of the steel slag and asphalt changed from 5 to 4, while that of limestone changed from 4 to 2. **Figures 3A,B** present test photos showing the asphalt adhesion of limestone and steel slag at 6 min. It is clear that the adhesion of steel slag/asphalt is much better than that of limestone/asphalt. This result indicates that the interface between steel slag and asphalt has a stronger resistance to high temperature and water immersion than the limestone–asphalt interface. This indirectly explains why the cohesion of SSAMs is only slightly reduced after long-term water immersion.

In the asphalt mixtures, the main function of asphalt is to provide the required cohesion and stabilizing force. When asphalt is gradually stripped from the asphalt mixture, the cohesion and stability also decrease, which consequently reduces the deformation resistance of the asphalt mixture.

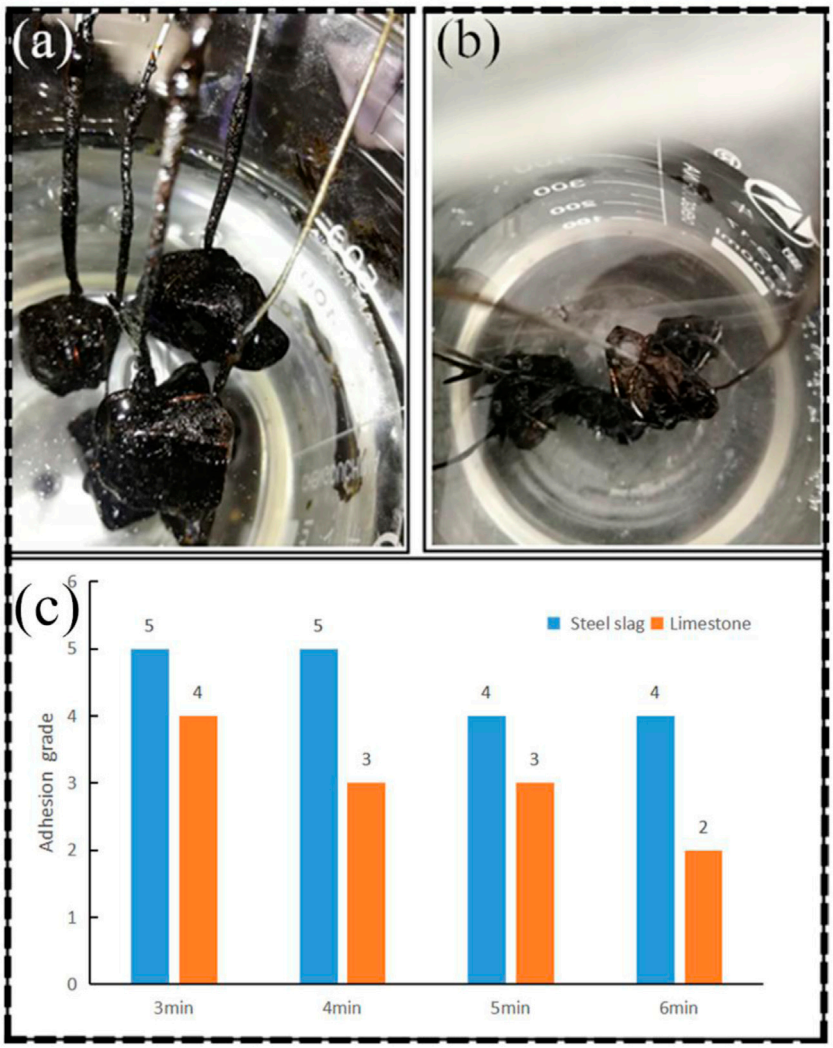

FIGURE 3 | Adhesion tests between aggregates and asphalt: **(A)** steel slag aggregate adhesion test at 6 min; **(B)** limestone aggregate adhesion test at 6 min; and **(C)** results of aggregate adhesion.

Microscopic Tests

The longitudinal resolution of AFM images is less than 0.01 nm, which allows us to distinguish atomic level surface changes and to calculate the roughness of samples. Therefore, AFM was used to study the surface changes of steel slag before and after immersion.

The asphalt steel slag slices were soaked in trichloroethylene after immersion, and the asphalt on the surface was removed. Then, AFM scans were carried out on the steel slag slices. The testing process is shown in **Figure 4A**.

Figure 4B shows the electron microscope scanning diagram of a specimen after 60 days of immersion, revealing hexagonal plate-like crystals. **Figure 4C** presents the atomic force scanning diagram of the sample immersed for 120 days, which clearly shows crystals that make the steel slag surface uneven.

Using Gwyddion software for data visualization and analysis, the surface area data from atomic force scanning was obtained, as shown in **Figures 4D,E**.

According to **Figures 4D,E**, the ratios of the steel slag surface area to the scanning area were 1.29 and 1.93 before and after soaking, respectively. This means that over the same scanning area, the surface area of steel slag soaked in room temperature water for 120 days was 1.5 times of that of non-immersed steel slag aggregate.

The aforementioned phenomenon indicates that with the prolongation of the soaking time, water soaked the steel slag along cracks and initiated hydration reactions on the surface of steel slag. This increased the surface roughness of the steel slag aggregate and the internal friction angle of the SSAM. Higher internal friction can enhance the anti-deformation ability of an asphalt mixture, which also improves its anti-rutting performance.

Other Road Performance Tests

The water stability, low-temperature deformation performance, and fatigue performance of LAM and SSAM after immersion

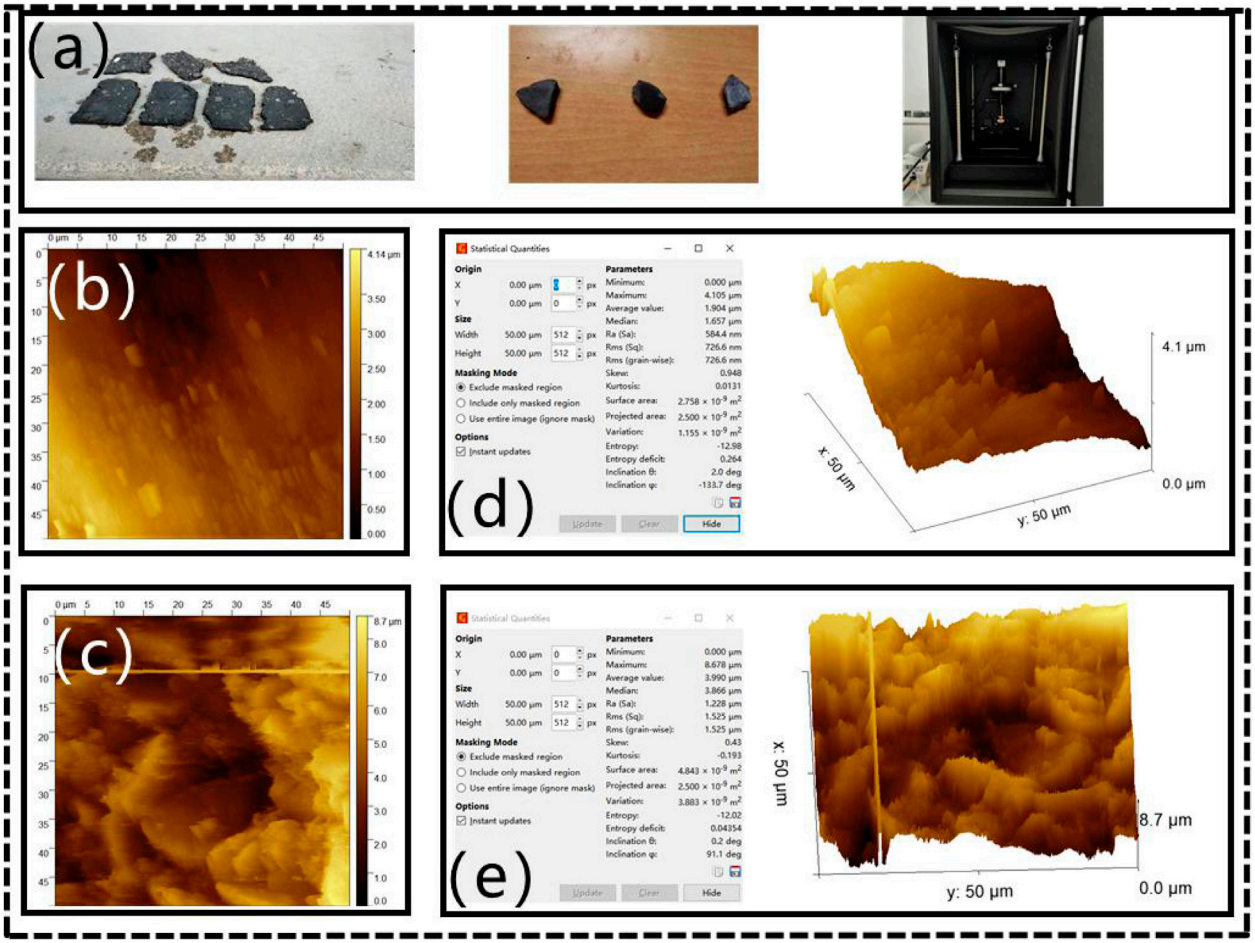

FIGURE 4 | Microscopic tests: **(A)** test preparation; **(B)** specimen after 60 days of water immersion; **(C)** specimen after 120 days of water immersion; **(D)** scanning area and surface area of steel slag aggregates before water immersion; and **(E)** scanning area and surface area of steel slag aggregates after immersion.

were tested to evaluate their water damage resistance and tensile deformation resistance. **Figure 5** illustrates the low-temperature bending test, the fatigue test, and the water stability test, and the results are presented in **Table 5**.

Table 5 indicates that when the SSAM specimen was immersed in water for 120 days, the residual stability, the freeze-thaw splitting strength ratio (TSR), and maximum bending tensile strain at failure met the specification requirements. Furthermore, SSAM had a higher fatigue life, which indicates that the SSAM still has excellent water damage resistance and low-temperature deformation capacity.

However, it should be noted that the expansion of the steel slag aggregate (less than 2%) and SSAM expansion (less than 1.5%) met the specification requirements. For a SSAM whose expansion does not meet the requirements, the TSR value and maximum bending tensile strain at failure would be significantly reduced. This is because SSAMs will expand and produce cracks, thus greatly reducing their deformation capacity.

As shown in **Figure 6A**, the Marshall specimen of the asphalt mixture with unqualified expansion in room temperature water for 120 days had large cracks on its surface, which were mainly caused by the large expansion of the steel slag aggregate. Based on **Figure 6B**, the stability of the Marshall specimen reached 23.68 kN; however, the maximum bending tensile strain of the asphalt mixture with unqualified expansion was only 500 με, and the fatigue life was 3,000 times, which greatly reduced the material's low-temperature tensile deformation resistance ability. When SSAM with unqualified expansion is used to pave roads, it can easily form cracks.

Therefore, the SSAM with qualified expansion has the growth resistance, excellent water damage resistance, and low-temperature deformation ability. However, the SSAM with unqualified expansion capacity is affected by moisture in the use process, and its low-temperature deformation performance and fatigue performance will be greatly reduced due to expansion cracks. In the process of production, it is inevitable that steel slag with unqualified expansion rate is used in asphalt pavement. In order to reduce the cracking caused by the expansion of steel slag, modified asphalt and fiber can be used in asphalt mixture (Jiang et al., 2020).

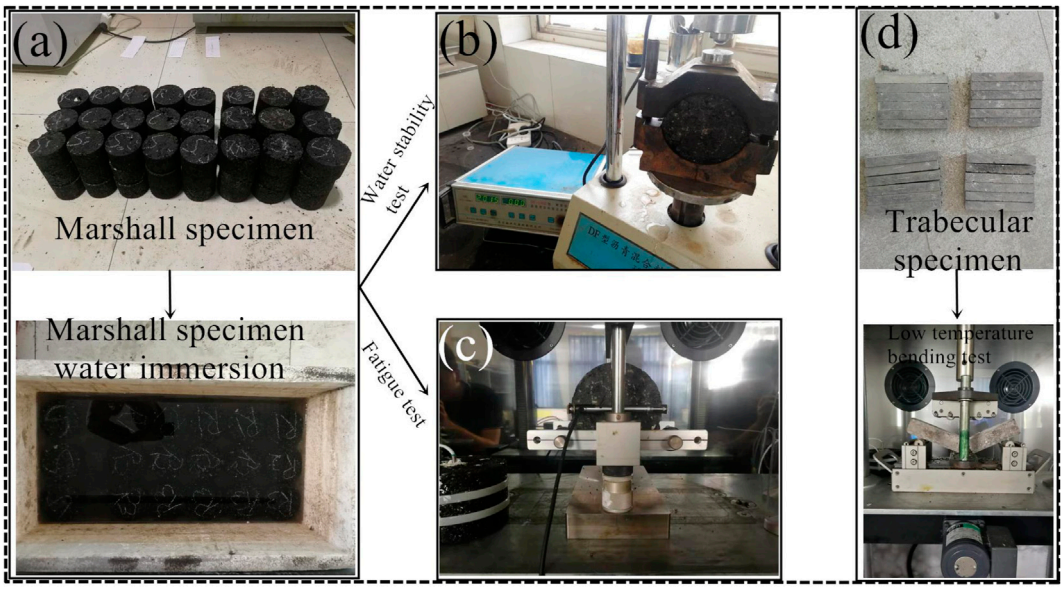

FIGURE 5 | Other road performance tests: **(A)** Marshall test piece; **(B)** water stability test; **(C)** fatigue test; and **(D)** low-temperature test.

TABLE 5 | Experimental data of water stability and low-temperature deformation performance.

Type of mixture	Residual stability (%)	TSR (%)	Maximum bending tensile strain at failure ($\mu\varepsilon$)	Fatigue life (times)
SSAM	90	85	2,235	16,607
LAM	75	68	1820	13,793
Requirements	≧80	≧75	≧2000	—

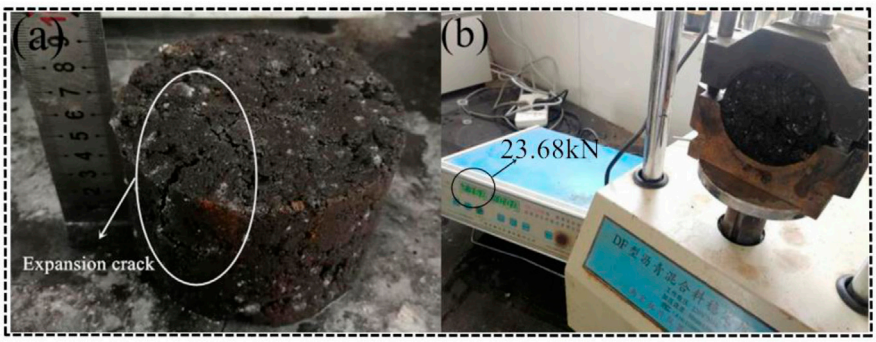

FIGURE 6 | Expansion cracking: **(A)** Marshall specimen after 120 days of immersion; **(B)** Marshall stability after 120 days of immersion.

Significance and Engineering Practice of the Research Results

In China, semirigid base asphalt pavement is the main part of asphalt road. The semirigid base has high stiffness, strong load diffusion capacity, and plays the role of structural bearing, while asphalt pavement only plays the role of functional layer. In order to study the failure mode of semirigid base asphalt pavement structure, ANSYS is used to simulate the structure. The pavement structure, material parameters, and mesh division are shown in **Figure 7A**, and the profile of pavement structure along the load center is shown in **Figure 7B**.

From **Figures 7C,D**, it is clear that the asphalt layer is in a high shear state, and the maximum shear stress appears on the road surface in the wheel gap center, meaning that the pavement

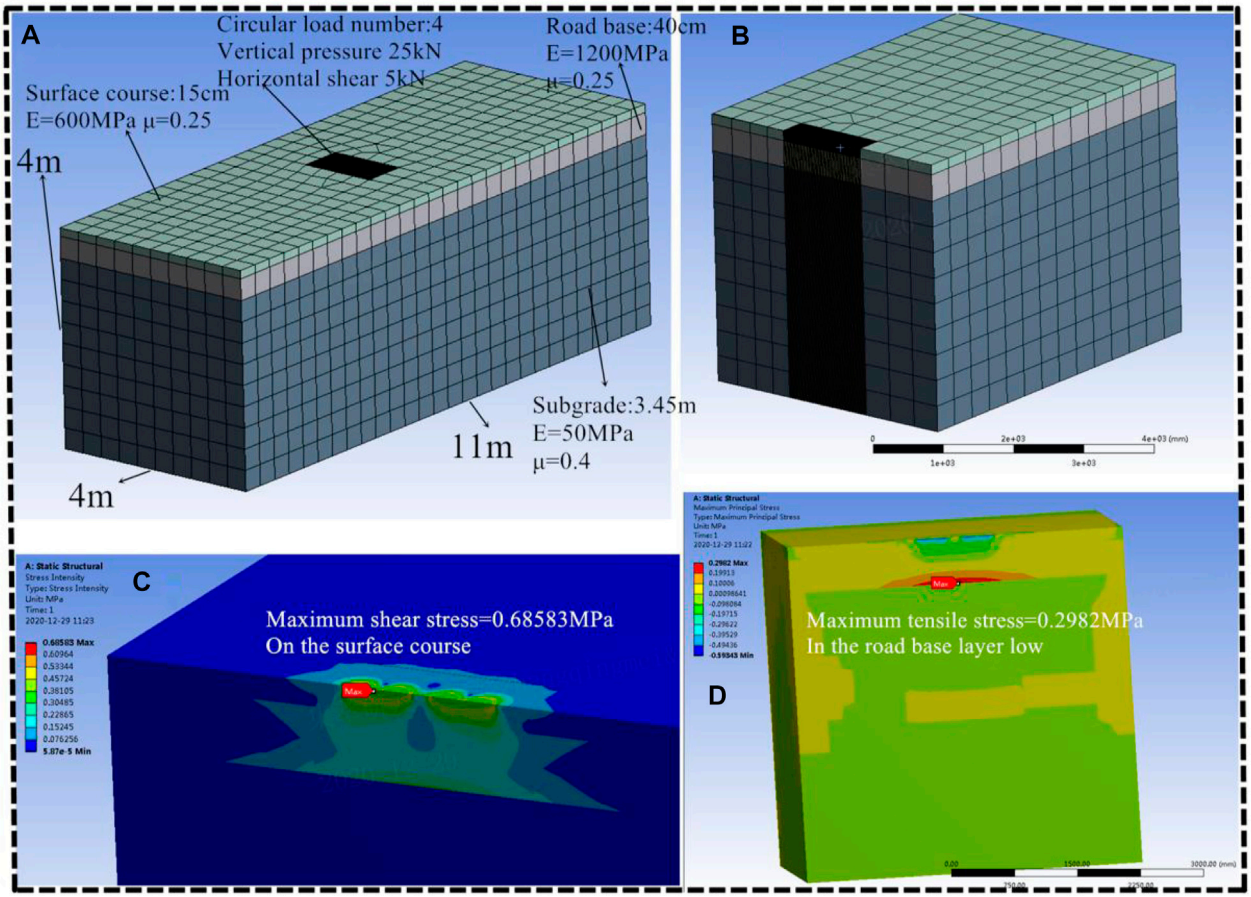

FIGURE 7 | Finite element analysis: **(A)** mesh dividing; **(B)** cross section; **(C)** stress intensity; and **(D)** maximum principal stress.

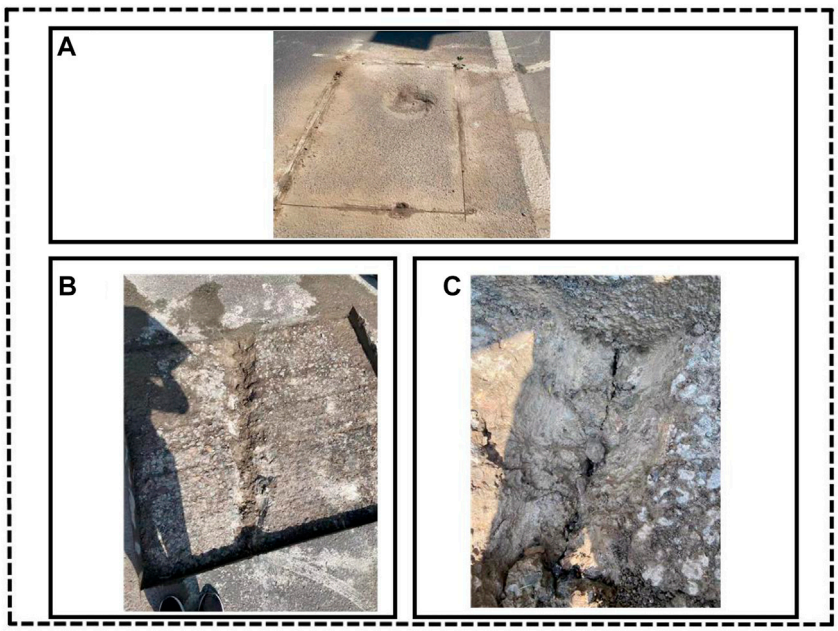

FIGURE 8 | Typical diseases: **(A)** local settlement of asphalt pavement; **(B)** removal of asphalt pavement surface; and **(C)** reflection crack of base course.

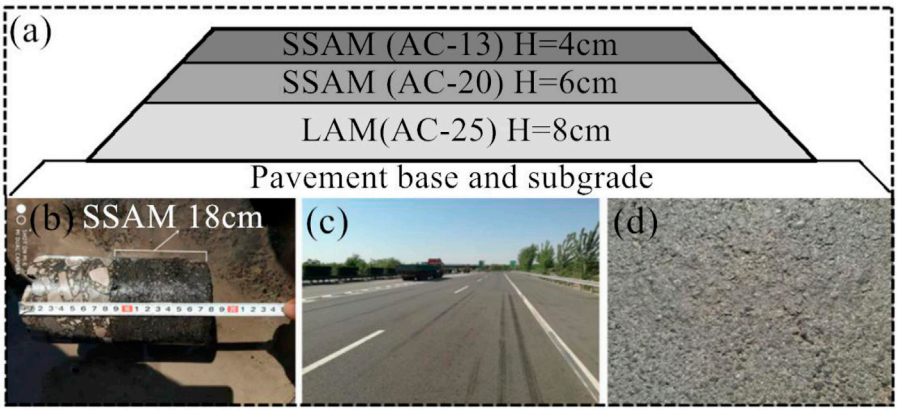

FIGURE 9 | Test road: **(A)** schematic diagram of a main line pavement structure; **(B)** core drilling sample; **(C)** condition of the test section; and **(D)** surface of the test section.

surface can easily undergo permanent deformation. The semirigid base course bears too much bending tensile stress, so the pavement can easily produce reflection cracks (**Figure 8**). Therefore, most of the pavement issues on China's expressways involve ruts and cracks. In the latest Chinese specifications, the design indices of semirigid pavement include the lowest layer tensile stress of the inorganic binder and the permanent deformation of the asphalt mixture layer.

Under the influence of water, the high-temperature deformation resistance of SSAMs will undergo a certain amount of growth. If the SSAM is paved on the surface of asphalt pavement, it will effectively reduce the permanent deformation of the asphalt pavement to alleviate the development of ruts in semirigid asphalt pavement.

To verify the feasibility of steel slag application in high-grade highways, steel slag with qualified expansion is used in the asphalt pavement surface of a highway in Tangshan city, Hebei Province. The pavement structure is shown in **Figure 9A**, and core sampling at a representative site location is shown in **Figure 9B**.

After two years of operation, the surface of the test section was smooth, and there was no cracking, loosening, rutting, or other pavement problems. Therefore, the material demonstrated shows good skid resistance and excellent road performance (**Figures 9C,D**).

CONCLUSION

1) After soaking SSAM and LAM in water for 120 days, the dynamic stability of LAM decreased by 73% relative to that before immersion, and the dynamic stability of SSAM after immersion increased by 50%.
2) Through triaxial compression tests, it was determined that the cohesion of SSAM did not decrease significantly, but that of LAM decreased by 27.1%; the internal friction angle of SSAM increased by 25.1%, and that of LAM decreased by 21.1%. The increase in the internal friction angle and stability of cohesion after immersion led to increased deformation resistance.
3) According to the asphalt adhesion tests, the adhesion between steel slag and asphalt was grade 4, and that of limestone was grade 2 after boiling for 6 min. The adhesion between steel slag and asphalt was superior to that between limestone and asphalt. Therefore, the reason why the cohesion did not decrease after long-term immersion was that steel slag and asphalt had excellent adhesion.
4) Based on the microscopic test, it was determined that hydration reactions occurred on the aggregate surface of the SSAM after immersion, which produced calcium hydroxide, and other crystals. These crystalline substances increased the surface roughness of the steel slag aggregate and the internal friction angle.
5) The SSAM with qualified expansion demonstrated growth resistance, excellent water damage resistance, and low-temperature deformation ability. However, the SSAM with unqualified expansion capacity was affected by moisture during use, and its low-temperature deformation performance was greatly reduced because of expansion cracks.
6) Through the ANSYS analysis, it was determined that the semirigid asphalt pavement could easily produce permanent deformations. Additionally, the high-temperature deformation resistance of SSAMs after contact with water could effectively reduce the permanent deformation of asphalt pavement, which alleviated the development of pavement ruts. The steel slag asphalt road that was open to traffic for two years exhibited no cracking, loosening, or rutting, which indicated that SSAMs with qualified expansion can be used in high-grade highways.

DATA AVAILABILITY STATEMENT

The original contributions presented in the study are included in the article/Supplementary Material, further inquiries can be directed to the corresponding author.

AUTHOR CONTRIBUTIONS

CW executed the experiment, wrote the manuscript, and conceived and designed the study and the experiment plan. CZ revised the manuscript and analyzed the experimental results.

FUNDING

The study was funded by the Natural Science Foundation of Hebei Province (e2012202161); Jiangsu transportation science and technology and achievement transformation project (2018Y25).

REFERENCES

Ameli, A., Hossein Pakshir, A., Babagoli, R., Norouzi, N., Nasr, D., and Davoudinezhad, S. (2020). Experimental Investigation of the Influence of Nano TiO2 on Rheological Properties of Binders and Performance of Stone Matrix Asphalt Mixtures Containing Steel Slag Aggregate. *Construction Building Mater.* 265, 120750. doi:10.1016/j.conbuildmat.2020.120750

Ameri, M., Hesami, S., and Goli, H. (2013). Laboratory Evaluation of Warm Mix Asphalt Mixtures Containing Electric Arc Furnace (EAF) Steel Slag. *Construction Building Mater.* 49, 611–617. doi:10.1016/j.conbuildmat.2013.08.034

Barišić, I., Netinger Grubeša, I., and Hackenberger Kutuzović, B. (2017). Multidisciplinary Approach to the Environmental Impact of Steel Slag Reused in Road Construction. *Road Mater. Pavement Des.* 18, 897–912. doi:10.1080/14680629.2016.1197143

Bonoli, A., Degli Esposti, A., and Magrini, C. (2020). A Case Study of Industrial Symbiosis to Reduce GHG Emissions: Performance Analysis and LCA of Asphalt Concretes Made with RAP Aggregates and Steel Slags. *Front. Mater.* 7. doi:10.3389/fmats.2020.572955

Chai, C., Cheng, Y., Zhang, Y., Zhu, B., and Liu, H. (2020). Mechanical Properties of Crumb Rubber and Basalt Fiber Composite Modified Porous Asphalt Concrete with Steel Slag as Aggregate. *Polymers* 12, 2552. doi:10.3390/polym12112552

Chen, J.-S., and Wei, S.-H. (2016). Engineering Properties and Performance of Asphalt Mixtures Incorporating Steel Slag. *Construction Building Mater.* 128, 148–153. doi:10.1016/j.conbuildmat.2016.10.027

Gao, J., Sha, A., Wang, Z., Tong, Z., and Liu, Z. (2017). Utilization of Steel Slag as Aggregate in Asphalt Mixtures for Microwave Deicing. *J. Clean. Prod.* 152, 429–442. doi:10.1016/j.jclepro.2017.03.113

Gulisano, F., Crucho, J., Gallego, J., and Picado-Santos, L. (2020). Microwave Healing Performance of Asphalt Mixture Containing Electric Arc Furnace (EAF) Slag and Graphene Nanoplatelets (GNPs). *Appl. Sci.* 10, 1428. doi:10.3390/app10041428

Jiang, Z., Hu, C., Liu, M., Easa, S. M., and Zheng, X. (2020). Characteristics of Morphology and Tensile Strength of Asphalt Mixtures under Impact Loading Using Split Hopkinson Pressure Bar. *Construction Building Mater.* 260, 120443. doi:10.1016/j.conbuildmat.2020.120443

Jiao, W., Sha, A., Liu, Z., Jiang, W., Hu, L., and Li, X. (2020). Utilization of Steel Slags to Produce thermal Conductive Asphalt Concretes for Snow Melting Pavements. *J. Clean. Prod.* 261, 121197. doi:10.1016/j.jclepro.2020.121197

Lian, C., Wang, Y., Liu, S., and Hao, Y. (2021). Experimental Study of the Dynamic Compressive and Tensile Strengths of Fly Ash and Slag Based Alkali-Activated Concrete Reinforced with Basalt Fibers. *Front. Mater.* 8. doi:10.3389/fmats.2021.651581

Liu, J., Yu, B., and Hong, Q. (2020). Molecular Dynamics Simulation of Distribution and Adhesion of Asphalt Components on Steel Slag. *Construction Building Mater.* 255, 119332. doi:10.1016/j.conbuildmat.2020.119332

Liu, W., Miao, P., and Wang, S.-Y. (2017). Increasing Microwave Heating Efficiency of Asphalt-Coated Aggregates Mixed with Modified Steel Slag Particles. *J. Mater. Civil Eng.* 29, 04017171. doi:10.1061/(ASCE)MT.1943-5533.0002026

Lyu, Z., Shen, A., Li, D., Guo, Y., Zhai, C., and Yang, X. (2021). Effect of Dry-Wet and Freeze-Thaw Repeated Cycles on Water Resistance of Steel Slag Asphalt Mixture. *Iran J. Sci. Technol. Trans. Civ Eng.* 45, 291–301. doi:10.1007/s40996-020-00454-1

Ma, L., Xu, D., Wang, S., and Gu, X. (2020). Expansion Inhibition of Steel Slag in Asphalt Mixture by a Surface Water Isolation Structure. *Road Mater. Pavement Des.* 21, 2215–2229. doi:10.1080/14680629.2019.1601588

Pathak, S., Choudhary, R., Kumar, A., and Shukla, S. K. (2020). Evaluation of Benefits of Open-Graded Friction Courses with Basic Oxygen Furnace Steel-Slag Aggregates for Hilly and High-Rainfall Regions in India. *J. Mater. Civil Eng.* 32, 04020356. doi:10.1061/(ASCE)MT.1943-5533.0003445

Pattanaik, M. L., Choudhary, R., Kumar, B., and Kumar, A. (2021). Mechanical Properties of Open Graded Friction Course Mixtures with Different Contents of Electric Arc Furnace Steel Slag as an Alternative Aggregate from Steel Industries. *Road Mater. Pavement Des.* 22, 268–292. doi:10.1080/14680629.2019.1620120

Preti, F., Noto, S., Accardo, C., Romeo, E., Montepara, A., and Tebaldi, G. (2019). Effect of Hyper-Modified Asphalt Binder and Steel Slags on Cracking and Rutting Behaviour of Wearing Course Mixtures. *Road Mater. Pavement Des.* 20, S678–S694. doi:10.1080/14680629.2019.1633746

Qazizadeh, M. J., Farhad, H., Kavussi, A., and Sadeghi, A. (2018). Evaluating the Fatigue Behavior of Asphalt Mixtures Containing Electric Arc Furnace and Basic Oxygen Furnace Slags Using Surface Free Energy Estimation. *J. Clean. Prod.* 188, 355–361. doi:10.1016/j.jclepro.2018.04.035

Tang, Y., Fang, S., Chen, J., Ma, L., Li, L., and Wu, X. (2020). Axial Compression Behavior of recycled-aggregate-concrete-filled GFRP-Steel Composite Tube Columns. *Eng. Structures* 216, 110676. doi:10.1016/j.engstruct.2020.110676

Tang, Y., Feng, W., Chen, Z., Nong, Y., Yao, M., and Liu, J. (2021a). Experimental and Theoretical Investigation on the Thermo-Mechanical Properties of Recycled Aggregate Concrete Containing Recycled Rubber. *Front. Mater.* 8. doi:10.3389/fmats.2021.655097

Tang, Y., Feng, W., Feng, W., Chen, J., Bao, D., and Li, L. (2021b). Compressive Properties of Rubber-Modified Recycled Aggregate concrete Subjected to Elevated Temperatures. *Construction Building Mater.* 268, 121181. doi:10.1016/j.conbuildmat.2020.121181

Wan, J., Wu, S., Xiao, Y., Chen, Z., and Zhang, D. (2018). Study on the Effective Composition of Steel Slag for Asphalt Mixture Induction Heating Purpose. *Construction Building Mater.* 178, 542–550. doi:10.1016/j.conbuildmat.2018.05.170

Wei, M., Wu, S., Cui, P., Yang, T., and Lv, Y. (2020). Thermal Exchange and Skid Resistance of Chip Seal with Various Aggregate Types and Morphologies. *Appl. Sci.* 10, 8192. doi:10.3390/app10228192

Zhu, B., Liu, H., Li, W., Wu, C., and Chai, C. (2020). Fracture Behavior of Permeable Asphalt Mixtures with Steel Slag under Low Temperature Based on Acoustic Emission Technique. *Sensors* 20, 5090. doi:10.3390/s20185090

Ziaee, S. A., and Behnia, K. (2020). Evaluating the Effect of Electric Arc Furnace Steel Slag on Dynamic and Static Mechanical Behavior of Warm Mix Asphalt Mixtures. *J. Clean. Prod.* 274, 123092. doi:10.1016/j.jclepro.2020.123092

Conflict of Interest: CW was employed by the company Jiangsu JITRI Road Engineering Technology and Equipment Research Institute Co., Ltd.

The remaining authors declare that the research was conducted in the absence of any commercial or financial relationships that could be construed as a potential conflict of interest.

Publisher's Note: All claims expressed in this article are solely those of the authors and do not necessarily represent those of their affiliated organizations, or those of the publisher, the editors and the reviewers. Any product that may be evaluated in this article, or claim that may be made by its manufacturer, is not guaranteed or endorsed by the publisher.

frontiers in Materials

ORIGINAL RESEARCH
published: 30 August 2021
doi: 10.3389/fmats.2021.739542

Microstructure and Mechanical Properties of Additively Manufactured Ni-Al Bronze Parts Using Cold Metal Transfer Process

Rongcheng Wang[1,2], Yang Zhao[2], Qing Chang[2], Fengshi Yin[1], Xiaoming Wang[2]*, Wenyu Wang[2], Zhiqiang Ren[2] and Guofeng Han[2]*

[1]School of Mechanical Engineering, Shandong University of Technology, Zibo, China, [2]National Key Laboratory for Remanufacturing, Army Academy of Armored Forces, Beijing, China

In this paper, the microstructure and mechanical properties of the SG-CuAl8Ni6 Ni-Al bronze straight wall were studied, which was fabricated by the cold metal transfer (CMT) arc additive manufacturing technology. This Ni-Al bronze cladding layer of SG-CuAl8Ni6 is composed mainly of α-Cu, residual β phase, rich Pb phase and κ phase. The microstructure of this multilayer single-channel Ni-Al bronze straight wall circulating presents the overall periodic law, which changes from fine cellular crystals, columnar crystals to dendritic crystals with the increase of the distance from the substrate. The Vickers hardness value of the Ni-Al bronze straight wall decreases with the distance of substrate are between 155 and 185 $HV_{0.5}$. The microhardness and elastic modulus of the Ni-Al bronze specimen are 1.57 times and 1.99 times higher than these of the brass matrix, respectively. The ultimate tensile strength (UTS) of the straight wall in the welding direction and 45° downward-sloping is greater than that of about 550 MPa in the stacking direction, and the elongation value in the welding direction is the highest. With the increase in interlayer temperature, the grain size increased gradually, and the tensile strength decreases slightly.

Keywords: cold metal transfer, additive manufacturing, microstructure, microhardness, tensile properties

OPEN ACCESS

Edited by:
Yunchao Tang,
Guangxi University, China

Reviewed by:
Baoqiang Cong,
Beihang University, China
Jianxin Xie,
University of Science and Technology Beijing, China
Sheng Lu,
Jiangsu University of Science and Technology, China

****Correspondence:***
Fengshi Yin
fsyin@sdut.edu.cn
Xiaoming Wang
uwangxm@126.com

Specialty section:
This article was submitted to Structural Materials, a section of the journal Frontiers in Materials

Received: *11 July 2021*
Accepted: *31 July 2021*
Published: *30 August 2021*

Citation:
Wang R, Zhao Y, Chang Q, Yin F, Wang X, Wang W, Ren Z and Han G (2021) Microstructure and Mechanical Properties of Additively Manufactured Ni-Al Bronze Parts Using Cold Metal Transfer Process. Front. Mater. 8:739542. doi: 10.3389/fmats.2021.739542

INTRODUCTION

Copper alloys, with its excellent thermal and electric conductivity as well as mechanical properties, are widely used in the electrical, lighting and machinery fields. They also have good corrosion resistance to seawater and marine organisms, and thus are suitable to manufacture parts in the shipbuilding industry (Wang et al., 2020a). And traditional manufacturing technology is difficult to realize the complex shape of copper alloy parts forming, resulting in high processing cost, low material utilization rate.

Additive manufacturing is a process of designing and fabricating layer by layer (Lamichhane et al., 2020; Mosallanejad et al., 2021), with a "bottom-up" characteristic and without restricting the production process of traditional process and complex shape structure (Tofail et al., 2017; Tang et al., 2021; Wang et al., 2016; Attar et al., 2020), which greatly improves the utilization of resources, reduces the costs of research and development (Aziz et al., 2021; Thompson et al., 2015; Ostovari Moghaddam et al., 2021), and is thus one of the key drivers for sustainable manufacturing, and a key strategy for circulation economy. Wang et al. (2021) used Laser Engineered Net Shaping technology,

have prepared Ti-Ni-C gradient composites with high hardness and wear resistance, which can be used for equipment, size and cutting tools, Hunter Martin et al. (2020) achieved grain refinement when using the laser additive manufacturing process by adding Al3Ta and Al3Zr to aluminum alloy powder materials, and believed that the method could also be extended to other alloys such as iron, nickel and titanium alloys. It has been shown that Laser additive manufacturing technology can improve production efficiency, have high material utilization rate, small shrinkage, and can obtain parts with excellent performance (Zhang and Chen, 2019; Chen et al., 2021). This point of view is also proven by Wang et al. (2020), who used SLM technology to prepare Cu-15Ni-8Sn alloy forming parts that showed good strength and toughness. Electronic beam additive manufacturing technology can achieve the rapid forming of complex parts with a minimum of steps, and the resulting density of components is high (Zhang and Chen, 2019). Roman Laptev et al. (2019) used electron beam additive manufacturing technology to obtain a Ti-6Al-4V alloy with a higher dislocation density and microhardness than that achieved by casting method with the same material. Focused electron beam deposition technology has also been shown to achieve high precision and complex profile manufacturing (Mutunga et al., 2019). However, additive manufacturing process has drawbacks such as large residual stress and an uneven microstructure (Sanaei and Fatemi, 2021), and the higher heat input needed creating further problems. For example, in the comparative study of Surinder Singh (Singh et al., 2019) on 316 L stainless steel laser cladding layer on the surface of a pure copper, it was found that the cladding layer was produced with a large number of holes, porosity and other defects, meaning that the strength, density and thermal conductivity of the pure copper cladding layer was lower than those of the cold spaying pure copper coating, because the high heat input leads to particle melting, high local temperature, high cooling rate and diffusion of carbon element in the cross-section.

Cold metal transfer (CMT) technology optimizes the connection between the additive process and wire feeding. The control system receives the short circuit signal of the welding wire for feedback, and controls the contact between the welding wire and the matrix, thereby forming a cyclic additive process (Cadiou et al., 2020). In addition to the advantages of high deposition efficiency and having a wide range of applied materials (Tanvir et al., 2021), compared to the other two additive manufacturing technologies, this technology also has the advantages of arc stability, less heat input and fewer spatters. Compared with pulsed metal inert gas (pulsed-MIG) technology, CMT additive ER5183 was confirmed by Derekar et al. (2020) to have lower porosity. Kim et al. (2020) have studied on nickel-aluminum bronze made of CMT and proved that CMT arc additive manufacturing technology can obtain better performance than casting forming workpiece. Pranav et al. (Nikam et al., 2020) used CMT to fabricated an ER2594 alloy straight wall and found that the tensile strength was better along the welding direction than in the stacking direction, but the percentage elongation of the samples was opposite due to having more slip systems in γ-FCC austenite. Wang et al. (2020) used CMT technology to deposit a 316 L part onto a stainless-steel plate, and found that the multi-layer structure had a periodic structure in the stacking direction, in transverse stacking direction has two alternating structure which the one is the areas materials remelted with dispersed grain orientation, and the other one is the areas located at the overlapping areas of adjacent with concentrated grain orientations. The yield and tensile strengths of covering the remelting zone were higher than those in the overlapping zone, and both of them were superior to those in the stacking direction. The optimization of CMT technology is mainly achieved by applying pulses. Wu et al. (2019) used the double-wire CMT + P process to obtain the 316 L stainless steel multilayer, and found that asynchronous arc striking and extinguishing can improve the forming. Increasing the wire feeding and decreasing the welding speed can increase the deposition rate, but it will cause the crystalline grains coarser due to the heat accumulation and reduction in the mechanical properties. Xie et al. (2020) proved that a fine-sized straight wall of 316 L stainless can be obtained by applying a pulsed CMT + P process, and that the microhardness changes parabolic along the stacking direction.

At present, research on CMT additive manufacturing mainly focuses on the section structure and the properties of steel and aluminum alloy by optimizing process parameters. There are few research papers on the properties of the copper alloy cladding layer manufactured by CMT arc additive manufacturing. In this paper, the microstructure, microhardness, tensile properties and corrosion resistance of Ni-Al Bronze forming parts manufactured by CMT arc additive are studied.

EXPERIMENTAL PROCEDURE

Materials

The substrate used in this research is brass alloy with the dimensions of 200 × 100 × 10 mm, containing 0.15 Fe, 1.5–2.5 Pb, 34.3–38.3 Zn and Cu in balance (in wt%), which is produced by Shanghai Meipin Industrial Co., Ltd. The SG-CuAl8Ni6 nickel-aluminum bronze welding wire with a diameter of Φ = 1.2 mm (Beijing Yida Kuntai Technology Co., Ltd.) was used for the CMT arc additive manufacturing. The welding wire has the following composition: 8.5–9.5 Al, 3.0–4.0 Fe, 1.0–2.0 Mn, 4.0–6.0 Ni, ≤0.02 Pb, ≤ 0.2 Si, ≤ 0.1 Zn, and Cu in balance (all in wt%).

CMT Arc Additive Manufacturing

The CMT arc additive manufacturing system used in this research is the ArcMan600 arc additive manufacturing system from Nanjing Enigma Automation CO., Ltd. as shown in **Figure 1A**. Prior to CMT arc additive manufacturing, the oxide film on the substrate surface was removed by mechanical grinding and ultrasonic cleaning. The CMT arc additive process parameters used are listed in **Table 1**. Before the experiment, the mathematical model of the multilayer single-channel was established. The model was imported and automatically sliced according to the printing parameters to generate the printing path. Through the layout simulation and

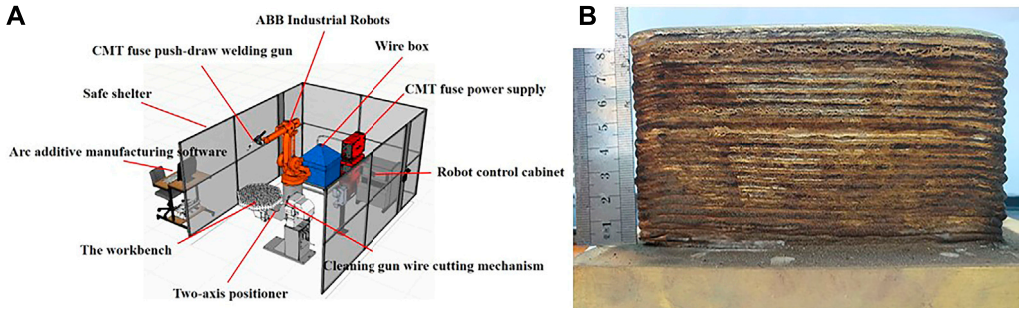

FIGURE 1 | CMT arc additive manufacturing equipment **(A)** and macro morphology of the parts **(B)**.

TABLE 1 | The CMT brazing process parameters in the additive manufacturing process.

Project	Parameters
Shielding gas	Argon (wt., 70%) +Helium (wt., 30%)
Gas flow rate	18 L/min
Wire feeding speed	9.0 m/min
Mean voltage and mean current	19.4 V + 210 A
Brazing speed	6.0 mm/s
Travel angle	90°
Electrode extension	15 mm

dynamic path simulation with an extremely high degree, the printing process is shown intuitively and visually. Based on the simulation of the printing process, a reciprocating additive method and five interlayer temperatures were selected to form up multilayer single-channel forming experimental specimens, 100, 150, 200, 250, and 300°C, respectively, with the dimensions of 150 × 10 × 90 mm, where, the interlayer temperature is controlled by the cooling time after the formation of the cladding layer, and the macro-morphology of the multilayer single-channel wall is shown in **Figure 1B**. The nickel-aluminum bronze straight wall line with five parameters was cut to obtain samples for metallographic, hardness, tensile and corrosion resistance experiments.

Microstructure Characterization

The SG-CuAl8Ni6 nickel-aluminum-bronze multilayer single-channel formation was cut using wire electro-discharge machine for a regional equidistant cutting, and a sample with a size of 5 × 5 × 3 mm was obtained, which was then polished. The microstructure of the polished section with and without corrosion by corrosive solution were observed using a quanta 250 field emission environmental scanning electron microscope (SEM, quanta 250, FEI, America). The corrosive solution was obtained by mixing 3 g $FeCl_3$, 10 ml concentrated hydrochloric acid and 100 ml absolute ethanol solution.

Process parameters in **Table 1** were used to obtain single-channel single cladding. X-ray diffraction (XRD, AXS D8 Advance, Bruker, Germany) was used to obtain XRD patterns of the cladding using Cu-K α radiation at a 2θ range of 10°–80° with a scan speed of 2 /min, and electron backscatter diffraction (EBSD, C-nano, Oxford Instruments, England) microstructural characterization was conducted using a JEOL 7001 F FE-SEM system equipped with a TSL/EDAX EBSD system containing a DigiView camera. These EBSD experiments were performed under a working distance of 15 mm at an acceleration voltage of 30 kV with a 70° tilt. After a process of argon ions polishing, the EBSD morphology of the bonding area between cladding layer and substrate, the inside of cladding layer and the top of cladding layer, were observed.

Mechanical Property Tests

To evaluate the formation quality, some mechanical property tests were used for the CMT arc additive manufactured SG-CuAl8Ni6 nickel-aluminum-bronze multilayer single-channel wall.

Hardness

The hardness of the SG-CuAl8Ni6 nickel-aluminum-bronze cladding specimen was measured using micro-hardness (MH-VK, China) at a load of 500 g with a dwell period of 15 s. Indentations were performed every 3 mm in the cladding layer area along the stacking direction. The inner area of the multi-layer single-channel formation was cut using wire electro-discharge machine cutting to obtain a sample of a size of 10 × 10 × 3 mm, and then polished. The nanoindentation test was conducted using a Nano Indenter (Agilent, G200, America) to measure the continuous load and displacement of each sample at five points by setting the maximum depth to 2,000 nm and holding the load time to 20 s, and thus the pressure depth-load curve was obtained.

Tensile Properties

Tensile tests were carried out on the sample at room temperature using a universal testing machine with a maximum 100 kN and a tensile rate ranging from 0.005 mm/min to 1,000 mm/min to determine the material's characteristic value and the deformation capacity of the sample. In this experiment, three samples were tested by being subjected to a low strain rate of 1 mm/min to fracture the specimens. The size of the plate-like tensile specimen used in this test was obtained in accordance with the Chinese national standard GB/T 34505-2017 copper and copper alloys materials-tensile testing at room temperature. The elongation,

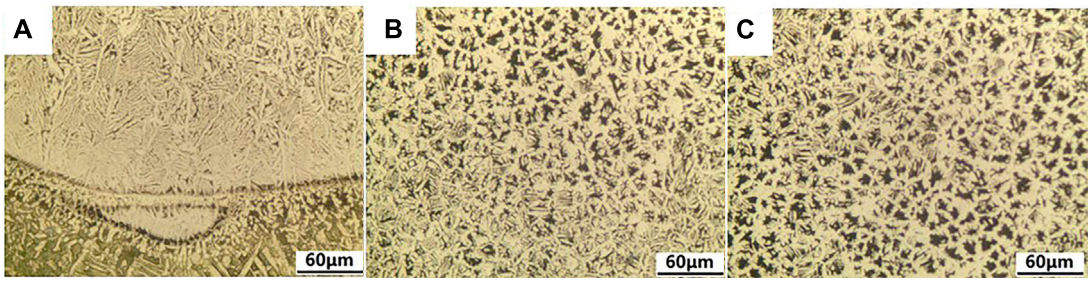

FIGURE 2 | The phase diagram of section of single-channel nickel-aluminum-bronze cladding layer manufactured by CMT arc additive **(A)**, the internal **(B)** and the top **(C)** of cladding layer.

tensile strength and yield of the sample were mainly tested, and after tensile testing, fracture morphology was observed by a quanta 250 field emission environmental scanning electron microscope (SEM).

Electrochemical Test

The electrochemical test was performed on the brass alloy substrate and nickel-aluminum-bronze cladding. The size of the sample was 10 × 10 × 1 mm, and then AB glue was used to encapsulate the sample with a reserved working area of 1 cm^2, after which absolute ethanol was used for cleaning. The electrochemical workstation (CHI-660E, CH Instruments Ins, America) was used to test the Tafel curve of the cladding layer and the substrate in 3.5% (mass fraction) NaCl solution (pH = 7). The electrochemical workstation adopts a standard three-electrode system, the working electrode is a copper alloy test sample, the auxiliary electrode is a platinum electrode, and the reference electrode is a saturated potassium chloride electrode. The polarization curve potential scan range is −1–1 V, and the scan rate is 0.5 mV/s.

RESULTS AND DISCUSSION

Microstructural Analysis

Figure 2 shows the section morphology of the single-channel nickel-aluminum-bronze samples observed by Metallographic microscope. As shown in **Figure 2A**, there is a black arc between the CMT arc additive manufactured nickel-aluminum-bronze cladding layer and the substrate, which shows good metallurgical bonding between the two. The cladding layer's internal microstructure presents an obvious gradient structure: the cladding layer and substrate combination area near the fusion line area of the microstructure are mainly for the tiny cell, in the region far away from the fusion line, columnar crystals grow perpendicular to the direction of welding (**Figure 2A**) and then gradually it turns to dendrites (**Figure 2B**). In the initial solidification stage, due to the low temperature of the base, the large temperature gradient of the melting pool in the binding region and small solidification speed are mainly small in the area near the melting line. With the solidification process, affected by the thermal diffusion, the base temperature gradually increases, the solidification temperature gradient at the solidification front decreases, and the microtissue is mainly presented as columnar crystals and branch crystal tissue growing in the reverse thermal dispersion direction. In **Figure 2C**, for the structure of the top of cladding, the direction of the temperature gradient is changed during the solidification process, the top of the solidification process is mainly affected by air cooling, the heat flow no longer runs perpendicular to the substrate surface, the temperature gradient is small, the solidification rate is high, thus a straight wall at the top of the regional direction dendrite tissue shows growth disorders, which are mainly for the branch crystal and the equiaxial crystal. It can be found that with the increase in the distance from the bonding zone, the grain size inside the cladding layer also gradually increases. This may be caused by the uneven solidification that takes place due to the different temperature gradients and undercooling degrees in the three regions, which in turn is caused by the heat dissipation of the air and matrix inside the cladding layer. Through a cross-sectional SEM observation, as shown in **Figure 3A**, bright white Pb particles with dispersion distribution can be identified inside the cladding layer. Due to the presence of a certain amount of Pb in the nickel-al-bronze alloy, monotectic crystals occur due to the influence of the high degree of undercooling during solidification, and the Pb-rich secondary phase particles are formed (Dong et al., 2019). Furthermore, the EDS analysis results (**Figure 3B**) and XRD analysis (**Figure 3C**) proved the existence of Pb phase.

Figure 3C shows the XRD diffraction pattern of the single-channel nickel-aluminum-bronze cladding layer. The analysis shows that the inner part of the cladding layer is composed of α-Cu, residual β phase (Martensite) (β-M), Pb and K phase at room temperature, as shown in **Figures 3D,E**, the cladding layer presents a duplex microstructure composed of the gray α-Cu phase matrix and the bright white β-Martensite. The process of additive manufacturing is the nickel-aluminum-bronze metal wire end melt and spread out quickly on the substrate, and then rapid solidification. The main process from liquid solidification to room temperature is as follows: Firstly, α, κ_I and β phase are precipitated in the liquid phase, α phase is the Cu-based solid solution with face-centered cubic structure, κ_I phase is mainly flower-shaped, and β phase is martensite with 2R and 3H

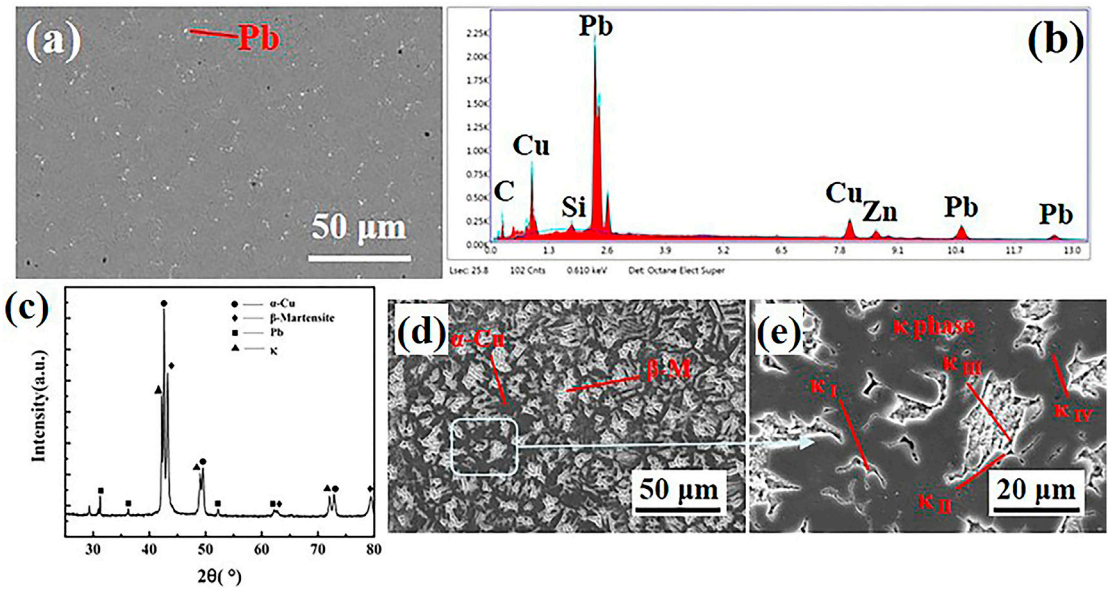

FIGURE 3 | Internal backscattered electron image **(A)** and EDS analysis **(B)** of cladding layer before corrosion, and the XRD diffraction pattern **(C)**, secondary electron images **(D,E)** of the single-channel nickel-aluminum-bronze cladding layer.

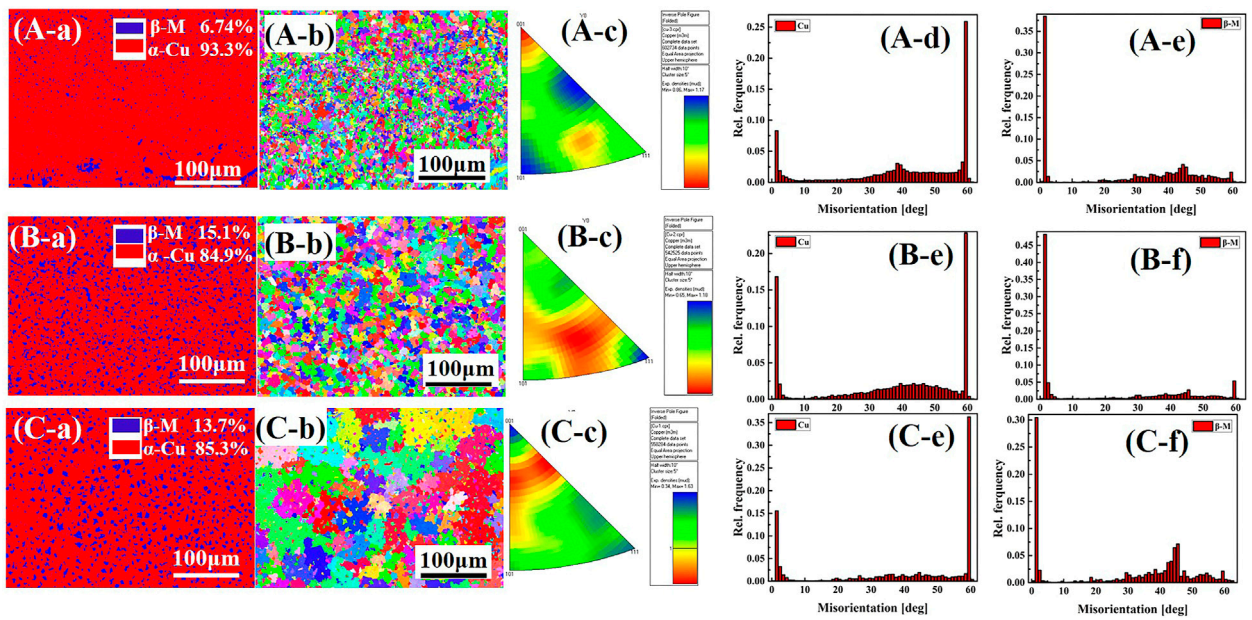

FIGURE 4 | The EBSD analysis results of the bonding area between the substrate and the cladding layer **(A)**, the inner area **(B)** and the top area **(C)** of the cladding layer, where (a) phase distribution diagrams, (b) grain boundary orientation diagram, (c) the anti-pole diagram of texture (d–e) the histogram of grain orientation difference.

structure. As the solidification process proceeds, κ_{II} phase is precipitated in the β phase and distributed around the α phase, mainly in the shape of spherical or flower, then the tiny spherical κ_{IV} phase precipitates out of the α phase, and then the β phase underwent eutectoid transformation: $\beta \rightarrow \alpha + \kappa_{III}$, the κ_{III} phase with spherical or layered structure.

The EBSD analysis results of the bonding area between the substrate and the cladding layer, the inner area of the cladding layer and the top area of the cladding layer, are shown in **Figure 4**, respectively. According to the phase distribution diagrams of different regions (**Figure 4**(A-a)-(C-a)), the structure is mainly α-Cu phase and residual β phase, α-Cu phase and β phase are

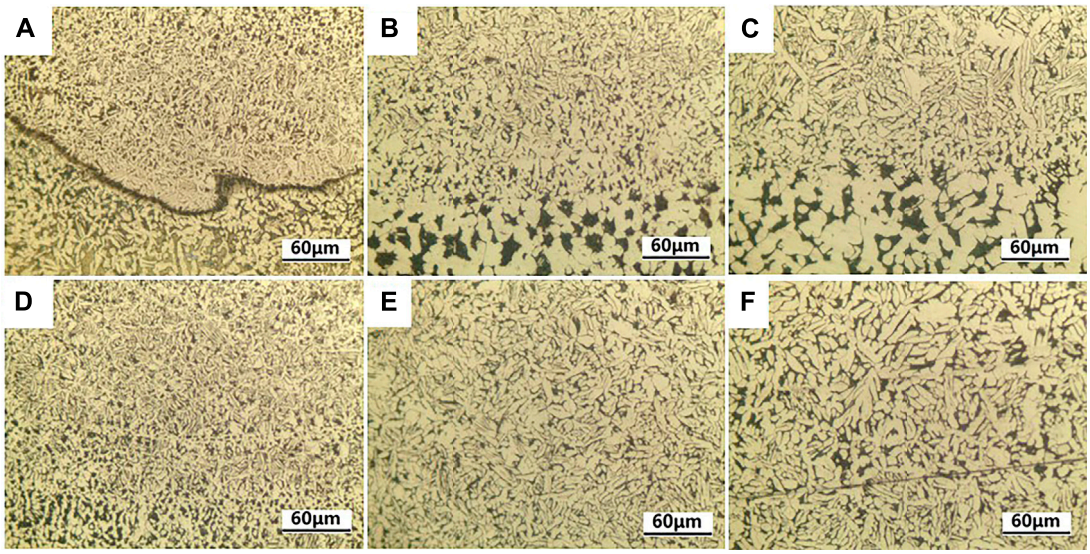

FIGURE 5 | When the interlayer temperature is 100°C, the microstructure of the CMT arc additive Ni-Al bronze straight wall along the height direction shows that **(A,B)** is the area near the matrix of the straight wall, **(C,D)** is the middle area of the wall, and **(E,F)** is the top area of the wall.

labeled in red and blue, respectively. And the proportion of β phase is 6.74% in the bonding zone, 15.1% in the interior and 13.7% at the top, respectively. Due to the influence of substrate and air heat dissipation during the solidification of cladding layer, the cooling rate in the bonding zone and the top zone is higher than that in the interior, the growth tendency of α phase in the interior is weakened, at the same time, the eutectoid transformation time of β-phase is short and the content of β-phase is high in the cladding layer. From the grain boundary orientation diagram (**Figure 4**(A-b)-(C-b)), and the anti-pole diagram of α-Cu texture (**Figure 4**(A-c)-(C-c)), it was obtained are equiaxed or nearly equiaxed in the near the bonding region and the top grains, the region away from the fusion line is columnar crystal and the inner region is mainly dendrite. And it can be seen that in the Cu phase, the grains have a strong alignment in the direction of the <001> crystal, and the texture in the sample decreases and then increases with the distance from the matrix, which means that the grain growth rate on the grain orientation decreases and then increases with the distance from the matrix. **Figures 4**(A-d,e)-(C-d,e) is the histogram of grain orientation difference, and it can be seen that the orientation difference of β phase in the cladding layer is the largest in the inner region, and the internal grains of Cu-phase gradually increase with the distance from the matrix. In summary, with the increasing distance from the matrix, the grain size inside the cladding layer gradually increases, and the content of β phase solid solution increases first and then decreases (Chai et al., 2017; Chen et al., 2019a; Chen et al., 2019b).

Based on the EBSD test results from the single-channel nickel-aluminum-bronze cladding layer, the microstructures of the samples manufactured by CMT arc additive in the direction of height were analyzed. The metallographic after corrosion was shown in **Figure 5**, and the internal structure of the straight wall is similar to that of the single cladding. **Figure 5A** shows the bonding zone between cladding layer and substrate, which, due to a low substrate temperature, have a bigger molten pool internal temperature gradient, to form the branch crystal because of the large undercooling degree. The bonding zone structures of the middle area of the wall shown in **Figure 5B**, it can be seen that on to the next layer of the material, by the arc found on a layer of cladding layer at the top of the remelting pool formation, it was suffering from the melting solidification effect. Above the remelting zone is mainly composed of small dense isometric and it reverses the growth of the heat flow direction's short columnar grain structure, leading away from the area, while the smaller branches of crystal formation are found in the forefront of the columnar crystal. Combine with the internal area structure of cladding layer of the central straight wall along the height direction (**Figures 5D–F**), it was found that the internal regional organizations of the straight wall appear in turn as dendrites, fine isometric, tiny columnar crystal, bulky columnar crystal and crystal growth direction and disorderly branch organization. Furthermore, when compared to the bottom of the organization, it can be seen that the size slightly increases. Combine with **Figure 2**, it can be conclusion that, the microstructure of the straight wall shows periodic. The formation of straight wall is the result of layer by layer accumulation. The temperature gradient and overcooling degree of each cladding are consistent with the single cladding fusion cladding, and due to the same temperature control in the accumulation process, the internal temperature gradient of each cladding changes the same. However, due to the influence of the heat dissipation mode, the heat dissipation speed slows down with the additive height increases, and the growth time increases, and the average grain size of each cladding gradually increases away from the substrate.

As shown in **Figure 6**, an observation of the different interlayer temperature microstructure cladding layers within

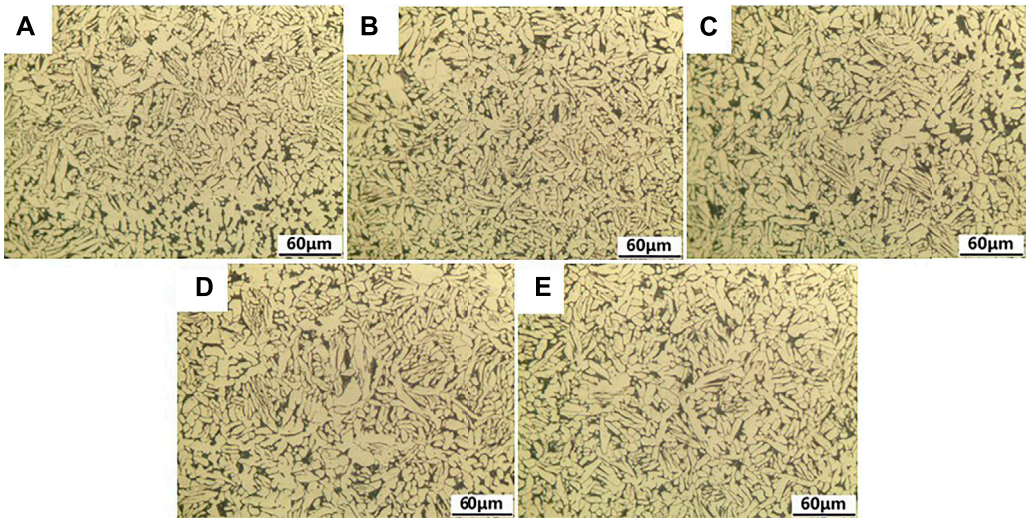

FIGURE 6 | The microstructure morphology of CMT arc additive nickel-aluminum-bronze along the height direction at different interlayer temperatures, **(A)** 100°C, **(B)** 150°C, **(C)** 200°C, **(D)** 250°C, **(E)** 300°C.

the same height, when the interlayer temperature was 300°C, the specimen's microstructure size was bigger than that at 100°C. With the increase of interlayer temperature, the preheating effect of the previous cladding layer is increased, and the growth time of microstructure is increased, which makes the microstructure size gradually increase with the increase of interlayer temperature.

The process of solidification and the cooling rate for the grain shape and size of the nickel-aluminum-bronze cladding layer presents the characteristics of directional solidification, and the grain growth direction and heat flow are in the opposite direction, mainly influenced by the temperature gradient. Adding the material in the manufacturing process is influenced by the arc's heat effect, and the fast wire ends and substrate molten pool formation will be achieved. Due to the low substrate temperature of the brass alloy and itself having good heat conduction effect, the interface formed within the molten pool is greater than the cold, and the setting rate is low. At this time, the substrate junctions in the cladding layer are mainly composed of a thin layer of cell crystal. As the solidification process continues, the temperature of the matrix and the planar crystal region continuously increases, while the temperature gradient of the solid-liquid interface decreases. At this time, the solidification rate is faster and the columnar crystals grow in the opposite direction to the heat flow in the solidification and crystallization process. As the solidification process further continues, the components in the liquid metal become more undercooled, fine secondary dendrites are laterally formed at the front of the columnar grain, and the growth direction of the dendrite runs in the direction of the reverse heat flow. The inner cladding layer and the upper region growing direction that works for directional performance results from the copper alloy thermal conductivity, excellent bonding pads on the bottom of the cladding layer and solidification. Temperature gradient is reduced to a small scope, the heat flow no longer runs perpendicular to the substrate surface, and there is a fast solidification, thus the internal cladding layer and the upper area direction dendrite tissue show growth disorders, which are mainly in the branch crystal and the equiaxial crystal. This is different from $Fe_{49.5}Mn_{30}Co_{10}Cr_{10}C_{0.5}$ multicomponent alloy (Chew et al., 2021) and Al-Co-Cr-Fe-Ni high entropy alloy (Shen et al., 2021), as the room temperature for the microstructure of Ni-Al bronze manufactured by CMT arc additive contains a large amount of dendritic microstructure. The increase of the interlayer temperature reduces the temperature gradient during the solidification process of the molten metal and extends the cooling time. Samples with a high interlayer temperature have a larger grain size.

Hardness Analysis

The obtained hardness changes of the straight wall are shown in **Figure 7**. The internal hardness of single channel cladding layer is shown in **Figure 7A**, it can be seen that the hardness in the bonding zone increases significantly and the internal hardness is stable. It can be seen that the Vickers hardness values of the Ni-Al bronze straight wall are between 155 $HV_{0.5}$ and 185 $HV_{0.5}$ from **Figure 7B**, which are all higher than the average Vickers hardness values of the matrix of 123.7 $HV_{0.5}$. The hardness of the cladding layer at the bottom of the straight wall is high, and Vickers hardness fluctuates and decreases with the increase of the distance from the bottom. The reason for this phenomenon is that when the next layer of additive manufacturing is carried out, the upper layer of the cladding layer will undergo a remelting solidification, and at this time, the temperature gradient is large and the solidification rate is fast, so metallurgical bonding occurs at the bonding interface and leads to the formation of compact and fine structures, which means that the hardness of the interlayer bonding is high, as hardness increases in this region. At the bottom of the straight wall, due to the strong heat conduction of the substrate and the large temperature gradient, the cooling speed of the first few cladding layers is

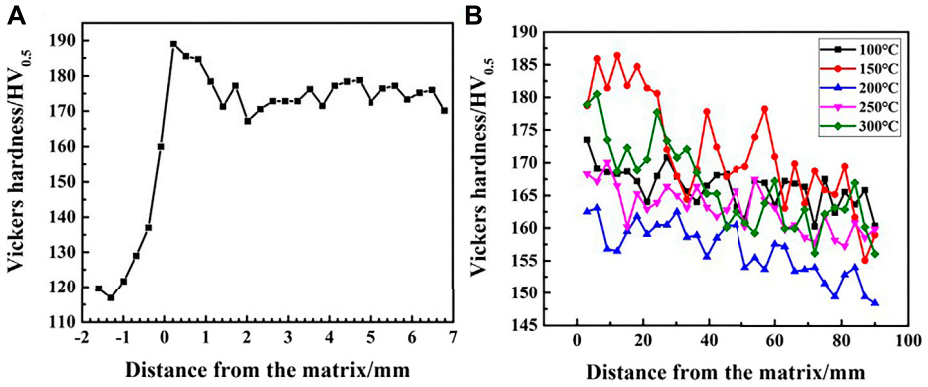

FIGURE 7 | The Vickers hardness of the nickel-aluminum-bronze cladding, **(A)** the single-channel Ni-Al bronze cladding layer **(B)** the multilayer single-channel forming.

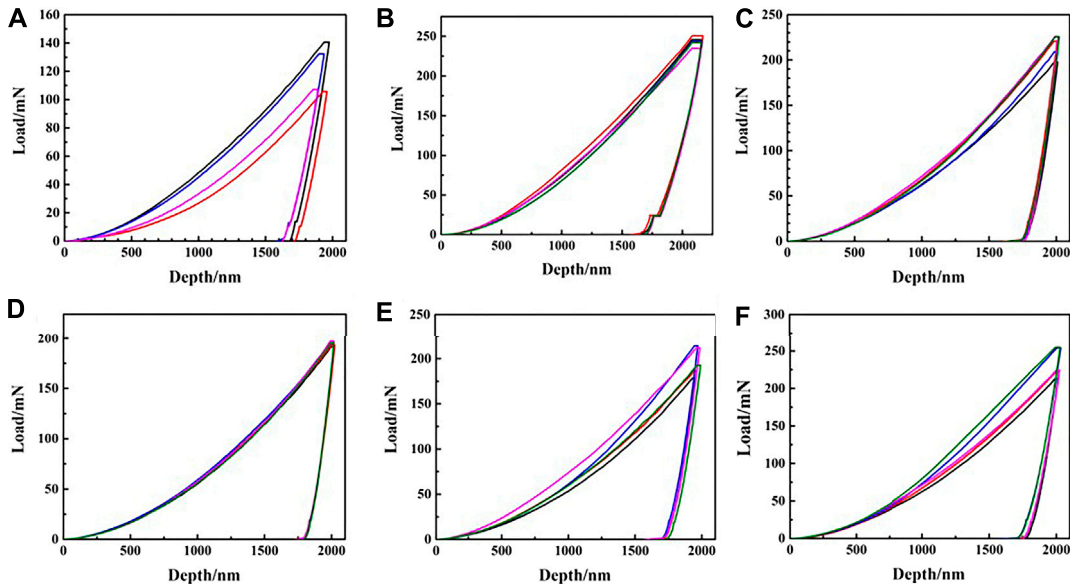

FIGURE 8 | The internal of the CMT arc additive nickel-aluminum-bronze depth-load curve at different interlayer temperatures, where **(A)** the substrate, **(B)** 100°C, **(C)** 150°C, **(D)** 200°C, **(E)** 250°C, **(F)** 300°C.

extremely fast, so the obtained microstructure is fine, uniform and dense, and the obtained hardness is higher. With the increase of the number of additive layers, the solidification heat dissipation of cladding layer is mainly transmitted by air heat dissipation and the previous cladding layer, which is weakened by the heat conduction of matrix and reduces the cooling rate. After solidification, the internal structure of cladding layer is coarsened and the Vickers hardness is reduced.

The depth-load curve of the sample in the central area of the straight wall is shown in **Figure 8**, and the obtained elastic modulus and hardness data are shown in **Figure 9**. As can be seen from **Figure 8**, under the condition of the same depth of pressure, the maximum load obtained by the Ni-Al bronze straight wall is about 200 mN, which is significantly higher than the that of brass matrix of 140 mN. It can be seen from **Figure 9** that the average microhardness of Ni-Al bronze straight wall is 2.40 GPa and that of the brass matrix is 1.53 GPa at different interlayer temperatures, indicating that the Ni-Al bronze straight wall is harder than brass matrix, and the microhardness of the Ni-Al bronze straight wall is 1.57 times higher than that of the brass matrix. The Ni-Al bronze straight wall's average elastic modulus is 122.79 GPa, while that of the brass matrix is 61.83 GPa. The elastic modulus of the Ni-Al bronze straight wall is 1.99 times higher than that of the brass matrix. The microhardness and elastic modulus of the Ni-Al bronze straight wall have no obvious rule to follow at different interlayer temperatures, and the process parameters of the surface interlayer temperature have no obvious effect on it.

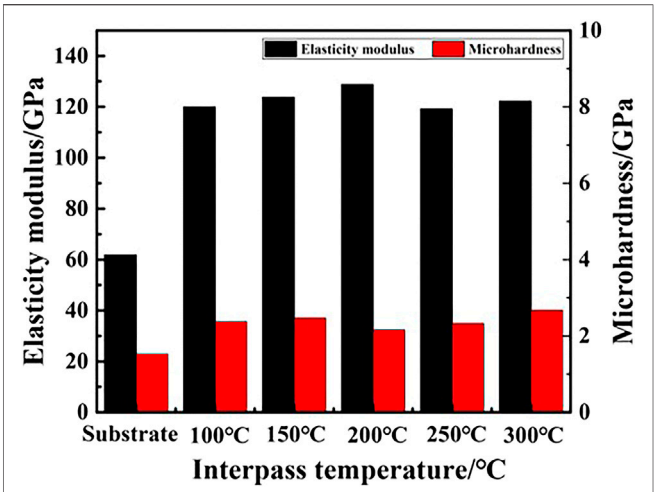

FIGURE 9 | Hardness and elastic modulus of brass substrate and CMT additive nickel-aluminum-bronze straight wall.

Tensile Behavior

As shown in **Figure 10**, the straight wall tensile samples for a straight wall inside different direction tensile samples of the stress-strain curve show no obvious yielding point to generate 0.2% of the residual deformation stress value as its yield strength $Rp_{0.2}$. Along with the loading process and with the load increasing more than the material yield strength's $Rp_{0.2}$, a deformation of the tensile specimen elastic occurred first, and then the specimen tensile process reached the plastic deformation stage, until the end of the straight wall tensile specimen fractured due to the plastic deformation, and the straight wall came under different interlayer temperature parameters, as opposed to the three directions of yield strength, tensile strength and elongation, as shown in **Table 2**. Combined with **Figure 10**, it can be seen that the welding direction and 45° downward-sloping direction for the specimen's tensile strength value, which were all at about 570 MPa, accumulated a significantly higher direction than the sample and the tensile strength of 550 MPa. Among them, the average elongation on the stacking direction, welding direction and 45° downward-sloping direction was 41.14, 54.00, and 41.04%, respectively, showing that the direction of welding in the specimen elongation value is the highest, but that the upward tensile specimen elongation is much higher than the known brass C35300 matrix 440 MPa tensile strength and its elongation of 25%. The tensile strength and elongation of the brass matrix were optimized by CMT arc additive Ni-Al bronze straight wall. By observing the longitudinal profile of the fracture running at the stacking, welding and 45° downward-sloping of the tensile samples at an interlaminar temperature of 100°C, as shown in **Figures 11A–C**, and the tensile samples' fracture location in the direction of accumulation is the internal interlaminar junction of the straight wall, while the fracture in the 45° downward-sloping direction is also inclined to the direction of the interlaminar junction.

Taking an interlayer temperature of 100°C as an example, the tensile fracture SEM morphology of the Ni-Al bronze straight wall in the stacking direction, welding direction, and 45° downward-sloping is shown in **Figures 11D,E**. From the diagram, it can be observed that the section is composed of tearing edges and oval dimples. And the dimples in the tensile specimen in the stacking direction are dense and the size is small,

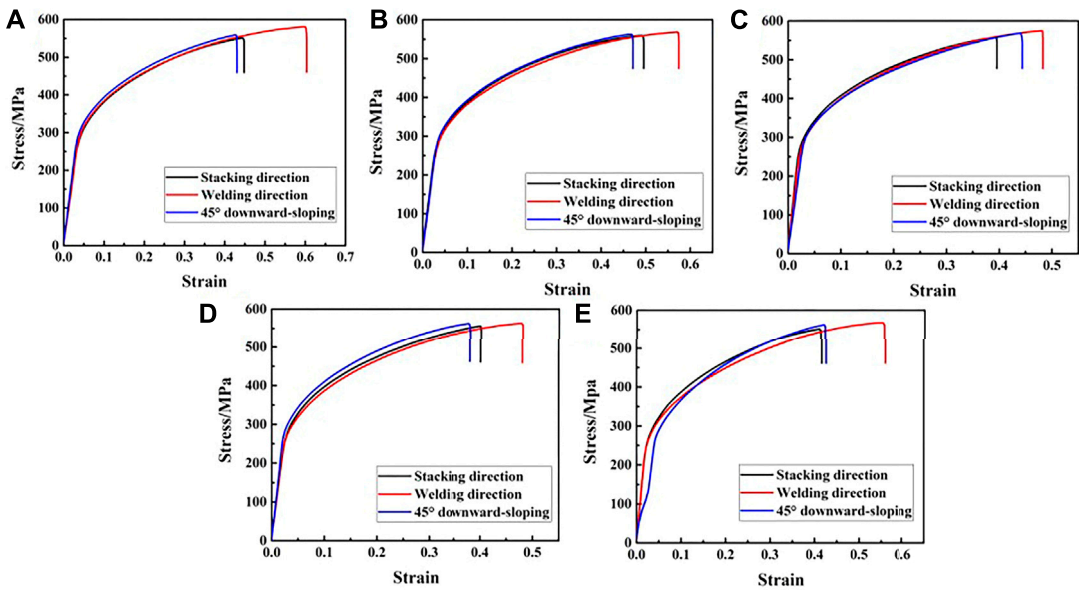

FIGURE 10 | Tensile curves of a nickel-aluminum-bronze straight wall in different directions, where the interlayer temperature **(A)** 100°C, **(B)** 150°C, **(C)** 200°C, **(D)** 250°C, **(E)** 300°C.

TABLE 2 | Tensile properties of CMT arc additive nickel-aluminum-bronze multilayer single-channel forming at different interlayer temperatures.

Interlayer temperature/°C	Stacking direction			Welding direction			45° downward-sloping		
	Yield strength/MPa	Tensile strength/MPa	Elongation/%	Yield strength/MPa	Tensile strength/MPa	Elongation/%	Yield strength/MPa	Tensile strength/MPa	Elongation/%
100	347.3	560.3	44.83	365.1	582.8	60.37	377.4	570.4	42.85
150	345.6	560.9	49.52	361.6	567.7	57.38	365.5	564.1	47.11
200	343.3	558.2	39.56	357.7	574.6	48.22	344.6	567.6	44.54
250	342.25	554.2	40.15	360.2	562.4	48.07	343.7	560.9	38.12
300	345.3	550.2	41.64	360.3	567.7	55.93	362.9	560.5	42.57

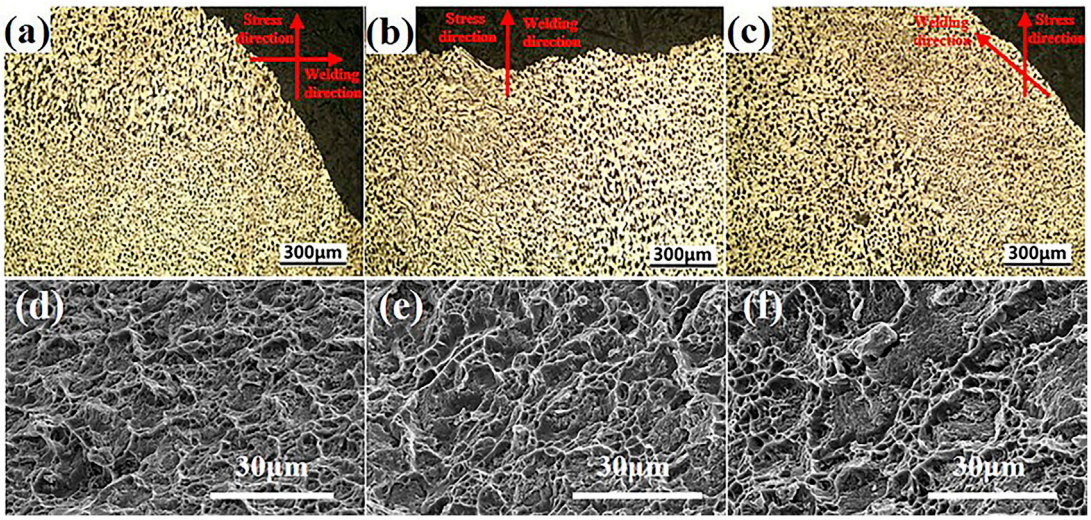

FIGURE 11 | Longitudinal section of the macroscopic fracture of the tensile specimen in the stacking direction of the nickel-aluminum-bronze straight wall with an interlayer temperature of 100°C, where **(A)** stacking direction, **(B)** welding direction, **(C)** 45° downward-sloping , and SEM morphology of tensile fractures in three directions of a nickel-aluminum-bronze straight wall with an interlayer temperature of 100°C, where **(D)** parallel to the stacking direction, **(E)** parallel to the welding direction, **(F)** 45° downward-sloping.

while the dimples in the welding direction are deeper and the size is larger, and their toughness is better than that in the stacking direction. By comparing the tensile samples along the welding direction's fracture morphology at different interlaminar temperatures in **Figure 12**, it can be found that with the increase of interlaminar temperatures, the size of the dimples inside the tensile fracture of the Ni-Al bronze straight wall slightly decreases, tensile properties deteriorate accordingly.

The formation process of the straight wall is composed of a layer-by-layer accumulation process, and the strength of the bonding zone between layers is low, being in fact lower than the overall tensile strength of the remelted solidified alloy. In other words, the tensile strength of the samples in the direction of accumulation is weakened by the influence of the interlayer bonding strength. C. Wang et al. (2020) studied the performance of the 316 L wall and found that it has a multi-layer structure. They studied the strength of the remelting and overlapping zones, and found that the yield strength and tensile strength of overlapping zone were low, while the strength of the stacking direction was the lowest. Pranav et al. (Nikam et al., 2020) found that the mechanical properties along the welding direction were better, which also proved this point of view. The internal structure of the straight wall is slightly increased by the increase of interlaminar temperature, but the size increase is very small, and the strength of the bonding zone is slightly reduced by the increase of interlaminar temperature. As a result, the tensile strength of the Ni-Al Bronze straight wall has a tendency of decrease with the increase of interlaminar temperature.

Corrosion Analysis

The obtained Tafel curve is shown in **Figure 13**, and the fitting results of the polarization curve are shown later. The self-corrosion potential of the wall is −0.32, −0.33, −0.31, −0.32, and −0.35 V at different interlayer temperatures (100, 150, 200, 250, 300°C), the current density of the self-corrosion current is 1.04×10^{-5}, 1.41×10^{-5}, 1.31×10^{-5}, 1.20×10^{-5}, 1.10×10^{-5} A/cm^2, the self-corrosion potential of the brass substrate is −0.55 V, the self-corrosion current density of the brass substrate is 5.37 × 10–5 A/cm^2. The self-corrosion potential of the Ni-Al bronze wall is increased by 0.20–0.24 V compared

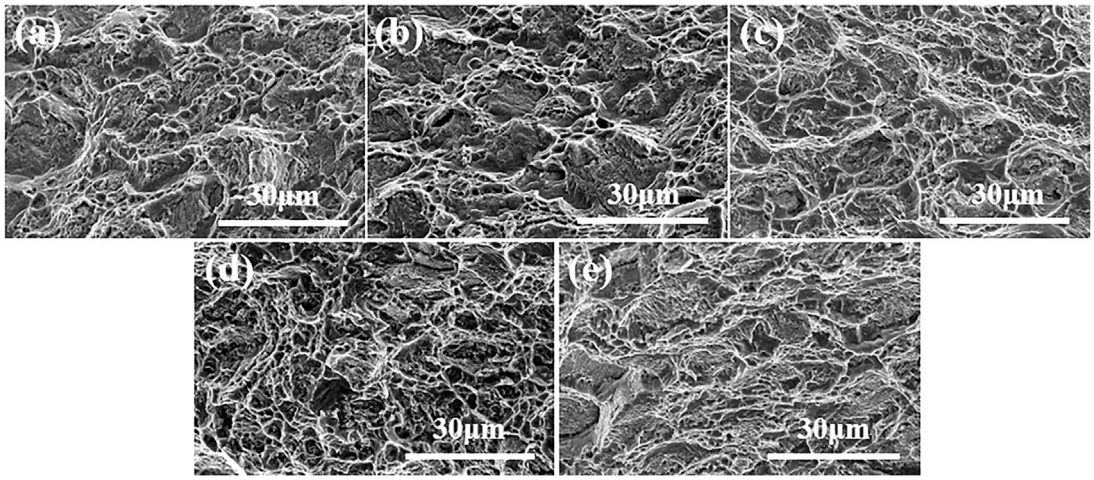

FIGURE 12 | The SEM morphology of the tensile fracture of the nickel-aluminum-bronze straight wall along the welding direction at different interlayer temperatures, where **(A)** 100°C, **(B)** 150°C, **(C)** 200°C, **(D)** 250°C, **(E)** 300°C.

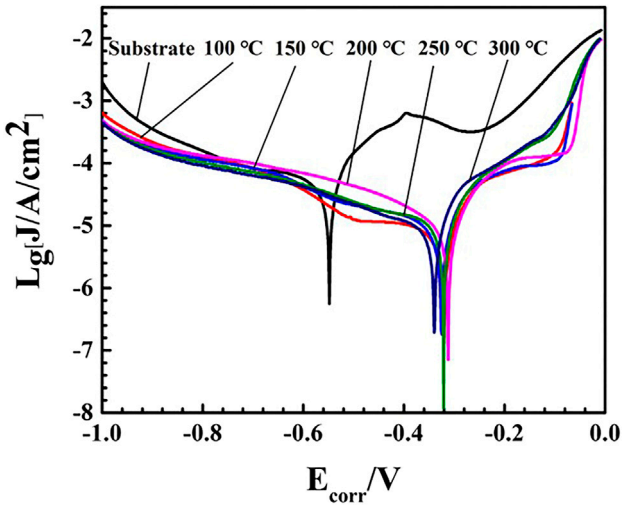

FIGURE 13 | The Tafel curve of a nickel-aluminum-bronze straight wall with a brass substrate and different interlayer temperatures.

with that of the brass matrix, and the self-corrosion current density of the Ni-Al bronze wall is decreased by 4×10^{-5} A/cm^2 compared with that of the brass matrix. It can be seen that the corrosion resistance of the nickel-aluminum-bronze straight wall is better than that of the brass matrix. By comparing the Tafel curves of the nickel-aluminum-bronze wall with the corrosion potential and the corrosion current density, it is found that there is no obvious increase or decrease rule, and the surface interlayer temperature has no obvious effect on the corrosion resistance of the straight wall material. As shown in **Figure 13**, the polarization curves of Ni-Al bronze samples and brass matrix samples are divided into anode and cathode regions. The cathode region is mainly characterized by a hydrogen evolution reaction, while the anode region is mainly characterized by three stages of the Ni-Al bronze corrosion process. First of all, copper in Ni-Al bronze alloy loses electrons to form Cu^+ by anodic action and Cl^- in electrolyte reaction to form CuCl and $CuCl_2^-$, which is shown by the increase in corrosion current density. Following this, due to the instability of CuCl, the dense Cu_2O oxide film is formed by hydrolysis reaction $2CuCl + H_2O \rightarrow 2Cu_2O + 2HCl$. Finally, with the increase of polarization potential, a new electrode reaction is initiated, which results in a rapid increase of corrosion current density.

A more positive the self-corrosion potential leads to a more difficult anodic polarization. The current density of self-corrosion reflects the speed of the corrosion reaction of the material. A smaller current density of self-corrosion results in a slower material's corrosion reaction. Without too many defects in the material, the corrosion resistance of the material is only related to the property of the material itself. The self-corrosion potential of the nickel-aluminum-bronze alloy is greater positive than the matrix, and the corrosion current density is thus smaller, meaning that the corrosion resistance is better than that of the brass matrix.

CONCLUSION

In this study, the microstructure and mechanical properties of an as-built SG-CuAl8Ni6 part manufactured by CMT wire and arc additive manufacturing were discussed in detail. The conclusions can be summarized as follows:

1) The Ni-Al bronze cladding layer of Sg-CuAl8Ni6 is mainly composed of α-Cu, residual β phase, Pb and κ phases. The microstructure of the single-channel Ni-Al bronze cladding has obvious gradient structure, which is successively presented as peritectic, columnar crystals growing in the direction of heat flow, dendritic crystals growing in the direction of

disorderly growth, and equiaxed grains. With the increase of the distance between the cladding layer and the matrix, the grain size inside the cladding layer increases gradually, and the content of β phase solid solution increases first and then decreases. In its structure, the microstructure of the monolayer of the multilayer and multi-pass Ni-Al bronze straight wall is similar to that of the monolayer single channel.

2) The Vickers hardness values of the Ni-Al bronze straight wall are between 155 and 185 $HV_{0.5}$, and the hardness of the wall overall trend of fluctuation decreases with the distance of substrate, and the hardness of single cladding in the bonding zone increases significantly and the internal hardness is stable. The obtained straight wall in the central area of the nano indentation test results show that the nickel-aluminum-bronze straight wall can achieve a maximum load that is controlled in 200 mN, which is higher than the brass substrate (140 mN). At the same time, the nickel-aluminum-bronze sample microhardness is 2.40 Gpa, and its modulus of elasticity is 122.79 Gpa. Its microhardness was 1.57 times of the brass substrates (1.53 Gpa), and the brass modulus of elasticity (61.83 Gpa) of 1.99 times, which is again better than that of the matrix.
3) The fracture of the straight wall tensile specimen is a ductile fracture, and its fracture morphology is mainly composed of tearing edge and oval dimples. The location of the fracture on the stacking direction is mainly concentrated in the combination area, and the tensile strength in the combination area is weak. The tensile strength of the straight wall in the welding direction and 45° downward-sloping direction is about 570 MPa, which is much higher than the that of about 550 MPa in stacking direction. The elongation in stacking direction, welding direction and 45° downward-sloping direction is 41.14%, 54.00, and 41.04% respectively, with the elongation in welding direction the highest.
4) The self-corrosion potential of the Ni-Al bronze wall is increased by 0.20–0.24 V compared with that of the brass matrix, and the self-corrosion current density of the Ni-Al bronze wall is decreased by $4 \times 10–5$ /cm^2 compared with that of the brass matrix. and the corrosion resistance of the wall is better than that of the substrate.
5) The hardness, tensile and corrosion resistance of the straight wall obtained are better than that of the matrix, but with the increase in interlayer temperature, the grain size increased gradually, and the tensile strength decreases slightly.

DATA AVAILABILITY STATEMENT

The original contributions presented in the study are included in the article/Supplementary Material, further inquiries can be directed to the corresponding authors.

AUTHOR CONTRIBUTIONS

RW: Conceptualization, Data curation, Formal analysis, Investigation, Validation, Writing-original draft. YZ: Conceptualization, Formal analysis, Supervision, Methodology. QC: Investigation, Methodology. FY: Conceptualization, Formal analysis, Supervision, Funding acquisition, Methodology, Resources. XW: Conceptualization, Supervision, Funding acquisition, Project administration, Resources. WW: Investigation, Methodology. ZR: Conceptualization, Supervision. GH: Data curation, Methodology.

FUNDING

This publication was supported by the National Key R&D Program of China (2018YFB1105800).

REFERENCES

Attar, H., Ehtemam-Haghighi, S., Soro, N., Kent, D., and Dargusch, M. S. (2020). Additive Manufacturing of Low-Cost Porous Titanium-Based Composites for Biomedical Applications: Advantages, Challenges and Opinion for Future Development. *J. Alloys Compd.* 827, 154263. doi:10.1016/j.jallcom.2020.154263

Aziz, N. A., Adnan, N. A. A., Wahab, D. A., and Azman, A. H. (2021). Component Design Optimisation Based on Artificial Intelligence in Support of Additive Manufacturing Repair and Restoration: Current Status and Future Outlook for Remanufacturing. *J. Clean. Prod.* 296, 126401. doi:10.1016/j.jclepro.2021.126401

Cadiou, S., Courtois, M., Carin, M., Berckmans, W., and Le masson, P. (2020). 3D Heat Transfer, Fluid Flow and Electromagnetic Model for Cold Metal Transfer Wire Arc Additive Manufacturing (CMT-WAAM). *Additive Manufacturing* 36, 101541. doi:10.1016/j.addma.2020.101541

Chai, L., Wang, S., Wu, H., Guo, N., Pan, H., Chen, L., et al. (2017). α→β Transformation Characteristics Revealed by Pulsed Laser-Induced Non-equilibrium Microstructures in Duplex-phase Zr alloy. *Sci. China Technol. Sci.* 60, 1255–1262. doi:10.1007/s11431-016-9038-y

Chen, K., Zeng, L., Li, Z., Chai, L., Wang, Y., Chen, L.-Y., et al. (2019). Effects of Laser Surface Alloying with Cr on Microstructure and Hardness of Commercial Purity Zr. *J. Alloys Compd.* 784, 1106–1112. doi:10.1016/j.jallcom.2019.01.097

Chen, L.-Y., Xu, T., Wang, H., Sang, P., Lu, S., Wang, Z.-X., et al. (2019). Phase Interaction Induced Texture in a Plasma Sprayed-Remelted NiCrBSi Coating during Solidification: An Electron Backscatter Diffraction Study. *Surf. Coat. Technol.* 358, 467–480. doi:10.1016/j.surfcoat.2018.11.019

Chen, L.-Y., Zhang, H.-Y., Zheng, C., Yang, H.-Y., Qin, P., Zhao, C., et al. (2021). Corrosion Behavior and Characteristics of Passive Films of Laser Powder Bed Fusion Produced Ti-6Al-4V in Dynamic Hank's Solution. *Mater. Des.* 208, 109907. doi:10.1016/j.matdes.2021.109907

Chew, Y., Zhu, Z. G., Weng, F., Gao, S. B., Ng, F. L., Lee, B. Y., et al. (2021). Microstructure and Mechanical Behavior of Laser Aided Additive Manufactured Low Carbon Interstitial Fe49.5Mn30Co10Cr10C0.5 Multicomponent alloy. *J. Mater. Sci. Technol.* 77, 38–46. doi:10.1016/j.jmst.2020.11.026

Derekar, K. S., Addison, A., Joshi, S. S., Zhang, X., Lawrence, J., Xu, L., et al. (2020). Effect of Pulsed Metal Inert Gas (Pulsed-MIG) and Cold Metal Transfer (CMT) Techniques on Hydrogen Dissolution in Wire Arc Additive Manufacturing (WAAM) of Aluminium. *Int. J. Adv. Manuf Technol.* 107, 311–331. doi:10.1007/s00170-020-04946-2

Dong, B. W., Jie, J. C., Yao, X. X., Liu, S. C., Chen, Y. H., Zhong, N., et al. (2019). Effect of Sn Addition on Morphology Evolution of Secondary Phase in Hypomonotectic Cu-Pb-Sn alloy during Solidification. *J. Alloys Compd.* 791, 936–946. doi:10.1016/j.jallcom.2019.03.388

Kim, J., Kim, J., and Pyo, C. (2020). Comparison of Mechanical Properties of Ni-Al-Bronze Alloy Fabricated through Wire Arc Additive Manufacturing with

Ni-Al-Bronze Alloy Fabricated through Casting. *Metals* 10 (9), 1164. doi:10.3390/met10091164

Lamichhane, T. N., Sethuraman, L., Dalagan, A., Wang, H., Keller, J., and Paranthaman, M. P. (2020). Additive Manufacturing of Soft Magnets for Electrical Machines-A Review. *Mater. Today Phys.* 15, 100255. doi:10.1016/j.mtphys.2020.100255

Laptev, R., Pushilina, N., Kashkarov, E., Syrtanov, M., Stepanova, E., Koptyug, A., et al. (2019). Influence of Beam Current on Microstructure of Electron Beam Melted Ti-6Al-4V alloy. *Prog. Nat. Sci. Mater. Int.* 29, 440–446. doi:10.1016/j.pnsc.2019.04.011

Martin, J. H., Yahata, B., Mayer, J., Mone, R., Stonkevitch, E., Miller, J., et al. (2020). Grain Refinement Mechanisms in Additively Manufactured Nano-Functionalized Aluminum. *Acta Materialia* 200, 1022–1037. doi:10.1016/j.actamat.2020.09.043

Mosallanejad, M. H., Niroumand, B., Aversa, A., and Saboori, A. (2021). *In-situ* Alloying in Laser-Based Additive Manufacturing Processes: A Critical Review. *J. Alloys Compd.* 872, 159567. doi:10.1016/j.jallcom.2021.159567

Mutunga, E., Winkler, R., Sattelkow, J., Rack, P. D., Plank, H., and Fowlkes, J. D. (2019). Impact of Electron-Beam Heating during 3D Nanoprinting. *ACS nano* 13, 5198–5213. doi:10.1021/acsnano.8b09341

Nikam, P. P., Arun, D., Ramkumar, K. D., and Sivashanmugam, N. (2020). Microstructure Characterization and Tensile Properties of CMT-Based Wire Plus Arc Additive Manufactured ER2594. *Mater. Characterization* 169, 110671. doi:10.1016/j.matchar.2020.110671

Ostovari Moghaddam, A., Shaburova, N. A., Samodurova, M. N., Abdollahzadeh, A., and Trofimov, E. A. (2021). Additive Manufacturing of High Entropy Alloys: A Practical Review. *J. Mater. Sci. Technol.* 77, 131–162. doi:10.1016/j.jmst.2020.11.029

Sanaei, N., and Fatemi, A. (2021). Defects in Additive Manufactured Metals and Their Effect on Fatigue Performance: A State-Of-The-Art Review. *Prog. Mater. Sci.* 117, 100724. doi:10.1016/j.pmatsci.2020.100724

Shen, Q., Kong, X., and Chen, X. (2021). Fabrication of Bulk Al-Co-Cr-Fe-Ni High-Entropy alloy Using Combined cable Wire Arc Additive Manufacturing (CCW-AAM): Microstructure and Mechanical Properties. *J. Mater. Sci. Technol.* 74, 136–142. doi:10.1016/j.jmst.2020.10.037

Singh, S., Singh, P., Singh, H., and Kumar Buddu, R. (2019). Characterization and Comparison of Copper Coatings Developed by Low Pressure Cold Spraying and Laser Cladding Techniques. *Mater. Today Proc.* 18, 830–840. doi:10.1016/j.matpr.2019.06.509

Tang, Y. T., Panwisawas, C., Ghoussoub, J. N., Gong, Y., Clark, J. W. G., Németh, A. A. N., et al. (2021). Alloys-by-design: Application to New Superalloys for Additive Manufacturing. *Acta Materialia* 202, 417–436. doi:10.1016/j.actamat.2020.09.023

Tanvir, A. N. M., Ahsan, M. R. U., Seo, G., Bates, B., Lee, C., Liaw, P. K., et al. (2021). Phase Stability and Mechanical Properties of Wire + Arc Additively Manufactured H13 Tool Steel at Elevated Temperatures. *J. Mater. Sci. Technol.* 67, 80–94. doi:10.1016/j.jmst.2020.04.085

Thompson, S. M., Bian, L., Shamsaei, N., and Yadollahi, A. (2015). An Overview of Direct Laser Deposition for Additive Manufacturing; Part I: Transport Phenomena, Modeling and Diagnostics. *Additive Manufacturing* 8, 36–62. doi:10.1016/j.addma.2015.07.001

Tofail, S. A. M., Koumoulos, E. P., Bandyopadhyay, A., Bose, S., O'Donoghue, L., and Charitidis, C. (2018). Additive Manufacturing: Scientific and Technological Challenges, Market Uptake and Opportunities. *Mater. Today* 21, 22–37. doi:10.1016/j.mattod.2017.07.001

Wang, C., Liu, T. G., Zhu, P., Lu, Y. H., and Shoji, T. (2020). Study on Microstructure and Tensile Properties of 316L Stainless Steel Fabricated by CMT Wire and Arc Additive Manufacturing. *Mater. Sci. Eng. A* 796 (7), 140006. doi:10.1016/j.msea.2020.140006

Wang, J., East, D., Morozov, E. V., Seeber, A., and Juan, P. E-D. (2021). Microstructure and Hardness Variation of Additively Manufactured Ti-Ni-C Functionally Graded Composites. *J. Alloys Compd.* 865, 158976. doi:10.1016/j.jallcom.2021.158976

Wang, J., Zhou, X. L., Li, J., Brochu, M., and Zhao, Y. F. (2020). Microstructures and Properties of SLM-Manufactured Cu-15Ni-8Sn alloy. *Additive Manufacturing* 31, 100921. doi:10.1016/j.addma.2019.100921

Wang, S., Shen, W., Guo, J., Yuan, T., Qiu, Y., and Tao, Q. (2020). Engineering Prediction of Fatigue Strength for Copper alloy Netting Structure by Experimental Method. *Aquacultural Eng.* 90, 102087. doi:10.1016/j.aquaeng.2020.102087

Wang, X., Xu, S., Zhou, S., Xu, W., Leary, M., Choong, P., et al. (2016). (Topological Design and Additive Manufacturing of Porous Metals for Bone Scaffolds and Orthopaedic Implants: A Review. *Biomaterials* 83, 127–141. doi:10.1016/j.biomaterials.2016.01.012

Wu, W., Xue, J., Zhang, Z., Ren, X., and Xie, B. (2019). Process Optimization on Multilayer Morphology during 316L Double-Wire CMT+P Deposition Process. *Metals* 9 (12), 1334. doi:10.3390/met9121334

Xie, B., Xue, J., and Ren, X. (2020). Wire Arc Deposition Additive Manufacturing and Experimental Study of 316L Stainless Steel by CMT + P Process. *Metals* 10 (11), 1419. doi:10.3390/met10111419

Zhang, L. C., and Chen, L. Y. (2019). A Review on Biomedical Titanium Alloys: Recent Progress and Prospect. *Adv. Eng. Mater.* 21, 1801215. doi:10.1002/adem.201801215

Conflict of Interest: The authors declare that the research was conducted in the absence of any commercial or financial relationships that could be construed as a potential conflict of interest.

Publisher's Note: All claims expressed in this article are solely those of the authors and do not necessarily represent those of their affiliated organizations, or those of the publisher, the editors and the reviewers. Any product that may be evaluated in this article, or claim that may be made by its manufacturer, is not guaranteed or endorsed by the publisher.

frontiers in Materials

ORIGINAL RESEARCH
published: 09 September 2021
doi: 10.3389/fmats.2021.731449

Dynamic Triaxial Test and Microscopic Study of Solidified Muddy Soil With Different Mixing Ratios and Curing Ages

Zhou Chen[1], Haocheng Xu[1], Mayao Cheng[1]*, Hanwen Lu[1], Zhijian Wang[2] and Peiyu Feng[3]*

[1]School of Transportation and Civil Engineering & Architecture, Foshan University, Foshan, China, [2]China Railway Guangzhou Group Co., Ltd., Guangzhou, China, [3]China Railway Siyuan Survey and Design Group Co, Ltd., Wuhan, China

Aiming to explore the optimal mixture ratio and curing age of solidified muddy soil under dynamic load, the paper intends to investigate whether the solidified muddy soil can be used as filling of high-speed railway subgrade. Based on the dynamic triaxial test, the investigation measured the dynamic strain and dynamic elastic modulus of solidified muddy soil under different mix ratios and curing ages, and also observed the microscopic morphology of solidified muddy soil samples by using scanning electron microscope. The results show that the addition of cement and curing agent significantly increases the dynamic strength and elastic modulus of muddy soil, which effectively improve the dynamic characteristics of muddy soil. The curing effect of the curing agent is more obvious with the increase of the dosage of cement and curing agent under different mix ratio. The content of curing agent plays a leading role in the hydration reaction between cement, curing agent and soil particles. Additionally, in case of the same test conditions, when the ratio of cement mass to dry silt mass is 1:20, the ratio of diluent volume to dry silt mass is 1:20, with 28 days of curing age, its curing effect will reach the best.

Keywords: solidified muddy soil, dynamic triaxial test, mixture ratio, curing age, SEM

OPEN ACCESS

Edited by:
Yunchao Tang,
Guangxi University, China

Reviewed by:
Neven Ukrainczyk,
Darmstadt University of Technology, Germany
Jie Wu,
Wuhan Polytechnic University, China
Chang-Fu Hu,
East China Jiaotong University, China

****Correspondence:***
Zhou Chen
gscz19861985@fosu.edu.cn
Mayao Cheng
chengmayao@163.com

Specialty section:
This article was submitted to Structural Materials, a section of the journal Frontiers in Materials

Received: *27 June 2021*
Accepted: *31 July 2021*
Published: *09 September 2021*

Citation:
Chen Z, Xu H, Cheng M, Lu H, Wang Z and Feng P (2021) Dynamic Triaxial Test and Microscopic Study of Solidified Muddy Soil With Different Mixing Ratios and Curing Ages. Front. Mater. 8:731449. doi: 10.3389/fmats.2021.731449

INTRODUCTION

The construction goal of the Guangdong-Hong Kong-Macao Greater Bay Area is bound to promote the great development of railway construction in Guangdong's Pearl River Delta. However, the treatment and utilization of the rich deep muddy soil in Guangdong's Pearl River Delta has always been a difficulty in practical engineering application (Zhou, 2013). At present, the treatment methods of muddy soil include vacuum preloading (Yan et al., 2010), curing method (Radovanovic et al., 2016), electroosmosis (Tang et al., 2017), mixing pile (Yang et al., 2011), etc. Whereas, due to the limitations of its high-water content, high compressibility and low strength, many deficiencies and limitations in the practical engineering application existed in the present methods (Pan et al., 2020). The muddy soil shallow reinforcement technology that has emerged in recent years can better improve the shortcomings of the appeal method. The core construction method is to shallowly strengthen the extremely low-strength muddy soil through foundation treatment (Xu et al., 2019; Dong et al., 2011), and partly use fly ash (Sani et al., 2018; Karthik et al., 2014; Takhelmayum et al., 2013) and soil-fly ash-lime (Consoli et al., 2014) for reinforcement, thereby forming a hard shell layer and improving the bearing capacity of foundation. Judging from the existing research (Shan et al., 2021; Huang et al., 2010; Kuna et al., 2016), the shallow reinforcement technology of muddy soil can

be achieved by natural drying, sand-filled cushion, shallow soil drainage, and chemical reinforcement. The *in-situ* solidification method with solidifying agent can greatly reduce the cost and construction period, help to recycle industrial waste materials, and save the cost of spoiled land acquisition during the construction process and the cost of earthwork transportation, which is a new hot spot in the research of shallow reinforcement of muddy soil. Since the mechanical properties of the solidified muddy soil are affected by various factors such as natural environment and external excitation, the mechanical properties of the solidified muddy soil filler become complicated. Therefore, in order to further grasp the engineering characteristics of the solidified muddy soil and ensure that it can serve the construction and operation of the project, it is necessary to carry out research on the solidification performance of the solidified muddy soil.

The effect of railway trains on the muddy soil is mainly the cyclic dynamic load. Therefore, research on the dynamic performance of the solidified muddy soil under the train load, In order to clarify the change of solidification effect, to ensure the stability of mechanical properties of solidified muddy soil is the primary prerequisite to ensure the safe and stable operation of the train. Whereas, the solidified muddy under the train load, the microscopic properties of soil can greatly determine its macroscopic working properties. Therefore, combined with microscopic experiments to observe the structural properties of solidified muddy soils, it is a concentrated expression of its complex physical and mechanical properties. The available literature shows (Tian et al., 2020) that for solidified soils with different mix ratios and the same age conditions, the dynamic strength and dynamic elastic modulus are very different. In addition, age is also an important factor affecting the curing effect. Scholars at home and abroad have done abundant laboratory experiments on the theory of soil dynamic performance under load. For example, Sun et al. (2020) carried out dynamic triaxial tests on the muddy soil after multiple freeze-thaw cycles under negative temperature load, and found that the lower the temperature, the dynamic stress and dynamic modulus of the muddy soil under the freeze-thaw cycle. The conclusion that the influence of dynamic characteristics is more obvious; Wang et al. (2019) studied and analyzed the deformation and strength of solidified muddy soil under cyclic loading; Arulrajah et al. (2018) carried out experiments on unconfined compressive strength of solidified muddy soil with various moisture content, different amounts of cement curing agents, and different curing ages. Jian et al. (2013) took water glass as an auxiliary material for cement curing agents, and studied the effect of water glass on the improvement of the mechanical properties and impermeability of solidified soil (Amir-Faryar and Aggour, 2016); made research on the deformation process of silt-solidified soil under dynamic load conditions, and concluded that the time interval of load application is a factor affecting the deformation of solidified soil; Li et al. (2014) used indoor geotechnical tests and on-site construction conditions to systematically study the effects of cement, lime, and fly ash as soil solidification agents on soil solidification, and summarized the development law of the influence of the mixing amount and age of various materials on the performance indexes of soil engineering. Liang et al. (2020) took Guizhou red clay as the research object and observed the changes in the microstructure of the red clay with a scanning electron microscope (SEM); Zhang et al. (2021) used SEM to study the diametric splitting tests of compacted bentonite. In recent years, developed countries such as Europe, America and Japan have gradually applied the technology of solidified muddy soil in railway subgrade filling (Liu et al., 2018). However, due to the late start in China, the research on the mechanical properties of solidified soil mostly focuses on static forces. There are inadequate studies on characteristics. Particularly, the application of solidified soil in railway engineering is less extensive.

Therefore, the paper applies shallow silty soil in a coastal area of the Pearl River Delta as raw material soil, inorganic liquid curing agent and 32.5 ordinary Portland cement as additives, and uses SDT-10 microcomputer-controlled electro-hydraulic servo soil dynamic three-axis testing machine to solidify muddy soil. The study also carries out indoor dynamic triaxial tests of different mix ratios, and different ages by combing the SEM test to conduct microscopic observations of the loaded soil samples. Finally, the paper analyzes the dynamic strength and dynamics of the solidified muddy soil. The changing law of elastic modulus can obtain the best mixing ratio and curing age for curing effect, which provides theoretical basis for related engineering practice. We analyze the dynamic strength and dynamic elastic modulus of solidified muddy soil to obtain the best mix ratio and curing age of solidified muddy soil, which provides a theoretical basis for related engineering practice.

Test Plan

Due to the low confining pressure of the superficial subgrade filling, the loading frequency of the subgrade filling under the train load should be less than 1.85 Hz (Tian, 2020). Therefore, the confining pressure and axial pressure of the proposed sample are 100 kPa, the loading frequency is 1 Hz, the cycle number is 1,000 for the solidified muddy soil with changing mix ratio, and the cycle number is 400 for the solidified muddy soil with changing the curing age. Secondly, sine wave waveforms are used to simulate the repeated effects of railway trains on subgrade soil. In order to consider the real stress state of the shallow muddy soil, the test method is adopted in the test process to first carry out isobaric consolidation of the sample with a dynamic triaxial instrument. Afterwards, the study applies axial dynamic force. The specific test control data are shown in **Table 1**.

Test Materials and Test Preparation

The silt used in this experiment was taken from the shallow silt at the bottom of a pond in the Pearl River Delta region. The sampling depth is 0.5–3.0 m; the curing agent is "Xiyang Brand" F type liquid curing agent; the cement is 32.5 ordinary Portland cement. The operation steps of the sample preparation process refer to the specific methods in the *Regulations for Railway Engineering Geotechnical Tests* (TB 10102–2010). At the same time, since the undisturbed silt soil will inevitably be disturbed by the external environment during the sampling and

TABLE 1 | Test control conditions.

Dynamic strain	Confining pressure/kPa	Axial load amplitude/N	Vibration frequency/Hz	Drainage conditions	Vibration loading times/time	Wave
	100	**100**	**1**	**Undrained**	**1,000,00**	**Sine wave**
Dynamic elastic modulus	confining pressure/kPa 100	Axial load amplitude/N 100	Vibration frequency/Hz 1	Drainage conditions Undrained	Load level 10	Wave Sine wave

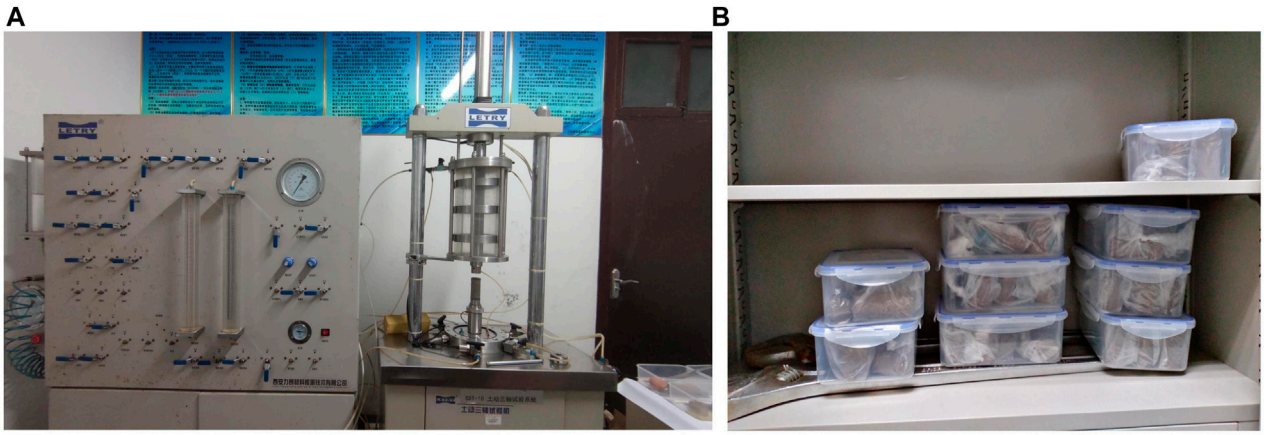

FIGURE 1 | Real scene of the equipment **(A)** SDT-10 microcomputer controlled electro-hydraulic servo soil dynamic triaxial testing machine **(B)** Scanning electron microscope.

transportation process. To eliminate the interference of the soil disturbance on the test results, the undisturbed muddy soil is reshaped before sample preparation. Further, the sample preparation is controlled. The moisture content is 30%, and the size of the prepared standard sample is diameter d = 39.1 mm, height h = 80 mm.

Sample Preparation Method

Firstly, the liquid curing agent and distilled water is diluted to a certain ratio to obtain the curing agent diluent. Further, the muddy soil to a constant weight is stored in a laboratory drying oven at 65°C, the dried muddy soil is pulverized into powder and by a pulverizer, that would pass through a 0.6 mm square hole sieve. Finally, powdery muddy soil is produced with a particle size of less than 0.6 mm. Additionally, the powdery silt is mixed with cement according to the proportion. The hardener diluent which is prepared in advance are added and more importantly mix them well. We prepare a number of solidified muddy soil standard samples with the sample preparation device, and put them in a plastic bag to wrap and seal the samples to cure to 7 days, 28 days and 90 days.

Test Equipment

Dynamic triaxial test equipment the SDT-10 microcomputer control electro-hydraulic servo soil dynamic triaxial testing machine which composed by seven parts, including axial pressure measurement and control system, confining pressure measurement and control system, pressure chamber, pressure chamber lifting mechanism, hydraulic oil source, electrical control system, computer display and control and data processing system, show in **Figure 1A**; Test Seal is saved as shown in **Figure 1B**.

TABLE 2 | Test mix ratio of solidified muddy soil.

Number	Cement mass g: dry sludge mass g	Diluent volume ml: dry sludge mass g
1	1:20	1:20
2	1:20	1:30
3	1:20	1:40
4	1:25	1:20
5	1:30	1:20

Tests on Dynamic Characteristics of Solidified Muddy Soil Under Different Mix Ratios

According to the above preparation being made, we equipped with standard test pieces of variable curing agent and cement content. In the experiment, a total of five sets of samples with different mix ratios were designed, with three parallel samples in each group. The specific mix ratios are shown in **Table 2**. The first group of curing age, they are 7, 28 days and 90 days respectively. Further, the maintenance age of the remaining groups was 28 days. According to < Standard for geotechnical testing

TABLE 3 | Cumulative strain change curve of different curing agent content under dynamic load.

Curing agent content	Cycles	1st test (mm)	2nd test (mm)	3rd test (mm)	Mean value (mm)	Standard deviation (%)
1:20	100	0.0175	0.0175	0.0184	0.0178	0.0424
	200	0.0182	0.0184	0.0181	0.0182	0.0125
	300	0.0186	0.0186	0.0183	0.0185	0.0141
	400	0.0183	0.0187	0.0188	0.0186	0.0216
	500	0.0184	0.0185	0.0195	0.0188	0.0497
	600	0.0189	0.0190	0.0188	0.0189	0.0082
	700	0.0196	0.0192	0.0185	0.0191	0.0455
	800	0.019	0.0188	0.0195	0.0191	0.0294
	900	0.0195	0.0195	0.0186	0.0192	0.0424
	1,000	0.0197	0.0194	0.0188	0.0193	0.0374
1:30	100	0.0232	0.0229	0.0224	0.0228	0.0330
	200	0.0244	0.0247	0.0256	0.0249	0.0510
	300	0.0263	0.0267	0.0265	0.0265	0.0163
	400	0.0276	0.0279	0.0267	0.0274	0.0510
	500	0.0283	0.0286	0.028	0.0283	0.0245
	600	0.0291	0.0296	0.028	0.0289	0.0668
	700	0.0292	0.0293	0.0297	0.0294	0.0216
	800	0.0301	0.0304	0.0293	0.0299	0.0464
	900	0.0302	0.0305	0.0299	0.0302	0.0245
	1,000	0.0303	0.0304	0.0311	0.0306	0.0356
1:40	100	0.0276	0.0276	0.0273	0.0275	0.0141
	200	0.0295	0.0295	0.0304	0.0298	0.0424
	300	0.0317	0.0315	0.0307	0.0313	0.0432
	400	0.0321	0.0325	0.0318	0.0321	0.0287
	500	0.0324	0.0325	0.0336	0.0328	0.0544
	600	0.0332	0.0328	0.034	0.0333	0.0499
	700	0.0339	0.0336	0.0339	0.0338	0.0141
	800	0.0342	0.0344	0.0338	0.0341	0.0249
	900	0.0348	0.035	0.0335	0.0344	0.0665
	1,000	0.0349	0.0347	0.0344	0.0347	0.0205

method > (GB/T 50,123–2019), We repeated each test for three times to show the scatters of the experimental results.

Test Results of Dynamic Characteristics of Solidified Muddy Soil Under Different Mix Ratios

Dynamic Strain Test Results

Table 3 and **Table 4** shows the cumulative strain of solidified Mucky soil under different mixing ratios and different cycles. From the data analysis in these tables, we can get the maximum value in the range of twice the average value plus the standard deviation, which shows that the test results are less discrete. **Figure 2** shows the cumulative strain curve of solidified muddy soil under different mixing ratios under different cycles. It can be seen from the figure that as the number of cycles increases, the cumulative strain of the sample also increases. In other words, the strain of the solidified silty soil is basically in a positive correlation with the number of cycles. Observing the development trend of the curve in the figure, it can be found out that the specimen compression is relatively large at the beginning of loading. When the number of cycles reaches a certain level, the strain growth rate of the specimen tends to slow down. This is because as the number of cycles increases, the inside of the sample gradually becomes dense. Whereas, the porosity inside the soil begins to decrease, the strength becomes higher and higher, and the corresponding strain begins to decrease.

From **Figure 2A**, it is easy to find that when the cement mass g is 1:20 than the dry sludge mass g, the cumulative strain is lower than 1:30 and 1:40. This is because as the content of the diluent increases, the crystals produced between the solidifying agent and the soil can make the connection between the soil particles closer. While the increase in molecular gravity makes many individual soil particles aggregate into small aggregates, thus forming a stable structure, the stiffness of the soil is improved. Therefore, the cumulative axial strain of the specimen becomes the smallest.

Comparing **Figure 2B**, when the cement mass g: dry sludge mass g is 1:20, the cumulative strain is lower than that at 1:30 and 1:40. The increase in cement content makes the contact between cement and curing agent closer, which results the hydrolysis and hydration reaction of cement and the liquid curing agent filling the pores in the soil structure well, thereby improving the stiffness of the silt soil.

Dynamic Elastic Modulus Test Results

The dynamic elastic modulus of silty soil refers to the relationship between the dynamic stress and the recoverable part of the

TABLE 4 | Cumulative strain change curve of different cement content under dynamic load.

Cement content	Cycles	1st test (mm)	2nd test (mm)	3rd test (mm)	Mean value (mm)	Standard deviation (%)
1:20	100	0.018	0.0181	0.0173	0.0178	0.0356
	200	0.018	0.0181	0.0185	0.0182	0.0216
	300	0.018	0.0181	0.0193	0.0185	0.0591
	400	0.019	0.019	0.0178	0.0186	0.0566
	500	0.0184	0.0187	0.0193	0.0188	0.0374
	600	0.0193	0.0188	0.0186	0.0189	0.0294
	700	0.0194	0.019	0.0189	0.0191	0.0216
	800	0.0194	0.019	0.019	0.0191	0.0189
	900	0.0189	0.0184	0.0202	0.0192	0.0759
	1,000	0.019	0.0189	0.02	0.0193	0.0497
1:25	100	0.0277	0.028	0.0281	0.0279	0.0170
	200	0.0325	0.0322	0.034	0.0329	0.0787
	300	0.036	0.0356	0.0373	0.0363	0.0726
	400	0.0395	0.0392	0.0386	0.0391	0.0374
	500	0.0413	0.0416	0.0413	0.0414	0.0141
	600	0.0433	0.043	0.0434	0.0432	0.0170
	700	0.0453	0.0456	0.0444	0.0451	0.0510
	800	0.0468	0.0464	0.0464	0.0465	0.0189
	900	0.0485	0.0482	0.0476	0.0481	0.0374
	1,000	0.0492	0.0493	0.0501	0.0495	0.0403
1:30	100	0.0255	0.0255	0.0257	0.0256	0.0094
	200	0.0268	0.0269	0.0274	0.0270	0.0262
	300	0.0281	0.0284	0.0272	0.0279	0.0510
	400	0.0282	0.0281	0.0295	0.0286	0.0638
	500	0.0289	0.0289	0.0298	0.0292	0.0424
	600	0.03	0.0301	0.029	0.0297	0.0497
	700	0.0299	0.0304	0.0301	0.0301	0.0205
	800	0.0306	0.0305	0.0307	0.0306	0.0082
	900	0.0313	0.0315	0.0301	0.0310	0.0618
	1,000	0.0309	0.0306	0.0325	0.0313	0.0834

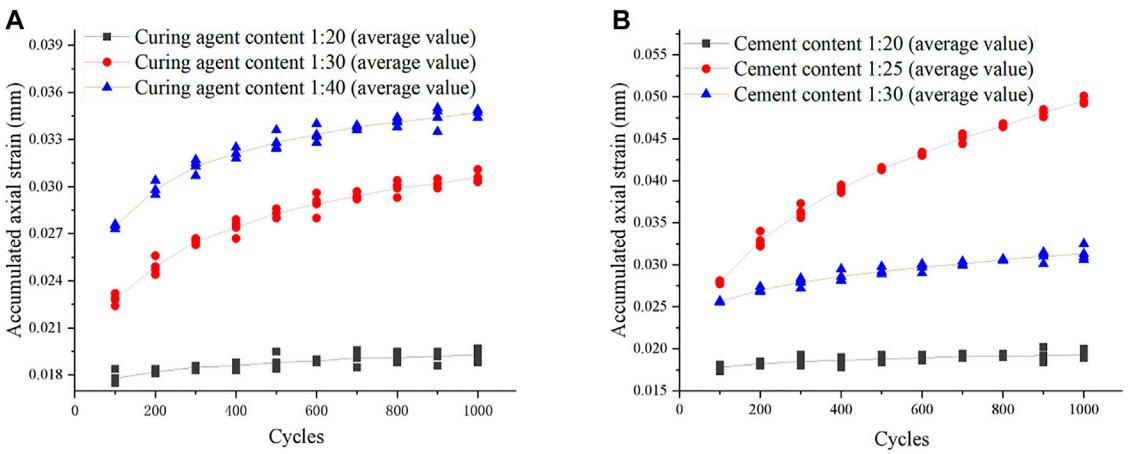

FIGURE 2 | Cumulative strain change curve of sample under dynamic load amplitude N = 100N and different cycle times **(A)** Different curing agent content **(B)** Different cement content.

dynamic strain in the soil (Oh and Vanapalli, 2014). Due to the periodic action of the dynamic load, a series of hysteretic curves appear between the dynamic stress and the dynamic strain. We also calculated the dynamic elastic modulus according to **formula (1)**:

$$E_d = \frac{\delta_{max} - \delta_{min}}{\varepsilon_{max} - \varepsilon_{min}} \quad (1)$$

In **formula (1)**, δ_{max}, δ_{min}, ε_{max}, and ε_{min} are the maximum and minimum values of stress and strain in the hysteresis curve,

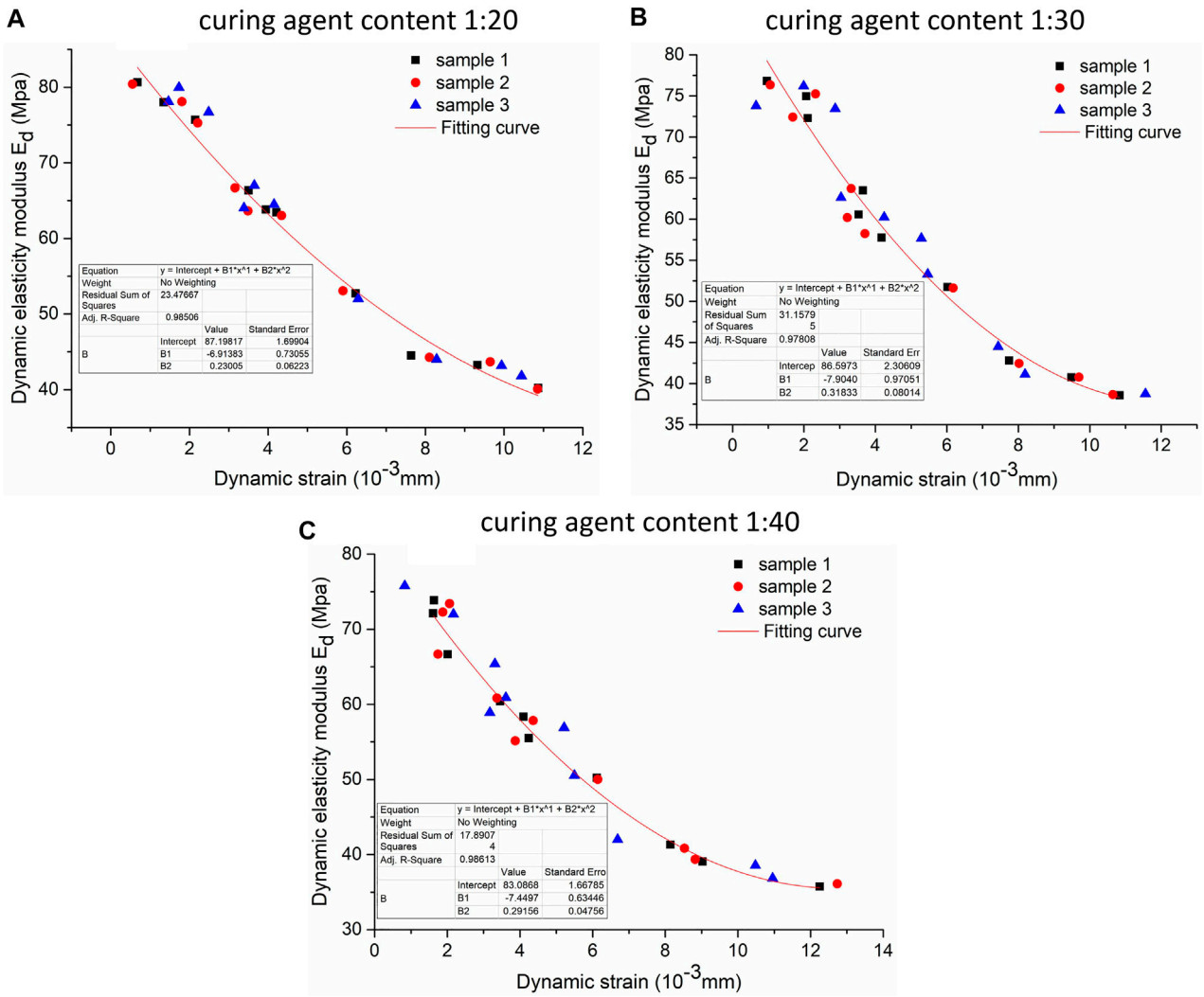

FIGURE 3 | Ed-εd relation curve under dynamic load amplitude N = 100N and different loading stages, Different curing agent content.

respectively. Firstly, we sort the E_d-ε_d data obtained in the experiment, as shown in **Figure 3** and **Figure 4**.

Figure 3 and **Figure 4** show the relationship between dynamic elastic modulus and dynamic strain of solidified muddy soil under different mix ratios. It can be included from the figure that the E_d-ε_d relationship curve of the solidified muddy soil under different mix ratios has the same trend, but the corresponding initial dynamic elastic modulus are different, and the specimens with high cement and curing agent content are initially elastic modulus is higher, indicating that as the amount of cement and curing agent increases, the initial dynamic elastic modulus of the solidified muddy soil can be effectively improved; As the number of loading stages increases, the corresponding dynamic strain increases and the dynamic elastic modulus decreases.

Comparing **Figure 3** and **Figure 4**, it can be found that when the ratio of cement mass to dry sludge mass is 1:20, and the ratio of diluent volume to dry sludge mass is 1:20, the sample produced lower strain under the same conditions. Because the higher the content of cement and curing agent, the higher the content of hydration products in the solidified muddy soil, the stronger the cementing force between soil particles, the denser the sample, the higher its stiffness, and the mechanical properties of the material are optimized, so the ability of the soil to resist deformation is enhanced. If the loading order increases, the sample becomes more and more hardened, Therefore its elastic deformation decreases, plastic deformation increases, and the dynamic elastic modulus decreases.

Test Results of Dynamic Characteristics of Solidified Muddy Soil Under Different Curing Ages

Table 5 shows the analysis of dynamic load amplitudes and final axial strain data of solidified muddy soil under different curing ages. From the table, the maximum values can be obtained in the

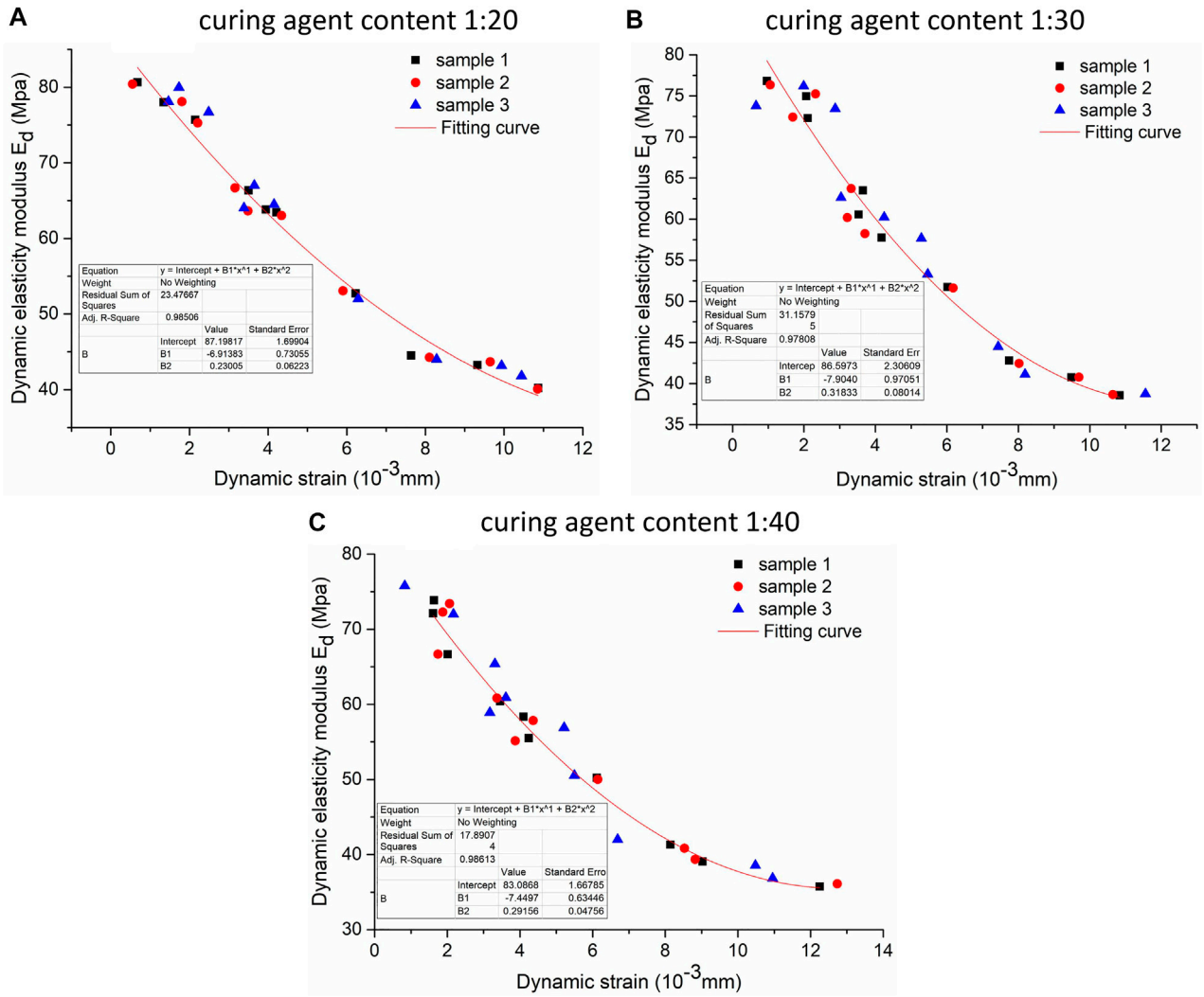

FIGURE 4 | Ed-εd relation curve under dynamic load amplitude N = 100N and different loading stages, Different cement content.

TABLE 5 | Final axial strain of solidified muddy soil at different curing ages.

Curing ages (d)	Amplitude (N)	1st test (mm)	2nd test (mm)	3rd test (mm)	Mean value (mm)	Standard deviation (%)
7	20	0.0048	0.0047	0.0059	0.0051	0.0544
	40	0.0076	0.0078	0.0087	0.0080	0.0478
	60	0.0211	0.0215	0.0204	0.0210	0.0455
	80	0.0288	0.0288	0.0276	0.0284	0.0566
	100	0.0332	0.0329	0.0339	0.0333	0.0419
28	20	0.0027	0.0022	0.0023	0.0024	0.0216
	40	0.0043	0.0041	0.0033	0.0039	0.0432
	60	0.006	0.0063	0.0061	0.0061	0.0125
	80	0.0093	0.0093	0.0082	0.0089	0.0519
	100	0.0118	0.0116	0.0129	0.0121	0.0572
90	20	0.0027	0.0028	0.0041	0.0032	0.0638
	40	0.0047	0.005	0.005	0.0049	0.0141
	60	0.0068	0.0071	0.0074	0.0071	0.0245
	80	0.0114	0.0118	0.0125	0.0119	0.0455
	100	0.0165	0.0168	0.0159	0.0164	0.0374

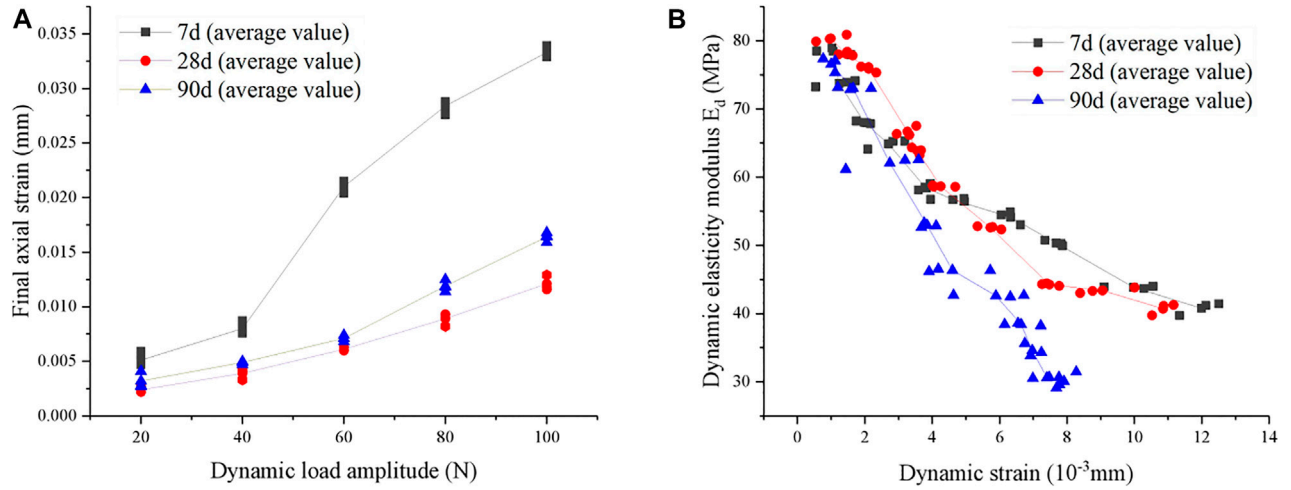

FIGURE 5 | Dynamic characteristics of solidified muddy soil at different curing ages **(A)** The curve between dynamic load amplitude and final axial strain **(B)** The curve between dynamic strain and dynamic elastic modulus.

range of two times the average value plus the standard deviation, it shows that the test results are less discrete. **Figure 5** shows the dynamic characteristics of solidified muddy soil under different curing age conditions. It can be seen from **Figure 5A** that with the increase of the dynamic load amplitude, the final axial strain of the solidified muddy soil also increases. More importantly, the final axial strain increases at different ages. When the final axial strain at 7 days is the largest, followed by 90 days, and the smallest at 28 days. Due to the hydration reaction between cement, curing agent, and muddy soil is slow, the reaction is insufficient when the curing age is 7 days. Consequently, the main effect of the early strength improvement is the physical filling effect. As the curing age reaches 28 days, the hydration reaction between cement, curing agent, and muddy soil is sufficient, which results those colloidal crystals fill and connect the molecular gaps between the soil well, improving the compactness of the muddy soil. Therefore, the strength of the solidified muddy soil continues to increase. Whereas, when the curing age reaches 90days, the rigidity of the solidified muddy soil begins to decrease, indicating that the curing effect of the curing agent is not indefinite. At last, the increase in age makes the curing agent possible to fail.

Table 6 shows the data analysis table of dynamic strain and dynamic modulus of elasticity of solidified muddy soil under different curing ages. From the table, the maximum relative error is 16.81% (curing ages 90 days), which shows that the experimental results are less discrete, the relative error and dispersion increase with the increase of age, indicating that the curing state becomes dispersed when the age reaches 90 days. According to **Figure 5B**, it can be inferred that when the curing age is 28 days, the initial dynamic elastic modulus of solidified muddy soil is larger than that of 7 days and 90 days. In cast that the curing age is 7 days, the hydration reaction between cement, curing agent, and muddy soil is insufficient. Further, the early stiffness improvement is mainly due to physical diffusion, the degree of improvement is therefore not obvious. When the curing age is 90 days, the dynamic elastic modulus of solidified silty soil tends to decrease over time. That is to say, the effect of the curing agent is weakened. Comparing the three curing ages, in case of dynamic elastic modulus of high solidified silty soil corresponding to 28 days, and the dynamic strain is the lowest, indicating that curing age of 28 days solidified muddy soil has the best hydration reaction effect. The gelling material greatly improves the cohesion between molecules, thereby effectively inhibiting the deformation of the silt soil particles.

Kang et al. (2017) showed that the dynamic constitutive relationship of soil under cyclic loading conforms to the following hyperbolic relationship through a large number of experimental studies, where:

$$\boldsymbol{\delta_d = \frac{\varepsilon_d}{a + b\varepsilon_d}} \tag{2}$$

In **formula (2)**, where δ_d is the dynamic stress, ε_d is the elastic dynamic strain, and a and b are the soil parameters. On basis of **formula (2)**, $1/E_d = a+b\varepsilon_d$ can be obtained, that is, the reciprocal of dynamic elastic modulus has a linear relationship with the magnitude of dynamic strain. Therefore, we accordingly draw the correlation curve of $1/E_d \sim \varepsilon_d$, as shown in **Figure 6**.

It can be concluded from **Figure 6** that the test points fit with the straight line well. However, it should be noted that the dispersion is very small, indicating that the curves are basically linear for solidified muddy soils of different ages under the same test conditions. The larger the slope, the faster the dynamic strain increases, and the faster the reciprocal of the dynamic elastic modulus increases, that is, the faster the dynamic elastic modulus decreases. The hyperbolic model can well reflect the relationship between the strain of solidified silt and the dynamic elastic modulus. From **Figure 6**, the curve slope of 28 days solidified muddy soil is smaller than that of 7 days and 90 days solidified muddy soil, its dynamic elastic modulus is therefore larger than that of the other two groups of solidified muddy soil, indicating that 28 days is the curing age with the best curing agent effect.

TABLE 6 | Dynamic elasticity modulus E_d of solidified muddy soil at different curing ages.

Curing ages (d)		Dynamic strain (10^{-3}mm)	Actual measurement E_d (Mpa)	Regression analysis E_d (Mpa)	Relative error (%)
7	1st test	1.025	78.904	74.427	6.02
		1.462	73.901	72.147	2.43
		2.165	67.841	68.650	1.18
		3.182	65.269	63.961	2.04
		3.589	58.128	62.208	6.56
		4.942	56.837	56.881	0.08
		6.046	54.444	53.109	2.51
		7.345	50.754	49.331	2.89
		10.279	43.671	43.425	0.57
		12.12	41.183	41.580	0.95
	2nd test	0.569	78.48	76.891	2.07
		1.71	74.119	70.890	4.56
		1.74	68.224	70.740	3.56
		2.832	65.247	65.526	0.43
		3.829	58.39	61.206	4.60
		4.947	56.446	56.863	0.73
		6.312	54.891	52.277	5.00
		7.819	50.277	48.130	4.46
		10.548	43.973	43.066	2.11
		12.505	41.419	41.375	0.11
	3rd test	1.579	77.951	71.551	8.94
		0.539	73.229	77.057	4.97
		2.057	67.929	69.174	1.80
		2.086	64.094	69.033	7.15
		3.943	59.033	60.739	2.81
		3.95	56.739	60.711	6.54
		6.617	53.015	51.360	3.22
		7.861	49.953	48.028	4.01
		9.098	43.891	45.364	3.25
		11.339	39.722	42.187	5.84
28	1st test	0.55	79.869	85.285	6.35
		1.223	77.985	79.858	2.34
		2.109	76.122	73.248	3.92
		3.32	66.193	65.196	1.53
		3.666	63.933	63.104	1.31
		4.016	58.763	61.082	3.80
		5.786	52.699	52.308	0.75
		7.4	44.417	46.422	4.32
		8.756	43.32	43.035	0.66
		10.867	41.129	40.595	1.31
	2nd test	0.955	80.261	81.977	2.09
		1.636	77.822	76.701	1.46
		1.89	76.186	74.825	1.82
		2.942	66.316	67.587	1.88
		3.395	64.316	64.734	0.65
		4.053	58.592	60.873	3.75
		6.047	52.339	51.220	2.18
		7.259	44.305	46.856	5.44
		8.388	42.999	43.814	1.86
		11.162	41.258	40.529	1.80
	3rd test	1.459	80.881	78.038	3.64
		1.477	78.379	77.901	0.61
		2.337	75.328	71.645	5.14
		3.523	67.513	63.957	5.56
		3.624	63.229	63.353	0.20
		4.681	58.589	57.501	1.89
		5.342	52.786	54.281	2.75
		7.766	44.05	45.368	2.90
		10.006	43.806	41.174	6.39
		10.521	39.743	40.759	2.49
90	1st test	1.116	77.044	74.376	3.59
		1.571	72.883	70.620	3.20
		3.189	62.487	58.239	7.29

(Continued on following page)

TABLE 6 | (*Continued*) Dynamic elasticity modulus E_d of solidified muddy soil at different curing ages.

Curing ages (d)		Dynamic strain (10^{-3}mm)	Actual measurement E_d (Mpa)	Regression analysis E_d (Mpa)	Relative error (%)
		4.113	52.869	51.853	1.96
		4.178	46.531	51.422	9.51
		6.316	42.45	38.633	9.88
		6.148	38.417	39.541	2.84
		7.238	34.308	33.939	1.09
		6.984	30.515	35.182	13.27
		7.773	29.594	31.442	5.88
	2nd test	0.761	77.344	77.391	0.06
		1.196	73.138	73.707	0.77
		3.593	62.572	55.386	12.97
		3.762	53.291	54.220	1.71
		3.903	46.175	53.261	13.30
		6.719	42.659	36.520	16.81
		6.544	38.587	37.426	3.10
		6.917	33.865	35.517	4.65
		7.47	30.676	32.835	6.58
		7.685	29.113	31.841	8.57
	3rd test	1.114	75.319	74.393	1.24
		2.183	73.014	65.758	11.03
		1.432	61.151	71.755	14.78
		3.675	52.615	54.818	4.02
		5.72	46.305	41.930	10.43
		4.628	42.691	48.509	11.99
		7.219	38.22	34.030	12.31
		6.746	35.628	36.382	2.07
		7.758	30.663	31.510	2.69
		8.272	31.445	29.263	7.46

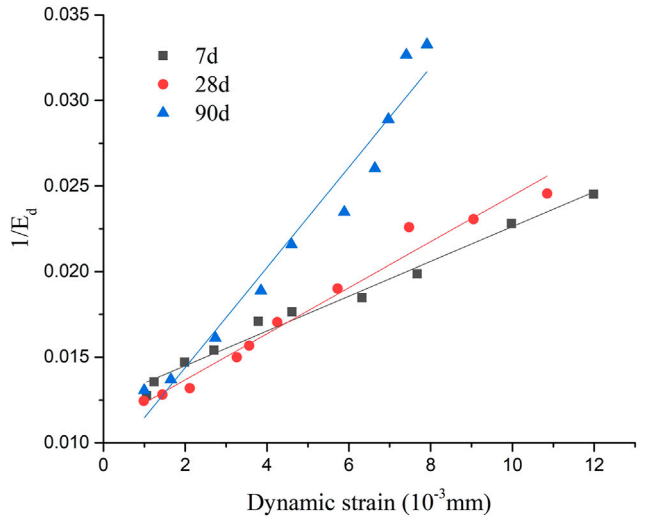

FIGURE 6 | Relationship curve of $1/E_d$~ε_d of solidified muddy soil at different curing ages.

INDOOR SCANNING ELECTRON MICROSCOPE MICROSCOPIC TEST

Test Principle and Scheme

In the experiment, through sampling the samples after the moving strain test and scanning electron microscopy test, the paper studies the quantitative structural characteristics of the solidified muddy soil by selecting typical sample maps aiming to reveal the microstructure characteristics of the solidified muddy soil. With the purposed of avoiding disturbing the structure of solidified muddy soil, we collected the powder samples with a surface thickness of about 3 mm with a soil cutter and placed in a sealed sample box. Furthermore, to eliminate the interference of moisture and the vacuum degree of the SEM vacuum system on the test results, it is necessary to dry the samples, so the samples were dried in an 80°C oven, and then transported back to the laboratory for SEM test observation. More specific experimental steps are as follows:

1) Take a powder sample with a thickness of about 3 mm on the surface of the test block after the dynamic triaxial test.
2) Put the powdered sample in the plastic box, label it and put it in the drying box for drying.
3) Sprinkle the powdered sample evenly on the sample stage, and use a scanning electron microscope (SEM) to scan and image the surface of the sample point by point.

Legend of the Sample Observed in the Test

Figures 7, **8** present examples of samples under different mixing ratios. It is shown from **Figure 7** with the increase of content of curing agent, curing muddy soil skeleton structure of microscopic particles form starts from single chip sorting clutter to sort stereospecificity obvious granular, which shows that with the increase of content of curing agent, cement, curing agent. The

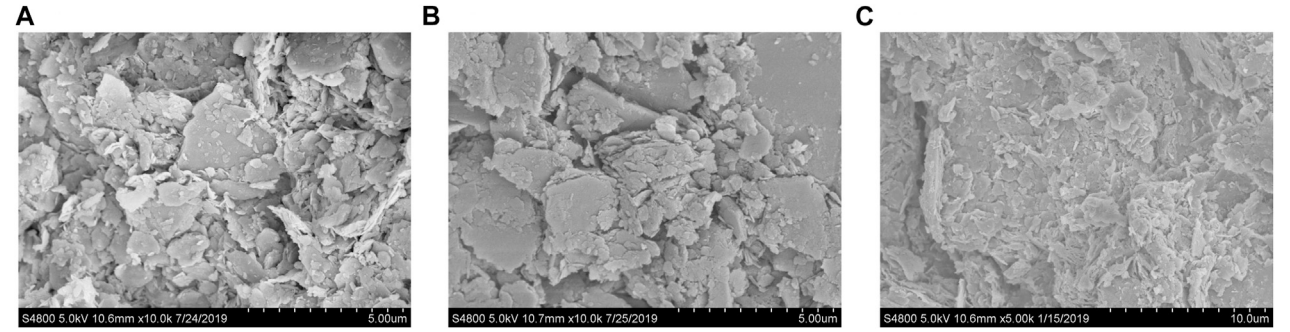

FIGURE 7 | SEM images of solidified muddy soil with different curing agent contents **(A)** Curing agent content (1:40) **(B)** Curing agent content (1:30) **(C)** Curing agent content (1:20).

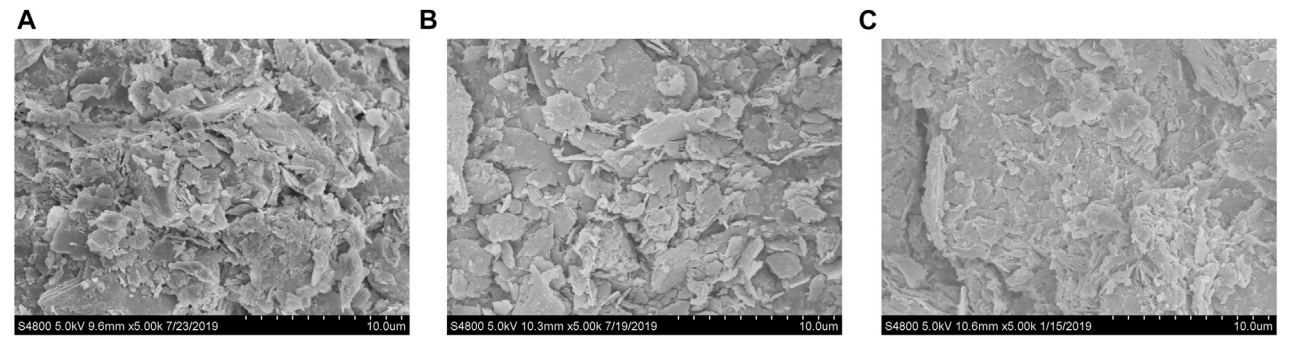

FIGURE 8 | SEM images of solidified muddy soil with different cement contents **(A)** Cement content (1:30) **(B)** Cement content (1:25) **(C)** Cement content (1:20).

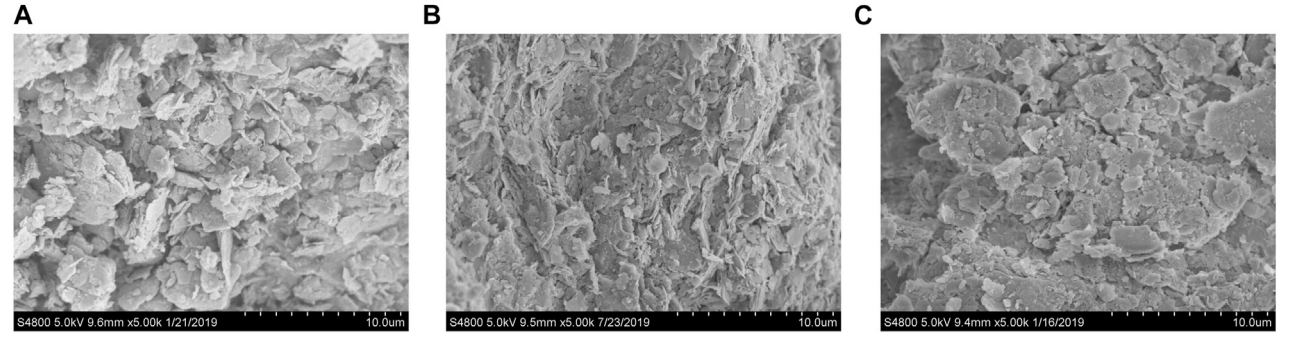

FIGURE 9 | SEM images of solidified muddy soil at different curing ages **(A)** 7 days **(B)** 28 days **(C)** 90 days

hydration reaction between soil particles can effectively adhere to the soil particle. It acts as a connecting "bridge" to fill in the particle gap, thus improving the structural properties of the solidified silty soil itself.

It is clear from **Figure 8**, following the increase of cement content, the contact area of the solidified mud soil microscopic particles started from dot and gradually become section. It is noted that the contact area increases. This is because the cement content increase cement, curing agent, hydration gel between the soil particles will flake silt particle conglomerate, particle clearance gradually be populated, internal close-grained, to form a whole structure. On the macroscopic level, the strength and stiffness of solidified silty soil are enhanced.

By comparing **Figure 7** and **Figure 8**, it can be concluded that the influence of content of curing agent on solidified silty soil is greater than that of changing the content of cement. This is because the content of curing agent plays a leading role in the

hydration reaction between cement, curing agent and soil particles. On another hand, the increasing curing agent content can effectively promote the growth of hydration gel products.

Figure 9 is an example of samples under different curing age conditions. It is found out that the curing age is 7 days. Consequently, the microstructure of solidified muddy soil presents a large number of flaky particles piled up. The surface of the soil particles is very rough, coupling with a lot of gaps in the internal structure. However, as the curing age reaches 28 days, a large amount of hydration gel material condenses the flaky particles. Especially, the hydration products penetrate into the interstices of the internal structure of the soil, bonding the soil particles together and making the surface relatively flat and smooth. While the curing age reaches 90 days, it will result in mutual slippage between the polymers. In this case, a small amount of rough monolithic particles appears, indicating that the curing effect decreases with the curing age reaching 90 days.

Dynamic triaxial test and SEM microscopic tests were combined to analyze the relationship of the solidified muddy and the mechanic property. From section 4 and section 5, we will find that there exists proportional relationship between micro-structure and mechanical property. On the one hand, the solidified muddy will change the structure by filling the particle gap, thus raising the compactness degree of soil. On the other hand, the cementation of the solidified muddy can effectively adhere the soil particles, thus raising the cohesive force of soil. The compactness degree and the cohesive force affect proportionally the dynamic elastic modulus and dynamic strain of the soil.

CONCLUSION

Through indoor dynamic triaxial test and SEM microscopic test on solidified muddy soil, the paper analyzes the influence of changing mix ratio and curing age on solidification effect according to the test results of dynamic characteristics of solidified muddy soil with different mix ratio and curing age. The corresponding conclusions are drawn as following:

1) Under the conditions of different mix ratios, with the increase in the mixing amount of cement and curing agent, the curing effect of the curing agent is more obvious. Particularly, the curing agent content dominates in the hydration reaction between cement, curing agent and soil particles. The mixing of cement and curing agent significantly improves the dynamic strength and dynamic elastic modulus of the powdery silty soil, and can effectively improve the dynamic characteristics of the powdery silty soil.
2) With the increase of the loading series, the corresponding dynamic strain increases. Whereas, the dynamic elastic modulus shows a downward trend. Particularly, the dynamic cohesion inside the structure increases, the soil gradually becomes compact, and its stiffness increases.
3) The theoretical curve predicted by adopting the hyperbolic model can fit with the relationship between dynamic stress and dynamic strain of solidified silty soil well.
4) The results show that the best mix ratio can be obtained when the ratio of cement mass to dry sludge mass is 1:20, additionally the ratio of diluent volume to dry sludge mass is 1:20. There is no adhesion between the particles in the silt soil sample, with only friction between the particles and the inlaid bite. After mixing cement and curing agent, part of the hydration products are wrapped on the surface of the soil particles in flocculent or fibrous form. Moreover, some hydration products fill the pores between the soil particles. However, with the increase of age, the hydration products stretch to the soil particles. Interstitials or pores between sand particles extend and overlap and begin to agglomerate. When its age reaches 28 days, the agglomeration is enhanced. Therefore, a grid-like spatial skeleton structure is gradually formed, which binds the soil particles into one body and strengthens the soil particles. The connection between the two has realized the improvement of the mechanical properties of the silt soil.
5) The solidifying agent strengthens the silt as the base layer or subbase layer of the road pavement. Additionally, its strength increases faster and more stable in the early stage, with a higher resistance to deformation. In coastal areas where silt soil is widely distributed, it is practical to use curing agent to reinforce the silt soil as the base or subbase of high-speed railway station buildings and railways. The research can solve the resource shortage problems such as insufficient fillers and stones. More importantly, the *in-situ* solidification can effectively reduce the damage to the natural environment, and achieve energy saving and reduction by recycling resources.
6) The paper basically focuses on the investigation of agitated silt soil to obtain regular conclusions. But the silt sample undergoes drying, crushing and other pretreatment operations, which may change some properties and cause a certain difference in the effect of silt *in-situ* solidification. It's necessary to be further studied regarding on the effect mechanism of curing agent on different silt soils and whether the effect is the same. The research on the mechanical properties of silt is limited to dynamic characteristics. While, it needs to be further studied on the changing laws of certain static mechanical indexes such as unconfined compressive strength, partial shear strength, compressibility, stability, etc. The future research is generally divided into two steps: 1) To further deepen the research on curing effect durability, 2) To further carry out research on on-site quality control approach combined with engineering practice so as to provide a more comprehensive theoretical basis for high-quality construction of actual projects.

DATA AVAILABILITY STATEMENT

The raw data supporting the conclusions of this article will be made available by the authors, without undue reservation.

AUTHOR CONTRIBUTIONS

ZC: Data curation, Formal analysis, Investigation,Methodology, Software,Visualization, Writing.—review and editing. HX: Formal analysis, Validation,Writing-review and editing. MC Formal analysis, Investigation,Methodology,Writing-original draft. HL: Data curation, Funding acquisition. ZW: Project administration. PF: Validation.

FUNDING

The work described in this paper was financially supported by the National Natural Science Foundation of China (Grant No. 51908146), Characteristic innovation projects of colleges and universities in Guangdong Province (2019KTSCX190) the Foshan self-funded science and technology plan project (Grant No. 1920001001539).

REFERENCES

Amir-Faryar, B., and Aggour, M. S. (2016). Effect of Fibre Inclusion on Dynamic Properties of clay. *Geomechanics and geoengineering* 11 (2), 104–113. doi:10.1080/17486025.2015.1029013

Arulrajah, A., Yaghoubi, M., Disfani, M. M., Horpibulsuk, S., Bo, M. W., and Leong, M. (2018). Evaluation of Fly Ash- and Slag-Based Geopolymers for the Improvement of a Soft marine clay by Deep Soil Mixing. *Soils and foundations* 58 (6), 1358–1370. doi:10.1016/j.sandf.2018.07.005

Consoli, N. C., da Rocha, C. G., and Silvani, C. (2014). Devising Dosages for Soil-Fly Ash-Lime Blends Based on Tensile Strength Controlling Equations. *Construction Building Mater.* 55 (Mar.), 238–245. doi:10.1016/j.conbuildmat.2014.01.044

Dong, Z. L., Zhang, G. X., Zhou, Q., Luo, Y., Qiu, Q., Li, Y., et al. (2011). RESEARCH AND APPLICATION OF IMPROVEMENT TECHNOLOGY OF SHALLOW ULTRA-SOFT SOIL FORMED BY HYDRAULIC RECLAMATION IN TIANJIN BINHAI NEW AREA. *Chin. J. Rock Mech. Eng.* 30 (005), 1073–1080. CNKI:SUN:YSLX.0.2011-05-027.

Huang, Y., Zhou, Z. Z., and Bo, J. (2010). Micro-experiments on a Soft Ground Improved by Cement-Mixed Soils with gypsum Additive. *Chin. J. Geotechnical Eng.* 32 (08), 1179–1183.

Jian, W. B., Sun, D., and Huang, C. X. (2013). Micromechanism of Cement-Sodium Silicate-Stabilized Soft Soils. *Chin. J. Geotechnical Eng.* 35 (S2), 632–637.

Kang, G.-o., Tsuchida, T., and Kim, Y.-s. (2017). Strength and Stiffness of Cement-Treated marine Dredged clay at Various Curing Stages. *Construction Building Mater.* 132 (FEB.1), 71–84. doi:10.1016/j.conbuildmat.2016.11.124

Karthik, S., Ashok, K., Gowtham, P., Elango, G., Gokul, D., and Thangaraj, S. (2014). Soil Stabilization by Using Fly Ash. *IOSR J. Mech. Civil Eng.* 10 (6), 20–26. doi:10.9790/1684-1062026

Kuna, K., Airey, G., and Thom, N. (2016). Development of a Tool to Assess *In-Situ* Curing of Foamed Bitumen Mixtures. *Construction Building Mater.* 124, 55–68. doi:10.1016/j.conbuildmat.2016.07.086

Li, H. L., Liu, K., and Shen, Y. (2014). Experimental Research on Road-Used Performance of Dredger Fill with Cement-Lime Curing. *J. Water Resour. Architectural Eng.* 12 (02), 51–57. doi:10.3969/j.issn.1672-1144.2014.02.011

Liang, S. H., Lu, Y. D., Pan, W. S., and Xiaozhou, Z. (2020). Study on Microstructure of Red Clay in Southern Guizhou Province Based on SEM. *Water Resour. Power* 38 (02), 151–154. CNKI:SUN:SDNY.0.2020-02-038.

Liu, S. Y., Zhang, T., and Cai, G. J. (2018). Research on Technology and Engineering Application of Silt Subgrade Solidified by Lignin-Based Industrial By-Product. *China J. Highw. &Transport* 31 (3), 1–11. doi:10.19721/j.cnki.1001-7372.2018.03.001

Oh, W. T., and Vanapalli, S. K. (2014). Semi-empirical Model for Estimating the Small-Strain Shear Modulus of Unsaturated Non-plastic Sandy Soils. *Geotech Geol. Eng.* 32 (2), 259–271. doi:10.1007/s10706-013-9708-5

Pan, C., Xie, X., Gen, J., and Wang, W. (2020). Effect of Stabilization/solidification on Mechanical and Phase Characteristics of Organic River silt by a Stabilizer. *Construction Building Mater.* 236 (2), 117538. doi:10.1016/j.conbuildmat.2019.117538

Radovanovic, D. D., Kamberovic, Z. J., Korac, M. S., and Rogan, J. R. (2016). Solidified Structure and Leaching Properties of Metallurgical Wastewater Treatment Sludge after Solidification/stabilization Process. *Environ. Lett.* 51 (1-2), 34–43. doi:10.1080/10934529.2015.1079104

Sani, A., Muhammad, N. Z., Mehan, A., and Joel, M. (2018). Optimization of Fly-Ash Dosage for the Stabilization of Gravel Soil Using Cement for Use as Flexible Pavement Material. *Adv. Sci. Lett.* 24 (6), 3914–3917. doi:10.1166/asl.2018.11510

Shan, W., Chen, H.-e., Yuan, X., Ma, W., and Li, H. (2021). Mechanism of Pore Water Seepage in Soil Reinforced by Step Vacuum Preloading. *Bull. Eng. Geol. Environ.* 80 (3), 2777–2787. doi:10.1007/s10064-020-02075-4

Sun, J., Gong, M. S., and Xiong, H. Q. (2020). Experimental Study of the Effect of Freeze-Thaw Cycles on Dynamic Characteristics of Silty Sand. *Rock Soil Mech.* 41 (03), 747–754. doi:10.16285/j.rsm.2019.0679

Takhelmayum, G., Savitha, A. L., and Gudi, K. (2013). Laboratory Study on Soil Stabilization Using Fly Ash Mixtures. *Int. J. Eng. Sci. Innovative Technol.* 2 (1), 477–482.

Tang, X., Xue, Z., Yang, Q., Li, T., and VanSeveren, M. (2017). Water Content and Shear Strength Evaluation of marine Soil after Electro-Osmosis Experiments. *Drying Technol.* 35 (14), 1696–1710. doi:10.1080/07373937.2016.1270299

Tian, Z. K. (2020). *Experimental Study and Numerical Simulation of Mechanical Properties of Solidified Silt Soil under Dynamic*. Ph. D. Thesis (Hengyang: University of south China).

Tian, Z. K., Peng, C., and Tan, Y. Q. (2020). Effect of Dynamic Action on Mechanical Properties of Composite Solidified Silt Soil. *J. Univ. South China(Science Technology)* 34 (02), 62–68. doi:10.19431/j.cnki.1673-0062.2020.02.010

Wang, J., Li, S., and Feng, T. (2019). A Method Analyzing Deformation of Anchor Foundations in Soft clay under Static and Cyclic Loads. *Appl. Ocean Res.* 84, 133–144. doi:10.1016/j.apor.2019.01.010

Xu, R. Q., Wang, X., Wen, J. Y., and Bingjian, Z. (2019). Curing Agent for Shallow Mucky Soil. *J. Shanghai Jiaotong Univ.* 53 (07), 805–811. doi:10.16183/j.cnki.jsjtu.2019.07.006

Yan, J., Wang, Q., and Zhang, J. (2010). Environmental Influence of Vacuum Preloading Dredging Project. *Proced. Environ. Sci.* 2, 1613–1621. doi:10.1016/j.proenv.2010.10.172

Yang, X. R., Zhang, L. Y., Li, H. C., and Dong, L. Y. (2011). Study and Analysis on Pile-Soil Stress Ratio of the Composite Foundation of Cement-Soil Mixing Pile under Flexible Foundation. *Amr* 335-336, 1145–1150. doi:10.4028/www.scientific.net/amr.335-336.1145

Zhang, J. R., Wang, L. J., Jiang, T., Zhao, J., Ren, M., Li, H., et al. (2021). Diametric Splitting Tests on Compacted Bentonite at Different High Suctions Based on PIV Technique. *J. Basic Sci. Eng.* 29 (03), 691–701. doi:10.16058/j.issn.1005-0930.2021.03.014

Zhou, H. (2013). *Study on Soft Soil Microstructure and Mechanism of Seepage and Consolidation in Pearl River Delta*. Ph. D. Thesis (Guangzhou: South China University of Technology).

Conflict of Interest: Author ZW, is employed by China Railway Guangzhou Group Co., Ltd. Author PF is employed by China Railway Siyuan Survey and Design Group Co, Ltd.

The remaining authors declare that the research was conducted in the absence of any commercial or financial relationships that could be construed as a potential conflict of interest.

Publisher's Note: All claims expressed in this article are solely those of the authors and do not necessarily represent those of their affiliated organizations, or those of the publisher, the editors and the reviewers. Any product that may be evaluated in this article, or claim that may be made by its manufacturer, is not guaranteed or endorsed by the publisher.

frontiers in Materials

ORIGINAL RESEARCH
published: 08 November 2021
doi: 10.3389/fmats.2021.778173

Optimization of Preparation of Foamed Concrete Based on Orthogonal Experiment and Range Analysis

Menglong Cong[1]*, *Shanshan Zhang*[2], *Dandan Sun*[1] and *Kunpeng Zhou*[1]

[1]College of Engineering, Inner Mongolia University for the Nationalities, Tongliao, China, [2]College of Information Science and Technology, Dalian Maritime University, Dalian, China

For the purpose of reducing the energy consumption and construction cost of buildings, the preparation process of geopolymer based foamed concrete, which is a novel material of the wall and roof of building, had been studied in detail. Water glass and sodium hydroxide were used as the alkali activator to excite the mixture consists of slag, fly ash and Kaolin to form the geopolymer matrix, and finally the foams generated using the physical foaming method were filled into the geopolymer matrix to produce geopolymer-based foamed concrete blocks. In the preparation process, firstly one of the four parameters of foam content, water-binder ratio, water glass content, and water glass modulus had been changed separately to study the influence of a single factor on the compressive strength, dry density, thermal conductivity and specific strength of foamed concrete blocks. The experimental results show that the above four factors have different degrees of influence on the concerned performances. Next, some representative combinations of these factors were constructed by orthogonal experiment method, and the influence degree of each combination on the concerned performances was determined by means of range analysis. According to the results of analysis, the most important influencing factor in terms of thermal conductivity was the water-binder ratio, followed by foam content, water glass modulus and water glass content. When the foam content is 1.58%, the water-binder ratio is 0.45, the water glass content is 30%, and the water glass modulus is 1.2, the thermal conductivity of the prepared geopolymer foam concrete reaches 0.044 W/(m·K), which satisfies the expected requirements for heating in severe cold areas.

Keywords: geopolymer, foamed concrete, orthogonal experiment, thermal conductivity, range analysis

OPEN ACCESS

Edited by:
Lin Xu,
Jilin University, China

Reviewed by:
Zhiling Hou,
Beijing University of Chemical Technology, China
Jiaoqing Pan,
Institute of Semiconductors (CAS), China

***Correspondence:**
Menglong Cong
congml@163.com

Specialty section:
This article was submitted to Polymeric and Composite Materials, a section of the journal Frontiers in Materials

Received: *16 September 2021*
Accepted: *21 October 2021*
Published: *08 November 2021*

Citation:
Cong M, Zhang S, Sun D and Zhou K (2021) Optimization of Preparation of Foamed Concrete Based on Orthogonal Experiment and Range Analysis. Front. Mater. 8:778173. doi: 10.3389/fmats.2021.778173

1 INTRODUCTION

With the development of society and the increase of population, the problem of energy shortage has become increasingly prominent, and countries all over the world have attached great importance to energy conservation and environmental protection in the construction industry (Huang, 2013). The Chinese government proposed the development of "applicable, economical and green buildings" in the "13th Five-Year Plan" (Fan et al., 2019). As an important part of the building, the design of the enclosure structure is closely related to the building energy consumption (Liu et al., 2014). In recent years, with the continuous enhancement of China's scientific research and economic strength, relevant functional departments have put forward higher requirements on building environmental

protection, and have successively introduced various policies and measures. With the strong support of these favorable policies, reforms in the construction sector have been deepened, and significant progress has been made in the research of building energy-saving technologies and building energy-saving materials (Chang et al., 2016). From the chemical composition, building insulation materials can be divided into organic materials (Silvestre et al., 2016), inorganic materials (Wang et al., 2020) and organic-inorganic composite materials (Yang et al., 2018). In China's building materials market, organic building materials such as polystyrene foam and polyurethane foam are common (Hou et al., 2018; He, 2017). Compared with inorganic materials, organic materials have the advantages of light weight and low thermal conductivity, which made them favored by the market. Apart from the above advantages, the problems of low ignition point and easy aging of organic building materials can't be ignored (Vuong et al., 2016). On the morning of March 9, 2021, an indoor fire in the Zhongxin Building in Shijiazhuang City, Hebei Province caused serious casualties and property losses because the fire spread to the insulation layer of the building's external walls. The intensification of fires caused by the inflammable insulation of the exterior wall of buildings such as this occurs many times a year, seriously endangering national health and economic construction. In order to reduce the fire threat caused by organic building materials, the Ministry of Housing and Urban-Rural Development of the People's Republic of China has issued a series of announcements to limit the excessive use of organic building materials (Xiao and Ding, 2013). Therefore, inorganic materials represented by foamed concrete have gradually become a research hotspot in the field of building materials (Yang et al., 2021).

Foamed concrete is a kind of lightweight and porous concrete that receives considerable attention from builders worldwide. The irregular voids inside are derived from the foaming agent mixture in the mortar (Amran et al., 2015). The urgent need for energy-saving and environmentally-friendly building technology has promoted the rapid promotion of foam concrete. Pure cement mixed with fine sand is commonly used for preparing foamed concrete with light weight and uniformly distributed discrete bubbles (Ramamurthy et al., 2009). In different countries such as the United Kingdom, Germany, Turkey, the Philippines and Thailand, foam concrete has become a common material required for construction (Mydin and Wang, 2011). In history, the Romans first realized that by adding blood to a mixture of small gravel, coarse sand and hot lime and stirring it with water, the resulting block containing small bubbles was more durable and practical (Hill, 2013). In 1923, Axel Eriksson was granted a patent for Portland cement-based foam concrete (Valore, 1954). After that, major improvements in production equipment and better superplasticizer and foaming agents have allowed foamed concrete to be used on a large scale, and a lot of efforts have been made to comprehensively study the characteristics and behavior of foamed concrete to simplify its usage in building structure application. Foamed concrete can be prepared by two techniques, which are called pre-foaming method and hybrid foaming method. For the former, it is necessary to prepare stable foam with the help of an air compressor, and then mix it with the basic mixture (consisting of cement, sand and water). For the latter, the foaming agent solution is mixed with the base mixture in a high-speed mixer. Since Davidovits introduced geopolymers, the concept of cement-free concrete has been formally put forward (Liu et al., 2016). The concrete can be prepared by a reaction between an alkaline solution and a raw material rich in silica and alumina, followed by curing and drying (Hardjito et al., 2004). The use of geopolymers to replace the ordinary Portland cement (OPC) to make concrete not only significantly reduces the CO2 emissions of the cement industry, but also realizes the reuse of industrial waste residues such as fly ash. In addition, geopolymer concrete also exhibits lower absorptivity than OPC concrete. As a relatively new material, the preparation process, proportion of doped components and material properties of foamed concrete are yet to be studied.

This article mainly studies the preparation technology of foamed concrete, and then expands it to introduce in detail the optimized design of the raw materials and doping ratio of foamed concrete to obtain the ideal compressive strength, dry density, thermal conductivity, and specific strength in the fresh and hardened state. The remainder of this paper is structured as follows: **Section 2** provides a complete solution of preparing the geopolymer-based foamed concrete referred in this article. Next, the influence of a single factor among foam content, water-binder ratio, water glass content and water glass modulus on the compressive strength, dry density, thermal conductivity, and specific strength of foamed concrete blocks are described and discussed in **Section 3**. Apart from this, the results of orthogonal experiment (Xuan and Leung, 2011) and range analysis (Tang et al., 2011) of the combination of various influencing factors will also be presented. At last, the conclusions are drawn in **Section 4**.

2 RAW MATERIALS AND PREPARATION METHOD OF FOAMED CONCRETE

2.1 Raw Materials

The most important raw material for preparing geopolymer-based foamed concrete is geopolymer. Its basic material is usually aluminosilicate in industrial waste residue, roasted clay or natural minerals produced after smelting, or a mixture of the above substances. Here we mixed Kaolin (Inner Mongolia Hongji Co., Ltd.), slag (Shenyang Huacheng Slag Powder Manufacturing Co., Ltd.) and fly ash (Tongliao General Power Plant Co., Ltd.) in a certain proportion to form the basic material of geopolymer. The main components of slag are calcium oxide and glass body. As a by-product of coal combustion, fly ash is usually classified as siliceous (class F) or cementitious (class C). In the experiment, class C fly ash (Type I) conforming to the ASTM C 618 standard was used as the auxiliary cementing material. The chemical composition of slag and fly ash are listed in **Table 1**. The alkali activator was made by water glass (Shandong Yousuo Chemical Technology Co., Ltd.) and sodium hydroxide (Shenyang Chemical Reagent Factory). In order to enhance the compressive strength of the geopolymer, in addition to the above-mentioned raw materials, a small amount of H46 hollow glass beads jointly developed by Ma'anshan Institute of Mining

TABLE 1 | Chemical composition of slag and fly ash.

Material	Mass fraction (weight %, dry basis)								
	SiO_2	Al_2O_3	CaO	Fe_2O_3	MgO	Na_2O	K_2O	TiO_2	FeS
Slag	25.68	15.64	49.51	2.36	4.65	0.38	0.41	0.39	0.98
Fly ash	57.66	28.47	3.25	5.43	2.36	2.83	—	—	—

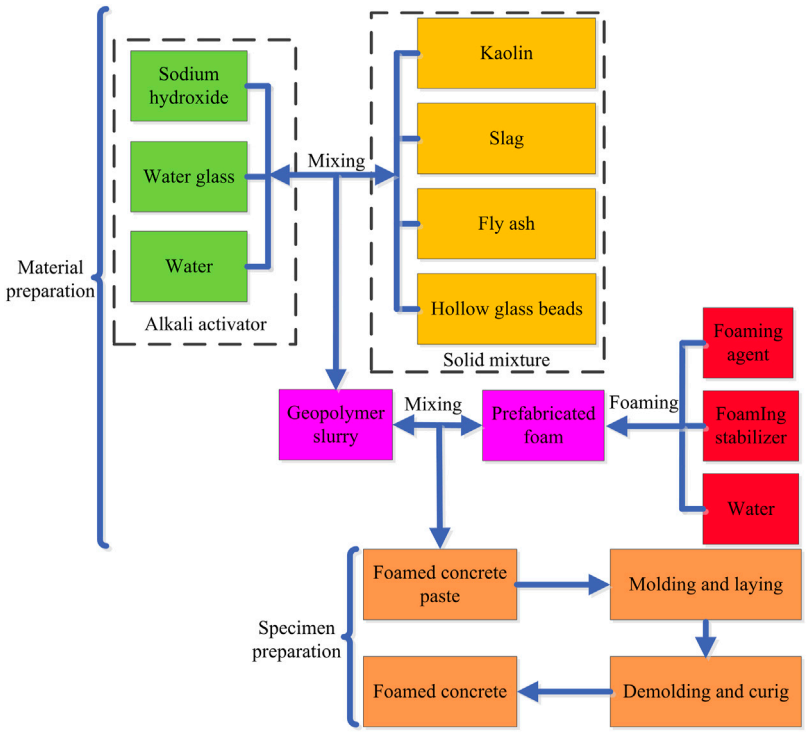

FIGURE 1 | The preparing process of geopolymer-based foamed concrete.

Research and Chinese Academy of Sciences were added. The physical foaming method is used to realize the preparation of geopolymer-based foamed concrete. The current physical foaming agents mainly include rosin, synthetic, protein, and composite. Among them, the composite has the highest foaming efficiency. The high-performance composite foaming agent produced by Qingdao Xinyu Machinery Technology Co., Ltd., was used in the experiments. The foaming agent used is a nearly colorless and transparent liquid, and the dilution ratio, pH value, bleeding and foam density are 50, 7.1, <20 ml and 50 kg/m^3, respectively. For extending and stabilizing the foam to maintain its long-term performance, hydroxypropyl methyl cellulose produced by a Beijing company was introduced as a foam stabilizer.

2.2 Preparation Method

The preparing process of geopolymer-based foamed concrete was shown in **Figure 1**. First, sodium hydroxide, water glass and water were mixed to form an alkali activator of the required modulus; subsequently, dry materials such as Kaolin, slag and fly ash are mixed in a certain proportion and poured into a pot and stir evenly (about 3 min); then, the prepared alkali activator was poured into the uniformly mixed powder and continue stirring to form a geopolymer slurry (about 1 min); finally, the prefabricated foam containing foam stabilizer was passed into a mixer filled with geopolymer slurry and quickly stirred for about 45 s to form a paste-like foamed concrete. In order to prevent the rapid loss of moisture and cause cracks, we poured the above paste into a mold and covered it with a film, and cured it in a standard curing chamber for 24 h under constant temperature and humidity (20 ± 2°C, RH 90%). After demolding, the environmental parameters were kept unchanged until the foamed concrete specimen reached the predetermined age of 28 days.

2.3 Evaluating the Properties of Foamed Concrete

The demoulded foam concrete blocks were divided to obtain 9 small blocks in 3 groups with a length, width and height of 10 cm. The measurement of the compressive strength and dry density of the foamed concrete in this test follows the relevant regulations in the industry standards of the Chinese construction industry (JG/T

TABLE 2 | Mixing ratio of geopolymer-based foam concrete with different foam content.

No.	Water-binder ratio (a.u.)	Slag (g)	Fly ash (g)	Water glass content (%)	Water glass modulus (a.u.)	Foam content (%)
1	0.45	1,150	270	30	1.0	0.30
2	0.45	1,150	270	30	1.0	0.62
3	0.45	1,150	270	30	1.0	0.94
4	0.45	1,150	270	30	1.0	1.26
5	0.45	1,150	270	30	1.0	1.58

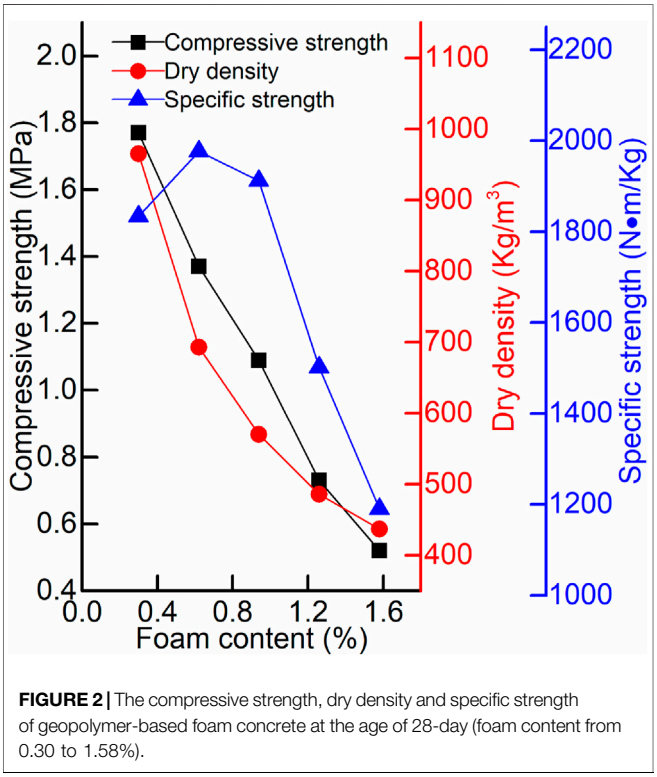

FIGURE 2 | The compressive strength, dry density and specific strength of geopolymer-based foam concrete at the age of 28-day (foam content from 0.30 to 1.58%).

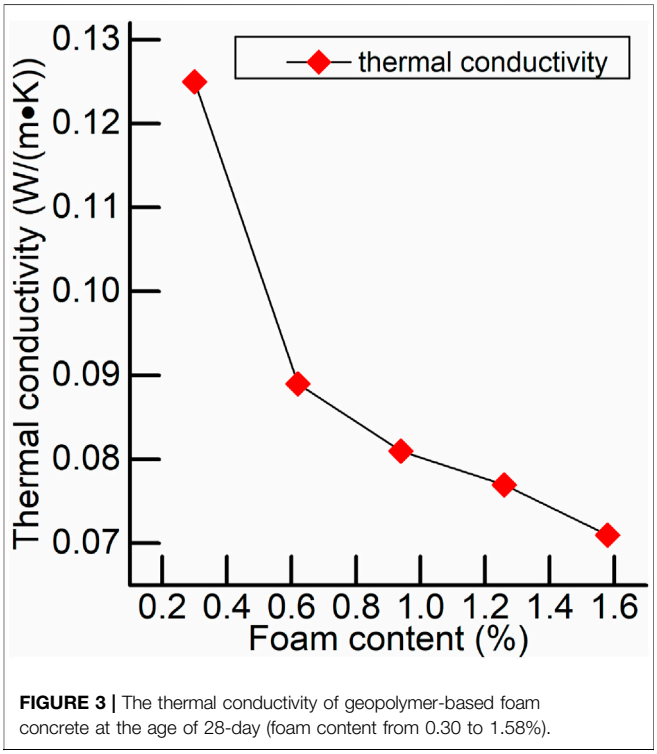

FIGURE 3 | The thermal conductivity of geopolymer-based foam concrete at the age of 28-day (foam content from 0.30 to 1.58%).

266-2011). Before carrying out the experiments, first put the test block in a drying box and dry it to a constant weight. Next, measure the length, width and height twice and then take the average to calculate the volume and surface area. Finally, the average values of each group were calculated using the volumes, surface areas and masses of the 3 test blocks. The IMDRY3001 thermal conductivity tester was used to measure the thermal conductivity. In order to ensure accurate and reliable measurement results, the upper and lower surfaces of the selected test block are required to be as parallel, smooth and uniform in thickness as possible. The compression strength test uses NYL-2000D universal press, and its pressurizing speed can be set to 0.5~1.5KN/s. During the pressurization process, the load is continuously and uniformly increased until the test block is damaged. At this time, the pressure reading of the universal press is recorded as the maximum failure load. The compressive strength f is expressed as

$$f = \frac{F}{A} \tag{1}$$

where F is the maximum failure load and A is the area of Surface. The calculation of dry density follows the following formula:

$$\rho_0 = \frac{m_0}{V} \tag{2}$$

In **Eq. 2**, ρ_0 is dry density, m_0 is quality after drying, and V is the volume. Compared with the simple compressive strength index, the specific strength S obtained after the introduction of dry density is more objective for foam concrete performance evaluation:

$$S = \frac{f}{\rho_0} \tag{3}$$

3 RESULTS AND DISCUSSION

3.1 Influencing Factors of Geopolymer-Based Foam Concrete

The performance of geopolymer-based foam concrete is affected by foam content, water-binder ratio, water glass content and

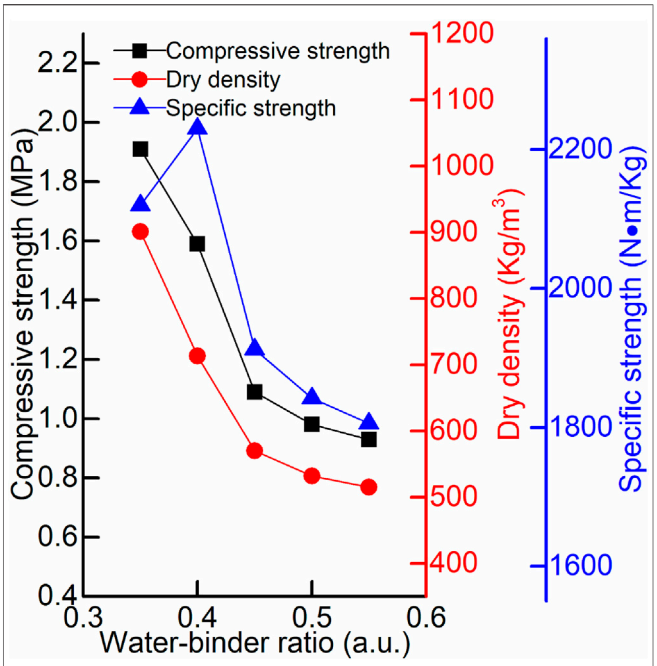

FIGURE 4 | The compressive strength, dry density and specific strength of geopolymer-based foam concrete at the age of 28-day (water-binder ratio from 0.35 to 0.55).

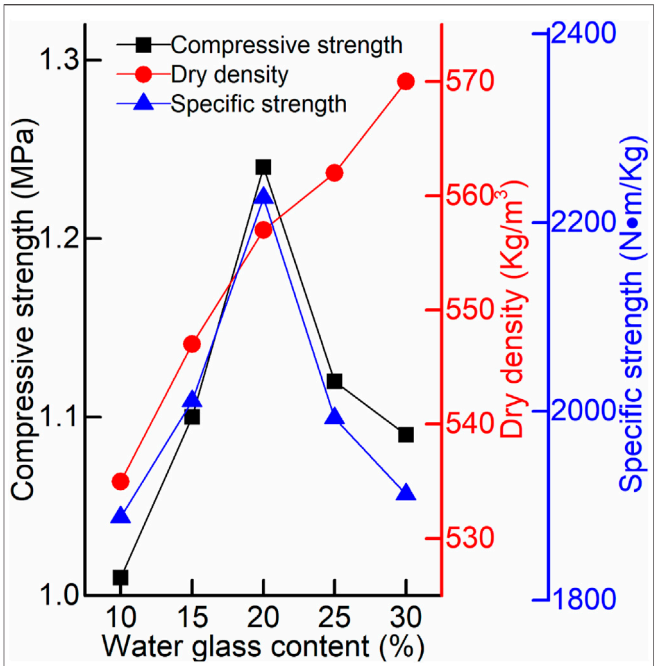

FIGURE 6 | The compressive strength, dry density and specific strength of geopolymer-based foam concrete at the age of 28-day (water glass content from 10 to 30%).

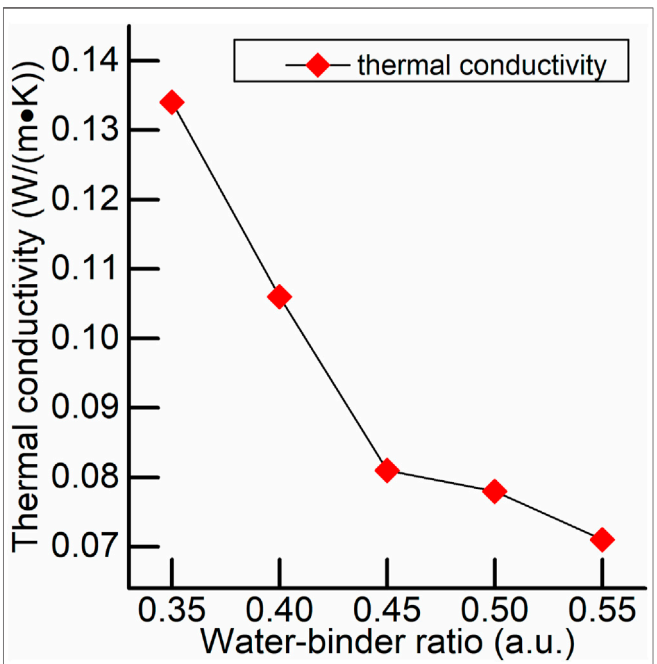

FIGURE 5 | The thermal conductivity of geopolymer-based foam concrete at the age of 28-day (water-binder ratio from 0.35 to 0.55).

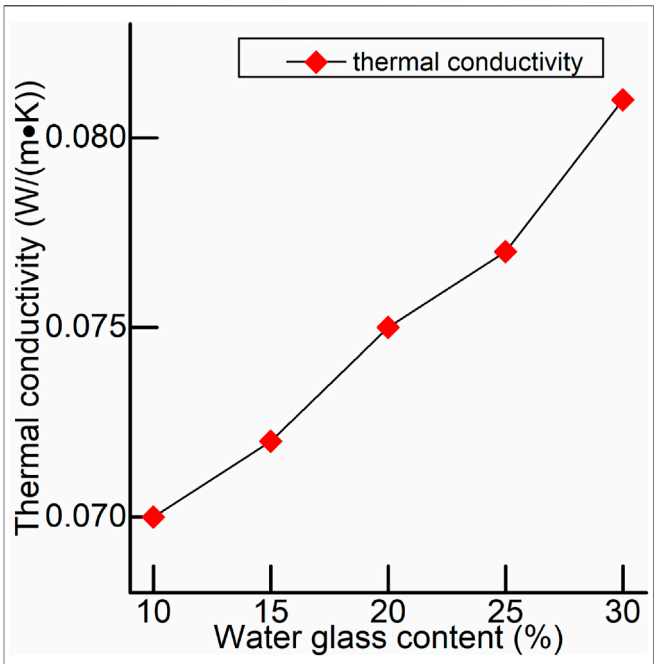

FIGURE 7 | The thermal conductivity of geopolymer-based foam concrete at the age of 28-day (water glass content from 10 to 30%).

water glass modulus. The foam content is defined as ratio of the mass of foaming agent and gelling material required to prepare the foam. The water-binder ratio refers to the ratio of the total water consumption to the mass of the cementations material in the material preparation process. The water glass content is the ratio of the pure water glass in the liquid water glass to the mass of

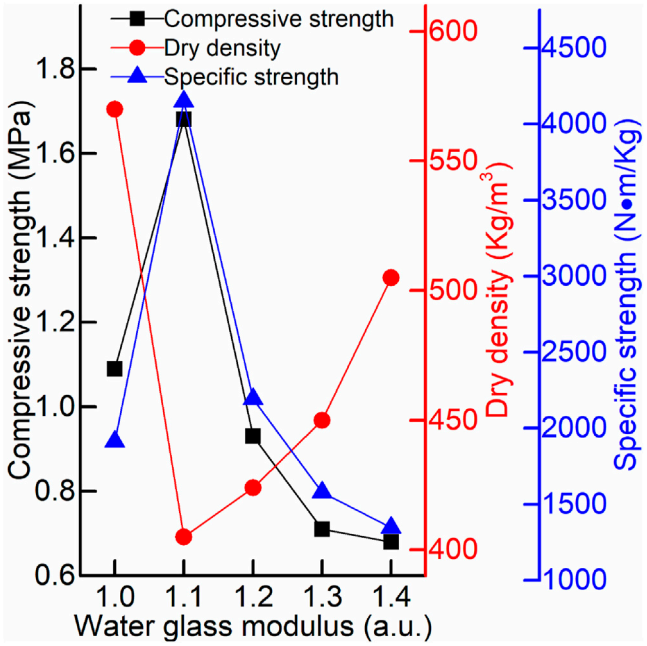

FIGURE 8 | The compressive strength, dry density and specific strength of geopolymer-based foam concrete at the age of 28-day (water glass modulus from 1.0 to 1.4).

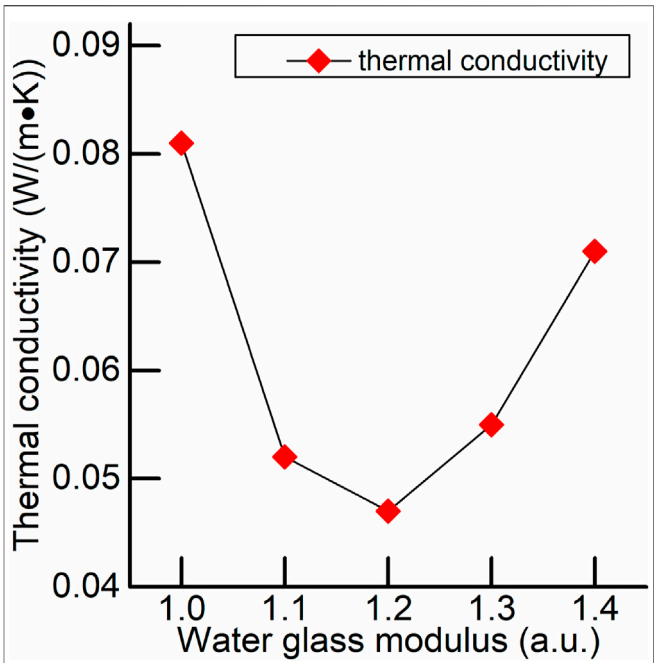

FIGURE 9 | The thermal conductivity of geopolymer-based foam concrete at the age of 28-day (water glass modulus from 1.0 to 1.4).

the cementitious material. The water glass modulus is n in the molecular formula of water glass (n in $Na_2O{\cdot}nSiO_2$).

3.1.1 Foam Content

For the research of influence of foam content on the performance of geopolymer-based foam concrete, the foam content was increased from 0.30 to 1.58% during the preparation process while keeping other conditions unchanged. The elementary mix proportions are summarized in **Table 2**. The compressive strength, dry density and specific strength of geopolymer-based foam concrete at the age of 28-day are shown in **Figure 2**. It can be found that the compressive strength and dry density of the geopolymer-based foamed concrete decreases continuously with the increase of the foam content. The above phenomenon is the result of the continuous decrease of the concrete density as the foam content increases. On the other hand, the continuous increase of foam content will cause the foam to burst and merge, which in turn makes the pores larger. Moreover, the curve of specific strength shows a trend of first increasing and then decreasing. This is because there is a significant change in the rate of decrease of the concrete dry density as the foam content increases. When the foam content increases to 0.62%, the specific strength reaches the maximum. As is shown in **Figure 3**, the thermal conductivity of foam concrete decreases with the increase of foam content, which indicates that the voids inside the concrete help to improve its thermal insulation performance.

3.1.2 Water-Binder Ratio

In **Table 2**, the foam content was fixed at 0.94%, the water-binder ratio was changed in the range of 0.35–0.55, and the preparation process was repeated. As the water-binder ratio increases, the consistency of the slurry decreases, the fluidity increases, and the stability of the concrete structure decreases. In addition, the shear resistance of the slurry to the bubbles is also continuously reduced, the bubbles continue to float up and tend to concentrate, and stress defects are prone to appear in the concentrated position. The above factors will cause the compressive strength and dry density of concrete to decrease, as shown in **Figure 4**. In the same way as above (**Figure 2**), the sudden change in the rate of decrease of the concrete dry density results in the fluctuation of the specific strength curve. When the water-binder ratio is between 0.35 and 0.45, the curve has an inflection point. The pores of foamed concrete increase with the water-binder ratio, which in turn leads to a decrease in thermal conductivity. The changing trend of the curve in **Figure 5** just confirms this process.

3.1.3 Water Glass Content

Among the materials listed in **Table 2**, the foam content was kept at 0.94% while the water glass content was gradually increased from 10 to 30%, and the preparation process was repeated. In **Figure 6**, with the increase in the amount of water glass, the compressive strength of the concrete first increases and then decreases. The main reason for this condition is the change in the degree of alkali excitation: as the content of water glass increases, the content of NaOH must be increased to keep the modulus of the water glass unchanged, resulting in stronger alkali excitation and compressive strength. However, when the content of water glass reaches a certain level, it will directly react with the geopolymer and weaken the excitation effect, thereby reducing the compressive strength. The increase of the water glass content

TABLE 3 | Scheme of the orthogonal experiments.

No.	Factors (A, B, C, and D)				Results	
	Foam content (%)	Water-binder ratio (a.u.)	Water glass content (%)	Water glass modulus (a.u.)	Specific strength (N·m/Kg)	Thermal conductivity (W/(m·K))
1	1 (0.30%)	1 (0.35)	1 (10%)	1 (1.0)	2011.3	0.165
2	1	2 (0.45)	2 (20%)	2 (1.2)	2997.5	0.088
3	1	3 (0.55)	3 (30%)	3 (1.4)	1157.2	0.101
4	2 (0.94%)	1	2	3	1519.9	0.126
5	2	2	3	1	1912.3	0.081
6	2	3	1	2	2067.6	0.077
7	3 (1.58%)	1	3	2	1671.1	0.094
8	3	2	1	3	607.8	0.068
9	3	3	2	1	1401.7	0.065

TABLE 4 | Analysis of the experimental results of specific strength.

Item	Factors (A, B, C and D)			
	Foam content (%)	Water-binder ratio (a.u.)	Water glass content (%)	Water glass modulus (a.u.)
K_1 (k_1)	6166.0(2055.3)	5202.3(1734.1)	4686.7(1562.2)	5325.3(1775.1)
K_2 (k_2)	5499.8(1833.3)	5517.6(1839.2)	5919.1(1973.0)	6736.2(2245.4)
K_3 (k_3)	3680.6(1226.9)	4626.5(1542.2)	4740.6(1580.2)	3284.9(1095.0)
R	828.4	297.0	410.8	1150.4
the optimal levels	1	2	1	1
the optimal combination	$A_1B_2C_2D_2$			
order of influencing factors	D>A>C>B			

TABLE 5 | Analysis of the experimental results of thermal conductivity.

Items	Factors (A, B, C and D)			
	Foam content (%)	Water-binder ratio (a.u.)	Water glass content (%)	Water glass modulus (a.u.)
K_1 (k_1)	0.354(0.118)	0.385(0.128)	0.310(0.103)	0.311(0.104)
K_2 (k_2)	0.284(0.095)	0.237(0.079)	0.279(0.093)	0.259(0.086)
K_3 (k_3)	0.227(0.076)	0.243(0.081)	0.276(0.092)	0.295(0.098)
R	0.042	0.049	0.011	0.018
the optimal levels	3	2	3	2
the optimal combination	$A_3B_2C_3D_2$			
order of influencing factors	B>A>D>C			

improves the stability of the unhardened concrete paste, that is, increases the shear resistance. As can be seen in **Figure 6**, the larger shear resistance causes a large amount of foam to break, reducing the voids of the concrete, and thereby increasing the dry density of the concrete. While the water glass content is increasing, the specific strength of the geopolymer-based foam concrete first increases and then decreases. When the water glass content is 20%, the specific strength reaches the maximum. The increase in the amount of water glass will reduce the voids of the foamed concrete, thereby accelerating the process of heat conduction, as described in the experimental results given in **Figure 7**.

3.1.4 Water Glass Modulus

The foam content listed in **Table 2** was kept at 0.94%, while the water glass modulus was gradually increased from 1.0 to 1.4. The compressive strength, dry density and specific strength of geopolymer-based foam concrete at the age of 28-day are shown in **Figure 8**. The increase in the modulus of the water glass causes a corresponding increase in the Si component. The appropriate increase of the Si component is conducive to the formation of C-S-H gel, thereby increasing the compressive strength of concrete and reducing its dry density. However, when the modulus of the water glass is too large, the alkaline solution will not be able to fully stimulate the activity of the slag because the pH value is not high enough. At this time, the changes in compressive strength and dry density are opposite to the above, and then the maximum value of the specific strength curve appears. In **Figure 9**, the fluctuation of the thermal conductivity curve indicates that a moderate increase in the modulus of the water glass produces more pores, but when it

reaches a certain level, the effect of increasing the pores is no longer obvious. Instead, the increase in dry density caused by the introduction of Si components dominates.

3.2 Orthogonal Experiment and Range Analysis

3.2.1 Orthogonal Experiment

Orthogonal experiments can not only reduce the number of repeated experiments, but also help to understand the overall experimental situation through the analysis of some representative points. For this research, the foam content, water-binder ratio, water glass content and water glass modulus are considered as independent factors. Within the optimal range of these factors, three typical values are taken for each to design the $L_9(3^4)$ orthogonal scheme shown in **Table 3**, where 9 represents the orthogonal combinations of factors, 3 represents the levels of each factor, and 4 represents the number of factors. As shown in **Table 3**, the orthogonal experiment table must satisfy orthogonality, representativeness and comprehensive comparability. Orthogonality requires that the number of occurrences of each level in the same column is equal. Representativeness means that the experimental points in the orthogonal experiment table are evenly distributed among all possible experimental points. The comprehensive comparability ensures that the interference of other factors is eliminated to the greatest extent in the effect of each level of each factor, so that the influence of different levels of the factor on the experimental indicators can be comprehensively compared.

3.2.2 Range Analysis

In order to meet the main requirements of light weight, sturdiness and heat preservation of building enclosure materials, the orthogonal experiments were carried out with specific strength and thermal conductivity as the indicators. Range analysis is an intuitive data processing method for orthogonal experiments. Through this method, the degree of influence of each factor on a certain indicator can be evaluated, and the optimal combination of each factor for the indicator can be obtained. In **Tables 4**, **5** used for data analysis, K_i represents the sum of experimental results corresponding to the ith level of a certain factor, and k_i in the bracket is the mean value of K_i. When k_i reaches the maximum value, i is the optimal level of this factor. Once the optimal levels of each factor are determined, the optimal combination can be obtained directly. The difference between the maximum and minimum values of k_i is the range R:

$$R = \max(k_i) - \min(k_i). \tag{4}$$

The larger the R value, the greater the influence of the change of this factor on the experimental results. According to this, the order of the factors affecting the certain indicator can be determined. From the results listed in **Table 4**, it can be seen that the water glass modulus has the greatest influence on the specific strength, followed by the foam content, the water glass content and the water-binder ratio. When the foam content, water-binder ratio, water glass content and water glass modulus are 0.30%, 0.45, 20%, and 1.2, the maximum specific strength can be obtained. Similarly, it can be seen from **Table 5** that the factors affecting the thermal conductivity are water-binder ratio, foam content, water glass modulus and water glass content in order. For severe cold regions, heat preservation is the basic requirement of building enclosure structure, so the optimal combination of parameters should correspond to the minimum value but not the maximum value of thermal conductivity. This explains why the optimal combination in **Table 5** is A3B2C3D2 instead of A1B1C1D1. The thermal conductivity obtained by a separate experiment is 0.044.

4 CONCLUSION

The preparation and characterization methods of geopolymer-based lightweight foam concrete are reported in the paper. The influences of foam content, water-binder ratio, water glass content and water glass modulus on the performance indicators of the prepared foam concrete are studied. Based on the experimental results, the following conclusions are drawn:

1) Compared with several other parameters, the water-binder ratio has the most significant effect on the thermal conductivity.
2) With the continuous increase in the foam content or water-binder ratio, the compressive strength, dry density and thermal conductivity of geopolymer-based foam concrete at the age of 28-day have been continuously reduced.
3) When the content of water glass increases, the compressive strength of geopolymer-based foam concrete at the age of 28-day first increases and then decreases, while the dry density and thermal conductivity continue to increase.
4) Through orthogonal optimization experiment and range analysis, it can be known that the optimal levels of foam content, water-binder ratio, water glass content and water glass modulus for thermal conductivity is 1.58%, 0.45, 30%, and 1.2.

DATA AVAILABILITY STATEMENT

The raw data supporting the conclusion of this article will be made available by the authors, without undue reservation.

AUTHOR CONTRIBUTIONS

The authors contributed to the present study as follows: MC and DS: conceptualization; MC and KZ: methodology; MC, SZ, and KZ: validation; MC: formal analysis, writing—original draft preparation; DS: investigation and writing—review and editing; SZ: resources, software, and visualization. All authors have read and agreed to the published version of the manuscript.

FUNDING

This research was funded by Natural Science Foundation of Inner Mongolia Autonomous Region (China), Grant number 2018BS06004; National Natural Science Foundation (China),

Grant number F030608; Scientific Research Project of Inner Mongolia University for the Nationalities (China), Grant number NMDYB19065.

REFERENCES

Amran, Y. H. M., Farzadnia, N., and Abang Ali, A. A. (2015). Properties and Applications of Foamed concrete; a Review. *Construction Building Mater.* 101 (P1), 990–1005. doi:10.1016/j.conbuildmat.2015.10.112

Chang, R.-d., Soebarto, V., Zhao, Z.-y., and Zillante, G. (2016). Facilitating the Transition to Sustainable Construction: China's Policies. *J. Clean. Prod.* 131, 534–544. doi:10.1016/j.jclepro.2016.04.147

Fan, J.-L., Wang, J.-X., Hu, J.-W., Wang, Y., and Zhang, X. (2019). Optimization of China's Provincial Renewable Energy Installation Plan for the 13th Five-Year Plan Based on Renewable Portfolio Standards. *Appl. Energ.* 254, 113757. doi:10.1016/j.apenergy.2019.113757

Hardjito, D., Wallah, S. E., Sumajouw, D. M. J., and Rangan, B. V. (2004). Factors Influencing the Compressive Strength of Fly Ash-Based Geopolymer concrete. *Civil Eng. Dimension.* 6 (2), 88–93. doi:10.9744/ced.6.2

He, M. (2017). Polyurethane Foam Technology in Green Building Eco-Efficiency Design (In Chinese). *Bull. Sci. Technol.* 33 (1), 174–177. doi:10.13774/j.cnki.kjtb.2017.01.037

Hill, D. (2013). Ancient Roman Concrete Could Hold Secrets to Improving Modern Construction. *Civ. Eng. Mag. Arch.* 83 (9), 44–45. doi:10.1061/ciegag.0000655

Hou, M., Wang, Y., Zhao, H., Zhang, Q., Xie, Q., Zhang, X., et al. (2018). Halogenated Flame Retardants in Building and Decoration Materials in China: Implications for Human Exposure via Inhalation and Dust Ingestion. *Chemosphere* 203, 291–299. doi:10.1016/j.chemosphere.2018.03.182

Huang, Y. (2013). Development of Foreign Building Saving-Energy Technology. *Adv. Mater. Res.* 671–674 (2), 2126–2128. doi:10.4028/www.scientific.net/AMR.671-674.2126

Liu, M. Y. J., Alengaram, U. J., Santhanam, M., Jumaat, M. Z., and Mo, K. H. (2016). Microstructural Investigations of palm Oil Fuel Ash and Fly Ash Based Binders in Lightweight Aggregate Foamed Geopolymer concrete. *Construction Building Mater.* 120, 112–122. doi:10.1016/j.conbuildmat.2016.05.076

Liu, Y., Yan, H., and Lam, J. C. (2014). Thermal comfort and Building Energy Consumption Implications – A Review. *Appl. Energ.* 115 (4), 164–173. doi:10.1016/j.apenergy.2013.10.062

Mydin, M. A. O., and Wang, Y. C. (2011). Structural Performance of Lightweight Steel-Foamed concrete-steel Composite walling System under Compression. *Thin-Walled Structures* 49 (1), 66–76. doi:10.1016/j.tws.2010.08.007

Ramamurthy, K., Kunhanandan Nambiar, E. K., and Indu Siva Ranjani, G. (2009). A Classification of Studies on Properties of Foam concrete. *Cement and Concrete Composites* 31 (6), 388–396. doi:10.1016/j.cemconcomp.2009.04.006

Silvestre, J., Pargana, N., de Brito, J., Pinheiro, M., and Durão, V. (2016). Insulation Cork Boards-Environmental Life Cycle Assessment of an Organic Construction Material. *Materials* 9 (5), 394. doi:10.3390/ma9050394

ACKNOWLEDGMENTS

We would also like to thank Mrs. Lynn for language editing.

Tang, S., Xu, Y., Zhu, G., and Fang, W. (2011). Orthogonal experiment Optimum Design in the Power of the Rotor on Straight-Bladed Vawt. *Energ. Proced.* 12, 856–861. doi:10.1016/j.egypro.2011.10.113

Valore, R. C. (1954). Cellular Concretes Part 1 Composition and Methods of Preparation. *ACI J. Proc.* 50 (5), 773–796. doi:10.14359/11794

Vuong, X. T., Prietzel, J., and Heitkamp, F. (2016). Measurement of Organic and Inorganic Carbon in Dolomite-Containing Samples. *Soil Use Manage* 32 (1), 53–59. doi:10.1111/sum.12233

Wang, Z., Gao, H., Liu, H., Liao, L., Mei, L., Lv, G., et al. (2020). Inorganic thermal Insulation Material Prepared from Pitchstone. *J. Building Eng.* 32 (2), 101745. doi:10.1016/j.jobe.2020.101745

Xiao, J., and Ding, T. (2013). Research on Recycled concrete and its Utilization in Building Structures in china. *Front. Struct. Civ. Eng.* 7 (3), 215–226. doi:10.1007/s11709-013-0212-z

Xuan, W., and Leung, D. (2011). Optimization of Biodiesel Production from Camelina Oil Using Orthogonal experiment. *Appl. Energ.* 88 (11), 3615–3624. doi:10.1016/j.apenergy.2011.04.041

Yang, H., Jiang, Y., Liu, H., Xie, D., Wan, C., Pan, H., et al. (2018). Mechanical, thermal and Fire Performance of an Inorganic-Organic Insulation Material Composed of Hollow Glass Microspheres and Phenolic Resin. *J. Colloid Interf. Sci.* 530, 163–170. doi:10.1016/j.jcis.2018.06.075

Yang, S., Yao, X., Li, J., Wang, X., Zhang, C., Wu, S., et al. (2021). Preparation and Properties of Ready-To-Use Low-Density Foamed concrete Derived from Industrial Solid Wastes. *Construction Building Mater.* 287 (1), 122946. doi:10.1016/j.conbuildmat.2021.122946

Conflict of Interest: The authors declare that the research was conducted in the absence of any commercial or financial relationships that could be construed as a potential conflict of interest.

Publisher's Note: All claims expressed in this article are solely those of the authors and do not necessarily represent those of their affiliated organizations, or those of the publisher, the editors and the reviewers. Any product that may be evaluated in this article, or claim that may be made by its manufacturer, is not guaranteed or endorsed by the publisher.

frontiers in Materials

ORIGINAL RESEARCH
published: 13 December 2021
doi: 10.3389/fmats.2021.788079

Study on Metakaolin Impact on Concrete Performance of Resisting Complex Ions Corrosion

Chen Xupeng[1]*, *Sun Zhuowen*[2] and *Pang Jianyong*[1]

[1]School of Civil Engineering and Architecture, Anhui University of Science and Engineering, Huainan, China, [2]School of Transportation and Civil Engineering, Nantong University, Nantong, China

The main purpose of this study is to determine the metakaolin (MK) impacts on the concrete durability when the concrete is subjected to joint corrosion of SO_4^{2-},Mg^{2+} and, Cl^-. Four groups of concrete test samples, which contained different MK contents, were designed and tested in order to see their physical property changes and macro-morphology differences during the cyclic corrosion process. And a series of approaches, including XRD, FTIR, SEM, and EDS, were applied to study the concrete phase composition changes and the micro-morphology features of all groups. According to the test results, when reaching 20 cycles, the concrete sample with 10% MK showed the best concrete physical properties; when reaching 120 cycles, the concrete with 5% MK content showed the best durability, produced similar amount of corrosion products to ordinary concrete, and presented relatively compacted micro-structure and small internal porosity. Mg^{2+} actually has a great impact on metakaolin. The corrosion product quantity increased significantly when MK admixture reached 15%. Due to the great number of produced M-S-H, the corrosive ions damaged the concrete for a second time, leading to serious aggregate peeling-off, powder surface of test samples, and porous micro-structure.

Keywords: concrete, metakaolin, dry-wet alternation, ion corrosion, micro-analysis

OPEN ACCESS

Edited by:
Dake Xu,
Northeastern University, China

Reviewed by:
Jie Hu,
South China University of Technology, China
Yang Zhou,
Southeast University, China

***Correspondence:**
Chen Xupeng
1933310001@stmail.ntu.edu.cn

Specialty section:
This article was submitted to "Structural Materials", a section of the journal Frontiers in Materials

Received: *04 October 2021*
Accepted: *15 November 2021*
Published: *13 December 2021*

Citation:
Xupeng C, Zhuowen S and Jianyong P (2021) Study on Metakaolin Impact on Concrete Performance of Resisting Complex Ions Corrosion. Front. Mater. 8:788079. doi: 10.3389/fmats.2021.788079

INTRODUCTION

With the rapid development of economy and continuous improvement of industrialization, large infrastructures, such as high-rise buildings, large bridges, and tunnels, have been constructed one after another. However, behind the huge economic benefits brought by the above-mentioned infrastructures, there is a great concern about the environmental pollution and energy consumption (Bildirici, 2019). The carbon dioxide (CO_2) produced due to cement production accounts for 8% of total CO_2 emission of the whole globe (Xi et al., 2016; Andrew, 2019). And for the reduction of greenhouse gas emission of the cement industry around the world, the most effective way is to minimize the cement use (Environment et al., 2018), which can be achieved by replacing certain proportion of cement by mineral admixture. Both the coal fly ash and blast furnace slag are the commonly used mineral admixtures (Supit and Shaikh, 2014; Juenger and Siddique, 2015; Hemalatha and Ramaswamy, 2017), but for common coal fly ash, though it can effectively reduce cement dosage and lower the economic cost, it has adverse effect on concrete performance at initial stage due to its low activity and large particle size (Jiang, 2005).

Metakaolin is a highly active pozzolanic material, which is produced by mineral resource of Kaolin burnt in 500–900°C temperature. Kaolin actually spreads widely with rich reserves around the

world. Taking China for instance, Kaolin reserve reaches 3 billion tons, among which, 3/4 hasn't been exploited and utilized. And this data only ranks fifth in the globe (Zhang et al., 2021a). The pozzolanic activity of metakaolin is even higher than silica fume (Wei et al., 2019), so that the metakaolin can engage in secondary reaction with $Ca(OH)_2$ during hydration process to produce large amount of C-S-H, as well as hydrated calcium aluminate and calcium sulphoaluminate hydrate. The hydration products can reduce the porosity of the concrete (Jiang et al., 2015), and enhance the cementious capability of the aggregates and the slurry (Mo et al., 2020). Zeng et al.(2014) believed that the metakaolin can reduce the pores in mortar, thereby refining the pore diameter inside the mortar. Besides, the metakaolin can also improve the mechanical properties of the concrete at the initial stage (Chen et al., 2021a), which perfectly solve the adverse effects brought by traditional mineral admixture (ordinary coal fly ash and blast furnace slag) to the concrete.

Sulfate has always been a key environmental factor that can seriously damage the concrete from both chemical and salt crystallization aspects. The chemical corrosion is represented by the SO_4^{2-} invasion into the concrete, which could result in micro structural damage and hydration product damage (Gu et al., 2019a). The salt crystallization corrosion is mainly represented by the gypsum crystal expansion and the mirabilite crystal separating-out, which produce crystal pressure inside the concrete (Feng et al., 2014). Many researchers have found that adding mineral admixture could help to improve the concrete performance in resisting sulfate corrosion (Huang et al., 2017; Nosouhian et al., 2019; Zhang et al., 2021b). Alapour et al. (Alapour and Hooton, 2017) determined from their study that, the application of certain amount of slag can delay the concrete deterioration caused by sulfate. Nabil M(Al-Akhras, 2006) believed that, replacing cement with 0–15% metakaolin can significantly enhance the concrete performance in resisting sulfate corrosion. However, in practical engineering, the concrete is usually subjected to corrosion brought by multiple types of ions, especially SO_4^{2-}, Mg^{2+}, and Cl^-. These three types of ions, which are widely distributed in saline soil and ocean, have the most serious adverse impact on concrete (Gu et al., 2019b). For the studies on metakaolin concrete when suffering corrosion brought by multiple types of ions, the test of Mardani (Mardani-Aghabaglou et al., 2014) showed that, facing the joint corrosion of Mg^{2+} and SO_4^{2-}, the adding of metakaolin would ease the damage brought by concrete expansion, but Lee et al. (2005) expressed the contrary opinion, believing that the adding of metakaolin could worsen the concrete damage when facing the joint corrosion of Mg^{2+} and SO_4^{2-}.

The aforementioned studies demonstrate the advantages of mineral admixtures. However, most of these studies focus on the concrete corrosion caused by a single type of corrosive ion, lacking studies on metakaolin concrete corrosion caused by multiple types of ions. And even the existing researches obtained contradictory conclusions. As a matter of fact, the concrete could be affected by the coupling effects of dry-wet alternation and corrosive ion corrosion, such as the large temperature difference and large water evaporation phenomenon in salt lake areas of West China region, and the alternated flood and tide ebb tides in coastal environment regions. The dry-wet alternation can increase the concrete porosity and accelerate the corrosive ion filtration (Qi et al., 2017), but its physical corrosion effect is usually ignored. Moreover there are also problems to be solved, for example: do various metakaolin contents have different impacts on corrosion brought by multiple types of corrosive ions? Will different corrosion time result in different results?

To solve the above problems, the dry-wet alternation test was carried out, in which, the 5%$MgSO_4$+3.5%NaCl solution was taken as the corrosion medium, the concretes were added with 5, 10, and 15% metakaolin respectively, and the ordinary concrete was taken as the control group, in order to study the influences of different metakaolin contents on the concrete performance in resisting corrosion brought by multiple types of corrosive ions. The compressive strength and mass of the concrete were measured for each cycle. And the comparison on differences among all groups of concretes was made as well. A series of micro analysis approaches, including the X-ray diffraction (XRD), Fourier transform infrared spectrum (FTIR), scanning electron microscope (SEM), and energy dispersive spectrum (EDS), were applied to explore the degradation mechanism of concretes with different metakaolin contents at the time of being eroded by multiple ions.

TEST PROCESS

Raw Material of Test

According to the industrial standards and the references of relevant literature (Peng et al., 2019; Zhou et al., 2021), the P.O. 42.5 ordinary Portland cement produced in Huainan City, and the white-color metakaolin with about 1.8 μm average particle size produced by Shanghai Lingdong Company were applied in this test. The chemical compositions of the metakaolin and the cement are as shown in **Table 1**. And for the aggregates, the gravels with 5–15 mm continuous gradation were used as the coarse aggregates, which are featured in 1,543 kg/m³ bulk density and 2,630 kg/m³ apparent density; and the medium sands coming from Huaihe River were used as the fine aggregates, which are with about 2.9 fineness modulus, 1,577 kg/m³ bulk density, and 2,621 kg/m³ apparent density. And the Polycarboxylate-based superplasticizer with about 37% water reduction rate was used as the water reducer in this test.

Mix Proportion and Preparation of Test Samples

Relative materials show (Abdul Razak and Wong, 2005; Pouhet and Cyr, 2016) that, the maximum content of metakaolin added into concrete shall be no more than 20%; and on the other hand, adding 5–15% metakaolin into the concrete could effectively improve the mechanical properties of the concrete. Therefore, the concrete proportioning was finally determined according to the JGJ55-2011 *Specification for mix proportion design of ordinary concrete* (as shown in **Table 2**). In this test, the metakaolin was

TABLE 1 | Cement and metakaolin chemical composition (%).

Composition	CaO	SiO_2	Al_2O_3	Fe_2O_3	SO_3	K_2O	P_2O_5	MgO	Na_2O	Loss
Cement	68.66	21.93	3.72	2.57	1.09	0.67	0.33	0.07	0.12	0.84
Metakaolin	0.04	57.03	41.06	0.71	0.13	0.16	0.11	0.08	0.11	0.57

TABLE 2 | Mix proportion of concrete (kg/m³).

Number	Sand	Aggregate	Cement	Metakaolin	Water	Water reducing agent
MK0	619	1,101	500	0	180	3
MK5	619	1,101	475	25	180	3.5
MK10	619	1,101	450	50	180	4
MK15	619	1,101	425	75	180	4.5

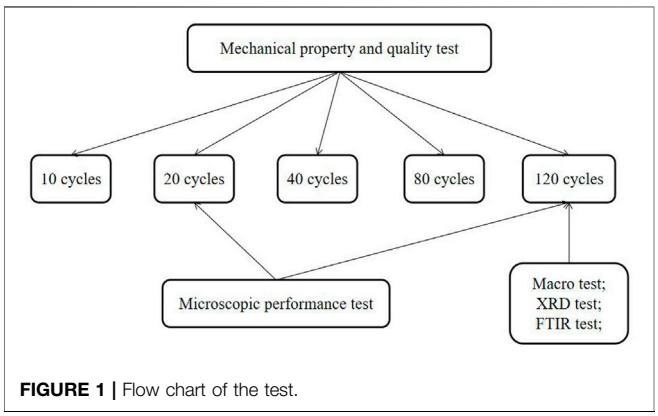

FIGURE 1 | Flow chart of the test.

used to equivalently replace 5, 10, and 15% Portland cements, based on which, the corresponding test samples were numbered as MK5, MK10, and MK15. Besides, the reference concrete was numbered as MK0 and taken as the control group. The concrete samples made for this test were non-standard blocks sized 100 × 100 × 100 mm. The process to make the concrete test samples is below: weigh and mix the sand and stone, and put the mixture into the mixer to mix for about 1 min, then weigh and mix the metakaolin and cement according to the ratio as shown in **Table 2** and mix for 2 mins until the cementing material and the aggregates are evenly mixed; finally, mix the water reducer with the clean water, and put the mixture into the mixer to mix with other materials evenly; after finishing the mixing, put the mixture into molds, and then move the molds to the vibration table to vibrate and compact; then put the molds aside and wait for 24 h; after that, demold and put the concrete samples in the standard curing room with (20 ± 2)°C temperature and over 95% humidity for 28 days before carrying out dry-wet alternation test.

Test Method

To simulate the physical and chemical corrosion in certain salt lake areas and coastal areas, the 5%$MgSO_4$+3.5%NaCl solution was taken as the corrosion medium, and the dry-wet alternation steps were determined according to the *Standard for test methods of long-term performance and durability of ordinary concrete* (GB/T50082-2009) (GB/T 50082-2009, 2009), the previous testing experience (Chen et al., 2021b), and the literature (Liu et al., 2020; Sun et al., 2021) for the test. The dry-wet alternation steps include: soak the test samples in the solution for 14 h → dry them in room temperature for 1 h → dry them in 60°C dryer for 8 h → cool them at room temperature for 1 h, totaling to 24 h per cycle. In order to maintain stable concentrations of all the solutions, we made new solutions and replaced every 10 days during the test. When the required cycles were reached, the tests on mechanical properties, mass, XRD, FTIR, macro, and micro performances were carried out on the test samples respectively. For specific flowchart of the test, please refer to **Figure 1**. Since the key study objects of this paper are the concretes that are added with different volumes of metakaolin, in order to show the differences among various groups of concrete samples obviously, the macro test, XRD test, and FTIR test were carried out when reaching the most representative "120 cycles".

When 10, 20, 40, 80, and 120 cycles were reached, the compressive strength and the mass of various groups of metakaolin concrete were tested. And the compressive-strength operation was performed according to GB/T50081-2002 specifications (GB/T 50081-2002, 2002). Since the test samples adopted in this test are non-standard blocks sized 100 × 100 × 100 mm, the coefficient of 0.95 was multiplied. Meanwhile the relative compressive strength was calculated according to **Eq. 1**. And the mass was measured by electronic balance (accurate to 0.01). Each test sample was weighed for three times, based on which, the average value was taken finally. And the rate-of-change of the mass was calculated by **Eq. 2**.

$$F_\alpha = 100\% \times \frac{F_N}{F_0} \tag{1}$$

Where F_α is the relative compressive strength, F_N is the compressive strength of concrete after N times of dry-wet alternation, F_0 is the MK concrete compressive strength that hasn't been eroded.

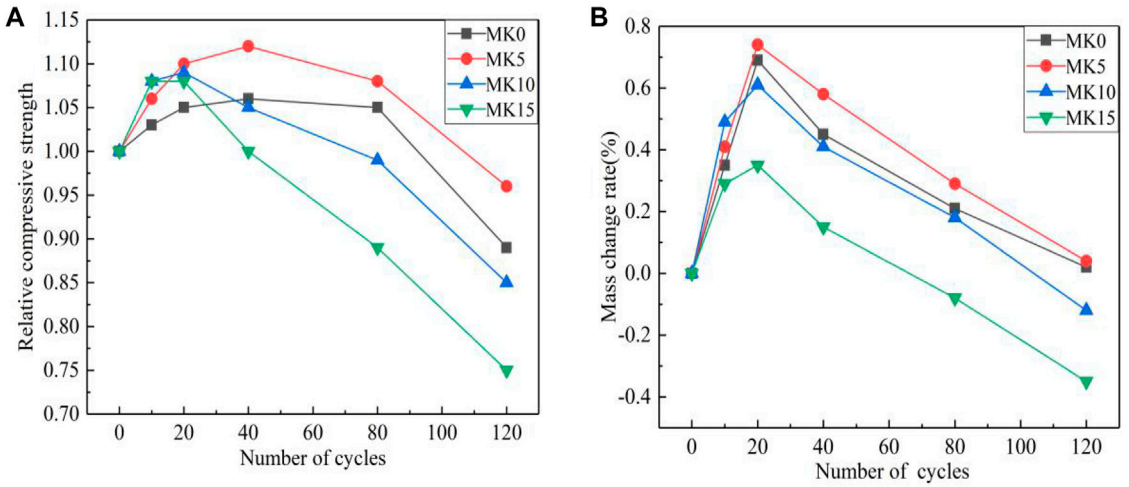

FIGURE 2 | Changes in physical properties of concrete: **(A)** Relative compressive strength; **(B)** Mass change rate.

$$\Delta M = 100\% \times \frac{M_N - M_0}{M_0} \quad (2)$$

Where ΔM is the mass change rate of the test sample, M_N is the test sample mass after N times of dry-wet alternations, and M_0 is the test sample mass before corrosion.

When reaching 120 cycles, XRD and FTIR tests were carried out on the concretes with different metakaolin contents in order to analyze the phase composition of the corrosion products. The D/max-2550 XRD machine with 5°~95°scanning range produced by Japan was used in this test. And the scanning step was set as 0.02 in the test; the NICOLET IS 50 infrared spectrometer with 350 cm^{-1}~7800 cm^{-1} wave number range produced by the USA was used for the FTIR test in this study.

When 20 and 120 cycles were reached, Hitachi S4800 cold field SEM produced by Japan and EDS machine were used to observe and analyze the micro morphology of each sample. The accelerating voltage is 5 KV. Adjust the magnification to 10,000 times when observing the samples with 20 cycles. For the samples with 120 cycles, set the magnification to 20,000 times or 50,000 times for observation. Before SEM observation, the mortar slices with 2–4 mm thickness were taken from the surface of the test samples and put into absolute ethyl alcohol to terminate hydration. After that, the slices were put into dryer with 60 ± 5°C temperature till reaching constant mass. The test samples were carried out with grinding and polishing treatment, as well as vacuuming and conductive coating treatment to improve the conductivity. Finally, the SEM test was carried out.

RESULTS

Changes of Physical Properties

Figure 2 shows the physical property changes of concretes added with 5, 10, and 15% metakaolin respectively. In general, the trend of relative compressive strength changes of the concrete added with metakaolin is: rising stage →flat stage→declining stage→rapid declining stage. And the trend of the mass changes is: rising stage →flat stage→declining stage.

For the corrosion time impact on concrete performance, at the initial stage (about 0–20 cycles), the corrosion products, such as ettringite and magnesium hydroxide, were produced firstly, which filled up the internal pores inside the concrete to some certain extent. This promoted the rising of the compressive strength and the mass of the concrete. Meanwhile due to the pozzolanic activity of the metakaolin, lots of hydration products were produced inside the concretes, so that the mass of the test samples increased slightly. However with the continuous increase of dry-wet alternation times, the corrosion products kept accumulating in quantity and volume, which resulted in cracking and mortar aggregates peeling-off on concrete surface. In this case, the compressive strength and the mass kept declining during this period.

For impacts of metakaolin contents on concrete performance, during 0–10 cycles, with the increase of metakaolin contents, the compressive strength improved gradually due to two reasons: first, the concrete during 0–10 cycles was still at hydration stage, and the large amount of Al_2O_3 contained in the metakaolin accelerated the hydration process (Coleman and Mcwhinnie, 2000); second, the small diameter of the metakaolin filled up the pores inside the cement, which resulted in particle gradation and improved the concrete compactness. However the metakaolin increase also brought with adverse effects. When the metakaolin content reached 10%, the relative compressive strength increased by 1.08% during the process of 0–10 cycles. But when the metakaolin content reached 15%, the increase of relative compressive strength still remained at 1.08%. That's because the metakaolin has large specific surface area, and its particles are in flake shape. Excessive content of metakaolin would induce agglomeration. Therefore, too much metakaolin is non-conductive to the concrete performance development (Vance et al., 2013). With the increase of cycles, the physical

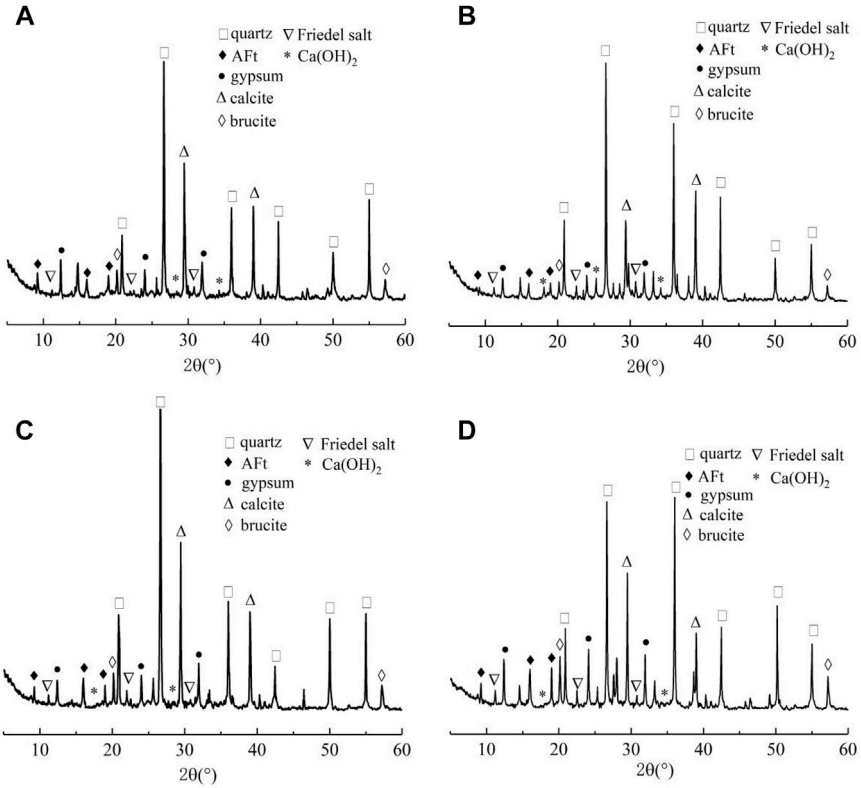

FIGURE 3 | XRD pattern of specimen when erosion days are 120 days: **(A)** MK0; **(B)** MK5; **(C)** MK10; **(D)** MK15.

property of each group of concrete samples are: MK5 > MK0 > MK10 > MK15. The metakaolin contains a great number of SiO_2, so it can promote the massive M-S-H generating. And the forming of M-S-H can soften the cement, inducing serious declining of the physical properties of the concrete. When reaching 120 cycles, the relative compressive strength of MK10 was only 0.85 while the mass changing rate was −0.12%. And the same two data of MK15 were 0.75% and −0.35% respectively. Compared with MK10 and MK15, MK5 physical properties always ranked at high position, reaching 0.96% relative compressive strength and 0.04% mass changing rate after 120 cycles. That's mainly because the metakaolin makes MK5 compact during the concrete hydration process, and the relatively small metakaolin content prevents massive generating of M-S-H, which reduces the chemical corrosion brought to the concrete.

Phase Composition Analysis

X-Ray Diffraction Analysis

The X-ray diffraction was applied to analyze the corrosion products, in order to further study the concrete degradation mechanism under corrosion of multiple types of ions, and study the influences of metakaolin content changes on the concrete phase composition.

Figure 3 shows the XRD maps of concrete with different metakaolin contents. With the changes of metakaolin contents, the phase compositions vary, which is mainly manifested in the disappearing and occurrence of diffraction peaks and the intensity changes. The two highest diffraction peaks in the figure are quartz and calcite, which are both from the aggregates of the concrete. Besides, it can be seen that the diffraction peaks of $Ca(OH)_2$ and Friedel salt of the four types of concretes are quite weak. That's because at the later stage of corrosion, the Mg^{2+} and SO_4^{2-} enter inside the concrete, consuming great number of $Ca(OH)_2$ and generating corrosion products of ettringite, gypsum, and magnesium hydroxide. This leads to sharp drop of pH value inside the test samples. Meanwhile, Friedel salt can decompose gradually in low-pH environment (Cheng et al., 2019). By making comparison on the four groups of concretes, it can be found that the diffraction peaks of $Ca(OH)_2$ and Friedel salt of MK5 were higher than those of MK0, MK10, and MK15, and on the other hand, the diffraction peaks of the its corrosion products, such as the ettringite, gypsum, and magnesium hydroxide, were lower than those of other groups. Based on the above, it can be deduced that, MK5 has better performance in resisting compound salts corrosion than the other two groups at this time. That is because in the early stage of corrosion, the concrete compactness is high due to the effect of metakaolin, and the corrosive ion diffusion speed is slowed down. After that, with the increase of corrosion time, it generated limited volume of M-S-H inside MK5 concrete, and the undecalcified C-S-H physically absorbed SO_4^{2-} and Cl^- (Yuan et al., 2009) to some extent, which reduced the generating of corrosion products, and improved the

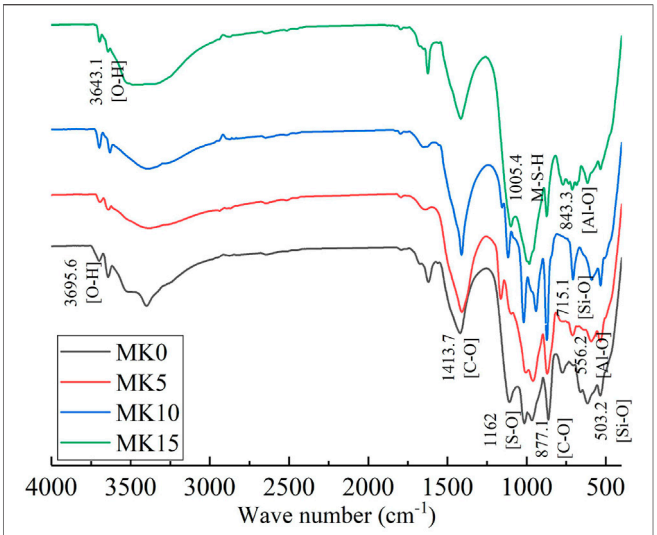

FIGURE 4 | FTIR diagram of concrete with different metakaolin content.

concrete durability. For MK0, MK10, and MK15, since these groups of samples had weaker performance in resisting corrosion and low pH than those of MK5 at this time, they experienced ettringite decomposition and weakened generating of secondary ettringite, but accelerated generating of gypsum. Besides, Mg^{2+} diffused faster in low pH environment (De Weerdt et al., 2019), which greatly increased the contents of M-S-H and magnesium hydroxide. And since the metakaolin contained massive active SiO_2, the increase of metakaolin content accelerated the generating of M-S-H, and resulted in worse damage to the concrete. Therefore the diffraction peaks of ettringite, gypsum, and magnesium hydroxide of MK10 are higher than those of MK5 and MK0. And the diffraction peaks of corrosion products in MK15 reach the maximum.

Fourier Transform Infrared Spectrum Analysis

It is hard to use X-ray diffraction to identify ettringite and thaumasite. Therefore the FTIR spectrum was applied for testing in this study, which can not only identify the ettringite and thaumasite, but also prove the existence of M-S-H.

Figure 4 shows the infrared spectrogram of the concretes with different metakaolin contents. It can be seen that stretching vibration peak of S-O(SO_4^{2-}) exist at 1,162 cm^{-1}. Besides, bending vibration peaks corresponding to Al-O bond also exist at wave numbers of 843.3 and 556.2 cm^{-1}. That's the evidence proving the existence of ettringite. The strong peaks at 877.1 and 1,413.7 cm^{-1} are induced by the bending and stretching vibrations of C-O bond (CO_3^{2-}). This indicates the existence of massive calcite (Wang et al., 2019) coming from the concrete aggregates. The silicon in the thaumasite and the hydroxyl combined in hexacoordinated form, generating the octahedron group. In this figure, the bending vibration peak of Si-O bond (SiO_6) appears at 503.2 cm^{-1}. And the stretching vibration peak corresponding to Si-O bond exists at 715.1 cm^{-1}. This indicates the existence of thaumasite in corrosion products (Deng et al., 2005).

It can be known from relative articles (Bernard et al., 2017) that, the characteristic peak of M-S-H in the figure appears at 1005.4 cm^{-1}. It can be seen that comparatively weak shoulder peaks of MK0 and MK5 appear at this position with similar peak sizes. This further indicates that, a few content of metakaolin added in concrete won't produce excessive M-S-H. MK10 shows comparatively sharp characteristic absorption peak here, indicating the enlargement of peak value at this position. The characteristic absorption peak of MK15 gets broader and the peak value increase further. Besides, compared to samples MK0 and MK5, peaks of MK10 and MK15 at 556.2 cm^{-1} become stronger with the increase of metakaolin contents. This shows that the ettringite content also increases gradually. Therefore the ettringite contents of MK15 and MK10 are higher than those of MK0 and MK5. This confirms to the conclusions obtained by XRD test. The characteristic absorption peak of O-H is at 3643.1 cm^{-1}, which is with small peak value. It means that the test samples contain $Ca(OH)_2$ (Song et al., 20142014) at this time, which is in extremely small amount. Through the XRD test and FTIR test, it can be known that the complex salt corrosion to the concrete produces complicated corrosion products. The generating of ettringite, gypsum, Friedel salt, magnesium hydroxide, M-S-H, and thaumasite consumes great number of $Ca(OH)_2$.

Macro Analysis

Figure 5 shows the macro-morphology images of the four types of concretes with different metakaolin contents that are subjected to corrosion of multiple types of ions after 120 cycles. Generally, three types of corrosive ions of Mg^{2+}, SO_4^{2-}, and Cl^- mainly cause peeling-off of surface aggregates, and cracking and peeling-off of corners. With the increase of metakaolin contents, the peeling-off of the surface mortar and aggregates seems more obvious.

MK0 is the ordinary concrete. It can be seen that significant deterioration appears on its edges. The edges are damaged and have small crack development. Holes can be seen on the bottom of the test samples. But the mortar particles peeling-off seems not serious on the surface of the concrete.

MK5 is the concrete with 5% metakaolin. Compared with MK0, MK5 is featured in better concrete integrity and less peeling-off of edges and corners, but significant surface aggregate peeling-off. Powders and slightly exposed coarse aggregates can be seen on the concrete surface. When the metakaolin content increases to 10%, large areas of aggregates peel off from the surface of MK10 concrete. Its exposed amount of coarse aggregates is significantly greater than that of the MK5, and is accompanied with big holes. When the metakaolin content reaches 15%, the damage to the concrete further gets worse. Compared with MK10, the surface mortar structure of MK 15 has been totally damaged by M-S-H. Edges of the test sample peel off. The concrete, as a whole, suffers serious damage.

Due to the high pozzolanic activity, the metakaolin could produce massive C-S-H in alkali environment. The two ions of calcium and magnesium are with similar radius of 4.1 and 4.3 radius respectively. So when the concrete is eroded by Mg^{2+}, the C-S-H could be easily decalcified and decomposed, forming non-cementing M-S-H. Besides, the active SiO_2 in metakaolin would

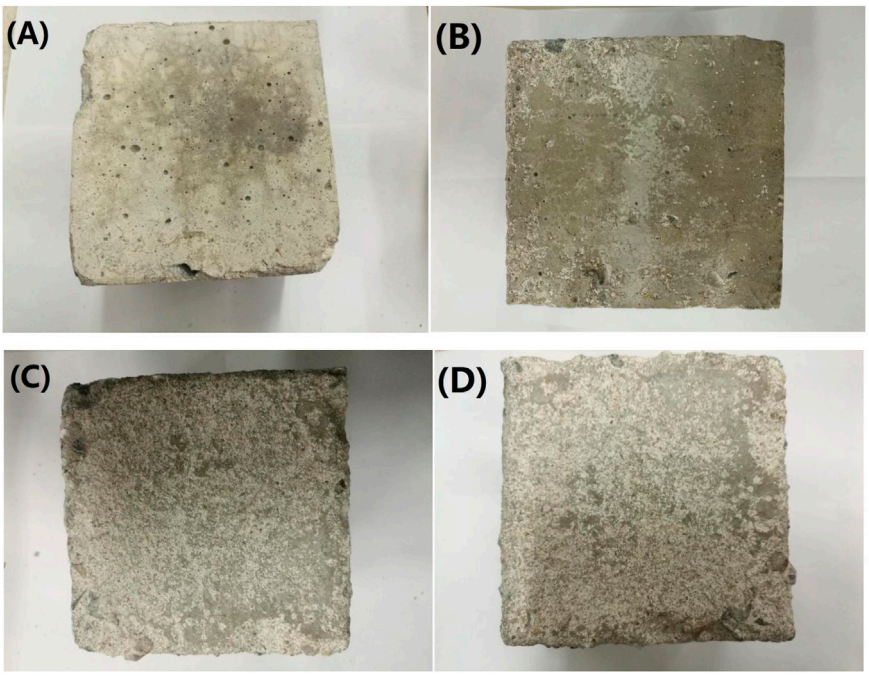

FIGURE 5 | Macro-morphology characteristics of the specimen when it is corroded by corrosive ions:**(A)** MK0; **(B)** MK5;**(C)** MK10; **(D)** MK15.

also promote the generating of M-S-H. Therefore, excessive metakaolin content would result in massive generating of M-S-H, seriously reducing the concrete durability.

Micro Analysis

Figure 6 shows the micro-morphology of the four groups of contents with different metakaolin contents after 20 cycles of corrosive ion corrosion. It can be seen that, at the initial stage of corrosion, thereare little corrosion products but many hydration products. The increase of metakaolin contents has a great impact on the micro-structure compactness and the pore characteristics of the concrete.

From **Figure 6**, it can be seen that, the MK0 micro-structure is compacted at this time. Besides the pores with different sizes on the surface, lots of needle-shaped ettringite inserted inside the pores can also be seen in this figure. Compared with MK0, the micro-structure of MK5 is more compacted. Though it has a small number of ettringite, the pores amount is comparatively reduced. Meanwhile at this time, most of the unhydrated particles and hydration products are closely connected. When the metakaolin content reaches 10%, the concrete surface is covered by massive C-S-H cementing materials in screen-shaped structure. Due to the high pozzolanic activity of the metakaolin, the cement and the metakaolin particles are covered by numerous hydration products, which further improves the compactness. However excessive metakaolin content would also result in agglomeration, reducing the concrete performance (Vance et al., 2013). That is also the reason causing the bad micro-structure connection, massive exposure of cement and metakaolin particles, and more significant pores and cracks of MK15 than the situations of MK10. Combining with the physical properties shown in **Figure 2**, it can be known that, concrete with proper metakaolin content has excellent durability at the early corrosion stage; when the metakaolin content reaches 10%, the concrete shows high compactness and most capable durability.

However when the corrosion time reaches 120 cycles, the micro-morphology of the four types of contents with different metakaolin contents are as shown in **Figure 7.** The EDS analysis was carried out in order to figure out the corrosion products, please see **Figure 8.**

When the corrosion reaches 120 cycles, the MK0 shows massive pores and very bad overall integrity. A small part of screen-shaped materials attach on its surface. The EDS analysis indicates that, the material was mainly composed of O,Ca,Si, and S. Therefore it can be inferred that the material is the hydration product C-S-H. At this time, there's only a little C-S-H, most of which have been converted into M-S-H. For MK5, it can be seen that many needle-shaped materials fill up the micro structure. And the EDS analysis results, as shown in **Figure 8B**, indicate that the material is mainly composed of Ca,S,Al, and O. According to the morphology features of this material (Sarkar et al., 2010; Nehdi et al., 2014), it can be inferred that the material is ettringite. These needle-shaped ettringite distribute randomly without any order, and are surrounded by a few pores and cracks. For MK10 with 10% metakaolin content, besides the needle-shaped ettringite, it also shows many plate-shaped corrosion products, which are proved to be composed of Ca,S, and O by EDS analysis. According to relative literature (Tan et al., 2017), it can be roughly judged that the material is gypsum. And at this time, the gypsum

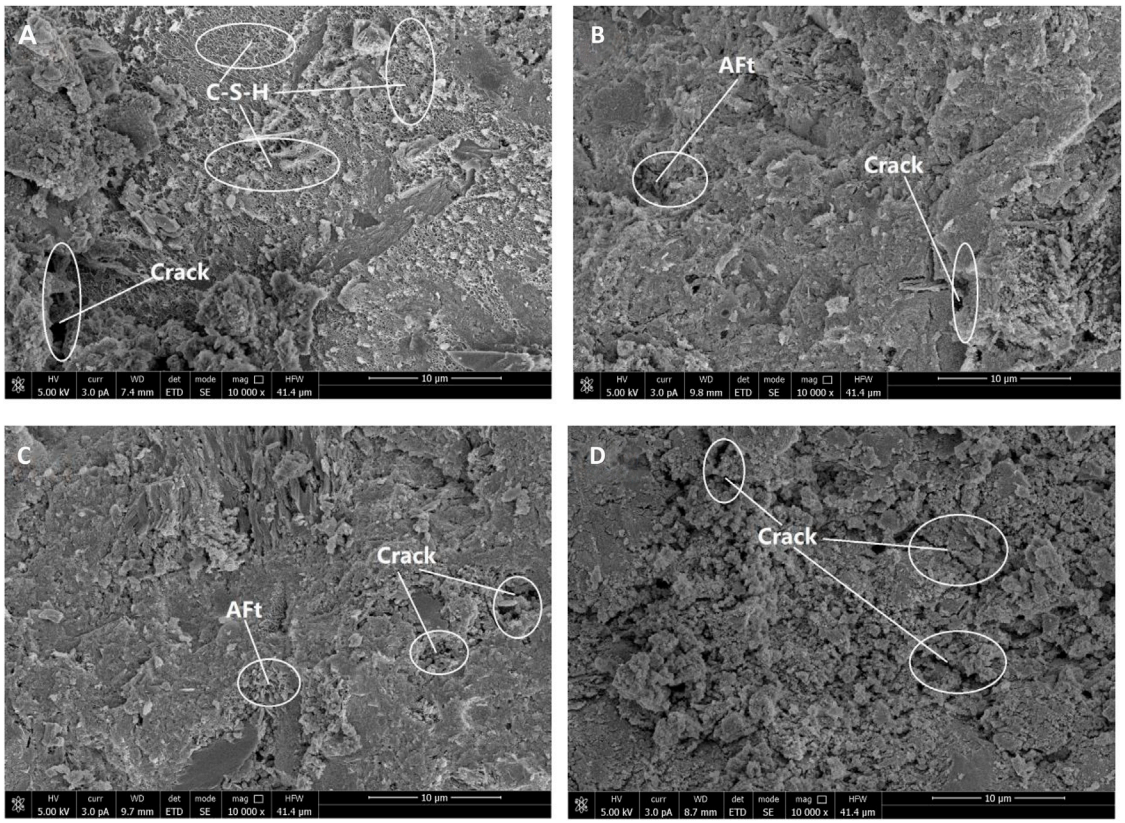

FIGURE 6 | Microscopic morphology of each group of concrete with 20 cycles: **(A)** MK0; **(B)** MK5; **(C)** MK10; **(D)** MK15.

crystal has developed abnormally large and overlapped. They interact and exist in the pores of the concrete, with part of the crystals covered by the surrounded M-S-H. Since MK10 contains more metakaolin, with the increase of corrosion time, the M-S-H content gradually increases, which leads to the increase of aggregate peeling-off and pores on the concrete surface. This not only provides channels to the SO_4^{2-} invasion, but also the space for corrosion product stacking. The SO_4^{2-} invasion again brings the test samples with secondary corrosion damage. When the metakaolin content reaches 15%, the concrete shows very bad internal connection of its micro structure, significantly increased pores with large sizes, and loose and porous characteristics. Besides, massive needle-shaped ettringite can also be seen. Compared with the ettringite shape of MK5, the ettringite of MK15 is thin and compact, which might be the secondary ettringite caused by the secondary M-S-H damage to the test samples. Meanwhile a certain amount of flocculent material is found around the pores, please refer to EDS of **Figure 8D**. This material is mainly composed of Mg,Si,O, and S. According to the micro morphology features (Li et al., 2014), it can be judged that the material might be M-S-H. Combining with the macro-morphology figure, when the operation reached 120 cycles, the concrete turns to have increased internal pores and cracks (**Figure 7**) due to the joint effects of expansion stress of corrosion products, pressure of salt crystals, and surface tension formed by the solution in the capillary pores during the dry-wet alternation process. The increased internal pores and cracks connect with the surface cracks, which result in the peeling-off of concrete edges and corners (**Figure 5**), thereby causing rapid reduction of concrete mass and compressive strength.

The results of 120 cycles are quite different from the those of 20 cycles. This is the later stage of corrosion. According to the XRD analysis and the FTIR analysis, the MK10 and MK15 are featured in loose and porous micro structure due to the M-S-H impact at this time. But MK5 still has closely connected hydration products, comparative compact micro structure, relatively small amount of corrosion products (**Figures 3**, **4**), and optimal durability.

DISCUSSIONS

Impacts of Single SO_4^{2-} on Metakaolin Concrete

There are many studies carried out on single SO_4^{2-} impacts on metakaolin concrete. NaBil M added 0~15% metakaolin in the concrete. With the increase of metakaolin content, the concrete performance in resisting sulfate salt corrosion enhances accordingly (Al-Akhras, 2006). The sulfate salt corrosion to the metakaolin concrete mainly produces ettringite, gypsum, and mirabilite crystal (Hu and He, 2020). During the SO_4^{2-}

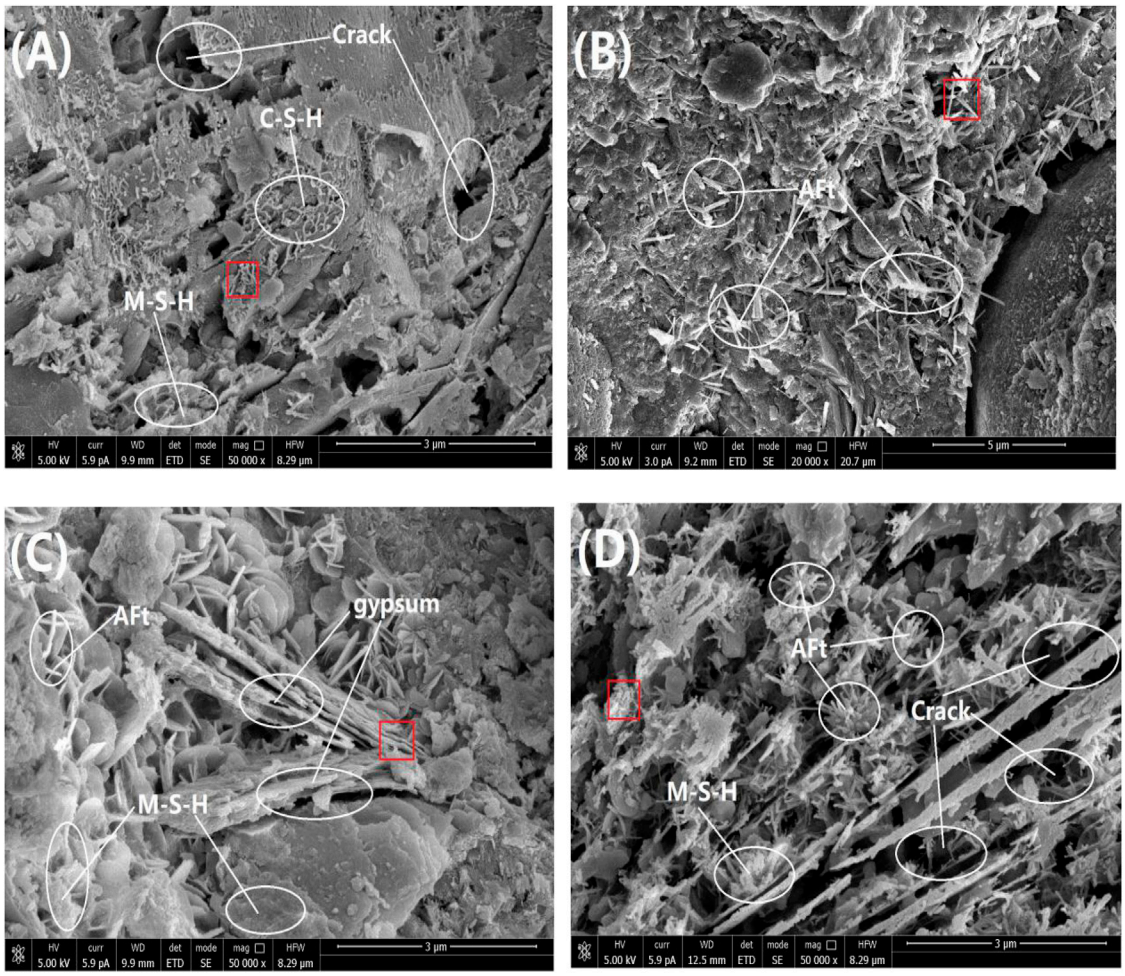

FIGURE 7 | Microscopic morphology of each group of concrete with 120 cycles: **(A)** MK0; **(B)** MK5; **(C)** MK10; **(D)** MK15.

corrosion to the concrete, the tricalcium aluminate and $Ca(OH)_2$ react with SO_4^{2-} and produce excessive ettringite and gypsum, which can seriously damage the concrete performance. The reason why the metakaolin is conductive in improving concrete's resistance to sulfate salt (Zheng et al., 2021) can be concluded into two points: first, the replacement of part of cement by metakaolin reduces the tricalcium aluminate content in the cement accordingly, thereby reducing the generated volume of corrosion products; second, due to the high pozzolanic activity, the metakaolin could react with $Ca(OH)_2$ inside the concrete, and produce massive C-S-H and C-A-S-H, which narrow the pores inside the concrete and enhance the compactness of the concrete.

The key point of this paper is the impact of compound salts on metakaolin concrete. Being different from the single SO_4^{2-} corrosion, with the increase of metakaolin content, the concrete's resistance to compound salts corrosion increases first, and then reduces. The main reason explaining this phenomenon is the M-S-H impact. Single SO_4^{2-} corrosion to metakaolin concrete only produces ettringite and gypsum. But the compound salts corrosion could produce complicated corrosion products, which includes M-S-H, magnesium hydroxide, thaumasite, and Friedel salt besides the ettringite and gypsum. Therefore under the joint effects of the corrosion products, the metakaolin concrete performance drops rapidly.

Joint Effects of Corrosive Ions

The mechanism of corrosive ions of SO_4^{2-},Mg^{2+}, and Cl^- on the concrete is complicated. The corrosion of multiple types of ions usually exist at the same time, and could promote or inhibit the corrosion effect of each other.

For Cl^-, it has little corrosive effect inside the concrete, instead, it mainly erodes the rebars. However the chloride salt could affect the corrosion of O_4^{2-} and Mg^{2+} to some certain extent during the corrosion process. At the early stage of corrosion, since Cl^- could diffuse rapidly due to its small volume, it could combine with Al prior to SO_4^{2-}, and generate Friedel salt (as shown in **Eq. 3**), thereby preventing the generating of ettringite (Deng et al., 2005). In this case, it can be said that Cl^- and $SO_4^{2-}$are mutually inhibited. But at the latter stage of the corrosion, with the reduction of the hydration products inside the test samples, the pH value of the corrosive layer of concrete reduces. As a

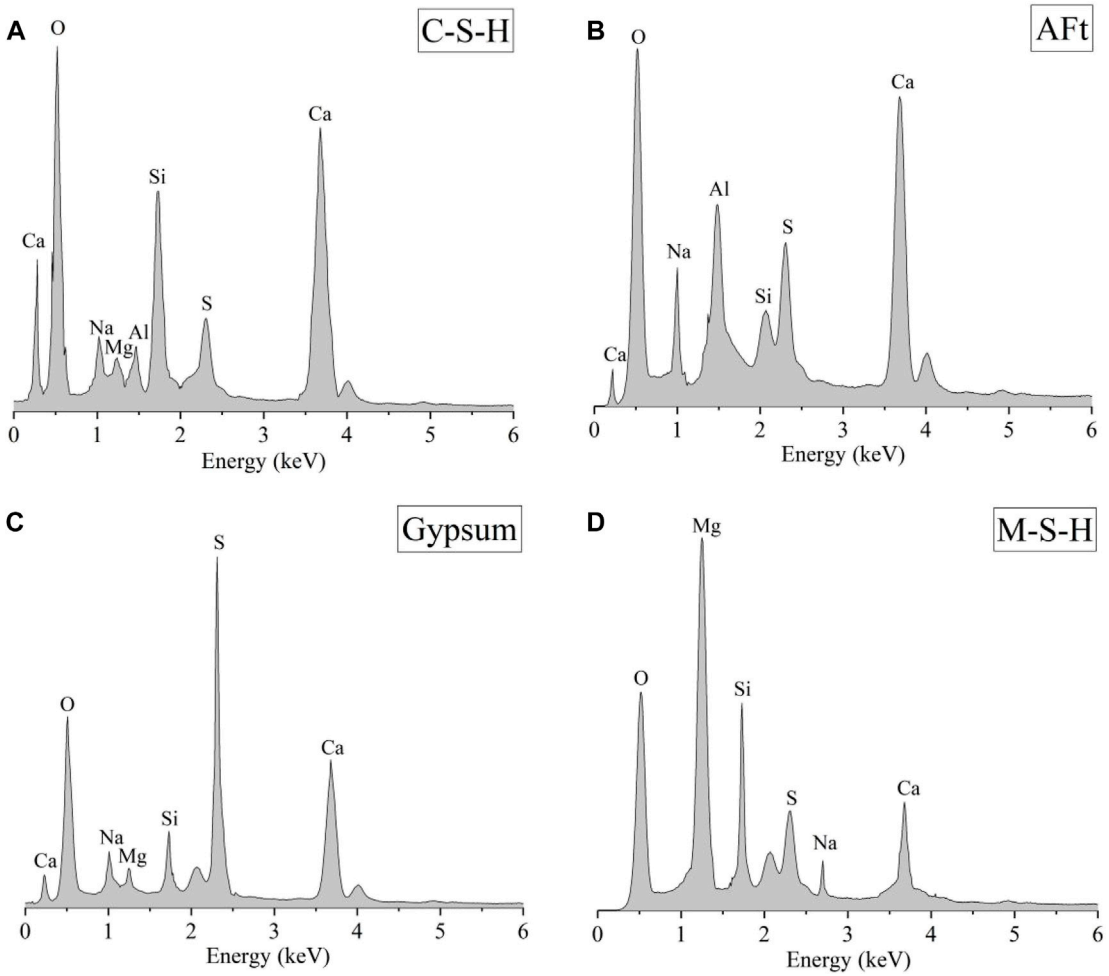

FIGURE 8 | EDS spectrum when the number of cycles is 120:**(A)** C-S-H; **(B)** AFt; **(C)** Gypsum; **(D)** M-S-H.

matter of fact, Friedel salt is unstable in low pH environment, and could hydrolyze (as shown in **Eq. 4**) to release massive free Cl^- inside the concrete. These free Cl^- could diffuse to deeper position of the test samples (Cheng et al., 2019).

Mg^{2+} is one of the main reasons causing pH value reduction, because Mg^{2+} could combine with $Ca(OH)_2$ inside the concrete to generate magnesium hydroxide with very-low solubility (**Eq. 5**). This could damage the alkali environment. Meanwhile, Ca^{2+} inside the hydration product C-S-H decalcifies and forms non-cementing M-S-H (**Eq. 6**), which could result in aggregate peeling-off from the surface of the concrete.

Iron synergy has great impact on concrete. With the increase of corrosion time, the pH value inside the test sample decreases further, Mg^{2+} diffusion accelerates, and the Friedel salt decomposes and generate a great number of Cl^- inside the concrete. Meanwhile the accelerating of Mg^{2+} invasion results in more generated M-S-H inside the concrete, which leads to the aggregate peeling-off, and the increase of internal cracks and pores of the test samples. This promotes the secondary invasion of SO_4^{2-} into the concrete, which produces more ettringite and gypsum, and results in secondary expansion damage to the concrete.

$$2Cl^- + Ca_3Al_2O_6 + Ca(OH)_2 + 10H_2O \rightarrow Ca_3Al_2O_6 \cdot CaCl_2 \cdot 10H_2O + 2OH^- \quad (3)$$

$$Ca_3Al_2O_6 \cdot CaCl_2 \cdot 10H_2O \rightarrow 2Al(OH)_4^- + 4Ca^{2+} + 2Cl^- + 4OH^- + 2H_2O \quad (4)$$

$$Mg^{2+} + Ca(OH)_2 \rightarrow Ca^{2+} + Mg(OH)_2 \quad (5)$$

$$3Mg^{2+} + 3CaO \cdot 2SiO_2 \cdot 3H_2O \rightarrow 3Ca^{2+} + 3MgO \cdot 2SiO_2 \cdot 3H_2O \quad (6)$$

CONCLUSION

In this paper, the impacts of different metakaolin contents on concrete durability under dry-wet alternation and joint corrosion of multiple types of ions were systematically analyzed. According to the results, conclusions as follows are obtained:

1) Under the corrosion of multiple types of corrosive ions, with the increase of the corrosion time, the physical properties of the test samples show tendency of rising first and then declining. At the early stage of corrosion (20 cycles), the concrete with 10% metakaolin content has the optimal physical properties. At the latter stage of the corrosion (120 cycles), concrete with 5% metakaolin content shows the optimal physical properties.
2) Main corrosion products generated by the joint corrosion of multiple types of corrosive ions on concrete under dry-wet alternation are: ettringite, gypsum, Friedel salt, magnesium hydroxide, M-S-H, and thaumasite. The corrosion product quantity of the concrete with 5% metakaolin is similar to that of the ornidary concrete. But with the increase of metakaolin, the quantity of corrosion products increase, especially the M-S-H shows the most significant increase in quantity.
3) When suffering joint corrosion of multiple types of corrosive ions, the metakaolin concrete, from the macro aspect, shows aggregate peeling-off and crack generating. The test sample represents powder-state surface. The increase of added metakaolin results in the increase of the surface aggregate peeling-off.
4) 10% metakaolin makes the micro structure of the concrete more compact at the early stage; then at the later stage, 5% metakaolin can improve the connection of the internal micro structure of the test sample, reducing pores. Since Mg^{2+} has very great impact on metakaolin concrete, excessive metakaolin leads to significant reduction of concrete durability, and loose and porous micro morphology.

DATA AVAILABILITY STATEMENT

The original contributions presented in the study are included in the article/supplementary material, further inquiries can be directed to the corresponding author.

AUTHOR CONTRIBUTIONS

CX wrote most of this manuscript. CX was in charge of implementing most of the materials manufacturing and properties testing. PJ and SZ are responsible for providing funds and checking manuscripts. All authors have read and agreed to the published version of the manuscript.

FUNDING

This research was funded by the Key Projects of Natural Science Research in Colleges and universities of AnhuiProvince, Grantnumber KJ2019A1043; Science and Technology Project of Jiangsu Provincial Department of Housing and Urban Rural Development, Grant number 2019ZD001190.

REFERENCES

Abdul Razak, H., and Wong, H. S. (2005). Strength Estimation Model for High-Strength concrete Incorporating Metakaolin and Silica Fume. *Cem. Concr. Res.* 35, 688–695. doi:10.1016/j.cemconres.2004.05.040

Al-Akhras, N. M. (2006). Durability of Metakaolin concrete to Sulfate Attack. *Cem. Concr. Res.* 36, 1727–1734. doi:10.1016/j.cemconres.2006.03.026

Alapour, F., and Hooton, R. D. (2017). Sulfate Resistance of Portland and Slag Cement Concretes Exposed to Sodium Sulfate for 38 Years. *ACI Mater. J.* 114, 477–490. doi:10.14359/51689678

Andrew, R. M. (2019). Global CO2 Emissions from Cement Production,1928-2018. *Earth Syst. Sci. Data.* 4, 1675–1710. doi:10.5194/essd-11-1675-2019

Bernard, E., Lothenbach, B., Rentsch, D., Pochard, I., and Dauzères, A. (2017). Formation of Magnesium Silicate Hydrates (M-S-H). *Phys. Chem. Earth, Parts A/B/C* 99, 142–157. doi:10.1016/j.pce.2017.02.005

Bildirici, M. E. (2019). Cement Production, Environmental Pollution, and Economic Growth: Evidence from China and USA. *Clean. Techn Environ. Pol.* 21, 783–793. doi:10.1007/s10098-019-01667-3

Chen, X., SunPang, Z. J., and Pang, J. (2021). A Research on Durability Degradation of Mineral Admixture Concrete. *Materials* 14, 1752. doi:10.3390/ma14071752

Chen, X., Sun, Z., and Pang, J. (2021). Effects of Various Corrosive Ions on Metakaolin Concrete. *Crystals* 11, 1108. doi:10.3390/cryst11091108

Cheng, S., Shui, Z., Sun, T., Gao, X., and Guo, C. (2019). Effects of Sulfate and Magnesium Ion on the Chloride Transportation Behavior and Binding Capacity of Portland Cement Mortar. *Constr. Build. Mater.* 204, 265–275. doi:10.1016/j.conbuildmat.2019.01.132

Coleman, N. J., and Mcwhinnie, W. R. (2000). The Solid State Chemistry of Metakaolin-Blended Ordinary Portland Cement. *J. Mater. Sci.* 35, 2701–2710. doi:10.1023/a:1004753926277

De Weerdt, K., Lothenbach, B., and Geiker, M. R. (2019). Comparing Chloride Ingress from Seawater and NaCl Solution in Portland Cement Mortar. *Cem. Concr. Res.* 115, 80–89. doi:10.1016/j.cemconres.2018.09.014

Deng, D. H., Xiao, J., Yuan, Q., Zhang, W. N., and Liu, Y. X. (2005). On Thaumasite Incementitious Materials. *J. Build. Mater.* 8, 400–409.

Environment, U., Scrivener, K. L., John, V. M., and Gartner, E. (2018). Eco-efficient Cements: Potential Economically Viable Solutions for a low-CO2 Cement-Based Materials Industry. *Cem. Concr. Res.* 114, 2–26. doi:10.1016/j.cemconres.2018.03.015

Feng, P., Miao, C., and Bullard, J. W. (2014). A Model of Phase Stability, Microstructure and Properties during Leaching of Portland Cement Binders. *Cem. Concr. Compos.* 49, 9–19. doi:10.1016/j.cemconcomp.2014.01.006

GB/T 50081-2002 (2002). *Standard for Test Method of Mechanical Properties on Ordinary Concrete*. Beijing,China: China Building Industry Press.

GB/T 50082-2009 (2009). *Standard for Test Method of Long-Term Performance and Durability of Ordinary Concrete*. Beijing, China: Chinese Standard Institution Press.

Gu, Y., Martin, R.-P., Omikrine Metalssi, O., Fen-Chong, T., and Dangla, P. (2019). Pore Size Analyses of Cement Paste Exposed to External Sulfate Attack and Delayed Ettringite Formation. *Cement Concr. Res.* 123, 105766. doi:10.1016/j.cemconres.2019.05.011

Gu, Y., Martin, R.-P., Omikrine Metalssi, O., Fen-Chong, T., and Dangla, P. (2019). Pore Size Analyses of Cement Paste Exposed to External Sulfate Attack and Delayed Ettringite Formation. *Cem. Concr. Res.* 123, 105766. doi:10.1016/j.cemconres.2019.05.011

Hemalatha, T., and Ramaswamy, A. (2017). A Review on Fly Ash Characteristics - towards Promoting High Volume Utilization in Developing Sustainable concrete. *J. Clean. Prod.* 147, 546–559. doi:10.1016/j.jclepro.2017.01.114

Hu, L., and He, Z. (2020). A Fresh Perspective on Effect of Metakaolin and limestone Powder on Sulfate Resistance of Cement-Based Materials. *Constr. Build. Mater.* 262, 119847. doi:10.1016/j.conbuildmat.2020.119847

Huang, H., Gao, X., Wang, H., and Ye, H. (2017). Influence of rice Husk Ash on Strength and Permeability of Ultra-high Performance concrete. *Constr. Build. Mater.* 149, 621–628. doi:10.1016/j.conbuildmat.2017.05.155

Jiang, G., Rong, Z., and Sun, W. (2015). Effects of Metakaolin on Mechanical Properties, Pore Structure and Hydration Heat of Mortars at 0.17 W/b Ratio. *Constr. Build. Mater.* 93, 564–572. doi:10.1016/j.conbuildmat.2015.06.036

Jiang, Y. (2005). Study on Early Cracking Resistant Mechanical Characteristics of Fly-Ash Concrete. *Large Dam Saf.* 03, 34–37.

Juenger, M. C. G., and Siddique, R. (2015). Recent Advances in Understanding the Role of Supplementary Cementitious Materials in concrete. *Cem. Concr. Res.* 78, 71–80. doi:10.1016/j.cemconres.2015.03.018

Lee, S. T., Moon, H. Y., Hooton, R. D., and Kim, J. P. (2005). Effect of Solution Concentrations and Replacement Levels of Metakaolin on the Resistance of Mortars Exposed to Magnesium Sulfate Solutions. *Cem. Concr. Res.* 35, 1314–1323. doi:10.1016/j.cemconres.2004.10.035

Li, Z., Zhang, T., Hu, J., Tang, Y., Niu, Y., Wei, J., et al. (2014). Characterization of Reaction Products and Reaction Process of MgO-SiO2-H2o System at Room Temperature. *Constr. Build. Mater.* 61, 252–259. doi:10.1016/j.conbuildmat.2014.03.004

Liu, F., Zhang, T., Luo, T., Zhou, M., Zhang, K., and Ma, W. (2020). Study on the Deterioration of Concrete under Dry-Wet Cycle and Sulfate Attack. *Materials* 13, 4095. doi:10.3390/ma13184095

Mardani-Aghabaglou, A., İnan Sezer, G., and Ramyar, K. (2014). Comparison of Fly Ash, Silica Fume and Metakaolin from Mechanical Properties and Durability Performance of Mortar Mixtures View point. *Constr. Build. Mater.* 70, 17–25. doi:10.1016/j.conbuildmat.2014.07.089

Mo, Z., Wang, R., and Gao, X. (2020). Hydration and Mechanical Properties of UHPC Matrix Containing limestone and Different Levels of Metakaolin. *Constr. Build. Mater.* 256, 119454. doi:10.1016/j.conbuildmat.2020.119454

Nehdi, M. L., Suleiman, A. R., and Soliman, A. M. (2014). Investigation of concrete Exposed to Dual Sulfate Attack. *Cem. Concr. Res.* 64, 42–53. doi:10.1016/j.cemconres.2014.06.002

Nosouhian, F., Fincan, M., Shanahan, N., Stetsko, Y. P., Riding, K. A., and Zayed, A. (2019). Effects of Slag Characteristics on Sulfate Durability of Portland Cement-Slag Blended Systems. *Constr. Build. Mater.* 229, 116882. doi:10.1016/j.conbuildmat.2019.116882

Peng, H., Cui, C., Cai, C. S., Liu, Y., and Liu, Z. (2019). Microstructure and Microhardness Property of the Interface between a metakaolin/GGBFS-Based Geopolymer Paste and Granite Aggregate. *Constr. Build. Mater.* 221, 263–273. doi:10.1016/j.conbuildmat.2019.06.090

Pouhet, R., and Cyr, M. (2016). Formulation and Performance of Flash Metakaolin Geopolymer Concretes. *Constr. Build. Mater.* 120, 150–160. doi:10.1016/j.conbuildmat.2016.05.061

Qi, B., Gao, J., Chen, F., and Shen, D. (2017). Evaluation of the Damage Process of Recycled Aggregate concrete under Sulfate Attack and Wetting-Drying Cycles. *Constr. Build. Mater.* 138, 254–262. doi:10.1016/j.conbuildmat.2017.02.022

Sarkar, S., Mahadevan, S., Meeussen, J. C. L., van der Sloot, H., and Kosson, D. S. (2010). Numerical Simulation of Cementitious Materials Degradation under External Sulfate Attack. *Cem. Concr. Compos.* 32, 241–252. doi:10.1016/j.cemconcomp.2009.12.005

Song, K.-I., Song, J.-K., Lee, B. Y., and Yang, K.-H. (2014). Carbonation Characteristics of Alkali-Activated Blast-Furnace Slag Mortar. *Adv. Mater. Sci. Eng.* 2014, 1–11. doi:10.1155/2014/326458

Sun, X., Hua, Y., Mao, S., and Zhang, Y. (2021). Experimental Research on the Influence of Dry-Wet Cycle on Concrete Compressive Strength. *IOP Conf. Ser. Earth Environ. Sci.* 714, 032016. doi:10.1088/1755-1315/714/3/032016

Supit, S. W. M., and Shaikh, F. U. A. (2014). Durability Properties of High Volume Fly Ash concrete Containing Nano-Silica. *Mater. Struct.* 48, 2431–2445. doi:10.1617/s11527-014-0329-0

Tan, Y., Yu, H., Ma, H., Zhang, Y., and Wu, C. (2017). Study on the Micro-crack Evolution of concrete Subjected to Stress Corrosion and Magnesium Sulfate. *Constr. Build. Mater.* 141, 453–460. doi:10.1016/j.conbuildmat.2017.02.127

Vance, K., Aguayo, M., Oey, T., Sant, G., and Neithalath, N. (2013). Hydration and Strength Development in Ternary portland Cement Blends Containing limestone and Fly Ash or Metakaolin. *Cem. Concr. Compos.* 39, 93–103. doi:10.1016/j.cemconcomp.2013.03.028

Wang, J., Niu, D., Hui, H., and Wang, B. (2019). Study on Durability Degradation of Shotcrete Lining Eroded by Compound Salt. *J. Civil Eng.* 52, 79–90. doi:10.15951/j.tmgcxb.2019.09.006

Wei, J., Gencturk, B., Jain, A., and Hanifehzadeh, M. (2019). Mitigating Alkali-Silica Reaction Induced concrete Degradation through Cement Substitution by Metakaolin and Bentonite. *Appl. Clay Sci.* 182, 105257. doi:10.1016/j.clay.2019.105257

Xi, F., Davis, S. J., Ciais, P., Crawford-Brown, D., Guan, D., Pade, C., et al. (2016). Substantial Global Carbon Uptake by Cement Carbonation. *Nat. Geosci.* 9, 880–883. doi:10.1038/ngeo2840

Yuan, Q., Shi, C., De Schutter, G., Audenaert, K., and Deng, D. (2009). Chloride Binding of Cement-Based Materials Subjected to External Chloride Environment - A Review. *Constr. Build. Mater.* 23, 1–13. doi:10.1016/j.conbuildmat.2008.02.004

Zeng, J., Shui, Z., and Wang, S. (2014). Hydration and Pore Structure of Steam Cured High-Strength Mortar with Metakaolin and Slag at Early Age. *J. Cent. South Univ. (Natural Sci. Edition)* 45, 2857–2863.

Zhang, T., Wang, T., Wang, K., Xu, C., and Ye, F. (2021). Development and Characterization of NaCl-KCl/Kaolin Composites for thermal Energy Storage. *Solar Energy* 227, 468–476. doi:10.1016/j.solener.2021.09.020

Zhang, J., Tan, H., Bao, M., Liu, X., Luo, Z., and Wang, P. (2021). Low Carbon Cementitious Materials: Sodium Sulfate Activated Ultra-fine Slag/fly Ash Blends at Ambient Temperature. *J. Clean. Prod.* 280, 124363. doi:10.1016/j.jclepro.2020.124363

Zheng, S., Qi, L., He, R., Wu, J., and Wang, Z. (2021). Erosion Damage and Expansion Evolution of Interfacial Transition Zone in concrete under Dry-Wet Cycles and Sulfate Erosion. *Constr. Build. Mater.* 307, 124954. doi:10.1016/j.conbuildmat.2021.124954

Zhou, Y., Peng, Z., Chen, L., Huang, J., and Ma, T. (2021). The Influence of Two Types of Alkali Activators on the Microstructure and Performance of Supersulfated Cement concrete： Mitigating the Strength and Carbonation Resistance. *Cem. Concr. Compos.* 118, 103947. doi:10.1016/j.cemconcomp.2021.103947

Conflict of Interest: The authors declare that the research was conducted in the absence of any commercial or financial relationships that could be construed as a potential conflict of interest.

Publisher's Note: All claims expressed in this article are solely those of the authors and do not necessarily represent those of their affiliated organizations, or those of the publisher, the editors and the reviewers. Any product that may be evaluated in this article, or claim that may be made by its manufacturer, is not guaranteed or endorsed by the publisher.

frontiers in Materials

ORIGINAL RESEARCH
published: 20 December 2021
doi: 10.3389/fmats.2021.722343

An Experimental Study on the Seismic Performance of High-Strength Composite Shear Walls

Min Gan[1,2], *Yu Yu*[1,2]* *and Huakun Zhang*[1,2]

[1]School of Civil Engineering, Chongqing University, Chongqing, China, [2]Key Laboratory of New Technology for Construction of Cities in Mountain Area (Chongqing University), Ministry of Education, Chongqing, China

In order to study the seismic performance of high-strength concrete composite shear walls with embedded steel strips, four tests for high-strength concrete composite shear walls with embedded steel strips (SPRCW-1 to SPRCW-4) were constructed and tested. Based on the test results, a discussion is provided in the present study on the hysteresis curve, backbone curves, and strain of steel plate and distributed reinforcement of high-strength concrete mid-rise and high-rise composite shear walls with embedded steel strips under different steel ratios and different steel strip positions. The test results reveal that in high-strength composite shear walls with embedded steel strips, the ductility of the test specimen can be effectively improved when the ratio of the steel strip reaches a certain level. In parallel, when the embedded steel strip is placed on both sides of the walls, the steel strip can function better. The ultimate displacement is better than when the steel strip is placed in the middle of the walls, and can effectively improve the seismic performance of the walls. The scheme with embedded steel strips is more convenient and economical for construction, which is suitable for popularization and application in middle-high buildings in highly seismic regions.

Keywords: high-strength composite shear walls, seismic performance, hysteresis curve, backbone curves, strain analysis

OPEN ACCESS

Edited by:
Yunchao Tang,
Zhongkai University of Agriculture and Engineering, China

Reviewed by:
Sun Qing,
Xi'an Jiaotong University, China
Roham Rafiee,
University of Tehran, Iran
Haytham F. Isleem,
Tsinghua University, China

***Correspondence:**
Yu Yu
cquyuy@163.com

Specialty section:
This article was submitted to Polymeric and Composite Materials, a section of the journal Frontiers in Materials

Received: *08 June 2021*
Accepted: *11 November 2021*
Published: *20 December 2021*

Citation:
Gan M, Yu Y and Zhang H (2021) An Experimental Study on the Seismic Performance of High-Strength Composite Shear Walls. Front. Mater. 8:722343. doi: 10.3389/fmats.2021.722343

INTRODUCTION

Despite having large dimension, high rigidity, and high bearing capacity, the ductility and energy dissipation capacity of shear walls of middle-high building structures in highly seismic regions are poor and can be severely damaged when strong earthquakes occur. The bearing capacity will diminish quickly and become ineffective in the occurrence of an earthquake and the seismic performance of the walls will not be fully exerted. In the present paper, an attempt was made to combine superior performances of concrete composite shear walls with slotted steel plates, such as adjustable rigidity and guided failure mode, through which the construction of two long steel plates (shear studs welded on both sides of the steel plate) in the walls of mid-rise and high-rise concrete shear walls was proposed. According to the different positions and dimensions of the long steel plates, different parameters of slotted steel plates were replaced, thereby reducing the steel ratio and the difficulty in manufacturing shear walls with slotted steel plates and saving the engineering cost. Additionally, cold-formed steel was also built into the edge members, to ensure that the plasticity of the walls could be fully utilized while not excessively increasing the rigidity of the shear walls. In the present paper, the seismic performance of high-strength concrete composite shear walls under

different positions of steel strips and different steel ratios in the walls was explored, which provides a theoretical basis for improving the seismic performance of high-strength concrete shear walls.

Many studies and tests have been conducted on concrete shear walls with steel plates. Jiang et al. (2019a) investigated the performance of steel-concrete bolt connections in precast reinforced concrete shear walls. Bahrami and Yavari (2019) discussed the performance of reinforced concrete shear walls on both sides of steel plate under cyclic loading. To determine the ultimate shear strength of steel-concrete shear walls (composite shear walls with double steel plates), Labibzadeh and Hamidi (2019) conducted research to find a new analytical formula. Through numerical studies, Ayazi and Shafaei (2019) performed tests on the seismic performance of shear walls with high performance fiber reinforced concrete slabs and steel plates. Blandon et al. (2018) introduced and discussed the quasi-static cyclic tests of four slender, thin and light reinforced concrete walls with different geometric structures, steel properties, and reinforcement arrangement. To reduce the post-earthquake damage of reinforced concrete shear walls, including permanent lateral deformation and concrete damage, TolouKian and Cruz-Noguez (2018) explored three new methods. Lim and Kim (2017) and Lim et al. (2018) conducted an experimental study on the seismic performance of precast concrete beams. In different places in a nuclear power plant, Lee et al. (2018) studied the shear behavior of seismic connections between cast-in-situ reinforced concrete slabs and steel plate-concrete composite shear walls. Farzampour et al. (2015) predicted and analyzed the performance of shear walls with perforated corrugated steel plates. Rafiee and Sharifi (2019) investigated random vibrations and failure analysis of composite pipe. Kassem and Elsheikh (2010), Moretti et al. (2020), and Zhou et al. (2020) proposed analytical methods for predicting the shear strength and performance of structural shear walls. Edin et al. (2019) and Ebadi and Farajloomanesh (2020) studied seismic performance parameters of shear walls, and proposed a design method based on the actual sharing of story shear wall and peripheral frame. Jiang et al. (2019b) proposed a new type of replaceable coupling beam damper to improve the seismic performance of reinforced concrete coupling beam shear wall.

In the present paper, an attempt was made to combine the advantageous qualities of concrete composite shear walls with slotted steel plates, such as adjustable rigidity and guided failure mode, through which the construction of two long steel plates (shear studs welded on both sides of the steel plate) in medium-high concrete shear walls was proposed. According to the different positions and dimensions of the long steel plates, different parameters of slotted steel plates were replaced, which can reduce the steel ratio and the difficulty in manufacturing shear walls with slotted steel plates and save engineering costs. Research on structural rigidity, mechanical performance, and crack development law of high-strength concrete composite shear walls with steel strips in the walls in different positions and different steel ratios is of considerable practical significance.

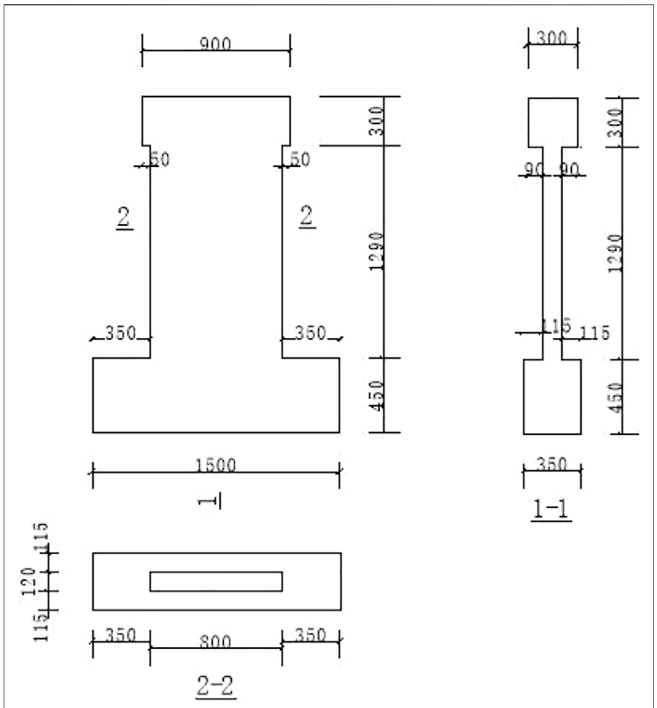

FIGURE 1 | Dimensions of test specimen.

TEST OVERVIEW

Test Design

Test Specimen Design

The dimensions of the high-strength concrete mid-rise and high-rise shear walls test specimens with embedded steel strips (SPRCW-1 to SPRCW-4) in the present test are shown in **Figure 1**. The horizontal load applied by the horizontally arranged actuator acted directly on the upper loading beam, and the lower support was arranged to provide embedded restraint to the walls.

The serial numbers of the test specimens were: SPRCW-1 (the steel plate with a high steel ratio arranged in the middle), SPRCW-2 (the steel plate with a low steel ratio arranged in the middle), SPRCW-3 (the steel plate with a low steel ratio arranged on the middle both sides), and SPRCW-4 (the steel plate with a high steel ratio arranged on the middle both sides). Among said specimens, the two test parameters of the steel plate ratio and the position of embedded steel strips were different for the four high-strength concrete medium-high shear walls test specimens (SPRCW-1 to SPRCW4) with embedded steel strips, while the other parameters were consistent. Details of the parameters of the four test specimens are shown in **Table 1**.

See **Figure 2** for the SPRCW-1 construction drawing. The differences between the four test specimens are explained as follows.

1) The steel ratio of SPRCW-1 was 1.6%, the distance between the outer edge of the steel plate was 247 mm, the distance

TABLE 1 | Table of parameters of test specimens.

Number of test specimens		SPRCW – 1	SPRCW – 2	SPRCW – 3	SPRCW – 4
Formwork of shear walls	Walls width/mm	800	800	800	800
	Walls thickness/mm	120	120	120	120
	Net walls height/mm	1290	1290	1290	1290
	Vertically arranged reinforcement in walls	A6.5@200	A6.5@200	A6.5@200	A6.5@200
	Horizontally arranged reinforcement in walls	A6.5@200	A6.5@200	A6.5@200	A6.5@200
	Ratio of horizontally arranged reinforcement	0.276%	0.276%	0.276%	0.276%
	Vertically arranged reinforcement in walls	A6.5@160	A6.5@160	A6.5@160	A6.5@160
	Ratio of vertically arranged reinforcement	0.345%	0.345%	0.345%	0.345%
	Section of embedded column/mm^2	120 × 160	120 × 160	120 × 160	120 × 160
	Height of edge column/mm	1290	1290	1290	1290
	Vertically arranged reinforcement in embedded column	6A8	6A8	6A8	6A8
	Ratio of reinforcement in embedded column	1.57%	1.57%	1.57%	1.57%
	Cold-formed section steel in embedded column	[60 × 30 × 2.2	[60 × 30 × 2.2	[60 × 30 × 2.2	[60 × 30 × 2.2
	Steel ratio of cold-formed section steel	1.32%	1.32%	1.32%	1.32%
	Stirrup in embedded column	A6.5@100	A6.5@100	A6.5@100	A6.5@100
	Reinforcement ratio per unit volume	0.97%	0.97%	0.97%	0.97%
	Dimension of steel plate	2050 × 80	2050 × 80	2050 × 80	2050 × 80
	Thickness of steel plate	6mm	6mm	6mm	6mm
	Location of steel plate	Middle	Middle	Both sides	Both sides
Upper loading beam	Height/mm	300	300	300	300
	Width/mm	300	300	300	300
	Length/mm	900	900	900	900
	Main reinforcement	4C20	4C20	4C20	4C20
	Stirrup	A8@100	A8@100	A8@100	A8@100
Lower loading beam	Height/mm	500	500	500	500
	Width/mm	400	400	400	400
	Length/mm	1600	1600	1600	1600
	Main reinforcement	8C20	8C20	8C20	8C20
	Stirrup	A8@100	A8@100	A8@100	A8@100

between the inner edge of the steel plate and the axis of symmetry was 25 mm, and the edge members on both sides were provided with cold-formed thin-walled steel, respectively, with a steel ratio of 1.43%.

2) The steel ratio of SPRCW-2 was 1.0%, the distance between the outer edge of the steel plate was 270 mm, the distance between the inner edge of the steel plate and the symmetry axis was 50 mm, and the edge members on both sides were provided with cold-formed thin-walled steel, respectively, with a steel ratio of 1.43%.
3) The steel ratio of SPRCW-3 was 1.0%, the distance between the outer edge of the steel plate was 195 mm, the distance between the inner edge of the steel plate and the symmetry axis was 125 mm, and the edge members on both sides were provided with cold-formed thin-walled steel, respectively, with a steel ratio of 1.43%.
4) The steel ratio of SPRCW-4 was 1.6%, the distance between the outer edge of the steel plate was 170 mm, the distance between the inner edge of the steel plate and the axis of symmetry was 104 mm, and the edge members on both sides were provided with cold-formed thin-walled steel, respectively, with a steel ratio of 1.43%.

Mechanical Properties of Steel

The present material property test was conducted in the Material Mechanics Laboratory of Chongqing University. As for the sampling and dimension of the test specimens, 12 test specimens were made according to the national standard, *Metallic Materials-Tensile Test Method at Room Temperature* (GB/GB/T 228–2010) (GB/T 228, 2010). The material property test was designed to determine the mechanical property parameters of cold-formed thin-walled steel, Q235A hot-rolled steel plate and HPB300 reinforcement used under uniaxial tension: elastic modulus E, yield stress σ_y, ultimate tensile strength σ_u, and yield strain $\mu\varepsilon$. The results of the uniaxial tensile test are shown in **Table 2**.

Measured Strength of Concrete and Axial Load of Test Specimen

The five test specimens in the present test were made of C60 concrete. The test specimens were made, poured, and cured at the same time. The dimensions of the test specimens were 150 × 150 × 150 mm. During the 28-day curing period and on the test day, cube compressive strength tests were, respectively conducted on test specimens, and the average values were taken. See **Table 3** for details.

Test Equipment and Loading Protocol

Test Equipment

Following the *Specifications of Testing Methods for Earthquake Resistant Buildings* (JGJ101-2015) (JGJ 101, 2015), quasi-static tests in repeated low-cycle loadings with fixed axial load were conducted. A repeated low-cycle loading test device was used, which consisted of a vertical and a horizontal loading device. The vertical load was controlled by hydraulic jacks through ball bearings, and the maximum bearing capacity of the single

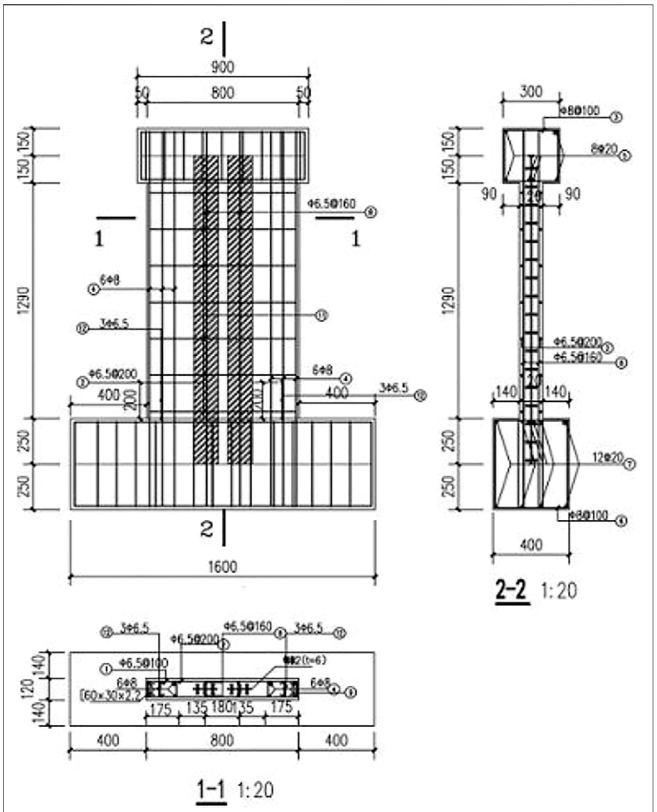

FIGURE 2 | Construction drawing of SPRCW-1.

vertical ball bearing was 120 KN. During the test, an oil pump was manually controlled to ensure the stability of the vertical load. The horizontal loading device was mainly comprised of reaction walls, a horizontal actuator, and a horizontal connecting device, wherein the end part of the horizontal actuator was connected to the horizontal connecting device through hinges. A horizontal load was mainly applied by the horizontal actuator, one end of the actuator was connected to a loading beam of the test specimen, and one end of the actuator acted on the reaction walls. The schematic diagram of the test equipment is shown in **Figure 3**.

Loading Protocol for Test

In the present test, the quasi-static test method was adopted for loading. During the test, the vertical load was controlled to remain unchanged while the horizontal load changed continuously according to the axial load ratio. The loading process was as follows:

1) In the preloaded stage, first, a 150 KN axial load was preloaded on the top of the test specimen, and then unloaded to 0 KN, to eliminate the nonuniformity of the internal load of the test specimen. After the axial load was loaded to a predetermined value, the test equipment was tested in the normal working state thereof by one cycle of loading in both the forward and backward directions with a 20 KN horizontal load.
2) After the first stage of work was completed, a positive horizontal load was applied, which was progressively increasing by 20, 40, 60, and 80 KN until the first crack appeared, and the crack load P_{cr} was recorded. Subsequently, the horizontal load was unloaded to 0 KN in three steps, and a backward load was applied to find the backward cracking load.
3) After the second stage of work was completed, the displacement loading stage began. With the initial position after the axial force was applied as the initial starting point, two cycles of loading were conducted according to the displacement control for each load. The first cyclic displacement was equally divided into three steps of loading, and the second cyclic displacement was completed by one cycle of loading. Loading ended when the test specimen completely lost bearing capacity or when out-of-plane

TABLE 2 | Material properties of steel.

Steel type	Yield strength (MPa)	Ultimate strength (MPa)	Elastic modulus (MPa)	Yield strain ($\mu\varepsilon$)
2.2 mm section steel	384.2	414.1	212,491.7	1808
Q235A	302.8	450.1	202,043.2	1495
φ6.5	419	607.7	254,663.6	1645
φ8	329.3	494.6	201,135.0	1637

TABLE 3 | Concrete strength and axial load ratio.

Number of test specimen	Measured strength value of 150 mm cube test specimen (N/mm^2)	Design value of concrete strength (N/mm^2)	Axial load of test specimen (KN)	Axial load ratio in test	Designed compression ratio
SPRCW – 1	55.2	25.68	826	0.16	0.4
SPRCW – 2	58.1	27.03	869	0.16	0.4
SPRCW – 3	58.8	27.36	879	0.16	0.4
SPRCW – 4	54.8	25.5	820	0.16	0.4

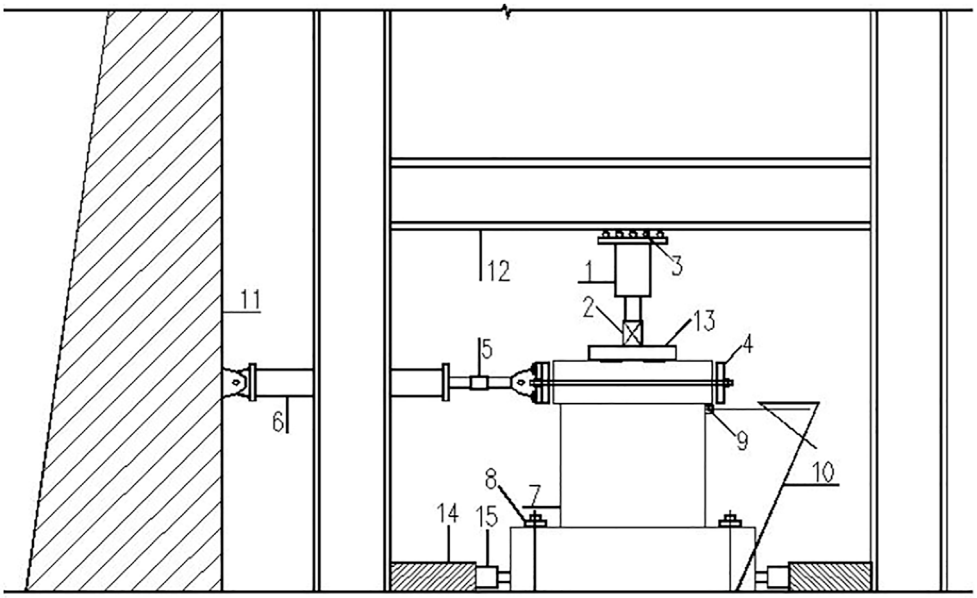

1-150T Vertical Hydraulic Jack	2-150T Vertical Sensor	3-Sliding Support
4-Horizontal Connection Device	5-150T Horizontal Sensor	6-150T Horizontal Actuator
7-Test Specimen	8-Anchor Bolt	9-Displacement Meter
10-Slotted-angle Shelving	11-Reaction walls	12- Reaction Beam
13-Loading Distribution Beam	14-Support	15-30T Jack

FIGURE 3 | Loading setup.

instability caused loading difficulty. See **Figure 4** for the test loading protocol.

ANALYSIS OF TEST RESULTS OF SEISMIC PERFORMANCE

Comparative Analysis of Hysteresis Curves and Characteristics

The load-displacement curves of test specimens obtained in quasi-static loading tests are referred to as hysteresis curves, and the closed graph formed by hysteresis curve is referred to as the hysteresis loop. The internal area of the hysteresis loop has an energy dimension, which can reflect the energy consumption caused by plastic deformation of the member under loading cycles. Under the maximum displacement of the same cycle, the fuller the hysteresis loop, the stronger the plastic deformation capacity of the member. The hysteresis curve of a test specimen can comprehensively reflect the seismic performance indexes, such as energy dissipation capacity, deformation capacity, and bearing capacity of the structure in linear and nonlinear stages. The hysteresis curves of SPRCW-1 to SPRCW-4 are shown in **Figure 5**.

According to **Figure 5**, based on the comparison results, an observation can be made that SPRCW-1 to SPRCW-4 followed the same rule, described as follows:

1) From the beginning of loading to the cracking stage, the test specimens were in an elastic state. After loading and unloading, the specimens could basically return to the original state through displacement, and the hysteresis curve changed linearly.
2) From the beginning of the displacement loading cycle to the occurrence of wall yielding, the horizontal load of the four test specimens obviously increased with the increase of the horizontal displacement, and small residual deformation occurred during unloading. The envelope area of the hysteresis curve was small, indicating that plastic deformation existed but only accounted for a small proportion. The five test specimens were basically in the elastic stage.
3) At the initial stage of the hysteresis curve after yielding, the walls of the four test specimens all exhibited obvious oblique cracks, especially at the bottom of the walls. The four test specimens all produced large residual deformation, thereby causing the envelope area of the curves of the four test specimens to gradually increase after yielding. After

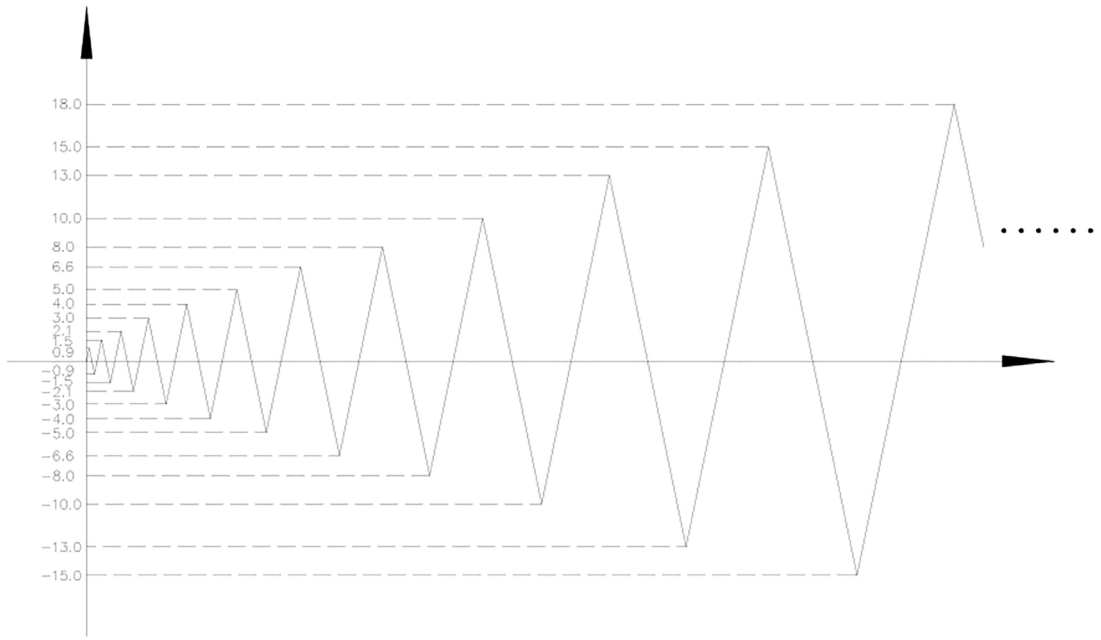

FIGURE 4 | Loading protocol during displacement control.

yielding, no relative displacement occurred between the steel plates and the concrete of the four test specimens, indicating the test specimens had good energy dissipation capacity and plastic deformation capacity.

4) At the later stage of the yield stage, the bearing capacity of the test specimen increased slowly with the increase of horizontal displacement. At the same displacement loading stage, the bearing capacity of the second cycle was slightly smaller than that of the first cycle, and the phenomenon became increasingly obvious after the specimen yielded, indicating that the residual strain caused by structural damage after the specimen yielded became increasingly larger.

According to **Figure 5**, based on the comparison, an observation can be made that the hysteresis curves of SPRCW-1 to SPRCW-4 exhibited the following differences:

1) SPRCW-2 had a large shear failure, and shear-type inclined cracks developed too early. As such, the test specimen reached the strength yield point earlier than the desired state, and after reaching the maximum bearing capacity point, the strength and rigidity of the test specimen decreased obviously. Before and after the failure, the bearing capacity of the test specimen dropped sharply, exhibiting a brittle failure characteristic to a certain degree. By comparing the hysteresis curves of SPRCW-2 and SPRCW-3, an observation can be made that under the same steel ratio, the ultimate bearing capacity of SPRCW-3 increased by 6%, and the slope of the hysteresis curve decreased slowly. After reaching the ultimate bearing capacity, the stiffness of the test specimen degraded slowly, and the ductility and energy dissipation capacity were better than those of SPRCW-2, indicating that when the steel strip was placed on both sides of the walls, the bearing capacity and ductility of the walls would be improved.
2) At the beginning, the hysteresis loops of the four test specimens all opened in a curve shape. With the increase of displacement, the walls gradually inclined to the displacement axis after yielding, and the stiffness gradually deteriorated. According to the hysteresis curves of the four specimens, although the hysteresis curves of the four specimens were full, the degrees of stiffness degradation were different. By comparing SPRCW-1 to SPRCW-4, when the steel plate was placed on both sides of the walls, the hysteresis loop was fuller, the curve dropped slowly, the energy consumption was relatively good, and the stiffness degradation was slow. After yielding, the section steel shear walls gradually began to pinch, indicating that the reinforcement and section steel inside the walls began to slip.
3) By comparing the descending process of the hysteresis curve of four specimens, SPRCW-1 to SPRCW-4, an observation can be made that the higher the steel ratio, the slower the descending and the better the ductility, indicating that the ductility of the shear walls could be effectively improved by appropriately increasing the steel ratio.

Comparative Analysis of Backbone Curves

The backbone curves of the test specimens were formed by connecting the extreme points of the load in the various steps of forward and backward displacement loading in the test process to the envelope. Backbone curves refer to the track of the maximum peak of horizontal force during the test and are an important data model to study the non-linear performance of structural specimens, which reflects the characteristics of stress and deformation of specimens in different stages, including ductility,

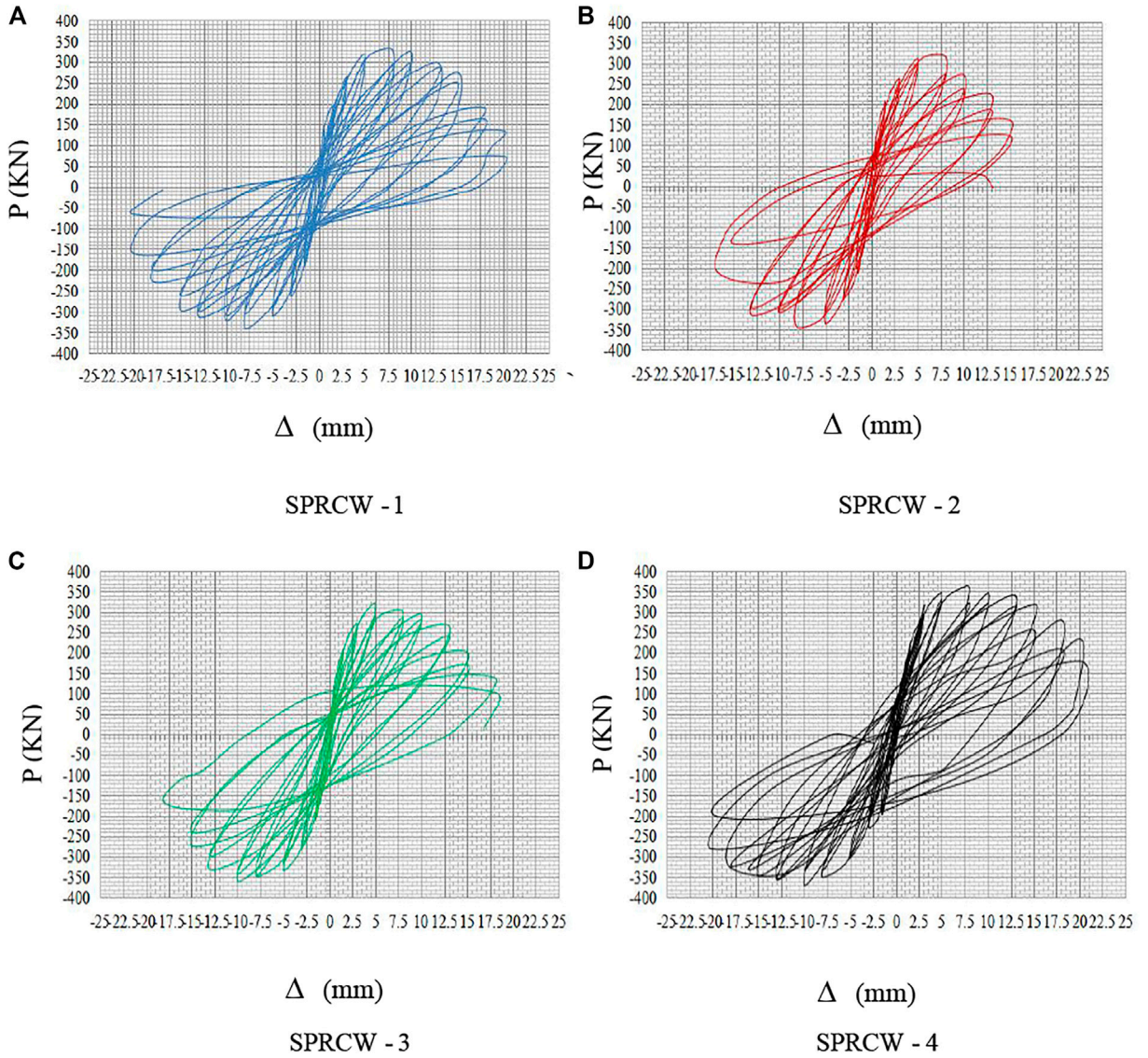

FIGURE 5 | Hysteresis curves diagram of test specimens.

stiffness, strength, and other performance indicators. The backbone curves of SPRCW-1 to SPRCW-4 are shown in **Figure 6**.

From the characteristic points of the backbone curves of the four test specimens, the descending section of the backbone curves of test specimen SPRCW-2 was steeper, and thus, the deformation capacity was weaker. For SPRCW-1, the inside steel plate of test specimen SPRCW-1 was placed on the same position, but the relative steel ratio was increased by 1.6%, and the descending section of backbone curves was relatively smooth, with good deformation capacity and ductility. Compared with SPRCW-3 and SPRCW-4, an observation can be made that after reaching the peak load point, the descending section of SPRCW-4 with higher relative steel ratio was almost horizontal for a long distance. During backward loading, the slope of the curve from failure to complete loss of bearing capacity was still slightly smaller than that of SPRCW-3, indicating that the test specimen with higher steel ratio not only had better deformation capacity and ductility, but also had better energy dissipation capacity after failure occurred. Compared with SPRCW-3 and SPRCW-4 with the same steel ratio but different steel plate positions, an observation can be made that although the performances of the two test specimens were better than those of the first two test specimens, the downward slope of the backbone curves of SPRCW-3 were larger and the downward trend was faster compared with SPRCW-4, indicating that the different positions of steel plates could effectively inhibit the premature failure of the test specimen, and could help to ensure the rigidity of the specimens, thereby improving the deformation ability and energy consumption ability thereof to a certain degree. When comparing and analyzing tests of SPRCW-2 and SPRCW-3, the aforementioned characteristics were also present, confirming the aforementioned experimental conclusion to

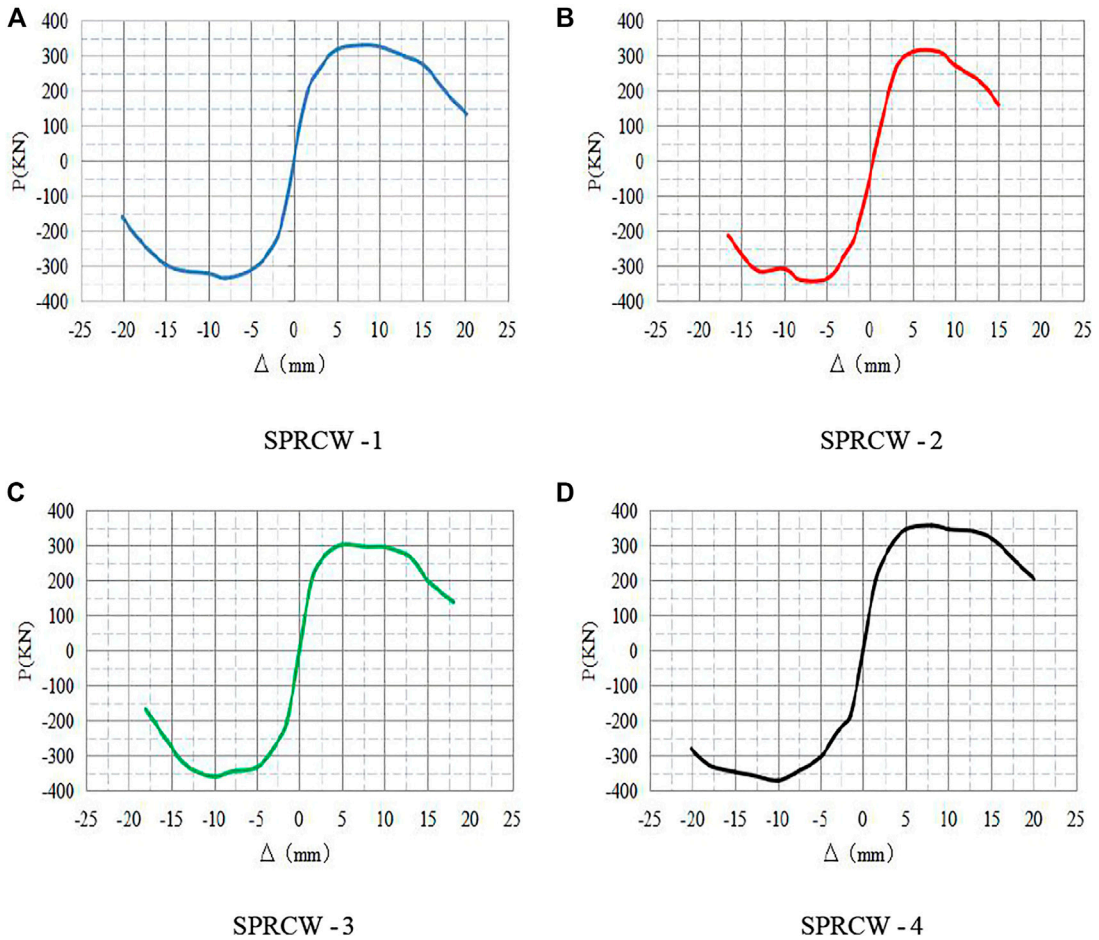

FIGURE 6 | Backbone curves of the test specimens.

some extent. The results of comparative analysis of the five specimens reveal that when the load peak point was reached, the displacement of the five specimens was basically the same, but the bearing capacity was obviously different. The peak loads were as follows: SPRCW-4 > SPRCW-1 > SPRCW-3 > SPRCW-2. Comparing SPRCW-1 with SPRCW-2, and SPRCW-3 with SPRCW-4, respectively, an observation can be directly made from the backbone curves that the higher the steel ratio, the higher the bearing capacity of the test specimens. Comparing SPRCW-1 to SPRCW-4, an observation can be directly made from the backbone curves that the steel plates were located at different positions. When the steel plates were closer to both sides of the walls, the greater the rigidity of the test specimen and the higher the bearing capacity. To summarize, an observation can be directly made from the backbone curves that the seismic performance of the composite shear walls could be effectively improved when the steel ratio was larger.

Strain Analysis of Steel Plates

Stress Distribution Law of Steel Plates in the Walls

In order to compare and analyze the different strain laws of steel strip in composite shear walls during loading, the reduced stress of measurement points under various displacement cycles of steel plate was obtained by arranging triaxial 45°strain rosette (shown in **Figure 7**) at the lower part of steel strip in the walls, to allow for the functions of steel strips at different positions and steel strips with different steel ratios in mid-rise and high-rise shear walls to be further elucidated.

The principal stress of the steel strip could be calculated by **Equation 1**:

$$\sigma_{\substack{\max \\ \min}} = \frac{E}{2(1-\nu)}(\varepsilon_0 + \varepsilon_{90}) \pm \frac{E}{\sqrt{2}(1+\nu)}\sqrt{(\varepsilon_0 + \varepsilon_{90})^2 + (\varepsilon_0 - \varepsilon_{90})^2} \tag{1}$$

In the calculation, the assumption is that there is no displacement parallel to the neutral surface at each point in the plane of the plate, and the stress of each point in the steel plate along the thickness direction is zero, that is, $\sigma_2 = 0$. According to the fourth strength theory ($\sigma_1 = \sigma_{max}$, $\sigma_3 = \sigma_{min}$), the following reduced stress could be obtained (Sun et al., 2021):

$$\sigma_{cr} = \sqrt{\frac{(\sigma_1 - \sigma_3)^2 + (\sigma_2 - \sigma_3)^2 (\sigma_3 - \sigma_1)^2}{2}} = \sqrt{\frac{\sigma_{\max}^2 + \sigma_{\min}^2 + (\sigma_{\min} - \sigma_{\max})^2}{2}} \quad (2)$$

where E_s is 2.02 105 (MPa), υ is 0.25, and $\sigma_{cr} \geq f_y$, indicating that the steel plate reaches the yield strength. As for reduced stress, the strain data corresponding to the tensile side of the steel plate when the test specimen was loaded to the peak value in the first cycle were used, that is, the strain box collected the data of the tensile steel plate when the first-step displacement cycle was loaded forward and backward. The data results are shown in **Figure 8** and **Table 4**.

The shear modulus of steel strips could be calculated by **Equation 3**:

$$G = \frac{E}{2(1+\nu)} \quad (3)$$

In the calculation, if each point in the plane of the plate had no displacement parallel to the neutral surface, that is, assuming that each point in the steel plate had zero deformation along the thickness direction, then:

$$\varepsilon_x = \varepsilon_{0^\circ}; \varepsilon_y = \varepsilon_{90^\circ}$$
$$\varepsilon_{45^\circ} = \frac{\varepsilon_{0^\circ} + \varepsilon_{90^\circ}}{2} + \frac{\varepsilon_{0^\circ} - \varepsilon_{90^\circ}}{2}\cos(2 \times 45^\circ) - \frac{\gamma_{xy}}{2}\sin(2 \times 45^\circ) \quad (4)$$

The in-plane shear deformation could be calculated as follows:

$$\gamma_{xy} = \varepsilon_{0^\circ} + \varepsilon_{90^\circ} - 2\varepsilon_{45^\circ} \quad (5)$$

Therefore, the shear stress could be denoted as follows:

$$\tau_{xy} = G\gamma_{xy} \quad (6)$$

where Poisson's ratio ν is 0.25, and τ_{xy} is greater than 0.7 times of the ultimate tensile strength of the steel plate (450.1 × 0.7 = 315.07 MPa), indicating the steel plate has reached the shear yield strength. As for shear stress, the strain data corresponding to the tensile side of the steel plate when the test specimen was loaded to the peak value in the first cycle were used, that is, the data collected by the strain box when the steel plate was in tension when the first-step displacement cycle was loaded forward and backward. The data results are shown in **Figure 9** and **Table 5**.

From **Figures 8** and **9** and **Tables 4** and **5**, the following observations can be made:

1) With the increase of horizontal load, the strain in the three directions of the strain rosette in the steel strip would increase correspondingly, resulting in a corresponding increase in the reduced stress and shear stress. Before the walls cracked, the steel plate and the concrete would jointly bear the tensile and compressive stress and shear stress. When the strain rosette was located at the position where the main tensile stress reached the tensile strength of the concrete, the concrete would crack rapidly, the tensile concrete at the crack would fail, and the stress would drop to zero. At this time, the tensile and compressive stress and shear stress on the walls would suddenly increase, which would lead to the sudden increase of the reduced stress and shear stress that can be seen in **Tables 4** and **5**. However, because of bonding stress, cracks would close during unloading, leading to a drop in strain gauge data after reloading, thereby causing a short-term drop in reduced stress and shear stress of some steel observation points after the sudden increase.
2) With the continuous increase of horizontal displacement, by comparing two groups of test specimens, SPRCW-1 and SPRCW-4, SPRCW-2 and SPRCW-3, an observation can be made from the four identical measurement points that the displacement of steel plate with the sudden increase of reduced stress and shear stress of specimens SPRCW-3 and SPRCW-4 on both sides of the walls body occurred later, indicating that the arrangement of steel plate on both sides of the walls could effectively limit the development of cracks.
3) Comparing the four identical measurement points of two groups of test specimens, SPRCW-1 and SPRCW-2, and SPRCW-3 and SPRCW-4, respectively, an observation can be made that the shear stress of the two test specimens SPRCW-2 and SPRCW-3 with lower steel ratio was smaller in the early stage, and the yield increased rapidly in the later stage. At the same time, the shear stress of the test specimens SPRCW-1 and SPRCW-4 with higher steel ratio exhibited a gradual increased trend with the increase of displacement. Thus, when the steel ratio was small, the shear strength of the steel plate in the composite shear walls could not be fully exerted, the rigidity of the walls degraded rapidly, and the energy dissipation capacity was relatively poor.
4) Comparing the four same measurement points of SPRCW-1 and SPRCW-4, and SPRCW-2 and SPRCW-3, respectively, an observation can be made that when the positions of steel plates in the walls were different, based on the reduced stress and

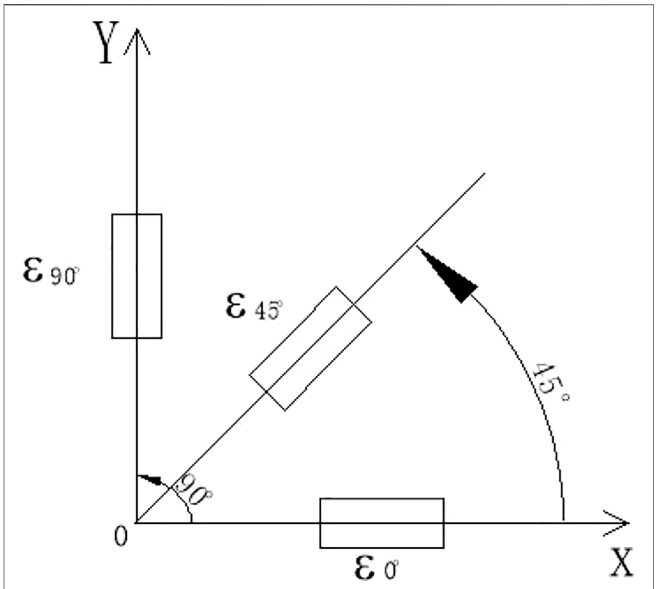

FIGURE 7 | Triaxial 45° strain rosette.

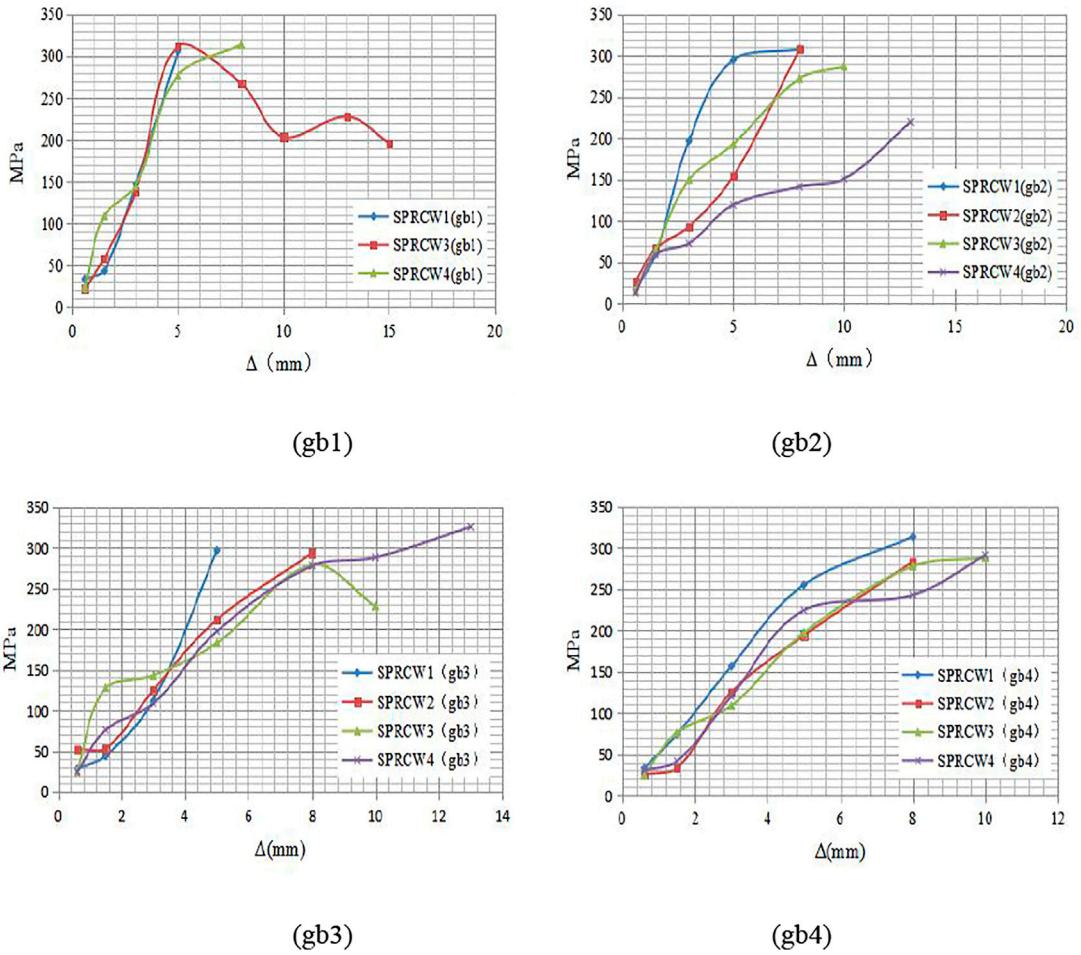

FIGURE 8 | Comparative analysis diagram of reduced stress of steel plates of SPRCW-1 to SPRCW-4.

TABLE 4 | Reduced stress on tensile side of steel plate.

Measurement point	Test specimen No.	Horizontal displacement (mm)							
		Crack	1.5	3	5	8	10	13	15
gb1	SPRCW-1	33.42	43.23	146.95	305.29				
	SPRCW-2	Bad track	Bad track	Bad track	Bad track	Bad track	Bad track	Bad track	Bad track
	SPRCW-3	22.54	57.94	138.69	312	267.02	203.26	227.77	195.87
	SPRCW-4	24.78	108.74	145.61	277.06	314.07			
gb2	SPRCW-1	16.83	59.24	196.61	295.12	308.07			
	SPRCW-2	26.36	66.14	92.66	154.16	308.27			
	SPRCW-3	15.51	64.54	149.64	193.01	272.70	287.29		
	SPRCW-4	12.27	59.36	72.58	119.17	141.44	150.73	219.71	
gb3	SPRCW-1	27.83	43.97	112.31	296.6				
	SPRCW-2	52.13	52.93	124.95	211.39	293.44			
	SPRCW-3	25.09	127.68	142.95	182.75	279.06	227.94		
	SPRCW-4	24.12	75.91	108.50	197.04	277.66	288.14	325.74	
gb4	SPRCW-1	32.90	73.88	156.51	255.15	313.43			
	SPRCW-2	25.26	32.83	125.12	193.74	283.29			
	SPRCW-3	24.12	75.91	108.50	197.04	277.66	288.14		
	SPRCW-4	29.90	41.19	120.09	224.26	242.82	291.04		

Note: The data in the table are the strain values obtained by forward loading in the first cycle.

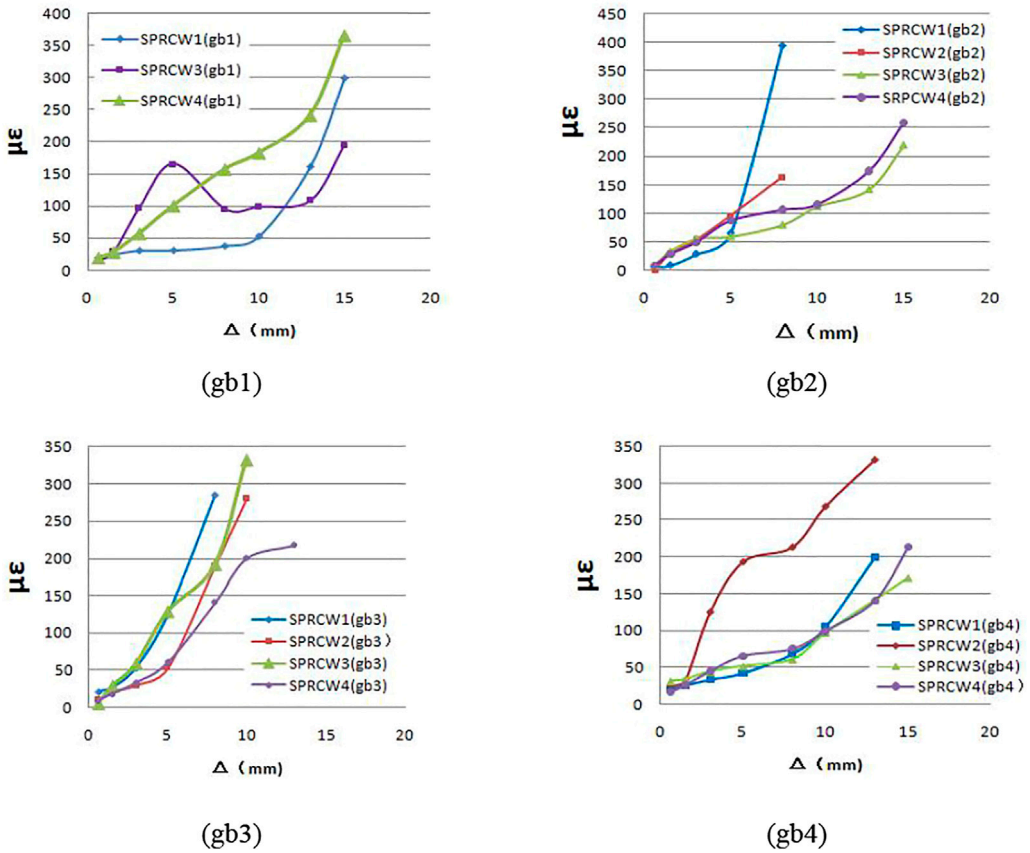

FIGURE 9 | Comparative analysis diagram of shear stress of steel plates of SPRCW-1 to SPRCW-4.

TABLE 5 | Shear stress on tensile side of steel plate.

Measurement point	Test specimen No.	Horizontal displacement (mm)							
		Crack	1.5	3	5	8	10	13	15
gb1	SPRCW-1	14.22	23.52	29.9	30.06	36.95	52.28	161.11	299.28
	SPRCW-2	Bad track	Bad track	Bad track	Bad track	Bad track	Bad track	Bad track	Bad track
	SPRCW-3	15.43	29.41	98.01	166.45	95.99	99.22	108.84	195.87
	SPRCW-4	19.56	28.44	57.20	100.59	157.56	182.85	241.59	365.78
gb2	SPRCW-1	5.25	8.32	28.28	64.72	394.95			
	SPRCW-2	7.76	30.63	54.06	96.72	164.03			
	SPRCW-3	8.56	33.21	55.59	59.39	79.99	111.99	142.13	219.71
	SPRCW-4	9.29	29.33	49.93	87.83	106.68	116.19	174.37	258.80
gb3	SPRCW-1	20.93	26.34	53.41	124.51	284.34			
	SPRCW-2	9.45	20.52	29.55	52.52	190.12	280.21		
	SPRCW-3	4.77	28.36	58.60	128.63	192.30	332.74		
	SPRCW-4	8.64	18.18	32.80	60.43	141.48	200.14	217.27	
gb4	SPRCW-1	19.64	25.05	32.81	41.78	67.87	104.56	199.42	
	SPRCW-2	25.26	32.83	125.12	193.74	113.52	268.90	332.41	
	SPRCW-3	31.43	33.61	44.36	51.63	60.68	96.88	141.24	170.97
	SPRCW-4	16.73	26.10	45.09	65.93	75.31	99.63	141.08	213.64

shear stress curves converted from the strain rosettes at the same measurement point, the stress growth rates were different when the steel plates were placed in different positions of the walls. When placed on both sides of the walls, the curve was relatively smooth, and thus, different steel plate positions could be found to have a certain influence on the energy dissipation capacity and stiffness degradation of the walls.

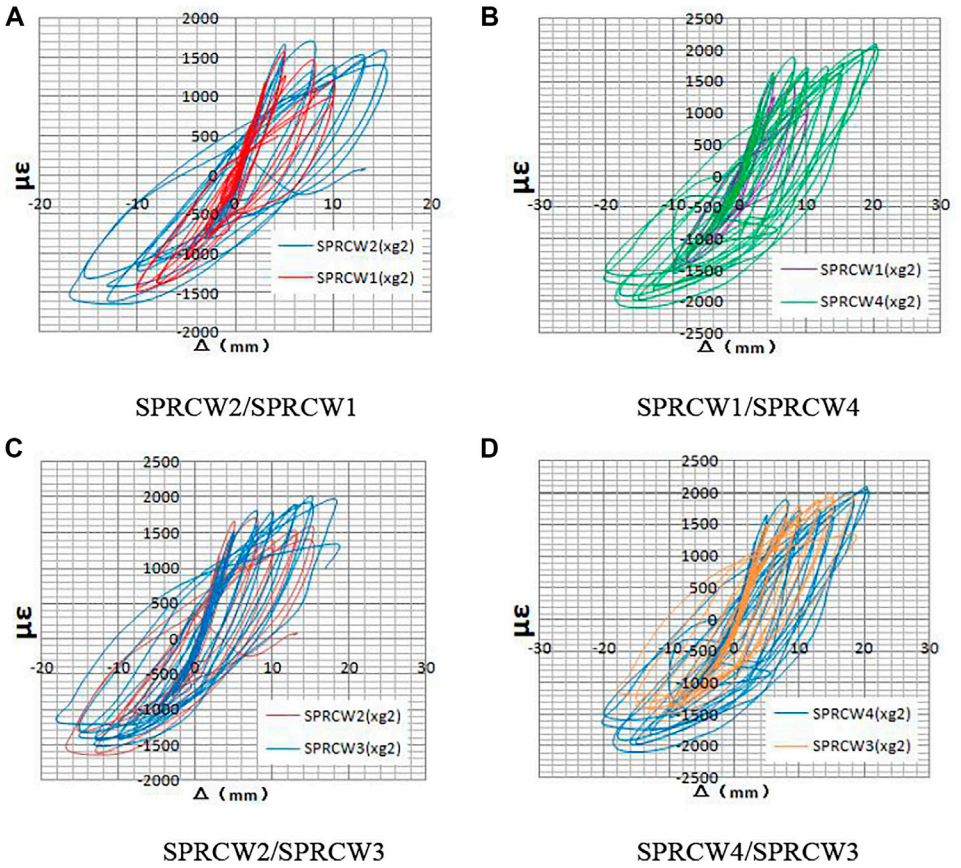

FIGURE 10 | Strain comparison diagram of cold-formed steel on xg2.

Comparative Analysis of Cold-Formed Steel Strain in SPRCW-1 to SPRCW-4 Concealed Column

Under the conditions of different steel ratios and different steel strip arrangement positions, SPRCW-1 to SPRCW-4 were equipped with cold-formed thin-walled steel with the same form and steel ratio. To compare the hysteresis curves of section steel strain before the strain gauge was damaged, four representative measurement points, xg2, xg3, xg7,s and xg8, which were located at the same position of four composite shear walls test specimens from SPRCW-1 to SPRCW-4, were taken. The detailed strain values of each measurement point in each stage are shown in **Figures 10–13**.

The strain hysteresis curves in **Figures 10–13** are the strain-displacement curves of four measurement points of section steel in the embedded column before the strain gauge was damaged due to cracks in the walls. An observation can be made from said figures that the overall trend of the section steel strain was basically the same, and the strain value at the measurement point increased continuously to the peak value and then gradually fell back with the increase of displacement. Before the strain gauge was damaged, the extreme strain values of the section steel in SPRCW-1 and SPRCW-4 embedded columns were greater than those of SPRCW-2 and SPRCW-3, indicating that the bending bearing capacities of the section steel in SPRCW-1 and SPRCW-4 embedded columns were fully utilized, and the bending and shearing resistances of the walls could be simultaneously improved when the steel ratio in the walls was high, thereby ensuring the balanced development of the bending deformation and shearing deformation of the walls during the whole loading process. The full utilization of the strength of the section steel material in the embedded column also reveals that the walls had higher bearing capacity and strong bending resistance, and the test specimen had better ductility.

Compared with SPRCW-1 and SPRCW-2, the time taken to reach the strain extreme values for SPRCW-4 and SPRCW-3 was longer. The four different measurement points all reflect such phenomenon to varying degrees, revealing that when the steel strip in the walls was placed on both sides with the same steel ratio, the flexural rigidity of the composite shear walls slowly diminished, and the shear deformation composition was smaller. Moreover, when the steel strip in the walls was located on both sides, the ductility of the composite shear walls would be effectively improved.

Strain Analysis of Reinforcement

Strain Analysis of Horizontally Arranged Reinforcement

The layout of horizontally arranged reinforcement in SPRCW-1 to SPRCW-4 walls was the same. Representative measurement points with the same positions were,

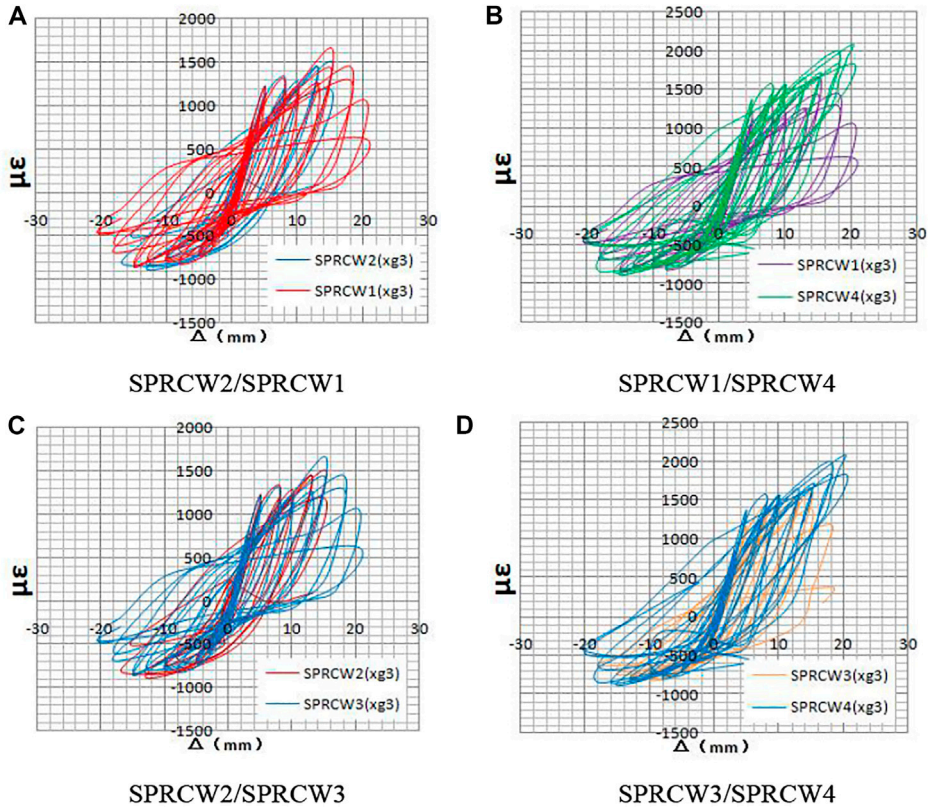

FIGURE 11 | Strain comparison diagram of cold-formed steel on xg3.

respectively, selected for comparative analysis. See **Figure 14** and **Table 6** for detailed strain values of each measurement point in each stage.

From **Figure 14** and **Table 6**, the following observations can be made.

By comparing and analyzing the hysteresis curves of horizontally arranged reinforcement in the middle and lower part of the walls, when △ = 3 mm, the strain of horizontally arranged reinforcement of SPRCW-2 was found to increase sharply after the walls yielded, and the horizontally arranged reinforcement yielded before △ = 15 mm. However, the other three test specimens were close to yielding only after △ = 15 and 18 mm, respectively. As such, an assumption could be made that with the increase of the steel ratio of the walls, the stress of the horizontally arranged reinforcement in the walls could be effectively increased, and the yield of the horizontally arranged reinforcement could be delayed. The effect of changing the position of the steel plate in the walls was not as obvious as that of increasing the steel ratio.

Strain Analysis of Vertically Arranged Reinforcement in Embedded Columns in the Walls

The bending resistance of shear walls was affected by the vertically arranged steel reinforcement in the embedded columns on both sides of the walls. Representative measurement points of vertically arranged steel reinforcement in the embedded columns were selected. See **Figures 15–17** and **Table 7** for the strain values of each measurement point in each stage.

The strain hysteresis curves in **Figures 15–17** are the strain-displacement relation curves of the three measurement points of the longitudinally arranged reinforcement in the embedded column before the strain gauge was damaged due to cracks in the walls. From **Figures 15–17** and **Table 7**, an observation can be made that the strain values of the five test specimens of composite shear walls were different at all steps of the displacement loading stage, but the overall strain trend of longitudinally arranged reinforcement in the embedded column was basically the same. With the increase of displacement, the strain value at the measurement point continuously increased to the peak value and then gradually decreased. Before the strain gauge was damaged, the extreme strain values of vertically arranged reinforcement of SPRCW-1 and SPRCW-4 were greater than those of SPRCW-2 and SPRCW-3, indicating that the bending bearing capacities of vertically arranged reinforcement of SPRCW-1 and SPRCW-4 had been fully utilized. When the steel ratio in the walls was high, the bending and shearing resistance of the walls could be simultaneously improved, thereby ensuring the balanced development of the bending deformation and shearing deformation of the walls in the whole loading

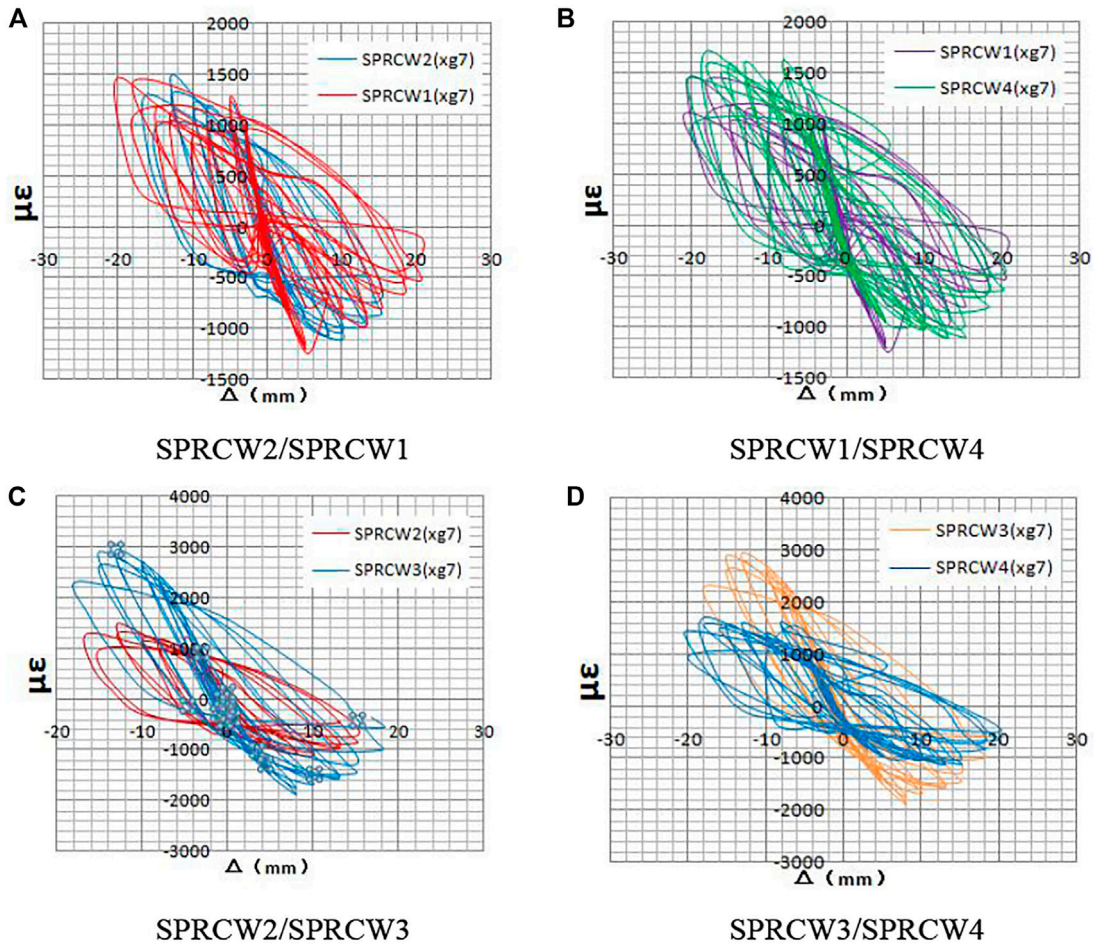

FIGURE 12 | Strain comparison diagram of cold-formed steel on xg7.

process. The full utilization of the vertically arranged reinforcement strength also indicates that the walls had higher bearing capacity, strong bending resistance, and the test specimen had better ductility.

When the vertically arranged reinforcement reached the same strain extreme value, compared with SPRCW-1 and SPRCW-2, SPRCW-4 and SPRCW-3 took a longer time. Such findings were more obvious at the ag3 measurement point, indicating that when the steel strip in the walls was placed on both sides with the same steel ratio, the flexural rigidity of the composite shear walls slowly diminished, and the shear deformation composition became smaller. Moreover, when the steel strip in the walls was located on both sides, the ductility of the composite shear walls would be effectively improved.

Comparative Analysis of Specimen Deformation Capacity

Deformation capacity is an important index for measuring the superiority of seismic performance of members. The ductility coefficient was used to quantitatively evaluate the deformation capacity of the members in the occurrence of an earthquake. When the structure or member had large ductility, the structure or member would consume sufficient energy due to plastic deformation, such that the structural bearing capacity would not be reduced rapidly under the condition of certain deformation of the member. As such, the design goal of being repairable after a medium earthquake and not collapsing after a large earthquake was achieved.

A visual comparison of the yield displacement of the four specimens is shown in **Table 8**. A conclusion can be drawn that the yield displacement relationship of the four specimens was as follows: SPRCW-4 > SPRCW-1, SPRCW-2 > SPRCW-3. The comparison of SPRCW-1 with SPRCW-2 and SPRCW-3 with SPRCW-4 reveals that the yield displacement of specimens with high steel ratio increased slightly but had little effect. Compared with SPRCW-4 and SPRCW-1, for SPRCW-4 and SPRCW-2, the yield displacement increased by 11.05 and 28.26%, respectively, indicating that different positions of steel plates could have a relatively obvious impact on the yield displacement, which is the same as the comparison law of yield load of the four specimens. Comparing the test results of SPRCW-3 and SPRCW-2, the yield displacement of SPRCW-3 was 9.43% higher than that of SPRCW-2, thereby verifying the aforementioned conclusion. However, when the steel ratio was relatively large, the effect of

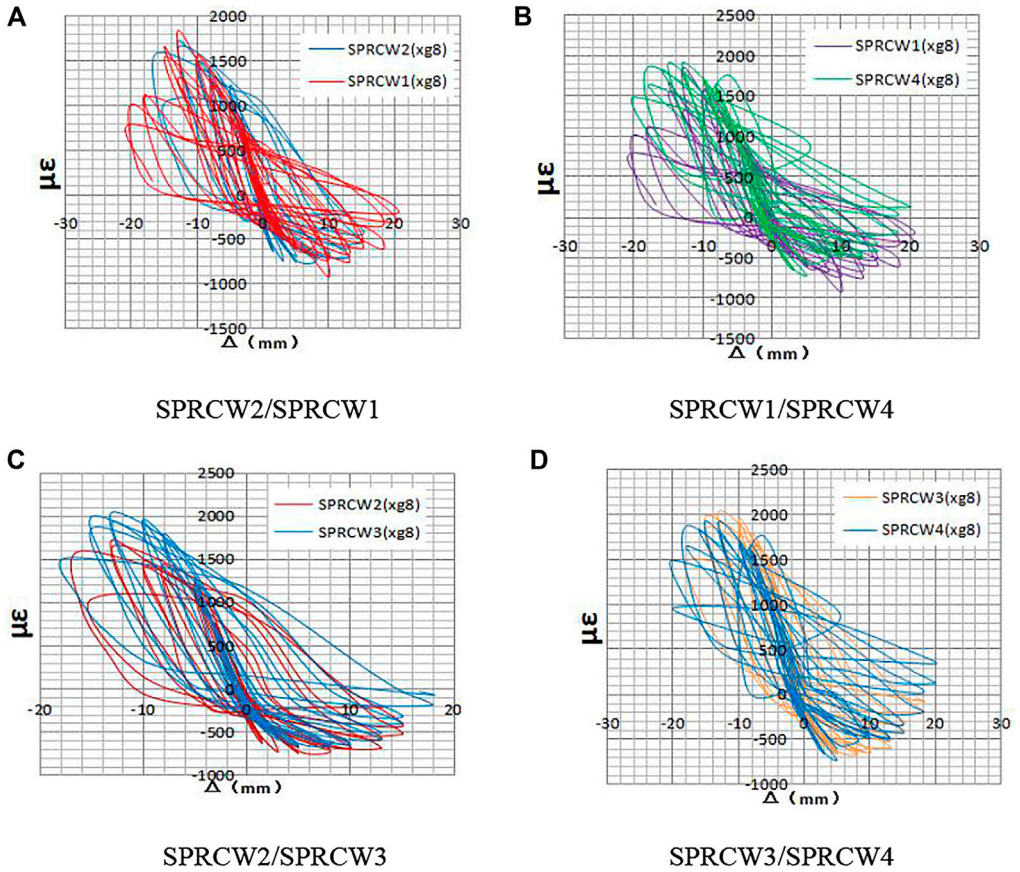

FIGURE 13 | Strain comparison diagram of cold-formed steel on xg8.

adjusting the position of wall steel plate was more obvious in improving the yield displacement.

The limit displacements of the four specimens are shown in **Table 8**. An observation can be made that the magnitude relationship was as follows: SPRCW-4 >SPRCW-1 >SPRCW-3 > SPRCW-2. Compared with SPRCW-1 and SPRCW-2, for SPRCW-3 and SPRCW-4, the limit displacements of the two groups of specimens increased by 24.12 and 29.16%, respectively, indicating that the extreme yield displacement of the specimens with higher steel ratio was significantly improved. Compared with SPRCW-4 and SPRCW-1, for SPRCW-4 and SPRCW-2, the limit displacement increased by 14.44 and 6.37%, respectively, indicating that different positions of steel plates could have a relatively obvious impact on the limit displacement, which is the same as the comparison law of the limit load of the four specimens.

The comparison of ductility coefficient between four specimens and ordinary high-strength concrete shear wall is shown in **Table 8** and the following observations can be made: 1) compared with ordinary high-strength concrete shear wall, the ductility coefficients of SPRCW-1 ~ 4 were increased by 78.17, 65.71, 77.22, and 83.59%, respectively, indicating that the ductility of specimens could be significantly improved by adding cold-formed steel diagonal bracing or setting steel plate strip in the wall body; 2) the ductility coefficient of SPRCW-1 relative to SPRCW-4 was reduced by 3.04%, and that of SPRCW-2 relative to SPRCW-3 was reduced by 8.67%, indicating that changing the position of the steel plate strip in the wall body could improve the ductility effect of the shear wall; and 3) the ductility coefficient of SPRCW-2 relative to SPRCW-1 was reduced by 7.52%, and that of SPRCW-3 relative to SPRCW-4 was reduced by 1.96%, indicating that changing the position of the steel plate strip in the wall could improve the ductility of the shear wall.

Comparative Analysis of Energy Consumption Capacity

The following observations can be made from the comparison between **Tables 9** and **10**:

1) The overall trend of the equivalent viscous damping coefficients of SPRCW-1-4 increased with the increase of displacement, which could be attributed to the increase of displacement increasing the energy consumption, such that the equivalent viscous damping coefficient would increase accordingly. The equivalent viscous damping coefficient increases with the increase of specimen cracking, crack development, yield of built-in section steel and steel plate, reinforcement, later plastic deformation of wall body, and aggregate bite dislocation between concrete cracks.

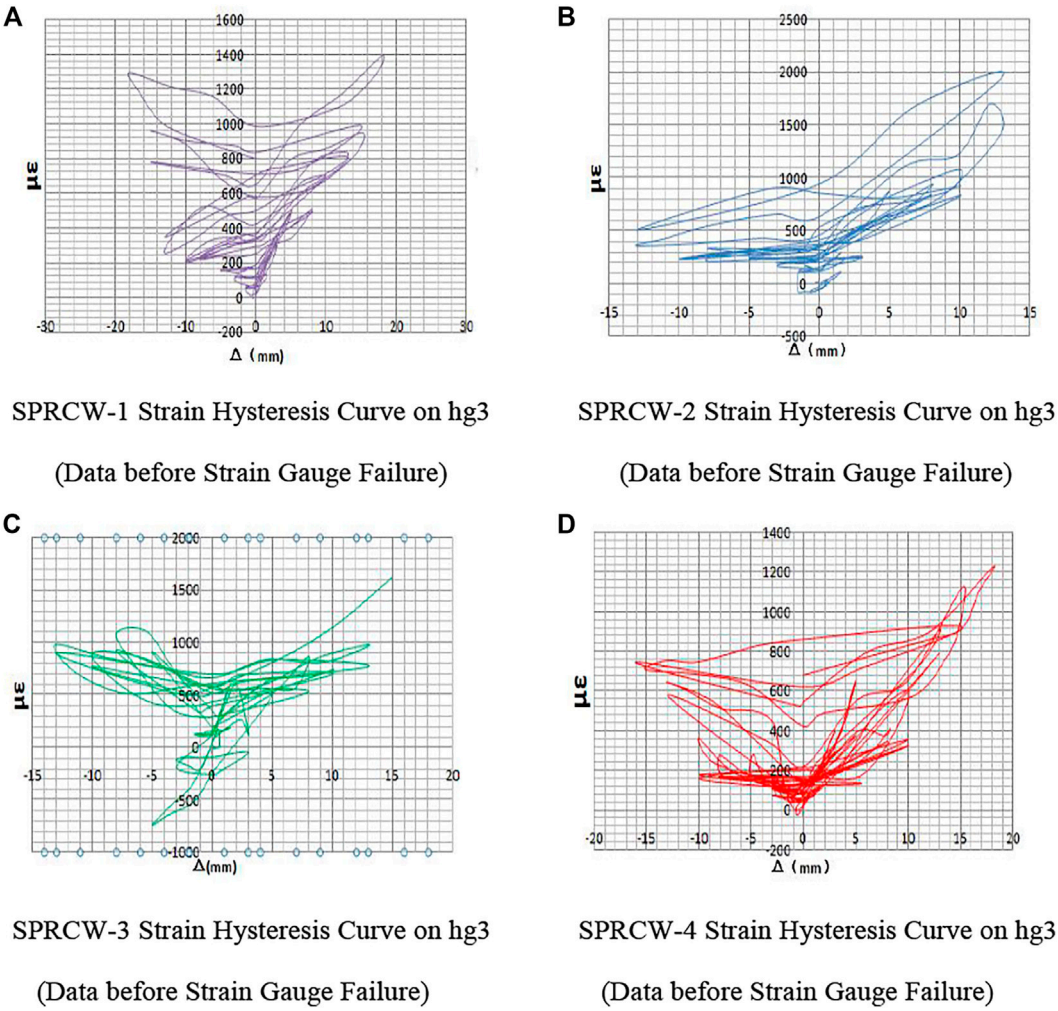

FIGURE 14 | Strain comparison diagram on hg3.

TABLE 6 | Strain statistics on measurement points of horizontally arranged reinforcement.

Measurement point	Test specimen No.	Horizontal displacement (mm)							
		1.5	3	5	8	10	13	15	18
hg-3	SPRCW-1	134	299	488	507	701	833	946	1,392
	SPRCW-2	117	260	896	944	1,085	1705	Overflow	Overflow
	SPRCW-3	184	397	657	869	743	981	1624	Overflow
	SPRCW-4	105	169	373	412	603	908	1122	1,225

2) In the two groups of comparison specimens, SPRCW-1 and SPRCW-4, and SPRCW-2 and SPRCW-3, the relative value of equivalent viscosity coefficient of SPRCW-2 in each displacement cycle stage from yield displacement to ultimate displacement was greater than SPRCW-3. The relative value of equivalent viscosity coefficient of SPRCW-1 was found also to be larger than that of SPRCW-4 under the same displacement controlled loading from yield displacement to ultimate displacement. Such findings reveal that under the same displacement control loading, when the steel plate in the wall was placed in the middle of the wall, the pinch of the specimen could be more effectively prevented, and the energy dissipation capacity of the structural wall could be improved.
3) In the comparison specimens of SPRCW-1, SPRCW-2, SPRCW-3, and SPRCW-4, the relative value of the equivalent viscosity coefficient of SPRCW-2 in each displacement cycle stage was close to SPRCW-1 at the

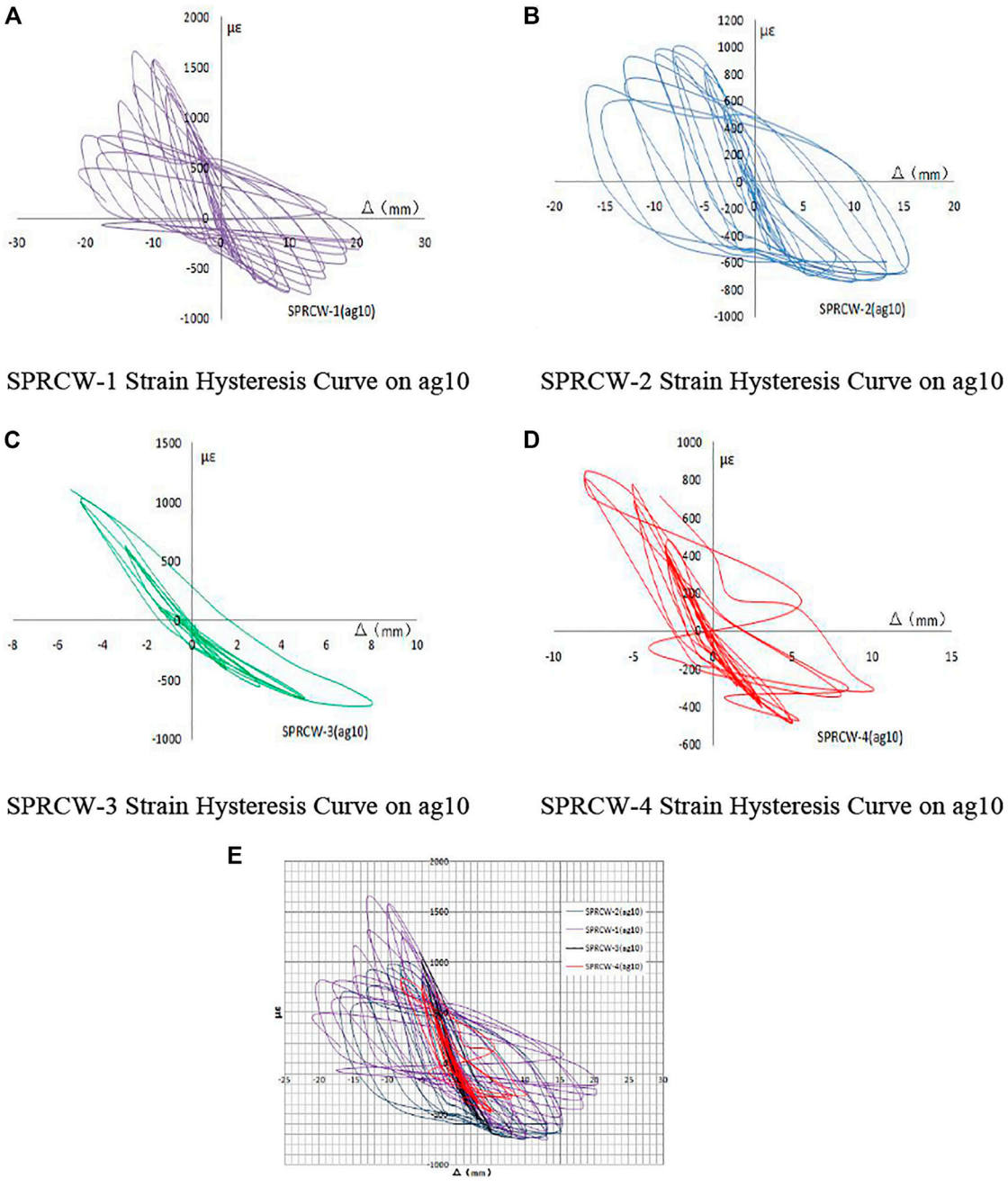

FIGURE 15 | Strain comparison diagram on ag10.

initial stage of the yield displacement to the ultimate displacement stage. SPRCW-3 was found to also be close to the relative value of equivalent viscosity coefficient of SPRCW-4 at the initial stage from yield displacement to ultimate displacement. In the later stage from yield displacement to ultimate displacement, the specimens with higher steel ratio in both groups had slightly lower equivalent viscous damping coefficients of SPRCW-1 and SPRCW-4, indicating that in the later stage from yield displacement to ultimate displacement, a slight pinch phenomenon would occur in the composite shear wall when the steel ratio of steel plate in the wall body was high, which is consistent with the hysteretic curves of SPRCW-1 and SPRCW-4.

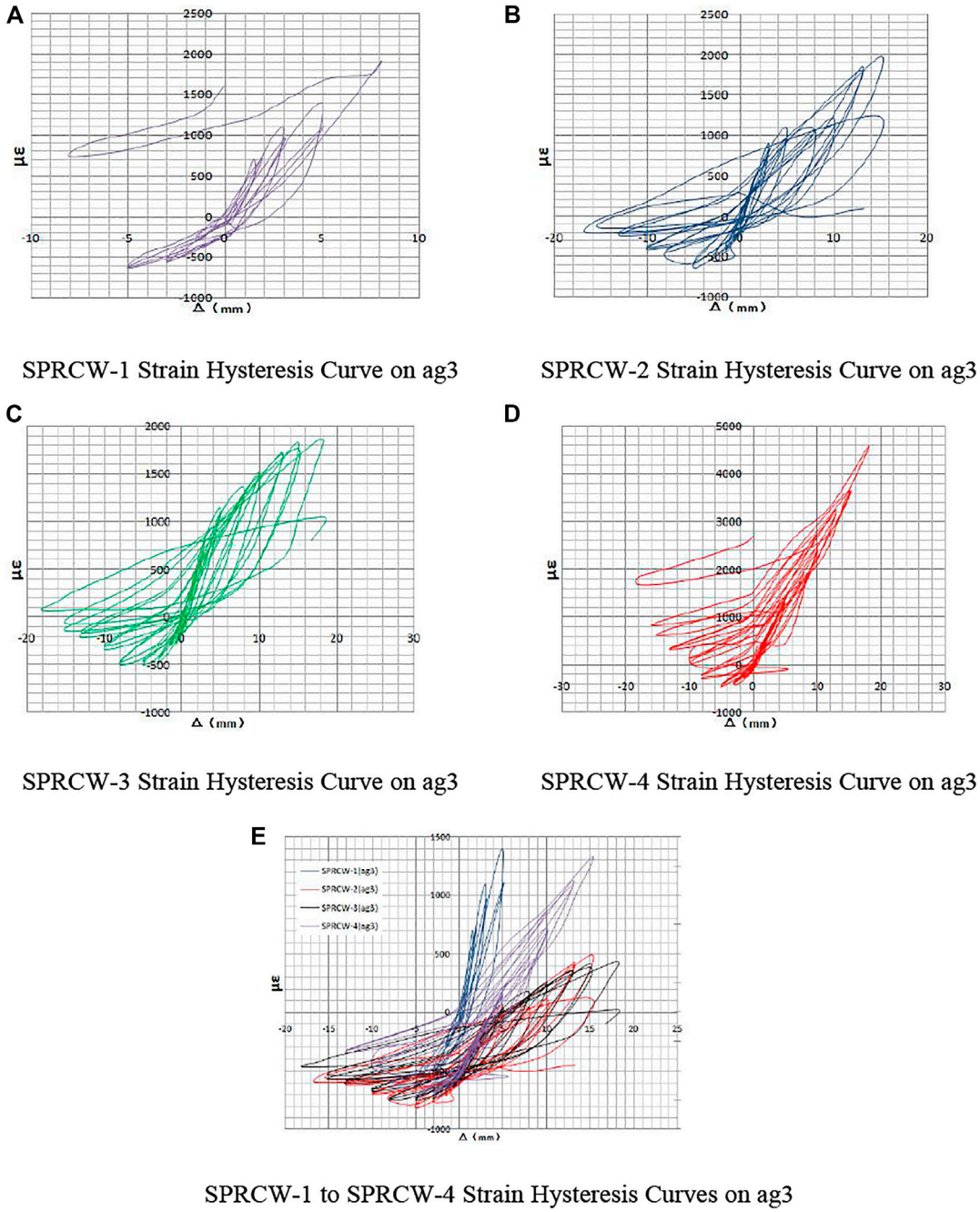

FIGURE 16 | Strain comparison diagram on ag3.

Comparative Analysis of Strength Attenuation Law

During the loading process, the bearing capacity of members would be reduced due to deformation and damage. In the study of structural earthquake resistance, the structural strength is generally measured by the strength attenuation coefficient. The strength attenuation coefficient of the present test was calculated using the following formula:

$$\beta = \frac{P_2}{P_1} \tag{7}$$

where P_1 is the extreme value of horizontal bearing capacity in the first cycle during each displacement cycle, and P_2 is the extreme value of horizontal bearing capacity in the second cycle during each displacement cycle.

Figure 18 shows the strength attenuation curves of five specimens of composite shear wall and section steel shear

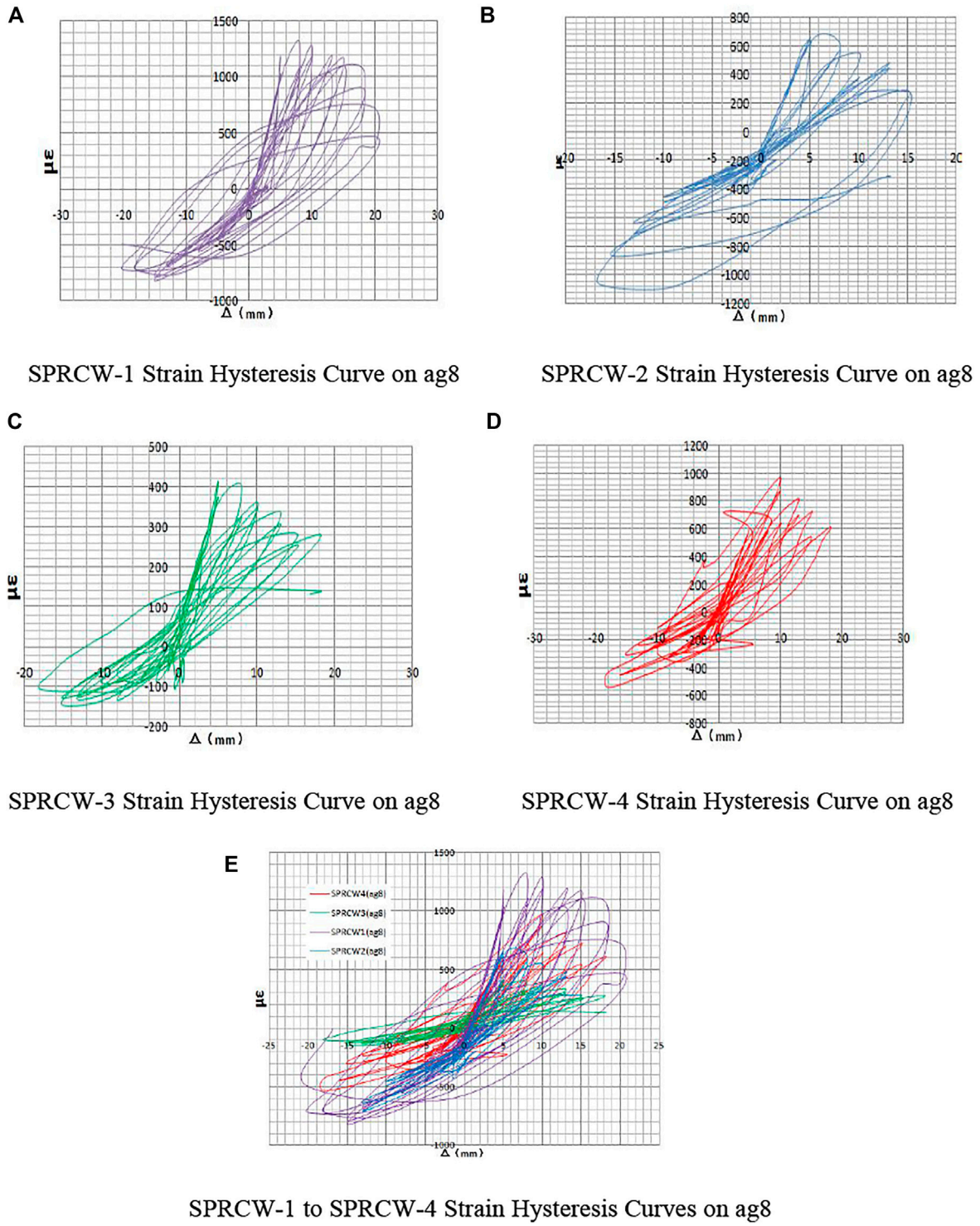

FIGURE 17 | Strain comparison diagram on ag8.

wall under different parameters, which can be seen as follows:

1) Before the SPRCW-1-4 strength attenuation coefficient reached the limit displacement β, a crack developed, and the steel plate in the wall body began to directly participate in resisting part of the external force, such that the bearing capacity of the specimen was slightly improved before reaching the ultimate bearing capacity. An observation can be made from the SPRCW-1-4 test phenomenon that the steel plate had a

TABLE 7 | Strain statistics on measurement points of vertically arranged reinforcement in embedded columns in the walls at different stages.

Measurement point	Test specimen No.	Horizontal displacement (mm)							
		1.5	3	5	8	10	13	15	18
ag-3	SPRCW-1	703	1087	1383	1897	Overflow	Overflow	Overflow	Overflow
	SPRCW-2	475	907	1091	1221	1424	1981	Overflow	Overflow
	SPRCW-3	278	508	1345	1480	1832	1866	Overflow	Overflow
	SPRCW-4	480	881	1311	1885	2385	Overflow	Overflow	Overflow
ag-8	SPRCW-1	13	305	1175	1317	1289	1035	1106	1086
	SPRCW-2	-195	25	618	630	554	385	282	Overflow
	SPRCW-3	10	192	413	403	360	338	284	281
	SPRCW-4	-3	273	597	682	740	818	914	990
ag-10	SPRCW-1	223	723	931	1225	1575	1646	1154	818
	SPRCW-2	30	466	867	1001	953	899	702	Overflow
	SPRCW-3	109	627	1023	1104	Overflow	Overflow	Overflow	Overflow
	SPRCW-4	228	473	643	842	Overflow	Overflow	Overflow	Overflow

Note: The data in the table are the strain values obtained by forward loading in the first cycle of loading.

TABLE 8 | Ductility coefficient of the specimens.

Number of test specimen	Yield displacement (mm)	Limit displacement (mm)	Ductility coefficient	Relative value of ductility coefficient
SPRCW – 1	2.787	15.492	5.559	1.075
SPRCW – 2	2.414	12.481	5.170	1
SPRCW – 3	2.616	13.726	5.618	1.087
SPRCW – 4	3.095	17.729	5.728	1.107

TABLE 9 | Relative energy dissipation coefficient.

Cycle serial number	Relative energy dissipation coefficient of each loading stage				
	SPRCW-1	SPRCW-2	SPRCW-3	SPRCW-4	
1	1.191	0.837	0.578	0.648	Cracking
2	0.921	0.658	0.521	0.581	Δ = 1.5 *mm*
3	0.632	0.569	0.498	0.746	Δ = 3 *mm*
4	0.723	0.636	0.517	0.4853	Δ = 5 *mm*
5	0.891	0.927	0.728	0.801	Δ = 8 *mm*
6	0.780	0.825	0.704	0.723	Δ = 10 *mm*
7	0.914	1.012	0.920	0.764	Δ = 13 *mm*
8	0.977	1.577	1.108	0.824	Δ = 15 *mm*
9	1.234		1.767	1.32	Δ = 18 *mm*
10	1.401			1.552	Δ = 20 *mm*

TABLE 10 | Equivalent viscous damping coefficient.

Cycle serial number	Equivalent viscous damping coefficient at each loading stage				
	SPRCW-1	SPRCW-2	SPRCW-3	SPRCW-4	
1	18.963	13.323	9.200	10.320	Cracking
2	14.661	10.467	8.292	9.253	Δ = 1.5 *mm*
3	10.054	9.057	7.933	11.874	Δ = 3 *mm*
4	11.507	10.119	8.226	7.712	Δ = 5 *mm*
5	14.182	14.750	11.583	12.744	Δ = 8 *mm*
6	12.409	13.127	11.197	11.503	Δ = 10 *mm*
7	14.555	16.113	14.649	12.152	Δ = 13 *mm*
8	15.542	25.094	17.642	13.119	Δ = 15 *mm*
9	19.629		28.130	20.990	Δ = 18 *mm*
10	22.304			24.705	Δ = 20 *mm*

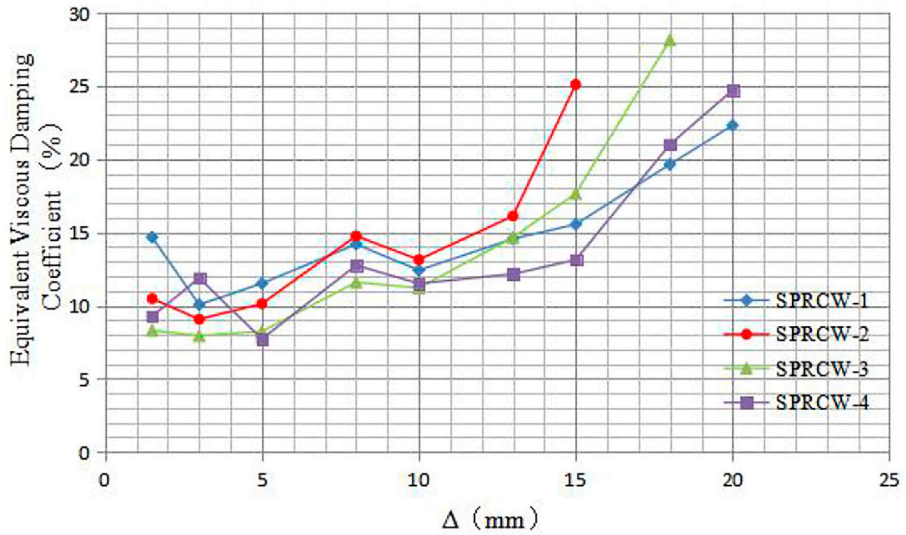

FIGURE 18 | Strength attenuation curves.

certain inhibitory effect on the development of wall cracks and through inclined cracks, which could effectively reduce the damage of the test piece, to improve the ability of the test piece to resist external effects to varying degrees. The built-in steel strip could effectively maintain the bearing capacity of the wall. When the bearing capacity of the specimen decreased to about 85% of the ultimate bearing capacity thereof, the value would drop rapidly, and the specimen would become damaged.

2) The strength attenuation coefficient curve of SPRCW-2 decreased the earliest and the fastest. Although the strength attenuation coefficient curve of SPRCW-3 decreased earlier, the decrease was slower compared with SPRCW-2. The attenuation rates of SPRCW-3 and SPRCW-4 were the same. After exceeding the limit displacement, SPRCW-4 decreased more slowly, indicating that when the steel ratio of the built-in steel plate belt in the wall was high, the built-in steel plate belt could delay the degradation of structural strength.

CONCLUSION

According to the performance of the four test specimens of composite shear walls under quasi-static loading, the seismic performance indexes of the four test specimens were calculated, analyzed, and compared in the present paper. The following conclusions were drawn:

1) By comparing the hysteresis curves and backbone curves of the four specimens, placing steel strips and angle steel embedded supports in the walls was found to be able to improve the bearing capacity of the shear walls to a certain extent. By comparing the hysteresis curves of SPRCW-2 and SPRCW-3, under the same steel ratio, the ultimate bearing capacity of SPRCW-3 was found to increase by 6%, and the slope of hysteresis curve was found to decrease slowly. The effect was more obvious when the steel ratio of the internal steel plate in the walls was higher, and angle steel embedded support could improve the bearing capacity of the walls most obviously.
2) Before the strain gauge was damaged, the extreme strain values of the section steel in SPRCW-1 and SPRCW-4 embedded columns were greater than those of SPRCW-2 and SPRCW-3, indicating that the bending bearing capacity of the section steel in SPRCW-1 and SPRCW-4 embedded columns was fully utilized, and the bending and shearing resistance of the walls could be simultaneously improved when the steel ratio in the walls was high, thereby ensuring the balanced development of the bending deformation and shearing deformation of the walls during the whole loading process.
3) Comparing the strain analysis results of the steel plate, the section steel, and the reinforcement of the four test specimens of composite shear walls, a conclusion could be drawn that the reasonable position of steel plate with a certain steel ratio and steel plate in the walls could effectively inhibit the shear deformation of the results, make the walls have strong shear rigidity, and ensure that the bending bearing capacity of vertically arranged reinforcement in the walls was fully utilized, thereby ensuring the structure had better ductility and energy dissipation capacity. Compared with SPRCW-1 and SPRCW-2, SPRCW-4 and SPRCW-3 took a longer time, indicating that when the steel strip in the walls was placed on both sides with the same steel ratio, the flexural rigidity of the composite shear walls slowly diminished, and the shear deformation composition became smaller.
4) Comparing the strength attenuation law of four specimens, the built-in steel plate and angle steel concealed support was found to be able to delay the attenuation speed of the structural bearing capacity, to improve the seismic performance of the structure. The location of the adjusting steel plate had little effect on slowing the decay rate of the structural bearing capacity, while increasing the rate of steel

distribution could effectively slow down the decay rate of the structural bearing capacity to a certain extent. However, the effect was not as obvious as that of the steel shear wall with a concealed bracing angle.

DATA AVAILABILITY STATEMENT

The original contributions presented in the study are included in the article/Supplementary Material. Further inquiries can be directed to the corresponding author.

AUTHOR CONTRIBUTIONS

YY analyzed the experiments and wrote the manuscript. MG, YY, and HZ revised the manuscript.

FUNDING

This study was supported by the National Natural Science Foundation of China (Grant No. 41372356), we gratefully acknowledge this support.

REFERENCES

Ayazi, A., and Shafaei, S. (2019). Steel-concrete Composite Shear walls Using Precast High Performance Fiber Reinforced concrete Panels. *Struct. Des. Tall Spec. Build* 28, 10e1617. doi:10.1002/tal.1617

Bahrami, A., and Yavari, M. (2019). Performance of Steel-concrete Shear walls with Two Sided Reinforced concrete. *Int. J. Eng. Technol. innovation* 9, 228–239.

Blandon, C. A., Arteta, C. A., Bonett, R. L., Carrillo, J., Beyer, K., and Almeida, J. P. (2018). Response of Thin Lightly-Reinforced concrete walls under Cyclic Loading. *Eng. structures* 176, 175–187. doi:10.1016/j.engstruct.2018.08.089

Ebadi, P., and Farajloomanesh, S. (2020). Seismic Design Philosophy of Special Steel Plate Shear walls. *Mag. civil Eng.* 95, 3–18. doi:10.18720/MCE.95.1

Edin, H. M. S., Ashour, A., and Galal, K. (2019). Seismic Performance Parameters of Fully Grouted Reinforced Masonry Squat Shear walls. *Eng. structures* 187, 518–527. doi:10.1016/j.engstruct.2019.02.06

Farzampour, A., Laman, J. A., and Mofid, M. (2015). Behavior Prediction of Corrugated Steel Plate Shear walls with Openings. *J. constructional steel Res.* 114, 258–268. doi:10.1016/j.jcsr.2015.07.018

GB/T 228 (2010). *Technical Specification for Tensile Test of Metal Materials at Room Temperature*. Beijing: China standard press.

JGJ 101 (2015). *Technical Specification for Seismic Tests of Buildings*. Beijing: China standard press.

Jiang, H., Li, S., and He, L. (2019). Experimental Study on a New Damper Using Combinations of Viscoelastic Material and Low-Yield-Point Steel Plates. *Front. Mater.* 6, 100. doi:10.3389/fmats.2019.00100

Jiang, H., Qiu, H., Sun, J., and Yang, Y. (2019). Behavior of Steel-concrete Composite Bolted Connector in Precast Reinforced concrete Shear wall. *Adv. Struct. Eng.* 22, 2572–2582. doi:10.1177/1369433219846957

Kassem, W., and Elsheikh, A. (2010). Estimation of Shear Strength of Structural Shear walls. *J. Struct. Eng.* 136, 1215–1224. doi:10.1061/(ASCE)ST.1943-541X.0000218

Labibzadeh, M., and Hamidi, R. (2019). A Design Formula for Lateral Load Resistance of concrete Filled Double-Steel-Plate walls with Small Height-To-Length Ratio. *KSCE J. Civ Eng.* 23, 3493–3508. doi:10.1007/s12205-019-1588-7

Lee, K.-J., Hwang, K.-M., Hahm, K.-W., and Yi, S.-T. (2018). Shear Strength of Joints between Reinforced concrete Slabs and Steel-Plate-concrete walls. *Proc. Inst. civil Eng. - structures buildings* 171, 739–754. doi:10.1680/jstbu.16.00138

Lim, W.-Y., Kang, T. H.-K., and Hong, S.-G. (2018). Effect of Reinforcement Details on Seismic Behavior of Precast Concrete Wall-Steel Coupling Beam Systems. *ACI Struct. J.* 115, 1751–1763. doi:10.14359/51702414

Lim, W.-Y., and Kim, S. (2017). Experimental Assessment of Seismic Vulnerability of Precast concrete Beam-To-Beam Connections with Steel Slit Damper. *Int. J. Steel Struct.* 17, 1249–1260. doi:10.1007/s13296-017-9030-9

Moretti, M. L., Kono, S., and Obara, T. (2020). On the Shear Strength of Reinforced Concrete Walls. *Sj* 117, 293–304. doi:10.14359/51724668

Rafiee, R., and Sharifi, P. (2019). Stochastic Failure Analysis of Composite Pipes Subjected to Random Excitation. *Construction building Mater.* 224, 950–961. doi:10.1016/j.conbuildmat.2019.07.107

Sun, X. F., Fang, X. S., and Guan, L. T. (2021). *Mechanics of Materials*. Beijing: Higher education press. (in Chinese).

Tolou Kian, M. J., and Cruz-Noguez, C. (2018). Reinforced concrete Shear walls Detailed with Innovative Materials: Seismic Performance. *J. Compos. Constr.* 22, 04018052. doi:10.1061/(ASCE)CC.1943-5614.0000893

Zhou, Z., Qian, J., and Huang, W. (2020). Shear Strength of Steel Plate Reinforced concrete Shear wall. *Adv. Struct. Eng.* 23, 1629–1643. doi:10.1177/1369433219898100

Conflict of Interest: The authors declare that the research was conducted in the absence of any commercial or financial relationships that could be construed as a potential conflict of interest.

Publisher's Note: All claims expressed in this article are solely those of the authors and do not necessarily represent those of their affiliated organizations, or those of the publisher, the editors, and the reviewers. Any product that may be evaluated in this article, or claim that may be made by its manufacturer, is not guaranteed or endorsed by the publisher.

frontiers in Materials

ORIGINAL RESEARCH
published: 20 December 2021
doi: 10.3389/fmats.2021.788746

Incorporation of Partially Hydrolyzed Polyacrylamide With Zwitterionic Units and Poly(Ethylene Glycol) Units Toward Enhanced Tolerances to High Salinity and High Temperature

Gang Lu[1,2], Jikuan Zhao[3], Shaoqi Li[3], Yuquan Chen[3], Chunfang Li[3], Youqi Wang[1,2] and Dongxiang Li[4]**

[1]State Key Laboratory of Shale Oil and Gas Enrichment Mechanisms and Effective Development, Beijing, China, [2]Research and Development Center for the Sustainable Development of Continental Sandstone Mature Oilfield by National Energy Administration, Beijing, China, [3]College of Chemistry and Molecular Engineering, Qingdao University of Science and Technology, Qingdao, China, [4]State Key Laboratory Base of Eco-chemical Engineering, Qingdao University of Science and Technology, Qingdao, China

OPEN ACCESS

Edited by:
Haibing Xia,
Shandong University, China

Reviewed by:
Tifeng Jiao,
Yanshan University, China
Wanli Kang,
China University of Petroleum (Huadong), China

***Correspondence:**
Jikuan Zhao
forestzhao@qust.edu.cn
Dongxiang Li
lidx@iccas.ac.cn

Specialty section:
This article was submitted to Polymeric and Composite Materials, a section of the journal Frontiers in Materials

Received: 03 October 2021
Accepted: 09 November 2021
Published: 20 December 2021

Citation:
Lu G, Zhao J, Li S, Chen Y, Li C, Wang Y and Li D (2021) Incorporation of Partially Hydrolyzed Polyacrylamide With Zwitterionic Units and Poly(Ethylene Glycol) Units Toward Enhanced Tolerances to High Salinity and High Temperature. Front. Mater. 8:788746. doi: 10.3389/fmats.2021.788746

Partially hydrolyzed polyacrylamide (HPAM) was widely implemented to improve the rheological properties of displacing fluids, but the high temperature and salinity of the reservoir brine limited their applications. Herein, copolymers including HPAM, zwitterion-modified HPAM (z-HPAM), PEG-modified HPAM (p-HPAM), and zwitterion/PEG-modified HPAM (zp-HPAM) were prepared by free radical polymerization in an aqueous solution. The viscosity of these copolymers under different temperature and salinity was measured in aqueous solution. It is found that the viscosity of the HPAM under the harsh condition (90°C, 20×10^4 mg/L salinity) is only 9.6% of that value under the normal condition (25°C, pure water), while the z-HPAM can significantly improve salt resistance by the effects of salting-in effect and intermolecular electrostatic crosslinking, showing a viscosity retention of 22.9% under the harsh condition. The addition of PEG-containing monomer can strengthen hydrogen bonding between the polymer chains and form a sterically ordered structure with improved salinity and temperature resistance. The synergistic effect of zwitterion units and PEG units endows the zp-HPAM with good salinity and temperature resistance; thus, the sample viscosity under the harsh condition remains 170 mPa s, which retains 29% of the value under the normal condition. The enhanced rheology properties of the zp-HPAM under the harsh condition are significant for the enhanced oil recovery of water-soluble polymer flooding.

Keywords: partially hydrolyzed polyacrylamide, viscosity, high salinity and high temperature, zwitteronic polymer, poly(ethylene glycol)

INTRODUCTION

Polymer flooding has better viscoelasticity and better sweep efficiency than simple water flooding for the enhanced oil recovery (Wever et al., 2011; Abidin et al., 2012; Wang et al., 2019). Especially in recent decades, water-soluble polymers such as partially hydrolyzed polyacrylamide (HPAM) have been widely implemented to improve the rheological properties of displacing fluids. However, such

HPAM flooding system is limited by temperature and salinity of the reservoir brine because the viscosity of the displacing fluids will be severely reduced under the harsh conditions above 75°C and 3×10^4 mg/L salinity in most oil reservoirs (Kamal et al., 2015). There are many reasons for the viscosity loss of water-soluble polymer fluids. For example, at high temperatures, (1) some polymer molecules will undergo thermal degradation and hydrolysis, and then the shortening of the polymer chain will result in a significant decrease in the intermolecular friction; (2) intensive thermal motion of the polymer chain reduces the stacking and tangling of the polymers; and (3) intensive thermal motion of solvent water molecules thins the hydration layer on the polymer chain, and the subsequent coiling and collapsing of the polymer chains cause the microscopic phase separation of the polymers from water. Otherwise, under a high salinity, (4) the strong "salting-out" effect promotes the phase separation of the polymers from water, because monovalent cations can shield the electrostatic repulsion among the carboxylate charges along the HPAM chains and compress the electric double layer of hydration film on the polymer surface, causing the polymer chain to coil and collapse (Liang et al., 2019); meanwhile, divalent ions, particularly Ca^{2+} and Mg^{2+}, can complex with the carboxylate groups, leading to the precipitation of the HPAM chains in the brines (Peng and Wu, 1999).

In the past years, to overcome the negative impact of high temperature on the HPAM fluid systems, the concept of "thermoviscosifying polymer" was proposed to have a response to high temperature and bring a rise of the system viscosity (L'Alloret et al., 1995; Hourdet et al., 1997; Petit et al., 2007). Such polymers, like poly (N-isoprpylacrylamide) and poly (ethylene glycol) (PEG), with a character of lower critical solution temperature (LCST), were attached to the skeleton of the HPAM; then, the thermally triggered response of these polymers brought an increase of the viscosity and elastic modulus at temperatures above LCST (Chen et al., 2013; Sarsenbekuly et al., 2017b; Chen et al., 2020; Li et al., 2021). Moreover, the dynamic simulation demonstrated that the HPAM incorporated with PEG units should have larger viscosity and stronger salt tolerance at high temperature because the modified monomers with alkyl ether bonds bring a steric hindrance and will reduce the curliness of the molecule chains (Yao et al., 2012; Zhang et al., 2015). Meanwhile, the incorporation of HPAM by hydrophobic long-alkyl groups displayed enhanced temperature and salinity tolerance (Lai et al., 2013; Liu et al., 2013; Ye et al., 2014; Gou et al., 2015c; Sarsenbekuly et al., 2017a), the modified HPAM by hydrophilic sulfonate groups also exhibited relatively high viscosity at high salinity and temperature (Gou et al., 2014; Li et al., 2018; Zhang et al., 2018; Hu et al., 2019; Ji et al., 2020; Tchameni et al., 2020), and even the incorporated HPAM by both long-alkyl groups and sulfonate groups showed improved rheological properties and salt resistance (Yuan et al., 2013; Deng et al., 2014; Gou et al., 2015b), but these results were not sufficient to meet the viscosity requirements of the polymer fluids in the brines from high-temperature and high-salt reservoirs. In addition, the structures of β-cyclodextrin in the HPAM skeleton displayed better temperature and salt tolerance due to the hydrophobic associating effect (Liu et al., 2013; Wei et al., 2015; Pu et al., 2016; Zhang et al., 2018; Peng et al., 2019), and some nature polysaccharides as flooding polymers were found to have a relatively low viscosity dependence on temperature and salinity (Gou et al., 2017; Liang et al., 2019), but the cost of polysaccharides, as well as β-cyclodextrin, limited their practice in the oil fields.

Zwitterionic polymers are composed of the main backbone chain and many side chains with positive and negative ions (Ladd et al., 2008). They are very hydrophilic because the solvation of zwitterions on the polymer chains can produce high solvent water retention and form a deeply hydrated layer around the polymer chains through anionic and cationic hydration (Leng et al., 2015). They also have strong salt affinity because the zwitterions on the polymer chains can electrostatically adsorb salt counterions in water (Li et al., 2020). So, zwitterionic polymers readily stretch in salt solution and have greater solubility in salt solution than in pure water (Mary et al., 2007), which is named as anti-polyelectrolyte behavior, i.e., "salting-in" effect (Yang et al., 2015; Xiao et al., 2018). Obviously, such superhydrophilicity and "salting-in" effect of zwitterionic polymers can reduce the dehydration of polymer chains at high temperatures, and thus can possibly overcome the "salting-out" effect of polymers under high salinity. Unfortunately, only little literature has focused on this topic for the enhanced oil recovery (Gou et al., 2015a; Dai et al., 2017; Liu et al., 2020). A modified HPAM with zwitterionic betaine groups and long alkyl groups reported by Kang et al. showed salt thickening behavior; a salt thickening mechanism was proposed that the destroyed inner salt bond of zwitterionic betaine groups in salt solution brought a greater hydrodynamic diameter of polymer molecules, and the inter-molecular hydrophobic interaction of the long alkyl groups in salt solution produced a stronger hydrophobic association (Zhu et al., 2017).

Herein, both zwitterionic sulfobetaine acrylate monomer and PEG-containing acrylate monomer were copolymerized with acrylamide (AM) and acrylic acid (AA) to prepare zwitterion-modified HPAM (z-HPAM), PEG-modified HPAM (p-HPAM), and zwitterion/PEG-modified HPAM (zp-HPAM) in order to study the rheological properties at different salinities and temperatures. The structures of these copolymers are shown in **Scheme 1**. It is found that zwitterionic sulfobetaine-unit incorporated HPAM (z-HPAM) obviously increases the viscosity under high salinity and high temperature, the incorporated HPAM with PEG units (p-HPAM) also exhibits enhanced salinity and temperature tolerance. The optimized zp-HPAM containing zwitterionic units and PEG units shows relatively high viscosity and good viscosity retention at 90°C in a synthetic brine of 20×10^4 mg/L salinity. The synergistic combination of zwitterionic units and PEG units in the zp-HPAM is considered to enhance the tolerance to high salinity and high temperature.

EXPERIMENTAL

Materials

Acrylamide (AM, 99%), acrylic acid (AA, >99%), and zwitterionic monomer [2-(Methacryloyloxy)ethyl]dimethyl-(3-sulfopropyl) ammonium inner salt (MDSA) were supplied by Shanghai Aladdin Biochemical Technology Co., Ltd., China.

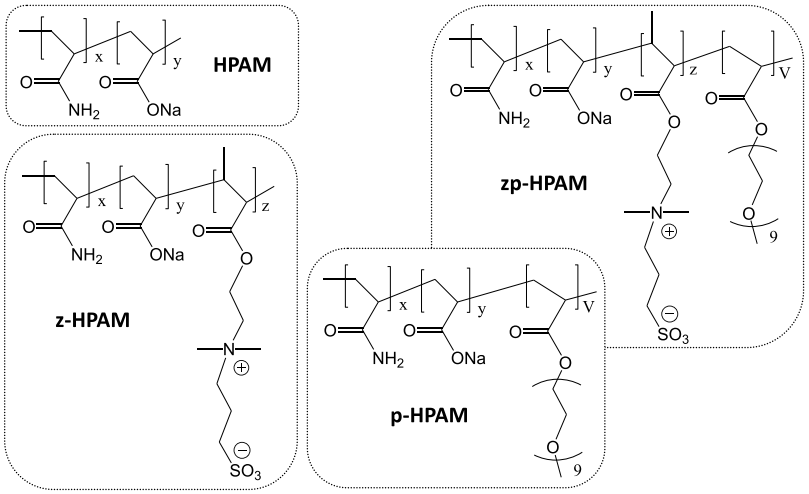

SCHEME 1 | Molecular structures of HPAM, zwitterion-modified HPAM (z-HPAM), PEG-modified HPAM (p-HPAM) and zwitterion/PEG-modified HPAM (zp-HPAM).

Poly(ethylene glycol) monomethyl ether acrylate ($H_2C = CHCO_2(CH_2CH_2O)_nCH_3$, $n \approx 9$, PEGMA) was provided by Shanghai Xianding Biotechnology Co., Ltd. Potassium persulfate ($K_2S_2O_8$), NaOH, anhydrous alcohol, NaCl, $MgCl_2$, and $CaCl_2$ were purchased from Sinopharm Chemical Reagent Co., Ltd. All reagents were of analytical grade and used directly without further purification. All aqueous solutions were prepared using ultrapure water with a resistivity of 18.25 MΩ cm.

Synthesis of Copolymers

For the copolymer synthesis, the total mass of AM and AA was fixed at 20 g, and a calculated volume of water was used to dilute the reactants to a monomer concentration of 10 wt%. In a typical process, a certain amount of AM, AA, and zwitterionic monomer MDSA were respectively dissolved in water, and the AA solution was then neutralized by isostoichiometric NaOH. All solutions were added to a 500-ml round-bottom three-necked flask, and a certain amount of PEGMA was added into the mixture. The monomers' molar ratio, namely, n_{AM}:n_{AA}:n_{MDSA}:n_{PEGMA}, was signed as x/y/z/V (x + y = 10) to label the sample. Next, the reaction solution was placed into a water bath at 70°C and bubbled with N_2 under stirring at least for 30 min to exclude dissolved oxygen. Subsequently, 10 ml of aqueous solution of potassium persulfate (0.57% of the total monomer mass) was added to the reaction mixture to initiate free radical polymerization. The reaction mixture was stirred under N_2 atmosphere for 3 h to form a viscous copolymer solution.

Characterization

For the measurements of ^{1}H NMR spectroscopy and FT-IR spectroscopy, the copolymer samples were precipitated and washed with anhydrous ethanol to remove water, unreacted monomers, and initiator, followed by a drying under vacuum at 50°C for 10 h. ^{1}H NMR spectra were recorded on a Bruker AV 500 MHz spectrometer in D_2O at 25°C. FT-IR spectra were measured on a Bruker Vertex 70 spectrometer according to the KBr-disk method between 4000 and 400 cm^{-1}. Morphology observation of the copolymer solutions was performed on a JSM-6700F scanning electron microscopy (SEM) with a voltage of 5.0 kV, in which the copolymer solutions (2.5wt%) were first dropped onto quartz sheets, quickly frozen in liquid nitrogen, and then freeze-dried before being coated with gold.

Preparation of Salt Solutions and Viscosity Measurements

In order to prepare solutions for viscosity measurement, the as-obtained 10 wt% copolymer solution was diluted with water and continually stirred to obtain a homogeneous solution of 5 wt% copolymers. Then, different amounts of salts were dissolved in deionized water to prepare synthetic brines, in which the molar ratio of $Na^+/Ca^{2+}/Mg^{2+}$ was fixed at 25.3/1/1.6. Thereafter, 50 ml of copolymer solution (5 wt%) was mixed with 50 ml of synthetic brines to obtain a series of copolymer solutions with different salinities from 1×10^4 to 20×10^4 mg/L of the total dissolved solids (TDS). All viscosity measurements were carried out on a Rheolab QC (Anton Paar, Austria) rotational rheometer using CC39 concentric-cylinder testing cup between 25 and 90°C by ascending shear rate ramps from 0.1 to 100 s^{-1}. The shear viscosity at different temperature was recorded at a fixed shear rate of 100 s^{-1}.

RESULTS AND DISCUSSION

FT-IR and NMR Characterization

The free radical polymerization of AM, AA, sulfobetaine methacrylate, and poly(ethylene glycol) methacrylate was

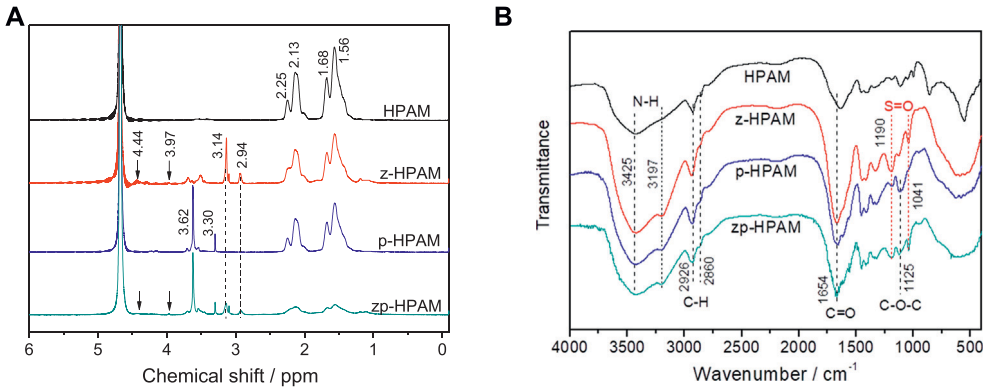

FIGURE 1 | ^{1}H NMR spectra **(A)** and FT-IR spectra **(B)** of HPAM (n_{AM}/n_{AA} = 9/1), z-HPAM ($n_{AM}/n_{AA}/n_{MDSA}$ = 9/1/1), p-HPAM ($n_{AM}/n_{AA}/n_{PEGMA}$ = 9/1/0.14), and zp-HPAM ($n_{AM}/n_{AA}/n_{MDSA}/n_{PEGMA}$ = 9/1/1/0.14).

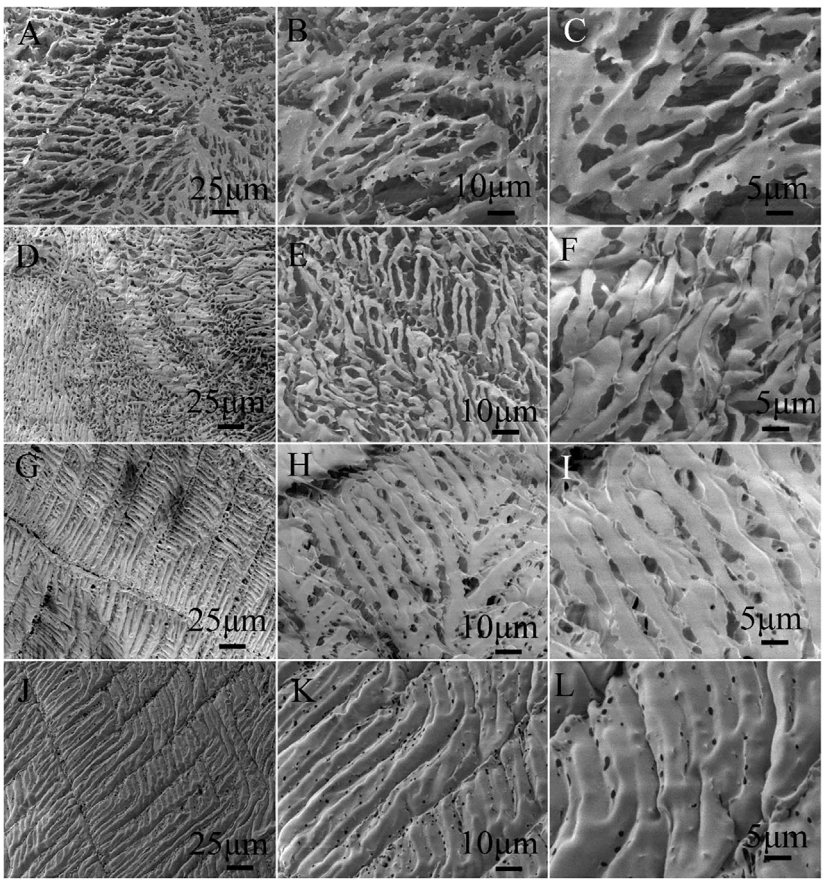

FIGURE 2 | SEM images of freeze-dried HPAM (n_{AM}/n_{AA} = 9/1) **(A,B,C)**, z-HPAM ($n_{AM}/n_{AA}/n_{MDSA}$ = 9/1/1) **(D,E,F)**, p-HPAM ($n_{AM}/n_{AA}/n_{PEGMA}$ = 9/1/0.14) **(G,H,I)**, and zp-HPAM ($n_{AM}/n_{AA}/n_{MDSA}/n_{PEGMA}$ = 9/1/1/0.14) **(J,K,L)**.

initiated by commonly used potassium persulfate. The as-obtained copolymer samples of HPAM, zwitterion-modified HPAM (z-HPAM), PEG-modified HPAM (p-HPAM), and zwitterion/PEG-modified HPAM (zp-HPAM) were characterized by ^{1}H NMR spectra, as shown in **Figure 1A**. For all samples, the peak at 4.68 ppm is due to residue solvent water, while the peaks at 1.56, 1.68, 2.13, and 2.25 ppm are ascribed to the skeleton of acrylate and acrylamide. The characteristic peaks

at 4.44, 3.97, 3.14, and 2.94 ppm reveal the presence of zwitterionic sulfobetaine groups in the z-HPAM and the zp-HPAM (Chang et al., 2006; Han et al., 2013), while in the p-HPAM and the zp-HPAM, the peaks at 3.62 and 3.30 ppm correspond to the O-CH_2 and O-CH_3 unit of PEG, respectively. In the FT-IR spectra of these samples (**Figure 1B**), the typical peaks at 3,425 and 3,197 cm^{-1} are attributed to N-H bonds, while those at 2,860 and 2,925 cm^{-1} are ascribed to CH_2 groups, and that peak around 1,654 cm^{-1} represents carbonyl groups in all samples. The characteristic peaks at 1,041 and 1,190 cm^{-1} in the z-HPAM and the zp-HPAM are caused by the symmetric stretching vibration of sulfonate groups from the zwitterionic units (Zhao et al., 2010), while that broad peak at 1,125 cm^{-1} in the p-HPAM and the zp-HPAM is evidence of C-O-C groups in the PEG units. All these results demonstrate that the designed copolymers have been successfully synthesized by the free radical polymerization.

SEM Characterization

The freeze-dried samples of HPAM, z-HPAM, p-HPAM, and zp-HPAM solutions were observed by SEM to investigate the microscopic structure of these copolymers in solution, as shown in **Figure 2**. It is found that the HPAM sample (**Figures 2A–C**) shows an irregular spatial network, which should be attributed to the aggregation and entanglement caused by the hydrogen-bond interaction between the amide and carboxyl groups in the polymer chains. The z-HPAM sample (**Figures 2D–F**) displays a more compact network and the pore size in the network is significantly reduced; the reason should be ascribed to the additional intermolecular electrostatic crosslinking *via* the ion pairing of two zwitterionic groups attached on different polymer chains. However, an ordered structure can be found in the sample of p-HPAM (**Figures 2G–I**), which should be related with the "comb-like" structure of the PEGMA segments in the copolymer skeleton, because the additional hydrogen-bond interaction between the PEG units and amide groups in the p-HPAM sample can facilitate the formation of the ordered structure. Comparing **Figures 2G–I** and **Figure 2J–L**, the network structure of the later zp-HPAM sample is more ordered than that of the p-HPAM, and the pore size of the zp-HPAM network is much smaller than that of the p-HPAM, which may mean more crosslinking sites in the spatial structure. We think that such a dense and ordered structure reveals that the zp-HPAM chains have more spatial crosslinking sites in the solution, and thus forming more uniform spatial distribution.

In aqueous solution, the HPAM sample exhibits a loose spatial network through the hydrogen bonding interaction of the amide and carboxylate, but in the z-HPAM sample, the additional crosslinking effect from the zwitterionic units promotes a formation of a denser network structure. However, for p-HPAM and zp-HPAM samples, the presence of PEG units strengthens the hydrogen bonding interaction and promotes the association of polymer chains to form ordered structures. The enhanced hydrogen bonding by the PEG units and the electrostatic crosslinking by the zwitterionic units in the zp-HPAM sample help to form a more uniform and stable spatial network, which will be beneficial to maintain the system viscosity under the harsh conditions.

Viscosity of HPAM and Zwitterion-Modified HPAM

The homogeneous copolymer solutions with a concentration of 2.5 wt% were used to measure the rheology properties in pure water and the synthetic brines, and the apparent viscosity of these solutions was recorded at the fixed shear rate of 100 s^{-1}. **Figure 3A** shows the apparent viscosity change of the HPAM and the z-HPAM at 25°C under different salinity. It is found that the viscosity of the HPAM rapidly drops from 105 mPa s to 70 mPa s when the salinity exceeds 1×10^4 mg/L. However, after adding 10% MDSA to AM/AA in copolymerization, the obtained z-HPAM is found to be more viscous than the HPAM, with a viscosity value between 140 and 190 mPa s. It is worth noting that changing the AM/AA molar ratio from 9/1 to 9.5/0.5 has little effect on the solution viscosity at different salinities. The viscosity of the z-HPAM solution decreases first and then gradually increases with the salinity increasing. The final viscosity under the highest salinity (20×10^4 mg/L) is similar to that value in pure water, which is better than the sufitiobetaine-modified HPAM as reported by Gou et al. (2015a). The salt thickening of the z-HPAM under high salinity can be ascribed to the following possible reasons: (1) The "salting-in" effect of zwitterionic units can overcome the viscosity reduction of the HPAM skeleton by the "salting-out" effect (Mary et al., 2007; Yang et al., 2015; Xiao et al., 2018; Li et al., 2020). The modified HPAM with zwitterionic betaine groups were found to have a larger hydrodynamic diameter in salt solution than in pure water, because the better solubility of zwitterionic betaine groups in salt solution can partially offset the coiling of polymer chains (Zhu et al., 2017). (2) The intermolecular ion pairing of the zwitterionic ions attached on different polymer chains can generate electrostatic crosslinking sites between different polymer chains. (3) The intermolecular crosslinking sites can be formed by the bridging of the divalent cations (Ca^{2+} and Mg^{2+}) in the synthetic brine (Zhu et al., 2017; Bai et al., 2021). **Figure 3B** shows the change in the viscosity of the z-HPAM ($n_{AM}/n_{AA}/n_{MDSA}$ = 9/1/1) with respect to salinity at different temperatures. The viscosity in the highest salinity solution is found to be approximately 70% of that value in pure water between 35°C and 75°C, whereas at 90°C, the viscosity value increases under higher salinities. Interestingly, the viscosity value at 90°C under 20×10^4 mg/L salinity reaches 42.8 mPa s, which is about 1.6 times the value at 90°C in pure water.

Figures 3C,D show the viscosity change of the HPAM (n_{AM}/n_{AA} = 9/1) and the z-HPAM ($n_{AM}/n_{AA}/n_{MDSA}$ = 9/1/1) with temperature at different salinities. It is clear that the viscosity of HPAM in pure water or in the synthetic brines gradually decreases to about 10 mPa s as the temperature rises to 90°C (**Figure 3C**), and the viscosity retention rate at 90°C changes in a range of 10.7%–13.8% of the corresponding value at 25°C under different salinities. The viscosity under the harsh condition (i.e., 90°C, 20×10^4 mg/L salinity, the same below) only retains 9.6% of the value under the normal condition

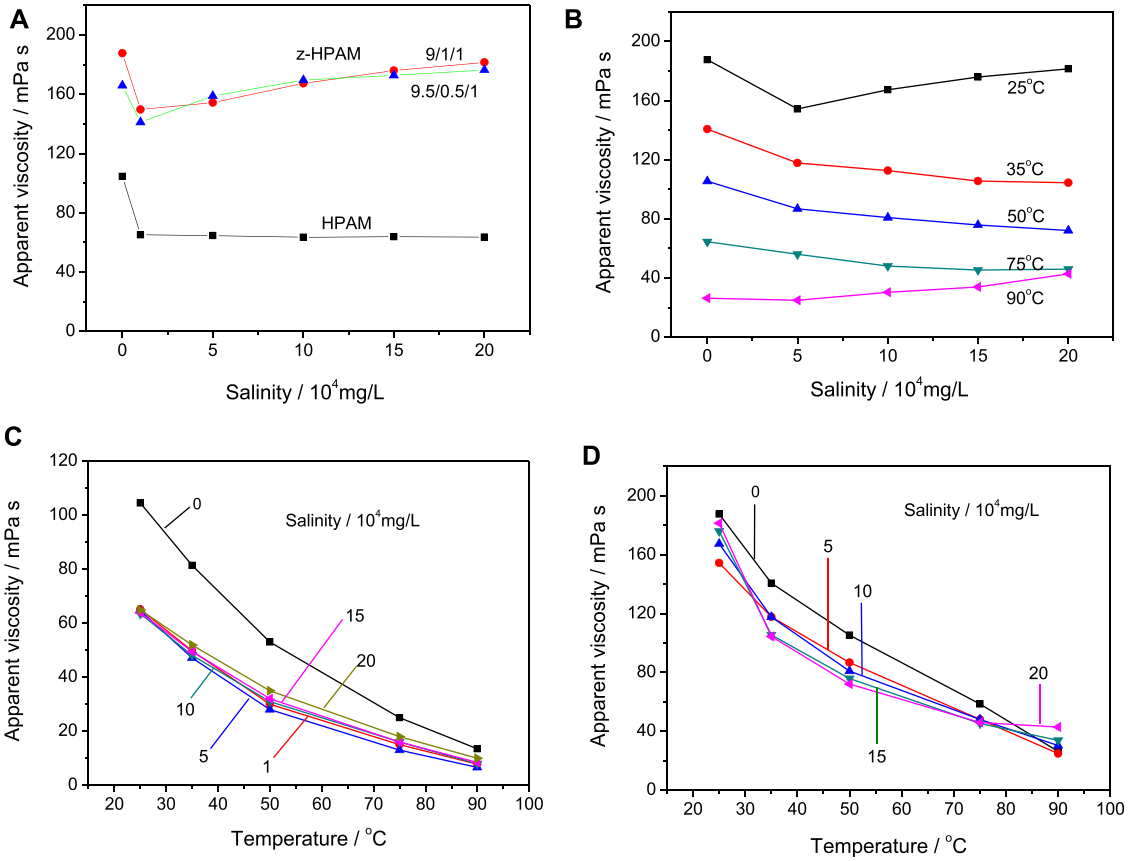

FIGURE 3 | Solution viscosity change of HPAM (n_{AM}/n_{AA} = 9/1) and z-HPAM ($n_{AM}/n_{AA}/n_{MDSA}$ = 9/1/1 or 9.5/0.5/1) to salinity **(A)**, that of z-HPAM ($n_{AM}/n_{AA}/n_{MDSA}$ = 9/1/1) to salinity **(B)**, and that of HPAM (n_{AM}/n_{AA} = 9/1) **(C)** and z-HPAM ($n_{AM}/n_{AA}/n_{MDSA}$ = 9/1/1) **(D)** to temperature.

TABLE 1 | Viscosity (mPa·s) of HPAM and zwitterion-modified HPAM at 90°C.

Components ($n_{AM}/n_{AA}/n_{MDSA}$)	Salinity/10^4 mg/L					
	0	1	5	10	15	20
9/1/1	26.3	—	24.9	30.3	33.8	42.8
9/1/0.5	18.5	10.9	—	11.1	—	11.7
9/1/0.25	8.7	4.1	—	5.6	—	7.5
9/1/0	13.5	7.8	6.6	7.9	8.4	10.0

(i.e., 25°C in pure water, the same below). For the z-HPAM sample (**Figure 3D**), the viscosity data similarly show a decrease with increasing temperature. From 35°C to 75°C, the viscosity of the z-HPAM at higher salinities (10–20 × 10^4 mg/L) is lower than that at lower salinity cases (0–5 × 10^4 mg/L), but at 90°C, the viscosity at the highest salinity is greater than that of low salinity. The viscosity retention rate at 90°C gradually increases from 14.1% to 23.6% of the value at 25°C under different salinities from 0 to 20 × 10^4 mg/L. Such viscosity retention values of the z-HPAM at 90°C are much larger than those of the HPAM at 90°C, indicating an enhanced tolerance to high temperature under the harsh condition. In addition, the viscosity retention rate under the harsh condition is 22.9% of that under the normal condition.

Table 1 shows the viscosity data of the z-HPAM with different zwitterion content at 90°C under different salinities. Obviously, the viscosity of z-HPAM decreases first and then increases at different salinities, which should be attributed to the "salting-in" and "electrostatic crosslinking" effects of zwitterionic units (Li et al., 2020). Noticeably, the viscosity value obviously decreases at any salinity when the zwitterion content is reduced. When the zwitterion content is 5% relative to AM/AA ($n_{AM}/n_{AA}/n_{MDSA}$ = 9/1/0.5), the z-HPAM sample shows viscosity values similar to those of the HPAM, and when the zwitterion content is 10% ($n_{AM}/n_{AA}/n_{MDSA}$ = 9/1/1), the viscosity is much larger than that of the HPAM. Therefore, we think the content of 10% zwitterionic monomer to AM/AA ($n_{AM}/n_{AA}/n_{MDSA}$ = 9/1/1) is effective for enhancing viscosity under high salinities, and the presence of zwitterionic units can also improve the tolerance to high temperature.

Viscosity of PEG-Modified HPAM

The polymers of PEG-containing acrylates were reported to have a thermally triggered response to temperature rising (Han et al., 2003; Ali and Stöver, 2004; Li et al., 2007), and the dynamic simulation demonstrated that the HPAM incorporated with PEG-containing units should have higher viscosity and stronger salt resistance (Yao et al., 2012; Zhang et al., 2015). In this work, poly(ethylene glycol) monomethyl ether acrylate

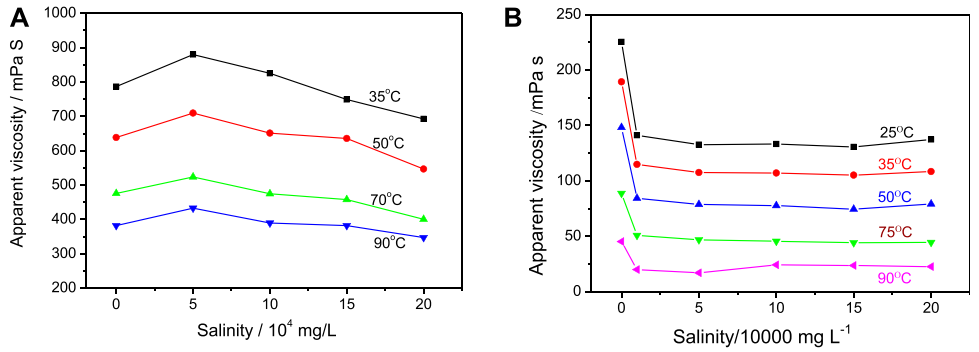

FIGURE 4 | Solution viscosity change of p-HPAM ($n_{AM}/n_{AA}/n_{PEGMA}$ = 9/1/0.14) **(A)** and ($n_{AM}/n_{AA}/n_{PEGMA}$ = 9/1/0.12) **(B)** to salinity at different temperature.

(PEGMA) with a long PEG tail was used to modify HPAM. It was found that the viscosity of the synthesis solution was greatly increased when adding PEGMA in the copolymerization. When the molar content of PEGMA to AM/AA reached 2.0%, the resulting p-HPAM solution after the polymerization reaction showed typical viscoelasticity, and it was difficult to obtain a homogenous copolymer solution through diluting and stirring. In our experiment, a relatively homogenous solution of the p-HPAM was obtained when the PEGMA content was 1.4% (i.e., $n_{AM}/n_{AA}/n_{PEGMA}$ = 9/1/0.14). The rheological results of this p-HPAM sample are shown in **Figure 4A**. The viscosity values at different conditions are relatively large, ranging from 350 to 880 mPa s. As the salinity increases, the sample viscosity increases at 5 × 10^4 mg/L salinity, but gradually decreases when the salinity increases from 10 × 10^4 to 20 × 10^4 mg/L. The viscosity values at the highest salinity are about 80%–90% of those values in pure water at a same temperature. From another view, the viscosity data can be rearranged according to the temperature change (Supporting information, **Supplementary Figure S1A**). It is found that the p-HPAM solution at any salinity shows a viscosity decrease with increasing temperature. Under the same salinity, the viscosity values at 90°C (between 347 and 433 mPa s) are about half of the values at 35°C (between 693 and 787 mPa s). The viscosity retention under 20 × 10^4 mg/L salinity at 90°C is about 44% of the value in pure water at 35°C.

In addition, another p-HPAM sample with a lower PEGMA content ($n_{AM}/n_{AA}/n_{PEGMA}$ = 9/1/0.12) was prepared and characterized by the rheological properties. The solution viscosity values to salinity change are shown in **Figure 4B** (the rearranged data to temperature change are shown in **Supplementary Figure S1B**). The viscosity of this sample ranges from 20 to 225 mPa s under all measurement conditions, which is obviously smaller than those of the last p-HPAM sample. The viscosity retention rate of this sample under the harsh condition is only 16% of the value in pure water at 35°C and only 10% of the value in pure water at 25°C. Thus, the PEGMA content in the p-HPAM shows a great influence on the viscosity of the sample and its tolerance to the environmental salinity and temperature. Moreover, based on the comparison of **Figures 4A,B**, the p-HPAM ($n_{AM}/n_{AA}/n_{PEGMA}$ = 9/1/0.14) has better salinity tolerance than the sample with lower PEGMA ($n_{AM}/n_{AA}/n_{PEGMA}$ = 9/1/0.12).

Viscosity of Zwitterion/PEG-Modified HPAM

Zwitterion-modified HPAM (z-HPAM) is found to have better rheological properties at high salinity and high temperature than the unmodified HPAM. Similarly, the modified HPAM by PEG units (p-HPAM) exhibits better viscosity retention than the unmodified HPAM at high salinity and high temperature. If both zwitterionic units and PEG units are incorporated into the HPAM skeleton together, we believe that the obtained zwitterion/PEG-modified HPAM (zp-HPAM) may have a synergistic effect on the rheological properties at high salinity and high temperature. Therefore, the zp-HPAM samples were prepared, in which the molar amount of MSDA relative to AM/AA was fixed at 10% and that of PEGMA was 1.4%, 1.0%, and 0.6% for comparison. The viscosity data of these samples are plotted with salinity change (**Figures 5A–C**) and temperature change (**Supplementary Figures S2A–C**), respectively. For the sample containing 1.4% PEGMA, the measured viscosity varies from 70 to 1,200 mPa s under all measurement conditions. When the temperature rises from 25°C to 75°C (**Figure 5A**), the solution viscosity first decreases along with the salinity increase until the salinity reaches 10 × 10^4 mg/L; then, as the salinity rises from 10 × 10^4 mg/L to 20 × 10^4 mg/L, the solution viscosity increases instead. The viscosity at 20 × 10^4 mg/L salinity maintains more than 70% retention of the value in pure water at a same temperature. However, at 90°C, the solution viscosity is relatively stable under different salinities. Moreover, it is clear that the solution viscosity obviously decreases with the temperature increasing from 25°C to 90°C (**Supplementary Figure S2A**). The viscosity curve at low salinity (1 × 10^4 mg/L and 5 × 10^4 mg/L) or the highest salinity (20 × 10^4 mg/L) is above the viscosity curve at middle salinity (10 × 10^4 mg/L and 15 × 10^4 mg/L), which indicates that the sample solution has a lower viscosity under the middle salinity.

For the sample with 1.0% PEGMA, the viscosity value varies between 30 and 430 mPa s under all measurement conditions (**Figure 5B**), which is obviously lower than the last sample.

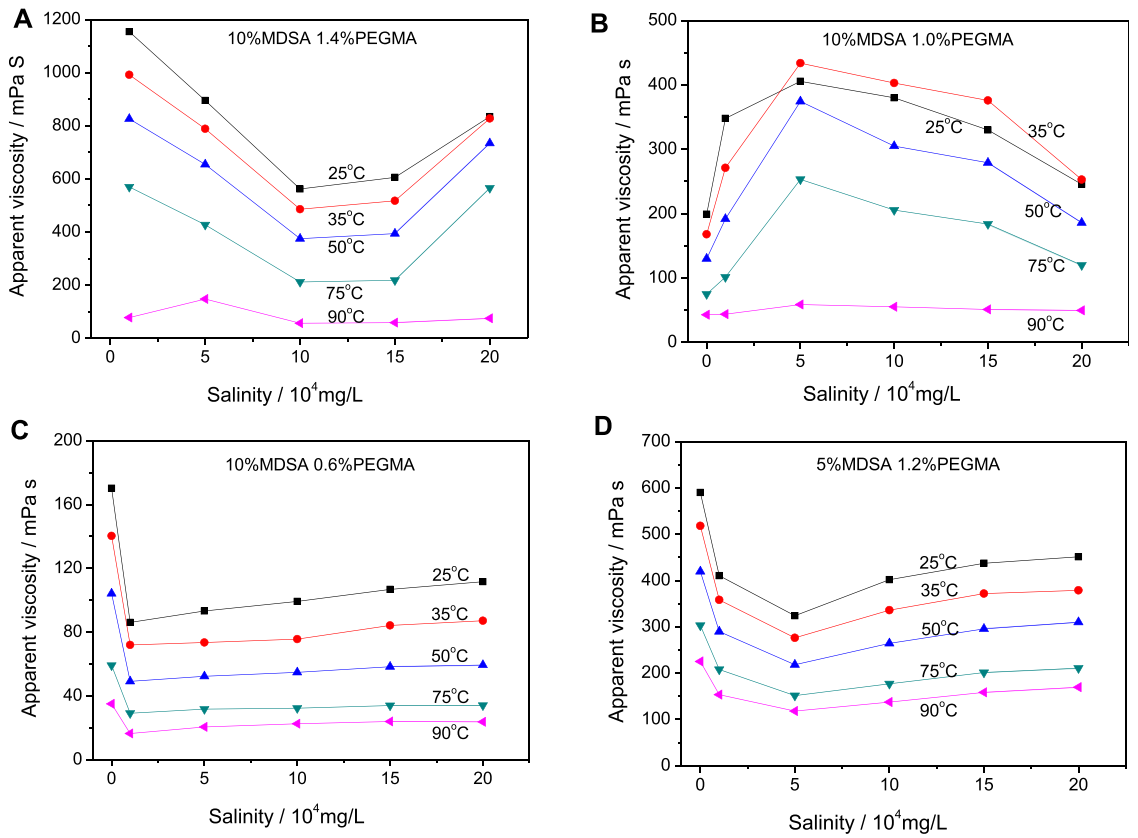

FIGURE 5 | Solution viscosity change of zp-HPAM with $n_{AM}/n_{AA}/n_{MDSA}/n_{PEGMA}$ of 9/1/1/0.14 **(A)**, 9/1/1/0.10 **(B)**, 9/1/1/0.06 **(C)**, and 9/1/0.5/0.12 **(D)** to salinity at different temperature.

Interestingly, under low salinity from 0 to 5 × 10^4 mg/L, the sample viscosity gradually increases. Then, with the salinity rising from 10 × 10^4 mg/L to 20 × 10^4 mg/L, the sample viscosity decreases in turn. Noticeably, at any same temperature, the viscosity of the sample under 20 × 10^4 mg/L is greater than that in pure water. Moreover, the sample in pure water or under a salinity of 1 × 10^4 mg/L shows a gradual decrease in viscosity from 25 to 90°C (**Supplementary Figure S2B**). However, as the salinity is above 5 × 10^4 mg/L, the sample viscosity increases first between 25°C and 35°C, and then decreases between 35°C and 90°C. It is also noticeable that the viscosity curves under the middle salinity (from 5 × 10^4 mg/L to 15 × 10^4 mg/L) are above those under other salinity cases (0, 1 × 10^4 mg/L and 20 × 10^4 mg/L). The final viscosity under the harsh condition is 39.7 mPa s, a 20% retention rate of the value under the normal condition.

Figure 5C and **Supplementary Figure S2C** show the viscosity data of the sample with 0.6% PEGMA. It is found that the measured solution viscosity varies between 16.5 and 170 mPa s, which is lower than the last two samples. In pure water, the sample solution viscosity varies between 170.2 and 35.1 mPa s at different temperatures (**Figure 5C**), but when the salinity reaches 1 × 10^4 mg/L, the viscosity drops sharply to about a half of that in pure water. Then, as the salinity increases, the solution viscosity slowly increases. When the salinity reaches 20 × 10^4 mg/L, the viscosity is about 60% of that in pure water at the same temperature. Moreover, the solution viscosity gradually decreases with increasing temperature under all salinities (**Supplementary Figure S2C**). The final viscosity under the harsh condition remains only 12% of that under the normal condition.

Comparing the curves in **Figures 5A,B**, the sample with 1.4% PEGMA has a higher viscosity in pure water, and the viscosity change shows concave curves with the increase of the salinity (**Figure 5A**), whereas the sample with 1.0% PEGMA has a lower viscosity in pure water, and the viscosity change shows convex curves with the salinity increasing (**Figure 5B**). Considering that the high viscosity of the sample with 1.4% PEGMA under low salinity will cause difficulty for fluid pumping in practices, the sample with 1.0% PEGMA is considered as the best one. Moreover, all three samples show a basic downward trend with the temperature increasing (**Supplementary Figures S2A–C**), but the viscosity of the zp-HPAM samples with 1.4 and 1.0% PEGMA drops sharply when the temperature increases from 75 to 90°C, which implies rapidly lowered viscosity tolerance at 90°C. Obviously, the significant difference in the salinity and temperature resistance of these zp-HPAM samples should be attributed to the different PEGMA content,

which will seriously affect the synergistic interaction of the zwitterion units and the PEG units.

It should be noted that the lowered tolerance of the zp-HPAM samples at 90°C (**Supplementary Figures S2A,B**) should be ascribed to the presence of the zwitterionic units because the p-HPAM samples (**Supplementary Figures S1A,B**) have exhibited relatively good environment tolerance at 90°C. So, we think that the environmental tolerance of the zp-HPAM at 90°C may be improved if lowering the zwitterion content. Therefore, the ratio of $n_{AM}/n_{AA}/n_{MDSA}/n_{PEGMA}$ in a new zp-HPAM sample was optimized to be 9/1/0.5/0.12. **Figure 5D** and **Supplementary Figure S2D** show the rheological properties of this zp-HPAM sample. At any temperature, the viscosity decreases first and then increases with the salinity increasing (**Figure 5D**) and the corresponding viscosity retentions under 20×10^4 mg/L salinity rise to 53%–73% of those values in pure water. In pure water, the sample viscosity retention at 90°C is about 38% of that value at 25°C (**Supplementary Figure S2D**), which is comparable with the hydrophobically associating polyacrylamide under similar conditions (Zheng and Huang, 2019). Though the viscosity of the sample in the synthetic brines gradually decreases with the temperature increasing, the final viscosity at the harsh condition remains 170 mPa s, a 29% retention of the value under the normal condition. This retention rate can be considered as a significant value for the HPAM-based fluid systems under the harsh condition.

CONCLUSION

The copolymers of HPAM, zwitterion-modified HPAM (z-HPAM), PEG-modified HPAM, and zwitterion/PEG-modified HPAM (zp-HPAM) were prepared by the free radical polymerization. The rheological properties of these copolymers in the aqueous solutions were studied under different salinities and temperatures. The following points were mainly concluded: (1) The viscosity of the HPAM under the harsh condition was only 9.6% of the value under the normal condition, while the z-HPAM significantly enhanced the viscosity retention to 22.9% under the harsh condition due to the salting-in effect and the electrostatic crosslinking by the divalent cations and the zwitterion units. (2) The PEG units in the p-HPAM samples improved the salinity and temperature resistances because they could strengthen the hydrogen bonding between the polymer chains and form a spatially ordered structure. (3) The zp-HPAM samples with the zwitterion and PEG units showed a complex impact on the rheological properties, the optimized zp-HPAM sample under the harsh condition exhibited a viscosity value of 170 mPa s and a viscosity retention rate up to 29% of the value under the normal condition. The good salinity and temperature tolerances of the zp-HPAM samples should be attributed to the synergistic effects of the zwitterion and PEG units. The enhanced rheological properties of the zp-HPAM under the harsh condition should be significant for the enhanced oil recovery in the water-soluble polymer flooding.

DATA AVAILABILITY STATEMENT

The original contributions presented in the study are included in the article/**Supplementary Material**. Further inquiries can be directed to the corresponding authors.

AUTHOR CONTRIBUTIONS

DL, GL, and JZ contributed to the conception and design of the study. SL, YC, YW, and CL performed the data collection and software treatment. GL and JZ performed the data analysis. DL gave a draft of the manuscript. GL, JZ, and DL wrote sections of the manuscript. All authors contributed to manuscript revision, read, and approved the submitted version.

SUPPLEMENTARY MATERIAL

The Supplementary Material for this article can be found online at: https://www.frontiersin.org/articles/10.3389/fmats.2021.788746/full#supplementary-material

REFERENCES

Abidin, A. Z., Puspasari, T., and Nugroho, W. A. (2012). Polymers for Enhanced Oil Recovery Technology. *Proced. Chem.* 4, 11–16. doi:10.1016/j.proche.2012.06.002

Ali, M. M., and Stöver, H. D. H. (2004). Well-Defined Amphiphilic Thermosensitive Copolymers Based on Poly(ethylene Glycol Monomethacrylate) and Methyl Methacrylate Prepared by Atom Transfer Radical Polymerization. *Macromolecules* 37 (14), 5219–5227. doi:10.1021/ma030485m

Bai, J., Wang, R., Ju, M., Zhou, J., Zhang, L., and Jiao, T. (2021). Facile Preparation and High Performance of Wearable Strain Sensors Based on Ionically Cross-Linked Composite Hydrogels. *Sci. China Mater.* 64 (4), 942–952. doi:10.1007/s40843-020-1507-0

Chang, Y., Chen, S., Zhang, Z., and Jiang, S. (2006). Highly Protein-Resistant Coatings from Well-Defined Diblock Copolymers Containing Sulfobetaines. *Langmuir* 22 (5), 2222–2226. doi:10.1021/la052962v

Chen, H., Liu, H., Zhang, S., and Feng, Y. (2020). Smart Thermoviscosifying Polymer for Improving Drag Reduction in Slick-Water Hydrofracking. *Fuel* 278, 118408. doi:10.1016/j.fuel.2020.118408

Chen, Q., Wang, Y., Lu, Z., and Feng, Y. (2013). Thermoviscosifying Polymer Used for Enhanced Oil Recovery: Rheological Behaviors and Core Flooding Test. *Polym. Bull.* 70 (2), 391–401. doi:10.1007/s00289-012-0798-7

Dai, C., Xu, Z., Wu, Y., Zou, C., Wu, X., Wang, T., et al. (2017). Design and Study of a Novel Thermal-Resistant and Shear-Stable Amphoteric Polyacrylamide in High-Salinity Solution. *Polymers* 9 (7), 296. doi:10.3390/polym9070296

Deng, Q., Li, H., Li, Y., Cao, X., Yang, Y., and Song, X. (2014). Rheological Properties and Salt Resistance of a Hydrophobically Associating Polyacrylamide. *Aust. J. Chem.* 67 (10), 1396–1402. doi:10.1071/ch14204

Gou, S., He, Y., Ma, Y., Luo, S., Zhang, Q., Jing, D., et al. (2015a). A Water-Soluble Antimicrobial Acrylamide Copolymer Containing Sulfitobetaine for Enhanced Oil Recovery. *RSC Adv.* 5 (64), 51549–51558. doi:10.1039/c5ra07495a

Gou, S., He, Y., Zhou, L., Zhao, P., Zhang, Q., Li, S., et al. (2015b). An Anti-biodegradable Hydrophobic Sulfonate-Based Acrylamide Copolymer

Containing 2,4-dichlorophenoxy for Enhanced Oil Recovery. *New J. Chem.* 39 (12), 9265–9274. doi:10.1039/c5nj01821h

Gou, S., Li, S., Feng, M., Zhang, Q., Pan, Q., Wen, J., et al. (2017). Novel Biodegradable Graft-Modified Water-Soluble Copolymer Using Acrylamide and Konjac Glucomannan for Enhanced Oil Recovery. *Ind. Eng. Chem. Res.* 56 (4), 942–951. doi:10.1021/acs.iecr.6b04649

Gou, S., Liu, M., Ye, Z., Zhou, L., Jiang, W., Cai, X., et al. (2014). Modification of a Nicotinic Acid Functionalized Water-Soluble Acrylamide Sulfonate Copolymer for Chemically Enhanced Oil Recovery. *J. Appl. Polym. Sci.* 131 (8), a–n. doi:10.1002/app.40166

Gou, S., Luo, S., Liu, T., Zhao, P., He, Y., Pan, Q., et al. (2015c). A Novel Water-Soluble Hydrophobically Associating Polyacrylamide Based on Oleic Imidazoline and Sulfonate for Enhanced Oil Recovery. *New J. Chem.* 39 (10), 7805–7814. doi:10.1039/c5nj01153a

Han, D., Letteri, R., Chan-Seng, D., Emrick, T., and Tu, H. (2013). Examination of Zwitterionic Polymers and Gels Subjected to Mechanical Constraints. *Polymer* 54 (12), 2887–2894. doi:10.1016/j.polymer.2013.04.003

Han, S., Hagiwara, M., and Ishizone, T. (2003). Synthesis of Thermally Sensitive Water-Soluble Polymethacrylates by Living Anionic Polymerizations of Oligo(ethylene Glycol) Methyl Ether Methacrylates. *Macromolecules* 36 (22), 8312–8319. doi:10.1021/ma0347971

Hourdet, D., L'Alloret, F., and Audebert, R. (1997). Synthesis of Thermoassociative Copolymers. *Polymer* 38 (10), 2535–2547. doi:10.1016/S0032-3861(96)00808-7

Hu, X., Ke, Y., Zhao, Y., Lu, S., Deng, Q., Yu, C., et al. (2019). Synthesis, Characterization and Solution Properties of β-cyclodextrin-functionalized Polyacrylamide/montmorillonite Nanocomposites. *Colloids Surf. A: Physicochemical Eng. Aspects* 560, 336–343. doi:10.1016/j.colsurfa.2018.10.035

Ji, Y. F., Cao, X. L., Zhu, Y. W., Xu, H., Sun, X. Z., and Li, H. T. (2020). Synthesis Of Super High Molecular Weight Copolymer Of AM/Naa/AMPS By Oxidation-Reduction And Controlled Radical Polymerization. *Pet. Sci.* 17 (1), 242–254. doi:10.1007/s12182-019-00385-1

Kamal, M. S., Sultan, A. S., Al-Mubaiyedh, U. A., and Hussein, I. A. (2015). Review on Polymer Flooding: Rheology, Adsorption, Stability, and Field Applications of Various Polymer Systems. *Polym. Rev.* 55 (3), 491–530. doi:10.1080/15583724.2014.982821

L'Alloret, F., Hourdet, D., and Audebert, R. (1995). Aqueous Solution Behavior of New Thermoassociative Polymers. *Colloid Polym. Sci.* 273 (12), 1163–1173. doi:10.1007/BF00653085

Ladd, J., Zhang, Z., Chen, S., Hower, J. C., and Jiang, S. (2008). Zwitterionic Polymers Exhibiting High Resistance to Nonspecific Protein Adsorption from Human Serum and Plasma. *Biomacromolecules* 9 (5), 1357–1361. doi:10.1021/bm701301s

Lai, N., Dong, W., Ye, Z., Dong, J., Qin, X., Chen, W., et al. (2013). A Water-Soluble Acrylamide Hydrophobically Associating Polymer: Synthesis, Characterization, and Properties as EOR Chemical. *J. Appl. Polym. Sci.* 129 (4), 1888–1896. doi:10.1002/app.38893

Leng, C., Hung, H.-C., Sun, S., Wang, D., Li, Y., Jiang, S., et al. (2015). Probing the Surface Hydration of Nonfouling Zwitterionic and PEG Materials in Contact with Proteins. *ACS Appl. Mater. Inter.* 7 (30), 16881–16888. doi:10.1021/acsami.5b05627

Li, D., Cui, Y., Wang, K., He, Q., Yan, X., and Li, J. (2007). Thermosensitive Nanostructures Comprising Gold Nanoparticles Grafted with Block Copolymers. *Adv. Funct. Mater.* 17 (16), 3134–3140. doi:10.1002/adfm.200700427

Li, D., Wei, Q., Wu, C., Zhang, X., Xue, Q., Zheng, T., et al. (2020). Superhydrophilicity and strong Salt-Affinity: Zwitterionic Polymer Grafted Surfaces with Significant Potentials Particularly in Biological Systems. *Adv. Colloid Interf. Sci.* 278, 102141. doi:10.1016/j.cis.2020.102141

Li, F., Zhu, W.-x., Yu, D.-z., Song, H., and Wang, K.-l. (2018). Rheological Properties and Enhanced Oil Recovery Performance of a Novel Sulfonate Polyacrylamide. *J. Macromolecular Sci. A* 55 (6), 449–454. doi:10.1080/10601325.2018.1470462

Li, S., Braun, O., Lauber, L., Leblanc, T., Su, X., and Feng, Y. (2021). Enhancing Oil Recovery from High-Temperature and High-Salinity Reservoirs with Smart Thermoviscosifying Polymers: A Laboratory Study. *Fuel* 288, 119777. doi:10.1016/j.fuel.2020.119777

Liang, K., Han, P., Chen, Q., Su, X., and Feng, Y. (2019). Comparative Study on Enhancing Oil Recovery under High Temperature and High Salinity: Polysaccharides versus Synthetic Polymer. *ACS Omega* 4 (6), 10620–10628. doi:10.1021/acsomega.9b00717

Liu, L., Gou, S., Zhang, H., Zhou, L., Tang, L., and Liu, L. (2020). A Zwitterionic Polymer Containing a Hydrophobic Group: Enhanced Rheological Properties. *New J. Chem.* 44 (23), 9703–9711. doi:10.1039/d0nj01687j

Liu, X., Jiang, W., Gou, S., Ye, Z., Feng, M., Lai, N., et al. (2013). Synthesis and Evaluation of Novel Water-Soluble Copolymers Based on Acrylamide and Modular β-cyclodextrin. *Carbohydr. Polym.* 96 (1), 47–56. doi:10.1016/j.carbpol.2013.03.053

Mary, P., Bendejacq, D. D., Labeau, M.-P., and Dupuis, P. (2007). Reconciling Low- and High-Salt Solution Behavior of Sulfobetaine Polyzwitterions. *J. Phys. Chem. B* 111 (27), 7767–7777. doi:10.1021/jp071995b

Peng, C., Gou, S., Wu, Q., Zhou, L., Zhang, H., and Fei, Y. (2019). Modified Acrylamide Copolymers Based on β-cyclodextrin and Twin-Tail Structures for Enhanced Oil Recovery through Host-Guest Interactions. *New J. Chem.* 43 (14), 5363–5373. doi:10.1039/c8nj06432f

Peng, S., and Wu, C. (1999). Light Scattering Study of the Formation and Structure of Partially Hydrolyzed Poly(acrylamide)/Calcium(II) Complexes. *Macromolecules* 32 (3), 585–589. doi:10.1021/ma9809031

Petit, L., Karakasyan, C., Pantoustier, N., and Hourdet, D. (2007). Synthesis of Graft Polyacrylamide with Responsive Self-Assembling Properties in Aqueous media. *Polymer* 48 (24), 7098–7112. doi:10.1016/j.polymer.2007.09.040

Pu, W., Du, D., Liu, R., Li, K., and Huang, T. (2016). Synthesis and Evaluation of β-cyclodextrin-functionalized Hydrophobically Associating Polyacrylamide. *RSC Adv.* 6 (98), 96006–96014. doi:10.1039/c6ra14209e

Sarsenbekuly, B., Kang, W., Fan, H., Yang, H., Dai, C., Zhao, B., et al. (2017a). Study of Salt Tolerance and Temperature Resistance of a Hydrophobically Modified Polyacrylamide Based Novel Functional Polymer for EOR. *Colloids Surf. A: Physicochemical Eng. Aspects* 514, 91–97. doi:10.1016/j.colsurfa.2016.10.051

Sarsenbekuly, B., Kang, W., Yang, H., Zhao, B., Aidarova, S., Yu, B., et al. (2017b). Evaluation of Rheological Properties of a Novel Thermo-Viscosifying Functional Polymer for Enhanced Oil Recovery. *Colloids Surf. A: Physicochemical Eng. Aspects* 532, 405–410. doi:10.1016/j.colsurfa.2017.04.053

Tchameni, A. P., Xie, B., Zhang, H., Zhao, L., Luo, M., and Wen, J. (2020). Thermo-associating Polymers Based on Cross-Linked 2-Acrylamido-Methylpropane Sulfonic Acid, Part A: Synthesis and Solution Behavior. *Colloids Surf. A: Physicochemical Eng. Aspects* 593, 124611. doi:10.1016/j.colsurfa.2020.124611

Wang, Z. M., Song, G.-L., and Zhang, J. (2019). Corrosion Control in CO2 Enhanced Oil Recovery from a Perspective of Multiphase Fluids. *Front. Mater.* 6, 272. doi:10.3389/fmats.2019.00272

Wei, B., Romero-Zerón, L., and Rodrigue, D. (2015). Improved Viscoelasticity of Xanthan Gum through Self-Association with Surfactant: β-cyclodextrin Inclusion Complexes for Applications in Enhanced Oil Recovery. *Polym. Eng. Sci.* 55 (3), 523–532. doi:10.1002/pen.23912

Wever, D. A. Z., Picchioni, F., and Broekhuis, A. A. (2011). Polymers for Enhanced Oil Recovery: A Paradigm for Structure-Property Relationship in Aqueous Solution. *Prog. Polym. Sci.* 36 (11), 1558–1628. doi:10.1016/j.progpolymsci.2011.05.006

Xiao, S., Ren, B., Huang, L., Shen, M., Zhang, Y., Zhong, M., et al. (2018). Salt-responsive Zwitterionic Polymer Brushes with Anti-polyelectrolyte Property. *Curr. Opin. Chem. Eng.* 19, 86–93. doi:10.1016/j.coche.2017.12.008

Yang, J., Chen, H., Xiao, S., Shen, M., Chen, F., Fan, P., et al. (2015). Salt-Responsive Zwitterionic Polymer Brushes with Tunable Friction and Antifouling Properties. *Langmuir* 31 (33), 9125–9133. doi:10.1021/acs.langmuir.5b02119

Yao, L., Chen, P., Ding, B., Luo, J., Jiang, B., and Zhou, G. (2012). Molecular Design of Modified Polyacrylamide for the Salt Tolerance. *J. Mol. Model.* 18 (9), 4529–4545. doi:10.1007/s00894-012-1447-7

Ye, Z., Zhang, X., Chen, H., Han, L., Lv, C., Su, Z., et al. (2014). Synthesis and Characterization of an Associative Polymer with an Octylphenyl Polyoxyethylene Side Chain as a Potential Enhanced-Oil-Recovery Chemical. *J. Appl. Polym. Sci.* 131 (20). doi:10.1002/app.41024

Yuan, R., Li, Y., Li, C., Fang, H., and Wang, W. (2013). Study about How the Metal Cationic Ions Affect the Properties of Partially Hydrolyzed Hydrophobically Modified Polyacrylamide (HMHPAM) in Aqueous Solution. *Colloids Surf. A: Physicochemical Eng. Aspects* 434, 16–24. doi:10.1016/j.colsurfa.2013.05.036

Zhang, C., Wang, P., and Song, G. (2018). Performance Evaluation of STARPAM Polymer and Application in High Temperature and Salinity Reservoir. *Int. J. Anal. Chem.* 2018, 1–13. doi:10.1155/2018/9653953

Zhang, P., Yao, L., Luo, J.-h., Ding, B., Zhou, G., and Jiang, B. (2015). Dynamics Simulation on the Associative Properties of Amphiphilic Functional Monomer Modified Polyacrylamide Copolymers. *Chin. J. Polym. Sci.* 33 (4), 540–553. doi:10.1007/s10118-015-1605-3

Zhao, Y.-H., Wee, K.-H., and Bai, R. (2010). Highly Hydrophilic and Low-Protein-Fouling Polypropylene Membrane Prepared by Surface Modification with Sulfobetaine-Based Zwitterionic Polymer through a Combined Surface Polymerization Method. *J. Membr. Sci.* 362 (1), 326–333. doi:10.1016/j.memsci.2010.06.037

Zheng, C., and Huang, Z. (2019). Self-assembly of Hydrophobic Associating Polyacrylamide Prepared by Aqueous Dispersion Polymerization. *J. Dispersion Sci. Tech.* 40 (9), 1317–1325. doi:10.1080/01932691.2018.1511434

Zhu, Z., Kang, W., Yang, H., Wang, P., Zhang, X., Yin, X., et al. (2017). Study on Salt Thickening Mechanism of the Amphiphilic Polymer with Betaine Zwitterionic Group by β-cyclodextrin Inclusion Method. *Colloid Polym. Sci.* 295 (10), 1887–1895. doi:10.1007/s00396-017-4169-7

Conflict of Interest: The authors declare that the research was conducted in the absence of any commercial or financial relationships that could be construed as a potential conflict of interest.

Publisher's Note: All claims expressed in this article are solely those of the authors and do not necessarily represent those of their affiliated organizations, or those of the publisher, the editors, and the reviewers. Any product that may be evaluated in this article, or claim that may be made by its manufacturer, is not guaranteed or endorsed by the publisher.

frontiers in Materials

ORIGINAL RESEARCH
published: 05 January 2022
doi: 10.3389/fmats.2021.818596

Sulfurization of Electrodeposited Sb/Cu Precursors for $CuSbS_2$: Potential Absorber Materials for Thin-Film Solar Cells

Aimei Zhao[1], Yanping Wang[1], Bing Li[1], Dongmei Xiang[1], Zhuo Peng[1], Yujie Yuan[1], Yupeng Xing[1], Liyong Yao[2], Jinlian Bi[1] and Wei Li[1]**

[1]Tianjin Key Laboratory of Film Electronic and Communication Devices, School of Integrated Circuit Science and Engineering, Tianjin University of Technology, Tianjin, China, [2]Tianjin Institute of Power Source, Tianjin, China

$CuSbS_2$, as a direct bandgap semiconductor, is a promising candidate for fabricating flexible thin-film solar cells due to its low grain growth temperature (300°C–450°C). Uniform and highly crystalline $CuSbS_2$ thin films are crucial to improving device performance. However, uniform $CuSbS_2$ is difficult to obtain during electrodeposition and post-sulfurization due to the "dendritic" deposition of Cu on Mo substrates. In this study, Sb/Cu layers were sequentially pulse electrodeposited on Mo substrates. By adjusting the pulse parameters, smooth and uniform Sb layers were prepared on Mo, and a flat Cu layer was obtained on Sb without any dendritic clusters. A two-step annealing process was employed to fabricate $CuSbS_2$ thin films. The effects of temperature on phases and morphologies were investigated. $CuSbS_2$ thin films with good crystallinity were obtained at 360°C. As the annealing temperature increased, the crystallinity of the films decreased. The $CuSbS_2$ phase transformed into a Cu_3SbS_4 phase with the temperature increase to 400°C. Finally, a 0.90% efficient solar cell was obtained using the $CuSbS_2$ thin films annealed at 360°C.

Keywords: $CuSbS_2$, pulse electrodeposition, Sb/Cu layer, post-sulfurization, thin-film solar cell

OPEN ACCESS

Edited by:
Xiaotian Wang,
Southwest University, China

Reviewed by:
Fangyang Liu,
Central South University, China
Hongkun Cai,
Nankai University, China

****Correspondence:***
Jinlian Bi
bijinlian815@126.com
Wei Li
cliwei618@126.com

Specialty section:
This article was submitted to Thin Solid Films, a section of the journal Frontiers in Materials

Received: *19 November 2021*
Accepted: *06 December 2021*
Published: *05 January 2022*

Citation:
Zhao A, Wang Y, Li B, Xiang D, Peng Z, Yuan Y, Xing Y, Yao L, Bi J and Li W (2022) Sulfurization of Electrodeposited Sb/Cu Precursors for $CuSbS_2$: Potential Absorber Materials for Thin-Film Solar Cells. Front. Mater. 8:818596. doi: 10.3389/fmats.2021.818596

INTRODUCTION

$CuSbS_2$ is a direct bandgap material, which can be adjusted between 1.4 and 1.6 eV (Medina-Montes et al., 2018; Pal et al., 2020), and its optical absorption coefficient is greater than $10^5\ cm^{-1}$ (Vinayakumar et al., 2019). Its grain growth temperature is within 300°C–450°C (Yang et al., 2014; Riha et al., 2017), which is lower than those of Cu (In, Ga) Se_2 and Cu_2ZnSnS_4. It is an excellent alternative material for flexible photovoltaic devices due to its low grain growth temperature. Various techniques, such as spray pyrolysis (Ramos Aquino et al., 2016; Wan et al., 2019; Zhou et al., 2021), ink (Banu et al., 2016; Banu et al., 2019), chemical bath deposition (Macías et al., 2017; Loranca-Ramos et al., 2018), sputtering (de Souza Lucas et al., 2016; Kang et al., 2018), evaporation (Rabhi et al., 2009; Wan et al., 2016), and electrodeposition (Septina et al., 2014; García et al., 2020), have been employed to fabricate $CuSbS_2$ thin films. Wan et al., (2016) fabricated stoichiometric $CuSbS_2$ thin films and Mo/$CuSbS_2$/CdS/ZnO/ZnO: Al/Ag structure solar cells via a two-stage co-evaporation, achieving a 1.9% efficiency with a 520-mV open-circuit voltage. Macías et al., (2017) fabricated $CuSbS_2$ thin films via a chemical bath method and treated the films at 380°C, achieving an encouraging efficiency of 0.6%. Zhang et al.(2019) fabricated Mo/$CuSbS_2$/CdS/ZnO/Al

structure cells via a one-step sputtering method and obtained a photovoltaic conversion efficiency of 2.55% with a 622-mV open-circuit voltage. The best efficiency of 3.22% was obtained by Banu et al., (2016).

Compared with other deposition methods, electrodeposition has the advantages of low equipment cost, simple operation, and high material usage rate (Lincot et al., 2004; Bhattacharya et al., 2012; Oliva et al., 2013; Vauche et al., 2016). Therefore, fabricating $CuSbS_2$ thin films *via* electrodeposition has been favored by researchers. The highest efficiency of $CuSbS_2$ thin films fabricated *via* electrodeposition is 3.13% (Septina et al., 2014), which is far lower than the maximum theoretical conversion efficiency of 22.9% (SLME) (Yu et al., 2013). The main factor limiting the further improvement of $CuSbS_2$ thin-film solar cells are 1) rough electrodeposited metal precursors lead the thickness and composition distribution to be nonuniform (Yuan et al., 2009; Gao et al., 2020)and 2) secondary phases, such as Sb_2S_3, $Cu_{12}Sb_4S_{13}$, and Cu_3SbS_4, easily form during annealing (Kang et al., 2018; Pal et al., 2020).

Zhang et al. (2016) have demonstrated the crystallinity of $CuSbS_2$ thin films fabricated by electrodepositing Mo/Cu/Sb metal layers followed by sulfurizing in 20% H_2S + Ar atmosphere for 1 h at 450°C. However, the surface roughness of the Mo/Cu/Sb metal layers was large, which further deteriorated the uniformity of $CuSbS_2$ thin films. Although Bi et al. (2016) eliminated the dendritic morphology of Cu on Mo *via* a pulse current electrodeposition method, the problem of dendritic clusters appeared again after the Cu thickness was reduced. To fabricate dendritic-cluster-free and smooth Cu films *via* electrodeposition, numerous studies have been conducted (Norkus et al., 2005; Moffat et al., 2007; Lee et al., 2012). Among them, adding organic additives in the electrodepositing solution could help reduce the surface roughness of Cu films and improve their flatness (Long et al., 2006; Favry et al., 2008). However, organic additives could easily be incorporated into the films as impurities, which would deteriorate the properties of the devices.

In this study, to solve the problem of rough metal precursors on Mo substrates, first, a smooth Sb layer was electrodeposited on a Mo substrate, and then, a Cu layer was electrodeposited on the Sb layer. A compact, flat, and uniform Sb/Cu layer was fabricated on a Mo substrate using the pulse current electrodeposition method. The metal stacking layer with the Sb/Cu atomic ratio of 1.7 was employed to fabricate $CuSbS_2$. In addition, the influences of temperature on structures, compositions, phases, and morphologies of $CuSbS_2$ thin films were systematically studied. Ultimately, 0.90% efficient $CuSbS_2$ solar cells were fabricated with a 13.58-mA/cm^2 current density.

MATERIALS AND METHODS

Preparation of the Sb/Cu Precursor

Mo back contact layer (1 μm) was fabricated on a clean soda-lime glass (SLG) *via* DC magnetron sputtering. Before the electrodeposition process, the fabricated SLG/Mo substrate was ultrasonically cleaned in alcohol for 30 min, followed by cleaning with deionized water to obtain a clean, oil-free Mo substrate. Afterward, Sb and Cu metal layers were fabricated on the Mo substrate *via* pulse electrodeposition at room temperature. An Sb solution was prepared using 0.3-M $SbCl_3$ and 2.2-M HCl, whereas a Cu solution was prepared using 0.8-M $CuSO_4$ and 0.76-M H_2SO_4. The diagram of the square wave pulse is shown in **Supplementary Figure S1**. There are three independent parameters: pulse current density (i_m), pulse on time (T_{on}), and pulse off time (T_{off}) in pulse electrodeposition. T_{off} is beneficial to recover ion concentration near a cathode and improve the coating quality. The T_{on}/T_{off} ratios of the electrodeposited Sb film were set to 1:1, 1:3, and 1:5; the pulse current densities were 31.25, 62.5, and 125 mA/cm^2; and the pulse frequency was 10,000 Hz. The T_{on}/T_{off} ratio of the electrodeposited Cu film was 1:3, the pulse current density was 62.5 mA/cm^2, and the pulse frequency was 10,000 Hz. The deposition charge densities of the Sb layer were varied from 0.5 to 1.275 C/cm^2. The pulse working conditions were provided by GKPT-FB4-24 V/10 A pulse/DC power supply manufactured by Shenzhen Shicheng Company, China.

Sulfurization of the Metal Precursor

$CuSbS_2$ thin films were fabricated by annealing Mo/Sb/Cu precursors in a double temperature quartz tube furnace. The alloyed precursor and 1-g sulfur powder (excess) were, respectively, placed in different temperature zones of the double temperature quartz tube furnace. The sulfur source temperature was maintained at 260°C with a 10°C/min heating rate. First, the metal stacks were annealed at 320°C in Ar atmosphere for 10 min and then sulfurized at 300°C–400°C for another 30 min. After free cooling to room temperature, the $CuSbS_2$ thin films were removed from the furnace.

Preparation of Devices

$CuSbS_2$ thin-film solar cells were prepared with the traditional structure of Mo/$CuSbS_2$/CdS/i-ZnO/ZnO: Al/Ni/Al. A CdS buffer layer of 50 nm was prepared via the chemical water bath method on $CuSbS_2$ thin films. The i-ZnO thin films with approximately 50-μm thickness were deposited on CdS thin films by AC magnetron sputtering; then, the Al-ZnO thin films with 500–800 nm thickness were deposited by DC sputtering. Finally, a Ni layer of 50 nm and an Al layer of 1 μm were deposited by electron beam evaporation as the collector. The effective area of the cell was 0.12 cm^2.

Characterization

The structure of the $CuSbS_2$ thin films was analyzed using X-ray diffractometry (XRD, Rigaku Smart Lab) and Raman spectrometry (Raman, Renishaw). The excitation wavelength of the Raman spectrometer was 532 nm. The surface roughness of the films was observed via atomic force microscopy (AFM, Dimension ICON). The morphology of the films and the elemental composition and distribution (EDS) of the samples were observed via field emission scanning electron microscopy (FE-SEM, Quanta FEG 250). The element composition and chemical states of the films were measured via energy-dispersive X-ray spectrometry (XPS,

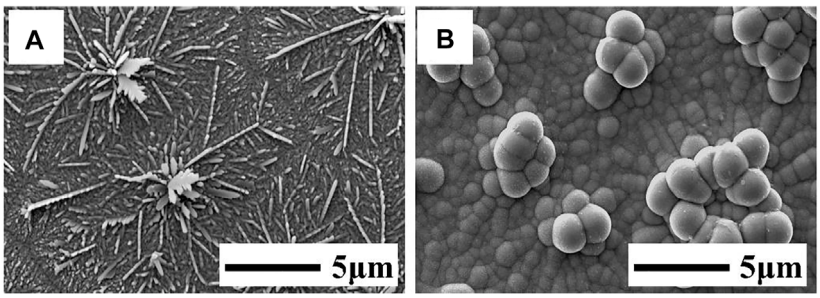

FIGURE 1 | SEM images of the **(A)** Mo/Cu and **(B)** Mo/Cu/Sb layers.

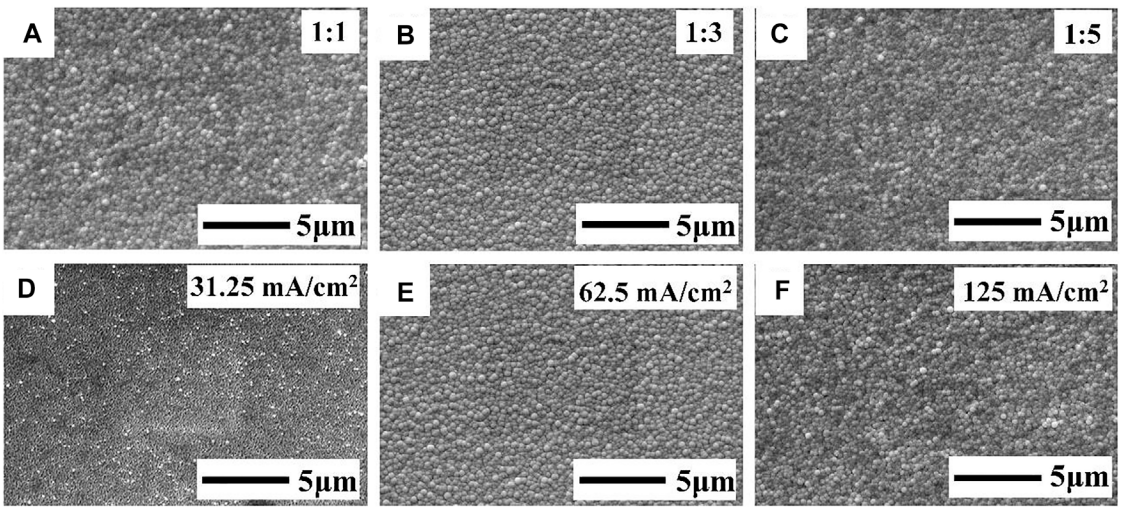

FIGURE 2 | FE-SEM images of the Sb film on the Mo substrate deposited with **(A–C)** T_{on}/T_{off} ratios of 1:1, 1:3, and 1:5, respectively, and a pulse current density of 62.5 mA/cm2; **(D–F)** pulse current densities of 31.25, 62.5, and 125 mA/cm^2 and a T_{on}/T_{off} ratio of 1:3.

ESCALAB250Xi). The J–V characteristics of $CuSbS_2$ solar cells were measured under a standard AM_1.5 spectrum using a solar simulator; the illumination intensity was 1000 WM^{-2}.

RESULTS AND DISCUSSION

Characteristics of the Sb/Cu Metal Precursors

Figure 1 shows the SEM images of Cu and Cu/Sb deposited on the Mo substrate. From **Figure 1A**, a "dendritic" morphology was formed by directly depositing the Cu layer on the Mo substrate. It was because the growth of Cu on Mo showed a three-dimensional island mode (Mercier et al., 2013). The growth rate of the Cu nucleus tended to be higher than the nucleation rate, inducing Cu to form a dendritic morphology (Budevski et al., 2000). The Sb layer electrodeposited on such a rough Cu underlayer usually resulted in a coarse Cu/Sb layer with bulging clusters on the Sb surface (**Figure 1B**). The non-uniform composition distribution of the rough Cu/Sb precursor tended to form copper-rich and -poor phases during annealing, which would increase the leakage current of the device and deteriorate its performance (Oliva et al., 2013; Kwon et al., 2014).

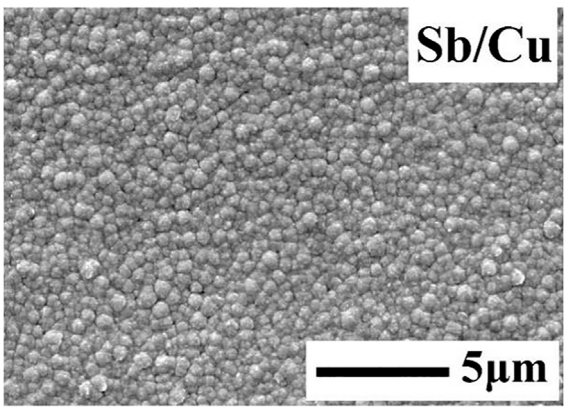

FIGURE 3 | SEM image of the Mo/Sb/Cu layer.

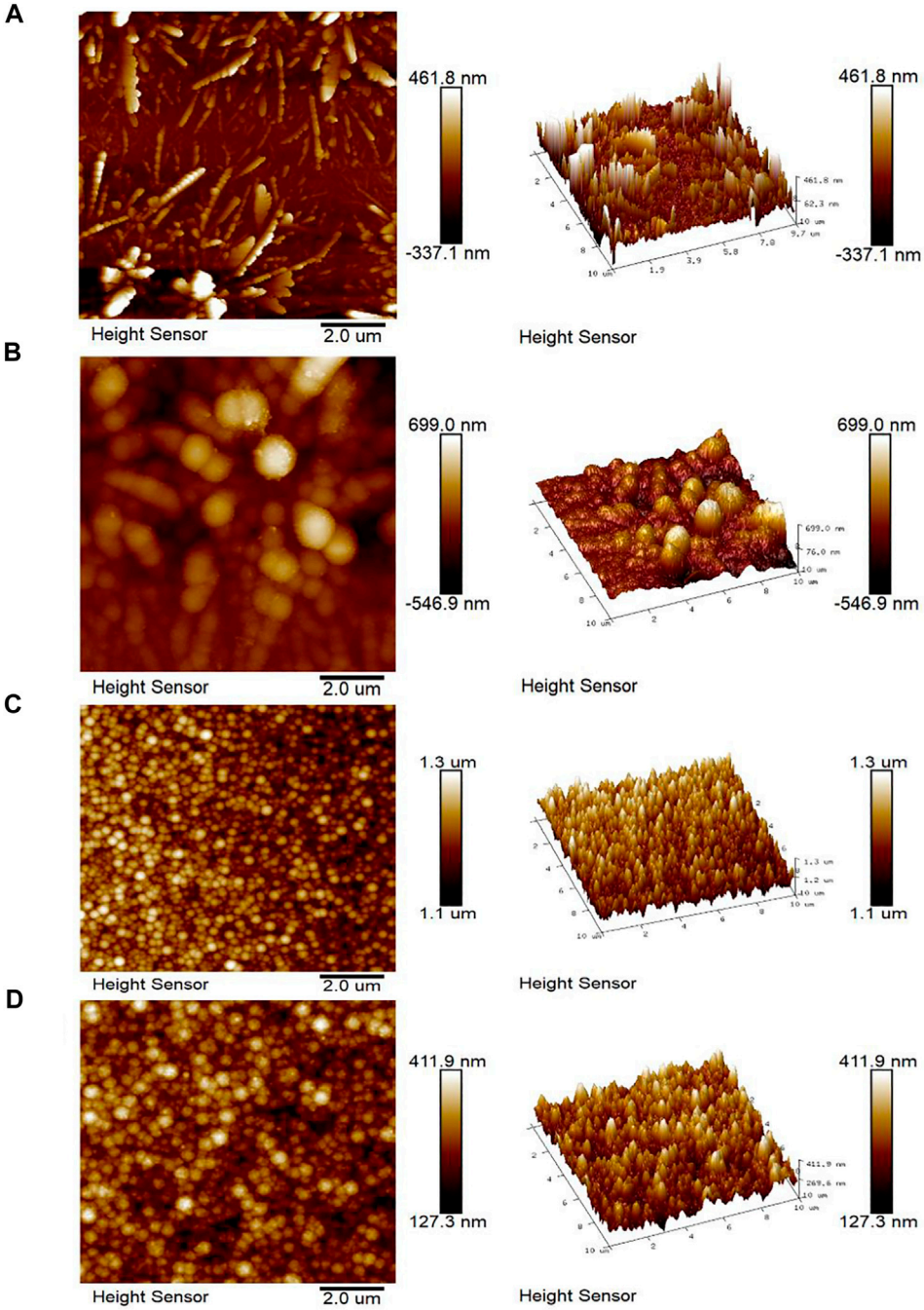

FIGURE 4 | AFM diagrams of the **(A)** Mo/Cu, **(B)** Mo/Cu/Sb, **(C)** Mo/Sb, and **(D)** Mo/Sb/Cu layers.

TABLE 1 | Surface roughness of the Mo/Cu, Mo/Cu/Sb, Mo/Sb, and Mo/Sb/Cu layers.

Samples	R_a (nm)
Mo/Cu	96
Mo/Cu/Sb	112
Mo/Sb	21.8
Mo/Sb/Cu	30.4

To eliminate the "dendritic" morphology, the Mo/Sb/Cu stack was employed to obtain a flat and uniform metal precursor. **Figure 2** shows the SEM images of the Sb layer on Mo prepared via the pulse current electrodeposition method. In **Figures 2A–C**, the T_{on}/T_{off} ratio was set to 1:1, 1:3, and 1:5, with the pulse current density of 62.5 mA/cm^2; small spherical grains can be observed. The size of the spherical grains was relatively non-uniform with

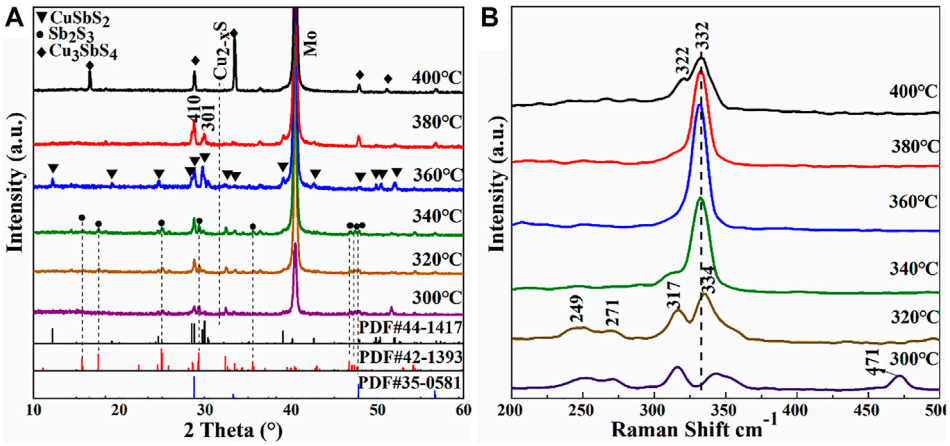

FIGURE 5 | (A) XRD patterns and **(B)** Raman spectra of $CuSbS_2$ thin films sulfurized at different substrate temperatures: 300°, 320°, 340°, 360°, 380°, and 400°C.

the T_{on}/T_{off} ratio of 1:1. The spherical grain size tended to be uniform with the decrease in the T_{on}/T_{off} ratio, and the surface of Sb films became smooth and compact. When the ratio decreased to 1:5, the Sb grains became nonuniform again. It might be because the decreased T_{on}/T_{off} ratio increased the peak current density, which led the growth rate of the Sb nucleus to be higher than the nucleation rate (Grujicic and Pesic, 2002).

Figures 2D–F show the FE-SEM images of Sb deposited with different pulse current densities: 31.25, 62.5, and 125 mA/cm^2. The T_{on}/T_{off} ratio was set to 1:3. The Sb surface was covered with a layer of insect-like particles with a pulse current density of 31.25 mA/cm^2. It might be because the Sb film was not fully nucleated and grew up when the current density was too low. When the pulse current density increased to 62.5 mA/cm^2, a uniform and compact Sb film was obtained. However, an uneven surface appeared when the pulse current density increased to 125 mA/cm^2, which might be due to the concentration polarization near the surface of Sb film at high pulse current density. Finally, a uniform, flat, and compact Sb film could be fabricated on the Mo substrate with a T_{on}/T_{off} ratio of 1:3 and a pulse current density of 62.5 mA/cm^2.

The Sb film deposited with a pulse current density of 62.5 mA/cm^2 and T_{on}/T_{off} of 1:3 (**Figure 2B**) was chosen as the substrate to deposit the Cu layer. The Cu was deposited with a pulse current density of 62.5 mA/cm^2 and a pulse frequency of 10,000 Hz. **Figure 3** shows a smooth, compact Cu layer without any dendritic clusters being obtained.

Figure 4 presents the AFM images of Mo/Cu, Mo/Cu/Sb, Mo/Sb, and Mo/Sb/Cu layers. The average roughness (R_a) of each layer was calculated using an atomic force microscope assistant software (**Table 1**). The average roughness (R_a) of Mo/Cu (96 nm) was larger than that of Mo/Sb (21.8 nm). As the underlying layer, the surface roughness of the Mo/Cu/Sb layer (112 nm) was larger than that of the Mo/Sb/Cu layer (30.4 nm), indicating that the uniformity of Mo/Sb/Cu was higher than that of Mo/Cu/Sb. Therefore, the new structure of Mo/Sb/Cu was chosen as the metal precursor to fabricate $CuSbS_2$ absorbers.

Analysis of the Composition, Phase, and Morphology of the $CuSbS_2$ Thin Film

Sb_2S_3 is easy to evaporate in the sulfurization process due to its high saturated vapor pressure, resulting in the loss of Sb elements. Therefore, the Sb/Cu metal-stack layers with an atomic ratio of 1.7 were sulfurized to prepare $CuSbS_2$ absorbers. **Figure 5A** shows the XRD patterns of the $CuSbS_2$ thin films annealed at 300, 320, 340, 360, 380, and 400°C for 30 min. The sample sulfurized at 300°C detected the $CuSbS_2$ chalcostibite compound (JCPDS No. 44-1417) and weak diffraction peaks of Sb_2S_3 (JCPDS No. 42-1393) and $Cu_{2-x}S$. The $CuSbS_2$ phase was generated by the reaction of Cu and Sb chalcogenides. Cu was completely transformed into Cu-S at 200°C, whereas Sb reacted with S to form Sb_2S_3 at approximately 300°C. When the temperature was sufficiently high (300°C), the binary sulfides of Cu and Sb reacted to form the $CuSbS_2$ ternary compound. The specific reaction equations are as follows (Colombara et al., 2012):

$$2Cu(s) + S_2(g) \rightarrow 2CuS(s) \quad (1)$$

$$4Sb(s) + 3S_2(g) \rightarrow 2Sb_2S_3(s) \quad (2)$$

$$4CuS(s) + 2Sb_2S_3(s) \rightarrow 4CuSbS_2(s) + S_2(g) \quad (3)$$

With the increase in temperature, the intensity of the Sb_2S_3 secondary phase decreased and the crystallinity of $CuSbS_2$ thin films improved. In the temperature range of 320°C–340°C, the films mainly comprised $CuSbS_2$ and Sb_2S_3 phases. However, the diffraction peak intensity of $CuSbS_2$ gradually increased with the temperature increase, whereas the intensity of the Sb_2S_3 peak gradually decreased. At 360°C, the typical bimodal structure of the $CuSbS_2$ phase was observed in the range of 28°–31°. In addition, the $CuSbS_2$ thin film showed the (301) preferred orientation. No other obvious secondary phases were observed, indicating that the film was relatively pure. Sb_2S_3 might have evaporated during high-temperature sulfurization due to its relatively high saturated vapor pressure (Colombara et al., 2011; Colombara et al., 2012).

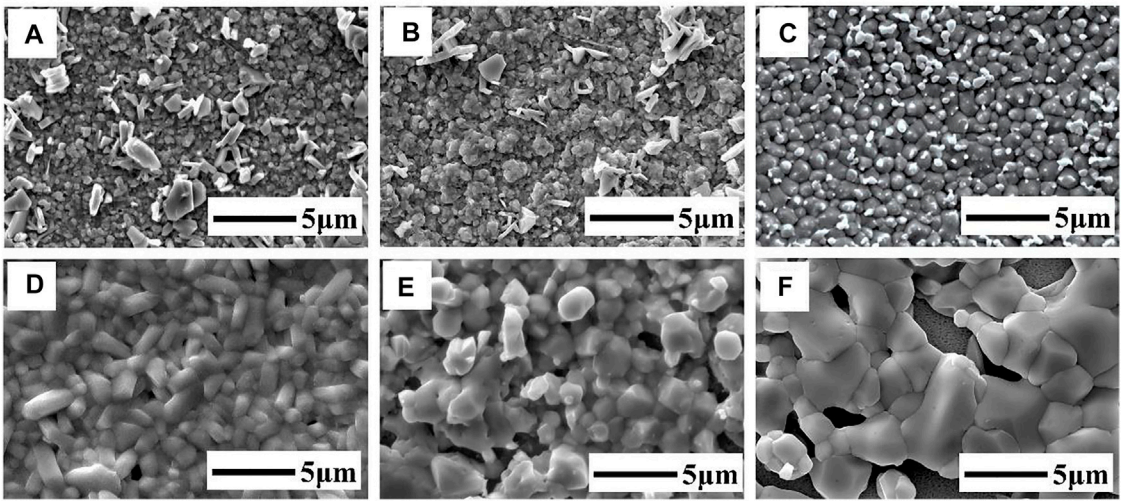

FIGURE 6 | FE-SEM images of the $CuSbS_2$ thin films annealed at different temperatures: **(A)** 300°C, **(B)** 320°C, **(C)** 340°C, **(D)** 360°C, **(E)** 380°C, **(F)** 400°C.

When the temperature increased to 380°C, the diffraction peak of $CuSbS_2$ began to decrease; the preferential orientation of the $CuSbS_2$ thin films changed from (301) to (410). When the annealing temperature increased to 400°C, the films became Cu-rich due to the loss of a large amount of Sb, and the $CuSbS_2$ phase transformed into the Cu_3SbS_4 phase (JCPDS No. 35-0581). $CuSbS_2$ tended to decompose into Cu_3SbS_4 and Sb_2S_3. The diffraction peak of Sb_2S_3 was not detected, because Sb_2S_3 evaporated due to its low melting point. The decomposition reaction was as follows:

$$9CuSbS_2(s) \rightarrow 3Cu_3SbS_4(s) + 2Sb(s) + 2Sb_2S_3(g) \quad (4)$$

TABLE 2 | Elemental compositions of thin films annealed at different temperatures measured *via* EDS.

Temperature (°C)	Atomic percent (at%)		Ratio		
	Cu	Sb	S	Cu/Sb	S/(Cu + Sb)
300	40.22	15.81	43.97	2.54	0.78
320	39.38	15.78	44.84	2.49	0.81
340	38.77	16.22	45.01	2.39	0.82
360	27.65	26.03	46.32	1.06	0.86
380	30.50	21.53	47.97	1.41	0.92
400	40.50	14.40	45.10	2.81	0.82

Figure 5B presents the Raman spectra of films annealed at different sulfurization temperatures. Raman vibration peaks at 249, 317, and 339–332 cm^{-1} all corresponded to the $CuSbS_2$ phase, as reported previously (Vinayakumar et al., 2017; Chalapathi et al., 2018). Moreover, the Raman peak at 471 cm^{-1} of the film sulfurized at 300°C corresponded to the $Cu_{2-x}S$ phase (Hurma and Kose, 2016), which agreed with the XRD results. Besides, the Raman peak at 271 cm^{-1} of the films sulfurized in the temperature range of 300°C–340°C corresponded to the Sb_2S_3 secondary phase (Efthimiopoulos et al., 2016). No $Cu_{2-x}S$ phase was detected in the films annealed in the temperature range of 320°C–340°C, indicating that $Cu_{2-x}S$ and Sb_2S_3 had reacted completely to form $CuSbS_2$. At 360°C, there was a prominent peak at 332 cm^{-1}, which corresponded to $CuSbS_2$. With the increase in the crystallization degree, the secondary peaks at 317 cm^{-1} disappeared and only the main peak located at 332 cm^{-1} remained. At 400°C, a shoulder at 322 cm^{-1} appeared due to the existence of the Cu_3SbS_4 phase (Chalapathi et al., 2018).

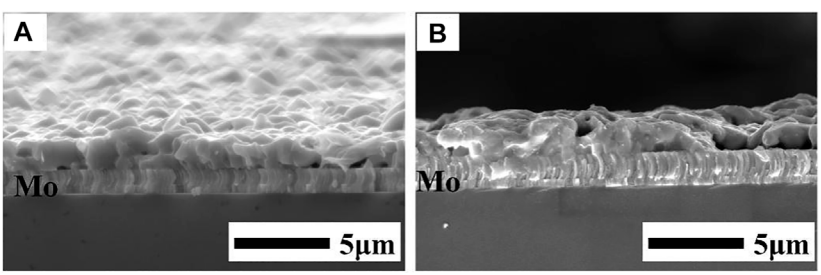

FIGURE 7 | Cross-sectional SEM images of $CuSbS_2$ thin films annealed at **(A)** 360°C and **(B)** 380°C.

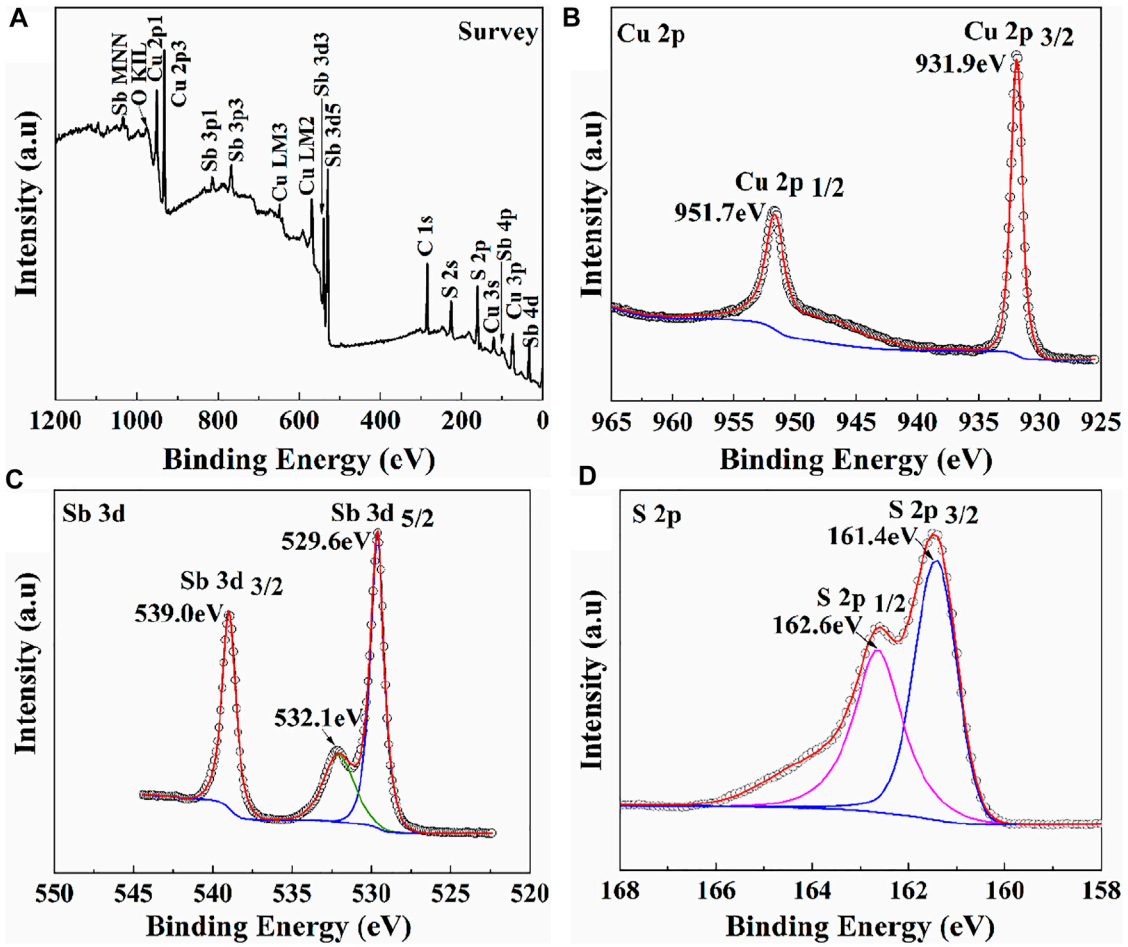

FIGURE 8 | XPS of the $CuSbS_2$ thin films prepared at 360°C. **(A)** Survey, **(B)** Cu 2p core level, **(C)** Sb 3 days core level, and **(D)** S 2p core level.

The elemental compositions of the films at different annealing temperatures were determined via EDS (**Table 2**). The compositions of Cu, Sb, and S were very sensitive to the annealing temperature. The films were rich in copper and poor in antimony due to the high volatility of Sb_2S_3. The Cu/Sb ratio was approximately 2.5 in the temperature range of 300°C–340°C, and the ratio decreased with the increase in temperature. This is because Sb was not fully sulfurized into Sb_2S_3 and did not fully participate in the reaction to generate $CuSbS_2$. When the temperature increased to 360°C, CuS and Sb_2S_3 fully reacted to produce $CuSbS_2$, the film showed only a slight Cu-rich composition and the Cu/Sb ratio of the film decreased to 1.06. Sb loss was significant when the temperature further increased to 400°C. The Cu/Sb ratio increased to 2.81 at 400°C, which should be due to the decomposition of the membrane into Cu_3SbS_4.

Figure 6 shows the FE-SEM images of the films sulfurized at different temperatures. The morphologies of the $CuSbS_2$ thin films changed with the increase in temperature. As shown in **Figure 6A**, fine grains and white rod-shaped grains were

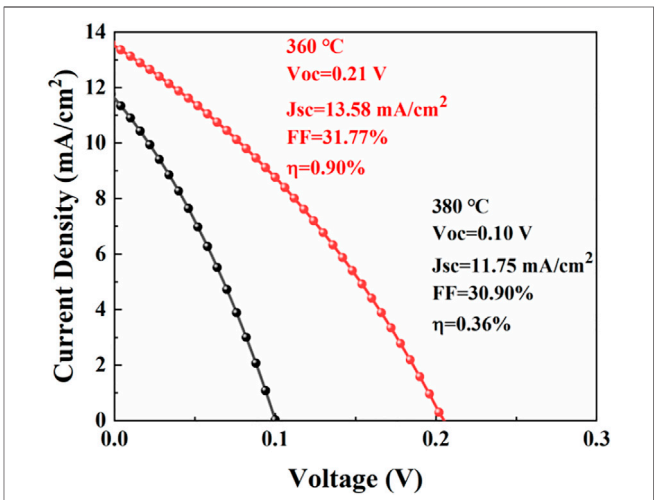

FIGURE 9 | J–V curves of the $CuSbS_2$ thin-film solar cells based on absorbers annealed at 360° and 380°C for 30 min.

TABLE 3 | Device parameters of the $CuSbS_2$ thin-film solar cells based on absorbers annealed at 360°C and 380°C for 30 min.

Temperature (°C)	Eff (%)	V_{oc} (V)	J_{sc} (mA/cm^2)	FF (%)	Area (cm^2)
360	0.90	0.21	13.58	31.77	0.12
380	0.36	0.10	11.75	30.90	0.12

observed on the film surface. EDS analysis showed that the white rod-shaped grains were Cu- and S-rich phases. In the temperature range of 320°C–340°C, grains began to aggregate and grow up. With the increase in temperature, the grain sizes increased. In the temperature range of 360°C–380°C, micron-sized rod-like grains were formed and the crystallization degree and compactness of $CuSbS_2$ thin films improved. Notably, the surface morphology of the film changed significantly with the increase in temperature due to the low reaction and formation temperature of $CuSbS_2$. However, further increasing the growth temperature to 400°C, the pores formed on the film surfaces. Combined with the XRD and Raman analyses, this phenomenon might be due to the decomposition of the $CuSbS_2$ phase—where a large amount of Sb loss destroyed the completeness of the film. A relatively pure $CuSbS_2$ thin film could be obtained in the temperature range of 360°C–380°C.

Figure 7 shows the cross-sectional FE-SEM images of the films sulfurized at 360 and 380°C. The thickness of the films was approximately 1.2 μm without fine-grain layers at the bottom of the film. At 360°C, the adhesion between the annealed Mo and $CuSbS_2$ thin films was good and columnar large grains were formed. The $CuSbS_2$ grain sizes increased with the increase in the sulfurization temperature to 380°C. Compared with the films prepared at 380°C, the films prepared at 360°C were more uniform and denser. The crystallinity of the $CuSbS_2$ thin films annealed at 360°C was high and more suitable to prepare $CuSbS_2$ devices.

XPS Analysis of the $CuSbS_2$ Thin Films

XPS was employed to measure the chemical states of elements in the $CuSbS_2$ thin films sulfurized at 360°C (**Figure 8**). From **Figure 8A**, the main elements of $CuSbS_2$ thin films were Cu, Sb, and S, indicating no additional doping element in the $CuSbS_2$ thin film. As shown in **Figures 8B–D**, the binding energies of Cu $2p_{1/2}$ and $2P_{3/2}$ were 931.9 and 951.7 eV, respectively, with an interval of 19.8 eV, which agreed with the reported binding energies of Cu^+ in $CuSbS_2$ (Wan et al., 2016). The binding energies of Sb $3d_{5/2}$ and $3d_{3/2}$ were 529.6 and 539.0 eV, respectively, with an interval of 9.4 eV, which agreed with Sb^{3+} (Vinayakumar et al., 2017). The peak at 532.1 eV corresponded to the oxygen adsorbed on the thin film. The binding energies of S $2p_{3/2}$ and $2p_{1/2}$ were 161.4 and 162.6 eV, respectively, with an interval of 1.2 eV, which corresponded to the binding energies of S^{2-} in $CuSbS_2$ (van Embden et al., 2020). The results agreed with the chemical states of standard $CuSbS_2$, which proved the pure phase $CuSbS_2$ thin films to be prepared at the annealing temperature of 360°C.

The $CuSbS_2$ thin films annealed at 360°C and 380°C were selected to prepare solar cells. The J–V curves of the $CuSbS_2$ thin-film solar cells are shown in **Figure 9**. The device parameters are listed in **Table 3**. The photovoltaic conversion efficiency (η) of the device, based on the $CuSbS_2$ thin films annealed at 360°C, was 0.90% with an open-circuit voltage (V_{oc}) of 0.21 V, a current density (J_{sc}) of 13.58 mA/cm^2, and a filling factor (FF) of 31.77%. However, the photovoltaic conversion efficiency of the device, based on the $CuSbS_2$ film annealed at 380°C, was only 0.36% with an open-circuit voltage(V_{oc}) of 0.10 V, a current density of 11.75 mA/cm^2. The $CuSbS_2$ thin films annealed at 360°C were more compact than those annealed at 380°C (**Figures 6D,E**). The voids in the $CuSbS_2$ thin films could influence carrier transportation, which would reduce the current density. Combined with the XRD analysis, the crystal-preferred orientation of the $CuSbS_2$ thin films changed from (301) to (410) with an increase in annealing temperature. Based on the analysis of the Cu (In, Ga) Se_2-preferred orientation (Kim et al., 2018), the changed-preferred orientation of $CuSbS_2$ might induce different defect densities, which would influence the open-circuit voltage. In addition, the band structure diagram of $CuSbS_2$ thin film solar cells is shown in **Supplementary Figure S2**.

CONCLUSION

In this study, Sb/Cu metal layers were prepared on Mo substrates *via* the pulse current electrodeposition method. By adjusting the pulse parameters (T_{on}/T_{off} of 1:3, a pulse current density of 62.5 mA/cm^2, and a pulse current frequency of 10,000 Hz), a compact and uniform Sb layer was prepared on the Mo substrate. With this uniform Sb underlayer, dense, uniform, and smooth Cu layers without dendric clusters were realized. A two-step sulfurization process was employed to fabricate $CuSbS_2$ absorbers. The influences of annealing temperature on the composition, phase, and morphology of $CuSbS_2$ thin films were studied. A compact and relatively pure $CuSbS_2$ thin film was fabricated at 360°C. Finally, a 0.90% efficiency of $CuSbS_2$ thin-film solar cell was obtained with an open-circuit voltage of 0.21 V, a short circuit current density of 13.58 mA/cm^2, and an FF of 31.77%.

DATA AVAILABILITY STATEMENT

The original contributions presented in the study are included in the article/**Supplementary Material**, further inquiries can be directed to the corresponding authors.

AUTHOR CONTRIBUTIONS

AZ: Conceptualization, Formal analysis, Writing-Original Draft, Writing—Review and Editing. YW: Visualization, Project administration. BL: Data Curation. DX: Data Curation. ZP: Resources. YY: Project administration, Writing-Review and Editing. YX: Data Curation, Project administration. LY: Visualization, Project administration. JB: Validation, Investigation, Writing-Review and Editing, Supervision. WL: Validation, Investigation, Writing-Review and Editing, Supervision.

FUNDING

This work was supported by the National Natural Science Foundation of China (61804108 and 62074084).

SUPPLEMENTARY MATERIAL

The Supplementary Material for this article can be found online at: https://www.frontiersin.org/articles/10.3389/fmats.2021.818596/full#supplementary-material

REFERENCES

Banu, S., Ahn, S. J., Ahn, S. K., Yoon, K., and Cho, A. (2016). Fabrication and Characterization of Cost-Efficient CuSbS2 Thin Film Solar Cells Using Hybrid Inks. *Solar Energ. Mater. Solar Cell* 151, 14–23. doi:10.1016/j.solmat.2016.02.013

Banu, S., Cho, Y., Kim, K., Ahn, S. K., Gwak, J., and Cho, A. (2019). Phase Transition Behavior and Defect Analysis of CuSbS2 Thin Films for Photovoltaic Application Prepared by Hybrid Inks. *Solar Energy* 188, 1209–1220. doi:10.1016/j.solener.2019.07.019

Bhattacharya, R. N., Oh, M. K., and Kim, Y. (2012). CIGS-based Solar Cells Prepared from Electrodeposited Precursor Films. *Solar Energ. Mater. Solar Cell* 98, 198–202. doi:10.1016/j.solmat.2011.10.026

Bi, J., Yao, L., Ao, J., Gao, S., Sun, G., He, Q., et al. (2016). Pulse Electro-Deposition of Copper on Molybdenum for Cu(In,Ga)Se2 and Cu2ZnSnSe4 Solar Cell Applications. *J. Power Sourc.* 326, 211–219. doi:10.1016/j.jpowsour.2016.07.005

Budevski, E., Staikov, G., and Lorenz, W. J. (2000). Electrocrystallization Nucleation and Growth Phenomena. *Electrochim. Acta* 45 (15-16), 2559–2574. doi:10.1016/S0013-4686(00)00353-4

Chalapathi, U., Poornaprakash, B., Ahn, C. H., and Park, S. H. (2018). Two-stage Processed CuSbS2 Thin Films for Photovoltaics: Effect of Cu/Sb Ratio. *Ceramics Int.* 44 (12), 14844–14849. doi:10.1016/j.ceramint.2018.05.117

Colombara, D., Peter, L. M., Rogers, K. D., and Hutchings, K. (2012). Thermochemical and Kinetic Aspects of the Sulfurization of Cu-Sb and Cu-Bi Thin Films. *J. Solid State. Chem.* 186, 36–46. doi:10.1016/j.jssc.2011.11.025

Colombara, D., Peter, L. M., Rogers, K. D., Painter, J. D., and Roncallo, S. (2011). Formation of CuSbS2 and CuSbSe2 Thin Films via Chalcogenisation of Sb-Cu Metal Precursors. *Thin Solid Films* 519 (21), 7438–7443. doi:10.1016/j.tsf.2011.01.140

de Souza Lucas, F. W., Welch, A. W., Baranowski, L. L., Dippo, P. C., Hempel, H., Unold, T., et al. (2016). Effects of Thermochemical Treatment on CuSbS2 Photovoltaic Absorber Quality and Solar Cell Reproducibility. *J. Phys. Chem. C* 120 (33), 18377–18385. doi:10.1021/acs.jpcc.6b04206

Efthimiopoulos, I., Buchan, C., and Wang, Y. (2016). Structural Properties of Sb2S3 under Pressure: Evidence of an Electronic Topological Transition. *Sci. Rep.* 6, 24246. doi:10.1038/srep24246

Favry, É., Frederich, N., Meunier, A., Omnès, L., Jomard, F., and Etcheberry, A. (2008). Investigation of Organics Adsorption and Inclusion at the Growing Interfaces during the Damascene Process. *Electrochimica Acta* 53 (23), 7004–7011. doi:10.1016/j.electacta.2008.01.108

Gao, Q., Ao, J., Bi, J., Yao, L., Zhang, Z., Zhang, Y., et al. (2020). A Novel Metal Precursor Structure for Electrodepositing Ultrathin CIGSe Thin-Film Solar Cell with High Efficiency. *ACS Appl. Mater. Inter.* 12 (21), 24403–24410. doi:10.1021/acsami.0c01008

García, R. G. A., Cerdán-Pasarán, A., Perez, E. A. R., Pal, M., Hernández, M. M., and Mathews, N. R. (2020). Phase Pure CuSbS2 Thin Films by Heat Treatment of Electrodeposited Sb2S3/Cu Layers. *J. Solid State. Electrochem.* 24 (1), 185–194. doi:10.1007/s10008-019-04475-3

Grujicic, D., and Pesic, B. (2002). Electrodeposition of Copper: the Nucleation Mechanisms. *Electrochimica Acta* 47 (18), 2901–2912. doi:10.1016/S0013-4686(02)00161-5

Hurma, T., and Kose, S. (2016). XRD Raman Analysis and Optical Properties of CuS Nanostructured Film. *Optik* 127 (15), 6000–6006. doi:10.1016/j.ijleo.2016.04.019

Kang, L., Zhao, L., Jiang, L., Yan, C., Sun, K., Ng, B. K., et al. (2018). *In Situ* growth of CuSbS2 Thin Films by Reactive Co-sputtering for Solar Cells. *Mater. Sci. Semiconduc Process.* 84, 101–106. doi:10.1016/j.mssp.2018.05.004

Kim, S., Yoo, H., Rana, T. R., Enkhbat, T., Han, G., Kim, J., et al. (2018). Effect of Crystal Orientation and Conduction Band Grading of Absorber on Efficiency of Cu(In,Ga)Se2 Solar Cells Grown on Flexible Polyimide Foil at Low Temperature. *Adv. Energ. Mater.* 8 (26), 1801501. doi:10.1002/aenm.201801501

Kwon, Y. H., Kim, S. K., Kim, S.-W., and Cho, H. K. (2014). Artificially Controlled Two-step Electrodeposition of Cu and Cu/In Metal Precursors with Improved Surface Roughness for Solar Applications. *J. Electrochem. Soc.* 161 (9), D447–D452. doi:10.1149/2.0771409jes

Lee, S. M., Ikeda, S., Harada, Y. O. T., and Matsumura, M. (2012). Structural Regulation of Electrochemically Deposited Copper Layers for Fabrication of Thin Film Solar Cells with a CuInS2 Photoabsorber. *J. Non-Crystalline Sol.* 358 (17), 2424–2427. doi:10.1016/j.jnoncrysol.2011.12.043

Lincot, D., Guillemoles, J. F., Taunier, S., Guimard, D., Sicx-Kurdi, J., Chaumont, A., et al. (2004). Chalcopyrite Thin Film Solar Cells by Electrodeposition. *Solar Energy* 77 (6), 725–737. doi:10.1016/j.solener.2004.05.02410.1016/j.solener.2004.05.024

Long, J. G., Searson, P. C., and Vereecken, P. M. (2006). Electrochemical Characterization of Adsorption-Desorption of the Cuprous-Suppressor-Chloride Complex during Electrodeposition of Copper. *J. Electrochem. Soc.* 153 (4), C258. doi:10.1149/1.2168050

Loranca-Ramos, F. E., Diliegros-Godines, C. J., Silva González, R., and Pal, M. (2018). Structural, Optical and Electrical Properties of Copper Antimony Sulfide Thin Films Grown by a Citrate-Assisted Single Chemical bath Deposition. *Appl. Surf. Sci.* 427, 1099–1106. doi:10.1016/j.apsusc.2017.08.027

Macías, C., Lugo, S., Benítez, Á., López, I., Kharissov, B., Vázquez, A., et al. (2017). Thin Film Solar Cell Based on CuSbS 2 Absorber Prepared by Chemical bath Deposition (CBD). *Mater. Res. Bull.* 87, 161–166. doi:10.1016/j.materresbull.2016.11.028

Medina-Montes, M. I., Campos-González, E., Morales-Luna, M., Sánchez, T. G., Becerril-Silva, M., Mayén-Hernández, S. A., et al. (2018). Development of Phase-Pure CuSbS2 Thin Films by Annealing Thermally Evaporated CuS/Sb2S3 Stacking Layer for Solar Cell Applications. *Mater. Sci. Semiconductor Process.* 80, 74–84. doi:10.1016/j.mssp.2018.02.029

Mercier, D., Delbos, E., El Belghiti, H., Vigneron, J., Bouttemy, M., and Etcheberry, A. (2013). Study of Copper Electrodeposition Mechanism on Molybdenum Substrate. *J. Electrochem. Soc.* 160 (12), D3103–D3109. doi:10.1149/2.017312jes

Moffat, T. P., Wheeler, D., Kim, S. K., and Josell, D. (2007). Curvature Enhanced Adsorbate Coverage Mechanism for Bottom-Up Superfilling and Bump Control in Damascene Processing. *Electrochimica Acta* 53 (1), 145–154. doi:10.1016/j.electacta.2007.03.025

Norkus, E., Vaškelis, A., Jačiauskiene, J., VaičIuniene, J., Gaidamauskas, E., and Macalady, D. L. (2005). Environmentally Friendly Natural Polyhydroxylic Compounds in Electroless Copper Plating Baths: Application of Xylitol, D-Mannitol and D-Sorbitol as Copper(II) Ligands. *J. Appl. Electrochem.* 35 (1), 41–47. doi:10.1007/s10800-004-2056-7

Oliva, F., Broussillou, C., Annibaliano, M., Frederich, N., Grand, P. P., Roussy, A., et al. (2013). Formation Mechanisms of Cu(In,Ga)Se2 Solar Cells Prepared

from Electrodeposited Precursors. *Thin Solid Films* 535, 127–132. doi:10.1016/j.tsf.2012.11.106

Pal, M., Diliegros-Godines, C. J., Gupta, G. K., Mathews, N. R., and Dixit, A. (2020). Structural Evolution of Chemically Deposited Binary Stacks of Sb 2 S 3 -CuS to Phase-pure CuSbS 2 Thin Films and Evaluation of Device Parameters of CuSbS 2/CdS Heterojunction. *Int. J. Energ. Res.* 44 (7), 5881–5894. doi:10.1002/er.5359

Rabhi, A., Kanzari, M., and Rezig, B. (2009). Optical and Structural Properties of CuSbS2 Thin Films Grown by thermal Evaporation Method. *Thin Solid Films* 517 (7), 2477–2480. doi:10.1016/j.tsf.2008.11.021

Ramos Aquino, J. A., Rodriguez Vela, D. L., Shaji, S., Avellaneda, D. A., and Krishnan, B. (2016). Spray Pyrolysed Thin Films of Copper Antimony Sulfide as Photovoltaic Absorber. *Phys. Status Solidi C* 13 (1), 24–29. doi:10.1002/pssc.201510102

Riha, S. C., Koegel, A. A., Emery, J. D., Pellin, M. J., and Martinson, A. B. F. (2017). Low-Temperature Atomic Layer Deposition of CuSbS2 for Thin-Film Photovoltaics. *ACS Appl. Mater. Inter.* 9 (5), 4667–4673. doi:10.1021/acsami.6b13033

Septina, W., Ikeda, S., Iga, Y., Harada, T., and Matsumura, M. (2014). Thin Film Solar Cell Based on CuSbS2 Absorber Fabricated from an Electrochemically Deposited Metal Stack. *Thin Solid Films* 550, 700–704. doi:10.1016/j.tsf.2013.11.046

van Embden, J., Mendes, J. O., Jasieniak, J. J., Chesman, A. S. R., and Della Gaspera, E. (2020). Solution-Processed CuSbS2 Thin Films and Superstrate Solar Cells with CdS/In2S3 Buffer Layers. *ACS Appl. Energ. Mater.* 3 (8), 7885–7895. doi:10.1021/acsaem.0c01296

Vauche, L., Risch, L., Sánchez, Y., Dimitrievska, M., Pasquinelli, M., Goislard de Monsabert, T., et al. (2016). 8.2% Pure Selenide Kesterite Thin-Film Solar Cells from Large-Area Electrodeposited Precursors. *Prog. Photovolt: Res. Appli.* 24 (1), 38–51. doi:10.1002/pip.2643

Vinayakumar, V., Shaji, S., Avellaneda, D. A., Aguilar Martinez, J. A., and Krishnan, B. (2019). Highly Oriented CuSbS2 Thin Films by Rapid thermal Processing of Pre-annealed Sb2S3-Cu Layers for PV Applications. *Mater. Sci. Semiconductor Process.* 91, 81–89. doi:10.1016/j.mssp.2018.11.007

Vinayakumar, V., Shaji, S., Avellaneda, D., Das Roy, T. K., Castillo, G. A., Martinez, J. A. A., et al. (2017). CuSbS2 Thin Films by Rapid thermal Processing of Sb2S3-Cu Stack Layers for Photovoltaic Application. *Solar Energ. Mater. Solar Cell* 164, 19–27. doi:10.1016/j.solmat.2017.02.005

Wan, L., Guo, X., Fang, Y., Mao, X., Guo, H., Xu, J., et al. (2019). Spray Pyrolysis Deposited CuSbS2 Absorber Layers for Thin-Film Solar Cells. *J. Mater. Sci. Mater. Electron.* 30 (24), 21485–21494. doi:10.1007/s10854-019-02531-2

Wan, L., Ma, C., Hu, K., Zhou, R., Mao, X., Pan, S., et al. (2016). Two-stage Co-evaporated CuSbS2 Thin Films for Solar Cells. *J. Alloys Comp.* 680, 182–190. doi:10.1016/j.jallcom.2016.04.193

Yang, B., Wang, L., Han, J., Zhou, Y., Song, H., Chen, S., et al. (2014). CuSbS2 as a Promising Earth-Abundant Photovoltaic Absorber Material: A Combined Theoretical and Experimental Study. *Chem. Mater.* 26 (10), 3135–3143. doi:10.1021/cm500516v

Yu, L., Kokenyesi, R. S., Keszler, D. A., and Zunger, A. (2013). Inverse Design of High Absorption Thin-Film Photovoltaic Materials. *Adv. Energ. Mater.* 3 (1), 43–48. doi:10.1002/aenm.201200538

Yuan, M., Mitzi, D. B., Liu, W., Kellock, A. J., Chey, S. J., and Deline, V. R. (2009). Optimization of CIGS-Based PV Device through Antimony Doping. *Chem. Mater.* 22 (2), 285–287. doi:10.1021/cm903428f

Zhang, L., Li, Y., Li, X., Li, C., Zhang, R., Delaunay, J. J., et al. (2016). Solution-processed CuSbS2 Thin Film: A Promising Earth-Abundant Photocathode for Efficient Visible-Light-Driven Hydrogen Evolution. *Nano Energy* 28, 135–142. doi:10.1016/j.nanoen.2016.08.036

Zhang, Y., Huang, J., Yan, C., Sun, K., Cui, X., Liu, F., et al. (2019). High Open-Circuit Voltage CuSbS2 Solar Cells Achieved through the Formation of Epitaxial Growth of CdS/CuSbS2 Hetero-Interface by post-annealing Treatment. *Prog. Photovolt Res. Appl.* 27 (1), 37–43. doi:10.1002/pip.3061

Zhou, R., Liu, X., Zhang, S., Liu, L., Wan, L., Guo, H., et al. (2021). Spray-coated Copper Antimony Sulfide (CuSbS2) Thin Film: A Novel Counter Electrode for Quantum Dot-Sensitized Solar Cells. *Mater. Sci. Semiconductor Process.* 124, 105613. doi:10.1016/j.mssp.2020.105613

Conflict of Interest: LY was employed by the company Tianjin Institute of Power Source.

The remaining authors declare that the research was conducted in the absence of any commercial or financial relationships that could be construed as a potential conflict of interest.

Publisher's Note: All claims expressed in this article are solely those of the authors and do not necessarily represent those of their affiliated organizations, or those of the publisher, the editors and the reviewers. Any product that may be evaluated in this article, or claim that may be made by its manufacturer, is not guaranteed or endorsed by the publisher.

frontiers in Materials

ORIGINAL RESEARCH
published: 28 January 2022
doi: 10.3389/fmats.2021.802136

Formation and Evolution of the Corrosion Scales on Super 13Cr Stainless Steel in a Formate Completion Fluid With Aggressive Substances

Xiaoqi Yue[1,2], Luyao Huang[3], Zhihao Qu[1], Zhile Yang[1], Lei Zhang[1] and Yong Hua[4]**

[1]Institute of Advanced Materials and Technology, Beijing, China, [2]Shunde Graduate School, Foshan, China, [3]State Key Laboratory of Advanced Power Transmission Technology, Global Energy Interconnection Research Institute Co., Ltd., Beijing, China, [4]School of Materials Science and Engineering, China University of Petroleum (East China), Qingdao, China

The formation and evolution of the corrosion scales on the super 13Cr stainless steel (SS) surface after exposure in a formate completion fluid with the presence of various aggressive substances was investigated. The results indicate that the formation of Fe_3O_4 covered the surface of super 13Cr SS as the inner layer accompanied with outer scattered FeS. The corrosion rate was below 0.07 mm/year after 120 h of exposure in the formate fluid at 180°C under N_2 environments; the presence of aggressive substances such as sulfide and CO_2 in the formate fluid promoted the proceeding of anodic dissolution in the early period, and the ingress of CO_2 progressively increased the general corrosion rate to 1.7 mm/year. For CO_2-containing conditions, the formation of $FeCr_2O_4$ and $Cr(OH)_3$ was detected in the inner corrosion product layers, and the precipitation of "sheet"-shaped iron carbonate ($FeCO_3$) was detected as the outer layer. The accumulation rate of corrosion products increases by two orders of magnitude with the ingress of CO_2, corresponding to thicker corrosion products, but the dissolution rate is still three orders of magnitude higher than when CO_2 was absent.

Keywords: potassium formate, super 13Cr SS, high temperature, thermodynamics, kinetics

OPEN ACCESS

Edited by:
Dake Xu,
Northeastern University, China

Reviewed by:
Ziming Wang,
Xiamen University, China
Mahmood Aliofkhazraei,
Tarbiat Modares University, Iran

****Correspondence:***
Lei Zhang
zhanglei@ustb.edu.cn
Yong Hua
leo.huayong@gmail.com

Specialty section:
This article was submitted to Environmental Degradation of Materials, a section of the journal Frontiers in Materials

Received: *26 October 2021*
Accepted: *06 December 2021*
Published: *28 January 2022*

Citation:
Yue X, Huang L, Qu Z, Yang Z, Zhang L and Hua Y (2022) Formation and Evolution of the Corrosion Scales on Super 13Cr Stainless Steel in a Formate Completion Fluid With Aggressive Substances. Front. Mater. 8:802136. doi: 10.3389/fmats.2021.802136

INTRODUCTION

The exploitation and production of ultra-deep reservoirs for future energy supply have been highlighted as a practical strategy to achieve the effective application of fossil energy. The Tarim Basin, where exists abundant natural gas in the depth between 6,500–8,000 m, has been constructed with 52 wells in Kuqa from 2012 (Liu et al., 2019a). Due to the high pressure (115–140 MPa), high temperature (170°C–190°C), and complex corrosive medium, the corrosion issues of highly dense brine-based completion fluids on tubing and casing materials in ultra-deep high-temperature wells have become a research hot spot in the course of oil and gas exploitation (Yue et al., 2020a; Li et al., 2020; Zhao et al., 2020). The considered competition fluids are mainly the bromine salt completion fluids (KBr, $ZnBr_2$, and $CaBr_2$) (Liu et al., 2014; Liu et al., 2019b) and/or formate brines (NaCOOH, KCOOH, and CsCOOH) (Bungert et al., 2000; Leth-Olsen, 2004; Zhu et al., 2011b). In the past decades, one of the major issues is the localized corrosion by using bromine salts due to the presence

of Br^- (Hoar and Jacob, 1967; Refaey et al., 2005). Recently, formate brines with filtrate viscosity and low-water activities are more potential to be a safe option for the deep wells (the average depth >6,000 m), and also the operating temperature can be over 150°C (Howard and others, 1995; Bungert et al., 2000). Clarke states that the formate brines have many advantages during drilling and completion processes at a temperature up to 160°C, such as preventing the thermal degradation for the conventional drilling and completion fluid polymers (Clarke-Sturman and Sturla, 1988). Among formate brines, KCOOH solution has been widely used as the alternative option for such arduous conditions based on its large solubility and low corrosivity (Leth-Olsen, 2004).

Tubing materials experienced low-corrosion risk in formate brines at a high temperature of 180°C (Li et al., 2018), compared with that of immersing in the CO_2-saturated formation water (Zhu et al., 2011a, 2015a; Hua et al., 2019a). However, corrosion control of the tubing material during the completion period remains an obstinate issue for corrosion engineers due to the intrinsically complicated corrosion processes, especially in the presence of sulfide impurity or CO_2 ingress under such harsh environments. The sulfides were introduced as an impurity by the synthesis of KCOOH where it is inevitable to exit sulfides in the industrial-grade purification process of CO from the exhaust gas (Teng et al., 2016). The CO_2 influx in annulus protection fluids will react with formate brines and form trace amounts of formic acid, which acts as a catalyst in the reactivity of formate (Bungert et al., 2000) and promotes the corrosion process on the material surface (Yang et al., 2019). Sekine et al. (Sekine and Chinda, 1984) stated that the formic acid can be corrosive with an increasing content of KCOOH in the solution due to the dissolved KCOOH increased the solution electrical conductivity. Recently, materials such as super 13%Cr martensite stainless steel (S13Cr) has been considered as a tubing and casing material for such hash conditions based on its good corrosion resistance, low cost, and excellent mechanical properties. Along with the growing understanding of the influence of aggressive substances on the corrosive of formate brines (Bungert et al., 2000; Howard et al., 2009), further study of the corrosion behavior of S13Cr immersed in the formate brines as well as the evolution of the corrosion scales on the surface is urgently pressed. It has been reported that both Fe and Cr elements in the matrix significantly contributed to the corrosion-resistant stainless steel (SS) in an acidized KCOOH solution by comparing the polarization curves between pure metal and 304 SS; Ni promotes the stability of the passive film on the surface as well as the mechanical property (Sekine and Chinda, 1984). Hakon (Leth-Olsen, 2004) found that the formation of the corrosion product scales on 13Cr SS in formate fluids did not act as an effective barrier against corrosion, showing high-corrosion rates after several weeks of exposure, and the surface was covered by nonuniformed crystalline $FeCO_3$, especially at 180°C (Leth-Olsen and others, 2005). Although the formation of the $FeCO_3$ layer plays a dominant role in retarding the corrosion rate, the corrosion resistance of S13Cr SS corresponds to a complicated corrosion product scales formation and evolution process, and that the amorphous/nanocrystalline inner layer provides better corrosion protection than outer $FeCO_3$ precipitation[21–25] under the ultra-deep well conditions [temperatures beyond 180°C (Zhao et al., 2018; Yue et al., 2020a, 2020b, 2020c; Zhao et al., 2021a)]. The systematic study on the formation and evolution of the corrosion product scales on the S13Cr SS surface immersed in a formate fluid under HTHP condition, especially with the presence of aggressive substances such as sulfide or CO_2 is rare.

TABLE 1 | Elemental composition of super 13Cr SS (wt%).

C	Si	Mn	P	S	Cr	Mo	Ni	Fe
0.041	0.34	0.34	≤0.001	≤0.001	12.8	1.92	4.78	Balance

It has been reported that the formation of the corrosion products under a CO_2–H_2S coexistence environment was related to H_2S and CO_2 concentration (Banaś et al., 2007; Pessu et al., 2017; Li et al., 2021). Having acidic media such as CO_2 and H_2S can promote the ionic conductivity in the solution (Vedage et al., 1993; Zhao et al., 2021b). Ding et al. (2013) discovered that the anodic dissolution was accelerated by high-H_2S/CO_2 partial pressures where both H_2S and CO_2 reduced the stability of the corrosion product scales (He et al., 2009). The composition of corrosion products may vary as H_2S concentration increases. The corrosion products have been reported to become more complicated (generating several FeS compounds in addition to $FeCO_3$), indicating porous in feature and results in less corrosion protection (Vedage et al., 1993). If the p_{CO2}/p_{H2S} ratio is between 20 and 500, there is a possibility that the iron sulfide layer covers the surface locally, and pitting corrosion dominates degradation due to the galvanic corrosion between covered and bare surfaces, which is usually improved by adding inhibitors (Xu et al., 2018; Askari et al., 2021; Hamza et al., 2021).

This article complements the literature gaps by systematically investigating the corrosion behavior of S13Cr immersed in a formate fluid via studying the influence of sulfide or CO_2 on the corrosion product kinetics. The weight-loss method is implemented to review the extent of general corrosion, and the nature and morphology of the corrosion products are identified using a combination of scanning electron microscopy (SEM), energy-dispersive X-ray spectroscopy (EDS), X-ray diffraction (XRD), and Raman spectroscopy in order to identify the role CO_2 plays on the corrosion product scale composition and morphology. This article mainly discussed the corrosion risk caused by potential aggressive substances (sulfide and CO_2 ingress) that may be introduced in the formate fluid as the application in the oil and gas industry and revealed the surface interaction mechanisms on the corrosion product scale of S13Cr SS at severe annulus environments.

EXPERIMENTAL PROCEDURE

Material Preparation

The material used was an API-P110 grade S13Cr (UNS S41425) SS with heat-treated through normalization and tempering at

TABLE 2 | Chemical composition of formation water.

Composition	KCOOH	DI Water	K_2S
Content (g/100 g)	54.60	45.36	0.04

the autoclave were purged with high pressure N_2/CO_2 and evacuated by lines 2 and 4 to remove the O_2 content within the system. The prepared, de-aerated brine was carefully transferred from the sparging vessel into the closed autoclave containing the test specimens at an ambient

TABLE 3 | Test matrix for corrosion tests under different conditions.

Material	T, °C	P_{N2} at 25°C, bar	p_{CO2} at 25°C, bar	pH	Total pressure, bar	Immersion time, hours (T = 180°C)
S13Cr SS	180	10	0	10.55	26	5
						48
						120
		0	10	6.80	34	5
						48
						120

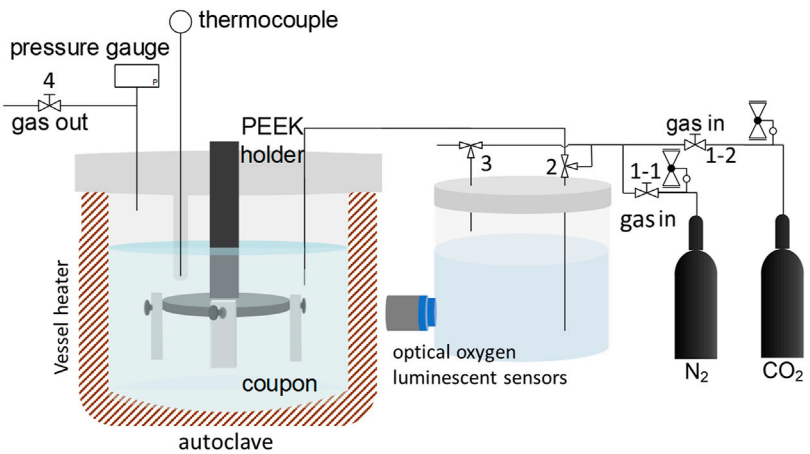

FIGURE 1 | Schematic diagram of the high-temperature and high-pressure autoclave and the location of mass loss samples.

980°C and 590°C, respectively. The chemical composition (wt%) of the material is listed in **Table 1**. Coupon specimens for immersion tests were machined to the dimension of 30 mm × 13 mm × 3 mm. Before each test, the specimens were ground to 1,200 grit using silicon carbide paper, then rinsed with deionized water and acetone, and dried.

Test Methods

The test solutions simulated the composition of the completion fluid from the Tarim field (1.5 g/ml in density) containing potassium formate (>97.1%) and deionized water. The chemical composition is listed in **Table 2**. The formate completion fluid usually uses CO purified from industrial tail gas as a synthetic raw material, containing sulfide due to the existence of a certain amount of K_2S in KCOOH. The solution was de-aerated by saturating with N_2 (gas in 1–1) or CO_2 (gas in 1–2) in a separate container overnight before testing. The dissolved oxygen was detected using optical oxygen luminescent sensors (HACH, K1100) to ensure the O_2 content within the solution was below 5 ppb. All lines to

pressure and temperature. Then, the autoclave was pressurized and stabilized at 10 bar N_2 or CO_2 at 25°C, respectively. The solution was heated to 180°C, and the final pressure was 26 bar under an N_2 condition and 34 bar under a CO_2 condition, as shown in **Table 3**. The immersion time for corrosion tests began once the solution temperature reached 180°C in the autoclave (**Supplementary Figure S1**).

A 316L SS static autoclave was utilized to conduct all the weight loss tests as schematically shown in **Figure 1**. For mass loss experiments, three coupons were mounted on a designed PEEK holder and fully immersed in the test solution. All tests were performed at 180°C with an N_2 or CO_2 partial pressure of 10 bar at 25°C, and the volume to surface ratio was kept at approximately 30 ml/cm^2 (three samples within the autoclave).

The original weight (m_0) of coupons was measured before the test, while the final weight (m_1) was obtained after the removal of corrosion products (ASTM G1-03 standard) (Metals, 2011). The corrosion rate (C_R) was reported in mm/year according to the obtained weight loss *via* **Eq. 1**:

$$C_R = \frac{87600\,(m_0 - m_1)}{t\rho A}, \quad (1)$$

where t represents the immersion time in hours, ρ is steel density in g/cm^3, and A is the exposed surface area in cm^2.

The thermodynamically stable states for S13Cr SS were evaluated by the Pourbaix diagram using OLI software[4]. The equilibrium of the aqueous and vapor phase was calculated using Stream Analyzer. Custom was selected as the type of calculation, and the volume of the total inflow was fixed. For thermodynamic calculation, the calculated stream was used in the Corrosion Analyzer. An alloy containing 12% Cr and 88% Fe was selected as the contact surface. In order to determine the total metal cation concentration, metal activities were changed, and the thermodynamics after the mass loss was calculated by iterating over Stream Analyzer.

Surface Analyses

The coupons after immersion tests were scanned using a scanning electron microscope equipped with an energy-dispersive X-ray detector (SEM/EDS), and X-ray diffraction (XRD) and Raman spectroscopy were performed on the surface to determine the morphology and chemical composition of the crystalline and amorphous corrosion products formed on the surface. The crystalline corrosion product was scanned over a 2-theta range from 10–90° at 0.033°/s on an area of 10 mm × 10 mm using a D8 Advance instrument (Bruker) with Cu Kα radiation; while the surface heterogeneities at the microscopic scale of the corrosion product was detected by confocal Raman microscopy using a LabRAM HR Evolution instrument (HORIBA) with a wavelength of 473 nm combined with a confocal imaging mode to focus on the injection area using the spot size of 1 μm access to frequencies from 200 to 1,200 cm^{-1}. The pit depth was measured by laser scanning confocal microscope (LSCM) measurements after removing the corrosion products according to the standard G46-94 (Metals, 2011, 46). An average pit depth from the 10 deepest pits was used to evaluate the localized corrosion rate (*LCR*) by the following formula:

$$LCR = \frac{8.76h}{t} + C_R, \quad (2)$$

where h is the pitting depth in μm after removing corrosion products.

RESULTS

Figure 2 compares the general corrosion rates of S13Cr SS exposed to the formate fluid saturated with N_2 or CO_2 at 180°C and various immersion times. The highest corrosion rates were observed at the first 5 h under both N_2 and CO_2 saturated conditions at 180°C. It can be seen that the corrosion rate of S13Cr SS was high (21.94 mm/year) when CO_2 was introduced into the formate fluid, in comparison with the value of 1.177 mm/year under the N_2 condition. The average mass loss tended to increase with time prolonged; however the slope of the increasing curve decreased with time, which indicates

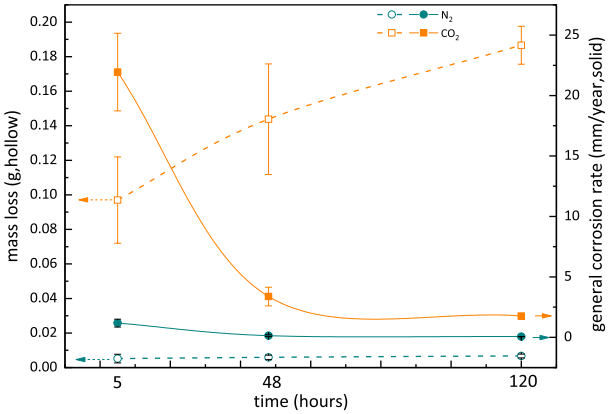

FIGURE 2 | Total mass loss and corrosion rates of S13Cr SS under the 180°C formate condition with N_2/CO_2 saturated after 5, 48, and 120 h.

the corrosion rates of S13Cr SS decreased with immersion time, showing a sharply reduction from 5 to 48 h. For a long immersion time of 120 h, the corrosion rate for S13Cr SS was maintained at 0.063 mm/year under the N_2 condition, whereas a higher corrosion rate of 1.76 mm/year was recorded after the introduction of CO_2.

The SEM morphology of the corrosion product scales formed on the S13Cr SS surface at various immersion times is given in **Figure 3**. For the condition with N_2, the polishing marks were still visible on the surface after 5 h of exposure (**Figure 3A**). It is interesting to note that the corrosion products with a "spherical" shape were observed after 48 h of exposure (**Figure 3B**) and increased in number after 120 h (**Figure 3C**). The EDS results in **Supplementary Figure S2** indicate that the scattered corrosion products were sulfur-rich. **Figures 3D–F** show the microscopic morphology of S13Cr SS in the formate solution saturated with CO_2 at various immersion times and 180°C, indicating the corrosion product scales covered the entire surface with time prolonged. It is noted that the spherical corrosion products rapidly precipitated and are visible on a cracked corrosion product layer after 5 h of exposure, as shown in **Figure 3D**. The higher magnification showed that the spherical products present a spherical-shaped structure in morphology. After 48 h of exposure, the presence of "sheet"-shaped corrosion products randomly covered the inner layer, as shown in **Figure 3E**. At 120 h, the sheet-shaped corrosion products gathered into clusters and fully covered the surface, as shown in **Figure 3F**.

Figure 4 illustrates the XRD patterns of the corrosion product scales formed on the surface of S13Cr SS at various immersion times. In the absence of CO_2, as shown in **Figure 4A**, no crystalline corrosion products were detected after 5 h of immersion time at 180°C. The peaks of FeS at (100), (101), and (111) were detected for the samples immersed in the solution after 48 h which corresponded to a disordered tetragonal mackinawite structure as spherical MkB (Wolthers et al., 2003) and agreed with the spherical feature observed through SEM/EDS in **Figure 3E**.

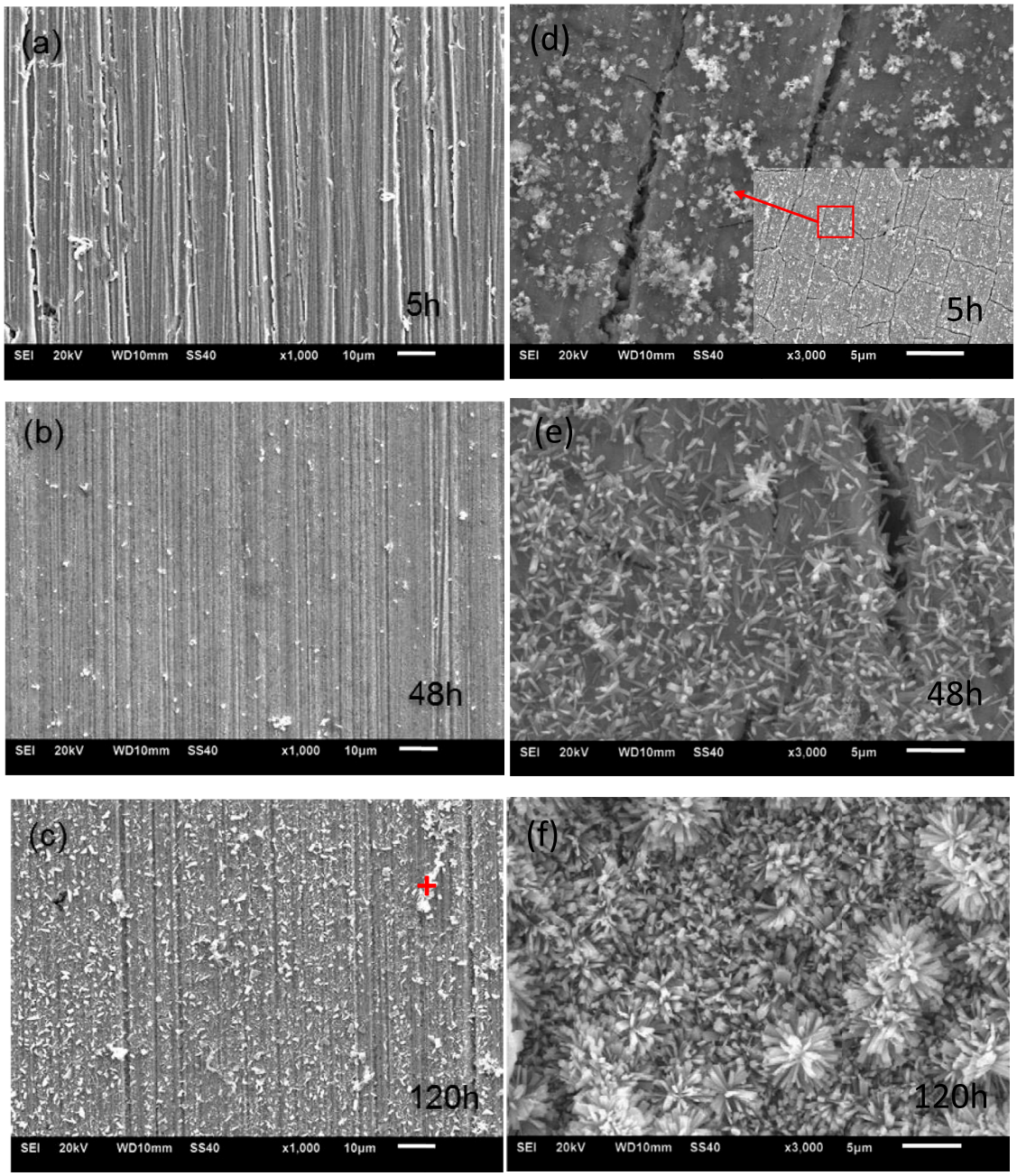

FIGURE 3 | SEM morphology of the corrosion products formed on S13Cr SS exposed to the 180°C formate fluid with **(A–C)** N_2 and **(D–F)** CO_2 saturated.

Figure 4B illustrates the overall XRD patterns of the corrosion product scales of S13Cr SS in CO_2-saturated formate fluids at various immersion times. The corrosion products are mainly $FeCO_3$ when the samples were exposed to the CO_2-saturated formate solution after 5, 48, and 120 h. However, both peaks for MkA (disordered sheet-like mackinawite) and MkB were detected in the first 5 h. Unlike spherical MkB, MkA has been reported to display sheet-like precipitated aqueous FeS clusters (Wolthers et al., 2003), which display a similar morphology with $FeCO_3$ in the context of this study. The proportion of these two end-member phases was reported to highly depend on the pH value, and thus the formation of MkA at (101) instead of MkB at (101) can be related to the pH drop caused by CO_2 infusion. It is also noted that an enhanced austenite peak located at 43.58° was detected, which suggests that the preferential dissolution of martensite took place on the surface in the early stages. However, neither the peaks of austenite nor martensite was detected after 120 h of exposure.

To identify the inner corrosion product layer, Raman spectroscopy was used to supplement XRD measurements.

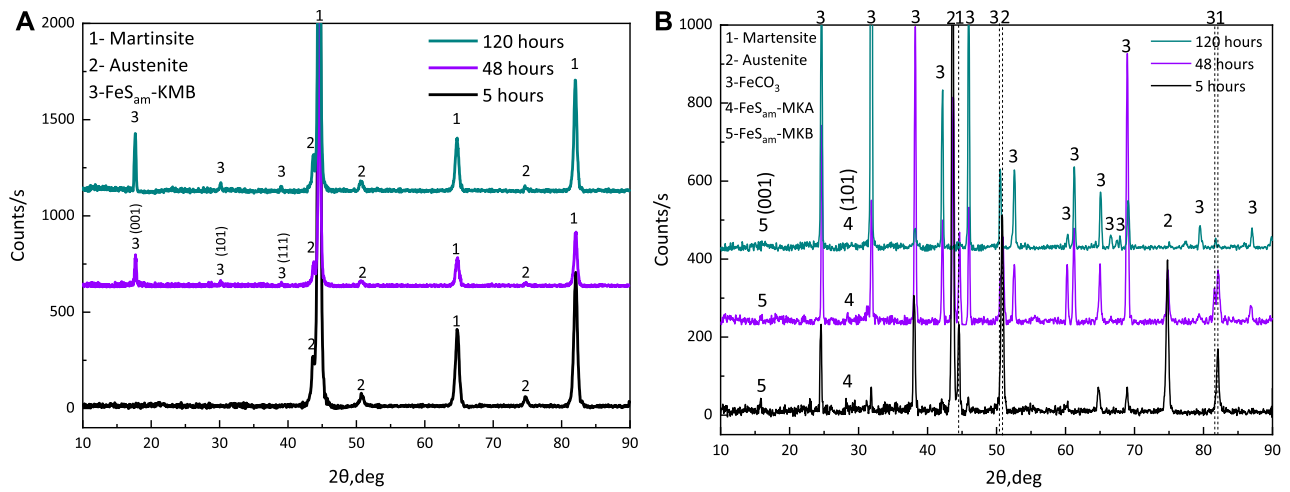

FIGURE 4 | XRD patterns of the corrosion scale formed on S13Cr SS under the 180°C formate condition with **(A)** N_2 or **(B)** CO_2 saturated after 5, 48, and 120 h.

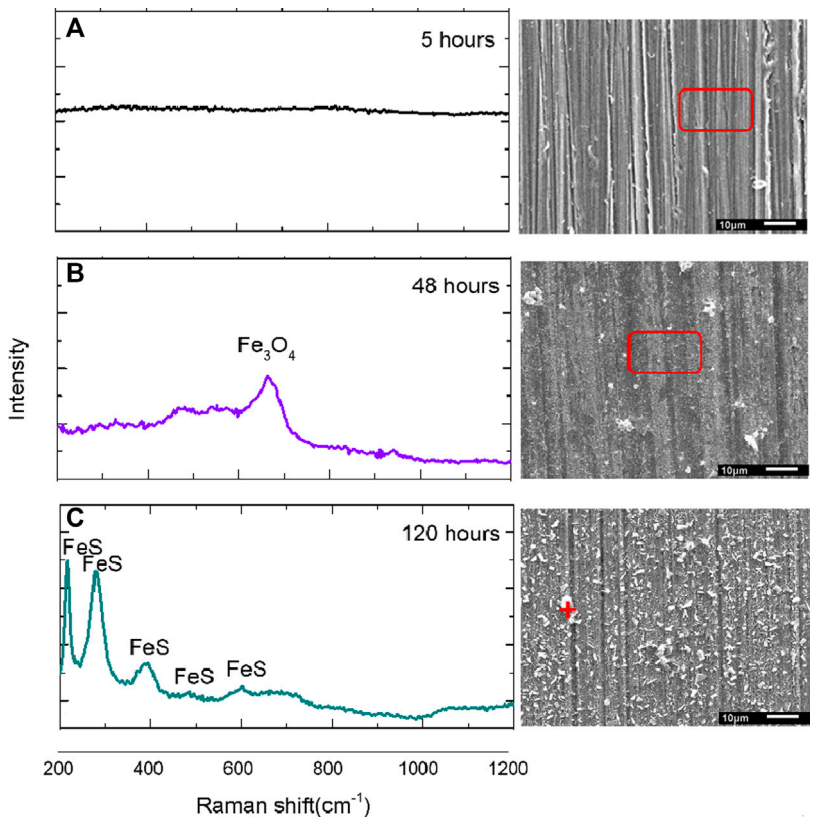

FIGURE 5 | Raman spectra of the corrosion scale formed on S13Cr SS in the formate fluid at 180°C after **(A)** 5 h, **(B)** 48 h, and **(C)** 120 h immersion time.

The Raman spectra in **Figure 5** relate to three local scans conducted on the S13Cr SS surface at various immersion times. For 5 h (**Figure 5A**), there was no corrosion product scale detected on the surface. The spectrum in **Figure 5B** indicates that the peak at around 662 cm^{-1} is representative of Fe_3O_4, and the scan in **Figure 5C** indicates that the peaks corresponding to Fe(II)-S(-II) are located at 213, 282, 384, 485, and 595 cm^{-1} (Genchev and Erbe, 2016).

The Raman spectra in **Figure 6** relate to six local scans conducted on the corroded S13Cr SS surface exposed to the

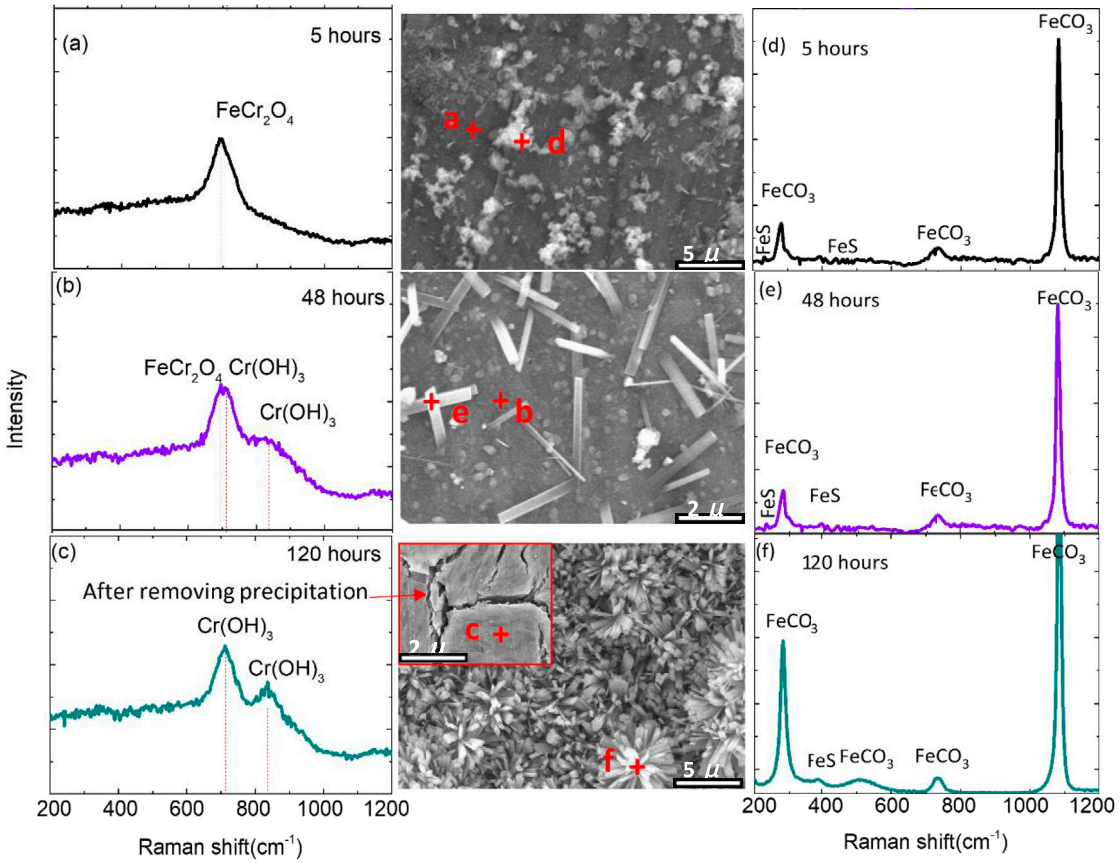

FIGURE 6 | Raman spectra of the corrosion scale formed on S13Cr SS after **(A,D)** 5 h, **(B,E)** 48 h, and **(C,F)** 120 h immersion time under CO_2-saturated formate condition at 180°C.

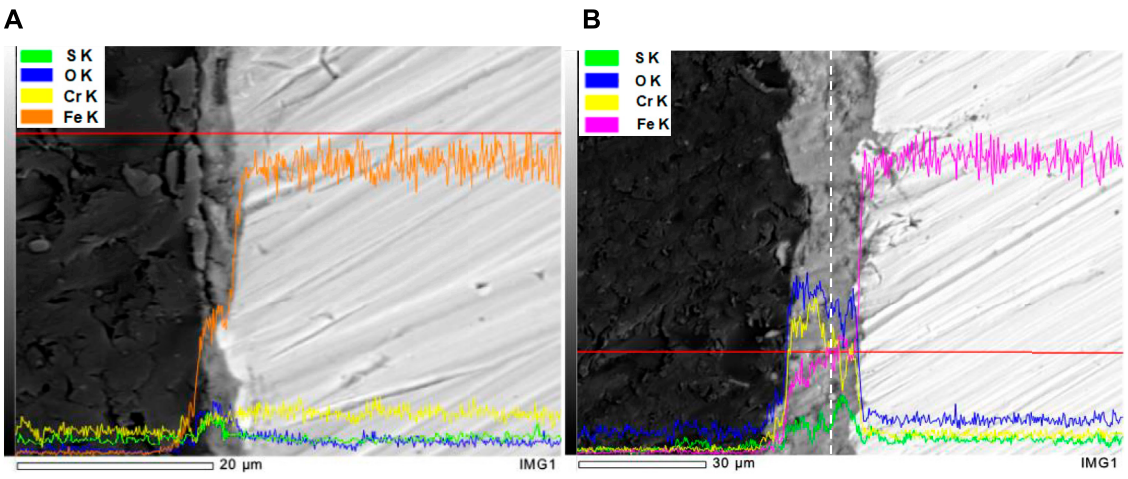

FIGURE 7 | Cross section of the corrosion scale formed on S13Cr SS exposed to the formate fluid in **(A)** N_2 and **(B)** saturated CO_2 after 120 h at 180°C.

CO_2-saturated formate fluids at various immersion times. The selected points were scanned on the outer layer and inner layer after 5, 48, and 120 h of immersion time. The spectrum in **Figure 6A** indicates that the peak at around 695 cm^{-1} is representative of $FeCr_2O_4$ (Anthony et al., 1990), and the scan in **Figure 6B** suggests the peaks corresponding to $FeCr_2O_4$ and $Cr(OH)_3$. For the sample exposed to 120 h (**Figure 6C**), the corroded sample surface was covered with $Cr(OH)_3$ which is

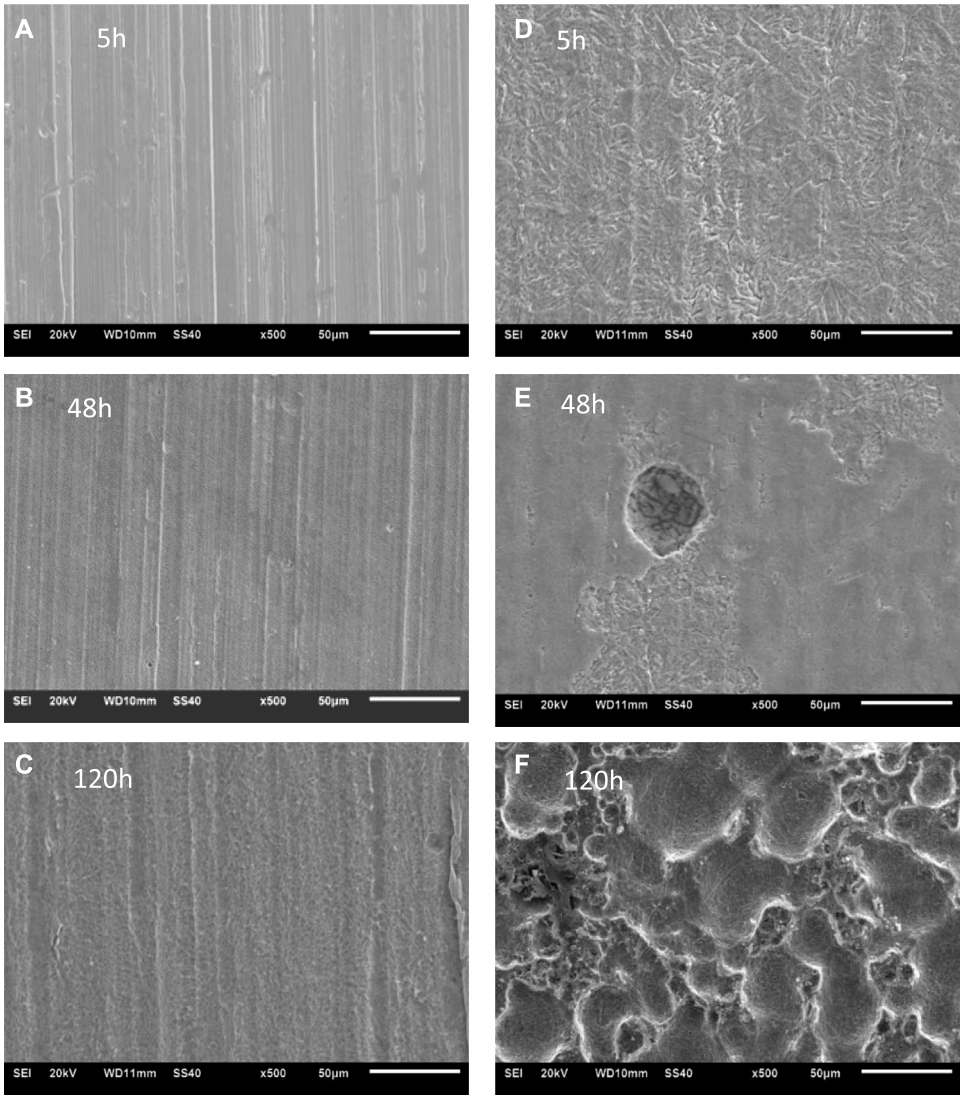

FIGURE 8 | SEM images of corroded S13Cr SS samples exposed under the 180°C formate condition with **(A–C)** N_2 and **(D–F)** CO_2 saturated after removing the corrosion products.

located at 707 cm^{-1} (Zhu et al., 2015b). The composition of the inner layer cannot be detected by XRD from 5 to 120 h, indicating the amorphous feature of this layer.

Figures 6D,E,F illustrate the conducted Raman spectra on the outer crystalline corrosion product layer. The results indicate that the "spherical"-like and "sheet"-like (scattered/cluster) corrosion products correspond to the mixture of $FeCO_3$ and FeS, respectively; the strong peaks of $FeCO_3$ are located at 187, 292, 730, and 1,087 cm^{-1} (Ondrus et al., 2003), and the weak peaks of FeS are located at 213 and 384 cm^{-1} (Genchev and Erbe, 2016). It should be noted that fewer peaks of FeS were detected on the outer surface of S13Cr SS, which could be related to the domination of forming $FeCO_3$ or the transformation from MkB to MkA.

Figure 7 illustrated the cross-sectional of corrosion product scales formed on the surface of S13Cr SS after 120 h under an N_2/CO_2-saturated formate condition at 180°C. As shown in **Figure 7A**, the thickness of the Fe_3O_4 layer was approximately 2.7 μm after 120 h of immersion in the formate fluid. The enrichment of S can be detected in the outer part of the corrosion product scale, which indicates the precipitation of FeS with time, consistent with the observation from top view. **Figure 7B** showed the corrosion product scale thickened to a thickness of 20 μm for CO_2-saturated condition at 120 h. The enrichment of Cr within the corrosion product scale can be related to the formation of $FeCr_2O_4$ and $Cr(OH)_3$, which is in agreement with the inner layer feature observed through Raman spectra in **Figure 6**. Besides, the enrichment of S was detected in the inner layer of the corrosion product, which can be resulted in the preferential precipitation of FeS in the early period. It should be noted that the EDS detection cannot separate S and Mo during line scan;

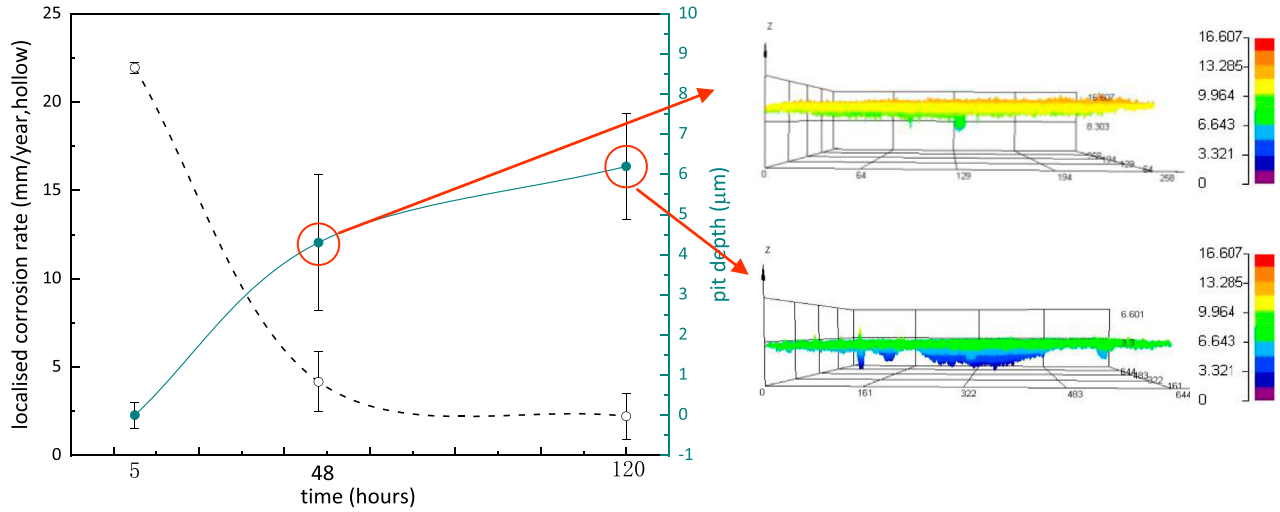

FIGURE 9 | Localized corrosion rate and pitting profilometry of corroded S13Cr SS samples after removing the corrosion products.

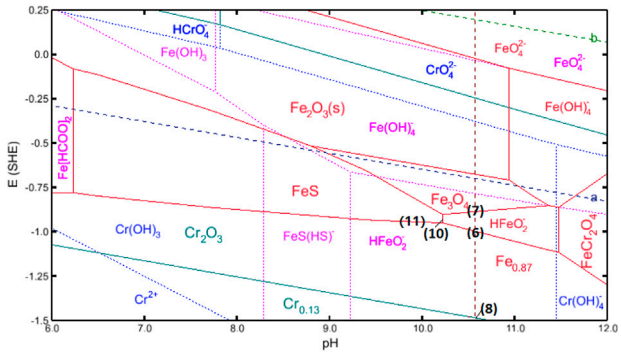

FIGURE 10 | Pourbaix diagram for S13Cr SS under the formate condition with the presence of sulfide at 180°C.

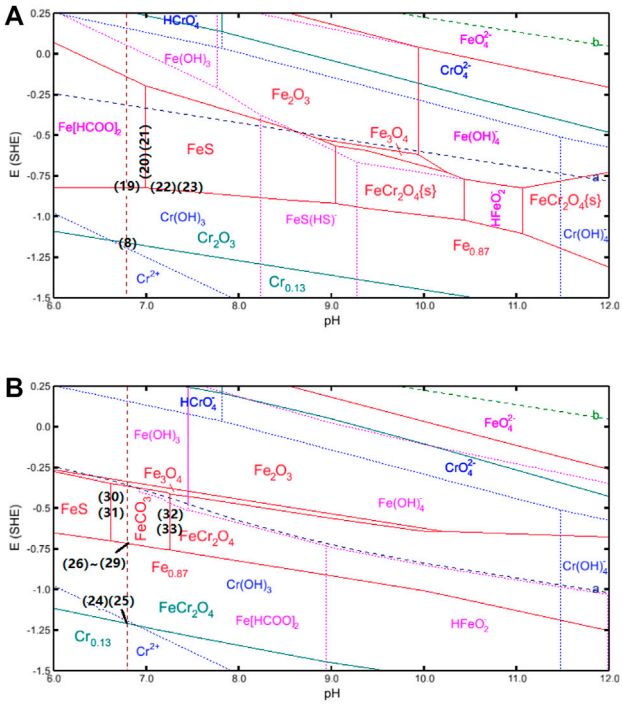

FIGURE 11 | Pourbaix diagram for S13Cr SS under the formate condition with the presence of CO_2 and sulfide at 180°C after **(A)** 0 and **(B)** 5 h of mass loss (0.098 g mass loss per sample).

therefore, the distribution of S within a film can be interfered with by Mo in the matrix.

The SEM images of corroded S13Cr SS samples after removing the corrosion products were observed in **Figure 8**. Compared to the condition with the infusion of CO_2, S13Cr suffered slight corrosion in the N_2-saturated formate fluid from 5 to 120 h. The polish marks were still visible; however, they became shallow as the immersion time prolonged. In the CO_2-saturated condition, the corrosion product scale can be detected at 5 h (**Figure 4** and **Figure 6**), and the surface of S13Cr SS was significantly corroded as shown in **Figure 8B**. As shown in **Figure 8D**, the localized attack can be observed on the surface of S13Cr after 48 h of immersion in the CO_2-saturated formate fluid. After 120 h, the few localized corrosion developed to a more severe attack (**Figure 8F**).

The localized corrosion rate of S13Cr SS immersed in CO_2-saturated formate fluids was calculated based on the analysis of *LSCM* measurements on the surface. The highest localized corrosion rate of 0.8 mm/year was determined in the first 48 h. From 48 to 120 h, the development of the pit grew slowly, and the localized corrosion rate declined to 0.45 mm/year after 120 h (note that the error bars were derived from the depth difference of the top ten pits, and the higher value at 48 and 120 h indicates the inhomogeneous development of pitting corrosion), which can be related to the formation of $Cr(OH)_3$ and $FeCO_3$ covering the surface and blocking the aggressive ions such as S (**Figure 9**).

DISCUSSION

The Formation of the Corrosion Product Scales in Thermodynamics

The formation of the thermodynamically stable corrosion scales on the surface can be predicted *via* Pourbaix diagrams by Corrosion Analyzer in the OLI system. **Figure 10** shows the conducting Pourbaix diagram for Cr and Fe in simulated completion fluids (formate saturated with N_2); a total metal cation concentration of 10^{-5} mol/l was considered (12% Cr cations and 88% Fe cations) at 180°C (Zhao et al., 2019; Yue et al., 2020c). It is acknowledged that the cathodic process contains the following reactions (Yue et al., 2017) and is provided as the navy dash line [a] in **Figure 13**:

$$2H^+(aq) + 2e^- \rightarrow H_2(g), \quad (3)$$

$$2HCOOH(aq) + 2e^- \rightarrow H_2(g) + 2COOH^-(aq), \quad (4)$$

$$2H_2O + 2e^- \rightarrow H_2(g) + 2OH^-(aq), \quad (5)$$

Where reaction (**Eq. 3**) can be negligible under the pH beyond 10.5, and concentration of HCOOH is negligible as it can be deduced from its pK_a [4.40 in diluted solutions at 180°C (HwaáKim et al., 1996)]. Therefore, reaction (**Eq. 5**) dominates the cathodic reactions in this case.

The initial corrosion rate was relatively high under such high-temperature conditions, which can be attributed to the fast metal dissolution in the absence of the protective layers (solid/insoluble products), and the results are in agreement with our previous research (Yue et al., 2020a; Yue et al., 2020b; Yue et al., 2020c):

$$Fe + 2H_2O \leftrightarrow HFeO_2^- + 3H^+ + 2e^-. \quad (6)$$

The corrosion rates were reduced sharply after 48 h, accompanied by the detection of the inner Fe_3O_4 layer, suggesting that the inner Fe_3O_4 layer plays a major role in blocking the ion transportation and retarding the corrosion process at the material interface. According to the Pourbaix diagram, the formation of Fe_3O_4 becomes thermodynamically favorable in formate fluids at 180°C and pH 10.55, suggesting the oxidation of the anion $HFeO^{2-}$ (**Eq. 7**):

$$3HFeO_2^- \leftrightarrow Fe_3O_4 + H_2O + OH^- + 2e^-. \quad (7)$$

For S13Cr SS, the formation of Cr_2O_3 is expected by reaction (**Eq. 8**) which coexists with $Cr(OH)_3$ (reaction **Eq. 9**) in aqueous. However, neither was detected from the Raman analyses and suggests that the amount of Cr_2O_3 and $Cr(OH)_3$ may be neglected compared to magnetite in the current system so these products may not be detected.

$$2Cr + 3H_2O \leftrightarrow Cr_2O_3 + 6H^+ + 6e^-, \quad (8)$$

$$Cr_2O_3 + 3H_2O \leftrightarrow 2Cr(OH)_3. \quad (9)$$

The dissolution of the substrate in the early period by reaction (**Eq. 6**) causes a reduction of pH and subsequently drives the formation of FeS by the following reaction when the interface pH value reaches 10.2:

$$HFeO_2^- + S^{2-} + H_2O \leftrightarrow FeS + 3OH^-, \quad (10)$$

$$Fe + S^{2-} \leftrightarrow FeS + 2e^-, \quad (11)$$

where reaction (**Eq. 10**) is considered as the formation of FeS via precipitation, while the reaction (11) represented the solid reaction for FeS (Rickard, 1995; Liu et al., 2017).

For the environment containing CO_2, as shown in **Figure 11**, the hydrogen evolution reaction line (navy dash line [a]) indicates a positive shift, which can be related to the change in the ion activity induced by CO_2. The presence of CO_2 can dissolve in the formate solution and hydrate to form H_2CO_3 through the following reactions (Ikeda et al., 1983):

$$CO_2(g) \leftrightarrow CO_2(aq); \quad (12)$$

$$CO_2(aq) + H_2O \leftrightarrow H_2CO_3(aq). \quad (13)$$

The weak acid H_2CO_3 in the formate solution can be dissociated in two steps, as shown in reactions (**Eq. 14**) and (**Eq. 15**) (Nesic et al., 1996b). It is noted that the formation of H_2CO_3 causes a reduced pH to 6.8 and can further react with formate ions to form HCOOH *via* reaction (**Eq. 16**) (Bungert et al., 2000).

$$H_2CO_3(aq) \leftrightarrow HCO_3^-(aq) + H^+(aq); \quad (14)$$

$$HCO_3^-(aq) \leftrightarrow CO_3^{2-}(aq) + H^+(aq); \quad (15)$$

$$H_2CO_3(aq) + COOH^-(aq) \leftrightarrow HCCOH(aq) + HCO_3^-(aq). \quad (16)$$

The cathodic reactions in the CO_2-saturated formate solution include not only the reactions (**Eqs 3–5**) but also the following reactions (Kahyarian and Nesic, 2020):

$$2H_2CO_3(aq) + 2e^- \rightarrow H_2(g) + 2HCO_3^-(aq); \quad (17)$$

$$2HCO_3^-(aq) + 2e^- \rightarrow H_2(g) + CO_3^{2-}(aq). \quad (18)$$

The reactions (**Eq. 4**), (**Eq. 18**), and (**Eq. 19**) are subsequently accelerated, indicating the fast metal dissolution process at the material interface under the CO_2-saturated condition compared to that of the N_2-balanced condition. The following anodic reaction is considered in the early stage as shown in **Figure 11A**:

$$Fe + 2HCOO^- \leftrightarrow Fe[HCOO]_2(aq) + 2e^-. \quad (19)$$

It is noted that the surface is covered by scattered FeS, suggesting that FeS becomes thermodynamically stable under the current experimental conditions. According to the constructing Pourbaix diagram, as shown in **Figure 11A**, the FeS phase becomes thermodynamically stable at pH 7.0, which indicates the formation of FeS at high pH. The following reactions are derived by the pH rise:

$$Fe[HCOO]_2(aq) + H_2S \leftrightarrow FeS + 2HCOOH, \quad (20)$$

$$Fe[HCOO]_2(aq) + HS^- \leftrightarrow FeS + HCOOH + HCOO^-. \quad (21)$$

Besides, reactions (**Eq. 22**) and (**Eq. 23**) can also occur based on the potential drive as the pH increase to 7.

$$Fe + H_2S \leftrightarrow FeS + 2H^+ + 2e^-, \quad (22)$$

$$Fe + HS^- \leftrightarrow FeS + H^+ + 2e^-. \quad (23)$$

After 5 h of mass loss, the increase in mass loss with immersion times made $FeCr_2O_4$ thermodynamically stable for

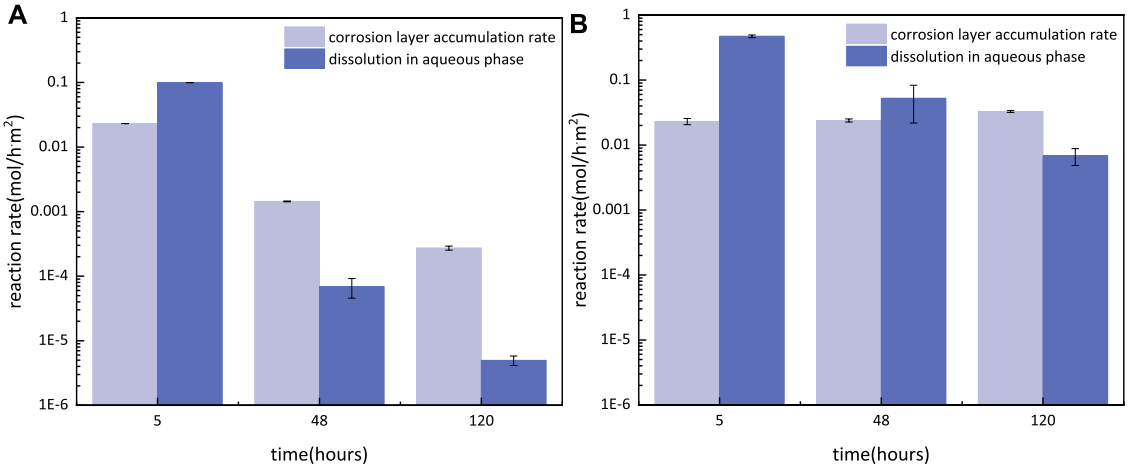

FIGURE 12 | *CLAR* and *DR* of S13Cr SS under the 180°C formate condition with N_2/CO_2 saturated after 5, 48, and 120 h.

Cr in solid-state (the calzo phase in **Figure 11B**) according to the following reactions (Hua et al., 2019b) in the Pourbaix diagram:

$$Fe(s) + 2Cr(s) + 4H_2O \rightarrow FeCr_2O_4(s) + 8H^+(aq) + 8e^-; \quad (24)$$

$$Fe[HCOO]_2(aq) + 2Cr + 4H_2O \leftrightarrow FeCr_2O_4(s) + 2HCOOH + 6H^+ + 6e^-, \quad (25)$$

Besides, $FeCO_3$ becomes the thermodynamically stable product after abundant cations in the aqueous, arising via both thermodynamic reactions (**Eqs 26–29**) (Nesic et al., 1996a) and transformation from FeS and $FeCr_2O_4$ derived by pH change according to reactions (**Eqs 30–33**):

$$Fe[\mathrm{HCOO}]_2(aq) + CO_3^{2-} \leftrightarrow FeCO_3(s) + 2HCOO^-; \quad (26)$$

$$Fe[\mathrm{HCOO}]_2(aq) + HCO_3^- \leftrightarrow FeCO_3(s) + \mathrm{HCOOH} + \mathrm{HCOO}^-; \quad (27)$$

$$Fe + CO_3^{2-} \leftrightarrow FeCO_3 + 2e^-, \quad (28)$$

$$Fe + HCO_3^- \leftrightarrow FeCO_3 + H^+ + 2e^-, \quad (29)$$

$$FeS + CO_3^{2-} \leftrightarrow FeCO_3 + S^{2-}, \quad (30)$$

$$FeS + HCO_3^- \leftrightarrow FeCO_3 + HS^-, \quad (31)$$

$$FeCr_2O_4 + CO_3^{2-} + 2H_2O + 2H^+ \leftrightarrow FeCO_3 + 2Cr(OH)_3, \quad (32)$$

$$FeCr_2O_4 + HCO_3^- + 2H_2O + H^+ \leftrightarrow FeCO_3 + 2Cr(OH)_3, \quad (33)$$

Although the reactions of corrosion products can be predicted by thermodynamics, it should be noted that the dominant reaction as the growth of corrosion products cannot be defined by thermodynamics and that is the limitation of using the Pourbaix diagram.

The Formation of the Corrosion Product Scales in Kinetics

The corrosion rate (C_R) consists of the reaction rate from corrosion layer accumulation (*CLAR*) and the dissolution in the aqueous phase (*DR*) (Sun and Nešic, 2008), which can be calculated by the weight of coupons with the corrosion product (m_a) according to **Eq. 34** and **Eq. 35** and is shown in **Figure 12**.

$$CLAR = \frac{m_a - m_1}{M \cdot V}, \quad (34)$$

$$DR = \frac{m_0 - (m_a - m_1)}{56 \cdot V}, \quad (35)$$

where M is the mol mass of the main corrosion product, and V is the volume of solution. To simplify the calculation, the S13Cr SS is assumed to be dissolved into iron ions (56 g/mol).

According to the observation in **Figure 3**, fewer outer FeS/$FeCO_3$ crystals accumulate on the surface at 5 h, which indicates that the *CLAR* mainly corresponded to the formation of the inner layer consisting of $Fe_3O_4/FeCr_2O_4$. It is interesting to note that the *CLAR* of both Fe_3O_4 and $FeCr_2O_4$ was 0.023 mol/hm^2, suggesting that more metal dissolution was transferred into Fe $[HCOO]_2$ in CO_2-saturated formates than the formation of $HFeO_2^-$ under N_2 conditions.

Under the N_2 condition, the *DR* decreased to the level below 1E-4 mol/hm^2 at 48 h, indicating the protection of the inner layer as a barrier against active metal dissolutions. The reaction rate for the growth of the corrosion products decreased with exposure time and reached to the value of 2.7E-4 mol/hm^2 after 120 h.

Under the CO_2-saturated condition, the *CLAR* slightly increased after 48 h of immersion, which can be attributed to the formation of the outer layer consisting of $FeCO_3$/FeS on the surface. The reduction in *DR* at 48 h, however, is still higher than *CLAR*, indicating the continuous releasing of metal ions from the substrate. As the immersion time prolonged, forming the fully covered outer layer to further block the flux of aggressive ions, resulted in a lower level of *DR* combined with an increased *CLAR* at 120 h. However, the *CLAR* in CO_2-saturated conditions was two orders of magnitude higher than that in N_2 conditions at 120 h, consistent with the results in **Figure 7B** where it shows a thicker corrosion product scale. Besides, the *DR* was still three orders of magnitude higher than that in the N_2 condition at 120 h. These results suggest that the dissolution of metal into ions occurred under the protection of the double-layered corrosion product scale.

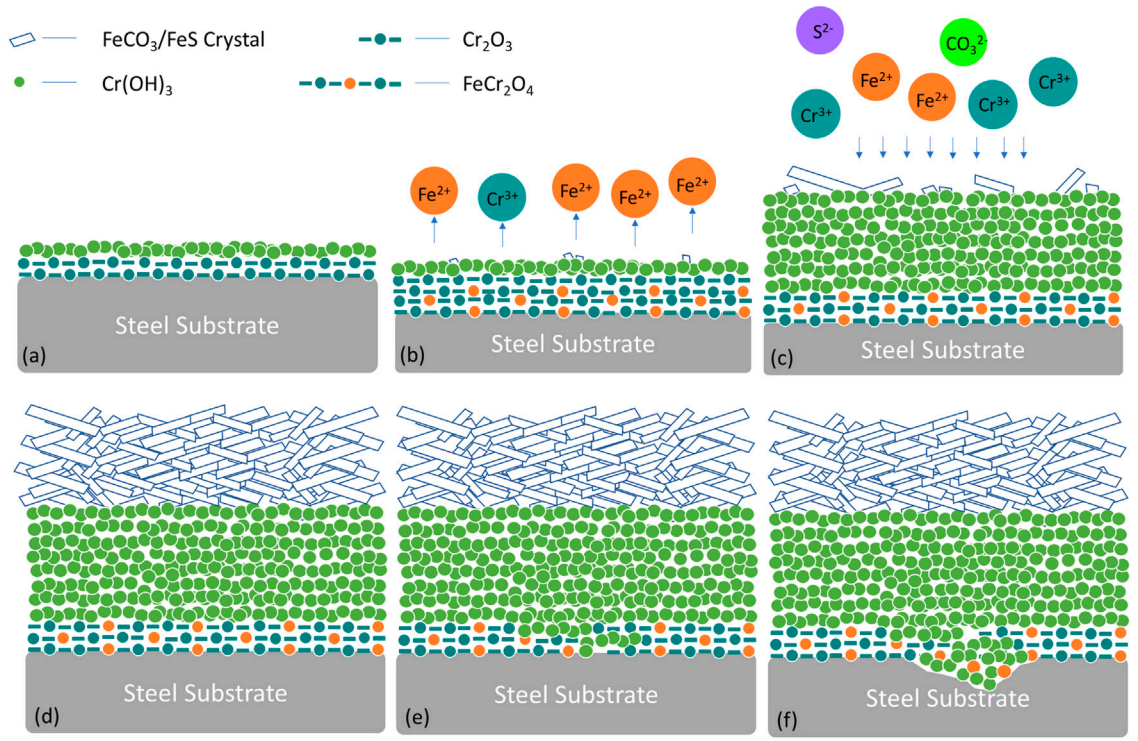

FIGURE 13 | Schematic diagram of **(A–D)** the sequence of the formation of the outer and inner layers of the double-layered corrosion products and **(E–F)** the development of localized corrosion in CO_2-saturated formate solution at 180°C.

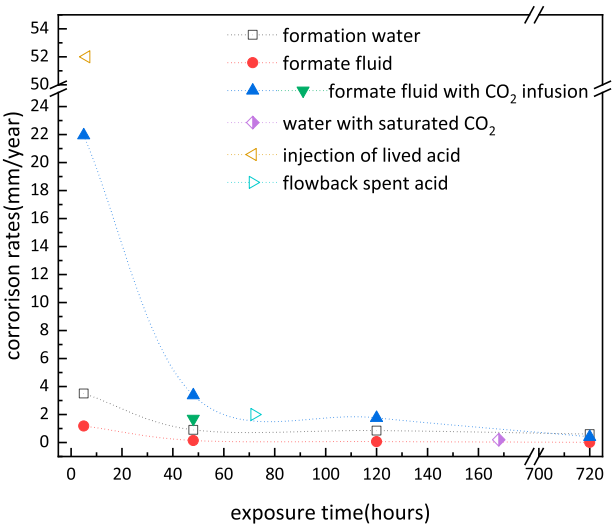

FIGURE 14 | Comparison of measured uniform corrosion rates of S13Cr with data obtained from the literature under ultra-deep downhole conditions (180°C).

Although the multi-layered corrosion product scales covered and protected the surface of S13Cr SS under the CO_2-containing condition, high *DR* suggests the presence of defects in the corrosion products consisting of FeS, $Cr(OH)_3$, and $FeCO_3$. The previous literature has reported that the formation of the $FeCO_3$ and $Cr(OH)_3$ on S13Cr SS was controlled by the dissolution–precipitation process and resulted in relatively high defections (Guo et al., 2012; Li et al., 2019b; Zhao et al., 2019). However, the formation of the compact structures for spinel products such as Fe_3O_4 and $FeCr_2O_4$ was considered to provide better corrosion protection than that of the precipitation type (Yue et al., 2020a, 2020b, 2020c; Liu et al., 2021). Besides, the outer corrosion products with sheet-shaped clusters characterized as a looser structure which may cause pore connectivity within the outer layer. Wang et al. (Li et al., 2019a; Wang et al., 2021) illustrated that the localized corrosion at CO_2-containing environments was corresponding to the connected pores in the corrosion product scale. The fast kinetics resulted in the small pore sizes as the quicker formation of crystalline $FeCO_3$. Therefore, the formation of the porous outer layer with high *CLAR* can induce the localized corrosion for S13Cr under CO_2-saturated conditions. In contrast, the outer FeS scattered on the compact inner layer with low *CLAR* in the formate fluid without CO_2, showing general corrosion after removal of the corrosion product layer (**Figure 8**).

The evolution of the double-layered corrosion products in CO_2-saturated formate solutions is illustrated in **Figure 13**. As shown in **Figure 13B**, the formation of $FeCr_2O_4$ acts as the protective layer (in **Figure 13A**). The $FeCr_2O_4$ can be destabilized and gradually transferred into $Cr(OH)_3$. **Figure 13C** illustrates the precipitation of $Cr(OH)_3$ in the inner layer due to its extremely low solubility product constant (Xu et al., 2013; Liu et al., 2015). Consequently, a Cr-rich inner layer appears instead of a passive film on the surface

when the CO_2-saturated formate fluid was at 180°C. A Cr-rich inner layer can decrease the corrosion rate at low pH; however, it should be noted that the corrosion scale displayed porous with high defects because $FeCO_3$/FeS grows irregularly and discontinuously, which allows anions to penetrate through the outer layer of corrosion product scales.

Note that there were no Cl^- ions present in the formate fluid, which indicates a relatively low localized corrosion risk. However, the hydrolysis of Cr^{3+} caused an acidified environment within the inner layer of corrosion products. When the pH dropped below 7.3 (**Figure 11B**), the oxide layer would dissolve. The hydrolytic action of dissolved Cr^{3+} would subsequently decrease the pH value and result in the development of localized corrosion, as shown in **Figures 13D,E**.

Figure 14 compares the measured corrosion rate in the formate fluid (tubing outer wall and casing) with those obtained from the literature both in formate fluid and formation water (tubing inner wall) (Leth-Olsen, 2004; Sunaba et al., 2014; Zhao et al., 2018; Qi et al., 2019; Yue et al., 2020b). It reveals that S13Cr shows a lower corrosion rate in the formate fluid than that in formation water. The high corrosion rates were only obtained in the CO_2 infusion formate fluid (showing the same corrosion rate with CO_2-saturated H_2O), which indicates that CO_2 is the governing factor in the ultra-deep downhole condition. It is noted that the highest corrosion rate occurred during the injection of lived acid, and the localized corrosion occurs at the defect of the corrosion product scale (Qi et al., 2019). The CO_2 would ingress into completion fluid once the localized corrosion induced tubing perforation, which would cause a dramatic increase in the corrosion rate for S13Cr in completion fluid.

CONCLUSION

The research has focused on clarifying the influence of sulfide impurity and CO_2 ingress on the corrosion of S13Cr SS as well as the evolution of the corrosion product scales under both CO_2-free and CO_2-saturated formate fluid conditions. From this work, the following conclusions can be drawn:

- Under N_2-deoxygenated formate fluid conditions, the general corrosion rate of S13Cr SS reached 1.177 mm/year after 5 h and reduced to 0.067 mm/year after 120 h of exposure, compared to high corrosion rates of 21.94 and 1.76 mm/year for samples exposed to the CO_2-saturated formate fluid condition after 5 and 120 h, respectively.
- A thin Fe_3O_4 layer was detected on S13Cr SS under N_2-deoxygenated formate fluid conditions. The presence of sulfide in formate brine can result in the formation of disordered tetragonal mackinawite MkB after 120 h of exposure. With the ingress of CO_2, the formation of the inner corrosion product layer on S13Cr SS was composed of $FeCr_2O_4$ after 5 h and then transformed to $Cr(OH)_3$ with time prolonged. The acidification on the surface results in the formation of a combination of disordered mackinawite of MkA and MkB, accompanied by the formation of a unique $FeCO_3$ morphology which presented as "sheet" crystalline after 48 h of exposure and developed into clusters after 120 h.
- For the system containing sulfide, the formation of FeS, Fe_3O_4, and $HFeO_2^-$ became thermodynamically stable. The reaction rate of $HFeO_2^-$ was higher in the first 5 h, whereas the accumulation for solid products as a barrier layer became favorable in kinetics after 48 h. Under CO_2-saturated conditions, the formation of Fe $[HCOO]_2$, FeS, $FeCr_2O_4$, $Cr(OH)_3$, and $FeCO_3$ became thermodynamically stable. Both the reaction rates for dissolution and corrosion layer accumulation are high from 5 to 120 h. The thicker corrosion product did not provide effective protection and induced localized corrosion after 48 h of exposure.

DATA AVAILABILITY STATEMENT

The original contributions presented in the study are included in the article/**Supplementary Material**; further inquiries can be directed to the corresponding authors.

AUTHOR CONTRIBUTIONS

XY, YH, and LZ contributed to the conception and design of the study. LH, XY, and ZQ organized the database. XY and ZY performed the statistical analysis. XY wrote the first draft of the manuscript. All authors contributed to manuscript revision and read and approved the submitted version.

FUNDING

This work was supported by the National Natural Science Foundation of China (Grant Nos. 51871027 and 52101069), the China Postdoctoral Science Foundation (No. 2021M690345), and the Postdoctoral Research Foundation of Shunde Graduate School of University of Science and Technology Beijing (Nos. 2020BH013 and 2020BH010).

SUPPLEMENTARY MATERIAL

The Supplementary Material for this article can be found online at: https://www.frontiersin.org/articles/10.3389/fmats.2021.802136/full#supplementary-material

REFERENCES

Anthony, J. W., Bideaux, R. A., Bladh, K. W., and Nichols, M. C. (1990). *Handbook of Mineralogy*. Tucson: Mineral Data Publ.

Askari, M., Aliofkhazraei, M., Jafari, R., Hamghalam, P., and Hajizadeh, A. (2021). Downhole Corrosion Inhibitors for Oil and Gas Production - a Review. *Appl. Surf. Sci. Adv.* 6, 100128. doi:10.1016/j.apsadv.2021.100128

Banaś, J., Lelek-Borkowska, U., Mazurkiewicz, B., and Solarski, W. (2007). Effect of CO2 and H2S on the Composition and Stability of Passive Film on Iron Alloys

in Geothermal Water. *Electrochimica Acta* 52, 5704–5714. doi:10.1016/j.electacta.2007.01.086

Bungert, D., Maikranz, S., Sundermann, R., Downs, J., Benton, W., Dick, M., et al. (2000). "The Evolution and Application of Formate Brines in High-Temperature/high-Pressure Operations," in IADC/SPE Drilling Conference (London: Society of Petroleum Engineers). doi:10.2118/59191-ms

Clarke-Sturman, A., and Sturla, P. (1988). Aqueous Polysaccharide Compositions. *Eur. patent* 259, 16.

Ding, J., Zhang, L., Li, D., Lu, M., Xue, J., and Zhong, W. (2013). Corrosion and Stress Corrosion Cracking Behavior of 316L Austenitic Stainless Steel in High H2S-CO2-Cl− Environment. *J. Mater. Sci.* 48, 3708–3715. doi:10.1007/s10853-013-7168-1

Genchev, G., and Erbe, A. (2016). Raman Spectroscopy of Mackinawite FeS in Anodic Iron Sulfide Corrosion Products. *J. Electrochem. Soc.* 163, C333–C338. doi:10.1149/2.1151606jes

Guo, S., Xu, L., Zhang, L., Chang, W., and Lu, M. (2012). Corrosion of alloy Steels Containing 2% Chromium in CO2 Environments. *Corrosion Sci.* 63, 246–258.

Hamza, A., Hussein, I. A., Jalab, R., Saad, M., and Mahmoud, M. (2021). Review of Iron Sulfide Scale Removal and Inhibition in Oil and Gas Wells: Current Status and Perspectives. *Energy Fuels* 35, 14401–14421. doi:10.1021/acs.energyfuels.1c02177

He, W., Knudsen, O. Ø., and Diplas, S. (2009). Corrosion of Stainless Steel 316L in Simulated Formation Water Environment with CO2-H2S-Cl−. *Corrosion Sci.* 51, 2811–2819. doi:10.1016/j.corsci.2009.08.010

Hoar, T. P., and Jacob, W. R. (1967). Breakdown of Passivity of Stainless Steel by Halide Ions. *Nature* 216, 1299–1301. doi:10.1038/2161299a0

Howard, S. K., Downs, J., and others (2009). "Formate Brines for HP/HT Well Control: New Insights into the Role and Importance of the Carbonate/Bicarbonate Additive Package," in SPE International Symposium on Oilfield Chemistry (London: Society of Petroleum Engineers). doi:10.2118/121550-ms

Howard, S. K., and others (1995). "Formate Brines for Drilling and Completion: State of the Art," in SPE Annual Technical Conference and Exhibition (London: Society of Petroleum Engineers). doi:10.2118/30498-ms

Hua, Y., Barker, R., Wang, C., and Neville, A. (2019a). "Comparison of Corrosion Products/Scales on X65 Carbon Steel in a NaCl Solution and a Complex Brine at Different CO 2 Partial Pressures," in *CORROSION 2019* (Houston, Texas, USA: NACE International).

Hua, Y., Xu, S., Wang, Y., Taleb, W., Sun, J., Zhang, L., et al. (2019b). The Formation of FeCO3 and Fe3O4 on Carbon Steel and Their Protective Capabilities against CO2 Corrosion at Elevated Temperature and Pressure. *Corrosion Sci.* 157, 16. doi:10.1016/j.corsci.2019.06.016

Ikeda, A., Ueda, M., and Mukai, S. (1983). *CO2 Corrosion Behavior and Mechanism of Carbon Steel and Alloy Steel*.

Kahyarian, A., and Nesic, S. (2020). On the Mechanism of Carbon Dioxide Corrosion of Mild Steel: Experimental Investigation and Mathematical Modeling at Elevated Pressures and Non-ideal Solutions. *Corrosion Sci.* 173, 108719. doi:10.1016/j.corsci.2020.108719

Kim, M. H., Kim, C. S., Lee, H. W., and Kim, K. (1996). Temperature Dependence of Dissociation Constants for Formic Acid and 2,6-dinitrophenol in Aqueous Solutions up to 175 °C. *J. Chem. Soc. Faraday Trans.* 92, 4951–4956. doi:10.1039/ft9969204951

Leth-Olsen, H. (2005). "CO2 Corrosion in Bromide and Formate Well Completion Brines," in SPE International Symposium on Oilfield Corrosion (London: Society of Petroleum Engineers). doi:10.2118/95072-ms

Leth-Olsen, H. (2004). "CO2 Corrosion of Steel in Formate Brines for Well Applications," in CORROSION 2004 (New Orleans, Luisiana, USA: NACE-04357).

Li, D., Zhang, L., Wang, X., Yang, Z., Yue, X., Lu, M., et al. (2018). "Study on the Corrosion Performance of C110 Tubing in Formate Completion Fluid at High Temperature," in *CORROSION 2018* (Houston, Texas, USA: NACE International).

Li, J., Zhang, Z., Zhu, G., Li, T., Zhao, K., Chi, L., et al. (2020). The Origin and Accumulation of Ultra-deep Oil in Halahatang Area, Northern Tarim Basin. *J. Pet. Sci. Eng.* 195, 107898. doi:10.1016/j.petrol.2020.107898

Li, L., Yan, J., Xiao, J., Sun, L., Fan, H., and Wang, J. (2021). A Comparative Study of Corrosion Behavior of S-phase with AISI 304 Austenitic Stainless Steel in H2S/CO2/Cl- media. *Corrosion Sci.* 187, 109472. doi:10.1016/j.corsci.2021.109472

Li, S., Zeng, Z., Harris, M. A., Sánchez, L. J., and Cong, H. (2019a). CO2 Corrosion of Low Carbon Steel under the Joint Effects of Time-Temperature-Salt Concentration. *Front. Mater.* 6, 10. doi:10.3389/fmats.2019.00010

Li, X., Zhao, Y., Qi, W., Xie, J., Wang, J., Liu, B., et al. (2019b). Effect of Extremely Aggressive Environment on the Nature of Corrosion Scales of HP-13Cr Stainless Steel. *Appl. Surf. Sci.* 469, 146–161. doi:10.1016/j.apsusc.2018.10.237

Liu, H., Cao, L., Xie, J., Yang, X., Zeng, N., Zhang, X., et al. (2019a). "Research and Practice of Full Life Cycle Well Integrity in HTHP Well, Tarim Oilfield," in International Petroleum Technology Conference. doi:10.2523/19403-ms

Liu, H., Sun, J., Qian, J., Wang, B., Shi, S., Zhu, Y., et al. (2021). Revealing the Temperature Effects on the Corrosion Behaviour of 2205 Duplex Stainless Steel from Passivation to Activation in a CO2-containing Geothermal Environment. *Corrosion Sci.* 187, 109495. doi:10.1016/j.corsci.2021.109495

Liu, W., Lu, S.-L., Zhang, Y., Fang, Z.-C., Wang, X.-M., and Lu, M.-X. (2015). Corrosion Performance of 3% Cr Steel in CO2-H2S Environment Compared with Carbon Steel. *Mater. Corrosion* 66, 1232–1244.

Liu, W., Shi, T., Li, S., Lu, Q., Zhang, Z., Feng, S., et al. (2019b). Failure Analysis of a Fracture Tubing Used in the Formate Annulus protection Fluid. *Eng. Fail. Anal.* 95, 248–262. doi:10.1016/j.engfailanal.2018.09.009

Liu, Y., Xu, L., Lu, M., Meng, Y., Zhu, J., and Zhang, L. (2014). Corrosion Mechanism of 13Cr Stainless Steel in Completion Fluid of High Temperature and High Concentration Bromine Salt. *Appl. Surf. Sci.* 314, 768–776. doi:10.1016/j.apsusc.2014.07.067

Liu, Y., Zhang, Z., Bhandari, N., Dai, Z., Yan, F., Ruan, G., et al. (2017). New Approach to Study Iron Sulfide Precipitation Kinetics, Solubility, and Phase Transformation. *Ind. Eng. Chem. Res.* 56, 9016–9027. doi:10.1021/acs.iecr.7b01615

Metals, A. C. G.-1 on. C. of. (2011). *Standard Practice for Preparing, Cleaning, and Evaluating Corrosion Test Specimens*. West Conshohocken, Pennsylvania, USA: ASTM international.

Nesic, S., Postlethwaite, J., and Olsen, S. (1996a). An Electrochemical Model for Prediction of Corrosion of Mild Steel in Aqueous Carbon Dioxide Solutions. *Corrosion* 52, 280–294. doi:10.5006/1.3293640

Nesic, S., Thevenot, N., Crolet, J. L., and Drazic, D. (1996b). "Electrochemical Properties of Iron Dissolution in the Presence of CO2 - Basics Revisited," in *NACE-96003* (Denver, Colorado: NACE International), 23.

Ondrus, P., Veselovsky, F., Gabasova, A., Hlousek, J., Srein, V., Vavrin, I., et al. (2003). Primary Minerals of the Jáchymov Ore District. *J. Geosciences* 48, 19–147.

Pessu, F., Barker, R., and Neville, A. (2017). Pitting and Uniform Corrosion of X65 Carbon Steel in Sour Corrosion Environments: the Influence of CO2, H2S, and Temperature. *Corrosion* 73, 1168–1183. doi:10.5006/2454

Qi, W., Wang, J., Li, X., Cui, Y., Zhao, Y., Xie, J., et al. (2019). Effect of Oxide Scale on Corrosion Behavior of HP-13Cr Stainless Steel during Well Completion Process. *J. Mater. Sci. Technol.* 64, 9. doi:10.1016/j.jmst.2019.10.009

Refaey, S. A. M., Taha, F., and El-Malak, A. M. A. (2005). Corrosion and Inhibition of Stainless Steel Pitting Corrosion in Alkaline Medium and the Effect of Cl− and Br− Anions. *Appl. Surf. Sci.* 242, 114–120. doi:10.1016/j.apsusc.2004.08.003

Rickard, D. (1995). Kinetics of FeS Precipitation: Part 1. Competing Reaction Mechanisms. *Geochimica et cosmochimica acta* 59, 4367–4379. doi:10.1016/0016-7037(95)00251-t

Sekine, I., and Chinda, A. (1984). Comparison of the Corrosion Behavior of Pure Fe, Ni, Cr, and Type 304 Stainless Steel in Formic Acid Solution. *Corrosion* 40, 95–100. doi:10.5006/1.3593929

Sun, W., and Nešić, S. (2008). Kinetics of Corrosion Layer Formation: Part 1-Iron Carbonate Layers in Carbon Dioxide Corrosion. *Corrosion* 64, 334–346. doi:10.5006/1.3278477

Sunaba, T., Ito, T., Miyata, Y., Asakura, S., Shinohara, T., Yakou, T., et al. (2014). Influence of Chloride Ions on Corrosion of Modified Martensitic Stainless Steels at High Temperatures under a CO2Environment. *Corrosion* 70, 988–999. doi:10.5006/1141

Teng, X., Yang, X., and Xu, T. (2016). *Formate Completion Fluid Technology*. Beijing: Petroleum Industry Press.

Vedage, H., Ramanarayanan, T. A., Mumford, J. D., and Smith, S. N. (1993). Electrochemical Growth of Iron Sulfide Films in H2S-Saturated Chloride media. *Corrosion* 49, 114–121. doi:10.5006/1.3299205

Wang, C., Hua, Y., Nadimi, S., Taleb, W., Barker, R., Li, Y., et al. (2021). Determination of Thickness and Air-Void Distribution within the Iron Carbonate Layers Using X-ray Computed Tomography. *Corrosion Sci.* 179, 109153. doi:10.1016/j.corsci.2020.109153

Wolthers, M., Van der Gaast, S. J., and Rickard, D. (2003). The Structure of Disordered Mackinawite. *Am. Mineral.* 88, 2007–2015. doi:10.2138/am-2003-11-1245

Xu, B., Yuan, B., Wang, Y., and Zhu, L. (2018). H2S-CO2 Mixture Corrosion-Resistant Fe2O3-Amended Wellbore Cement for Sour Gas Storage and Production wells. *Construction Building Mater.* 188, 161–169. doi:10.1016/j.conbuildmat.2018.08.120

Xu, L., Guo, S., Chang, W., Chen, T., Hu, L., and Lu, M. (2013). Corrosion of Cr Bearing Low alloy Pipeline Steel in CO2 Environment at Static and Flowing Conditions. *Appl. Surf. Sci.* 270, 395–404. doi:10.1016/j.apsusc.2013.01.036

Yang, Z., Du, C., Li, W., Zhang, L., Wang, Z., Li, D., et al. (2019). "Effects of pH Buffer on the Corrosion Behavior of C110 Tubing in Formate Completion Fluid with the Mix of CO2 at High Temperature," in NACE International Corrosion Conference Proceedings (Houston, Texas, USA: NACE International), 1–11.

Yue, X., Zhang, L., Li, D., Honda, H., Lu, M., Wang, Z., et al. (2017). Effect of Traces of Dissolved Oxygen on the Passivation Stability of Super 13Cr Stainless Steel under High CO2/H2S Conditions. *Int. J. Electrochem. Sci.* 12, 7853–7868. doi:10.20964/2017.08.33

Yue, X., Zhang, L., Ma, L., Lu, M., Neville, A., and Hua, Y. (2020a). Influence of a Small Velocity Variation on the Evolution of the Corrosion Products and Corrosion Behaviour of Super 13Cr SS in a Geothermal CO2 Containing Environment. *Corrosion Sci.* 178, 108983.

Yue, X., Zhang, L., Sun, C., Xu, S., Wang, C., Lu, M., et al. (2020b). A Thermodynamic and Kinetic Study of the Formation and Evolution of Corrosion Product Scales on 13Cr Stainless Steel in a Geothermal Environment. *Corrosion Sci.* 169, 108640. doi:10.1016/j.corsci.2020.108640

Yue, X., Zhang, L., Wang, Y., Xu, S., Wang, C., Lu, M., et al. (2020c). Evolution and Characterization of the Film Formed on Super 13Cr Stainless Steel in CO2-saturated Formation Water at High Temperature. *Corrosion Sci.* 163, 108277. doi:10.1016/j.corsci.2019.108277

Zhao, Y., Chang, L., Zhang, T., Xie, J., Chen, Y., Xu, D., et al. (2020). Effect of the Flow Velocity on the Corrosion Behavior of UNS S41426 Stainless Steel in the Extremely Aggressive Oilfield Environment for the Tarim Area. *CORROSION* 76, 654–665. doi:10.5006/2813

Zhao, Y., Hua, Y., Liu, B., Li, X., Xie, J., Zeng, G., et al. (2021a). The Development of a Mechanistic-Chemometrics Model with Multi-Degree of freedom for Pitting Corrosion of HP-13Cr Stainless Steel under Extremely Oilfield Environments. *Corrosion Sci.* 181, 109237. doi:10.1016/j.corsci.2021.109237

Zhao, Y., Li, X., Zhang, C., Zhang, T., Xie, J., Zeng, G., et al. (2018). Investigation of the Rotation Speed on Corrosion Behavior of HP-13Cr Stainless Steel in the Extremely Aggressive Oilfield Environment by Using the Rotating Cage Test. *Corrosion Sci.* 145, 307–319. doi:10.1016/j.corsci.2018.10.011

Zhao, Y., Xie, J., Zeng, G., Zhang, T., Xu, D., and Wang, F. (2019). Pourbaix Diagram for HP-13Cr Stainless Steel in the Aggressive Oilfield Environment Characterized by High Temperature, High CO2 Partial Pressure and High Salinity. *Electrochimica Acta* 293, 116–127. doi:10.1016/j.electacta.2018.08.156

Zhao, Y., Zhang, T., Xiong, H., and Wang, F. (2021b). Bridge for the Thermodynamics and Kinetics of Electrochemical Corrosion: Modeling on Dissolution, Ionization, Diffusion and Deposition in Metal/solution Interface. *Corrosion Sci.* 191, 109763. doi:10.1016/j.corsci.2021.109763

Zhu, J., Xu, L., and Lu, M. (2015a). Electrochemical Impedance Spectroscopy Study of the Corrosion of 3Cr Pipeline Steel in Simulated CO2-saturated Oilfield Formation Waters. *Corrosion* 71, 854–864. doi:10.5006/1494

Zhu, J., Xu, L., Lu, M., Zhang, L., and Chang, W. (2015b). Interaction Effect between Cr(OH)3 Passive Layer Formation and Inhibitor Adsorption on 3Cr Steel Surface. *RSC Adv.* 5, 18518–18522. doi:10.1039/c4ra15519j

Zhu, S. D., Wei, J. F., Bai, Z. Q., Zhou, G. S., Miao, J., and Cai, R. (2011a). Failure Analysis of P110 Tubing String in the Ultra-deep Oil Well. *Eng. Fail. Anal.* 18, 950–962. doi:10.1016/j.engfailanal.2010.11.013

Zhu, S. D., Wei, J. F., Cai, R., Bai, Z. Q., and Zhou, G. S. (2011b). Corrosion Failure Analysis of High Strength Grade Super 13Cr-110 Tubing String. *Eng. Fail. Anal.* 18, 2222–2231. doi:10.1016/j.engfailanal.2011.07.017

Conflict of Interest: Author LH was employed by company State Key Laboratory of Advanced Power Transmission Technology, Global Energy Interconnection Research Institute Co., Ltd.,.

The remaining authors declare that the research was conducted in the absence of any commercial or financial relationships that could be construed as a potential conflict of interest.

Publisher's Note: All claims expressed in this article are solely those of the authors and do not necessarily represent those of their affiliated organizations, or those of the publisher, the editors, and the reviewers. Any product that may be evaluated in this article, or claim that may be made by its manufacturer, is not guaranteed or endorsed by the publisher.

Advantages of publishing in Frontiers

OPEN ACCESS
Articles are free to read for greatest visibility and readership

FAST PUBLICATION
Around 90 days from submission to decision

HIGH QUALITY PEER-REVIEW
Rigorous, collaborative, and constructive peer-review

TRANSPARENT PEER-REVIEW
Editors and reviewers acknowledged by name on published articles

Frontiers
Avenue du Tribunal-Fédéral 34
1005 Lausanne | Switzerland

Visit us: www.frontiersin.org
Contact us: frontiersin.org/about/contact

REPRODUCIBILITY OF RESEARCH
Support open data and methods to enhance research reproducibility

DIGITAL PUBLISHING
Articles designed for optimal readership across devices

FOLLOW US
@frontiersin

IMPACT METRICS
Advanced article metrics track visibility across digital media

EXTENSIVE PROMOTION
Marketing and promotion of impactful research

LOOP RESEARCH NETWORK
Our network increases your article's readership